



HO CHI MINH CITY UNIVERSITY OF TECHNOLOGY
National Key Laboratory of Digital Control
and System Engineering (DCSELab)
Department of Aerospace Engineering

ISIUS INTERNATIONAL SOCIETY OF
INTELLIGENT UNMANNED SYSTEMS



ICIUS 2021

PROCEEDINGS OF THE 17TH INTERNATIONAL CONFERENCE ON INTELLIGENT UNMANNED SYSTEMS

Ho Chi Minh City University of Technology, VNU - HCM
Ho Chi Minh City, Vietnam

August
25th-27th, 2021



VNU-HCM PRESS

***PROCEEDINGS OF THE 17TH INTERNATIONAL
CONFERENCE ON INTELLIGENT UNMANNED SYSTEMS
(ICIUS 2021)***

ORGANIZER



**Ho Chi Minh City University of Technology
National Key Laboratory of Digital Control and
System Engineering (DCSELab)
Department of Aerospace Engineering**



**International Society of Intelligent Unmanned
Systems**

SPONSORS



**Vietnam National University Ho Chi Minh City
(VNU-HCM)**



**Ho Chi Minh City University of Technology
(HCMUT)**



Department of Science and Technology (DOST)



Office of Naval Research Global (ONRG)

CONTENTS

WELCOME FROM CHAIR OF ICIUS-2021	viii
WELCOME ADDRESS OF PRESIDENT, ISIUS	ix
COMMITTEES.....	x
EDITORIAL BOARD	xii
CONFERENCE SCHEDULE.....	xiv
CONFERENCE PROGRAM.....	xvii
KEYNOTE LECTURES	xxv
FULL PAPERS.....	1
ICIUS-2021-1. Numerical Study of Aerodynamic Performance and Flow Characteristics of a Centrifugal Blower	2
<i>Thanh-Long Le*, Tran Trung Nghia, Hong Duc Thong, Mai Hoang Kim Son</i>	
ICIUS-2021-3. Decentralized Cubature Kalman Filter for Spacecraft Constellations Navigation... 11	
<i>Xingyu Zhou, Jie Ren*, Qin Tong and Dong Qiao</i>	
ICIUS-2021-4. An Adaptive Trajectory Tracking Scheme for Car-like Autonomous Vehicles in the Presence of Input Constraints	18
<i>Juqi Hu, Youmin Zhang* and Subhash Rakheja</i>	
ICIUS-2021-5. Connectivity Maintenance Control for Multiple UAVs with Input Saturation	26
<i>Xianghong Xue, Youmin Zhang* and Lingxia Mu</i>	
ICIUS-2021-7. Design and Flight of the KUBeetle Equipped with a Flapping-wing Mechanism Based on a Rack-pinion Mechanism	35
<i>Gi Heon Ha, Hoang Vu Phan, Tan-Hanh Pham and Hoon Cheol Park*</i>	
ICIUS-2021-8. CFD and FSI-based Parametric Study on Tail Fin for High-speed Underwater Locomotion.....	42
<i>Thanh Tien Dao, Khanh Nguyen and Hoon Cheol Park*</i>	
ICIUS-2021-9. Numerical Investigation on Aerodynamic Performance of Airfoil with Different Cambers	50
<i>Min Zhao, Yao Zou and Wei He*</i>	

ICIUS-2021-10. Effects of Wing Kinematics on Aerodynamic Efficiency of an Insect-inspired Flapping-wing Micro Air Vehicle in Hover.....	57
<i>Khanh Nguyen, Loan Thi Kim Au, Hoang-Vu Phan, Tien Thanh Dao, and Hoon Cheol Park*</i>	
ICIUS-2021-11. Design and Test of a Propulsion System for a Robotic Flying Fish	65
<i>Tan Hanh Pham and Hoon Cheol Park*</i>	
ICIUS-2021-13. Aerodynamic and Structural Performances of a Single-stage Transonic Axial Compressor with Blade Fillet Radius	73
<i>Chu Hoang Quan* and Dinh Cong Truong</i>	
ICIUS-2021-14. Study on the Loading Redistribution during Braking Maneuver of a Tanker Semi-trailer – The Effect of the Configuration of the Baffles	85
<i>Thong Duc Hong*, Thien Phuoc Huynh, Hieu Trung Le and Thanh-Long Le</i>	
ICIUS-2021-15. Trajectory Tracking for Caterfillar Vehicles with Uncertain Parameters Using a Model Reference Adaptive Controller	103
<i>Dae Hwan Kim*, Hyun Jong Kim and Tan Tien Nguyen</i>	
ICIUS-2021-16. Motion Control for Two Wheeled Mobile Inverted Pendulums Using a MIMO Robust Servo Controller Systems.....	112
<i>Dae Hwan Kim*, Huy Hung Nguyen and Sang Bong Kim</i>	
ICIUS-2021-17. Design, Analysis and Simulation of V-frame Octocopter.....	121
<i>Tri Bien Minh*, Hien Vo and Luan Hua Thanh</i>	
ICIUS-2021-19. Hybrid Transmission Line Kite Thread Removal Robot	132
<i>Katherine Carlos, Nickita Chen, Fida Hussain, Wenzheng Liu, Sheryl Mourin, Rini Akmeliawati* and Lei Chen</i>	
ICIUS-2021-20. Experimental Study of the Thrust Generation Performance of the Tapered Biomimetic Fin with Cupping Effect	140
<i>Arie Sukma Jaya* and Muljo Widodo Kartidjo</i>	
ICIUS-2021-21. A Numerical Study on the Design of a Cold Heat Storage Device in a Liquefied Air Energy Storage System (LAES).....	148
<i>Hyunjong Kim*, Juyeol Ryu, Kwansu Kim, Jungtae Kim, Dae Hwan Kim and Jongpo Park</i>	
ICIUS-2021-22. Computational Fluid Dynamics Based Propeller Design Improvement for High Altitude Long Endurance (HALE) UAV.....	156
<i>Mochammad Agoes Moelyadi, Fatwa Azam Maulana* and Ema Amalia</i>	
ICIUS-2021-26. Determination of Longitudinal Dynamic Derivatives of High-altitude Long Endurance UAV Using Computational Fluid Dynamics	164

Mochammad Agoes Moelyadi, Rais Fadillah and Ema Amalia*

ICIUS-2021-27. Drone Detection and Localization Using Omnidirectional Cameras173

Kieren Chua, Loh Yu Kang and Sutthiphong Srigrarom*

ICIUS-2021-28. Design and Implementation of a Hardware-in-the-Loop UAV System for Forest Fire Monitoring.....186

*Hossein Jamshidi and Youmin Zhang**

ICIUS-2021-29. Developing CMOS MEMS Flow Sensors on a Flapping Wing Surface.....193

Lung-Jieh Yang, Reshmi Waikhom and Horng-Yuan Shih*

ICIUS-2021-30. Characteristic of Paddle Squeezing Angle and AMBU Bag Air Volume in Bag Valve Mask Ventilator.....202

Cong Toai Truong, Kim Hieu Huynh, Van Tu Duong, Huy Hung Nguyen, Le An Pham and Tan Tien Nguyen*

ICIUS-2021-31. Tracking of High-speed and Aggressively-maneuvered Aerial Targets by Kalman-Kernelized and Kalman-Discriminative Correlation Filters (K-KCF & K-DCF).....213

*Shao Xuan Seah, Niven Junliang Sie and Sutthiphong Srigrarom**

ICIUS-2021-32. Wing Rotation Mechanism to Enhance Flapping Lift.....224

Lung. J. Yang, Vivek. J. Joseph, Saravana Kompala and Neethish. K. Unnam*

ICIUS-2021-33. Development of Communication System for Amphibious Multicopter232

*Yuta Motoki and Masafumi Miwa**

ICIUS-2021-35. Design of Robust Controller Applied for Series Elastic Actuators in Controlling Humanoid's Joint.....238

*Anh Khoa Lanh Luu, Van Tu Duong, Huy Hung Nguyen, Sang Bong Kim and Tan Tien Nguyen**

ICIUS-2021-36. Simulate Deformation and Stress of 3-Axis CNC Milling Machine Body in Outsoles Mold Machining249

*Thanh Luan Bui, Vinh Tuong Vuong, Duc Dat Do and Tan Tien Nguyen**

ICIUS-2021-37. Study on Designing of Coaxial BLDC Applied for Underwater Vehicle259

*Thien Phuc Tran, Cuong Quoc Thai Lam, Ngoc Quan Duong, Huy Hung Nguyen and Tan Tien Nguyen**

ICIUS-2021-38. Effectiveness Evaluation of Vacuum Pressure as Contributing Factor to Lightweight Seasoning Packets Distribution System.....268

*Tuan Huynh Thanh, Nhat Nguyen Le Minh, Van Tu Duong and Tan Tien Nguyen**

ICIUS-2021-39. Active Door Preventing Infectious Air of Hospital Isolation Room	277
<i>Vo Nhut Quang Mo, Duy Anh Nguyen, Tan Huy Nguyen, Phuc Long Duong, Dae Hwan Kim, Le An Pham and Tan Tien Nguyen*</i>	
ICIUS-2021-40. Design of Powered Air Purifying Respirator Used for Healthcare Workers	285
<i>An Thanh Vo Ta, Thanh Long Le*, Ngoc Dang Tran, Le An Pham, Hoang Long Phan and Tan Tien Nguyen</i>	
ICIUS-2021-41. Design and Implementation of Upper Limb Rehabilitation Exoskeleton for Post-stroke Patients.....	294
<i>Binh Vo Dang Phuong, Xuan Thang Nguyen, Van Tu Duong, Huy Hung Nguyen and Tan Tien Nguyen*</i>	
ICIUS-2021-42. Optimal Oil Lubrication for Ball Slide-guide of CNC Milling Machine Using Taguchi Method.....	302
<i>Huy Hung Nguyen, Quoc Dat Le, Hoang Long Phan, Van Tu Duong and Tan Tien Nguyen*</i>	
ICIUS-2021-43. An Optimal Method for Distributing Tolerance of Milling Spindle's Components.	310
<i>Xuan Quang Ngo, Van Tu Duong, Thanh Luan Bui, Huy Hung Nguyen and Tan Tien Nguyen*</i>	
ICIUS-2021-44. Design of Three Axes of CNC Milling Machine Using Lucas Design for Assembly.	319
<i>Viet Toan Vu, Van Tu Duong*, Thanh Luan Bui, Huy Hung Nguyen and Tan Tien Nguyen</i>	
ICIUS-2021-45. One-leg Stance of Humanoid Robot Using Active Balance Control	333
<i>Tri Duc Tran, Anh Khoa Lanh Luu, Van Tu Duong, Huy Hung Nguyen and Tan Tien Nguyen*</i>	
ICIUS-2021-48. Design and Evaluate the Hardware Framework in Mechanical Ventilator	348
<i>Anh Son Tran, Ngoc Anh Thu Vuong and Ha Quang Thinh Ngo*</i>	
ICIUS-2021-49. Towards Motion Capture Using a Swarms of Drones.....	357
<i>John Page*, Faqihza Mukhlis and Michael Bain</i>	
ICIUS-2021-50. Experimental Modelling of Flapping-wing Micro Air Vehicle	363
<i>Steven Aurecianus, Gi Heon Ha, Hoang Vu Phan, Hoon Cheol Park and Taesam Kang*</i>	
ICIUS-2021-51. Multi-terrain Hexapod Robot for Search and Rescue Mission	369
<i>R. Akmeiliawati*, D. Harvey, N. Mudisi, S. Lakshmanan, I. Iro and M. Ijala</i>	
ICIUS-2021-52. Laser-equipped Drone for Weed Management	377
<i>R. Akmeiliawati*, N. Sergiienko, L. Verbi, L. Hunter, A. Scarfo, C. Alt and B. Pedler</i>	
ICIUS-2021-53. A Smart Assistant Tool for Ship Machinery Arrangement Using Genetic Algorithm.....	385

*Trinh Duc Minh, Nguyen Duy Anh and Tat-Hien Le**

ICIUS-2021-54. LULC Classification with Modified HarDNet-MSEG on Sentinel-2 Satellite Images.....392

Laphonchai Jirachuphun, Pudit Tempattarachoke, Panin Pienroj, Photchara Ratsamee and Nattee Niparnan*

ICIUS-2021-55. A Comparison of Kalman Filters for Unmanned Aerial Vehicles Attitude Estimation Using Real Flight Test Data404

Dung Van Vu, Thanh Truong Nguyen, Dong Thanh Nguyen and Thap Khac Nguyen*

ICIUS-2021-56. Long Range Delivery Experiment Using a VTOL Type UAV - A Case Study of the Medical Supply Delivery Between Remote Islands412

Kazuo Watanabe, Masafumi Miwa and Shinya Takatsuka*

ICIUS-2021-58. Using Telematics to Improve EMTs' Response Times After Traffic Accidents Saving up to 2000 Lives per Year.....419

*Mark Haley**

ICIUS-2021-59. Demonstration of a Visible Light Communication System Using LED and Low-cost Low-quality Camera.....426

*Nguyen Hoang Nam**

ICIUS-2021-60. Low-cost 2D LIDAR System on Autonomous Robot for 3D Scanning and Modeling Unknown Areas.....434

*Hoang-Nam Nguyen**

ICIUS-2021-61. A Novel Approach in Simulation of Flow over Sphere from Low to High Reynolds Numbers.....442

Anh Huy Huynh, Buu Hung Tran, Thi Hong Hieu Le, Ngoc Hien Nguyen and Quang Le Dang*

ICIUS-2021-62. Path Planning Technology of Unmanned Vehicle Based on Improved Deep Reinforcement Learning451

*Luhe Wang, Jinwen Hu, Zhao Xu and Lei Lu**

ICIUS-2021-66. Obstacle Avoidance System on an Omni X Drone Based on Neural Network, Computer Vision and Mavlink Protocol.....462

Tran Quang Khoi, Ngo Khanh Hieu, Le Dinh Anh Huy and Truong Lu Tien*

ICIUS-2021-67. Implementing Lean and Sweep Method for Optimization of Gas Turbine Blade by Computational Fluid Dynamics.....472

*Zung Pham Ngoc, Anh Nguyen Tuan, Vu Hoang Nhu and Nhu Van Nguyen**

ICIUS-2021-68. Combustion Analysis for Small Gas Turbine Engine by Using Computational Fluid Dynamics (CFD)480

Quoc-Huy Nghiem, Cong-Anh Pham, Quang-Hai Nguyen and Nhu-Van Nguyen*

ICIUS-2021-69. The Comparison Results of Numerical Simulation with Experimental Data for Axial Turbine of Small Turbojet Engine487

Hung Vu Xuan, Anh Pham Tuan, Lanh Chu Duy, Nhu Van Nguyen*

ICIUS-2021-70. The Control Methodology for Jet Engine of Unknown Characteristics493

Huy Hoang Nguyen, Van Son Bui, Thanh Nam Trinh, Nhu Van Nguyen and Quang Hai Nguyen*

ICIUS-2021-71. Reverse Engineering and Aerodynamic Analysis of a High-speed UAV Inverted V-tail Using XFRL5501

Do Hoang Huy, Ngo Khanh Hieu*

ICIUS-2021-72. Numerical Study of the Laminar Separation Bubble during Drag Crisis over the Teardrop Model512

Thi Hong Hieu Le, Dinh-An Nguyen and Ngoc Hien Nguyen*



WELCOME MESSAGE

Nguyen Tan Tien, Assoc. Professor, Director of National Key Laboratory of Digital Control and System Engineering (DCSELab) - Ho Chi Minh City University of Technology, Vietnam

General Chair of the International Conference on Intelligent Unmanned Systems, August 25th -27th, Ho Chi Minh City, Vietnam

On behalf of the ICIUS2021 organizing committee, I am honored and delighted to welcome you to the 17th International Conference on Intelligent Unmanned Systems (ICIUS2021), to be held from August 25th-27th, 2021 at Ho Chi Minh City University of Technology, Ho Chi Minh City, Vietnam. I believe we have chosen a venue that guarantees a successful technical conference amid the culture and scenery of Vietnam.

Vibrating with energy, innovation and traffic – lots of traffic – Ho Chi Minh City, formerly known as Saigon, the Pearl of the Far East, has a prominent history going back more than three hundred years. It is the economic heart of Vietnam and the main hub of the southern region. A freewheeling, cosmopolitan metropolis, HCMC's dynamic cityscape draws together the old and new Vietnam in the most compact of spaces, representing the city's past as well as its future. It is, therefore, my hope that many would participate in this conference to actively debate on the future of the intelligent unmanned systems.

Herein, I believe that ICIUS2021 will serve as an excellent venue for such discussions. We will do our utmost efforts to make this event successful. We do hope that the successful results of the conference will significantly contribute the improvement, the application and the real effect of our researches on Unmanned Systems, Mechatronics, Robotics and Biomimetic, Intelligent Systems, Space Robots, Control and Computation to develop our community. We cordially invite you to take part in this exciting opportunity for the intelligent unmanned systems.

Best wishes to all of you and your family!

Thank you.



ISIUS

WELCOME ADDRESS

Youmin Zhang, Professor, Concordia University, Canada
President of the International Society on Intelligent Unmanned Systems

Dear Participants and Attendees:

On behalf of the International Society of Intelligent Unmanned Systems (ISIUS) and as the President of ISIUS, it is my great privilege, pleasure and honor to welcome you to The 17th International Conference on Intelligent Unmanned System (ICIUS 2021) being held at Ho Chi Minh City, Vietnam during 25-27th August 2021 in both on-site and online manner under the challenging COVID-19 pandemic condition.

I am writing this welcome message while the COVID-19 pandemic is still spreading all over the world since the beginning of 2020. For this, I would like to specially thank all of you for your strong support and participation to this special ICIUS 2021 event under such a difficult time. I would like to thank the ICIUS 2021 Organizing Committee for their hard work in preparing this event. I would also like to thank the ISIUS former Presidents, three Vice-Presidents, all Technical Committee Members for their strong support either in organization to the ICIUS 2021 or papers submission, or both! Last but not least, I am thankful for the contributions of the General Chairs, Prof. Thi-Hong-Hieu Le and Tan-Tien Nguyen and the Conference Organizing Team towards this successful ICIUS 2021 event under the challenging pandemic condition!

As you know, ICIUS 2021 will be our 17th ICIUS conference up to now. Here, I would like to share you a short history of ICIUS. The conference has been successful for many years in Seoul, Korea (2005, 2006), Bali, Indonesia (2007, 2010, 2015), Nanjing, China (2008), Jeju, Korea (2009, 2018), Chiba, Japan (2011), Singapore (2012), Jaipur, India (2013), Montreal, Canada (2014), Xi'an, China (2016), Tamsui, Taiwan (2017), and Beijing, China (2019). Since its start in 2005, ICIUS has become a well-established annual conference which addresses the rapidly developing field of unmanned systems (including Unmanned Aerial Vehicles (UAVs), Unmanned Ground Vehicles (UGVs), Unmanned Surface Vehicles (USVs), and Unmanned Underwater Vehicles (UUVs), etc.), robotics, automation, intelligent systems, and biomimetics while providing participants and attendees insight into the paths ahead for fundamental research, system development and technology deployment around the world. Let us all hope that ICIUS will grow further in the future, especially once the COVID-19 pandemic is over. I wish that ICIUS can attract more researchers to be a representative international conference on unmanned systems and intelligent systems worldwide. Therefore, for future success of ICIUS, I would like to ask for and thank you for your continuous support!

We wish you a satisfying and pleasant attendance in ICIUS 2021. Once again, I am most grateful for your participation and support, no matter on-site or online. I wish we can meet physically in the near future!

Finally, I would like to thank everyone who are involved in preparing ICIUS 2021 for their hard work and bravery! Thank you very much!

COMMITTEES

Steering Committees

- **Youmin Zhang**, Concordia University, Canada
- **Agus Budiyo**, Institute of Technology Bandung, Indonesia
- **Lung-Jieh Yang**, Tamkang University, Taiwan
- **Masafumi Miwa**, Tokushima University, Japan
- **Sutthiphong Srigrarom**, National University of Singapore, Singapore
- **Thien-Phuc Tran**, Ho Chi Minh City University of Technology, Vietnam
- **Wei He**, University of Science & Technology, Beijing, China

International Advisory Committees

- **Bruce W. Jo**, State University of New York at Stony Brook, USA
- **Dae-Hwan Kim**, State University of New York at Stony Brook, USA
- **Debopam Das**, IIT Kanpur, India
- **Hyun-Jong Kim**, Institute for Advanced Engineering, Korea
- **Quang Ha**, University Technology of Sydney, Australia
- **Rini Akmeliawati**, University of Adelaide Australia
- **Taesam Kang**, Konkuk University, Korea

Honorary Chairs

- **Muljowidodo**, Institute of Technology Bandung, Indonesia
- **Kenzo Nonami**, Chiba University, Japan
- **Kwang-Joon Yoon**, Konkuk University, Korea
- **Hoon Cheol Park**, Konkuk University, Korea
- **Sang-Bong Kim**, Pukyong National University, Korea

General Chairs

- **Tan Tien Nguyen**, Ho Chi Minh City University of Technology, Vietnam
- **Thi-Hong-Hieu Le**, Ho Chi Minh City University of Technology, Vietnam

General Secretary

- **Thanh-Long Le**, Ho Chi Minh City University of Technology, Vietnam
- **Thi Hoang Yen Nguyen**, Ho Chi Minh City University of Technology, Vietnam

Program Chairs

- **Hoang-Vu Phan**, Konkuk University, Korea
- **Huy-Hung Nguyen**, Saigon University, Vietnam
- **Khanh-Hieu Ngo**, Ho Chi Minh City University of Technology, Vietnam
- **Le-Quang Dang**, Ho Chi Minh City University of Technology, Vietnam
- **Ngoc-Hien Nguyen**, RMIT University, Australia
- **Quoc-Chi Nguyen**, Ho Chi Minh City University of Technology, Vietnam
- **Tat Hien Le**, Ho Chi Minh City University of Technology, Vietnam
- **Thanh-Long Le**, Ho Chi Minh City University of Technology, Vietnam
- **Thanh-Luan Bui**, Ho Chi Minh City University of Technology, Vietnam
- **Trong-Hieu Bui**, Ho Chi Minh City University of Technology, Vietnam
- **Van-Tu Duong**, Ho Chi Minh City University of Technology, Vietnam
- **Van-Sy Le**, Petro Vietnam University, Vietnam
- **Le-An Pham**, Ho Chi Minh City University of Medicine and Pharmacy, Vietnam

EDITORIAL BOARD

Tran Thanh Tinh, Ho Chi Minh City University of Technology, Vietnam
Ngo Dinh Tri, University of Centra Florida, USA
Daehwan Kim, State University of New York at Stony Brook, Korea
Taesam Kang, Konkuk University, South Korea
Nguyen Thien Tong, Ho Chi Minh City University of Technology, Vietnam
Le Tuan Phuong Nam, University of Thu Dau Mot, Vietnam
Au Thi Kim Loan, Sejong University, South Korea
Nguyen Ngoc Hien, RMIT, Australia
Tat-Hien Le, Ho Chi Minh City University of Technology, Vietnam
Hyunjong Kim, Institute for Advance Engineering, Republic of Korea
Rini Akmeliawati, The University of Adelaide, Australia
Duong Van Tu, Ho Chi Minh City University of Technology, Vietnam
Phan Hoang Vu, EPFL, Switzerland
Thanh-Long Le, Ho Chi Minh City University of Technology, Vietnam
Le Quang Dang, Ho Chi Minh City University of Technology, Vietnam
Nguyen Khanh, Konkuk University, South Korea
Nguyen Hoang Nam, Hanoi University of Science and Technology, Vietnam
Nguyen Quoc Chi, Ho Chi Minh City University of Technology, Vietnam
Tran-Phu Nguyen, Ho Chi Minh City University of Technology and Education, Vietnam
Wei He, University of Science and Technology Beijing, China
Nguyen Song Thanh Thao, Ho Chi Minh City University of Technology, Vietnam
Masafumi Miwa, Tokushima University, Japan
Nguyen Huu Tho, Nguyen Tat Thanh University, Vietnam
Bui Trong Hieu, Ho Chi Minh City University of Technology, Vietnam
Pham Huy Hoang, Ho Chi Minh City University of Technology, Vietnam
Quang Ha, University of Technology Sydney, Australia

Vo Bich Hien, Vietnamese German University, Vietnam

Comandur Venkatesan, IIT Jodhpur, India

Lung-Jieh Yang, Tamkang University, Taiwan

Hoon Cheol Park, Konkuk University, South Korea

Kenzo Nonami, Chiba University, Japan

Le Trung Chon, Ho Chi Minh City University of Technology, Vietnam

Nguyen Le Dung, Ho Chi Minh City University of Technology, Vietnam

Ngo Ha Quang Thinh, Ho Chi Minh City University of Technology, Vietnam

Sutthiphong Srigrarom, National University of Singapore, Singapore

Agus Budiyo, Indonesia Center for Technology Empowerment, Indonesia

Huynh Phuoc Thien, Cao Thang Technical College, Vietnam

Tran Trong Hy, Ho Chi Minh City University of Technology, Vietnam

Huynh Phu Minh Cuong, Ho Chi Minh City University of Technology, Vietnam

CONFERENCE SCHEDULE

Day 1- August 25th (Wednesday)	
2:00 - 4:00 PM (UTC/GMT +7:00)	Online Registration, Help Desk Networking

Day 2- August 26th (Thursday), Ho Chi Minh City University of Technology			
08:30 AM (UTC/GMT +7:00)	Networking		
9:00 - 09:20 AM (UTC/GMT +7:00)	Opening Ceremony Welcome Address: General Chair of ICIUS 2021, Prof. Nguyen Tan Tien, Director of National Key Laboratory of Digital Control and System Engineering (DCSELab) - Ho Chi Minh City University of Technology, Vietnam Introduction Address: President of ISIUS, Prof. Youmin Zhang, Concordia University, Canada		
9:20-9:50 AM (UTC/GMT +7:00)	Plenary Speech #1	Speaker: Prof. Kenzo Nonami, Chiba University, Japan Chair: Prof. Kwang-Joon Yoon Co-Chair: Dr. Nhu-Van Nguyen	
9:50-10:20 AM (UTC/GMT +7:00)	Plenary Speech #2	Speaker: Dr. Phan Hoang Vu, Laboratory of Intelligent Systems, Switzerland Chair: Prof. Nguyen Thien Tong Co-Chair: Prof. Lung-Jieh Yang	
10:20-10:45 AM (UTC/GMT +7:00)	Group Photo and Break		
Parallel Session #1			
10:45-12:10 AM (UTC/GMT +7:00)	(1A) Unmanned Systems Chair: Taesam Kang Co-chair: Tat-Hien Le #ICIUS-2021-4 #ICIUS-2021-5 #ICIUS-2021-8 #ICIUS-2021-11	(1B) Mechatronics, Robotics and Biomimetic Chair: Nguyen Quoc Chi Co-chair: Nguyen Ngoc Hien #ICIUS-2021-7 #ICIUS-2021-10 #ICIUS-2021-16 #ICIUS-2021-29	(1C) Intelligent Systems Chair: Agus Budiyo Co-chair: Rini Akmeliawati #ICIUS-2021-15 #ICIUS-2021-19 #ICIUS-2021-27 #ICIUS-2021-33

The 17th International Conference on Intelligent Unmanned Systems (ICIUS2021)
August 25th – 27th, 2021, Ho Chi Minh City University of Technology, VNU-HCM, Vietnam

12:10-1:30 PM (UTC/GMT +7:00)	Lunch		
	Parallel Session #2		
1:30-3:00 PM (UTC/GMT +7:00)	(2A) Unmanned Systems Chair: Masafumi Miwa Co-Chair: Ngo Dinh Tri #ICIUS-2021-20 #ICIUS-2021-28 #ICIUS-2021-31 #ICIUS-2021-37	(2B) Mechatronics, Robotics and Biomimetic Chair: Dae Hwan Kim Co-Chair: Phan Hoang Vu #ICIUS-2021-30 #ICIUS-2021-32 #ICIUS-2021-35 #ICIUS-2021-38	(2C) Intelligent Systems Chair: Lung-Jieh Yang Co-Chair: Duong Van Tu #ICIUS-2021-39 #ICIUS-2021-41 #ICIUS-2021-48 #ICIUS-2021-59
3:00-3:15 PM	Break		
	Parallel Session #3		
3:15-4:45 PM (UTC/GMT +7:00)	(3A) Unmanned Systems Chair: Hoon Cheol Park Co-Chair: Wei He #ICIUS-2021-49 #ICIUS-2021-50 #ICIUS-2021-51 #ICIUS-2021-62	(3B) Mechatronics, Robotics and Biomimetic Chair: Pham Huy Hoang Co-Chair: Hyun-Jong Kim #ICIUS-2021-40 #ICIUS-2021-42 #ICIUS-2021-43 #ICIUS-2021-44	(3C) Intelligent Systems Chair: Kenzo Nonami Co-Chair: Sutthiphong Srigrarom #ICIUS-2021-45 #ICIUS-2021-52 #ICIUS-2021-60 #ICIUS-2021-66

Day 3- August 27th (Friday), Ho Chi Minh City University of Technology

9:00-9:30 AM (UTC/GMT +7:00)	Plenary Speech #3	Speaker: Assoc. Prof Bruce Jo, Korea Chair: Prof. Nguyen Tan Tien Co-Chair: Dr. Nguyen Quoc Viet	
9:30-10:00 AM (UTC/GMT +7:00)	Plenary Speech #4	Speaker: Prof. Bin Jiang, Nanjing University of Aeronautics and Astronautics, P. R. China Chair: Prof. Youmin Zhang Co-Chair: Prof. Rini Akmeliawati	
10:00 -10:15 AM	Break		
	Parallel Session #4		
10:15- 11: 45 AM (UTC/GMT +7:00)	(4A) Unmanned Systems Chair: Sutthiphong Srigrarom Co-Chair: Quang Ha	(4D) Space Robots Chair: Vo Bich Hien Co-Chair: Ngo Dinh Tri #ICIUS-2021-3	(4E) Control and Computation Chair: Mochammad Agoes Moelyadi Co-chair: Tran Thanh Tinh

The 17th International Conference on Intelligent Unmanned Systems (ICIUS2021)
August 25th – 27th, 2021, Ho Chi Minh City University of Technology, VNU-HCM, Vietnam

	#ICIUS-2021-53 #ICIUS-2021-56 #ICIUS-2021-58 #ICIUS-2021-71	#ICIUS-2021-17 #ICIUS-2021-26 #ICIUS-2021-54	#ICIUS-2021-1 #ICIUS-2021-9 #ICIUS-2021-13 #ICIUS-2021-68
11:45 AM - 1:30 PM	Lunch		
	Parallel Session #5		
1:30-2:50 PM (UTC/GMT +7:00)	(5E-1) Control and Computation Chair: Nguyen Ngoc Hien Co-chair: Dang Le Quang #ICIUS-2021-21 #ICIUS-2021-36 #ICIUS-2021-61 #ICIUS-2021-67	(5E-2) Control and Computation Chair: Le Thanh Long Co-chair: Au Thi Kim Loan #ICIUS-2021-14 #ICIUS-2021-22 #ICIUS-2021-69 #ICIUS-2021-72	(5D) Space Robots Chair: Vo Bich Hien Co-Chair: Ngo Dinh Tri #ICIUS-2021-55 #ICIUS-2021-70
2:50 – 3:00 PM	Break - Networking		
	Parallel Session #6		
3:00 - 4:15 PM (UTC/GMT +7:00)	(6F) Industrial Session		(6G) Steering Committee Meeting
4:30 PM (UTC/GMT +7:00)	Closing Remarks and Paper Award		

CONFERENCE PROGRAM

Program is scheduled on Vietnam local time (UTC/GMT +7:00)

Date	Activities	Remarks
August 25th, 2021	Welcome	Venue: Ho Chi Minh City University of Technology Building C6, Lobby
2:00 - 4:00 PM		On-line Registration, Help Desk Networking

Date	Activities	Remarks
August 26th, 2021	Conference day #1	Venue: Ho Chi Minh City University of Technology Conference Hall B4
08:30 AM	Networking	
9:00-09:20 AM	Opening Ceremony	Welcome Address: General Chair of ICIUS 2021, Prof. Nguyen Tan Tien, Director of National Key Laboratory of Digital Control and System Engineering (DCSELab) - Ho Chi Minh City University of Technology, Vietnam Introduction Address: President of ISIUS, Prof. Youmin Zhang, Concordia University, Canada
9:20-9:50 AM	Plenary Speech #1	Title: LONGITUDINAL FLIGHT ACROSS TOKYO BAY BY DRONE AND FUTURE PROSPECTS Speaker: Prof. Kenzo Nonami Department of Mechanical Engineering, Chiba University, Japan Autonomous Control Systems Laboratory, Ltd. (ACSL) Chairman: Prof. Kwang-Joon Yoon Co-Chair: Dr. Nhu-Van Nguyen
9:50-10:20 AM	Plenary Speech #2	Title: COLLISION RECOVERY OF A BEETLE-INSPIRED FLAPPING-WING ROBOT Speaker: Dr. Hoang-Vu Phan Laboratory of Intelligent Systems, École Polytechnique Fédérale de Lausanne, Lausanne, Switzerland Chair: Prof. Nguyen Thien Tong Co-Chair: Prof. Lung-Jieh Yang
10:20-10:45		Group Photo and Break

Date	Activities			
10:50-12:10 AM	Parallel Session #1	<p>(1A) Unmanned Systems Chair: Taesam Kang Co-chair: Tat-Hien Le #ICIUS-2021-4 An Adaptive Trajectory Tracking Scheme for Car-like Autonomous Vehicles in the Presence of Input Constraints <i>Juqi Hu, Youmin Zhang* and Subhash Rakheja</i> #ICIUS-2021-5 Connectivity Maintenance Control for Multiple UAVs with Input Saturation <i>Xianghong Xue, Youmin Zhang* and Lingxia Mu</i> #ICIUS-2021-8 CFD and FSI-based Parametric Study on Tail Fin for High-speed Underwater Locomotion <i>Thanh Tien Dao, Khanh Nguyen and Hoon Cheol Park*</i> #ICIUS-2021-11 Design and Test of a Propulsion System for a Robotic Flying Fish <i>Tan-Hanh Pham, Hoon Cheol Park*</i></p>	<p>(1B) Mechatronics, Robotics and Biomimetic Chair: Nguyen Quoc Chi Co-chair: Nguyen Ngoc Hien #ICIUS-2021-7 Design and Flight of the KUBeetle Equipped with a Flapping-wing Mechanism Based on a Rack-pinion Mechanism <i>Gi Heon Ha, Hoang Vu Phan, Tan-Hanh Pham and Hoon Cheol Park*</i> #ICIUS-2021-10 Effects of Wing Kinematics on Aerodynamic Efficiency of an Insect-inspired Flapping-wing Micro Air Vehicle in Hover <i>Khanh Nguyen, Loan Thi Kim Au, Hoang-Vu Phan, Tien Thanh Dao and Hoon Cheol Park*</i> #ICIUS-2021-16 Motion Control for Two Wheeled Mobile Inverted Pendulums Using a MIMO Robust Servo Controller Systems <i>Dae Hwan Kim*, Huy Hung Nguyen and Sang Bong Kim</i> #ICIUS-2021-29 Developing CMOS MEMS Flow Sensors on a Flapping Wing Surface <i>Lung-Jieh Yang*, Reshmi Waikhom and Horng-Yuan Shih</i></p>	<p>(1C) Intelligent Systems Chair: Agus Budiyo Co-chair: Rini Akmeliawati #ICIUS-2021-15 Trajectory Tracking for Caterpillar Vehicles with Uncertain Parameters Using a Model Reference Adaptive Controller <i>Dae Hwan Kim*, Hyun Jong Kim and Tan Tien Nguyen</i> #ICIUS-2021-19 Hybrid Transmission Line Kite Thread Removal Robot <i>Katherine Carlos, Nickita Chen, Fida Hussain, Wenzheng Liu, Sheryl Mourin, Rini Akmeliawati* and Lei Chen</i> #ICIUS-2021-27 Drone Detection and Localization Using Omnidirectional Cameras <i>Kieren Chua, Loh Yu Kang* and Sutthiphong Srigrarom</i> #ICIUS-2021-33 Development of Communication System for Amphibious Multicopter <i>Yuta Motoki and Masafumi Miwa*</i></p>
12:10-1:30 PM	Lunch			

Date	Activities			
1:30-3:00 PM	Parallel Session #2	<p>(2A) Unmanned Systems Chair: Masafumi Miwa Co-Chair: Ngo Dinh Tri #ICIUS-2021-20 Experimental Study of the Thrust Generation Performance of the Tapered Biomimetic Fin with Cupping Effect <i>Arie Sukma Jaya* and Muljo Widodo Kartidjo</i> #ICIUS-2021-28 Design and Implementation of a Hardware-in-the-Loop UAV System for Forest Fire Monitoring <i>Hossein Jamshidi, Youmin Zhang*</i> #ICIUS-2021-31 Tracking of High-speed and Aggressively-maneuvered Aerial Targets by Kalman-Kernelized and Kalman-Discriminative Correlation Filters (K-KCF & K-DCF) <i>Shao Xuan Seah, Niven Junliang Sie and Sutthiphong Srigrarom*</i> #ICIUS-2021-37 Study on Designing of Coaxial BLDC Applied for Underwater Vehicle <i>Thien Phuc Tran, Cuong Quoc Thai Lam, Ngoc Quan Duong, Huy Hung Nguyen and Tan Tien Nguyen*</i></p>	<p>(2B) Mechatronics, Robotics and Biomimetic Chair: Dae Hwan Kim Co-Chair: Phan Hoang Vu #ICIUS-2021-30 Characteristic of Paddle Squeezing Angle and AMBU Bag Air Volume in Bag Valve Mask Ventilator <i>Cong Toai Truong, Kim Hieu Huynh, Van Tu Duong*, Huy Hung Nguyen, Le An Pham and Tan Tien Nguyen</i> #ICIUS-2021-32 Wing Rotation Mechanism to Enhance Flapping Lift..... <i>Lung. J. Yang, Vivek. J. Joseph*, Saravana Kompala and Neethish. K. Unnam</i> #ICIUS-2021-35 Design of Robust Controller Applied for Series Elastic Actuators in Controlling Humanoid's Joint <i>Anh Khoa Lanh Luu, Van Tu Duong, Huy Hung Nguyen, Sang Bong Kim and Tan Tien Nguyen*</i> #ICIUS-2021-38 Effectiveness Evaluation of Vacuum Pressure as Contributing Factor to Lightweight Seasoning Packets Distribution System <i>Tuan Huynh Thanh, Nhat Nguyen Le Minh, Van Tu Duong, and Tan Tien Nguyen*</i></p>	<p>(2C) Intelligent Systems Chair: Lung-Jieh Yang Co-Chair: Duong Van Tu #ICIUS-2021-39 Active Door Preventing Infectious Air of Hospital Isolation Room <i>Vo Nhut Quang Mo, Duy Anh Nguyen, Tan Huy Nguyen, Phuc Long Duong, Dae Hwan Kim, Le An Pham and Tan Tien Nguyen*</i> #ICIUS-2021-41 Design and Implementation of Upper Limb Rehabilitation Exoskeleton for Post-stroke Patients <i>Binh Vo Dang Phuong, Xuan Thang Nguyen, Van Tu Duong, Huy Hung Nguyen and Tan Tien Nguyen*</i> #ICIUS-2021-48 Design and Evaluate the Hardware Framework in Mechanical Ventilator <i>Anh Son Tran, Ngoc Anh Thu Vuong and Ha Quang Thinh Ngo*</i> #ICIUS-2021-59 Demonstration of a Visible Light Communication System Using LED and Low-cost Low-quality Camera <i>Nguyen Hoang Nam*</i></p>

Date	Activities			
3:00 - 3:15 PM	Break			
3:15 - 4:45 PM	Parallel Session #3	<p>(3A) Unmanned Systems Chair: Hoon Cheol Park Co-Chair: Wei-He #ICIUS-2021-49 Towards Motion Capture Using a Swarms of Drones <i>John Page*, Faqihza Mukhlis and Michael Bain</i> #ICIUS-2021-50 Experimental Modelling of Flapping-wing Micro Air Vehicle <i>Steven Aurecianus, Gi Heon Ha, Hoang Vu Phan, Hoon Cheol Park and Taesam Kang*</i> #ICIUS-2021-51 Multi-terrain Hexapod Robot for Search and Rescue Mission <i>R. Akmeliawati*, D. Harvey, N. Mudisi, S. Lakshmanan, I. Iro and M. Ijala</i> #ICIUS-2021-62 Path Planning Technology of Unmanned Vehicle Based on Improved Deep Reinforcement Learning <i>Luhe Wang, Jinwen Hu, Zhao Xu and Lei Lu*</i></p>	<p>(3B) Mechatronics, Robotics and Biomimetic Chair: Pham Huy Hoang Co-Chair: Hyun-Jong Kim #ICIUS-2021-40 Design of Powered Air Purifying Respirator Used for Healthcare Workers <i>An Thanh Vo Ta, Thanh Long Le*, Ngoc Dang Tran, Le An Pham, Hoang Long Phan and Tan Tien Nguyen</i> #ICIUS-2021-42 Optimal Oil Lubrication for Ball Slide-guide of CNC Milling Machine Using Taguchi Method <i>Huy Hung Nguyen, Quoc Dat Le, Hoang Long Phan, Van Tu Duong and Tan Tien Nguyen*</i> #ICIUS-2021-43 An Optimal Method for Distributing Tolerance of Milling Spindle's Components <i>Xuan Quang Ngo, Van Tu Duong, Thanh Luan Bui, Huy Hung Nguyen and Tan Tien Nguyen*</i> #ICIUS-2021-44 Design of Three Axes of CNC Milling Machine Using Lucas Design for Assembly <i>Viet Toan Vu, Van Tu Duong*, Thanh Luan Bui, Huy Hung Nguyen and Tan Tien Nguyen</i></p>	<p>(3C) Intelligent Systems Chair: Kenzo Nonami Co-Chair: Sutthiphong Srigrarom #ICIUS-2021-45 One-leg Stance of Humanoid Robot Using Active Balance Control <i>Tri Duc Tran, Anh Khoa Lanh Luu, Van Tu Duong, Huy Hung Nguyen and Tan Tien Nguyen*</i> #ICIUS-2021-52 Laser-equipped Drone for Weed Management <i>R. Akmeliawati*, N. Sergiienko, L. Verbi, L. Hunter, A. Scarfo, C. Alt and B. Pedler</i> #ICIUS-2021-60 Low-cost 2D LIDAR System on Autonomous Robot for 3D Scanning and Modeling Unknown Areas <i>Hoang-Nam Nguyen*</i> #ICIUS-2021-66 Obstacle Avoidance System on an Omni X Drone Based on Neural Network, Computer Vision and Mavlink Protocol <i>Tran Quang Khoi, Ngo Khanh Hieu*, Le Dinh Anh Huy, Truong Lu Tien</i></p>

The 17th International Conference on Intelligent Unmanned Systems (ICIUS2021)
August 25th – 27th, 2021, Ho Chi Minh City University of Technology, VNU-HCM, Vietnam

Date	Activities	
August 27th, 2021	Conference day #2	Venue: Ho Chi Minh City University of Technology Conference Hall B4
9:00 – 9:30 AM	Plenary Speech #3	<p>Title: DESIGN AND IMPLEMENTATION OF CAMBER MORPHING WINGS AND THEIR MECHANISMS</p> <p>Speaker: Associate Professor, Bruce W. Jo, Ph.D Department of Mechanical Engineering at State University of New York (SUNY), USA & Korea</p> <p>Chair: Prof. Nguyen Tan Tien Co-Chair: Dr. Nguyen Quoc Viet</p>
9:30 – 10:00 AM	Plenary Speech #4	<p>Title: ADAPTIVE DIAGNOSIS AND RECONFIGURATION CONTROL WITH FLIGHT CONTROL APPLICATIONS</p> <p>Speaker: Professor Bin Jiang College of Automation Engineering, Nanjing University of Aeronautics and Astronautics, P.R. China</p> <p>Chair: Prof. Youmin-Zhang Co-Chair: Prof. Rini Akmeliawati</p>
10:00 – 10:15 AM	Break	Networking

The 17th International Conference on Intelligent Unmanned Systems (ICIUS2021)
August 25th – 27th, 2021, Ho Chi Minh City University of Technology, VNU-HCM, Vietnam

Date	Activities			
10:15 - 11:45 AM	Parallel Session #4	<p>(4A) Unmanned Systems Chair: Sutthiphong Srigrarom Co-Chair: Quang Ha #ICIUS-2021-53 A Smart Assistant Tool for Ship Machinery Arrangement Using Genetic Algorithm <i>Trinh Duc Minh, Nguyen Duy Anh and Tat-Hien Le*</i> #ICIUS-2021-56 Long Range Delivery Experiment Using a VTOL Type UAV - A Case Study of the Medical Supply Delivery Between Remote Islands <i>Kazuo Watanabe*, Masafumi Miwa and Shinya Takatsuka</i> #ICIUS-2021-58 Using Telematics to Improve EMTs' Response Times After Traffic Accidents Saving up to 2000 Lives per Year <i>Mark Haley*</i> #ICIUS-2021-71 Reverse Engineering and Aerodynamic Analysis of a High-speed UAV Inverted V-tail Using XFRL5 <i>Do Hoang Huy*, Ngo Khanh Hieu</i></p>	<p>(4D) Space Robots Chair: Vo Bich Hien Co-Chair: Ngo Dinh Tri #ICIUS-2021-3 Decentralized Cubature Kalman Filter for Spacecraft Constellations Navigation <i>Xingyu Zhou, Jie Ren*, Qin Tong and Dong Qiao</i> #ICIUS-2021-17 Design, Analysis and Simulation of V-frame Octocopter <i>Tri Bien Minh*, Hien Vo and Luan Hua Thanh</i> #ICIUS-2021-26 Determination of Longitudinal Dynamic Derivatives of High-altitude Long Endurance UAV Using Computational Fluid Dynamics <i>Mochammad Agoes Moelyadi, Rais Fadillah* and Ema Amalia</i> #ICIUS-2021-54 LULC Classification with Modified HarDNet-MSEG on Sentinel-2 Satellite Images <i>Laphonchai Jirachuphun*, Pudit Tempattarachoke, Panin Pienroj, Photchara Ratsamee and Nattee Niparnan</i></p>	<p>(4E) Control and Computation Chair: Mochammad Agoes Moelyadi Co-chair: Tran Thanh Tinh #ICIUS-2021-1 Numerical Study of Aerodynamic Performance and Flow Characteristics of a Centrifugal Blower <i>Thanh-Long Le*, Tran Trung Nghia, Hong Duc Thong, Mai Hoang Kim Son</i> #ICIUS-2021-9 Numerical Investigation on Aerodynamic Performance of Airfoil with Different Cambers <i>Min Zhao, Yao Zou and Wei He*</i> #ICIUS-2021-13 Aerodynamic and Structural Performances of a Single-stage Transonic Axial Compressor with Blade Fillet Radius <i>Chu Hoang Quan* and Dinh Cong Truong</i> #ICIUS-2021-68 Combustion Analysis for Small Gas Turbine Engine by Using Computational Fluid Dynamics (CFD) <i>Quoc-Huy Nghiem*, Cong-Anh Pham, Quang-Hai Nguyen and Nhu-Van Nguyen</i></p>
11:45 - 1:30 PM	Lunch			

Date	Activities			
1:30 - 2:50 PM	Parallel Session #5	<p>(5E-1) Control and Computation Chair: Nguyen Ngoc Hien Co-chair: Dang Le Quang #ICIUS-2021-21 A Numerical Study on the Design of a Cold Heat Storage Device in a Liquefied Air Energy Storage System (LAES) <i>Hyunjong Kim*, Juyeol Ryu, Kwansu Kim, Jungtae Kim, Dae Hwan Kim and Jongpo Park</i> #ICIUS-2021-36 Simulate Deformation and Stress of 3-Axis CNC Milling Machine Body in Outsoles Mold Machining <i>Thanh Luan Bui, Vinh Tuong Vuong, Duc Dat Do and Tan Tien Nguyen*</i> #ICIUS-2021-61 A Novel Approach in Simulation of Flow over Sphere from Low to High Reynolds Numbers <i>Anh Huy Huynh, Buu Hung Tran, Thi Hong Hieu Le*, Ngoc Hien Nguyen and Quang Le Dang</i> #ICIUS-2021-67 Implementing Lean and Sweep Method for Optimization of Gas Turbine Blade by Computational Fluid Dynamics <i>Zung Pham Ngoc, Anh Nguyen Tuan, Vu Hoang Nhu and Nhu Van Nguyen*</i></p>	<p>(5E-2) Control and Computation Chair: Le Thanh Long Co-chair: Au Thi Kim Loan #ICIUS-2021-14 Study on the Loading Redistribution during Braking Maneuver of a Tanker Semi-trailer – The Effect of the Configuration of the Baffles <i>Thong Duc Hong*, Thien Phuoc Huynh, Hieu Trung Le and Thanh-Long Le</i> #ICIUS-2021-22 Computational Fluid Dynamics Based Propeller Design Improvement for High Altitude Long Endurance (HALE) UAV <i>Mochammad Agoes Moelyadi, Fatwa Azam Maulana* and Ema Amalia</i> #ICIUS-2021-69 The Comparison Results of Numerical Simulation with Experimental Data for Axial Turbine of Small Turbojet Engine <i>Hung Vu Xuan*, Anh Pham Tuan, Lanh Chu Duy, Nhu Van Nguyen</i> #ICIUS-2021-72 Numerical Study of the Laminar Separation Bubble during Drag Crisis over the Teardrop Model <i>Thi Hong Hieu Le*, Dinh-An Nguyen and Ngoc Hien Nguyen</i></p>	<p>(5D) Space Robots Chair: Vo Bich Hien Co-Chair: Ngo Dinh Tri #ICIUS-2021-55 A Comparison of Kalman Filters for Unmanned Aerial Vehicles Attitude Estimation Using Real Flight Test Data <i>Dung Van Vu*, Thanh Truong Nguyen, Dong Thanh Nguyen and Thap Khac Nguyen</i> #ICIUS-2021-70 The Control Methodology for Jet Engine of Unknown Characteristics <i>Huy Hoang Nguyen*, Van Son Bui, Thanh Nam Trinh, Nhu Van Nguyen and Quang Hai Nguyen</i></p>

The 17th International Conference on Intelligent Unmanned Systems (ICIUS2021)
August 25th – 27th, 2021, Ho Chi Minh City University of Technology, VNU-HCM, Vietnam

Date	Activities			
2:50 - 3:00 PM	Break Networking			
3:00 - 4:15 PM	Parallel Session #6	(6F) Industrial Session Viettel Aerospace Institute RT Robotics Agridrone DCSELab		(6G) Steering Committee Meeting
4:30 PM	Closing Remarks and Paper Award			

KEYNOTE LECTURE #1

Longitudinal Flight Across Tokyo Bay by Drone and Future Prospects

Professor Kenzo Nonami

Advanced Robotics Foundation, Tokyo, Japan

Email: nonami@arf.or.jp / nonami@faculty.chiba-u.jp

Abstract



On June 21, 2021, ARF (Advanced Robotics Foundation) and its affiliates succeeded in fully autonomous flying across Tokyo Bay with a flight distance of 50 km between Yokohama and Chiba, Japan(1). This was a complete BVLOS flight without any observer of Tokyo Bay by small drone like kite plane of 24kg. A drone connects Yokohama and Chiba, which are big cities of Yokohama with a population of 4 millions and Chiba with 1 million, using the ultra-low airspace over Tokyo Bay. This was a demonstration experiment to build a distribution highway. We actually transported 500,000 Japanese yens worth of implants and dental technicians. The drone was also an emergency drone that can carry out

the mission as a disaster prevention and mitigation system for natural disasters such as earthquakes and typhoon. It took two years from the conception to finish. It means that the technical hurdles for safely flying a long distance of 50 km in Tokyo Bay, where there is Tokyo International Airport (Haneda Airport) and many large ships go around, are extremely high. And it was not easy to get a flight permit from the Civil Aviation Bureau of the Ministry of Land, Infrastructure, Transport and Tourism of Japan. In this presentation, the progress of including technical issues, the future plans and prospects will be presented.

Short bio-sketch

Dr. Kenzo Nonami received Ph.D. degree in Mechanical Engineering in 1979 from Tokyo Metropolitan University. He was a research scientist and a senior research scientist at NASA in USA from 1985 to 1988. After that, he became an associate professor from 1988 to 1994. Since 1994, he has been a full professor in Department of Mechanical Engineering at Chiba University. Dr. Kenzo Nonami was Vice President of Chiba University from 2008 to 2014. He organized ICIUS 2011 in Chiba, Japan. Their high quality papers were published by Springer book with the title “Autonomous Control Systems and Vehicles”, edited by K.Nonami etc, 2013. Dr. Nonami founded a startup company in 2013 called Autonomous Control Systems Laboratory, Ltd. (ACSL) and is the CEO of this company. In December, 2018, ACSL listed the stock on the Tokyo Stock Exchange as IPO. Dr. Nonami is the chairman of Japan drone consortium, which includes more than 300 companies, and founded Advanced Robotics Foundation in June, 2019 as its president. ARF is focusing on the development of a new vertical takeoff and landing type unmanned airframe with a flight distance of 100 km or more, a payload of 5 kg or more, and a flight speed of 150 km / h or more for logistics and disaster response purposes.

KEYNOTE LECTURE #2

Collision Recovery of a Beetle-inspired Flapping-Wing Robot

Dr. Hoang-Vu Phan

School of Engineering, Swiss Federal Institute of Technology Lausanne (EPFL),
Lausanne, Switzerland
Email: vu.phan@epfl.ch

Abstract



In this study, we introduce the 16 g beetle-inspired, motor-driven, KUBeetle-S robot, which is truly insect-like in terms of tailless and two-winged configuration, attitude control approach, and hovering flight capability. The robot could remain for up to 9 minutes in the air, making it the lightest two-winged robot so far that can sustain free controlled flight with all onboard components. We then present a study on how beetles and the robot survive inflight wing collision. We demonstrated that the folding mechanism in the beetle's hindwing serves a crucial shock-absorbing function during in-flight collisions by collapsing and redeploying rapidly (< 5 ms) within a single stroke. We then built a beetle-inspired collapsible wing that can be passively folded and rapidly unfolded (< 7 ms). Implementing the wing on a flapping-wing robot, we showed that the folding mechanism enables the robot to fly safely after collisions. Otherwise, in absence of the folding mechanism, the robot tumbles. This initial result promises to develop a collision-tolerant robot for applications in confined space and cluttered environments.

Short bio-sketch

Dr. Hoang-Vu Phan received the B.S. degree in aerospace engineering from the Ho Chi Minh City University of Technology, Ho Chi Minh city, Vietnam in 2010, and M.S. and Ph.D. degrees in biomimetics and intelligent microsystems from Konkuk University, Seoul, South Korea in 2012 and 2017, respectively. He is currently a postdoctoral researcher at the Laboratory of Intelligent Systems at the Swiss Federal Institute of Technology Lausanne (EPFL), Switzerland. Prior to joining EPFL, he was a research assistant professor at the Department of Smart Vehicle Engineering, Konkuk University, Seoul, Korea (2017-2020). His research interests include biologically inspired flying robots, multimodal locomotion robots, and insect flight. He has published more than 25 SCI/SCIE journal papers, and more than 30 conference papers and abstracts. During his research, he released the 16 g KUBeetle robot, which is an insect-like, tailless, two-winged, hover-capable, flapping-wing robot that can sustain a long flight. He is currently the associate editor of International Journal of Micro Air Vehicles and editorial board member of Mathematical Problems in Engineering.

KEYNOTE LECTURE #3

Design and Implementation of Camber Morphing Wings and Their Mechanisms

Associate Professor, Bruce W. Jo
State University of New York (SUNY), Stony Brook University, Korea
E-mail: bruce.jo@stonybrook.edu

Abstract



Wing morphing technologies in general aim to optimize aircraft's efficiency by changing and adjusting the shape of wings in compliance with corresponding flight conditions. Among many types of wing morphing, suggested variable camber compliant morphing in airfoil morphing enables aircraft to have seamless, conformal, and energy and noise effective change of wing geometry that significantly reduces drag force or lift-drag ratio. Unlike typical approaches of using smart materials or partial morphing of trailing-edge, mechanism-driven camber morphing wing via linear actuators enables fixed wing aircraft wing to adjust camber rates conformally, dynamically, and firmly along the wing span. For realization of actual flight and control of camber morphing wing aircraft, it is of interest (1) to investigate the nature of structural and aerodynamical behaviors of camber morphing wings while flight, (2) to study differences and similarities between conventional wings and camber morphing wings in control aspects, (3) to design and implement the skin structure of camber morphing wings along with characteristics of 3D printed structure. This presentation covers overview of morphing technologies, motivation and benefits of camber morphing, design of control allocation aspect of camber morphing wings, and design and implementation of skin structure for camber morphing wings with perspectives of 3D/4D printing.

Short bio-sketch

Dr. Bruce W. Jo is an Associate Professor in the Department of Mechanical Engineering at State University of New York (SUNY), Stony Brook University in NY and Korea. Before that, he was a tenured Associate Professor at Tennessee State University (TSU), Nashville TN in 2018. A year later, he did his first sabbatical year at ORNL (Oak Ridge National Laboratory), Knoxville TN focused on 3D/4D manufacturing technology. Before he joined TSU in fall, 2014, he was working as a tenure-track Assistant Professor at Embry-Riddle Aeronautical University from 2011-2014 and Florida State University as Research Associate from 2010-2011. His main research interests are 1) design and control of morphorous structures (4D printing), 2) design of flight control systems, and 3) dynamics/kinematics and mechanism design of mechanical systems in applications of aerospace, mechanical, and robotic systems. He earned his Ph.D. in Mechanical Engineering from Columbia University, NY in 2010, and M.S. in Mechanical Engineering from New York University, NY in 2006.

KEYNOTE LECTURE #4

Adaptive Fault Diagnosis and Reconfiguration Control with Flight Control Applications

Professor Bin Jiang

College of Automation Engineering, Nanjing University of Aeronautics and Astronautics, P.R. China

Email: binjiang@nuaa.edu.cn

Abstract



Based on the background of the flight control systems, this talk focuses on the topic of adaptive fault accommodation for complex dynamic systems, and introduces a series of results of fault detection, estimation and accommodation for continuous time, hybrid systems and multi-agent systems. Their applications on the hot issues of satellites, near space vehicles, helicopters are investigated. Some perspectives along this direction are provided.

Short bio-sketch

Bin Jiang received the Ph.D. degree in Automatic Control from Northeastern University, Shenyang, China, in 1995. He had been postdoctoral fellow, research fellow, invited professor and visiting professor in Singapore, France, USA and Canada, respectively. Now he is a Chair Professor of Cheung Kong Scholar Program in Ministry of Education and Vice President at Nanjing University of Aeronautics and Astronautics, China. He has served as Subject Editor of Int. J. Control, Automaton and Systems, Associate Editor or Editorial Board Member for a number of journals such as IEEE Trans. On Cybernetics, IEEE Trans. On Control Systems Technology; Neurocomputing, J. of Franklin Institute, etc. He is a Fellow of IEEE, Chair of Control Systems Chapter in IEEE Nanjing Section, a member of IFAC Technical Committee on Fault Detection, Supervision, and Safety of Technical Processes. His research interests include intelligent fault diagnosis and fault tolerant control, and their applications to helicopters, satellites and high-speed trains.

He has been the principle investigator on several projects of National Natural Science Foundation of China. He is the author of 8 books and over 100 referred international journal papers. He won National Natural Science Award of China.

FULL PAPERS

Numerical Study of Aerodynamic Performance and Flow Characteristics of a Centrifugal Blower

Thanh-Long Le^{1,2,5*}, Tran Trung Nghia^{3,5}, Hong Duc Thong^{4,5}, Mai Hoang Kim Son^{1,5}

¹Faculty of Mechanical Engineering, Ho Chi Minh City University of Technology (HCMUT),
268 Ly Thuong Kiet Street, District 10, Ho Chi Minh City, Vietnam

²National Key Laboratory of Digital Control and System Engineering (DCSELab), HCMUT,
268 Ly Thuong Kiet Street, District 10, Ho Chi Minh City, Vietnam

³Faculty of Applied Science, Ho Chi Minh City University of Technology (HCMUT), 268 Ly
Thuong Kiet Street, District 10, Ho Chi Minh City, Vietnam

⁴Faculty of Transportation Engineering, Ho Chi Minh City University of Technology
(HCMUT), 268 Ly Thuong Kiet Street, District 10, Ho Chi Minh City, Vietnam

⁵Vietnam National University Ho Chi Minh City, Linh Trung Ward, Thu Duc City, Ho Chi
Minh City, Vietnam

*Corresponding author. E-mail: ltlong@hcmut.edu.vn

Abstract

This paper focuses on the effect of operating conditions such as impeller speed on the performance and flow characteristics of centrifugal fan. A physical model of the air blower consisting of these mainly parts in a blower system: collector, impeller, outlet flange and volute casing and the appropriate boundary conditions are set up by ANSYS software. Computation Fluid Dynamics (CFD) are performed for the numerical analysis. The calculation of blower performance parameters such as total pressure, efficiency and flow rate are based on the Reynolds averaged Navier-stokes equations and k- ϵ turbulence flow model. The numerical results show that changes in operating conditions have significant effects on the blower performance and the pressure maintained inside the blower is higher for a larger impeller rotational speed. The ability to predict the behavior of the air flow motion in a centrifugal blower is essential for obtaining the topology optimization design.

Keywords: Blower, Centrifugal fan, Air flow, Computational fluid dynamics, Numerical simulation.

1. Introduction

Air blower (also commonly known as Centrifugal Fans) is an equipment that increases the velocity of air or gas when it passes through equipped impellers. The impeller in air blower rotates and vacuum the air in the suction section. The trapped air is then pushed to the outlet side. The kinetic energy of blades increases the pressure of the air at the outlet. Because the mass flow rate and compactness of a centrifugal fan are better compared to those of an axial fan, air blowers have several technical applications in exhausting, aspirating, cooling, ventilating, conveying, etc. In recent years, there have been studies on air blowers when applied to different purposes, mainly on noise control, aerodynamic performance, blade design... Due to customer demands for reducing noise in the industry, household appliances, and rigorous noise regulations, much attention has been paid to the fan noise problem. By theoretical calculations and experimental measurements, Bazhenova presented the origin of aerodynamic sources on all rotational and rotational elements inside an air blower [1]. Chen et al. found that the main source of noise in

centrifugal fan is the volute surface [2]. Hence, there have been studies on noise reduction by improving volute design [3-4]. Noise reduction of air blower with the impeller improvement was studied by Prezelj et al. [5].

A very important research direction on air blower is the flow characteristics, which serves many different purposes to improve aerodynamic performance, user experience, economic efficiency, natural resources protection such as pressure and heat control, airpower efficiency, energy consumption, etc. Charapale et al. created a 3D air blower model consisting of the suction hood, impeller and volute, and applied CFD to calculate the airflow through blower [6]. Their results showed that CFD applications in air blower research give good results, therefore reducing the number of experiments and costs for any new air blower design studies. With this in mind, Ye et al. investigated performance and flow behaviors of the multi-blade centrifugal fan by CFD method [7]. It was showed that optimized bevel cutting edge blades change the fan's inlet structure and improve the flow performance of the fan. Patil et al. presented an improvement of centrifugal fan performance considering volute tongue clearance variation [8]. Four cases of impeller are 6%, 8%, 10%, and 12%. They found that the total pressure and efficiency increase by 19.52% and 21.90% by decreasing volute tongue clearance (12.5% to 6%). Zhou et al. optimized blade design of the centrifugal fan based on Hicks-Hence function and multi-objective genetic algorithm [9]. They pointed out that pressure efficiency, flow rate, and aerodynamic noise are improved, thus reducing energy consumption. This study provides useful and important ideas in the optimal design of centrifugal fans for buildings.

Previous studies have focused on analyzing the influence of impeller geometry and volute tongue on fan performance. However, the variation of the rotation speed while the other parameters remain the same also profoundly affects the ability of the centrifugal fan to exploit. With the advancement of computational models, scientists have more conditions to study about the air blower, serving the growing human civilization. In the present study, a 3D centrifugal fan design was developed using numerical methods for the inspection of flow conditions. The performance of the flow field is simulated by different standard operating conditions of the fan. Our main purpose is to compare results when input conditions are changed, thereby achieving the expected pressure, velocity values, and mass flow rate. From there, the optimal parameters for the design and manufacture of the air blower are drawn.

2. Methodology

2.1 Physical model

The geometry of the centrifugal fan is constructed using CAD software, represent all important features of a real fan. This consists of collector, impeller, outlet flange, and volute casing. This study concentrates on evaluating airflow through the blower, ignoring many solid parts which do not affect the calculation to simplify the computational process. The fan blades are thin blades of equal thickness and each profile is a simple arc curve. These important parameters determine the quality of the internal flow field. The model dimensions are ensured to be easily manufactured and widely used in many fields.

Blade's geometry includes two main parameters: fan diameters and blade angle. The blade profile varies could be constructed using the tangent circular arc method. The blade profile could be calculated through Eq. (1):

$$P = (R_2^2 - R_1^2) / [2(R_2 \cos \beta_2 - R_1 \cos \beta_1)] \quad (1)$$

where R_2 and R_1 are the impeller outer and inner radius, respectively. Likewise, β_2 and β_1 are the blade outlet and inlet angle, respectively. Figures 1, 2, and Table 1 show the 3D geometry of centrifugal fan, impeller, and data of the fan, respectively.

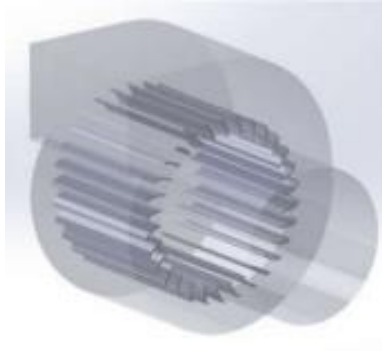


Figure 1. Basic structure of centrifugal fan model

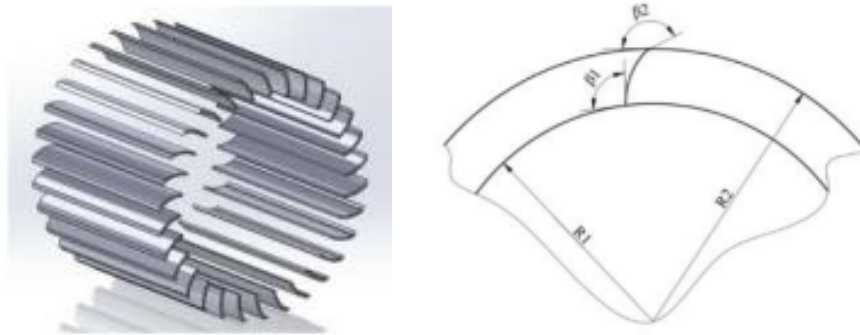


Figure 2. Blade physical model

Table I. Basic parameter of the fan

Fan structure	Dimension
Number of blades	30
Impeller length (mm)	100
Impeller outer radius, R_2 (mm)	62
Impeller inner radius, R_1 (mm)	50
Blade thickness (mm)	1.2
Blade inlet angle, β_1 ($^\circ$)	90
Blade outlet angle, β_2 ($^\circ$)	153
Volute width (mm)	105
Speed of fan (rpm)	2700

For the purpose of this study, which is obtaining the simulation's results, the governing continuity and momentum equations Reynolds averaged Navier-stokes equations for incompressible flow field at constant temperature are used:

$$\frac{\partial U_i}{\partial x_i} = 0 \tag{2}$$

$$\rho \frac{\partial U_i}{\partial t} + \rho U_j \frac{\partial U_i}{\partial x_j} = -P \frac{\partial p}{\partial x_i} + \frac{\partial}{\partial x_j} \left[\mu \frac{\partial u_i}{\partial x_j} - \overline{u_i u_j} \right] \quad (3)$$

where ρ is density; μ is dynamic viscosity; $U(U, V, W)$ is velocity vector; p is pressure; primes denote fluctuating components and $u'_i u'_j$ is Reynolds stress tensor. Because this system of equations has more unknown variables than equations to solve, the Boussinesq hypothesis relates the Reynold stress to the mean flow velocity gradients as:

$$-\overline{\rho u_i u_j} = \mu \left(\frac{\partial \overline{u_i}}{\partial x_j} + \frac{\partial \overline{u_j}}{\partial x_i} \right) - \frac{2}{3} \rho \delta_{ij} k \quad (4)$$

with δ_{ij} as the Kronecker delta and k as the turbulent kinetic energy; $k = \frac{1}{2} \overline{u_i u_i}$ and $\mu_t = C_\mu \rho \frac{k^2}{\epsilon}$.

In this paper, the reliable k- ϵ module was used. According to Gil Ho Yoon [10], this module is widely used for calculating turbulent flow by solving two transport equations: kinetic energy equation (k) and turbulent dissipation equation (ϵ). Thence, it can achieve better results in solving turbulence problems and reduce the number of calculations, which is very useful in the study and in industrial applications.

The kinetic energy equation (k) is:

$$\frac{\partial}{\partial t} (\rho k) + \frac{\partial}{\partial x_j} (\rho k u_j) = \frac{\partial}{\partial x_j} \left[\left(\mu + \frac{\mu_t}{\sigma_k} \right) \frac{\partial k}{\partial x_j} \right] + P_k + P_b - \rho - Y_M + S_k \quad (5)$$

The turbulent dissipation equation (ϵ) is:

$$\frac{\partial}{\partial t} (\rho \epsilon) + \frac{\partial}{\partial x_j} (\rho \epsilon_j) = \frac{\partial}{\partial x_j} \left[\left(\mu + \frac{\mu_t}{\sigma_\epsilon} \right) \frac{\partial \epsilon}{\partial x_j} \right] + \rho C_1 S_\epsilon - \rho C_2 \frac{\epsilon^2}{k + \sqrt{\nu \epsilon}} + C_{1\epsilon} \frac{\epsilon}{k} C_{3\epsilon} P_b + S_\epsilon \quad (6)$$

where:

$$C_1 = \max \left[0.43; \frac{\eta}{\eta + 5} \right];$$

$$\eta = S \frac{k}{\epsilon};$$

$$S = \sqrt{2 S_{ij} S_{ji}};$$

u_j : Velocity component in corresponding direction

$$\mu_t: \text{Eddy viscosity, } \mu_t = \rho C_\mu \frac{k^2}{\epsilon};$$

$$C_\mu = 0.09; \sigma_k = 1;$$

$$\sigma_\epsilon = 1.3; C_{1\epsilon} = 1.44;$$

The energy in the air delivered by the fan is the difference between outlet air energy and inlet air energy. This energy has two components: static and dynamic. Because the flow is equal for both inlet and outlet, we may calculate the total pressure of centrifugal fan by:

$$FTP = TP_2 - TP_1 = (SP_2 - SP_1) + (VP_2 - VP_1) \quad (7)$$

with:

FTP: Fan total pressure.

TP_2 , TP_1 : Total pressure in fan outlet and inlet.

SP_2 , SP_1 : Static pressure in fan outlet and inlet.

VP_2 , VP_1 : Dynamic pressure in fan outlet and inlet.

2.2 Numerical methods

Before generating the mesh, the processed fluid domain was divided into the impeller fluid domain, the volute fluid domain, the inlet, and the outlet fluid domain. The air blower is meshed using tetrahedral elements because they maintain good quality for complex shapes and the mesh element size for volute was kept constant throughout the analysis. The second-order upwind difference scheme is employed for the spatial discretization of the convection terms. The pressure–velocity coupling is handled using the SIMPLE algorithm. After grid generation, the mesh was carried out in Figure 3. There are 4264 nodes and 3632 elements used in total.

Module transient in ANSYS FLUENT was used to solve the flow inside the air blower. It is very important to include the relative motion between stationary and rotating parts of the air blower. The moving reference frame (MRF) model allows individuals' cell zones to rotate at different speeds. The domain is divided into separate zones and the fluid flow is solved in stationary or rotating coordinate systems. The wall of the impeller is defined as the moving wall with the rotating frame of reference and the other walls are defined as the stationary wall in the inertial frame of reference. Time step size was set at 0.01s.

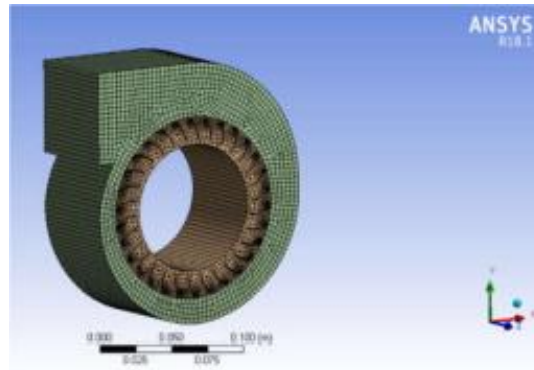


Figure 3. Meshed centrifugal fan

3. Results and Discussion

In this section, validation of the simulation results are given through the velocity and pressure contour of the fan and evaluating of the relation between total pressure and flow rate. The computational domain is air with the density of 1.225 kg/m^3 and the viscosity of $1.7894\text{e-}5 \text{ kg/ms}$. The intensity turbulent at the inlet is 5%.

Figure 4 represents the static pressure and velocity contour of the air blower in case the impeller rotates at 2700 revs/min. It was found that the low-velocity zones are moving away from the fan center and the high flow velocity is obviously near the impeller exit, caused by the asymmetry of the volute. The maximum value that the airflow velocity can achieve is 44.42 m/s at the center of the volute. The airstream enters the impeller from an axial direction and flows out by the centrifugal force. Moreover, the pressure value changes in an increasing direction from the inlet to the outlet of the centrifugal fan, reaching its maximum value of 99.18 Pa at the fan wall.

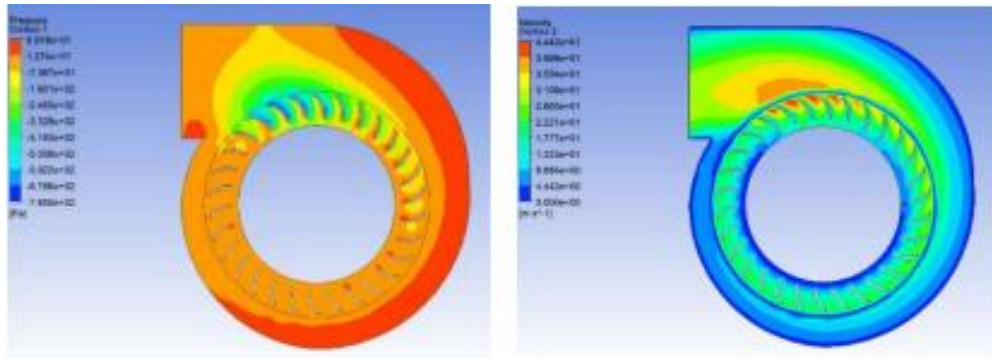


Figure 4. Pressure contour and velocity contour of fan at the speed of 2700 revs/min

Figures 5 and 6 show the static pressure and velocity contour of the air blower in case the impeller rotates at 2800 revs/min and 2600 revs/min. The distribution of pressure and velocity fields is no different from the first case study above. The centrifugal fan shell is where the maximum pressure and minimum velocity value gather. In comparison with the first case (2700 revs/min), the pressure and velocity values change proportionally with the rotational speed. As rotational speed increases, maximum pressure also increases, reaching 151.4 Pa, and the maximum velocity value is 46.9 m/s. Likewise, as rotational speed is reduced, the pressure value is lower than in the original case, 13.77 Pa, and the velocity decreases to 44 m/s.

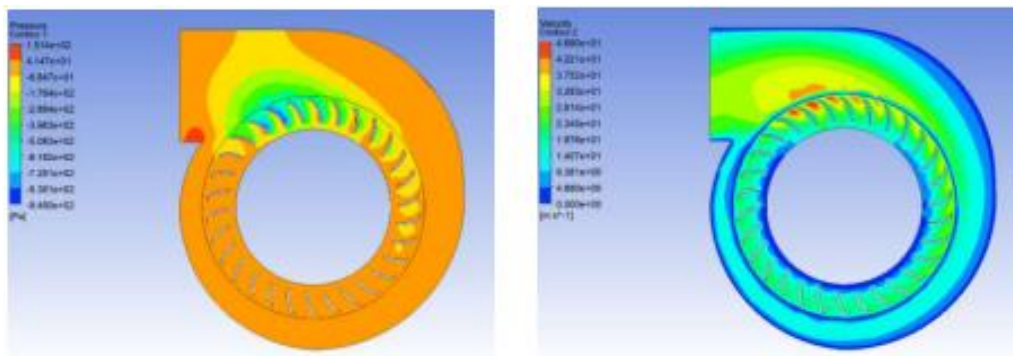


Figure 5. Pressure contour and velocity contour of fan at the speed of 2800 revs/min

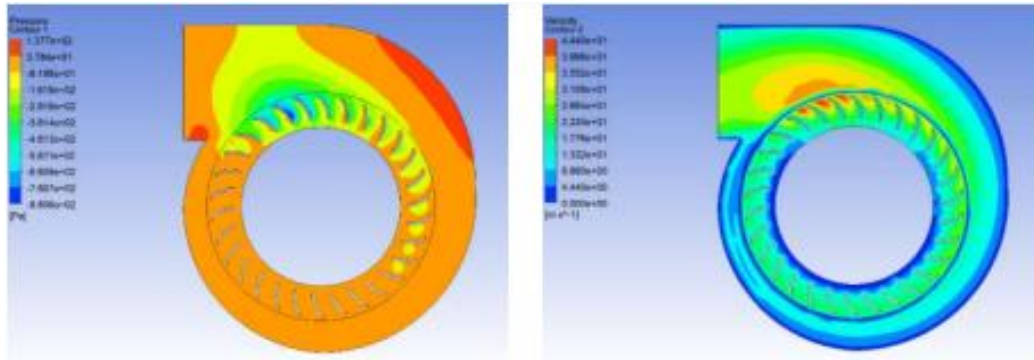


Figure 6. Pressure contour and velocity contour of fan at the speed of 2600 revs/min

Figure 7 compares the max total pressure values in the first five seconds of the fan at three different rotational speeds. The graph shows that a larger rotational speed will result in a larger max total pressure value. When operating at the speeds of 2800, 2700, and 2600 revs/min, the centrifugal maximum total pressure values are approximately 890, 820, and 770 Pa, respectively.

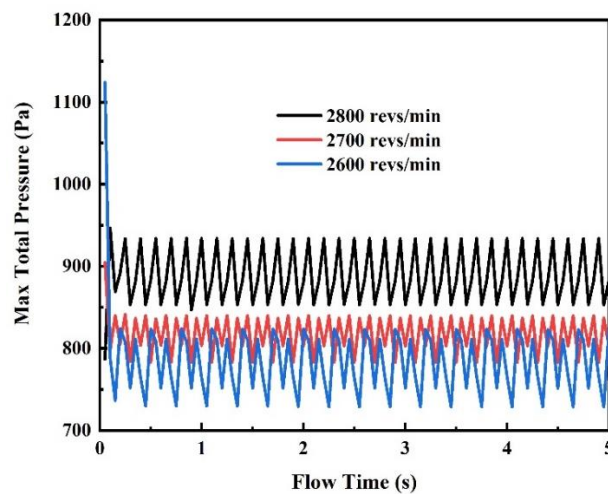


Figure 7. Max total pressure of the fan at three different rotational velocity in the first 5 seconds

To analyze more closely the influence of rotational speed on the performance of the centrifugal fan, this study considers the relationship between mass flow rate inlet and rotational speed as indicated in Figure 8. As can be seen from the results, there is no doubt that greater speed means greater suction, resulting in a larger inflow of air. The inlet flow rates of the blower are approximately 1.87, 1.83, and 1.80 kg/s at to the rotational speed of 2800, 2700, and 2600 revs/min, respectively. There are three stages in pressure development through a centrifugal fan impeller. In the first stage, the airflow is straight to the surface of the blades. The impellers split the air into small volumes. Here, the accumulation of air mass occurs, which is the compression of the air mass of small volume. In the second stage, the air pressure is pumped inside the working chamber. The relative velocity reduces as the air flows through the blade passage, leading to an additional increase in static pressure and dynamic pressure at the impeller outlet. In the final stage, the compressed air is discharged from the working chamber to the outlet. As the air moves radially through the impeller, the absolute velocity of the flow will increase, reaching maximum absolute velocity at the impeller outlet. This increase in the absolute velocity of the air leads to an increase in the kinetic energy and dynamic pressure across the impeller. This three-

stage process creates a repetitive up and down movement in the max total pressure and mass flow rate diagrams in Figures 7 and 8. With the centrifugal fan studied in this paper, when the rotational speed increases and decreases by 3.7%, the max total pressure of the centrifugal fan increased by 8.5% and decreased by 5%, respectively. Meanwhile, the mass flow rate increased by 2.2% and decreased by 1.6%, compared to the original results.

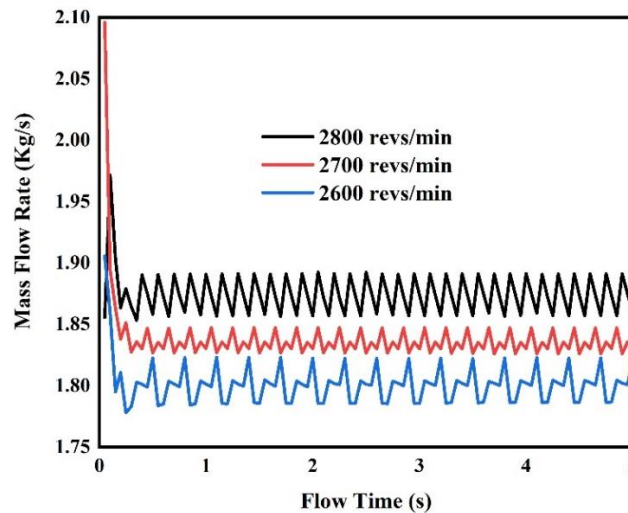


Figure 8. Mass Flow Rate of the fan at three different rotational velocity in first 5 seconds

4. Conclusion

In this paper, a centrifugal fan has been modeled, meshed, and analyzed to study the characteristics of the flow field such as pressure and velocity distribution. Moreover, by changing the impeller speed, the effect of different rotation speeds on the performance of a centrifugal fan such as total pressure and the mass flow rate was studied by CFD simulations and compared with the original speed. The numerical results show that the rotational speed has a great influence on the performance of the fan. The total pressure maintained inside the blower and the mass flow rate of the blower increase as the impeller rotational speed gets larger. The figures obtained from numerical results give the potential to upgrade and optimize the new design of the air blower in further studies. With the development of the computational method, the flow patterns of air inside the blower are analyzed, which will help in a better understanding of the flow behavior of the centrifugal fan. Therefore, the number of experiments is also reduced. It will help to reduce cost and lead time for any new design air blower studies.

Acknowledgement

We acknowledge the support of time and facilities from Ho Chi Minh City University of Technology (HCMUT), VNU-HCM for this study.

References

- [1] L. A. Bazhenova (2018), “Noise Sources of Aerodynamic Origin in Air Blowers”, *Acoustical Physics*, Vol. 64, pp. 356-364.
- [2] J. Chen, Y. He, Li Gui, C.X. Wang, L. Chen, Y.R. Li (2018), “Aerodynamic noise prediction of a centrifugal fan considering the volute effect using IBEM”, *Applied Acoustics*, Vol. 132, pp. 182-190.

- [3] Chen Wang, M.Q. Wang, K. Mai, H.Y. Li, N.T. Liu (2020), “Structure design of low-frequency broadband sound-absorbing volute for a multi-blade centrifugal fan”, *Applied Acoustics*, Vol. 165, 107315.
- [4] W.Y. Hao, J.J. Wang, X.M. He, Z.C. Zhu, Z.D. Wang, H. Yang, W. Zhang, Y.K. Wei (2020), “Reduction of aerodynamic noise of single-inlet centrifugal fan with inclined volute tongue”, *Measurement and Control*, Vol. 53 No. 7-8, pp. 1376-1387.
- [5] J. Prezelj and T. Novaković (2018), “Centrifugal fan with inclined blades for vacuum cleaner motor”, *Applied Acoustics*, Vol. 140, pp. 13-23.
- [6] U. D. Charapale and A. T. Mathew (2018), “Prediction of Flow in the Industrial Blower using Computational Fluid Dynamics”, *Materials Today: Proceedings*, Vol. 5 No. 2, pp. 12311-12319.
- [7] J.J. Ye, W.W. Liu, P. Duan, X.Y. Huang, J.D. Shao, Y. Zhang (2018), “Investigation of the performance and flow behaviors of the Multi-blade Centrifugal Fan based on the Computer Simulation Technology”, *Wireless Personal Communications*, Vol. 103, pp. 563-574.
- [8] S.R. Patil, S.T. Chavan, N.S. Jadhav, S.S. Vadgeri (2018), “Effect of Volute Tongue Clearance Variation on Performance of Centrifugal Blower by Numerical and Experimental Analysis”, *Materials Today: Proceedings*, Vol. 5 No. 2, pp. 3883-3894.
- [9] S.Q. Zhou, H.X. Zhou, K. Yang, H.B. Dong, Z.L. Gao (2021), “Research on blade design method of multi-blade centrifugal fan for building efficient ventilation based on Hicks-Henne function”, *Sustainable Energy Technologies and Assessments*, Vol. 43, 100971.
- [10] G.H. Yoon (2020), “Topology optimization method with finite elements based on the $k-\epsilon$ turbulence model”, *Computer Methods in Applied Mechanics and Engineering*, Vol. 361, 112784.

Decentralized Cubature Kalman Filter for Spacecraft Constellations Navigation

Xingyu Zhou¹, Jie Ren^{2,*}, Qin Tong³ and Dong Qiao⁴

^{1,2,4}School of Aerospace Engineering, Beijing Institute of Technology, Beijing, China, 100081

³Department of Precision Instrument, Tsinghua University, Beijing, China, 100084

*Corresponding author. E-mail: jieren21@live.com

Abstract

The high-degree cubature Kalman filter (CKF) algorithms have been widely used in spacecraft OD because of the higher accuracy. However, using high-degree CKFs for orbit determination of spacecraft constellations usually suffers from drawbacks related to computational burden. To release the navigation burden, a novel decentralized approach called Iterative Reduced Order cubature Kalman filter (IRCKF) is proposed in this paper. To decrease the state dimension in each filter, the proposed IRCKF is developed by decoupling the state model and the observation equation. In this way, each spacecraft only needs to estimate its own state. Furthermore, the measurement noise matrix is updated to compensate the accuracy. Finally, the proposed IRCKF is successfully applied into a 6-spacecraft constellation OD problem via comparing with the Integrated Navigation cubature Kalman filter (INCKF). Numerical simulations shows that the proposed method has a lower computation burden compared to an integrated navigation system, while keeping the same accuracy as INCKF, indicating that the proposed IRCKF is superior to INCKF.

Keywords: spacecraft constellation, orbit determination, high-precise filter, decentralized navigation

1. Introduction

Autonomous navigation, or orbit determination (OD), due to its considerable value in space systems engineering, has been of widespread interest in the last several decades [1]. The ability for spacecraft to determine their own states, without the help of ground-based tracking equipment, can improve their ‘intelligence’, survivability, and may also reduce the operational management costs [2,3].

The cooperation between spacecraft, making full use of inter-spacecraft measurements, has been widely used to improve navigation (or orbit determination) performance. Psiaki explored the cooperative orbit determination problem using Kalman filter [4]. Yim solved angle-only autonomous orbit determination of a dual satellite system using extend Kalman filter [5]. However, the filters employed above suffer some drawbacks in estimation accuracy. With increasing efforts to deal more accurately with the high nonlinearities and high dimension, the fifth-order cubature Kalman filter (fifth-order CKF) have been widely used [6-8].

However, the above researches are based on the centralized framework. In centralized framework, the cooperative navigation requires the main spacecraft to process all measurements collected by other spacecraft and estimates the all states. Therefore, the centralized framework using fifth-order CKF usually suffers from drawbacks related to efficiency, facing an increasing computation burden as the amount of spacecraft increases [9].

Thus, for constellations navigation, or similarly problems, a decentralized navigation system is necessary to distribute the navigation task. In this paper, a fifth-order CKF based decentralized approach is proposed to efficiently solve muti-spacecraft constellations cooperation navigation problems. The proposed method is developed by decoupling the observation equation, resulting

in each spacecraft only needing to estimate its own state using fifth-order CKF. The proposed method is promised to have a lower computational burden than the integrated methods.

2. Problem Formulation

In this section, the navigation problem, *i.e.*, the state model and the measurement model, are formulated.

2.1 State Model

In generally, a n -dimensional continuous nonlinear system consisted of the state equation and measurement equation, given by:

$$\begin{cases} \dot{\mathbf{x}} = \mathbf{f}(\mathbf{x}, t) + \mathbf{w} \\ \mathbf{z} = \mathbf{h}(\mathbf{x}) + \mathbf{v} \end{cases} \quad (1)$$

where $\mathbf{x} \in \mathbb{R}^n$ is the state vector continuous with respect to time t , $\mathbf{w} \in \mathbb{R}^n$ is the system noise, $\mathbf{z} \in \mathbb{R}^m$ is the measurement vector, and $\mathbf{v} \in \mathbb{R}^m$ is the Gaussian-distributed measurement noise.

Assuming that a constellation contains N spacecraft, noted as S_i ($i=1,2,\dots,N$) with the orbit states as $\mathbf{X}_i = [\mathbf{r}_i^T, \mathbf{v}_i^T]^T$. Thus, the state of the integrated system is given as $\mathbf{x} = [\mathbf{X}_1^T, \mathbf{X}_2^T, \dots, \mathbf{X}_N^T]^T$ and the dimension is $n = 6N$. In two-body dynamics, the state equation in Eq.(1) is rewritten as:

$$\dot{\mathbf{x}} = [\dot{\mathbf{X}}_1^T, \dot{\mathbf{X}}_2^T, \dots, \dot{\mathbf{X}}_N^T]^T = [\mathbf{f}^T(\mathbf{X}_1), \mathbf{f}^T(\mathbf{X}_2), \dots, \mathbf{f}^T(\mathbf{X}_N)]^T \quad (2)$$

$$\mathbf{f}(\mathbf{X}_i) = \mathbf{f}([\mathbf{r}_i^T, \mathbf{v}_i^T]^T) = [\mathbf{v}_i^T, -\mu \mathbf{r}_i^T / |\mathbf{r}_i|^3]^T, \quad i = 1, 2, \dots, N \quad (3)$$

where μ is the gravitational constant of the central gravity body.

2.2 Measurement Model

In our imaged scenario, the measurements of the system include both the internal measurements and external measurements, which are the inter-satellite range measurements and the starlight angles (*i.e.*, the angles between the line-of-sight of the remote stars and the central body, as shown in Figure 1), respectively.

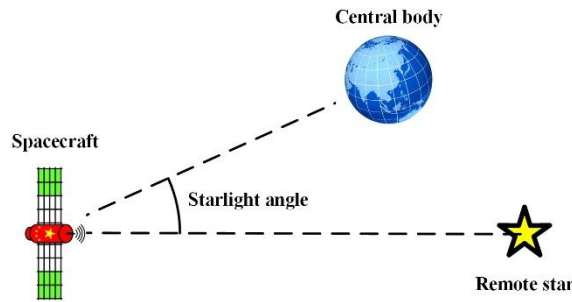


Figure 1. Measurement schematic of starlight angle.

Assuming that the spacecraft s_i can observe n_i stars ;

$$\mathbf{y}_{external} = \left[\left[\frac{\mathbf{r}_1}{|\mathbf{r}_1|} s_{1,1}, \dots, \frac{\mathbf{r}_1}{|\mathbf{r}_1|} s_{1,n_1} \right], \dots, \left[\frac{\mathbf{r}_N}{|\mathbf{r}_N|} s_{N,1}, \dots, \frac{\mathbf{r}_N}{|\mathbf{r}_N|} s_{N,n_N} \right] \right]^T + \mathbf{v}_{external} \quad (4)$$

and each spacecraft could measure the relative range with its neighboring spacecraft:

$$\mathbf{y}_{internal} = [|\mathbf{r}_1 - \mathbf{r}_2|, |\mathbf{r}_2 - \mathbf{r}_3|, \dots, |\mathbf{r}_{n-1} - \mathbf{r}_n|, |\mathbf{r}_n - \mathbf{r}_1|]^T + \mathbf{v}_{internal} \quad (5)$$

3. Decentralized Cubature Kalman Filter Method

In this section, first, the fifth-order cubature Kalman filter (fifth-order CKF) is briefly reviewed. Then, the IRCKF is detailed.

3.1 Fifth-order Cubature Kalman Filter

First, the fifth-order CKF is reviewed. The process of the filter method containing two steps, time updating step:

$$\begin{aligned}
 A_k &= Chol(\mathbf{P}_{k-1|k-1}) \\
 \boldsymbol{\chi}_{i,k-1|k-1} &= \boldsymbol{\zeta}_i + \mathbf{x}_{k-1|k-1} \\
 \boldsymbol{\chi}_{i,k|k-1}^* &= \mathbf{F}(\boldsymbol{\chi}_{i,k-1|k-1}) \\
 \mathbf{x}_{k|k-1} &= \sum_{i=0}^{2n^2} w_i \boldsymbol{\chi}_{i,k|k-1}^* \\
 \mathbf{P}_{k|k-1} &= \sum_{i=0}^{2n^2} w_i (\boldsymbol{\chi}_{i,k|k-1}^* - \mathbf{x}_{k|k-1})(\boldsymbol{\chi}_{i,k|k-1}^* - \mathbf{x}_{k|k-1})^T + \mathbf{Q}_k
 \end{aligned} \tag{6}$$

and measurement updating step:

$$\begin{aligned}
 A_k &= Chol(\mathbf{P}_{k|k-1}) \\
 \boldsymbol{\chi}_{i,k|k-1} &= \boldsymbol{\zeta}_i + \mathbf{x}_{k|k-1} \\
 \mathbf{z}_{i,k|k-1}^* &= \mathbf{h}(\boldsymbol{\chi}_{i,k|k-1}) \\
 \mathbf{z}_{k|k-1} &= \sum_{i=0}^{2n^2} w_i \mathbf{z}_{i,k|k-1}^* \\
 \mathbf{P}_{xz,k|k-1} &= \sum_{i=0}^{2n^2} w_i (\boldsymbol{\chi}_{i,k|k-1}^* - \mathbf{x}_{k|k-1})(\mathbf{z}_{i,k|k-1}^* - \mathbf{z}_{k|k-1})^T \\
 \mathbf{P}_{zz,k|k-1} &= \sum_{i=0}^{2n^2} w_i (\mathbf{z}_{i,k|k-1}^* - \mathbf{z}_{k|k-1})(\mathbf{z}_{i,k|k-1}^* - \mathbf{z}_{k|k-1})^T + \mathbf{R}_k \\
 \mathbf{K}_k &= \mathbf{P}_{xz,k|k-1} \mathbf{P}_{zz,k|k-1}^{-1} \\
 \mathbf{x}_{k|k} &= \mathbf{x}_{k|k-1} + \mathbf{K}_k (\mathbf{z}_k - \mathbf{z}_{k|k-1}) \\
 \mathbf{P}_{k|k} &= \mathbf{P}_{k|k-1} - \mathbf{K}_k \mathbf{P}_{zz,k|k-1} \mathbf{K}_k^T
 \end{aligned} \tag{7}$$

where $Chol(\square)$ represents the Cholesky decomposition method, $\boldsymbol{\chi}_{i,k|k-1}^*$ is the corresponding predicted state at time epoch t_k through executing state transfer function \mathbf{F} on the cubature point $\boldsymbol{\chi}_{i,k-1|k-1}$, $\mathbf{z}_{i,k|k-1}^*$ represents the measurements.

3.2 Iterative Reduced Order Cubature Kalman Filter

The navigation system (2), (3), (4) and (5) suffer from drawbacks related to efficiency, for it couples with an increasing computation burden as the amount of spacecraft increases. To reduce the navigation burden, the navigation system should be decentralized and each spacecraft operates a subsystem that estimates its own states using only measurements related to itself. The navigation subsystem of spacecraft S_i is given as:

$$\begin{cases} \dot{\mathbf{X}}_i = \mathbf{f}(\mathbf{X}_i) + \mathbf{w}_i \\ \mathbf{y}_i = \left[|\mathbf{r}_i - \mathbf{r}_{i-1}|, \left[\frac{\mathbf{r}_i}{|\mathbf{r}_i}| s_{i,1}, \dots, \frac{\mathbf{r}_i}{|\mathbf{r}_i}| s_{i,n_i} \right] \right] + \mathbf{v}_i \end{cases} \quad (8)$$

However, the accurate states of \mathbf{r}_{i-1} is not obtained when propagating if fifth-order CKF is used directly. Thus, the accuracy of the decentralized navigation is corrupted. To compensate, the IRCKF is developed by constructing a new measurement noise matrix, written as:

$$\bar{\mathbf{R}}_i(t_{k+1}) = \mathbf{H}_{i-1}(t_{k+1})\mathbf{P}_{i-1}(t_{k+1})[\mathbf{H}_{i-1}(t_{k+1})]^T + \mathbf{R}_i(t_{k+1}) \quad (9)$$

where $\mathbf{H}_{i-1}(t_{k+1})$ is the observation Jacobian matrix:

$$\mathbf{H}_i(t_{k+1}) = \left. \frac{\partial \mathbf{y}_i}{\partial \mathbf{X}_i} \right|_{\mathbf{X}_i = \hat{\mathbf{X}}_i^+(t_{k+1})} \quad (10)$$

4. Numerical Simulation

To demonstrate the effectiveness and practicality of the proposed IRCKF in solving real-world complicated spacecraft navigation problems, a constellation with 6 spacecraft in elliptic orbits is considered. Denote the spacecraft as S_i ($i=1,2,3,4,5,6$), the corresponding orbit states as $\mathbf{X}_i = [\mathbf{r}_i^T \ \mathbf{v}_i^T]^T$. The orbit elements are listed in Table I and the constellation is shown in Figure 2, where $i \in \{1,2,3,4,5,6\}$ represent spacecraft S_1 to S_6 in constellation. Spacecraft S_1 to S_6 have the same semi-major axis, eccentricity, inclination, and argument of periapse. The longitude of ascending node and true anomaly are both at 60-degree intervals.

Table I. Nominal orbit elements of an elliptic constellation

a/km	e	i/deg	Ω/deg	ω/deg	n/deg
26560	0.3	60	$60i-40$	10	$60i-40$

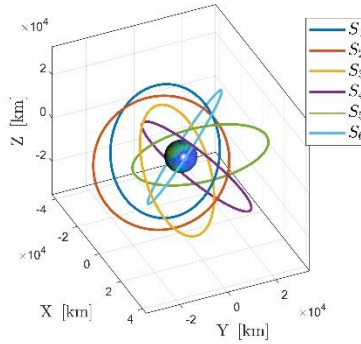


Figure 2. Configuration of an elliptic constellation

4.1 Observability analysis

First, the observability of the constellation system (2) (3) is analyzed. The observability matrix (OM) is used to measure the feasibility of a navigation system [1], and a theoretical analysis can be conducted based on the OM to show the observable states. Note that if the OM has a full rank, the whole system is observable and all states can be estimated by a navigation filter. Furthermore, the invertibility of the OM, i.e. the condition number (CN) of OM (note that

the CN could be computed by $\text{cond}(OM) = \|OM\| \cdot \|OM^{-1}\|$, is used to evaluate the degree of the observability of the system [3].

Figure 3 displays the observability of the navigation system. The upper stacked subplot illustrates the rank of OM, where the red line means the unobservable period and the blue line represents the observable period. What's more, the lower stacked subplot demonstrates the condition number (CN) of OM (note that in Figure 3, y-label represents the reciprocal of CN). It is clear that the navigation system discussed in this paper is observable.

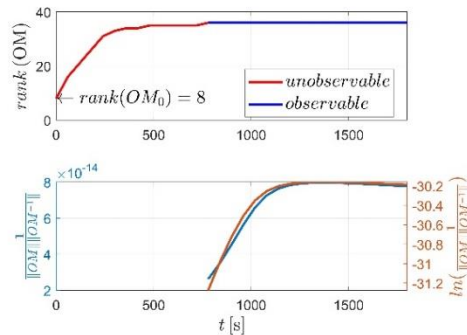
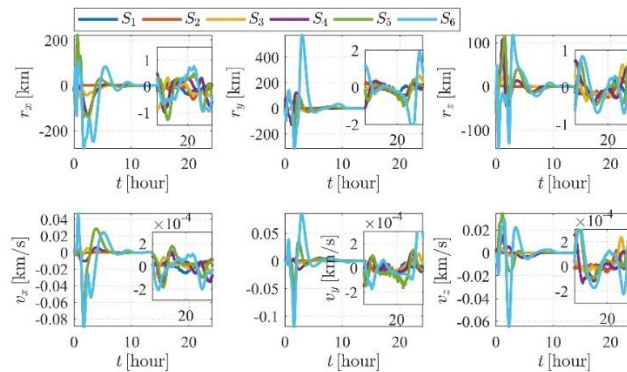


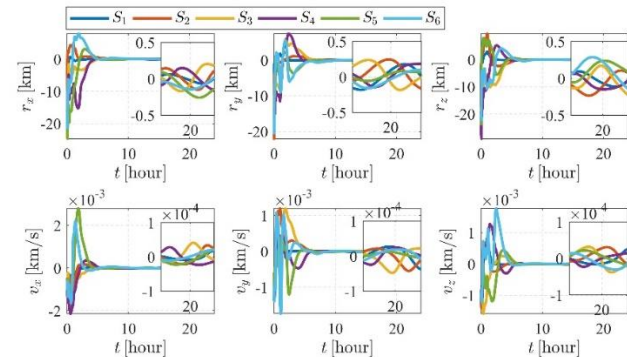
Figure 3. Observability results

4.2 Simulation results

The convergence performances of both integrated navigation cubature Kalman filter (INCKF) and IRCKF are shown in Figure 4. It is assumed that spacecraft S_1 observes two different stars and measures two starlight angles and each spacecraft in Table I has initial tri-axial position errors of 10 km.



(a) IRCKF



(b) INCKF

Figure 4. Orbit determination errors using IRCKF and INCKF

It is clearly observed that the both methods converge successfully, and the integrated navigation method has the faster convergence. It is because, using IREKF, the orbit of S_1 is first determined based on the absolute measurements. Then, the orbit of S_1 is determined based on the inter-satellite range measurements to S_1 by referring the orbit of S_1 . Likewise, the orbits of other spacecraft are successively determined. But the convergence performance from S_1 to S_6 gradually decreases.

Reducing the computation burden of the navigation system is the primary purpose of the proposed IRCKF. The run time of one-step estimation using three methods are shown in Figure 5, and the run time data is listed in Table II. The term IRCKF-I denotes single threaded computation using IRCKF, while IRCKF-II represents parallel computation. The simulations run on a computer with an AMD Ryzen 9 3950X 16-Core Processor 4.20 GHz. It can be seen that the run time of INCKF grows as a second-order power function with the number of spacecraft while IRCKF does not change. For constellation with six spacecraft, it takes only 0.0433 s for one-step estimation using IRCKF and parallel computation, which is only 1.47% of INCKF.

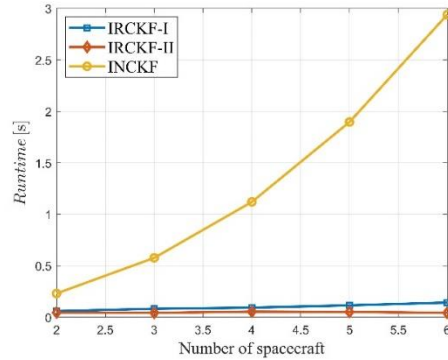


Figure 5. Run time of navigation simulations

Table II. Run time of one-step estimation using three different methods

	2	3	4	5	6
IRCKF-I	0.0598	0.0827	0.0933	0.1161	0.1425
IRCKF-II	0.0449	0.0431	0.0545	0.0517	0.0433
INCKF	0.2308	0.5771	1.1206	1.8969	2.9389

5. Conclusion

In this paper, a decentralized approach called Iterative Reduced Order Cubature Kalman Filter (IRCKF) is proposed for efficiently solving spacecraft constellations navigation problem. The performance of proposed IRCKF is tested through a six-spacecraft constellation navigation problem, then compared with corresponding integrated navigation method. Simulation shows that the time consumption of one-step prediction of proposed IRCKF is an order of magnitude less than that of the integrated navigation method. For the six-spacecraft constellation navigation problem, it takes the IRCKF about 0.1425 seconds to propagate one step while the integrated navigation method takes 2.9389 seconds. What's more, both the decentralized and integrated approaches converge successfully.

Acknowledgments

This research was funded by the National Natural Science Fund grant number 51827806, 11902359 and National Basic Scientific Research Project grant number JCKY2020903B002.

References

- [1] QIN, T., *et al.* 2019. Relative Orbit Determination Using Only Intersatellite Range Measurements. *Journal of Guidance Control and Dynamics*, 42, 703-710.
- [2] HABIB, T. M. A. 2013. Simultaneous spacecraft orbit estimation and control based on GPS measurements via extended Kalman filter. *The Egyptian Journal of Remote Sensing and Space Science*, 16, 11-16.
- [3] HU, Y., *et al.* 2020. Three-spacecraft autonomous orbit determination and observability analysis with inertial angles-only measurements. *Acta Astronautica*, 170, 106-121.
- [4] PSIAKI and MARK, L. 1999. Autonomous Orbit Determination for Two Spacecraft from Relative Position Measurements. *Journal of Guidance Control & Dynamics*, 22, 305-312.
- [5] YIM, J. R., *et al.* 2005. Autonomous orbit navigation of two spacecraft system using relative line of sight vector measurements. *Advances in the Astronautical Sciences*, 119.
- [6] ARASARATNAM, I. and HAYKIN, S. 2009. Cubature Kalman Filters. *IEEE Transactions on Automatic Control*, 54, 1254-1269.
- [7] ARASARATNAM, I., *et al.* 2010. Cubature Kalman Filtering for Continuous-Discrete Systems: Theory and Simulations. *IEEE Transactions on Signal Processing*, 58, 4977-4993.
- [8] SHI, Y., *et al.* 2014. Adaptive High-degree Cubature Kalman Filter with Unknown Noise Statistics. *Journal of Information & Computational Science*, 11, 6703-6712.
- [9] ARASARATNAM, I., *et al.* 2010. Cubature Kalman Filtering for Continuous-Discrete Systems: Theory and Simulations. *IEEE Transactions on Signal Processing*, 58, 4977-4993.

An Adaptive Trajectory Tracking Scheme for Car-like Autonomous Vehicles in the Presence of Input Constraints

Juqi Hu, Youmin Zhang* and Subhash Rakheja

Department of Mechanical, Industrial and Aerospace Engineering, Concordia University,
Montreal, Quebec H3G 1M8, Canada

*Corresponding author. E-mail: youmin.zhang@concordia.ca

Abstract

This paper focuses on the trajectory tracking control for low-speed autonomous vehicles in the presence of input constraints. Based on the backstepping control technique, an interesting adaptive control scheme is proposed by integrating the design of adaptive control gains with consideration of steering saturation. While the input boundaries are ensured, the proposed adaptive control scheme has a simple structure comparable to the existing tracking methods that do not consider input constraints or saturation. The design of the adaptive control gains is also based on enhancing the convergence rate of lateral tracking error and avoiding the sharp acceleration. Comparative experimental tests based on the latest Quanser self-driving car (QCar) platform have been conducted to verify the effectiveness of the proposed adaptive control scheme in tracking the reference trajectory without violating the input constraints.

Keywords: Adaptive control, Backstepping control, Car-like autonomous vehicles, Input constraints, Trajectory tracking control

Nomenclature

V	=	forward speed of the vehicle (m/s)
V_d	=	reference forward speed of the vehicle (m/s)
X_c	=	longitudinal position of the control point in the global frame (m)
X_d	=	reference longitudinal position of the control point in the global frame (m)
Y_c	=	lateral position of the control point in the global frame (m)
Y_d	=	reference lateral position of the control point in the global frame (m)
d_x	=	threshold distance of the longitudinal position error (m)
l	=	vehicle's wheelbase (m)
x_e	=	longitudinal position error in the local frame (m)
y_e	=	lateral position error in the local frame (m)
u_1^m	=	maximum forward speed of the vehicle (m/s)
u_2^m	=	maximum steering angle of the front wheel (rad)
α	=	tuning parameter of the adaptive gain \check{k}_2
δ	=	steering angle of the front wheel (rad)
δ_d	=	reference steering angle of the front wheel (rad)
σ	=	tuning parameter of the adaptive gain \check{k}_1
ψ_c	=	yaw angle of the vehicle (rad)
$\dot{\psi}_c$	=	yaw rate of the vehicle (rad/s)
ψ_d	=	reference yaw angle of the vehicle (rad)
$\dot{\psi}_d$	=	reference yaw rate of the vehicle (rad/s)
ψ_e	=	yaw angle error of the vehicle (rad)

1. Introduction

Car-like autonomous vehicles have attracted considerable attentions and efforts from academia and industry due to their flexible mobility and convenience for future transportation [1, 2]. As a result of nonholonomic constraints, trajectory tracking control for car-like autonomous vehicles as a special and important type of unmanned ground vehicles remains a challenging problem. The reported tracking control methods in literature can be categorized by geometric, dynamic, and kinematic model-based approaches [3-5]. When the car-like autonomous vehicles are driving at low speed, most dynamic effects of the vehicles are negligible. The designed trajectory tracking controllers based on kinematic model alone may still achieve acceptable tracking performances. Two major issues, however, should be considered for trajectory tracking for car-like vehicles based on kinematic model. One is the input constraints caused by the capability of the actuators. The overlarge value of the commanded inputs from the trajectory tracking controller would lead to large trajectory tracking errors or even system instability. The other concern is the operational range of the trajectory tracking controller. Clearly, a set of constant control gains seldom meets all driving scenarios. Accurate trajectory tracking with consideration of input constraints and adaptive gains would thus be desirable for practical implementation. In this paper, based on the backstepping control technique, a new trajectory tracking control scheme with adaptive gains is designed for the car-like autonomous vehicles. To make the trajectory tracking control more explicit, the lateral position error is creatively taken as a virtual input, resulting in a faster convergence rate of the lateral tracking error. The combined consideration of design of the adaptive control gains with steering saturation is not only ensured with respecting to the input boundaries but also largely reduces the tuning time and efforts. Problem formulation and the details about the design of the proposed adaptive control scheme will be presented in the following sections.

2. Kinematic Model and Problem Formulation

The low-speed autonomous vehicle is simplified by a bicycle model. It is easy to obtain the following geometric relationship as:

$$\begin{bmatrix} x_e \\ y_e \\ \psi_e \end{bmatrix} = \begin{bmatrix} \cos \psi_c & \sin \psi_c & 0 \\ -\sin \psi_c & \cos \psi_c & 0 \\ 0 & 0 & 1 \end{bmatrix} \begin{bmatrix} X_d - X_c \\ Y_d - Y_c \\ \psi_d - \psi_c \end{bmatrix} \quad (1)$$

and the kinematic motion equations are derived as:

$$\begin{cases} \dot{X}_c = V \cos \psi_c \\ \dot{Y}_c = V \sin \psi_c \\ \dot{\psi}_c = \frac{V}{l} \tan \delta \end{cases} \quad (2)$$

Taking the time derivative of (1) and combining it with (2), the dynamic equations of the tracking errors are obtained as:

$$\begin{cases} \dot{x}_e = -V + V_d \cos \psi_e + y_e \frac{V}{l} \tan \delta \\ \dot{y}_e = V_d \sin \psi_e - x_e \frac{V}{l} \tan \delta \\ \dot{\psi}_e = \dot{\psi}_d - \dot{\psi}_c = \frac{V_d}{l} \tan \delta_d - \frac{V}{l} \tan \delta \end{cases} \quad (3)$$

In this paper, only forward motion is considered ($V > 0$), the steering angle δ and the yaw angle ψ_c are confined within $[-0.5, 0.5]$ and $(-\pi, \pi]$, respectively, and it is also assumed that $|\psi_e| < \pi$. The actual controlled inputs to the car-like autonomous vehicle are the forward speed V and the steering angle δ , both of which have physical constraints in real-life applications. By

assuming that the reference position and angle information are known to the vehicle all the time, the trajectory tracking problem is transferred to finding an appropriate input vector $\mathbf{u} = [u_1, u_2]' = [V, \delta]'$ to make (x_e, y_e, ψ_e) converge to zero subject to the following input constraints:

$$|u_i| \leq u_i^m, i = 1, 2 \quad (4)$$

where $u_i^m, i = 1, 2$ are determined by the implementation capability of the actuators of the autonomous vehicle.

3. Adaptive Tracking Control Scheme

In this section, the adaptive nonlinear kinematic controller will be designed to stabilize the tracking error dynamics given by (3) with combined consideration of the input constraints in (4).

3.1 Backstepping Control without Input Constraints

Firstly, the kinematic model without input constraints is considered. As $\dot{\psi}_c$ equals $\frac{V}{l} \tan \delta$, (3) can be written in compact form as:

$$\begin{cases} \dot{x}_e &= -V + V_d \cos \psi_e + y_e \dot{\psi}_c \\ \dot{y}_e &= V_d \sin \psi_e - x_e \dot{\psi}_c \\ \dot{\psi}_e &= \dot{\psi}_d - \dot{\psi}_c \end{cases} \quad (5)$$

The tracking problem is then transformed to finding appropriate control inputs $\mathbf{u}^* = [u_1^*, u_2^*]' = [V, \dot{\psi}_c]'$ such that $(x_e, y_e, \psi_e) \rightarrow (0, 0, 0)$ as $t \rightarrow +\infty$. We choose the Lyapunov function candidate as:

$$V_1 = \frac{1}{2}(x_e^2 + y_e^2) \quad (6)$$

The derivative of V_1 along (5) is:

$$\dot{V}_1 = x_e(-u_1^* + V_d \cos \psi_e) + y_e V_d \sin \psi_e \quad (7)$$

As lateral position error y_e has an explicit reflection of trajectory tracking performance, we hereby regard it as a virtual input. If y_e varies along $y_e^d = -\frac{\check{k}_2}{V_d} \sin \psi_e$, and the input u_1^* is selected as $u_1^* = V_d \cos \psi_e + \check{k}_1 x_e$, then one can obtain:

$$\dot{V}_1 = -\check{k}_1 x_e^2 - \check{k}_2 (\sin \psi_e)^2 \quad (8)$$

where \check{k}_1 and \check{k}_2 are positive varying gains. Therefore, V_1 will converge to zero asymptotically, and thus both the longitudinal and lateral position errors will converge to zero asymptotically. Define $\tilde{y}_e = y_e - y_e^d$, the derivative of \tilde{y}_e is calculated as:

$$\dot{\tilde{y}}_e = V_d \sin \psi_e - \left(x_e + \frac{\check{k}_2 \cos \psi_e}{V_d} \right) u_2^* + \frac{\check{k}_2 \sin \psi_e + \check{k}_2 \cos \psi_e \dot{\psi}_d}{V_d} - \frac{\check{k}_2 \sin \psi_e \dot{V}_d}{V_d^2} \quad (9)$$

To ensure $\tilde{y}_e \rightarrow 0$ or $y_e \rightarrow y_e^d$ as $t \rightarrow +\infty$, we consider the Lyapunov function as:

$$V_2 = V_1 + \frac{1}{2} \tilde{y}_e^2 \quad (10)$$

The time derivative of V_2 can be derived as:

$$\dot{V}_2 = -\check{k}_1 x_e^2 - \check{k}_2 (\sin \psi_e)^2 + \tilde{y}_e \left\{ 2V_d \sin \psi_e - \left(x_e + \frac{\check{k}_2 \cos \psi_e}{V_d} \right) u_2^* + \frac{\check{k}_2 \sin \psi_e + \check{k}_2 \cos \psi_e \dot{\psi}_d}{V_d} - \frac{\check{k}_2 \sin \psi_e \dot{V}_d}{V_d^2} \right\} \quad (11)$$

If we select u_2^* in (11) as:

$$u_2^* = \frac{k_3 \tilde{y}_e + 2V_d \sin \psi_e + (\check{k}_2 \sin \psi_e + \check{k}_2 \cos \psi_e \dot{\psi}_d)/V_d - (\check{k}_2 \sin \psi_e \dot{V}_d)/V_d^2}{x_e + (\check{k}_2 \cos \psi_e)/V_d} \quad (12)$$

where

$$\tilde{y}_e = y_e + \frac{\check{k}_2}{V_d} \sin \psi_e \quad (13)$$

and k_3 is a positive constant gain. Then, \dot{V}_2 is obtained as:

$$\dot{V}_2 = -\check{k}_1 x_e^2 - \check{k}_2 (\sin \psi_e)^2 - k_3 \tilde{y}_e^2 \quad (14)$$

Obviously, $\dot{V}_2 \leq 0$ for $\forall t \in (0, +\infty)$. The control system will converge to the set defined as $\{x_e = 0, y_e = 0, \tilde{y}_e = 0\}$. As $\tilde{y}_e \rightarrow 0$, $y_e \rightarrow y_e^d = -\frac{\check{k}_2}{V_d} \sin \psi_e$. Since $\check{k}_2 > 0$, $V_d > 0$, and $|\psi_e| < \pi$, the yaw angle error ψ_e also converges to zero when $y_e \rightarrow 0$. The control objective of $(x_e, y_e, \psi_e) \rightarrow (0, 0, 0)$ as $t \rightarrow +\infty$ is thusly achieved. As the actual control of the car-like autonomous vehicle is \mathbf{u} instead of \mathbf{u}^* , the proposed control laws are transformed by:

$$u_1 = u_1^*, \quad u_2 = \tan^{-1} \left(\frac{l}{u_1} u_2^* \right) \quad (15)$$

3.2 Adaptive Gains and Input Constraints

The proposed control laws (15) are functions of control gains $[\check{k}_1, \check{k}_2, k_3]'$ and tracking errors $[x_e, y_e, \psi_e]'$. The adaptive gains \check{k}_1 and \check{k}_2 are designed with combined consideration of input constraints and avoidance of sharp acceleration, especially when there are large initial tracking errors. Recall that $u_1^* = V_d \cos \psi_e + \check{k}_1 x_e$, it is evident that $|u_1| = |u_1^*| \leq V_d + \check{k}_1 |x_e|$. Define d_x as the threshold distance of $|x_e|$ and $d_x > 0$. If $|x_e| \leq d_x$, then $|u_1| \leq V_d + \check{k}_1 d_x$. On the one hand, it should be ensured that $|u_1| \leq u_1^m$ for all the time. On the other hand, the vehicle is generally expected to move close to the trajectory quickly when the vehicle is far away from the reference trajectory ($|x_e| > d_x$). With combined consideration of these two effects, \check{k}_1 is designed as a piecewise function of $|x_e|$, consisting of a quadratic function ($|x_e| \leq d_x$) and a reciprocal function ($|x_e| > d_x$). The complete curve of \check{k}_1 is assumed continuous up to the first-order derivative at position $|x_e| = d_x$ to realize smooth variation in \check{k}_1 . After selecting $\check{k}_1 = \frac{\Delta^*}{d_x}$ at position where $|x_e| = d_x$, the designed control gain \check{k}_1 is described as:

$$\check{k}_1(|x_e|) = \begin{cases} -\frac{\Delta^*}{2d_x^3} |x_e|^2 + \frac{3\Delta^*}{2d_x}, & |x_e| \leq d_x \\ \frac{\Delta^*}{|x_e|}, & |x_e| > d_x \end{cases} \quad (16)$$

As suggested in [6], Δ^* can be simply set as $\Delta^* = u_1^m - V_d \tanh \frac{V_d}{\sigma}$ to drive the vehicle at the maximum speed when $|x_e| > d_x$, while ensuring $|u_1| \leq u_1^m$. However, this Δ^* will lead to sharp

acceleration when there are large initial errors. To ensure smooth motion, a new Δ^* is designed in this paper as:

$$\Delta^* = \frac{1}{2}(u_1^m + V_d) - V_d \tanh \frac{V_d}{\sigma} \quad (17)$$

The schematic of \check{k}_1 as a function of $|x_e|$ is plotted in Fig. 1.

Recall that we expect y_e to vary along y_e^d , \check{k}_2 can be designed as a function of V_d to compensate the influence of the forward speed on tracking results. For simplicity, \check{k}_2 is set as proportional to V_d :

$$\check{k}_2 = \alpha V_d, \quad \alpha > 0 \quad (18)$$

Based on the designed adaptive gains of \check{k}_1 and \check{k}_2 , the new input vector $\mathbf{u}^c = [u_1^c, u_2^c]^T$ is obtained as:

$$u_1^c = V_d \cos \psi_e + \check{k}_1(|x_e|)x_e \quad (19)$$

and

$$u_2^c = \tan^{-1} \left\{ \frac{l[k_3(y_e + \alpha \sin \psi_e) + 2V_d \sin \psi_e + \alpha \cos \psi_e \dot{\psi}_d]}{u_1^c(x_e + \alpha \cos \psi_e)} \right\} \quad (20)$$

Noted that both \check{k}_2 and \dot{V}_d disappeared because of algebraic simplification by selecting \check{k}_2 according to (18). While $u_1^c \leq u_1^m$ is always satisfied, adjusting k_3 alone cannot guarantee that the steering angle will not violating the constraint. Steering saturation is thus included, the final control laws are given by:

$$u_1 = u_1^c \quad (21)$$

and

$$u_2 = \begin{cases} u_2^c, & \text{if } |u_2^c| < u_2^m \\ u_2^m, & \text{if } u_2^c \geq u_2^m \\ -u_2^m, & \text{if } u_2^c \leq -u_2^m \end{cases} \quad (22)$$

to achieve acceptable trajectory tracking results for car-like autonomous vehicles. For low-speed car-like autonomous vehicles, using the control laws given by (21) and (22) will result in an approximate globally asymptotically stable equilibrium at $(x_e, y_e, \psi_e) = (0, 0, 0)$ for $V_d > 0$ and $|\psi_e| < \pi$. Details about the proof are referred to [6]. When the steering saturation is considered, the globally asymptotically stable region is quite large, although the accurate determination may be difficult.

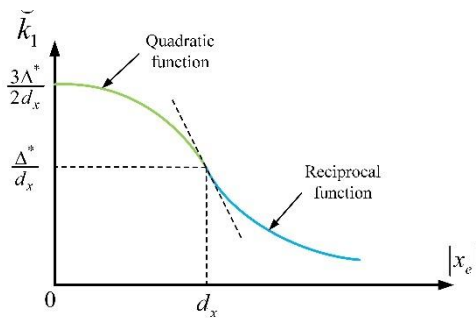


Figure 1. Variation of \check{k}_1 as a function of $|x_e|$

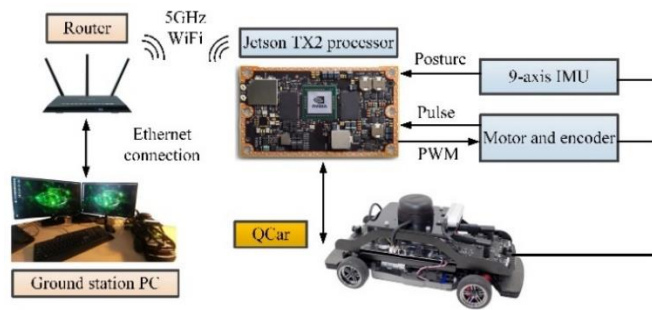


Figure 2. The schematic of the Quanser self-driving car (QCar) experiment setup

4. Experimental Results

To verify the effectiveness of the proposed control scheme in practice, experimental tests have been conducted on the Quanser self-driving car (QCar) platform. For the sake of comparative study, the performances of the controller in [5] (Controller I) and the controller in [6] (Controller II) were also investigated. To achieve acceptable tracking results, the control gains of Controller I was tuned as $[1.65, 1.65, 1.65]'$, the control parameters $\sigma = 0.3$, $\alpha = 0.75$ and $k_3 = 1.65$ are set the same for Controller II and the proposed controller. d_x was set at 1 m and 0.6 m for Controller II and the proposed controller, respectively. The QCar test videos can be viewed at <https://youtu.be/pqm3rxNFRHg> in our NAV Lab's website.

4.1 Experimental Setup

The schematic of the experimental setup is illustrated in Fig. 2. The key parameters of the QCar are listed as follows: $l = 0.256\text{ m}$, $u_1^m = 1.5\text{ m}$ and $u_2^m = 0.5\text{ rad}$. The motion of the QCar is controlled by a drive and steering servo motor, and an encoder measurement is also available. The onboard 9-axis inertial measurement unit (IMU) is used to obtain the real-time posture of the QCar. The onboard processor receives the commanded inputs from the ground station PC, sends the data collected from the IMU and the motor encoder to the ground station through Wi-Fi wireless communication, and generates appropriate pulse-width modulation (PWM) signal to the servo motor.

4.2 QCar Test Results

In the experiment, an S-shape trajectory was chosen as the reference trajectory. The equation of this trajectory was given as:

$$\begin{cases} X_d(t) &= 0.7 + 0.8 \sin(0.4t + 0.1) \\ Y_d(t) &= -2.2 + 2.2 \cos(0.2t + 0.1) \end{cases} \quad (23)$$

The reference speed V_d , yaw angle ψ_d and yaw rate $\dot{\psi}_d$ can all be obtained from (23). The initial posture of the QCar was $[-0.128, 0, 0]'$, and the large initial errors were calculated as $[0.908, -0.011, -0.137]'$.

The trajectory tracking results are presented in Fig. 3. The three controllers have shown similar tracking performances in longitudinal position error. While the proposed controller illustrates advantage in eliminating the lateral position error, it has the largest yaw angle error during the first turn. This is a slight sacrifice in order to achieve smooth accelerating for the proposed controller. However, the proposed controller has smaller tracking errors in lateral position and yaw angle during the second turn, as can be seen in Figs. 3(b) and 3(c). The resulting trajectories of the QCar are plotted in Fig. 3(d). The trajectory tracking performance of the Controller I is the worst, leaving an obvious deviation with the reference trajectory between the first and the second turn. By contrast, the proposed controller achieves high accuracy in trajectory tracking, which is comparable to the Controller II.

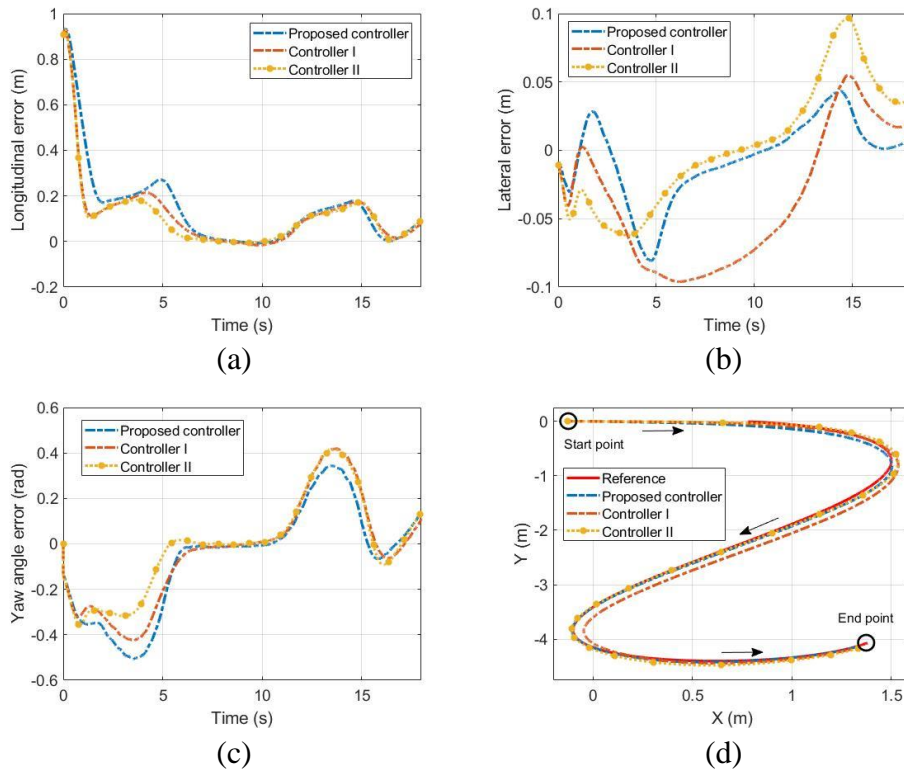


Figure 3. Tracking results of the S-shape trajectory with large initial errors

The commanded inputs of the three controllers are shown in Fig. 4. Due to large initial errors, the commanded velocity of Controller I and Controller II has both experienced a sharp increase to nearly the maximum speed at about 1 s. This may lead to very uncomfortable feeling in real driving. In contrast, the commanded velocity from the proposed controller varies smoothly with a much smaller peak value (less than 1 m/s). While the commanded steering angle of the proposed controller and the Controller II are guaranteed within the boundaries, the Controller I generates a steering angle exceeding the upper limit at the second turn, as can be seen in Fig. 4(b). It is worth noting that the proposed controller achieves comparable tracking performances with the Controller II, while at the same time ensuring a smooth motion of the vehicle. This is evident to see in Fig. 4(a).

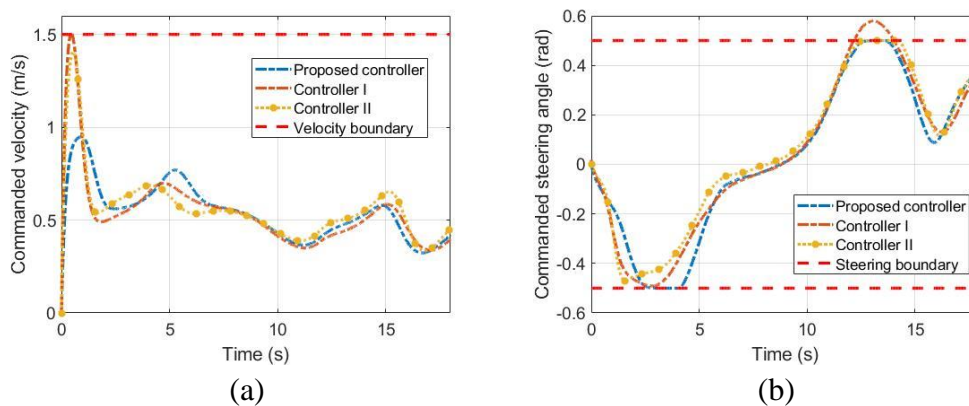


Figure 4. Commanded inputs for tracking the S-shape trajectory with large initial errors

5. Conclusion

This paper proposes an adaptive trajectory tracking control scheme for low-speed autonomous vehicles. The design of adaptive control gains and consideration of steering saturation are combined within the backstepping control technique. As control gains are designed to be adaptive to tracking error and reference speed, the demanded tuning efforts, which are generally neglected by the conventional methods, have reasonably reduced. Moreover, the proposed control scheme is able to address input constraints and to ensure smooth acceleration, while in the meanwhile enhancing the convergence rate of tracking errors. Experimental comparative results have shown the advantages and effectiveness of the proposed control scheme in trajectory tracking.

Acknowledgments

This work was partially supported by the Natural Sciences and Engineering Research Council of Canada (NSERC). The authors would like to thank the state-of-the-art self-driving car platform QCar from Quanser Inc., the technical and all supports from Quanser which make the experimental testing and validation of the developed control strategies possible.

References

- [1] Wu, X. *et al.*, (2019), "Backstepping trajectory tracking based on fuzzy sliding mode control for differential mobile robots", *Journal of Intelligent & Robotic Systems*, Vol. 96, No. 1, pp.109-121.
- [2] Mirzaeinejad, H. (2019), "Optimization-based nonlinear control laws with increased robustness for trajectory tracking of non-holonomic wheeled mobile robots", *Transportation Research Part C: Emerging Technologies*, Vol. 101, pp.1-17.
- [3] Lombard, A. *et al.*, (2020), "Curvature-based geometric approach for the lateral control of autonomous cars", *Journal of the Franklin Institute*, Vol. 357, No. 14, pp.9378-9398.
- [4] Setlur, P. *et al.*, (2006), "A trajectory tracking steer-by-wire control system for ground vehicles", *IEEE Transactions on Vehicular Technology*, Vol. 55, No. 1, pp.76-85.
- [5] Fang, H. *et al.*, (2006), "Trajectory tracking control of farm vehicles in presence of sliding", *Robotics and Autonomous Systems*, Vol. 54, No. 10, pp.828-839.
- [6] Hu, J. *et al.*, (2021), "Adaptive trajectory tracking for car-like vehicles with input constraints", *IEEE Transactions on Industrial Electronics* (Early Access), Date of Publication: Mar. 30, 2021. (DOI: 10.1109/TIE.2021.3068672).

Connectivity Maintenance Control for Multiple UAVs with Input SaturationXianghong Xue¹, Youmin Zhang^{2,*}, and Lingxia Mu¹¹Xi'an University of Technology, Xi'an, Shaanxi 710048, China²Concordia University, Montreal, Quebec H3G 1 M8, Canada

*Corresponding author. E-mail: youmin.zhang@concordia.ca

Abstract

The connectivity of the multi-UAV network is essential for distributed coordination control of multiple UAVs. However, the range limitation of communication links among UAVs, mixed with the UAVs' relative movements, creates a potential threat to disconnect the network. This paper studies connectivity maintenance controller design for multiple UAVs in the presence of input saturation. It is assumed that all UAVs can only obtain the states of their neighbors within their communication range. The multi-UAV network is modeled via a distance-induced proximity graph. A distributed controller with an indirect couplings control framework and a bounded artificial potential function is proposed. The framework endows each agent with a virtual proxy and couples initially adjacent agents through their virtual proxies. The UAV-proxy couplings address the actuator saturation constraints and make the UAV converge to its corresponding virtual proxy. The inter-proxy bounded artificial potential function is used to maintain the connectivity of the network and fulfill the coordination of all virtual proxies. Numerical simulations validate the effectiveness of the anti-saturation distributed connectivity maintenance controller.

Keywords: Unmanned aerial vehicle, Distributed coordination control, Connectivity maintenance, Input saturation

Nomenclature

\mathcal{F}_I	=	the inertial frame
\mathcal{F}_{B_i}	=	the body frame of the i -th UAV
\mathbf{p}_i	=	position of the i -th UAV with respect to \mathcal{F}_I
$\dot{\mathbf{p}}_i$	=	velocity of the i -th UAV with respect to \mathcal{F}_I
g	=	gravitational acceleration
\mathcal{G}	=	proximity graph
\mathcal{V}	=	vertex set of proximity graph \mathcal{G}
\mathcal{E}	=	edge set of proximity graph \mathcal{G}
\mathbf{A}	=	adjacency matrix of proximity graph \mathcal{G}
\mathbf{L}	=	Laplacian matrix of proximity graph \mathcal{G}
Δ	=	communication distance
\mathbf{u}_i	=	virtual control input
Φ	=	artificial potential function
$\hat{\mathbf{p}}_i$	=	the position of the i -th virtual proxy

1. Introduction

Formation control of multiple unmanned aerial vehicles (multi-UAVs) has received increasing attention due to its potential applications in remote sensing, search and rescue, real-time monitoring, surveillance, and so on (Shakhathreh *et al.*, 2019; Skorobogatov *et al.*, 2020). In the

past decades, the research interest of formation control methods is gradually shifting from centralized and decentralized control to distributed control (Chung, Paranjape *et al.*, 2018; Liu and Bucknall, 2018). Nevertheless, the distributed control of multi-UAVs is challenging since each UAV can only access its neighbors' information.

To realize distributed control of multi-UAVs, the communication network should be connected. In practice, the limited communication range, combined with the movements of UAVs, created a potential to destroy the connectivity of the network. Therefore, connectivity maintenance of the network must be taken into consideration during the design of distributed controllers of multi-UAVs. Connectivity maintenance has been widely studied in multi-agent systems during the last decade (Zavlanos and Pappas, 2007; Stephan *et al.*, 2017). Typical connectivity maintenance methods can be divided into local and global methods (Khateri *et al.*, 2019). The positive of a graph's algebraic connectivity is a typical metric to indicate that the graph is connected. The global methods preserve connectivity by maximizing algebraic connectivity of the network (Kim and Mesbahi, 2006; Qu *et al.*, 2014; Fang *et al.*, 2016). The local methods maintain the connectivity of the communication network through the interaction of local position and velocity information between agents (Ji and Egerstedt, 2007). These methods are mostly implemented by artificial potential functions (Cao and Ren, 2012). Recently, a local connectivity maintenance controller for multi-quadrotor aircraft was proposed (Cong *et al.*, 2020). However, the literature did not consider actuator input saturation.

The challenge now is to design distributed controllers for UAVs in consideration of connectivity maintenance under bounded actuation. Inspired by the literature (Wen *et al.*, 2012; Li *et al.*, 2013; Yang *et al.*, 2018), this paper proposes a distributed controller with indirect couplings and bounded artificial potential function. Firstly, the communication graph between UAVs is defined according to the relative distances between all UAVs. Then, a local second-order virtual proxy is designed for each UAV. The virtual proxy and the UAV are coupled with a saturated P+d controller. Moreover, a bounded artificial potential function is presented to achieve coordination of the adjacent virtual proxies. Finally, numerical simulations confirm the effectiveness of the anti-saturation distributed connectivity maintenance controller.

2. Preliminaries and Problem Statement

Consider two reference frames: 1) The inertial frame $\mathcal{F}_I = \{O_I x_I y_I z_I\}$ whose origin O_I is fixed at a point on the ground. The i -th UAV's position $\mathbf{p}_i = [p_{ix}, p_{iy}, p_{iz}]^\top$ and the velocity $\dot{\mathbf{p}}_i = [\dot{p}_{ix}, \dot{p}_{iy}, \dot{p}_{iz}]^\top$ are described in the inertial frame \mathcal{F}_I . The angular velocity of the i -th UAV in frame \mathcal{F}_{B_i} is denoted by $\boldsymbol{\omega}_i = [\omega_{ix}, \omega_{iy}, \omega_{iz}]^\top$. The rotation matrix $\mathbf{R}_i \in SO(3)$ is used to represent the i -th UAV's attitude. Then, the position dynamics of i -th UAV's can be described as (Zou and Meng, 2018)

$$m_i \ddot{\mathbf{p}}_i = -\mathbf{C}_i \dot{\mathbf{p}}_i - m_i g \mathbf{e}_3 + \mathbf{T}_i \mathbf{R}_i \mathbf{e}_3, \quad (11)$$

where m_i denotes the total mass of the i -th UAV, $\mathbf{C}_i = \text{Diag}(C_{i,1}, C_{i,2}, C_{i,3})$ represents the aerodynamic damping coefficients, and $\mathbf{e}_3 = [0, 0, 1]^\top$, $g = 9.81 \text{ m/s}^2$, \mathbf{T}_i is the total lift generated by the four propellers.

It can be found that the position dynamics is related with the attitude. In order to facilitate the design of the position controller, denote $\mathbf{u}_i = \mathbf{T}_i \mathbf{R}_i \mathbf{e}_3 - m_i g \mathbf{e}_3$, the position dynamics can be rewritten as

$$m_i \ddot{\mathbf{p}}_i = -\mathbf{C}_i \dot{\mathbf{p}}_i + \mathbf{u}_i. \quad (12)$$

The dynamic communication network between all UAVs can be modeled by distance-induced proximity graph. A proximity graph is denoted as $\mathcal{G}(\mathcal{V}, \mathcal{E})$, where $\mathcal{V} = \{1, 2, \dots, N\}$ denotes the vertex set and $\mathcal{E} \subset \mathcal{V} \times \mathcal{V}$ denotes the edge set. A path of \mathcal{G} is defined as an edge sequence $(i_1, i_2), (i_2, i_3), \dots$, where $(i_k, i_{k+1}) \in \mathcal{E} (k = 1, 2, \dots)$. A graph \mathcal{G} is called a connected graph if there is a path between any two vertices in \mathcal{V} (Mesbahi and Egerstedt, 2010). The vertex set represents the UAVs, and the edge set represents the communication relationship between the UAVs. Suppose all UAVs have the same sensing distance Δ . If the distance between the i -th UAV and the j -th UAV is smaller than Δ , then $(i, j) \in \mathcal{E}$. Then, the corresponding adjacency matrix $\mathbf{A}(\mathcal{G}) = [a_{ij}] \in \mathbb{R}^{N \times N}$ is defined as: $a_{ij} = 1$, if $(i, j) \in \mathcal{E}$; $a_{ij} = 0$, otherwise. The adjacency matrix $\mathbf{A}(\mathcal{G})$ can also be written as follows:

$$a_{ij}(t) = \begin{cases} 1, & \text{if } \|\mathbf{p}_{ij}(t)\| \leq \bar{\Delta}, i, j \in \mathcal{V}, \\ 0, & \text{otherwise,} \end{cases}$$

where $\mathbf{p}_{ij}(t) = \mathbf{p}_i(t) - \mathbf{p}_j(t)$, and $\bar{\Delta} = \Delta - \nu$ where $\nu > 0$ is a small constant.

The Laplacian matrix $\mathbf{L}(\mathcal{G}) = [l_{ij}] \in \mathbb{R}^{N \times N}$ is defined as: $l_{ij} = \sum_{j=1}^N a_{ij}$, if $i = j$; $l_{ij} = -a_{ij}$, if $i \neq j$.

Lemma 1. The Laplacian matrix $\mathbf{L}(\mathcal{G})$ is positive semidefinite if the graph \mathcal{G} is connected (Mesbahi and Egerstedt, 2010).

Assumption 1. The initial graph $\mathcal{G}(0)$ generated according to equation (4) is a connected graph.

Assumption 2. The desired formation \mathbf{p}_d satisfies the following conditions

$$d_{ij} < \Delta, \forall i \in \{1, \dots, N\}, j \in \mathcal{N}_i,$$

where $d_{ij} = \|\mathbf{p}_i^d - \mathbf{p}_j^d\|$ represents the desired distance between i -th UAV and j -th UAV.

Assumption 3. The saturation bound is enough to balance the gravity item $m_i g$ in equation (2), i.e., $\|m_i g \mathbf{e}_3\| \leq \bar{\mathbf{u}}_i$, where $\bar{\mathbf{u}}_i$ is the saturation bound for each UAV's control input.

Assumption 4. All UAVs are initially at rest, i.e., $\dot{\mathbf{p}}_i(0) = 0$.

Remark 1. From the results in (Wen *et al.*, 2012; Yang, Constantinescu and Shi, 2018) one knows that Assumptions 1 and 3 are mild and reasonable. Assumption 2 is also used in (Li *et al.*, 2013), which ensures the desired formation is reachable. It is generally infeasible for bounded control input to preserve the connectivity of a second-order system. An example is shown in (Yang *et al.*, 2018). Therefore, Assumption 4 is reasonable.

The objective of this paper is to design connectivity maintenance control laws \mathbf{u}_i with input saturation so that: 1) $\|\mathbf{p}_{ij}(t)\| \rightarrow d_{ij}, (i, j) \in \mathcal{E}, \dot{\mathbf{p}}_i(t) \rightarrow 0, i = 1, 2, \dots, N$ as $t \rightarrow \infty$ (i.e., the desired formation); 2) If $\|\mathbf{p}_{ij}(0)\| < \bar{\Delta}$, then $\|\mathbf{p}_{ij}(t)\| < \Delta, \forall t > 0, (i, j) \in \mathcal{E}$ (i.e., the initial connectivity maintenance).

3. Coordination Controller Design with Bounded Actuation

In this section, an indirect coupling framework coordination controller is proposed: 1) A virtual proxy with velocity-error damping is designed for each UAV; 2) the proxies are interconnected according to the communication relationship between the corresponding UAVs. The virtual proxy dynamics for i -th UAV is designed as

$$\begin{aligned} \hat{\boldsymbol{p}}_i(0) &= \boldsymbol{p}_i(0), \dot{\hat{\boldsymbol{p}}}_i(0) = 0, i = 1, \dots, N, \\ \ddot{\hat{\boldsymbol{p}}}_i &= \text{Sat}_i(\alpha_i \tilde{\boldsymbol{p}}_i) - \sum_{j=1}^N \alpha_{ij} \nabla_i \Phi(\|\hat{\boldsymbol{p}}_{ij}\|) - \beta_i \dot{\hat{\boldsymbol{p}}}_i, \end{aligned} \quad (13)$$

where $\hat{\boldsymbol{p}}_i$ denotes the position of the proxy of i -th UAV, $\tilde{\boldsymbol{p}}_i = \boldsymbol{p}_i - \hat{\boldsymbol{p}}_i$ represents the error between the UAV and its proxy, α_i and β_i are positive constant, $\text{Sat}_i(\boldsymbol{x})$ is a function saturates \boldsymbol{x} component-wise with the bound $\bar{\boldsymbol{u}}_i^k, k = 1, 2, 3$.

The bounded artificial potential function $\Phi(\|\hat{\boldsymbol{p}}_{ij}\|)$ is given as

$$\Phi(\|\hat{\boldsymbol{p}}_{ij}\|) = \begin{cases} P\Phi^f(\|\hat{\boldsymbol{p}}_{ij}\|), & \text{if } \|\hat{\boldsymbol{p}}_{ij}\| \in [0, d_{ij}], \\ P\Phi^c(\|\hat{\boldsymbol{p}}_{ij}\|), & \text{if } \|\hat{\boldsymbol{p}}_{ij}\| \in [d_{ij}, \hat{\Delta}], \end{cases} \quad (14)$$

where the formation potential function $\Phi^f(\|\hat{\boldsymbol{p}}_{ij}\|)$ and the connectivity maintenance potential function $\Phi^c(\|\hat{\boldsymbol{p}}_{ij}\|)$ are given as (Wen *et al.*, 2012)

$$\begin{aligned} \Phi^f(\|\hat{\boldsymbol{p}}_{ij}\|) &= \frac{(\|\hat{\boldsymbol{p}}_{ij}\| - d_{ij})^2 (\hat{\Delta} - \|\hat{\boldsymbol{p}}_{ij}\|)}{\|\hat{\boldsymbol{p}}_{ij}\| + \frac{d_{ij}^2 (\hat{\Delta} - \|\hat{\boldsymbol{p}}_{ij}\|)}{Q}}, \\ \Phi^c(\|\hat{\boldsymbol{p}}_{ij}\|) &= \frac{\|\hat{\boldsymbol{p}}_{ij}\| (\|\hat{\boldsymbol{p}}_{ij}\| - d_{ij})^2}{(\hat{\Delta} - \|\hat{\boldsymbol{p}}_{ij}\|) + \frac{\|\hat{\boldsymbol{p}}_{ij}\| (\hat{\Delta} - d_{ij})^2}{Q}} \end{aligned}$$

where $\hat{\Delta} = \Delta - \epsilon, \epsilon > 0$ is a small constant.

Remark 2. It is easy to verify that the potential function Φ monotonically increases in regard to $\|\hat{\boldsymbol{p}}_{ij}\|$ while $\|\hat{\boldsymbol{p}}_{ij}\| \in (d_{ij}, \hat{\Delta})$, and monotonically decreases while $\|\hat{\boldsymbol{p}}_{ij}\| \in (0, d_{ij})$. Therefore, the potential function reaches its only minimum value while $\|\hat{\boldsymbol{p}}_{ij}\| = d_{ij}$.

Remark 3. By the triangle inequality $\|\boldsymbol{p}_{ij}\| \leq \|\tilde{\boldsymbol{p}}_i\| + \|\hat{\boldsymbol{p}}_{ij}\| + \|\tilde{\boldsymbol{p}}_j\|$, it is enough to ensure $\|\boldsymbol{p}_{ij}\| \leq (0, \Delta), (i, j) \in \mathcal{E}$ while the following inequalities holds

$$\|\hat{\boldsymbol{p}}_{ij}\| \leq \hat{\Delta}, \|\tilde{\boldsymbol{p}}_i\| \leq \epsilon/2, \|\tilde{\boldsymbol{p}}_j\| \leq \epsilon/2. \quad (15)$$

Lemma 2. The virtual energy stored between i -th UAV and its virtual proxy is defined as

$$\psi_i(\tilde{\boldsymbol{p}}_i) = \int_0^{\tilde{\boldsymbol{p}}_i} \text{Sat}_i(\alpha_i \boldsymbol{\sigma})^\top d\boldsymbol{\sigma}. \quad (16)$$

Then, the function has the following properties (Yang *et al.*, 2019)

(i) $\psi_i(\tilde{\boldsymbol{p}}_i)$ is a convex function.

(ii) Within the domain $B(\mathbf{0}, (\epsilon/2)) = \{\tilde{\boldsymbol{p}}_i \mid \|\tilde{\boldsymbol{p}}_i\| \leq (\epsilon/2)\}$, $\psi_i(\tilde{\boldsymbol{p}}_i)$ achieves its maximum while $\|\tilde{\boldsymbol{p}}_i\| = (\epsilon/2)$ and its minimum while $\|\tilde{\boldsymbol{p}}_i\| = 0$.

(iii) Let

$$\psi_i^{\min} = \min_{\tilde{\mathbf{p}}_i} \psi_i(\tilde{\mathbf{p}}_i) = \int_0^{\tilde{p}_i} \text{Sat}_i(\alpha_i \sigma)^\top d\sigma, \text{ s.t. } \|\tilde{\mathbf{p}}_i\| = \frac{\epsilon}{2}. \quad (17)$$

If $\psi_i(\tilde{\mathbf{p}}_i) \leq \psi_i^{\min}$, then $\tilde{\mathbf{p}}_i \in B(\mathbf{0}, (\epsilon/2))$.

Theorem 1. Given a system with dynamics (2) and Assumptions 1-4, if the virtual control inputs are designed as follows:

$$\mathbf{u}_i = -\text{Sat}_i(\alpha_i \tilde{\mathbf{p}}_i) + m_i g \mathbf{e}_3. \quad (18)$$

Denote $M = |\mathcal{E}(0)|$, and let Q and P satisfy

$$Q \geq M\Phi(\bar{\Delta}), P = \frac{\min_{i=1,\dots,N} \{\psi_i^{\min}\}}{Q}. \quad (19)$$

One has the following results

- (i) $\|\mathbf{p}_{ij}(t)\| \rightarrow d_{ij}, (i, j) \in \mathcal{E}, \dot{\mathbf{p}}_i(t) \rightarrow 0, i = 1, 2, \dots, N$ as $t \rightarrow \infty$.
- (ii) If $\|\mathbf{p}_{ij}(0)\| < \bar{\Delta}$, then $\|\mathbf{p}_{ij}(t)\| < \Delta, \forall t > 0, (i, j) \in \mathcal{E}$.

Proof. Choose the Lyapunov function $V_1 = \frac{1}{2} \sum_{i=1}^N (\dot{\mathbf{p}}_i^\top m_i \dot{\mathbf{p}}_i + \hat{\mathbf{p}}_i^\top \dot{\mathbf{p}}_i)$. Taking the derivative of it and using (2), (3) and (8) yield that

$$\dot{V}_1(t) = -\sum_{i=1}^N \hat{\mathbf{p}}_i^\top \text{Sat}_i(\alpha_i \tilde{\mathbf{p}}_i) - \sum_{i=1}^N \hat{\mathbf{p}}_i^\top \sum_{j=1}^N a_{ij} \nabla_i \Phi(\|\hat{\mathbf{p}}_{ij}\|) - \beta_i \sum_{i=1}^N \hat{\mathbf{p}}_i^\top \dot{\mathbf{p}}_i. \quad (20)$$

Consider the Lyapunov function $V_2 = \frac{1}{2} \sum_{i=1}^N \sum_{j=1}^N a_{ij} \Phi(\|\hat{\mathbf{p}}_{ij}\|) + \sum_{i=1}^N \psi_i(\tilde{\mathbf{p}}_i)$. Its time derivative along (4) and (6) can be written as

$$\begin{aligned} \dot{V}_2(t) &= \frac{1}{2} \sum_{i=1}^N \sum_{j=1}^N a_{ij} [\nabla_i \Phi(\|\hat{\mathbf{p}}_{ij}\|) \dot{\mathbf{p}}_i + \nabla_j \Phi(\|\hat{\mathbf{p}}_{ij}\|) \dot{\mathbf{p}}_j] + \sum_{i=1}^N \hat{\mathbf{p}}_i^\top \text{Sat}_i(\alpha_i \tilde{\mathbf{p}}_i) \\ &= \sum_{i=1}^N \sum_{j=1}^N a_{ij} \nabla_i \Phi(\|\hat{\mathbf{p}}_{ij}\|) \dot{\mathbf{p}}_i + \sum_{i=1}^N \hat{\mathbf{p}}_i^\top \text{Sat}_i(\alpha_i \tilde{\mathbf{p}}_i). \end{aligned} \quad (21)$$

Consider the total Lyapunov function candidate

$$V = V_1 + V_2, \quad (22)$$

its derivative of V yields

$$\begin{aligned} \dot{V}(t) &= -\sum_{i=1}^N \hat{\mathbf{p}}_i^\top \text{Sat}_i(\alpha_i \tilde{\mathbf{p}}_i) - \sum_{i=1}^N \hat{\mathbf{p}}_i^\top \sum_{j=1}^N a_{ij} \nabla_i \Phi(\|\hat{\mathbf{p}}_{ij}\|) - \beta_i \sum_{i=1}^N \hat{\mathbf{p}}_i^\top \dot{\mathbf{p}}_i \\ &\quad + \sum_{i=1}^N \sum_{j=1}^N a_{ij} \nabla_i \Phi(\|\hat{\mathbf{p}}_{ij}\|) \dot{\mathbf{p}}_i + \sum_{i=1}^N \hat{\mathbf{p}}_i^\top \text{Sat}_i(\alpha_i \tilde{\mathbf{p}}_i) \\ &= -\beta_i \sum_{i=1}^N \hat{\mathbf{p}}_i^\top \dot{\mathbf{p}}_i. \end{aligned} \quad (23)$$

Therefore, $\dot{V}(t) \leq 0$ and $V(t) \leq V(0)$. It can be concluded that $\dot{\mathbf{p}}_i, \Phi(\hat{\mathbf{p}}_i), \psi(\tilde{\mathbf{p}}_i) \in \mathcal{L}_\infty$ and $\hat{\mathbf{p}}_i \in \mathcal{L}_2 \cap \mathcal{L}_\infty$. Thus, $\hat{\mathbf{p}}_i \rightarrow 0$ as $t \rightarrow \infty$. Since $\Phi(\hat{\mathbf{p}}_i)$ is continuously differentiable and bounded, we have $\nabla_i \Phi(\hat{\mathbf{p}}_i) \in \mathcal{L}_\infty$. Taking the derivative of equation (3) implies that $\ddot{\mathbf{p}}_i \in \mathcal{L}_\infty$ and $\ddot{\mathbf{p}}_i \rightarrow \mathbf{0}$. The secondary derivative of equation (5) further implies $\dot{\mathbf{p}}_i \rightarrow 0$. Therefore, $\dot{\mathbf{p}}_i \rightarrow \mathbf{0}, \nabla_i \Phi(\|\hat{\mathbf{p}}_i\|) \rightarrow \mathbf{0}, (i, j) \in \mathcal{E}$ and $\|\hat{\mathbf{p}}_i\| \rightarrow d_{ij}$. By noting $\ddot{\mathbf{p}}_i \rightarrow \mathbf{0}$ and $\dot{\mathbf{p}}_i \rightarrow \mathbf{0}$, equation (3) leads to $\tilde{\mathbf{p}}_i \rightarrow \mathbf{0}$. Overall, $\|\mathbf{p}_i\| \rightarrow d_{ij}, (i, j) \in \mathcal{E}$, i.e., the desired configuration is achieved. This completes the proof of (i).

Using the initial configuration given in equation (3) and Assumption 4, we have $V_1(0) = 0$ and $\psi_i(\tilde{\mathbf{p}}_i(0)) = 0$, for $i = 1, \dots, N$. Using (9), the Lyapunov function V yields

$$\begin{aligned} V(0) &= \frac{1}{2} \sum_{i=1}^N \sum_{j=1}^N a_{ij} \Phi(\|\hat{\mathbf{p}}_{ij}\|) < M\Phi(\bar{\Delta}) \\ &\leq \Phi(\hat{\Delta}) = PQ = \psi^{\min}. \end{aligned} \quad (24)$$

As $V(t) \leq V(0)$, it is obtained

$$V_2(t) \leq V(t) \leq V(0) < \Phi(\hat{\Delta}) = PQ = \psi^{\min}. \quad (25)$$

Suppose the maximum distance among all initial connected edges is $\|\hat{\mathbf{p}}_{lm}(t)\| = \hat{\Delta}$. This implies $V_p(t) \geq \Phi(\|\hat{\mathbf{p}}_{lm}(t)\|) = PQ$, which contradicts with equation (14). Therefore, all distances $\|\hat{\mathbf{p}}_{ij}(t)\| < \hat{\Delta}$, $(i, j) \in \mathcal{E}$. Using $\Phi(\|\hat{\mathbf{p}}_{ij}\|) \geq 0$ and (14), it is obtained that $\psi_i(\tilde{\mathbf{p}}_i) \leq \psi^{\min}$. Thus, from the property (3) of Lemma 2, it holds that $\|\tilde{\mathbf{p}}_i(t)\| \leq (\epsilon/2)$. Therefore, we have $\|\mathbf{p}_{ij}\| \leq \|\hat{\mathbf{p}}_{ij}\| + \|\tilde{\mathbf{p}}_i\| + \|\tilde{\mathbf{p}}_j\| \leq \hat{\Delta} + 2 \cdot (\epsilon/2) \leq \Delta$. This completes the proof of (ii).

Remark 4. In this article, in order to facilitate the analysis, we didn't consider the attitude dynamics of the UAVs. However, the attitude controllers to generate the virtual control inputs are given in (Kendoul *et al.*, 2010; Cong *et al.*, 2020).

4. Simulations

To confirm the effectiveness of the proposed controller, a simulation with three UAVs is presented in this section. The quality of all UAVs is $m_i = 0.5$ kg, $i = 1, 2, 3$. The aerodynamic damping coefficients are chosen as $\mathbf{C}_i = \text{Diag}(0.01, 0.01, 0.01)$. The initial positions of three UAVs are $\mathbf{p}_1(0) = [-10, -5, 0]^T$ m, $\mathbf{p}_2(0) = [0, 10, 0]^T$ m, $\mathbf{p}_3(0) = [5, 20, 0]^T$ m, the velocities are $\dot{\mathbf{p}}_i(0) = [0, 0, 0]^T$ (m/s), $i = 1, 2, 3$. The communication radius of each UAVs is set as $\Delta = 35$ m, and the desired distance between all UAVs are $d_{ij} = 20$ m, $i, j = 1, 2, 3$. The maximum virtual control inputs are $\bar{u} = 6$ N. It is easy to verify that the Assumptions 1-4 are satisfied. The control gains of formation controllers (3), (4) and (8) are chosen as follows: $Q = 100000$, $P = 0.002$, $\alpha = 0.2$, $\beta = 0.1$.

Figure 1 presents the distances between three UAVs over time, where the red line represents the communication distance between the UAVs. The figure indicates that none of the distances between the UAVs have never exceeded the communication range. Therefore, the connectivity of the graph is preserved. Figure 2 demonstrates that the velocities of all three UAVs eventually converge to zero. Figure 3 presents that the distance errors between the UAVs and its virtual proxy UAVs are not more than 1.2 m, and they finally converge to zero. Figure 4 shows that the velocity errors between the UAVs and their corresponding virtual proxies also eventually converge to zero.

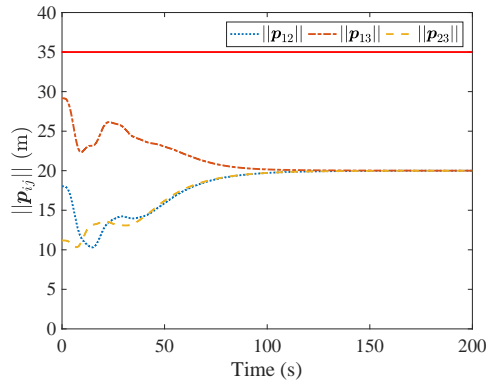


Figure 1. The distances between all UAVs

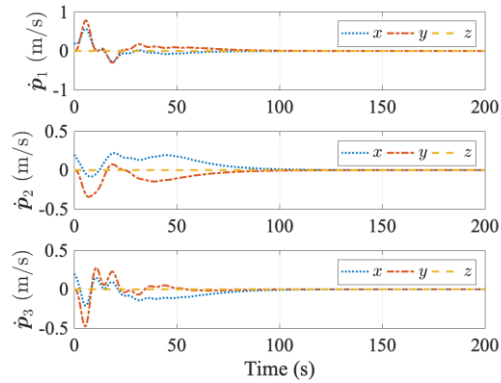


Figure 2. The velocities of UAVs

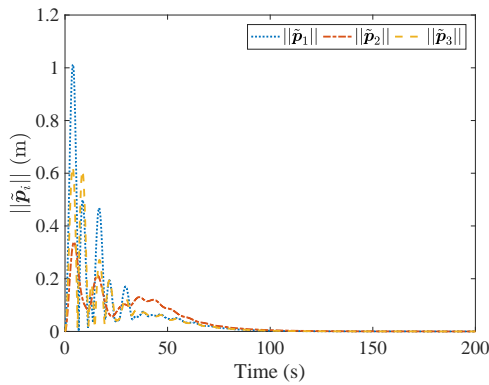


Figure 3. The UAV-proxy distance errors

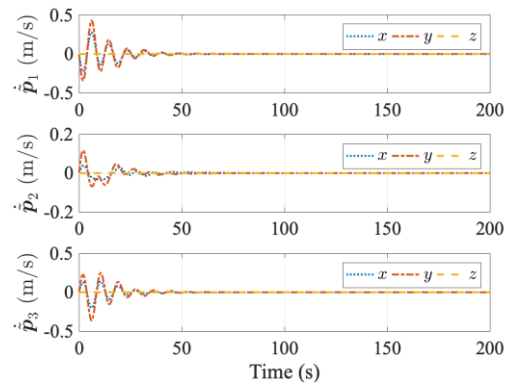


Figure 4. The UAV-proxy velocity errors

5. Conclusions

In this paper, a new connectivity maintenance controller has been developed for multiple UAVs in the presence of input saturation. Using an indirect coupling strategy with a bounded artificial potential function, the controller overcomes the actuator saturation constraints of the inputs. Stability analysis has shown that the position of all UAVs can converge to their desired formation. In future work, we will study the connectivity maintenance of a directed graph in the presence of actuator saturation.

Acknowledgments

This work was supported in part by the National Natural Science Foundation of China (Nos. 61833013 and 61903297) and the Natural Sciences and Engineering Research Council of Canada.

References

- [1] Cao, Y. and Ren, W. (2012), “Distributed coordinated tracking with reduced interaction via a variable structure approach”, IEEE Transactions on Automatic Control, Vol. 57, No. 1, pp. 33-48.
- [2] Chung, S.-J., Paranjape, A. A., Dames, P., Shen, S. and Kumar, V. (2018), “A survey on aerial swarm robotics”, IEEE Transactions on Robotics, Vol. 34, No. 4, pp. 837-855.
- [3] Cong, Y., Du, H., Jin, Q., Zhu, W. and Lin, X. (2020), “Formation control for

multiquadrotor aircraft: Connectivity preserving and collision avoidance”, *International Journal of Robust and Nonlinear Control*, Vol. 30, No. 6, pp. 2352-2366.

[4] Fang, H., Wei, Y., Chen, J. and Xin, B. (2016), “Flocking of second-order multiagent systems with connectivity preservation based on algebraic connectivity estimation”, *IEEE Transactions on Cybernetics*, Vol. 47, No. 4, pp. 1067-1077.

[5] Ji, M. and Egerstedt, M. (2007), “Distributed coordination control of multiagent systems while preserving connectedness”, *IEEE Transactions on Robotics*, Vol. 23, No. 4, pp. 693-703.

[6] Kendoul, F., Yu, Z. and Nonami, K. (2010), “Guidance and nonlinear control system for autonomous flight of minirotorcraft unmanned aerial vehicles”, *Journal of Field Robotics*, Vol. 27, No. 3, pp. 311-334.

[7] Khateri, K., Pourgholi, M., Montazeri, M. and Sabattini, L. (2019), “A comparison between decentralized local and global methods for connectivity maintenance of multi-robot networks”, *IEEE Robotics and Automation Letters*, Vol. 4, No. 2, pp. 633-640.

[8] Kim, Y. and Mesbahi, M. (2006), “On maximizing the second smallest eigenvalue of a state-dependent graph Laplacian”, *IEEE Transactions on Automatic Control*, Vol. 51, No. 1, pp. 116-120.

[9] Li, X., Sun, D. and Yang, J. (2013), “A bounded controller for multirobot navigation while maintaining network connectivity in the presence of obstacles”, *Automatica*, Vol. 49, No. 1, pp. 285-292.

[10] Liu, Y. and Bucknall, R. (2018), “A survey of formation control and motion planning of multiple unmanned vehicles”, *Robotica*, Vol. 36, No. 7, pp. 1019-1047.

[11] Mesbahi, M. and Egerstedt, M. (2010), *Graph theoretic methods in multiagent networks*, Princeton University Press, Princeton, pp. 15-16.

[12] Qu, Z., Li, C. and Lewis, F. (2014), “Cooperative control with distributed gain adaptation and connectivity estimation for directed networks”, *International Journal of Robust and Nonlinear Control*, Vol. 24, No. 3, pp. 450-476.

[13] Shakhathreh, H., Sawalmeh, A. H., Al-Fuqaha, A., Dou, Z., Almaita, E., Khalil, I., Othman, N. S., Khreishah, A. and Guizani, M. (2019), “Unmanned aerial vehicles (UAVs): A survey on civil applications and key research challenges”, *IEEE Access*, Vol. 7, pp. 48572-48634.

[14] Skorobogatov, G., Barrado, C. and Salami, E. (2020), “Multiple UAV systems: A survey”, *Unmanned Systems*, Vol. 8, No. 2, pp. 149-169.

[15] Stephan, J., Fink, J., Kumar, V. and Ribeiro, A. (2017), “Concurrent control of mobility and communication in multirobot systems”, *IEEE Transactions on Robotics*, Vol. 33, No. 5, pp. 1248-1254.

[16] Wen, G., Duan, Z., Su, H., Chen, G. and Yu, W. (2012), “A connectivity-preserving flocking algorithm for multi-agent dynamical systems with bounded potential function”, *IET Control Theory & Applications*, Vol. 6, No. 6, pp. 813-821.

[17] Yang, Y., Constantinescu, D. and Shi, Y. (2018), “Connectivity-preserving consensus of multi-agent systems with bounded actuation”, *arXiv preprint, arXiv:1803.09309*.

[18] Yang, Y., Shi, Y. and Constantinescu, D. (2019), “Connectivity-preserving synchronization of time-delay Euler-Lagrange networks with bounded actuation”, *IEEE*

Transactions on Cybernetics, Early Access, DOI: 10.1109/TCYB.2019.2914403.

[19] Zavlanos, M. M. and Pappas, G. J. (2007), “Potential fields for maintaining connectivity of mobile networks”, IEEE Transactions on Robotics, Vol. 23, No. 4, pp. 812-816.

[20] Zou, Y. and Meng, Z. (2018), “Immersion and invariance-based adaptive controller for quadrotor systems”, IEEE Transactions on Systems, Man, and Cybernetics: Systems, Vol. 49, No. 11, pp. 2288-2297.

Design and Flight of the KUBeetle Equipped with a Flapping-wing Mechanism Based on a Rack-pinion Mechanism

Gi Heon Ha¹, Hoang Vu Phan^{1,2}, Tan-Hanh Pham¹ and Hoon Cheol Park^{1,*}

¹Department of Smart Vehicle Engineering, Konkuk University, Seoul, South Korea, 05029

²Laboratory of Intelligent Systems, EPFL, Lausanne, Switzerland, 1015

*Corresponding author. E-mail: hcpark@konkuk.ac.kr

Abstract

The pulley-wire mechanism used in the flapping-wing mechanism of the KUBeetle-S, which is a tailless insect-like flapping-wing micro air vehicle (FW-MAV), is replaced with a rack-pinion mechanism for relatively easier and simpler fabrication. The robot is determined the gear ratio of the new mechanism, so that it can demonstrate similar performance to that of the previous KUBeetle. The gear ratio of 30:1 is chosen after comparing the thrusts and lift-to-power ratios of the flapping-wing mechanisms with various gear ratios. In addition, the control mechanism for stable attitude control and maneuverability of the robot is designed based on the same Stroke-Plane-Change (SPC) mechanism used in the KUBeetle-S. The 17.5 g robot fabricated by integrating the modified flapping-wing mechanism and the attitude control mechanism is named KUBeetle-RP. To guarantee flight stability, through several flight tests, the gain value of the attitude control system of the KUBeetle-RP is adjusted based on the PD control. Finally, KUBeetle-RP demonstrates a stable hovering flight for about 7 minutes.

Keywords: Insect flight, Biomimetics, Flapping-wing micro air vehicle (FW-MAV), Flapping-wing mechanism

1. Introduction

Recently, many engineers have been developing flapping-wing micro air vehicles (FW-MAV) that mimic the flight of insects. For a FW-MAV to fly, it needs to produce enough lift to overcome its weight and create control moments to maintain attitude and stability without a control surface at the tail. Due to this difficulty, only a few tailless FW-MAVs could demonstrate stable flight successfully [1-6]. KUBeetle-S [3] is recently developed. It weighs 15.8 g, drives wings with a single motor, and can fly for 8.8 minutes. The purpose of this work is to design and fabricate a flapping-wing mechanism that is easier and simpler to fabricate than that in the KUBeetle-S and then create a robot that integrates the new flapping-wing mechanism with the attitude control mechanism. Since the gear used for the reduction gear is a commercial one, there is a limitation in determining the reduction gear ratio. If a higher gear ratio is used, the size of the flapping-wing mechanism and weight will increase. Therefore, a proper gear ratio should be selected. To find a proper gear ratio that can perform similarly to the previous robot, the robot's thrust generation and lift-to-power ratios of the flapping-wing mechanisms with several gear ratios are investigated. The same attitude control mechanism used in the previous robots is adopted for stability and maneuverability. For stabilization and control, the same feedback control system in our previous robot is used. Finally, the robot demonstrated stable flight and endurance in a flight test.

2. KUBeetle-RP

2.1 Flapping-wing mechanism

The pulley-wire mechanism (Figure 1 left) applied to the flapping-wing mechanism of the KUBeetle-S [7] is difficult to fabricate and has the disadvantage of premature failure due to many linkages. On the other hand, the rack-pinion mechanism (Figure 1 right) is relatively easy to manufacture and has less possibility of failure. Therefore, the rack-pinion mechanism [8] was chosen for the flapping-wing mechanism. In the design of the flapping-wing mechanism, the flapping angle was designed at 180 degrees. Here, it is created over 190 degrees due to inertial force (Figure 2 right). If the flapping angle increases too much, the wingtips may touch each other, causing thrust and energy efficiency to drop. Therefore, the distance between the flapping axes (d) and the flapping angle (ψ) must be properly determined (Figure 2 left). Table I shows the distance and the flapping angle that can make the flapping-wing system produce a thrust large enough to overcome the robot weight. These values are obtained from several experiments.

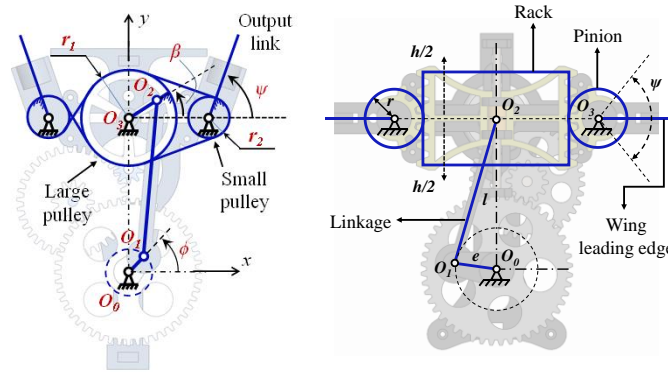


Figure 1. Pully-wire mechanism [7] (left) and rack-pinion mechanism (right)

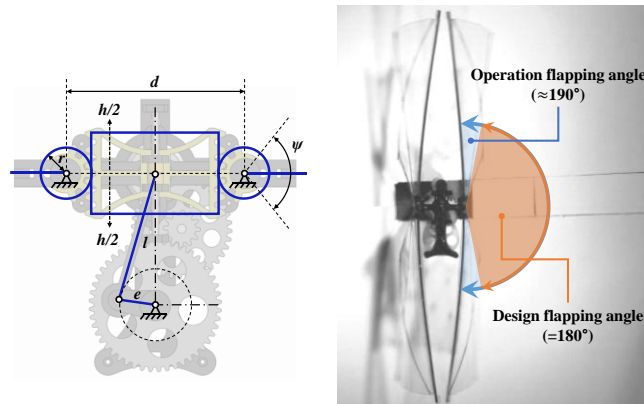


Figure 2. Major design parameters of the rack-pinion mechanism (left) and comparison of the design flapping angle and actual flapping angle (right)

Table I. Design parameters (d , ψ_{design}) and actual flapping angle (ψ_{actual}) of flapping-wing mechanisms with gear ratios

	24:1	30:1
d (mm)	20	22
ψ_{design} (degree)	170	175
ψ_{actual} (degree)	188	188

2.2 Measurement of force and power

To measure thrust and lift-to-power ratio, an experimental setup is constructed [3] as shown in Figure 3. A power supply (E36103A, Keysight) applies 3.7 V (V_s), which is equivalent to the nominal voltage of the battery used in the FW-MAV. The voltage (V_o) applied to the flapping-wing system and the resistor (R) are measured by using an oscilloscope (TDS 2024, Tektronix Inc.). The current (I) applied to the flapping-wing system was calculated as $I = (V_s - V_o)/R$. The power consumption (W) can be obtained by multiplying this current (I) and the voltage (V_o) applied to the flapping-wing system. At the same time, the thrust was measured by a load cell (Nano 17, ATI Industrial Automation Inc., force resolution ≈ 0.32 gf). Finally, the lift-to-power ratio was calculated by dividing the cycle average thrust by power consumption.

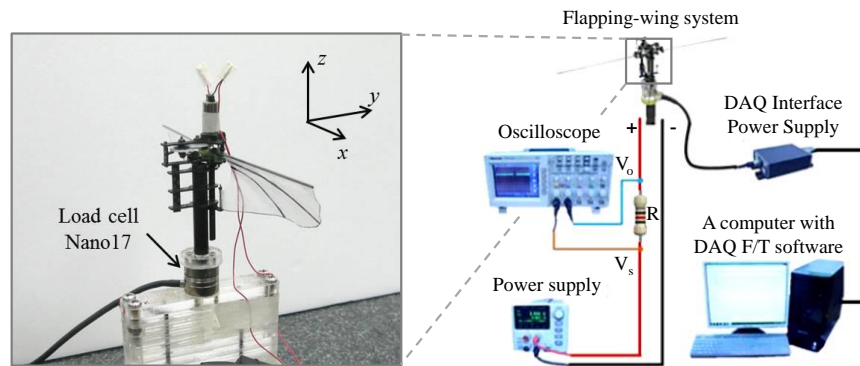


Figure 3. Experimental setup for thrust and lift-to-power ratio [3]

Since the operating flapping frequency of the flapping-wing mechanism at 3.7 V was measured at 17.8 Hz, the thrust and the lift-to-power ratio are measured at this flapping frequency as listed in Table II. The flapping-wing mechanisms with both gear ratios generated thrusts enough to overcome the robot's weight (~ 17.9 g). However, the flapping-wing mechanism with a gear ratio of 30:1 demonstrated a higher lift-to-power ratio (5.5). Therefore, the gear ratio of 30:1 is chosen for the flapping-wing mechanism.

Table II. Measured average thrust, power consumption and lift to power ratio at operation flapping frequency (17.8 Hz)

	24:1	30:1
Measured average thrust (gf)	21.45	20.64
Power consumption (W)	4.77	3.75
Lift to power ratio (gf/W)	4.49	5.50

2.3 Attitude control mechanism

The attitude control mechanism is for stable hovering and maneuvering of FW-MAV. The same SPC mechanism (Stroke Plane Change mechanism) used in the KUBeetle-S [9] is adopted. It is checked using a virtual model created by a 3D CAD software integration of the new flapping-wing mechanism and attitude control mechanism, and operation of the attitude control mechanism, as shown in Figure 4. After checking all possible troubles, a prototype is fabricated.

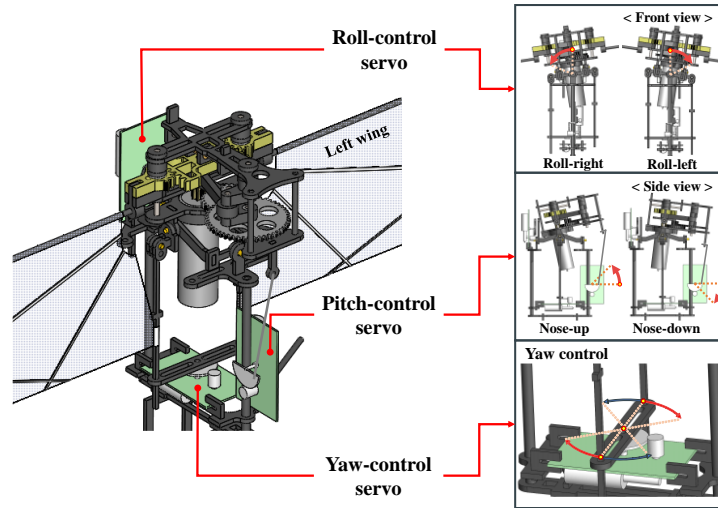


Figure 4. Principle of attitude control mechanism

2.4 Attitude stabilization system

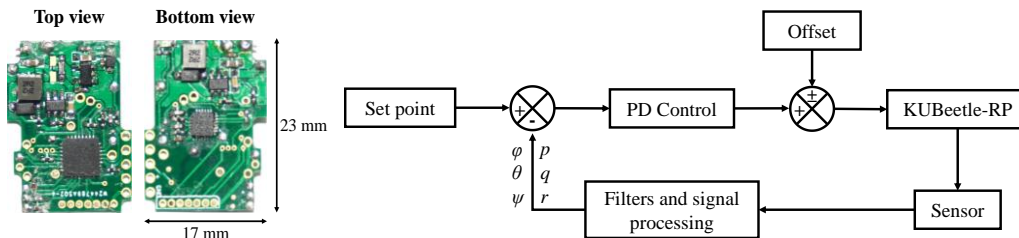


Figure 5. Feedback control board (left) and flow chart of the feedback controller (right) [10]

Since stable attitude control of the FW-MAV is impossible without feedback control, the same PD controller used in the KUBeetle-S [10] is adopted. When a control gain value that does not match is applied, flight stability cannot be maintained even if a feedback attitude control system is equipped. Therefore, through several flight tests, the control gain values are determined as summarized in Table III.

Table III. Gain values applied in KUBeetle-RP

	K_p (P gain value)	K_D (D gain value)
Roll	3.57	0.38
Pitch	3.20	0.33
Yaw	2	0.24

3. Flight test and endurance

3.1 KUBeetle-RP

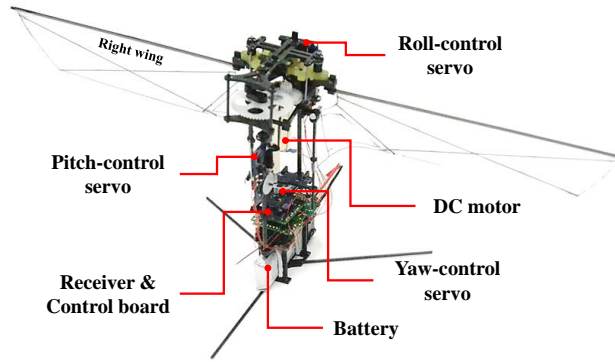


Figure 6. Prototype of the KUBeetle-RP

The robot in Figure 6 is named KUBeetle-RP because it is operated with a rack-pinion mechanism-based flapping-wing mechanism. As shown in Table IV, the major specifications of KUBeetle-RP are as follows: the gear ratio used in the flapping-wing mechanism is 30:1, and the wing area is 7% larger than in the KUBeetle-S. The total weight of the robot, including the feedback control system and battery, is 17.7g. Comparing KUBeetle-RP and KUBeetle-S, KUBeetle-RP is heavier by 12%. Because KUBeetle-RP adopts the higher gear ratio, the flapping-mechanism weight increases. Because the installation location of the feedback control system changes from top to bottom, the mainframe size increased.

Table IV. Comparison of major specifications of KUBeetle-S and KUBeetle-RP

	KUBeetle-S	KUBeetle-RP
Flapping mechanism gear ratio	28:1	30:1
Wing area (cm ²)	23.7	25.4
Wing length (cm)	9	9
Wing aspect ratio	3.2	3.2
Total weight (g)	15.8	17.7

3.2 Flight test and endurance

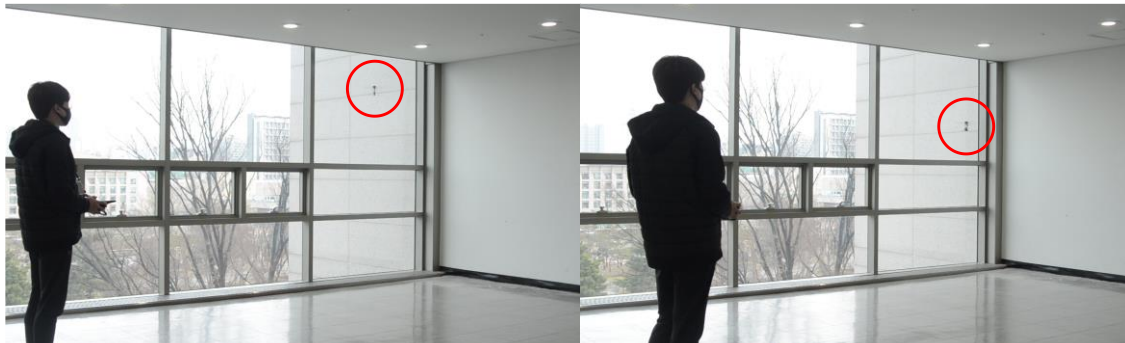




Figure 7. Flight test

Table V shows the main specification and endurance of the two types of KUBeetle-RP. KUBeetle-RP-1, with a gear ratio of 24:1, weights 16.8 g and has a flight time of 3 minutes and 50 seconds. KUBeetle-RP-2, with a gear ratio of 30:1, weights 17.7 g and has a flight time of 7 minutes.

Table V. Comparison of main specifications and endurance by KUBeetle-RP models

	 KUBeetle-RP-1	 KUBeetle-RP-2
Flapping mechanism gear ratio	24:1	30:1
Wing area (cm ²)	25.4	25.4
Wing length (cm)	9	9
Wing aspect ratio	3.2	3.2
Battery capacity (mAh)	150	150
Nominal voltage (V)	3.7	3.7
Height (cm)	8	8
Total weight (g)	16.8	17.7
Lift to power (gf/W)	4.5	5.5
Endurance	3 min 50 sec	7 min

4. Conclusion

For the flapping-wing mechanism, the rack-pinion mechanism is applied instead of the pulley-wire mechanism for another version of KUBeetle. To find the gear ratio of the flapping-wing mechanism that can perform similarly to KUBeetle-S, flapping-wing systems with two gear ratios (24:1, 30:1) fabricates. By comparing the lift-to-power ratios measured for the two systems, the gear ratio of the final flapping-wing mechanism is determined to be 30:1. For the attitude control mechanism, the SPC mechanism used in the previous KUBeetle is adopted. The final robot with an attitude control system weighs 17.7 g and demonstrates successful hovering flight for about 7 minutes.

Acknowledgments

This research is supported by a grant from LIG Nex1.

References

- [1] M. Keennon, K. Klingebiel, H. Won, and A. Andriukov (2012), “Development of the nano hummingbird: A tailless flapping wing micro air vehicle”, in Proc. 50th AIAA Aerosp. Sci. Meeting Including New Horizons Forum Aerosp., Nashville, TN, USA, pp.1-24.
- [2] Ma K. Y., Chirattananon P., Fuller S. B. and Wood R. J. (2013), “Controlled flight of a biologically inspired insect-scale robot”, *Science*, Vol. 340, pp.603-607.
- [3] Phan H. V., Aurecianus S., Au T. K. L., Kang T. S. and Park H. C. (2020), “Towards Long Endurance Flight of an Insect Inspired, Tailless, Two-Winged, Flapping Wing Flying Robot”, *IEEE Robotics And Automation Letters*, Vol. 5, No. 4, pp.5059-5066.
- [4] Roshanbin A., Altartouri H., Karasek M., Preumont A. (2017), “COLIBRI: a hovering flapping twin-wing robot”, *International Journal of Micro Air Vehicles*, Vol 9, No. 4, pp.270-282.
- [5] Karasek M., Muijres F.T., De Wagter C., Remes B.D.W, De Croon G (2018), “A tailless aerial robotic flapper reveals that flies use torque coupling in rapid banked turns”, *Science*, Vol. 361, pp.1089-1094
- [6] Tu Z., Fei F., Deng X. (2020), “Untethered flight of an at-scale dual-motor hummingbird robot with bio-inspired decoupled wings”, *IEEE Robotics and Automation Letters*, Vol. 5, No.3, pp.4191-4201
- [7] Phan H. V., Truong Q. T., Au T. K. L. and Park H. C. (2016), “Optimal flapping wing for maximum vertical aerodynamic force in hover: twisted or flat?”, *Bioinspiration & Biomimetics*, Vol. 11, No. 4, Paper No. 046007.
- [8] Nguyen T. A., Phan H. V., Au T. K. L. and Park H. C. (2016), “Experimental study on thrust and power of flapping-wing system based on rack-pinion mechanism”, *Bioinspiration & Biomimetics*, Vol. 11, No. 4, Paper No. 046001.
- [9] Phan H. V., Aurecianus S., Kang T. S. and Park H. C. (2019), “KUBeetle-S: An insect-like, tailless, hover-capable robot that can fly with a low torque control mechanism”, *Int. J. Micro Air Vehicle.*, Vol. 11, pp. 1-10.
- [10] Aurecianus S., Phan H. V., Kang T. S. and Park H. C. (2020), “Longitudinal mode model-based controller design for tailless flapping wing robot with loop shaping compensator”, *Bioinspiration & Biomimetics*, Vol. 15, No. 5, Paper No. 056004.

CFD and FSI-based Parametric Study on Tail Fin for High-speed Underwater Locomotion

Thanh Tien Dao¹, Khanh Nguyen¹ and Hoon Cheol Park^{1*}

¹Konkuk University, Seoul, Korea

*Corresponding author. E-mail: hcpark@konkuk.ac.kr

Abstract

Tail movement of fast-swimming fish in underwater environment has been widely studied in an effort to improve the swimming speed and efficiency of fish-like robots. In this study, we first investigated the effects of aspect ratio and area of tail on thrust and torque created by the tail fins with a uniform thickness using three-dimensional transient computational fluid dynamics (CFD) in ANSYS-Fluent. Furthermore, it is known that the flexibility of the tail can enhance thrust and efficiency. Therefore, we numerically investigated the effects of the stiffness of tail fin on the thrust and torque with different peduncle lengths and operating conditions such as frequency and tail-beat angle, and inflow velocity. The simulations for flexible tail were performed by using the two-way fluid-structure interaction (FSI) method in ANSYS Workbench. The results showed that the tail stiffness for high thrust generation differs for each operating condition. The tendency for each effect in this study can be used to find tails qualified for high-speed underwater locomotion.

Keywords: CFD, FSI, thrust, torque, tail fin, stiffness.

1. Introduction

The hydrodynamic characteristics of many underwater species have been widely studied because their principles are beneficial in enhancing swimming performance of fish-like robots such as swimming speed and energy efficiency. One of the most important factors determining a swimming ability of many types of fish is the characteristics of the tail fin as it contributes to thrust generation. Some research investigated the effect of tail shape on swimming performance by testing different tail shapes [1] [2]. It was found that the optimal tails of different swimming speeds are not the same shape. The fast-swimming fish, whose tail is crescent-shaped, have higher efficiency and better maneuverability than the other optimal bionic fish at low and moderate swimming speeds [1]. The experimental results on the performance of three tails, which differ in shape, at different Strouhal numbers in [2] shows that the swept tail, which is somehow similar to the crescent-shaped tail in [1], has the largest thrust generation at high Strouhal numbers, compared to that of the elliptical and rectangular tail shape.

The stiffness of the tail fin has also been examined, showing that the passive deformation due to the flexibility of tail could have a positive effect on the tail hydrodynamic performance [3] [4]. The numerical result in [3] shows that the flexible tail has a superior efficiency performance than the rigid tail operated in a low-inflow velocity and a low tail-beat frequency. Bending characteristics of the flexible tail is beneficial to enhance the swimming speed and efficiency as it can create more thrust under a lower required torque. A full three-dimensional CFD analysis on the pectoral fin and body interaction was performed based on the finite volume method in [5]. They found that hydrodynamic interactions exist between the pectoral-fin vortices and the undulating fish body. Taxiing with the caudal fin of flying fish was investigated by a CFD analysis in [6], which revealed that flying fish can accelerated along the water surface by taxiing with beating its caudal fin.

To find the optimal tails that can generate a larger thrust for high-swimming speed, we investigated the effect aspect ratio and area on the thrust and peak torque of the rigid tail using the ANSYS-Fluent, and the effect of stiffness and peduncle on thrust and propulsive efficiency of the flexible tail, according to the change of tail-beat angle and frequency. The fluid-structure interaction (FSI) method in ANSYS-Workbench was used in order to simulate the flexible tail.

2. Material and method

Figure 1 shows three-dimensional computational domain for the present numerical simulation, including the dynamic mesh region near the tail, in which the element size is fine, and the stationary mesh region, in which the element size is coarser to reduce the cost of computation. The length, width, and height of the domain are the same for all cases in the simulation, which are 2, 0.5, and 0.25m, respectively. Only a half of the tail fin in the z-axis is modeled using the symmetry plane of zx. For the turbulent flow, the k-epsilon model is used. A uniform tail with the thickness of 1 mm oscillates around a rotational axis with tail-beat angle Φ and tail-beat frequency f . The tail-beat motion was assumed harmonic in time. ANSYS-Fluent was used for the rigid tail and fluid-structure interaction component in ANSYS workbench was used for the flexible tail.

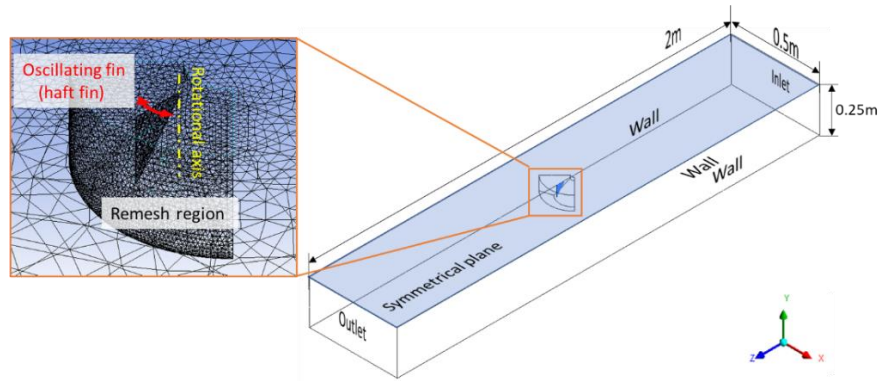


Figure 1. Three-dimensional computational domain

3. Result and discussion

3.1 Effect of tail aspect ratio

Table 1. Effect of tail aspect ratio

		20 deg	50 deg	80 deg
Average thrust (N)	AR=5.1	0.11	0.89	2.25
	AR=2.9	0.18	1.34	3.37
	AR=1.3	0.29	2.03	4.74
Peak torque (Nmm)	AR=5.1	63	241	456
	AR=2.9	127	506	959
	AR=1.3	350	1,255	2,305

The effect of tail aspect ratio on hydrodynamic performance was investigated by comparing the thrusts and peak torques produced by three triangle tails with the same area operating at a tail-beat frequency of 10 Hz and tail-beat angles of 20, 50, and 80°. Table 1 and Figure 2 show the cycle average thrust and peak torque for the three different tails. According to the change of the tail-beat angle from 20 to 80°, the thrust and torque greatly varied for all tails. The thrust was increased from 0.11 N to 2.25 N (~20 times) for AR=5.1 and from 0.29 N to 4.74 N (~16 times) for AR=1.3. Meanwhile, the change of torques was lesser, increased about 7 times for all tails.

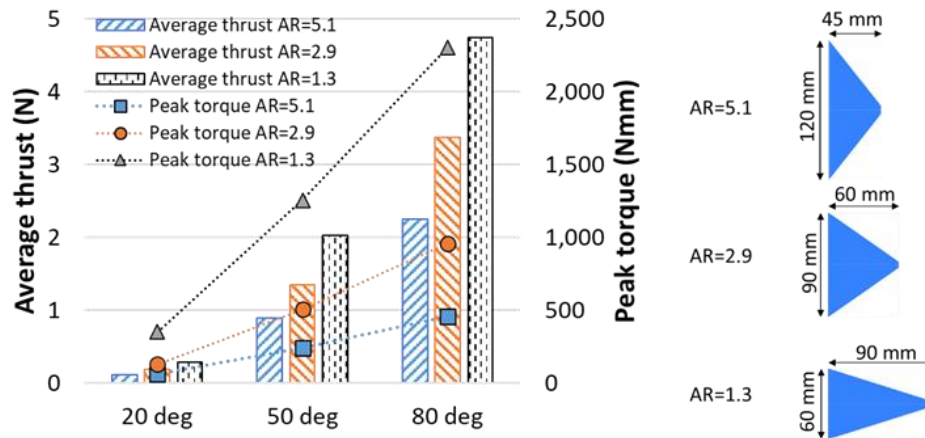


Figure 2. Effect of tail aspect ratio

As the tail aspect ratio reduced from 5.1 to 1.3, the thrust increased from 0.11 N to 0.29 N (~2.6 times) for a tail-beat angle of 20°, from 0.89 N to 2.03 N (~2.3 times) for a tail-beat angle of 50°, and from 2.25 N to 4.74 N (~2.1 times) for a tail-beat angle of 80°. To consider swimming efficiency, the torque was also examined. The increase rate of the peak torque was greater than that of the thrust. As the tail aspect ratio was reduced from 5.1 to 1.3, the peak torque increased from 63 Nmm to 350 Nmm (~5.6 times) for a tail-beat angle of 20°, from 241 Nmm to 1255 Nmm (~5.2 times) for a tail-beat angle of 50°, and from 457 Nmm to 2305 Nmm (~5 times) for a tail-beat angle of 80°.

3.2 Effect of tail area

With the same operating condition as the investigation of the effect of tail aspect ratio, three tails with the same aspect ratio but different areas were investigated to examine the effect of area on thrust and torque, as shown in Table 2 and Figure 3. With the value of average thrust and peak torque given in Table 2, we found two tendencies: the thrust is proportional to the square of area (area^2); meanwhile, the torque is proportional to the square of area multiplied by tail length ($\text{area}^2 \times \text{tail length}$). It was also found that the thrust and torque were significantly changed as the tail-beat angle was changed, and the increase rate in thrust was also greater than that of the torque, as the tail-beat angle increased.

Table 2. Effect of tail area

		20 deg	50 deg	80 deg
Average thrust (N)	Area x 1	0.11	0.89	2.25
	Area x 1.5	0.24	2.00	5.03
	Area x 2	0.44	3.58	9.11
Peak torque (Nmm)	Area x 1	63	241	457
	Area x 1.5	172	663	1,257
	Area x 2	356	1,364	2,585

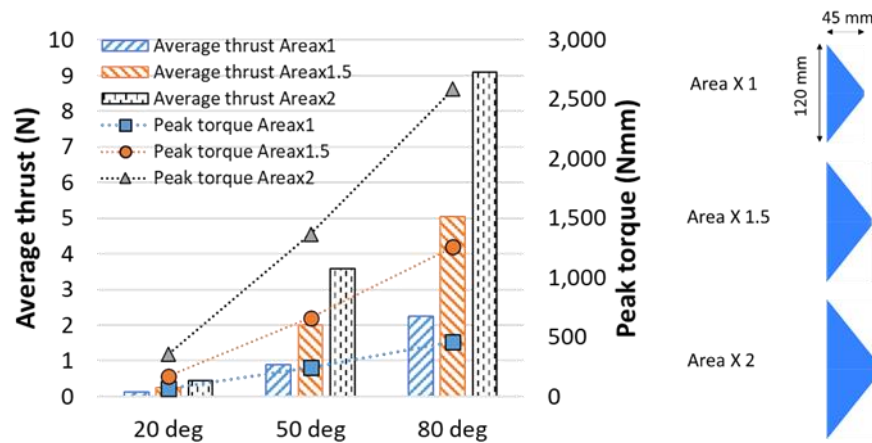


Figure 3. Effect of tail area

3.3 Effect of tail stiffness

3.3.1 Without inflow velocity

This simulation involved a FSI scheme to investigate the effect of the tail stiffness on hydrodynamic performance of the tail, using the system coupling component in ANSYS. Using the FSI method, the force from the fluid analysis in ANSYS-Fluent is transferred to the structure analysis in ANSYS - Mechanical, and reversely, the displacement from the structure analysis is transferred back to the fluid analysis.

The effect of stiffness by testing for the Young's modulus of 2, 5, 10, and 20 GPa of a triangular tail on the average thrust was investigated for frequencies of 5, 10, 15, and 20 Hz and tail-beat angles of 20, 50, 80° without inflow velocity, as shown in Figure 4. The stiffness which produces the highest average thrust (optimal stiffness) among the investigated Young's modulus varied with the tail-beat frequency. The optimal stiffness for a tail-beat angle of 20° increased from 2 GPa for frequencies of 5 and 10 Hz to 10 GPa for a frequency of 20 Hz. At tail-beat angles of 50 and 80°, the optimal stiffness increases from 2 GPa for frequencies of 5 Hz to 20 GPa for a frequency of 20 Hz. The optimal stiffness also varied according to the change of tail-beat angle, but the effect was less obvious than that due to change in the frequency.

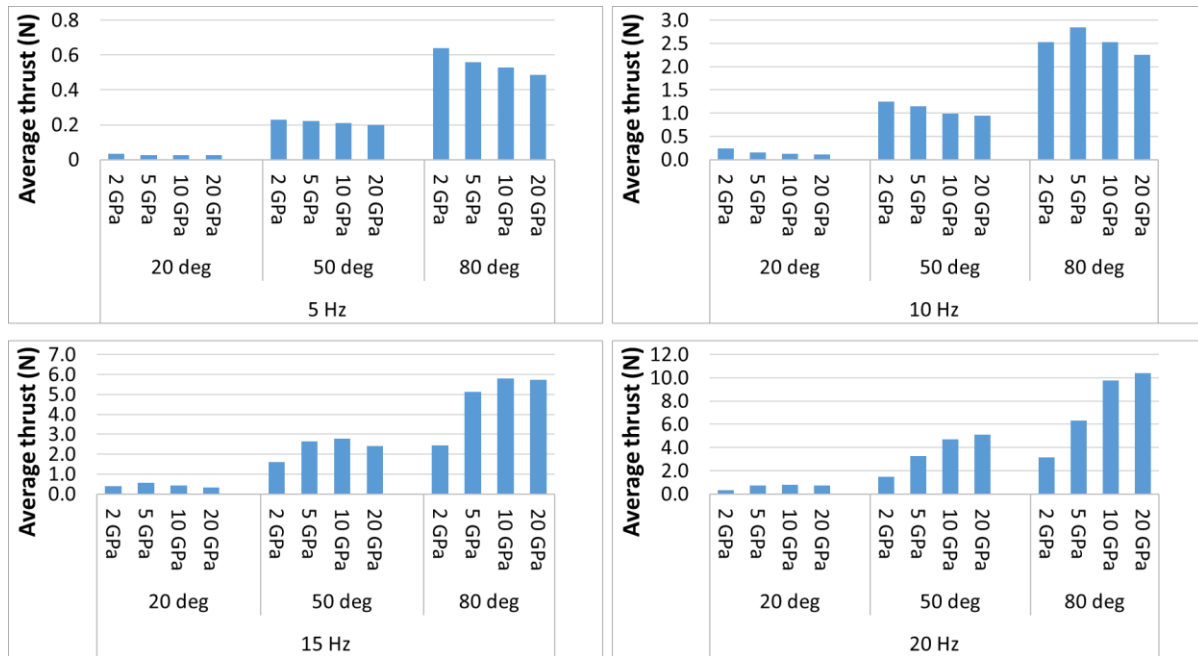


Figure 4. Effect of stiffness of tail without inflow velocity

3.3.2 With an inflow velocity of 1 m/s

With an inflow velocity of 1 m/s, the effect of tail stiffness on thrust and propulsive efficiency was investigated. The propulsive efficiency can be expressed as following equations:

$$\eta = P_T / P_R \quad (1)$$

$$P_T = T_{max} V \quad (2)$$

$$P_R = Q_{max} \omega \quad (3)$$

$$\omega = 2f\Phi, \quad (4)$$

where η is the propulsive efficiency, P_T is the thrust power, P_R is the required power, T_{max} is the maximum thrust (N), V is the inflow velocity of 1 m/s, Q_{max} is the maximum torque (Nm), ω is the angular velocity of the tail (rad/s), f is the frequency (Hz), and Φ is the tail-beat angle (rad). The tail used for the simulation is the tail with Area×1 in Figure 3.

The results are displayed in Figure 5. Generally, a tail with a larger tail-beat angle and higher stiffness produced a lower thrust for operating frequencies of 5 and 10 Hz. The thrusts (net thrust) are negative, which means that the tail operated in this condition has a velocity smaller than 1 m/s because the thrusts produced by tails are smaller than the drags. In these cases, the propulsive efficiency was not calculated since the thrust was negative.

When a tail was operated at frequencies of 15 and 20 Hz, the thrusts produced by the tail were larger than the drags. The net thrusts are positive, and the propulsive efficiencies can be calculated in these cases, as shown in Figure 5. As the tail-beat angles increased, the average thrusts increased significantly, while the propulsive efficiencies decreased slightly for both frequencies of 15 and 20 Hz. The thrust and propulsive efficiency also varied according to the change of frequency. As the frequency increased from 15 Hz to 20 Hz, the thrust increased, while the propulsive efficiency decreased for the same tail-beat angle and stiffness.

The stiffness that produces the highest thrust and propulsive efficiency also differed according to change of the tail-beat angle and frequency. At a frequency of 15 Hz, the highest thrust and propulsive efficiency were achieved for stiffness of 5 and 10 GPa at tail-beat angles of 50° and 80°. At a frequency of 20 Hz, the highest thrust and propulsive efficiency were recorded for stiffness of 20 GPa at both tail-beat angles of 50° and 80°, as shown in Figure 5.

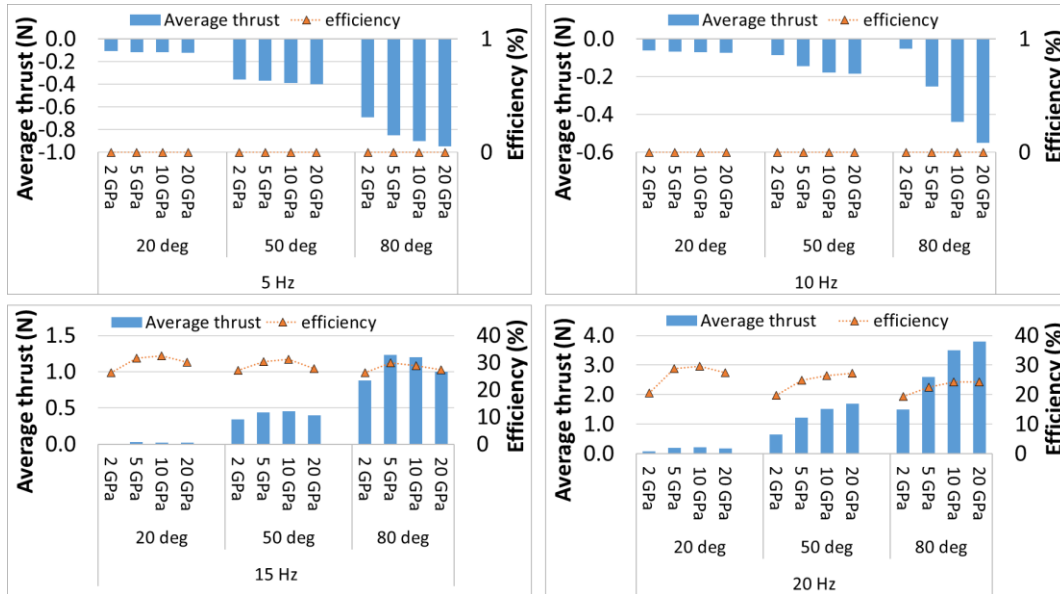


Figure 5. Effect of stiffness of tail with inflow velocity of 1 m/s

3.4 Effect of peduncle

Under a non-zero inflow velocity of 1 m/s, the flexible tail with the rigid peduncle was investigated to examine effect of peduncle on hydrodynamic performance at a tail-beat frequency of 10 Hz. Figure 6 shows the thrust and propulsive efficiency, and the parameter of this tail, which is Area×1 in Figure 3 with an extended rigid peduncle. In contrast to the tail without peduncle (Area×1 in Figure 3), the propulsive efficiency of the tail with the peduncle increased slightly as the tail-beat angle increased. The propulsive efficiency of the lowest stiffness was the highest for all tail-beat angles. All the thrusts are positive, while those of the tail without peduncle were negative at a frequency of 10 Hz, as shown in Figure 5.

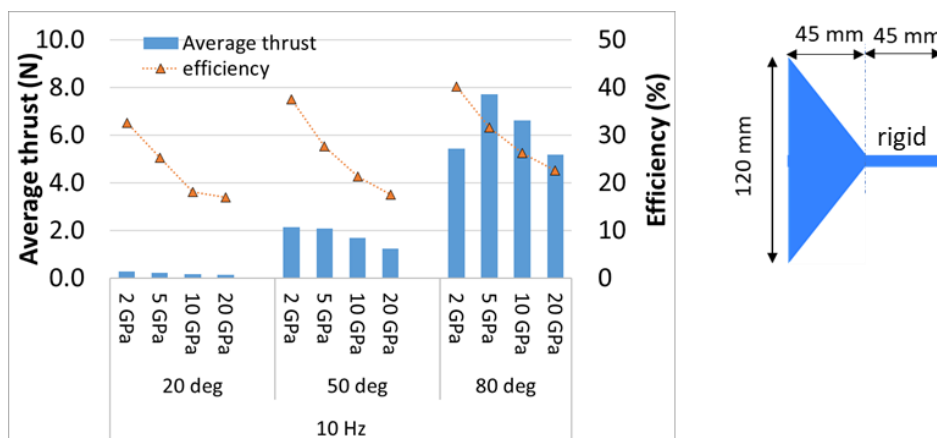


Figure 6. Effect of peduncle with inflow velocity of 1 m/s

4. Concluding remarks

In this study, a series of numerical simulations have been performed to investigate the effect of aspect ratio and area of tail fin on the thrust and torque generation, according to the change of tail-beat angle and tail-beat frequency without inflow velocity. For the rigid tails, the thrust increased significantly as the tail-beat angle increased. The torque also increased as the tail-beat angle increased. The increase rate of torque was less than half of that of the thrust. As the aspect ratio decreased, the thrust and torque increased, the increase rate of torque is more than 2 times larger than that of the thrust. For the effect of the tail area, it was found that the thrust was proportional to the square of area, meanwhile, the torque as proportional to the square of area multiplied by tail length.

The effect of the stiffness on the thrust and propulsive efficiency of the flexible tail was investigated with inflow velocities of 0 and 1 m/s. For an inflow velocity of 0 m/s, the stiffness which produced the highest average thrust varied according to the change of tail-beat frequency. For a low tail-beat frequency, the tail with a relatively low stiffness produced a larger thrust than that of the tail with a relatively high stiffness. However, for a high tail-beat frequency, the stiffer tail produced a larger thrust compared to that of the low-stiffness tail. The stiffness which produces the highest average thrust also varied according to the change of tail-beat angle, but the effect was less obvious than that of the tail-beat frequency. For an inflow velocity of 1 m/s, the net thrusts of the tail operated at frequencies of 5 and 10 Hz are negative, which means that the tail operated in this condition is not able to reach the swimming speed of 1 m/s. For the tail-beat frequencies of 15 and 20 Hz, the net thrusts were positive. As the tail-beat angle increased, the thrust increased significantly, while the propulsive efficiency decreased slightly.

The flexible tail with a rigid peduncle produced a positive net thrust operated at a frequency of 10 Hz, in contrast to the negative net thrust of the flexible tail without a peduncle. With a rigid peduncle, as the tail-beat angle increased, the propulsive efficiency increased slightly. In this case, the highest propulsive efficiency was achieved for the tail stiffness of 2 GPa for all tail-beat angles.

Results found in this paper can be used for designing a prototype fish robot that can swim fast underwater. We will report the progress in the near future.

Acknowledgement

This work was supported by the National Research Foundation of Korea (NRF) grant funded by the Korea government (MSIT) (2020R1F1A106827212).

References

- [1] Xin, Z. and Wu, C., 2013. Shape optimization of the caudal fin of the three-dimensional self-propelled swimming fish. *Science China Physics, Mechanics and Astronomy*, 56(2), pp.328-339..
- [2] Matta, A., Pendar, H., Battaglia, F. and Bayandor, J., 2020. Impact of Caudal Fin Shape on Thrust Production of a Thunniform Swimmer. *Journal of Bionic Engineering*, 17(2), pp.254-269..
- [3] Jaya, A.S. and Kartidjo, M.W., 2018. Performance evaluation of the shape and flexibility combination of the underwater biomimetic fin propulsion. *International Conference on Intelligent Unmanned Systems*, Jeju, South Korea

- [4] Shelton, R.M., Thornycroft, P.J. and Lauder, G.V., 2014. Undulatory locomotion of flexible foils as biomimetic models for understanding fish propulsion. *Journal of Experimental Biology*, 217(12), pp.2110-2120..
- [5] Yu, C.L., Ting S.C., Yeh, M.K., and Yang, J.T., 2011. Three-dimensional numerical simulation of hydrodynamic interactions between pectoral-fin vortices and body undulation in a swimming fish. *Physics of Fluids*, 23, 091901.
- [6] Deng J., Wang S., Zhang L., Mao X., 2019. Why does a flying fish taxi on sea surface before take-off? A hydrodynamic interpretation.
<https://www.biorxiv.org/content/biorxiv/early/2019/09/11/765560.full.pdf>

Numerical Investigation on Aerodynamic Performance of Airfoil with Different Cambers

Min Zhao¹, Yao Zou¹ and Wei He^{2*}

¹ School of Automation and Electrical Engineering, University of Science and Technology
Beijing, Beijing, China, 100083

² Institute of Artificial Intelligence, University of Science and Technology Beijing, Beijing,
China, 100083

*Corresponding author. E-mail: weihe@ieee.org

Abstract

Flapping-wing aerial vehicle (FAV) is a new type of aerial vehicle that mimics the flight mode of birds and insects. There are great differences in the structure and shape of the wings of birds and insects. The wings of birds are thicker and have a certain camber, while the wings of insects are thinner and most are corrugated. For the large bird-inspired FAV, the design of airfoil parameters is crucial for improving the performance of FAV. A numerical investigation into the effects of camber on aerodynamic performance is carried out through the solution of the two-dimensional incompressible unsteady Navier-Stokes equations using COMSOL Multiphysics software. The aerodynamic computational models with different airfoil camber are built based on the observation of flying creatures. The aerodynamic performance under low Reynolds number is analyzed using the finite element method coupled with the fluid-structure interaction (FSI) module. It is found that the appropriate wing camber can change the wing angle of attack effectively.

Keywords: Flapping-wing, Aerodynamic performance, Airfoil, FSI, COMSOL Multiphysics

Nomenclature

$\mathbf{u}_{\text{fluid}}$ = the velocity of the fluid
 $\mathbf{u}_{\text{solid}}$ = the deformation vector of the solid
 p = the hydrostatic pressure
 σ = the stress tensor
 \mathbf{I} = the identity tensor
 \mathbf{F} = the external force vector
 ρ = density of the fluid
 μ = viscosity of the fluid

1. Introduction

Flapping-wing flight is the common flight mode by flying creatures. There are nearly 1 million species of insects, more than 9000 species of birds and more than 1000 species of bats in nature. After billions of years of natural selection, many animals with flapping wings have superior flight and mobility capabilities. Flapping-wing aerial vehicle (FAV) operates in a flight mode that mimics insects, birds and bats. Compared with the fixed-wing and rotary-wing aircraft, flapping-wing flight has the unique advantages of bionic concealment, strong maneuverability and high energy utilization. With the great development potential, they have drawn considerable attention in military and civil applications. There are great differences in

wing structure and morphology among birds, bats and insects. The wings of birds are relatively thick and has a certain curvature, which are composed of muscles, bones, feathers and joints. Bats mainly control the flexible membrane wings by more than 24 joints. The wings of insects are thinner and has a corrugated airfoil, which is covered with veins and wing membranes. Due to the differences in wing structures and material properties, the aerodynamics of FAV wings is remarkably different from their counterparts in nature.

In recent years, with the rapid development of MEMS, 3D printing, intelligent material and bionics, the research of FAV has made considerable progress, such as Harvard University's RoboBee series [1–3], Delft University's Delfly series [4, 5], Konkuk University's KUBeetle series [6-8] and Festo's SmartBird [9] etc. These FAVs have different sizes and structures, while the research on aerodynamic characteristics of flapping wing is less. Compared with the flight of birds, insects and bats, the man-made flapping wing is obviously not the optimal structure. Traditional aerodynamics based on fixed wing and rotary wing flight patterns finds it difficult to explain the high lift mechanism of flapping wing. In order to improve the performance of flapping wing, many researchers are devoted to optimize the structure of flapping wing [10]. Flapping wing can offer some unique aerodynamic advantages over traditional fixed and rotary wing. However, the modeling and control are more difficult [11, 12] than the traditional aircrafts, especially the design and analysis of flapping systems. In flapping flight, both lift and thrust forces are produced simultaneously by flapping wings. For FAV systems, the most important subsystem is the flapping wing. Many flow simulation methods and experimental schemes are provided to find the most efficient flapping wing [13].

The steady aerodynamic characteristics of airfoils of different thickness and camber have been studied extensively. In order to reveal the influence of airfoil thickness and curvature on the aerodynamic performance of flapping wings, Bai et al. [14] studied the influence of different curvature airfoils on the aerodynamic performance of drosophilid-inspired flapping wings, and pointed out that positive curvature airfoils can effectively improve the lift and lift-drag ratio of flapping wings. Zhao et al. [15] carried out numerical calculations on the aerodynamic forces and aerodynamic efficiency of flapping wings with different airfoil thicknesses during upstrokes and downstrokes. The study showed that with the increase of the thickness of the airfoil, the thrust and propulsion efficiency of the flapping wing increased gradually, while the lift force of the flapping wing did not change significantly. Ashraf et al. [16] numerically studied the aerodynamic characteristics of flapping wings with different airfoil thicknesses and cambers in the combination of heaving and pitching motion, and found that the propulsive efficiency first increased and then decreased with the increase of the thickness of the airfoil, while the camber of the airfoil had little effect on the propulsive performance of the flapping wings. In addition, the study of Yu et al. [17] showed that the aerodynamic performance of flapping wings with different thicknesses presented different trends with the change of Reynolds number and Sternouhar number. In short, the influence of airfoil thickness and airfoil camber on the aerodynamic performance of flapping wings has not reached a consistent conclusion.

Both birds and insects have good flight ability, but the structure and shape of their flapping wing are different from each other. The wings of birds are relatively thick and often show a certain camber which has an important impact on its flight performance. For medium and large-scale bird-like FAV, the design of airfoil parameters is crucial to improve the aerodynamic performance of flapping wings. In this paper, the effect of airfoil on the aerodynamic performance is numerically studied using a partitioned Fluid-Structure Interaction (FSI) method. We presented four different flapping wing airfoils to study the effect of camber on the aerodynamic characteristics. A CFD simulation under 2D condition is applied to verify the effect

of cambers on aerodynamic forces. By the comparison of simulation results, the optimal camber is given out. The aim is to provide some theoretical guidance and technical reference for the aerodynamic design of FAV.

2. Numerical Simulation

In order to study the effect of camber on the aerodynamic characteristics, we developed four different airfoils inspired by birds, as shown in Figure 1. These four airfoils with chord length of 24cm have different cambers. We define camber as the distance from the highest point of the airfoil to the chord, where $h_1 = 30mm$, $h_2 = 25mm$, $h_3 = 20mm$, $h_4 = 15mm$.

The process of COMSOL simulation configuration includes: (1) Input airfoil coordinates data; (2) Construct the wind tunnel; (3) Select the materials for the wind tunnel and airfoil; (4) Set air as the space material for the wind tunnel; (5) Input the airfoil material parameters; (6) Set the airfoil as a linear elastic material; (7) Configure the wind tunnel entrance and wind velocity; (8) Configure the wind tunnel exit; (9) Configure the predetermined time-varying displacement function for airfoil; (10) Initiate mesh configuration; (11) Construct the triangular meshes of airfoil; (14) Scan the entire flapping wing; (12) Configure the fineness of the mesh size; (13) Complete configuration and initiate FEM calculation.

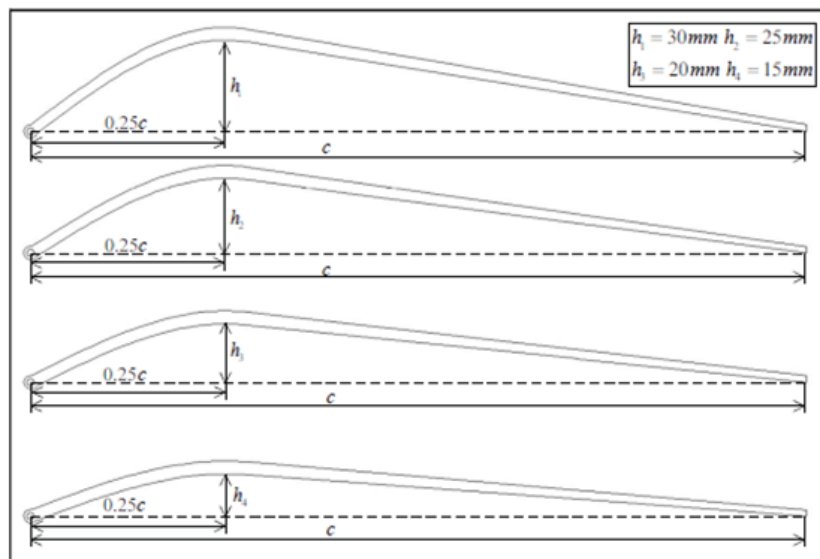
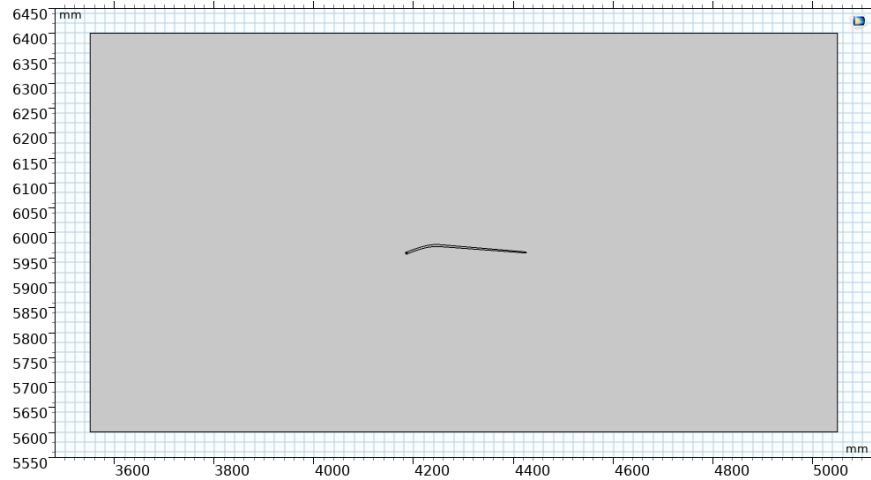


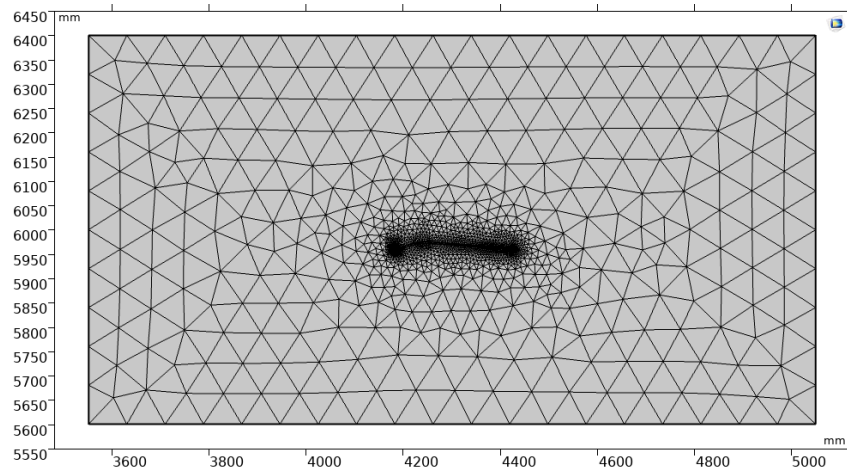
Figure 1. Schematic of different airfoils

2.1 Model

For the computational study, a fluid-structure interaction (FSI) analysis model is created for the proposed airfoil. The numerical calculation model of airfoil is shown in Figure 2. Based on COMSOL Multiphysics software, numerical simulations of different airfoils are conducted. The 2D geometry of airfoil is first imported, then a rectangle wind tunnel is established to serve as a surrounding boundary. The test section of the tunnel is taken as 1.5m*0.8m. The model of airfoil is placed at the center of the test section as a test object. Considering the calculation time and accuracy, we select fine mesh as the mesh size.



(a) Modeling of the airfoil



(b) The mesh form of airfoil

Figure 2. The numerical calculation model of airfoil

2.2 Methods

COMSOL Multiphysics is a finite-element-method (FEM) software package, specialized for dealing with the coupling phenomena, or multiphysics problems. Its outstanding capability of fluid-structure interaction (FSI) computation not only simulates the unsteady, moving-boundary flow field around airfoil, but also predicts the deformable airfoil surface profile due to the aeroelastic effect. Investigating the unsteady aerodynamics forces generated by flapping wings is an essential step toward understanding of interactions of flapping wings with fluids. The flapping motion of airfoil is realized by defining the displacement function. The numerical problem was solved using FSI physics in Computational Fluid Dynamic (CFD) module. The material properties of each part are shown in Table 1. We studied the aerodynamic performance of different airfoils in the virtual wind tunnel. The unsteady aerodynamic forces acting on 2D computational airfoils are studied by numerically solving the Navier-Stokes equations.

Table I. The material properties of airfoil and fluid.

Properties	Values
Young's modulus	1.04e11 Pa
Poisson's ratio	0.43
Density of airfoil	1500kg/m ³
Dynamic viscosity	1.8e-5 Pa·s
Density of fluid	1.29kg/m ³

Considering the flow around the wings to be compressible, the equations used by the solver are Navier Stokes equations as stated below:

$$\rho \frac{\partial \mathbf{u}_{fluid}}{\partial t} + \rho(\mathbf{u}_{fluid} \cdot \nabla) \mathbf{u}_{fluid} = \nabla \cdot [-p\mathbf{I} + \mu(\nabla \mathbf{u}_{fluid} + (\nabla \mathbf{u}_{fluid})^T) - \frac{2}{3} \mu(\nabla \cdot \mathbf{u}_{fluid})\mathbf{I}] + \mathbf{F} \quad (1)$$

$$\frac{\partial \rho}{\partial t} + \nabla \cdot (\rho \mathbf{u}_{fluid}) = 0 \quad (2)$$

$$\rho \frac{\partial^2 \mathbf{u}_{solid}}{\partial t^2} + \nabla \cdot \sigma = \mathbf{F}_v \quad (3)$$

3. Results and discussion

The surface pressure of different airfoils without flapping are shown in Figure 3. In order to visualize the relationship between aerodynamic forces and camber, the average lift and thrust are calculated. The average lift and thrust with different cambers are presented in Figure 4. In Figure 3, it is seen that as the camber of airfoil increases the region of the negative pressure tends towards the leading edge and the pressure difference is decreased. In Figure 4, we can observe that the camber of 20mm gets the largest average lift and average lift decreases as camber increase. However, we can find that the average thrust of the four flapping wings only has a small gap. In this paper, we only think about the motion of flapping up and down. Maybe the motion of flapping up and down does not contribute much to the generation of thrust.

4. Conclusion

A numerical investigation into the effects of camber on aerodynamic performance during the flight is carried out through the solution of the two-dimensional compressible unsteady Navier-Stokes equations using the computational fluid dynamics methods. The aerodynamic computational models with varying series airfoils are built based on the observation of flying creatures. We model four different airfoils with the camber of 15mm, 20mm, 25mm and 30mm. We have analyzed and compared the aerodynamics performance of airfoils with different cambers. The data presented in this study provide a guideline for the design of flapping wing. In the final design, we will choose the camber of 20mm as the flapping wing structure. Meanwhile, we will carry out the wind tunnel experiment to verify the rationality of our design in the future work.

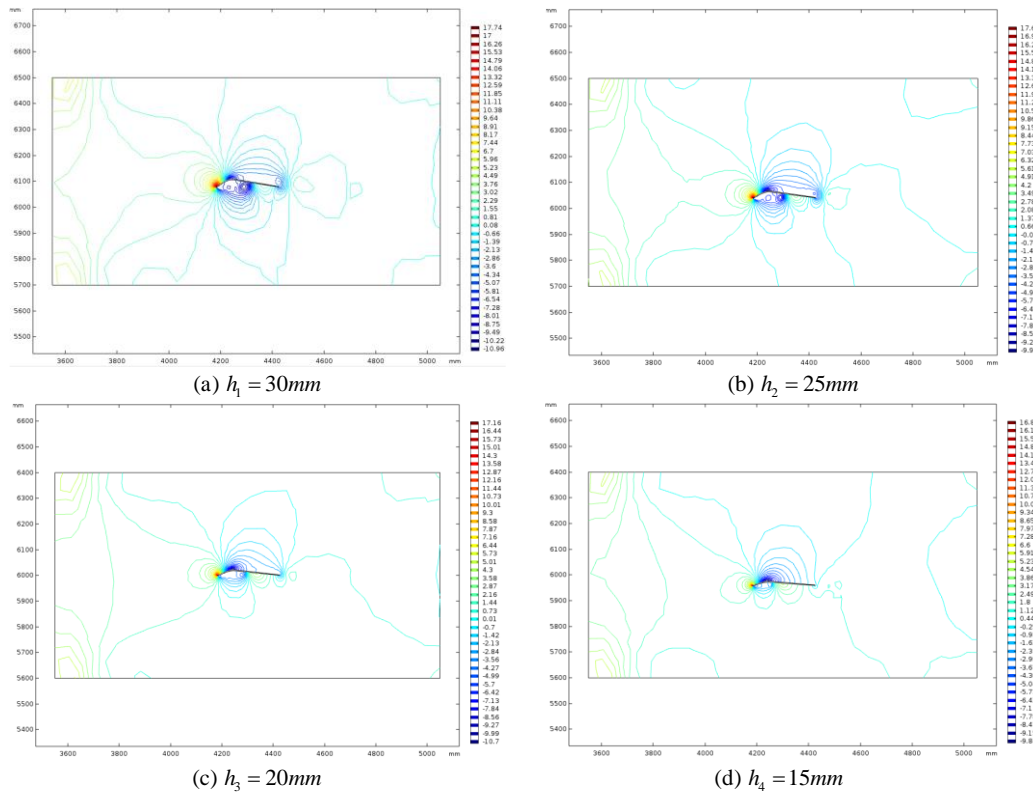


Figure 3. The surface pressure of different airfoils

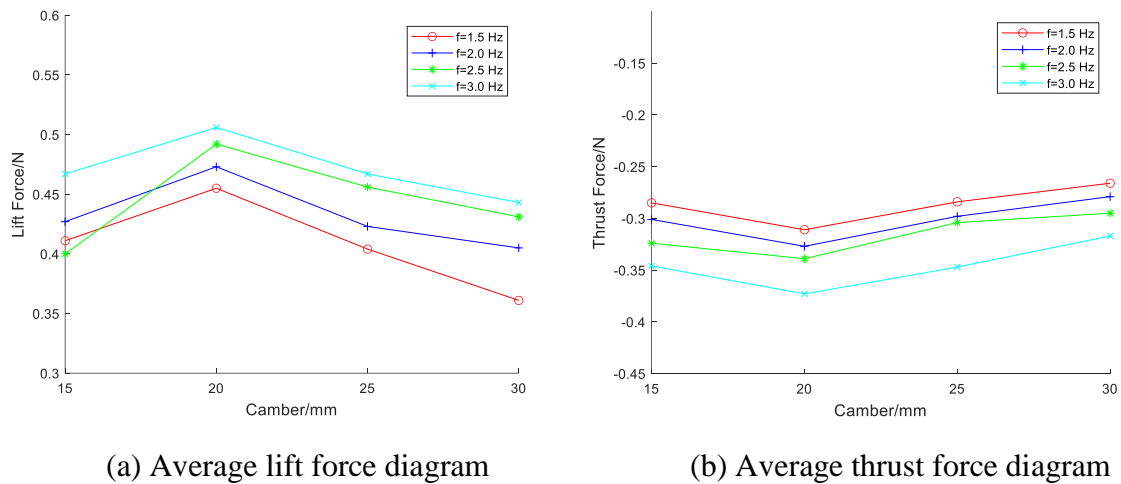


Figure 4. Average force values for different cambers

Acknowledgments

This work was supported by Fundamental Research Funds for the China Central Universities of USTB under Grant FRF-TP-19-001C2.

References

[1] Ma, K.Y., et al. (2013), “Controlled flight of a biologically inspired”, Science, Vol. 340 No. 6132, pp.603-607.

- [2] Chen, Y., et al. (2017), “A biologically inspired, flapping-wing, hybrid aerial-aquatic microrobot”, *Science Robotics*, Vol. 2 No. 11, eaao5619.
- [3] Chen, Y., et al. (2019), “Controlled flight of a microrobot powered by soft artificial muscles”, *Nature*, Vol. 575 No. 7782, pp. 324-329.
- [4] Holness, A. E., et al. (2018), “Characterizing and modeling the enhancement of lift and payload capacity resulting from thrust augmentation in a propeller-assisted flapping wing air vehicle”, *International Journal of Micro Air Vehicles*, Vol. 10 No. 1, pp. 50-69.
- [5] Karsek, M., et al. (2018), “A tailless aerial robotic flapper reveals that flies use torque coupling in rapid banked turns”, *Science*, Vol. 361No. 6407, pp. 1089-1094.
- [6] Kim, W.K., et al. (2009), “Effects of corrugation of the dragonfly wing on gliding performance”, *Journal of theoretical biology*, Vol. 260 No. 4, pp. 523-530.
- [7] 6Au, L., et al. (2020), “Effect of corrugation on the aerodynamic performance of three-dimensional flapping wings”, *Aerospace Science and Technology*, Vol. 105, 106041.
- [8] Phan, H.V. and Park, H.C. (2020), “Mechanisms of collision recovery in flying beetles and flapping-wing robots”, *Science*, Vol. 370 No. 6521, pp. 1214-1219.
- [9] Send, W., et al. (2012), “Artificial hinged-wing bird with active torsion and partially linear kinematics”, *Proceeding of 28th Congress of the International Council of the Aeronautical Sciences*.
- [10] He, W., et al. (2017), “Development of an autonomous flapping-wing aerial vehicle”, *Science China Information Sciences*, Vol. 60 No. 6, 063201.
- [11] He, W., et al. (2021), “Modeling and trajectory tracking control for flapping-wing micro aerial vehicles”, *IEEE/CAA Journal of Automatica Sinica*, Vol. 8 No. 1, pp. 148-156.
- [12] He, W., et al. (2018), “Iterative learning control for a flapping wing micro aerial vehicle under distributed disturbances”, *IEEE Transactions on Cybernetics*, Vol. 49 No. 4, pp. 1524-1535.
- [13] Shahzad, A., et al. (2018), “Effects of flexibility on the hovering performance of flapping wings with different shapes and aspect ratios”, *Journal of Fluids and Structures*, Vol. 81, pp. 69-96.
- [14] Peng, B., et al. (2009), “Aerodynamic Characteristics, Power Requirements and Camber Effects of the Pitching-Down Flapping Hovering”, *Journal of Bionic Engineering*, Vol. 6 No 2, pp. 120-134.
- [15] Zhao, L. and Yang, S., “Influence of Thickness Variation on the Flapping Performance of Symmetric NACA Airfoils in Plunging Motion”, *Mathematical Problems in Engineering*, Vol. 2010, pp. 1-19.
- [16] Ashraf, M.A., et al. (2011), “Reynolds number, thickness and camber effects on flapping airfoil propulsion”, *Journal of Fluids and Structures*, Vol. 27 No. 2, pp. 145-160.
- [17] Yu, M., et al. (2013), “High fidelity numerical simulation of airfoil thickness and kinematics effects on flapping airfoil propulsion”, *Journal of Fluids & Structures*, Vol. 42, pp. 166-186.

Effects of Wing Kinematics on Aerodynamic Efficiency of an Insect-inspired Flapping-wing Micro Air Vehicle in Hover

Khanh Nguyen¹, Loan Thi Kim Au¹, Hoang-Vu Phan¹, Tien Thanh Dao¹, and Hoon Cheol Park^{1,*}

¹Dpt. of Smart Vehicle Engineering, Artificial Muscle Research Center, Konkuk University, South Korea

*Corresponding author. E-mail: hcpark@konkuk.ac.kr

Abstract

In this work, we used a computational-fluid-dynamic method to investigate the effects of wing kinematics on aerodynamic efficiency of our hovering flapping-wing micro air vehicle (FW-MAV), named KUBeetle. From the measured wing kinematics, four wing kinematics were created to find out a wing motion that can produce high lift-to-drag ratio (L/D). Among the investigated cases, the wing kinematics version 3, which includes both camber and twist with an average angle of attack of about 37° , was selected, because of its 24 % improvement of L/D while maintaining similar lift of the measured wing kinematics. The results also showed that the camber plays an important role in the improvement of both lift and L/D , which are about 16.7 % and 10.6 %, respectively. Finally, the study confirmed that the modified wing kinematics version 3 is preferable for high aerodynamic efficiency of the KUBeetle robot, with 25 % improvement in L/D .

Keywords: Aerodynamic efficiency, Flapping-wing micro air vehicle, Computational fluid dynamics

Nomenclature

c_{\max} = maximum chord length (m) f = flapping frequency (Hz) h = mid-chord height (m)
 θ_m, θ_f = middle and full rotation angles ($^\circ$) α = angle of attack ($^\circ$) ψ = flapping angle ($^\circ$)

1. Introduction

Nowadays, since flying insects become a great source of inspiration, many scientists have been investigating their flapping-wing mechanisms for the development of flapping-wing micro air vehicles (FW-MAVs) (Sun, 2014). For actually flying FW-MAVs, there are still limitations in flight time. About 40% of the total power of a flapping-wing system is spent on producing aerodynamic forces, while about 20% is consumed to overcome inertial force (Phan *et al.*, 2018). To reduce the inertial power consumption, the wing mass must be as light as possible. However, the major portion of the power is still spent on force production. Thus, the improvement of aerodynamic efficiency is crucial to extend flight endurance of a FW-MAV. Besides, extensive optimizations of the wing deformation and kinematics have been considered. For example, (Okamoto *et al.*, 1996) experimentally compared a cambered wing and a thin flat plate. The conclusion was that the curved wing with 9% chord height increased the maximum lift coefficient and the slope of lift-to-drag ratio with respect to angles of attack (AoAs). Effect of wing twist on lift generation of flapping wings was investigated by (Truong *et al.*, 2013). The study showed that a wing with a negative twisting produced about 10% more vertical force, while consuming less power than the flat wing. In addition, (Gehrke *et al.*, 2021) tested a spanwise angle range for high aerodynamic efficiency and concluded that the low pitch angle kinematics increased aerodynamic efficiency by 93% but reduced the lift by 43%. In this study,

we performed a numerical simulation using ANSYS-Fluent to study the aerodynamic efficiency of the KUBeetle, a tailless FW-MAV, using the trailing-edge-change (TEC) system to control the moments (Truong *et al.*, 2013). Based on the simulation of the measured wing kinematics, four higher performing versions were then created.

2. Materials and methods

2.1 Wing kinematics of the KUBeetle

Similar to the previous works (Au and Park, 2019), the coordinate systems (Fig. 1a) are used to describe the wing motion, where $O_e x_e y_e z_e$ is the fixed coordinate system on the ground, while $O_b x_b y_b z_b$ is attached to the body. At the local spanwise location, the wing camber is defined as follows:

$$\text{Camber}(r) = \frac{h}{c} \times 100\% = \frac{1}{2} \tan(\theta_m - \theta_f) \times 100\%, \quad (1)$$

where h is the mid-chord height and c is the full-chord length. The middle rotation angle, θ_f is the angle between the stroke plane and the full-chord line connecting the leading edge and trailing edge. Meanwhile, the full rotation angle θ_m is the angle between the stroke plane and the mid-chord line connecting the leading edge and the mid-chord point. The local geometric angle of attack (α or AoA) is the angle between the inflow vector and the full chord line. The flapping angle between the feather axis and y -axis is denoted by ψ . The measured wing kinematics of the KUBeetle were captured using three high-speed digital cameras and showed in Figs. 1b (Truong *et al.*, 2013). The measured and fitted wing kinematics were specified at $0.25R$, $0.5R$, and $0.75R$. To reproduce the wing motion in CFD, the Fourier series function was used to fit the measured wing kinematics:

$$f(t) = a_0 + \sum_{k=1}^{n=9} [a_k \cos(2k\pi ft) + b_k \sin(2k\pi ft)], \quad (2)$$

where the coefficients a_0 , a_k , and b_k are designated in the user-defined-function of ANSYS-Fluent.

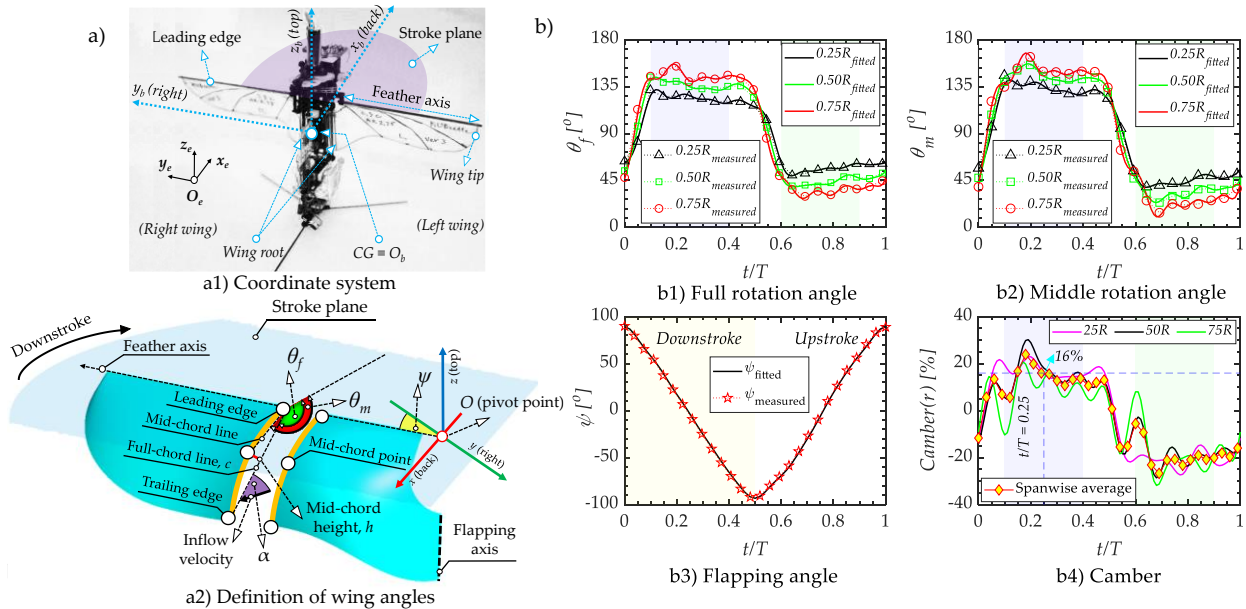


Figure 1. (a1) KUBeetle, (a2) wing angles, and (b) measured and fitted wing kinematics

2.2 Computational fluid dynamics (CFD) modeling

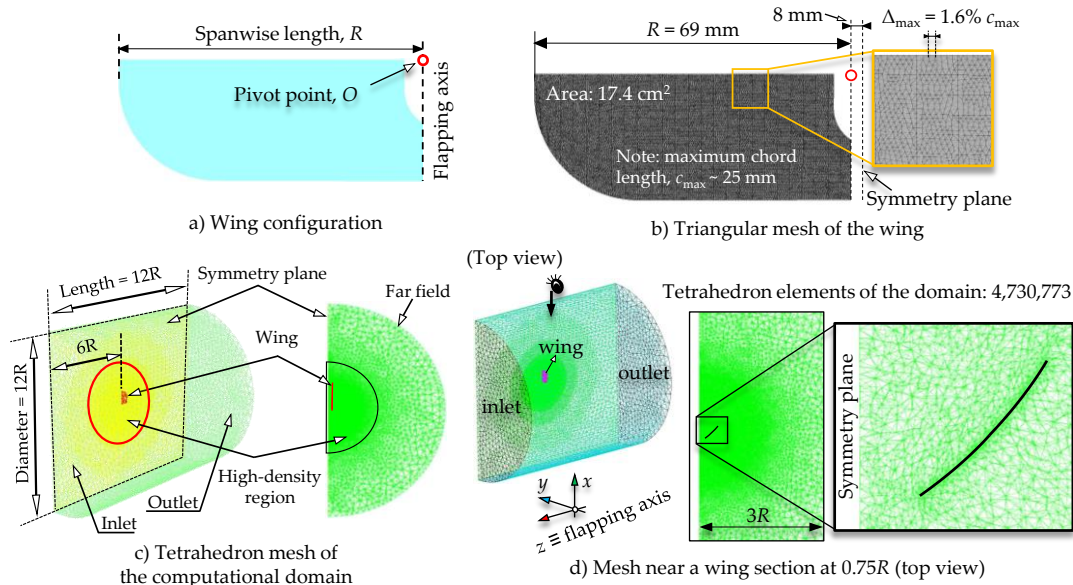


Figure 2. (a, b) Configuration and mesh of the wing, and (c, d) mesh details of computational domain

The CFD modeling in this paper (Fig. 2), is created by following the same mesh setting with that in (Au and Park, 2019), which provided the converged solutions. Therefore, the mesh independence study is assumed to be done for this work. Due to the symmetric flapping motion, only one wing is simulated (Fig. 2a). The wing is modeled by about 60,000 triangular elements, whose maximum element edge length is 0.4 mm, which is equivalent to 1.6 % of maximum chord length, c_{max} (Fig. 2b). The spanwise length, R is referenced to build the 3D computational domain (Fig. 2c). The domain is filled by about 4.7 million tetrahedral elements. The mesh is finest surrounding the wing in the high-density region, occupying about 50 % of the total elements. The maximum element edge length in this high-density region is 2.0 mm. Thus, the mesh size becomes coarser toward the far field. The Reynolds number of the KUBeetle is in the range of 10^3 to 10^4 along the wingspan, as reported in (Au and Park, 2019). In addition, there were essentially no differences in aerodynamic forces estimated by CFD between the laminar and turbulent flow options of a flapping dragonfly wing for Reynolds numbers of 500 and 30,000 (Young and Lai, 2008). Therefore, the same laminar flow option is employed in this work.

2.3 Method of wing kinematics modulation

We used the measured wing kinematics of the KUBeetle as the reference wing kinematics, named the TEC-WK, and modulated the wing kinematics to improve aerodynamic efficiency. In the modified wing kinematics, the flapping angle (ψ) is the same as that of the TEC-WK (Fig. 1b3). The implemental strategy to suggest a modified wing kinematics must ensure that all of the physical natures of the flapping wings are maintained, which is described as follows. As the first step, the spanwise-average camber of the TEC-WK is calculated at each time (t/T) using Eq. (1). Then, the camber at each time of the modified wing kinematics is assumed to be constant from the wing root to the tip, which is based on the spanwise-average camber of the TEC-WK computed at the same time. For example, the spanwise-average camber of the TEC-WK (Fig. 1b4) at $t/T = 0.25$ is about 16 %. Then, the camber of the modified wing kinematics at each spanwise location at the same time is suggested based on this spanwise-average camber of the TEC-WK.

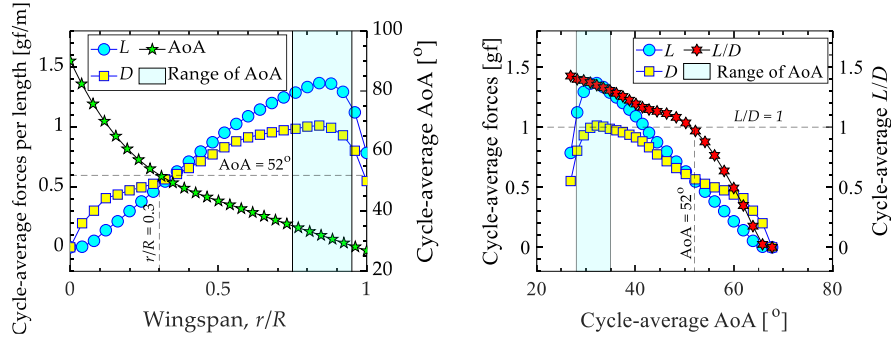


Figure 3. (a) Cycle-average forces and AoA, and (b) cycle-average forces and L/D

Second, Equation (3) expresses the definitions of AoAs. The AoAs of the TEC-WK are used to specify the AoAs of the modified wing kinematics:

$$\text{For downstroke: } \alpha = \pi - \theta_f \quad \text{and} \quad \text{for upstroke: } \alpha = \theta_f. \quad (3)$$

Table I. Details of AoAs (α), the spanwise-average camber, and the CFD results of five cases

	Stroke(s)	AoA (α) [°]				Camber [%]	Results			
		0.25 R	0.5 R	0.75 R	aver		L [gf]	D [gf]	L/D	
TEC-WK	Down	55.4	43.4	34.7	39.9	14.5	9.4	8.5	1.1	
	Up	55.8	43.5	35.6	40.7	19.5	10.8	9.4	1.2	
With camber but no twist	ver 1	Down	31.9	29.2	28.9	29.7	17.8	7.5	4.3	1.7
		Up	32.6	29.8	29.0	29.9	19.3	8.6	4.8	1.8
	ver 2	Down	33.9	31.2	30.6	31.4	17.9	7.9	4.9	1.6
		Up	34.2	31.4	30.5	31.5	19.3	8.8	5.4	1.6
With camber and twist	ver 3	Down	50.6	40.5	32.3	36.9	18.2	9.8	6.8	1.4
		Up	50.6	40.4	32.4	37.0	16.5	9.9	7.3	1.4
	ver 4	Down	45.6	40.5	35.5	38.0	19.7	10.3	7.3	1.4
		Up	45.4	40.4	35.3	37.8	18.1	10.5	8.0	1.3

In Fig. 3a, the left vertical axis indicates the cycle-average forces per length produced along the wingspan. The right vertical axis represents the cycle-average AoA over the spanwise location, which is interpolated based on the mean AoAs calculated at $0.25R$, $0.5R$, and $0.75R$ during the translational stages of the downstroke ($0.1 \leq t/T \leq 0.4$) and upstroke ($0.6 \leq t/T \leq 0.9$). Figure 3b presents the cycle-average lift (L), drag (D), and L/D versus the cycle-average AoA.

Note that the lift here is the force component in the vertical direction, while the drag is the horizontal force component of the resultant force. The shaded areas in the two plots stand for a AoA range of 28°–35°, where the lift and aerodynamic efficiency are relatively high. This AoA range corresponds to the spanwise locations from 0.75R to 0.95R (Fig. 3a), where a large portion of the aerodynamic force is generated in a wing. Another important note is that the L/D ratio at 0.3R is close to that at $\alpha \approx 52^\circ$, and it becomes less than one when $\alpha > 52^\circ$. Therefore, the cycle-average AoA of the modified wing kinematics must stay within the recommended range of 28°–35°. Third, using Eqs. (1) and (3), the AoAs of the modified wing kinematics are presented in Figs. 4a–d, based on their AoAs and spanwise-average camber (Fig. 4e). Finally, for the wing twist definition, the twist ratios of the TEC-WK at each time, which are defined in this work as the ratio of the AoA at the two locations of 0.25R and 0.75R to the AoA at 0.5R, are proportionally modulated for the modified wing kinematics. However, the cycle-average AoA at 0.25R is less than 50°, and that at 0.75R is in the range 28°–35°.

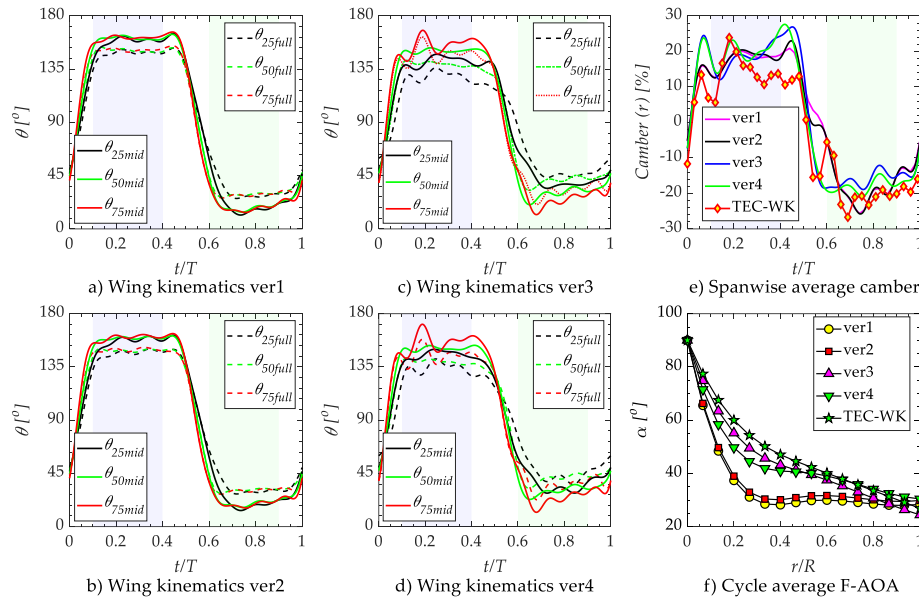


Figure 4. a–d) Modified wing kinematics, e) spanwise-average camber, and f) cycle-average F-AOA

Based on the guidelines, Table I and Figure 4 propose and present the four modified wing kinematics, which are named wing kinematics ver1, ver2, ver3, and ver4. Table I shows the half-cycle-average AoAs and spanwise-average camber of the five cases. Note that the average calculation is taken during $t/T = (0.1 - 0.4)$ in the downstroke, and $t/T = (0.6 - 0.9)$ in the upstroke. For the TEC-WK, the differences of the spanwise-average camber in the two half-strokes are relatively large, which implies that the camber of the TEC-WK is asymmetric. For example, the spanwise-average camber in the downstroke is 14.5 %, while in the upstroke it is 19.5 %. This explains why the lift is asymmetrically produced in the two half-strokes, *e.g.*, 9.4 gf (downstroke), and 10.8 gf (upstroke). Hence, the half-cycle-average camber of the TEC-WK is adjusted and applied in the modified wing kinematics to minimize the difference of lift produced by the two half-strokes of modified wing kinematics. Figures 4a–d present four modified wing kinematics. Figure 4e shows the spanwise-average cambers of the five cases. They are modified to ensure that the forces generated by the two half-strokes are close to each other, and their spanwise-average cambers are close to that of the TEC-WK. Figure 4f plots the distributions of their cycle-average AoAs along the wingspan. In Fig. 4f, since the cycle-average AoAs from

0.25R to the wing tip are similar in ver1 and ver2, we define that the cases ver1 and ver2 are with chordwise camber, but without spanwise twist.

3. Results

Table II shows the simulation results for the TEC-WK and five modified wing kinematics with the cycle-average AoAs and spanwise-average cambers. For the first two wing kinematics ver1 and ver2, the cycle-average AoAs are about 30°–32°. The spanwise-average cambers of ver1 and ver2 are about 18.6 %, which are close to that of the TEC-WK (about 17 %). Ver1 shows reduction of the lift and drag for about 20.7 % and 49.3 % respectively, resulting in a surge of the L/D for 57.5 %, compared to those of the TEC-WK. Meanwhile, the increase in the L/D for ver2 is about 44.3 %. On the other hand, ver3 and ver4 show the satisfactory lift production of about 20 gf. The spanwise-average camber of ver3 is about 17.2 %, and that of ver4 is about 18.9 %. The lift and drag of ver3 are 3 % and 21 %, respectively, lower than those of the TEC-WK, while the L/D increases by 24 %. Similarly, ver4 increases the L/D by 20 %. Even though ver1 and ver2 provided high L/D , their generated lifts are not enough to compensate for the weight. Moreover, it is challenging to develop a wing with constant AoA along the wingspan, while still forming a chordwise camber shape. Therefore, ver3 is chosen for further wing kinematics of the KUBeetle. In addition, to investigate the effect of chordwise camber, we removed the camber in ver3, and estimated the force generations, as shown in Table II for ver3* with the twist-only case. The results show that the camber (of ver3 case) increases the lift by 16.6 % and the drag by 4.4 %, resulting in 11.2 % improvement of the L/D , compared to the those of ver3*. Since the lift by ver3 is close to that by the TEC-WK, while the drag significantly decreased, the mechanism for force production is compared to that of the TEC-WK.

Table II. Cycle-average AOAs and CFD results for the TEC-WK and modified wing kinematics

Case(s)	Name	AoA [°]	Camber [%]	L [gf]	D [gf]	L/D
Reference	TEC-WK	40.3	17.0	20.3	17.95	1.13
Camber only	ver1	29.8	18.6	16.1 (-20.7 %)	9.1 (-49.3 %)	1.78 (+57.5 %)
	ver2	31.4	18.6	16.8 (-17.2 %)	10.3 (-42.6 %)	1.63 (+44.3 %)
Twist and camber	ver3	36.9	17.2	19.7 (-2.9 %)	14.1 (-21.4 %)	1.39 (+24.0 %)
	ver4	37.9	18.9	20.7 (+2.0 %)	15.3 (-14.8 %)	1.35 (+19.5 %)
Twist only	ver3*	36.9	0.0	16.9 (-16.7 %)	13.5 (-24.8 %)	1.25 (+10.6 %)

Figure 5 indicates the vortex structures over a flapping cycle for the measured wing kinematics in (a) and the modified wing kinematics ver3 in (b). The deformed wing shape and vortical structures of both cases are basically similar. However, the formed vorticities at $t/T = 0.1$, 0.2 and 0.6 of both cases are quite different. At $t/T = 0.1$ and 0.2, for the modified wing kinematics (Fig. 5b), stronger vortical structures and larger leading-edge separation (LES) are mainly formed and concentrated at the outboard wing compared to those formed by the measured wing kinematics (Fig. 5a). In contrast, at $t/T = 0.6$, the wing kinematics ver3 produces smaller LES at the outboard wing (Fig. 5b) compared to those by the measured wing kinematics (Fig. 5a). Figures 6a shows the lift (a1, a2) and drag (b1, b2) at point 1 ($t/T = 0.21$) and point 2 ($t/T = 0.54$) at $r/R = 0.88$ for both wing kinematics. Since lower pressure due to the larger LES enhances the lift generation. The modified wing kinematics ver3 increases the lift by 49.6 % at point 1 but reduces it by about 69.8 % at point 2 (see Figs. 6a1 and a2), which are compared to those of the

reference TEC-WK. As a result, the drag, which is defined here as the horizontal component of the resultant force, also increases by about 38.1 % at point 1 and reduces by 71.0 % at point 2 (see Figs. 6b1 and b2).

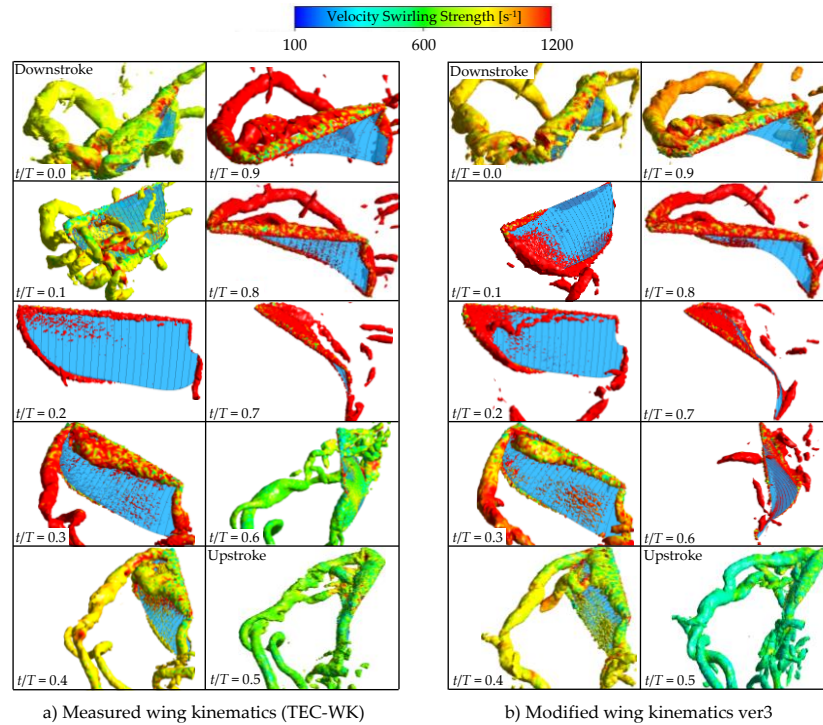


Figure 5. Vorticity of a) the measured wing kinematics, and b) the modified wing kinematics ver3

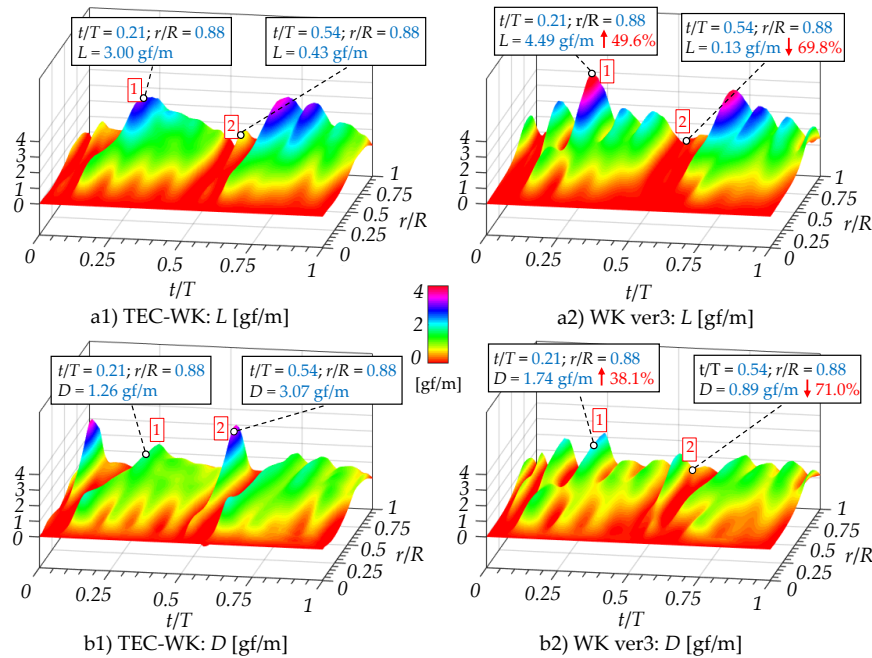


Figure 6. L (a1, a2) and D (b1, b2) for the measured wing kinematics and modified wing kinematics

4. Conclusions

This paper presented a CFD study on the aerodynamic efficiency of the KUBeetle that considered the effects of wing kinematics modulation. Based on the measured reference wing kinematics, four wing kinematics were investigated to find the proper one that improves L/D , while maintaining similar lift. The results of the modified wing kinematics ver3 with camber and twist outperformed the suggested cases, improving the aerodynamic efficiency by 24 %, while producing enough lift to compensate for the body weight. The study also confirmed that the chordwise camber (of ver3) improves both lift and L/D by about 16.7 % and 10.6 %, respectively. In conclusion, the modified wing kinematics ver3 may improve the L/D of the KUBeetle by about 25 %.

Acknowledgements

This research was supported by a National Research Foundation of Korea (NRF) grant, funded by the Korean government (MSIT) (NRF-2018R1A4A1024191).

References

- [1] Au, T.K.L. and Park, H.C. (2019), “Influence of center of gravity location on flight dynamic stability in a hovering tailless FW-MAV: Longitudinal Motion”, J. Bionic Eng., Vol. 16 No. 1, pp. 130–144.
- [2] Gehrke, A. and Mulleners, K. (2021), “Phenomenology and scaling of optimal flapping wing kinematics, Bioinspir. Biomim., Vol. 16 No. 2, p. 026016.
- [3] Okamoto, M., Yasuda, K. and Azuma, A. (1996), “Aerodynamic characteristics of the wings and body of a dragonfly”, J. Exp. Biol., Vol. 199 No. 2, pp. 281–294.
- [4] Phan, H.V. and Park, H.C. (2018), “Design and evaluation of a deformable wing configuration for economical hovering flight of an insect-like tailless flying robot”, Bioinspir. Biomim., Vol. 13 No. 3, p. 036009.
- [5] Sun, M. (2014), “Insect flight dynamics: stability and control”, Rev. Modern. Phys., Vol. 86, p. 615.
- [6] Truong, Q.T., Phan, H.V., Park, H.C. and Ko, J.H. (2013), “Effect of wing twisting on aerodynamic performance of flapping wing system”, AIAA journal, Vol. 51 No. 7, pp. 1612–1620.
- [7] Young, J., Lai, J.C. and Germain, C. (2008), “Simulation and parameter variation of flapping-wing motion based on dragonfly hovering”, AIAA journal, Vol. 46 No. 4, pp. 918–924.

Design and Test of a Propulsion System for a Robotic Flying Fish

Tan-Hanh Pham¹, Hoon Cheol Park^{1,*}

¹ Dpt. of Smart Vehicle Engineering, Artificial Muscle Research Center, Konkuk University,
Seoul 05029, Korea

* Corresponding author. E-mail: hcpark@konkuk.ac.kr

Abstract

Flying fish is a unique underwater animal that can escape from water to air, creating a very fast swimming speed of 10 m/s. Flying fish fall in the carangiform fish and produce propulsive force mainly by undulating their posterior body including caudal fin. In this work, we aim to design and fabricate a fish robot mimicking flying fish. As the first step of the research, we designed and tested a propulsion system that can create a fast tail-beat motion and produce a relatively large thrust. The required torque of the motor was calculated considering the gear ratio and the applied torque from tail based on the added mass model. Experimental results obtained from measurements indicate that propulsion system can generate a cycle average thrust of 0.88 N force at a tail-beat frequency of about 11 Hz when 12V is applied to the motor.

Keywords: Flying fish robot, Tail-beat mechanism, Propulsion system, Propulsive thrust

Nomenclature

N_g, N_p : gear ratio, pulley ratio	F_y : component force of tail motion in y direction (N)
α, β : tail-beat angle, reciprocating angle ($^\circ$)	$\Delta\theta, \Delta t$: angle interval, time interval
θ, w : tail angular position, angular velocity ($^\circ$)	Q_m, Q_a : motor torque, peak torque (N.m)
F_x : component force of tail motion in x direction (N)	EI: peduncle bending stiffness (N.m ²)

1. Introduction

Flying fish is a special creature, after million years of evolution, they have gain the abilities of fast swimming in the water, jumping out of the water and flying in the air. It is assumed that the main reasons for these abilities are escaping from underwater predators and storing their energy in a long expedition (Davenport, 1994). Flying fish is characterized by the capabilities of generating large thrust of tail under water and gliding in air with their pelvic and pectoral fins. Unlike insects and birds, flying fish can slide in air because of producing thrust created by propelling motion in water. Inspired by these exceptional characteristics, there are several research groups tried to create a model mimicking flying fish. Based on a constructed model of flying fish and some assumptions, the hydrodynamic forces for the model in the water media was estimated, and then a number of conceptual designs were introduced (Gao and Techet, 2011). In order to determine the effect of fish wings, a series of tests both pectoral fins and pelvic fins with dead fishes were undertaken in a wind tunnel, and several aspects of its effect were conjectured (Park and Choi, 2010). Following these results, a study determining the effect of fish wings during gliding flight phase was conducted on CFD environment (Deng *et al.*, 2019). However, there are no candidate that has ability to launch itself out of water and fly in air. Recently, a flying model that has a battery charged by a solar cell was designed by Stanford University, and it mimics the leaping glide of flying fish and flies in the air by its motor-driven propulsive

system without external powers (Marks, 2013). Furthermore, a Dolphin robot has capable of emerge out of water by itself was also designed (Yu *et al.*, 2016). As a design of the robot fish, Dolphin robot could emerge above the water level for over one second. In addition, a motor-based propulsion mechanism of carangiform fish robot was fabricated and then tested in water (Zhang and Zhang, 2018). They used a crank-rocker mechanism and a motor to drive the robotic fish. Meanwhile, by using a tensegrity structure that combines rigid bone elements and elastic cables, a motor-driven swimming robotic fish was also designed and tested in water (Shintake *et al.*, 2020). There are several additional fish robots developed in the last two decades (Clapham and Hu, 2015; Zhu *et al.*, 2019), but most of them are designed for only underwater swimming.

In this work, as the first stage of the design and fabrication of a robotic flying fish, a tail-beat propulsion system was designed and tested to eventually mimic the ability of flying fish, which can jump from water to air. In section 2, the design method of the propulsion system is described. Measurements presented in section 3. Result and discussion are shown in section 4. Conclusion is drawn in section 5.

2. Design Method

The flying fish robot includes a driving mechanism in a combination of a DC motor, reduction gear, four-bar linkage system, and a pulley-string mechanism. The DC motor (CL1625 Chaoli China) has the nominal spindle speed of 11,800 RPM at 12V and the stall torque of 16.8 mN.m. The reduction system consists of a reduction gear with a gear ratio of 14.4, a reduction pulley with a reduction ratio of 1.5 and a four-bar linkage. The reduction gear ratio was calculated as follows:

$$N_g = \frac{n_A}{n_B}, \quad (1)$$

where n_A and n_B are number teethes of gear A, B, respectively.

The pulley ratio was calculated as follows:

$$N_p = \frac{r_1}{r_2} \text{ and } \alpha = N_p \beta, \quad (2)$$

in which, r_1, r_2 are radii of the large and small pulleys, respectively, and α, β are tail-beat angle and reciprocating angle of the large pulley, respectively.

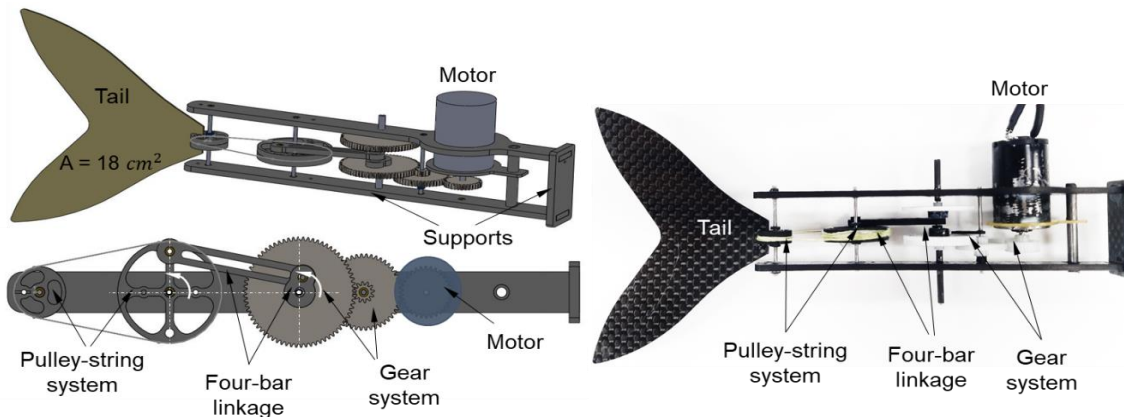


Figure 1. CAD model and construction of the propulsion system

The propagation ratio between links in the four-bar linkage mechanism can be computed as follows:

$$X = \sqrt{(O_0O_3)^2 + (O_2O_3)^2 + 2 \cdot O_0O_3 \cdot O_2O_3 \cdot \sin\left(\frac{\beta}{2}\right)} \quad (3)$$

$$Y = \sqrt{(O_0O_3)^2 + (O_2O_3)^2 - 2 \cdot O_0O_3 \cdot O_2O_3 \cdot \sin\left(\frac{\beta}{2}\right)} \quad (4)$$

$$O_0O_1 = \frac{X-Y}{2} \text{ and } O_1O_2 = \frac{X+Y}{2} \quad (5)$$

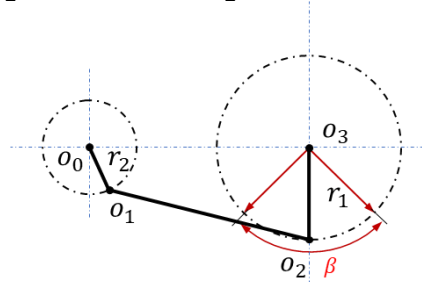


Figure 2. Parameters in the four-bar linkage

To obtain a set of approximate driving parameters, we calculated the applied torque for the tail. Motion of tail was assumed to be harmonic under water with a tail-beat angle of 60° at 10 Hz. A tail with an area of about 18 cm^2 was considered for the calculation. To estimate the applied torque created by tail, the method of added-mass was applied. In this approach, the acceleration of tail results in the acceleration of the water moving together with the tail. The accelerated water mass contributes to the thrust generation as the reaction. As shown in Figure 3a, the tail area made by the small length Δr and height $h(r_i)$ creates the force in the θ direction $(F_\theta)_j$ due to the tail-beat motion. The force can be decomposed into the two components, in the x and y directions as shown in Figure 3b, and they can be expressed by the following equations. At $t = t_j$ for $\theta = \theta_j$, if the tail-beat motion is in symmetry with respect to the x axis:

$$(F_x)_i = (F_{\theta_i})_i \sin\theta_j m_i r_i \ddot{\theta}_j \sin\theta_j, \quad (6)$$

$$(F_y)_i = (F_{\theta_j})_i \cos\theta_j = m_i r_i \ddot{\theta}_j \cos\theta_j, \quad (7)$$

$$\Sigma(F_y)_i = 0, \quad (8)$$

where $m_j = \rho \pi h^2(r_i) \Delta r$ as shown in Figure 3c, which is the added mass around the small tail section.

If the tail-beat motion is assumed harmonic in time with a period T, the angular position θ , angular velocity ($\dot{\theta}$) and angular acceleration ($\ddot{\theta}$) can be expressed by the following equations.

$$\theta(t) = \theta_0 \sin\left(\frac{2\pi}{T} t\right) \text{ with } \omega = \frac{2\pi}{T} = 2\pi f \left(f = \frac{1}{T}\right), \quad (9)$$

$$\dot{\theta}(t) = \theta_0 \omega \cos(\omega t), \quad (10)$$

Therefore, the angular acceleration (a_θ) in the θ direction at time t is expressed as follows:

$$a_\theta(t) = r \ddot{\theta}(t) = -r \theta_0 \omega^2 \sin(\omega t), \quad 0 \leq t \leq T. \quad (11)$$

If the shape of a tail fin is a trapezoid as shown in Figure 3, the added mass of the small section made by the small distance (Δr) and the height $h(r)$ can be expressed as follows:

$$h(r) = r_0 + \left(\frac{h_t - h_0}{R}\right) r, \quad (12)$$

$$m_i = m(r_i) = \rho \pi h^2(r_i) \Delta r. \quad (13)$$

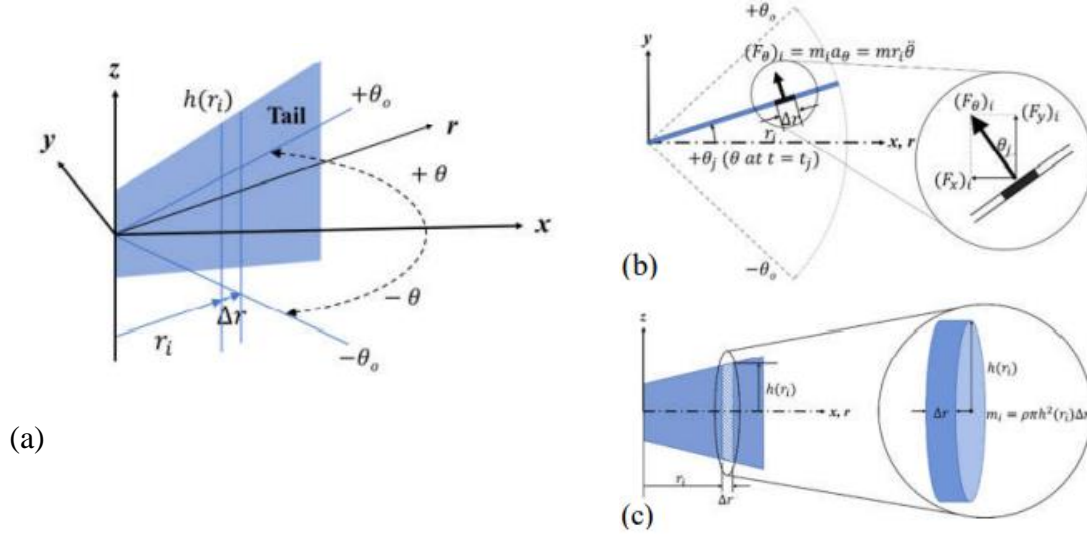


Figure 3. Tail-beat motion: (a) definition of the tail motion and section dr divided along the tail-length, (b) translational force components of tail, (c) cross-sectional area of the surrounding water and the added mass

When the number of the fin sections is N_R , which can be 10 to 20, the small fin length becomes:

$$\Delta r = \frac{R}{N_R}, \quad (14)$$

If the number of time steps is N_T , the small angle interval and time interval are respectively,

$$\Delta \theta = \frac{\theta_0}{N_T} \quad (N_T \sim 20), \quad (15)$$

$$\Delta T = \frac{T}{N_T}, \quad (16)$$

The position of the small fin section r_i , the time t_j , and the angular acceleration (a_θ) in the θ direction can be expressed as follows:

$$r_i = \Delta r \times i - \frac{\Delta r}{2} \quad (i = 1 \sim N_R), \quad (17)$$

$$t_j = t_0 + (j - 1)\Delta t \quad (j = 1 \sim (N_T + 1)), \quad t_0 = 0, \quad (18)$$

$$a_\theta(t_j)_i = r_i \ddot{\theta}(t_j) = -r_i(\theta_0 \omega^2) \sin(\omega t_j), \quad (19)$$

$(i = 1 \sim N_R, j = 1 \sim (N_T + 1)).$

Therefore, the force in the θ direction, created by the small fin section, can be expressed as following equation:

$$F_\theta(t_j)_i = m_i a_\theta(t_j)_i = m(r_i) a_\theta(t_j)_i = [\rho \pi h^2(r_i) \Delta r] \cdot [-r_i \theta_0 \omega^2 \sin(\omega t_j)], \quad (20)$$

Its x-component, which is a contribution to the thrust is written as follows:

$$F_x(t_j)_i = F_\theta(t_j)_i \cos \theta_j = [\rho \pi h^2(r_i) \Delta r] \cdot [-r_i \theta_0 \omega^2 \sin(\omega t_j)] \cos \theta_j, \quad (21)$$

Finally, the thrust produced by all the fin sections can be computed by summing the contributions of all the fin sections as follows:

$$F_{x,\text{total}} = \sum_{j=1}^{N_T} \left(\sum_{i=1}^{N_R} F_x(t_j)_i \right) \left(\frac{\Delta t}{T} \right). \quad (22)$$

For the tail shown in Figure 1, the estimated average thrust is 1.5 N and the applied peak torque Q_a is about 211 mN.m. Then the required motor torque Q_m , about 22 mN.m in this design, can be calculated using the following equation:

$$Q_m = \frac{N_p}{N_g} Q_a, \quad (23)$$

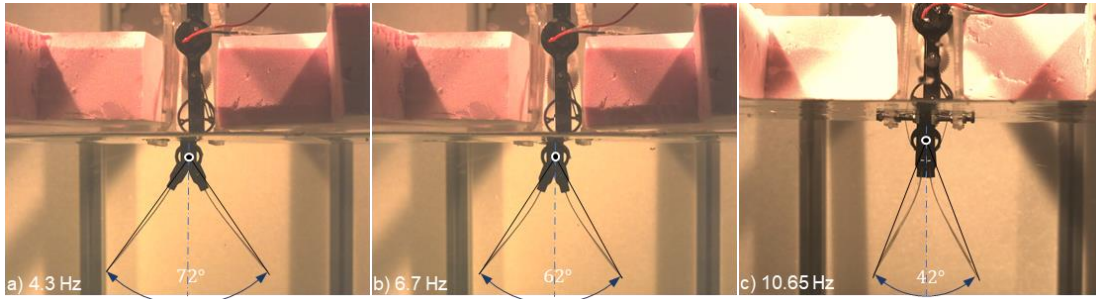


Figure 4. Tail-beat angle changing for a tail-beat frequency

3. Experimental Measurement

The thrust measurement was conducted in a glass water tank, which is 60 cm long, 30 cm wide, and 30 cm deep. Two aluminum extrusions were installed at a position above the water tank which were parallel to the water surface. A fixture made of plastic material was fixed on the aluminum extrusions and installed downward into the water tank. Then, the propulsion system was placed on the fixture and aligned in the vertical line. The tail was submerged in the water, and it moved in the lateral side.

To measure the tail-beat frequency for an applied voltage, a high-speed camera, with a film frame of 2,000 fps and a resolution of 1,024x1,024 pixels, was used to capture the motion of tail. Sequential images obtained from the camera were then analyzed to determine the tail-beat frequency. To measure thrusts generated by the tail-beat motion, a load cell capable of measuring three force and moment components (Nano17, ATI Industrial Automation, USA, force resolution of 0.0125 N and moment resolution of 0.0625 N.mm) was used. The load cell was vertically installed above the propulsion system.

To provide a best performance of swimming for flying fish robot, we investigated the effects of bending stiffness, peduncle length, and tail-beat angle on the thrust generation. Material of the tail plays an important role in generating thrust. Thus, three different bending stiffnesses were tested in this robot fish to compare the produced thrusts. The tails were made of carbon/epoxy and/or glass/epoxy with a thickness of 0.3, 0.4 and 0.5 mm.

4. Result and Discussion

The tail-beat propulsion system was designed and constructed for a tail-beat angle of 60°. However, the experimental results show that the tail-beat angle was reduced at high frequencies, and this phenomenon is illustrated in Figure.

Figure 5 shows a comparison of time histories of the measured thrust and estimated one by the added-mass model for a tail with a tail-beat angle of 60°. The measured thrust was filtered by a low pass filter with a cutoff frequency of 22 Hz. It is found that the predicted peak thrust was underestimated. However, the estimated average thrust was in good agreement with the measured one. At the tail-beat frequencies of 6.7 Hz and 10.65 Hz, the measured thrusts were 0.71 N and 0.88 N, respectively, while the theory results of those were 0.72 N and 0.85 N, respectively.

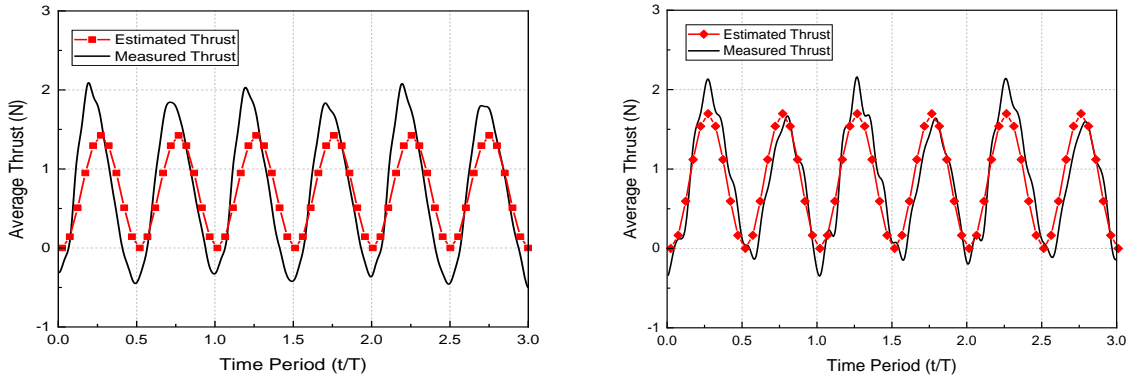


Figure 5. Average thrusts created by tail-beat mechanism: a) the generated thrusts at 6.7 Hz. b) the generated thrusts at 10.65 Hz

The effect of stiffness on the thrust generation is shown in Figure 6. The tail with a larger peduncle bending stiffness of 9.5EI (N.m²) shows lower frequency and produces lower average thrust for the same input voltage. The tail with a lower bending stiffness of 1EI (N.m²) creates faster frequency but produces lower thrust than the tail with 4.6EI (N.m²) at 12V. So, we have chosen the fin with a bending stiffness of 4.6EI, in which EI = 0.1125.

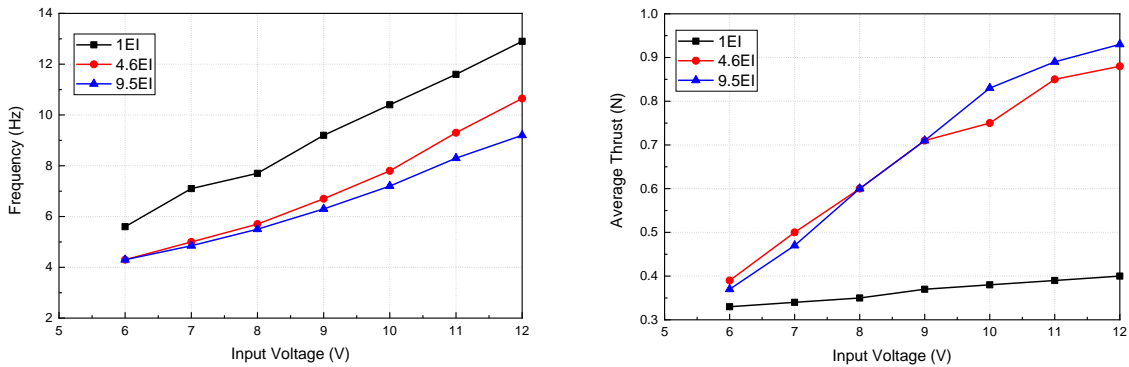


Figure 6. Effect of tail stiffness on produced thrust and frequency as depleted under the input voltage

For the tail with 4.6EI (N.m²), the tail peduncle length of 10 and 15 mm were tested. In Figure 7, the fin with a peduncle length of 15 mm moves more flexibly in water at a higher frequency, and it produces lower thrust for the same input voltage. Therefore, we have chosen the peduncle length of 10 mm.

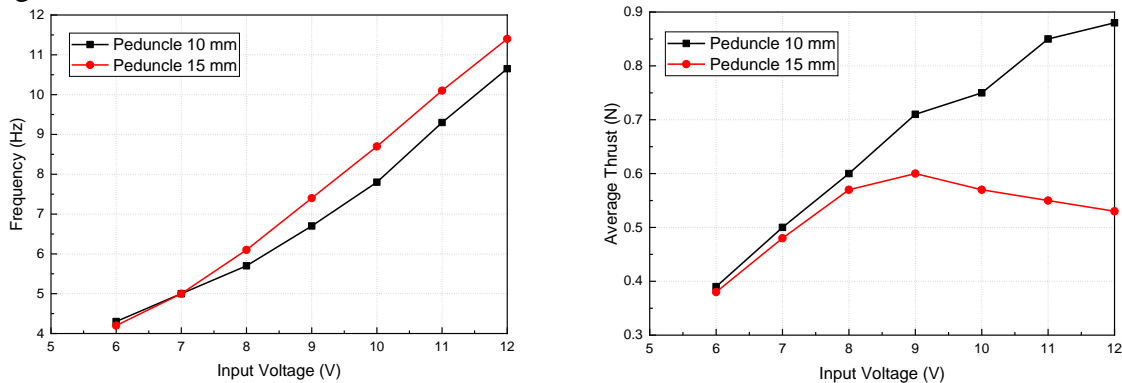


Figure 7. Effect of peduncle length on creating thrust and frequency

Using a tail with a bending stiffness of $4.6EI$ and a peduncle length of 10mm, this paper examined the effect of tail-beat angle (TB_A) in a range from 55° to 65° .

In the angle range, Figure 8 shows that the average thrust of tail becomes larger as the design tail-beat angle increases, while the frequency decreases. However, the actual tail-beat angle became smaller than the design tail-beat angle because of the bending deformation in the water as shown in Figure 8. Analyzing the actual tail-beat angle, the design tail-beat angle of 60° was chosen to apply for the future experiments.

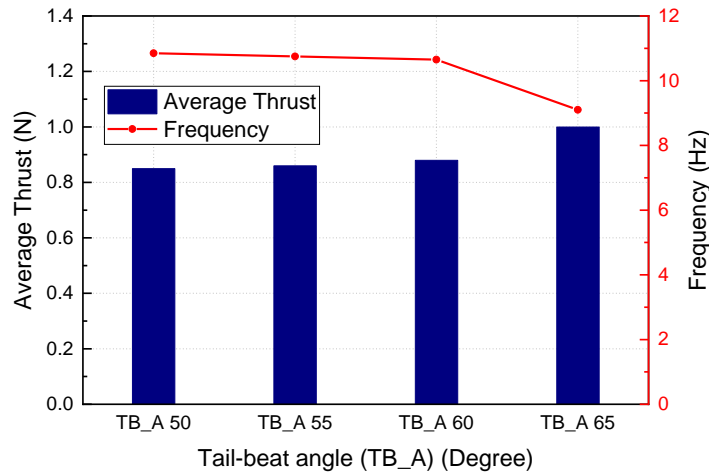


Figure 8. Comparison of thrust generation for various design tail-beat angle

5. Conclusion

In this work, we have presented a tail-beat propulsion mechanism for a robotic flying fish. For experimental purpose, the model was used to investigate the generating force capability. Force and frequency measurements were performed to provide quantitative data for the propulsion system. Through the experiments, the thrust generation characteristics of the system was identified in terms of the effects of bending stiffness of the tail, the effects of peduncle length, and the effects of tail-beat angle. For the high thrust generation, we chose the bending stiffness of $4.6EI$ ($N.m^2$) and the peduncle length of 10 mm. For these parameters, the maximum thrust was measured at the tail-beat angle of 65° and the frequency of tail-beat angle is about 9 Hz when the voltage of 12V was applied. Considering reduction in the tail-beat angle at a high frequency, we have chosen the tail-beat angle of 60° for fabrication of the flying fish robot in the future experiments.

Acknowledgement

This research was supported by National Research Foundation of Korea (NRF) grant, funded by the Korea government (MSIT) (NRF-2020R1F1A106827212).

References

- [1] Clapham, R.J. and Hu, H. (2015), "ISplash: Realizing fast carangiform swimming to outperform a real fish" In Robot Fish, pp. 193-218.
- [2] Davenport, J. (1994), "How and why do flying fish fly?", Reviews in Fish Biology and Fisheries, Vol. 4 No. 2, pp. 184-214.

- [3] Deng, J., Zhang, L., Liu, Z. and Mao, X. (2019), “Numerical prediction of aerodynamic performance for a flying fish during gliding flight”, *Bioinspiration and Biomimetics*, Vol. 14 No. 4, pp. 046009.
- [4] Gao, A. and Techet, A.H. (2011), “Design considerations for a robotic flying fish”, In *OCEANS'11 MTS/IEEE KONA*, pp. 1-8.
- [5] Marks, P. (2013), “Robot takes to the air on the wings of a fish”, *New scientist* 2916, pp. 22.
- [6] Park, H. and Choi, H. (2010), “Aerodynamic characteristics of flying fish in gliding flight”, *Journal of Experimental Biology*, Vol. 213 No.19, pp. 3269-3279.
- [7] Yu, J., Su, Z., Wu, Z. and Tan, M. (2016), “Development of a fast-swimming dolphin robot capable of leaping” *IEEE/ASME Transactions on Mechatronics*, Vol. 21 No. 5, pp. 2307-2316.
- [8] Zhang, R. and Zhang, H. (2018), “Simulation and Analysis for Propulsion Mechanism of Carangiform Robotic Fish on ADAMS”, In *2018 IEEE International Conference of Intelligent Robotic and Control Engineering (IRCE)*, pp. 1-5.
- [9] Shintake, J., Zappetti, D., Peter, T., Ikemoto, Y. and Floreano, D. (2020), “Bio-inspired Tensegrity Fish Robot” In *2020 IEEE International Conference on Robotics and Automation (ICRA)*, pp. 2887-2892.
- [10] Zhu, J., White, C., Wainwright, D. and Di Santo, V. (2019), “Tuna robotics: A high-frequency experimental platform exploring the performance space of swimming fishes”, *Science Robotics*, Vol. 4 No. 34.

Aerodynamic and Structural Performances of a Single-stage Transonic Axial Compressor with Blade Fillet Radius

Chu Hoang Quan^{1,*} and Dinh Cong Truong²

¹Le Quy Don Technical University, Hanoi, Vietnam, 11917

²Hanoi University of Science and Technology, Vietnam, 11615

*Corresponding author. E-mail: chu.h-quan.fas@lqdtu.edu.vn

Abstract

The study of Fluid-Structure Interaction (FSI) between airflow passing through blades and blades themselves is an important problem in turbomachinery. Using the commercial simulation software and the one-way FSI approach, this paper focus on the influence of a fillet radius of 2.5 mm, i.e., an additional geometry to the blades of a single-stage transonic axial compressor, NASA Stage 37, on its aerodynamic and structural performances. The aerodynamic results (i.e., total pressure ratio, adiabatic efficiency, stall margin), which are evaluated by solving the 3-D RANS equations with the k- ϵ turbulence model, are validated with experimental data. The structural outcomes (i.e., equivalent von-Mises stress, total deformation) determined after the CFD simulations are compared between the models with and without fillets. The numerical results show that there are small different values between the clean case and fillet case, 84.01% and 83.93% for peak efficiency, 2.07798 and 2.08228 for pressure ratio at near-stall condition, respectively. The stall margin significantly increases by 47.94%, from 10.21% in the case with fillet to 15.10% in the case without fillet. On the structural analysis, all structural performances declines when the blade fillets are added to the original design. At peak adiabatic efficiency condition, the maximal total deformation on the tip blade is slightly decreased while the maximal equivalent von-Mises stress on the rotor hub or the stator shroud is considerably reduced in the design with fillet as compared to the outlines of clean case.

Keywords: Single-stage transonic axial compressor, Fillet radius, 3-D RANS, 1-way FSI, Total pressure ratio, Adiabatic efficiency, Stall margin, von-Mises stress, Total deformation

Nomenclature

CFD	=	Computational Fluid Dynamics
CSD	=	Computational Structural Dynamics
EFF	=	Adiabatic efficiency (%)
PR	=	Pressure ratio
FSI	=	Fluid-Structure Interaction
SM	=	Stall margin (%)
RANS	=	Reynolds Averaged Navier-Stokes
max	=	Chocking mass flow point
peak	=	Peak adiabatic efficiency point
stall	=	Near-stall point
in	=	Inlet
out	=	Outlet
\dot{m}_{\max}	=	Mass flow rate at chocking condition (kg/s)

\dot{m}_{peak}	=	Mass flow rate at peak efficiency condition (kg/s)
\dot{m}_{stall}	=	Mass flow rate at near-stall condition (kg/s)
P_t	=	Total pressure (Pa)
PR_{peak}	=	Total pressure ratio at peak adiabatic efficiency condition (Pa)
PR_{stall}	=	Total pressure ratio at near-stall condition (Pa)
R_{RF}	=	Rotor fillet radius (cm)
R_{SF}	=	Stator fillet radius (cm)
T_t	=	Total temperature (°C)
γ	=	Specific heat ratio
η	=	Adiabatic efficiency (%)

1. Introduction

In turbomachinery, a real blade is often fabricated with a fillet, which is a smooth transition between the blade and the end-wall surfaces. Airflow through the blade root region in an axial compressor is a flow phenomenon influencing aerodynamic performances such as total pressure ratio, adiabatic efficiency, and stall margin. Many previous studies confirmed that this geometric feature could reduce endwall loss (or secondary flow loss). Kügeler *et al.* [1] gave a review of rotor blade fillets' effect in a 15-stage gas turbine compressor. Because of the presence of fillet geometry, there were a flow deflection reduction on the secondary flow and a corner stall decrease at the rotor hub and stator tip. In comparison with the clean case, the result for the fillet case was a higher throttling range. Matteo [2] presented the blade fillet effect of an axial 4.5 stage compressor on aerodynamic and structural performances. Since the crossflow section was lowered by fillet geometric feature, the flow deceleration increased, and the static pressure raised also if the total pressure was reduced. The stress distribution near the endwall zone was also influenced by the blade fillet. Meyer *et al.* [3] showed the experimental study on the high-speed compressor cascade without fillets and on three ones with different fillet radius (1 mm, 3 mm, and 5 mm). On the suction side, the fillets generated higher losses in the middle of the passage than in the side wall region. On the pressure side, additional losses in the corner area were produced by adding drag of these fillets. The effects of impeller blade fillets on aerodynamic performance were detected numerically in Oh [4]. At the corner of the hub pressure surface, there was a small scraping vortex in the case of clean blades, but this vortex disappeared in the case with blade fillets. Oh's study also demonstrated that the compressor performances dropped in the cause of shroud passage vortex, which grew toward the impeller exit with a higher vortex core in the case with blade fillets than in the case without fillets. Vasudevan [5] showed the experimental study of fillet radius' effects on the secondary flow modification and the generation of the losses under a low Reynolds number. It has been indicated that the presence of a uniform blade fillet decreased the overturning secondary flow and reduced marginally the endwall and mass averaged losses. A numerical study of the rotor blade fillet on aerodynamic performances in a transonic axial compressor, NASA Rotor 37, was found in Vu *et al.* [6]. By varying fillet radius compared to the maximum rotor chord length from 2% to 7%, mass flow rate fell while adiabatic efficiency and pressure ratio tended to rise slightly.

In Fluid-Structure Interaction (FSI) problems, there are reciprocal influences between one (or more) solid structure(s) and the surrounding (or internal) fluid flow. Numerous researchers applied the FSI approach to analysis study parameters in the turbomachine field such as pressure distribution, equivalent stress, rotor deflection, etc. Lerche *et al.* [7] predicted stresses on the blades of a single-stage centrifugal compressor by using the one-way FSI method. There was a

good agreement between numerical and experimental results when trying to determine a cause of failure. Wang *et al.* [8] presented a one-way FSI simulation on a 2-MW offshore wind turbine blades to define the mechanical properties for the full machine, such as stress and strain. These values gained a nice result in comparison with other scholar's figures, such as Chen *et al.* [9]. An evaluation matching total pressure ratio, efficiency, and stress between optimum and initial design of a NASA Rotor 37 was introduced by Song *et al.* [10]. The results using one-way FSI method showed that while total pressure ratio was constant, the adiabatic efficiency increased by 0.3% and the maximum stress decreased to 0.9 MPa. However, the authors did not talk about the influence of rotor rotation speed on the stress calculations. Applying FSI analysis and response surface method, Kang and Kim [11] submitted an optimum impeller design of a centrifugal compressor. At constant pressure, there were an efficiency increment by 1% and a stress decrement of 10% in the case of optimum design compared to the initial design. Dinh *et al.* [12] investigated the effects of rotor airflow bleed on aerodynamic and structural performances of a transonic single stage axial compressor, NASA Stage 37, using the FSI analysis. The numerical results were validated with the experiment data and showed the small growth of aerodynamic performances, such as about 0.09% and 0.51% increment in peak adiabatic efficiency and total pressure ratio, respectively, at peak efficiency condition. In the case of a reference bleeding airflow, there were a very small rising in von-Mises stress and a decreasing in total deformation on rotor tip leading edge in spanwise direction as compared to the results of smooth casing.

In the studies indicated above, Vu *et al.* [6] did not mention the effects of stator fillets and the structural performances, Dinh *et al.* [12] did not surveyed the influence of fillet radius on the compressor performances. Therefore, this paper deals with the one-way FSI method to determine the effects of blade fillet in the aerodynamic and structural performances of a single-stage transonic axial compressor, NASA Stage 37. Firstly, to prove the aerodynamic analysis, the fluid model of this compressor is solved using three-dimensional Reynolds Averaged Navier-Stokes (3D RANS) equations with the $k-\epsilon$ turbulence model. Secondly, to conduct the structural analysis, the blade surfaces of NASA Stage 37 structural model, such as blade tips, pressure sides and suction sides, carry the pressure load from the fluid model. Finally, the aerodynamic performance results (i.e., total pressure ratio, adiabatic efficiency, stall margin) are validated with experiment data. Due to the lack of experimental figures, the structural performance results (i.e., equivalent Von-Mises stress, total deformation) are compared between the models without fillet radius and the ones with fillet.

2. Numerical analysis

2.1 Compressor model

Reid and Moore [13] took an experimental research of the single-stage transonic axial compressor, NASA Stage 37, which had 36 rotor blades rotating at a speed of 17185.7 rpm for 100% speed design and 46 stator blades. The tip clearance values of this compressor were 0.4 mm under the rotor shroud and 0.762 mm over the stator hub. At peak adiabatic efficiency condition, where adiabatic efficiency was 84.00%, the total pressure ratio and mass flow rate had values of 2.00 and 20.74 kg/s, respectively. The figures of adiabatic efficiency and mass flow rate declined in the order to 79.30% and 19.6 kg/s, while the total pressure ratio reached a peak at 2.093 at near-stall condition. The reference data for temperature and pressure were correspondingly 288.15 K and 101.325 Pa. After the tests of Reid and Moore [13] on NASA Stage 37, Dunham [14] investigated an isolated rotor blade, NASA Rotor 37, with an additional geometry of 2.5 mm for a blade hub fillet radius. To facilitate comparisons of results between the clean blade case and the blade fillet case, the stator shroud radius is chosen as rotor hub radius

(i.e., 2.5 mm). Fig. 1 shows the 3D view of NASA Stage 37 model, where the main design geometries were described in Reid and Moore [13].

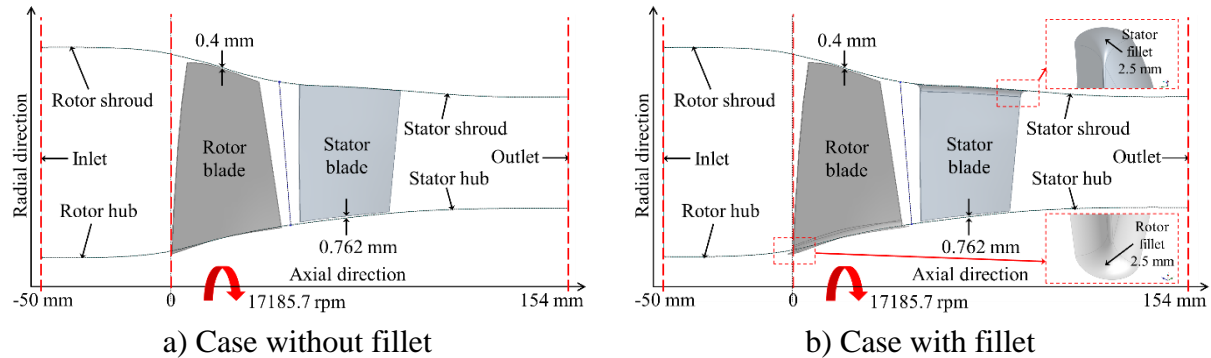


Figure 1. Meridional view of NASA Stage 37

2.2 Numerical fluid simulation

In the aerodynamic analysis, the 3D RANS equations with the $k-\epsilon$ turbulence model equations were solved using ANSYS CFX 19.1 [15]. The computational flow mesh of NASA Stage 37, as shown in Fig. 2, was automatically created by using TurboGrid®, where the rounded symmetric star topologies were applied for the leading edge and trailing edge zones. ANSYS CFX-Pre, CFX-Solver and CFX-Post were individually used to setup the boundary conditions, to solve the main equations and to show the postprocess results.

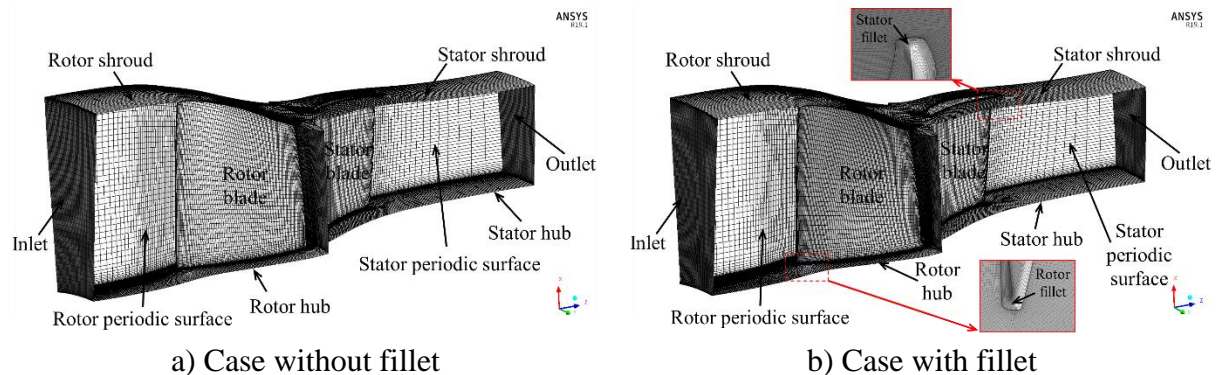


Figure 2. Computational flow mesh of NASA Stage 37

Air ideal gas was chosen as a material of the working fluid. An average static pressure was set for steady state simulation at the stator outlet boundary. A turbulence intensity of 5% was specified at the rotor inlet boundary. The adiabatic smooth wall condition is an option for the surfaces of blades, shrouds, and hubs. The general grid interface (GGI) method was used to connect the mesh between the stator and rotor domains. The frozen rotor method using specified pitch angles ($360^\circ/36 = 10^\circ$ for rotor and $360^\circ/46 = 7.826^\circ$ for stator) was applied at the interface between the rotor outlet and stator inlet surfaces. The two-equation turbulence model $k-\epsilon$ with a scalable wall function was used with y^+ value of the first nodes near the walls in a range from 20 to 100. The computational grid flow nodes for the clean case and the fillet case in this paper were total 851193 nodes (including 483183 nodes for rotor, 368010 nodes for stator) and total 865232 nodes (including 493128 nodes for rotor, 372104 nodes for stator), respectively.

The aerodynamic performance parameters in this study are the total pressure ratio (PR), adiabatic efficiency (η), stall margin (SM), which were described in Reid and Moore [13], as shown in the following equations:

$$PR = \frac{P_{t,out}}{P_{t,in}} \quad (1)$$

$$\eta = \frac{\left(\frac{P_{t,out}}{P_{t,in}}\right)^{\frac{\gamma-1}{\gamma}} - 1}{\frac{T_{t,out}}{T_{t,in}} - 1} \times 100\% \quad (2)$$

$$SM = \left(\frac{PR_{stall}}{PR_{peak}} \times \frac{\dot{m}_{peak}}{\dot{m}_{stall}} - 1\right) \times 100\% \quad (3)$$

2.3 Numerical structural simulation

In the structural analysis, the blade structures, which were imported from Design-Modeler, were affected by the pressure loads from the aerodynamic simulation results. The titanium alloy [16, 17] with the density of 4620 kg/m³, tensile and compressive yield strength of 930 MPa, and tensile ultimate strength of 1070 MPa were used for rotor blades. The structural steel [18, 19] with the density of 7850 kg/m³, tensile and compressive yield strength of 250 MPa and tensile ultimate strength of 460 MPa were used for stator blades. The structural models of this compressor, as shown in Fig. 3, were solved using ANSYS Mechanical 19.1 [20]. The rotor blade had a rotational velocity at 100% speed design, i.e., 17,185.7 rpm, but the rotor hub surface and the stator shroud surface were fixed support. The number of computational grid structural nodes for the clean case and the fillet case in this research were 44,156 total (including 28,669 nodes for rotor, 15,487 nodes for stator) and 45,124 nodes total (including 28,669 nodes for rotor, 16,455 nodes for stator), correspondingly.

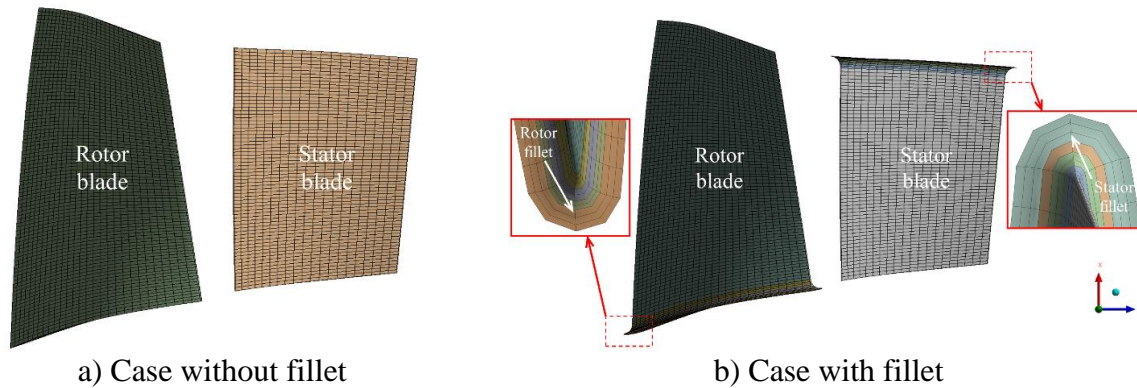


Figure 3. Computational structure mesh of NASA Stage 37

3. Results and Discussion

3.1 Validation

The last converged point, where the total pressure ratio reaches the maximal value, was determined as the near-stall condition using the convergence criteria by Chen *et al.* [21]. The performance curves were constructed by increasing the average static pressure at the stator outlet boundary from the choking condition (0 Pa) to the last stable convergence point. The simulation was carried out on PC utilizing 55/56 cores of [Dual CPU] Intel Xeon E5-2680 v4 @ 2.40GHz,

where most operating points took approximately 2 hours to finish but increased to over 3.5 hours at near-stall condition.

The experimental data of the NASA Stage 37, reported by Reid and Moore [13], were used to validate the numerical simulation in the clean blade case. Fig. 4a presents the performance curves of total pressure ratio and adiabatic efficiency obtained from numerical simulation in the comparison with several experimental points. The figures show that the numerical simulation was able to closely produce the data from the experiment. The simulated peak adiabatic efficiency is 84.01%, which is only slightly larger than the measurement, at 84.00%. In addition, the predicted total pressure ratio at peak efficiency condition is 1.99363, which is very close to the experimental result of 2.000. The compressor reached near-stall condition at 94.029% of the main choking mass flow rate, which is very close to the measured result, 93.645%. The predicted stall margin and experimental stall margin are also very similar, 10.21% compared to 10.00%. After the validation, the computational mesh of the clean blade case could apply for the case with fillet radius.

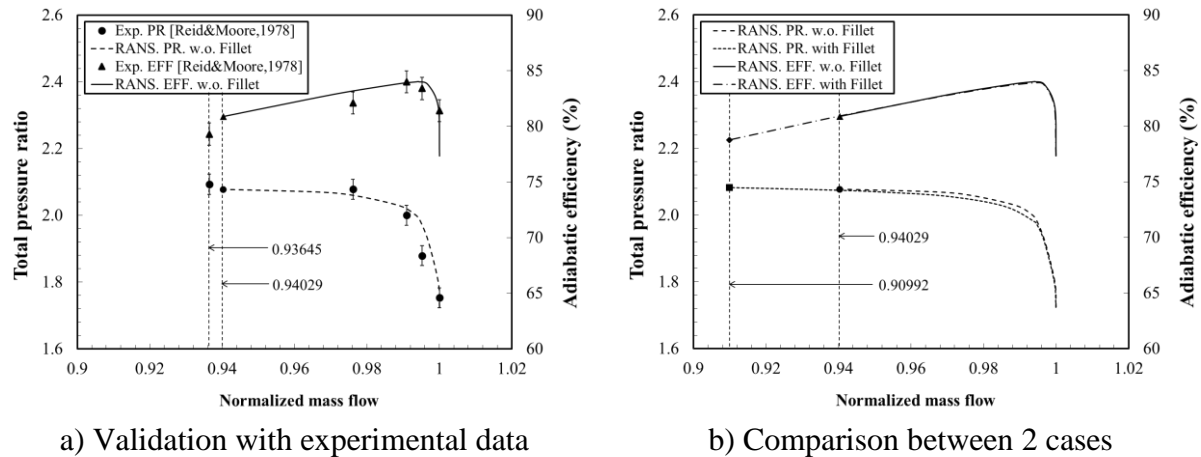


Figure 4. Compressor maps for validation and comparison purposes

3.2 Case with blade fillet

After validation of the case without fillet with the experimental data, the simulation results in the case of blade fillet 2.5 mm, as shown in Fig. 4b, were comprised with the figure of the clean blade. This image presents a large extension of normalized mass flow as the blade fillet delayed the near-stall condition from 0.94029 (clean case) to 0.90992 (fillet case) with a small decline of adiabatic efficiency from 84.01% (clean case) to 83.93% (fillet case). At peak adiabatic efficiency condition, the original design provided a superior total pressure ratio to that of the reference design (1.97721 compared to 1.99363). The blade fillet design extended the stall margin to 15.10 %, which is 47.89% higher than that of the clean case (10.21%). In more detail, Table I gives the aerodynamic simulation values of this compressor in comparison with the experiment data.

Table I. Fluid performance results

Case	Total pressure ratio		Normalized mass flow		Stall margin, %
	Peak efficiency	Near-stall	Peak efficiency	Near-stall	
Experience [13]	2.00000	2.09300	0.99092	0.93645	10.00
Without fillet	1.99363	2.07798	0.99421	0.94029	10.21
With fillet	1.97721	2.08228	0.99449	0.90992	15.10

At near-stall condition, Fig. 5 illustrates the Mach number contours on 98% span surface of NASA stage 37 with several the low-speed zones, corresponded to Mach number of 0.4. The first low-speed zones existing near the rotor leading edge area were significantly reduced from the clean case (Fig. 5a) to the fillet case (Fig. 5b). The second low-speed zones located around two sides of stator had two independent little zones in the case without fillet (Fig. 5a) and were combined into one bigger zone in the remaining case (Fig. 5b). This merger could be explained by the effect of fillet radius in the second case, where the airflow was continuous.

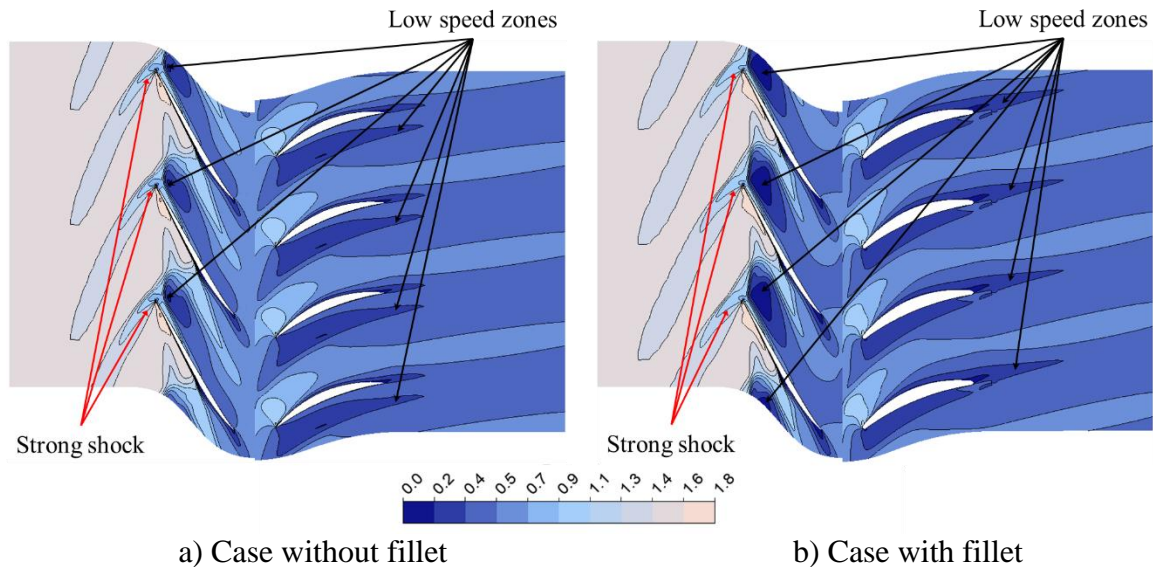


Figure 5. Relative Mach number contour at 98% span at near-stall condition

Moreover, there was also a strong shock attached at the leading-edge of rotor blade as shown in Fig. 5. This shock, as described in Dunham [14], interacted strongly with the suction side boundary layer of rotor blade. Therefore, this boundary layer after the shock might separate up to the trailing edge or reattach before this edge. This interesting phenomenon, which was simulated in Dinh *et al.* [12, 22, 24], Vuong *et al.* [23], and Pham *et al.* [25], is demonstrated in Fig. 6, where the surface streamlines are separated or reattached on the rotor blade suction side at peak adiabatic efficiency condition. In both cases, the separation line seemed to split the rotor blade suction surface into two parts, as shown in Fig.6. In the left region, the airflow direction was parallel to the axis, but it rolled up or was direction parallel to the separation line in the right region. The fillet case had a smaller scroll line area and more reattachment points in comparison with the clean case.

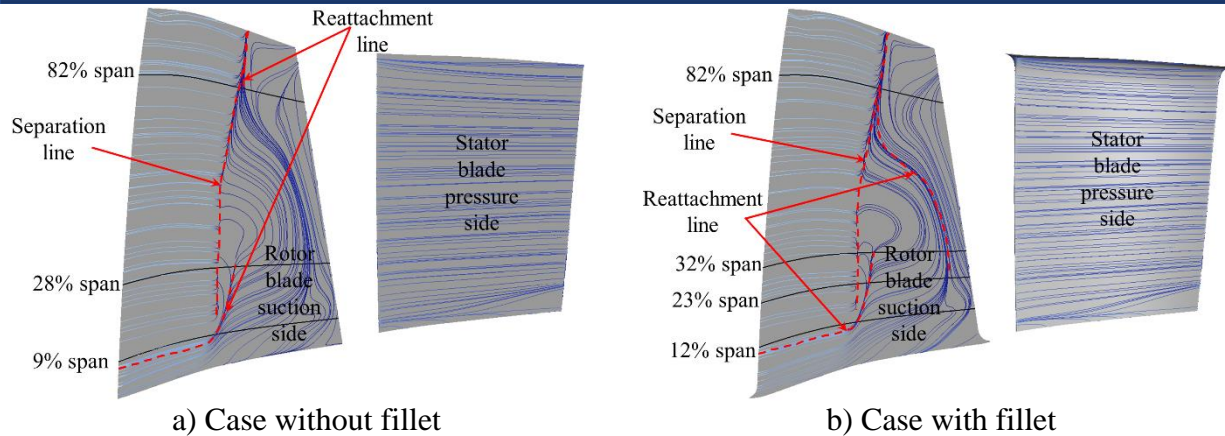


Figure 6. Blade streamlines at peak adiabatic efficiency condition

Fig. 7 shows how the airflow change from the leading-edge zone to the trailing-edge zone on the rotor blade pressure side. In fact, on the rotor hub surface, i.e., 0% span, due to the clean case had a sharp leading-edge, the streamlines were concentrated with a denser density than the ones in the fillet case. In opposition to the leading-edge zone, in the rotor blade trailing-edge zone, the airflow tending to get closer to the rotor blade pressure side appeared densely because of the fillet effect.

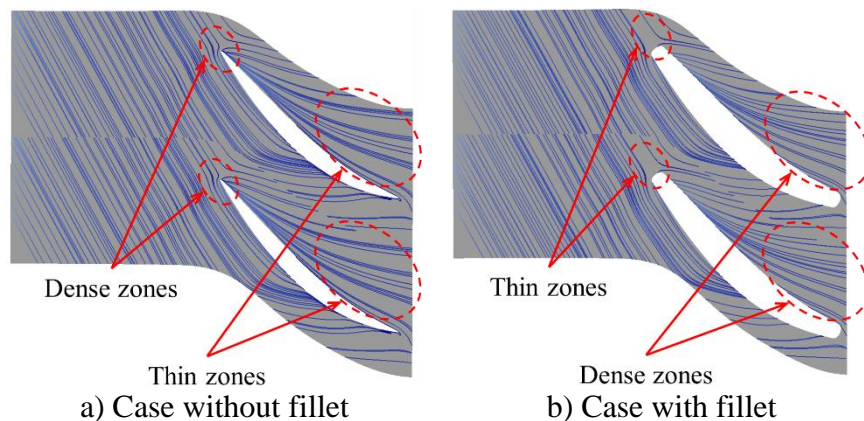


Figure 7. Rotor hub streamlines at peak adiabatic efficiency condition

In the clean case, a transition from blade surface to the end-wall surface is sudden, but the fillet can make this transition smoother in the reference design. This explains why airflow had a steadier state in the rotor blade trailing-edge zone in the case with fillet, as shown on Fig. 8. Fig. 5, 6, 7 and 8 provide the reasons for the enhancement of stall margin of a single-stage transonic axial compressor when the blade fillet is added.

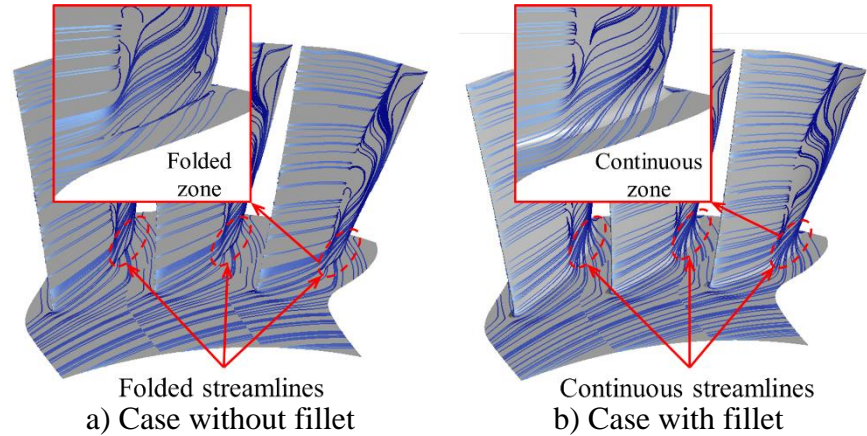


Figure 8. Streamlines on Rotor blade and hub at peak adiabatic efficiency condition

Fig. 9, 10 and Table II give some structural performance results. At peak efficiency condition, the maximal equivalent von-Mises stress for the clean case, as shown in Fig. 9, were considerably greater than for the fillet case, 326.44 MPa for rotor, 72.37 MPa for stator and 271.22 MPa for rotor, 58.92 MPa for stator, respectively. In both cases, the maximal equivalent von-Mises stress located on the leading-edge of the transition zone between blades and rotor hub or stator shroud. This shows the rationality in the relationship between the CFD and the CSD simulations. For example, in CFD simulation, the airflow concentrated with a denser density in the rotor blade trailing-edge zone. This location in CSD simulation also had the maximal stress.

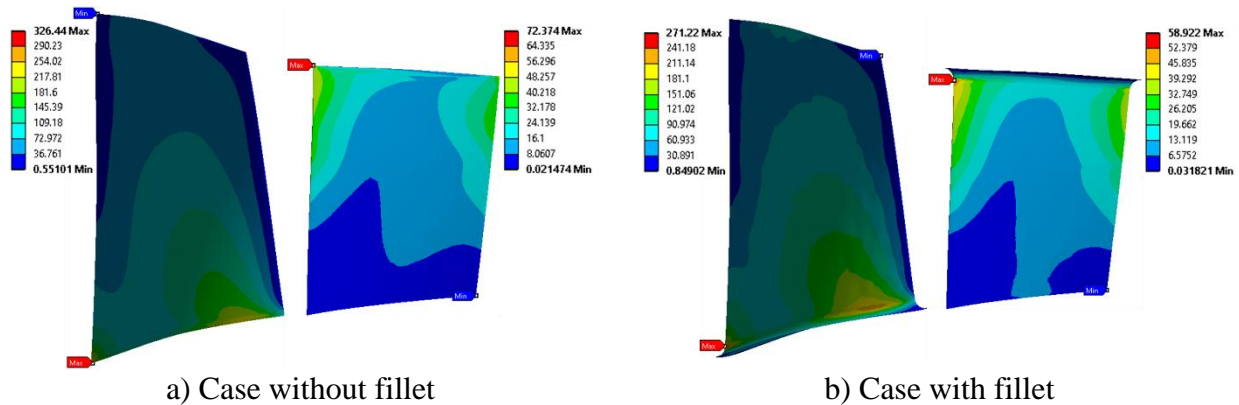


Figure 9. Equivalent von-Mises stress at peak adiabatic efficiency condition

Fig. 10 displays the total deformation at peak efficiency condition, where the maximal total deformations in the case with fillet were smaller than in the case without fillet, were in turn 1.2438 mm for rotor, 0.0897 mm for stator, and 1.2849 mm for rotor, 0.0995 mm for stator. In both cases, the maximal values are placed on the tip of leading-edge for rotor and stator.

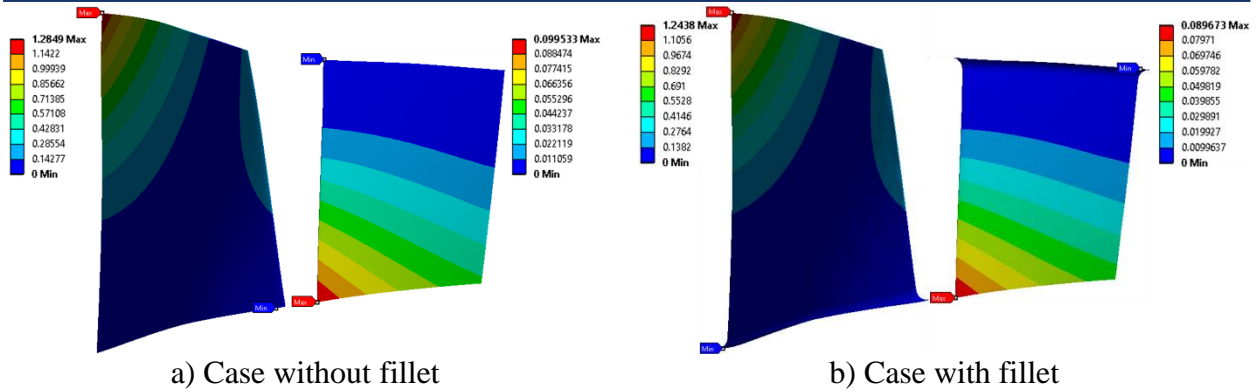


Figure 10. Total deformation at peak adiabatic efficiency condition

Table II provides the values of the maximal equivalent von-Mises stress and the maximal total deformation also at near-stall condition. In fact, all structural results at near-stall condition were slightly larger than the structural outcomes at peak adiabatic efficiency condition.

Table II. Structural performance results

Case		Maximal equivalent von-Mises stress, MPa		Maximal total deformation, mm	
		Peak efficiency	Near-stall	Peak efficiency	Near-stall
Without fillet	Rotor	326.44	328.77	1.2849	1.4054
	Stator	72.37	81.53	0.0995	0.1176
With fillet	Rotor	271.22	273.73	1.2438	1.3659
	Stator	58.92	72.55	0.0897	0.1105

4. Conclusion

The aerodynamic performances of a single stage transonic axial compressor, NASA stage 37 with an addition geometry, i.e., blade fillet 2.5 mm, were evaluated using 3-D RANS analysis. The CFD simulation results indicated that the reference design, i.e., the case with fillet, significantly delays the near-stall point from normalized mass flow rate of 0.94029 in the clean case to normalized mass flow rate of 0.90992. The results for total pressure ratio and adiabatic efficiency at peak efficiency condition in the fillet case were declined by 0.823% and 0.095%, respectively. The stall margin in the clean case is increased by 47.89% in the fillet case. The maximal equivalent Von-Mises stress of original design were considerably higher than the ones of reference case, by 16.92% for rotor and by 18.59% for stator at peak efficiency condition. The maximal total deformation of the case without fillet were also greater than the ones of the case with fillet, by 3.20% for rotor and by 9.91% for stator at peak efficiency condition. Based on the obtained results, there are some potential points for the future work, such as to optimize the geometry value of fillet radius, to analysis the two-way FSI, to find the better mesh for fluid model and structural model.

Acknowledgments

This study is funded by the Foundation for Science and Technology of Le Quy Don Technical University under grant number 20.1.048.

References

- [1] Kügeler, E., Nürnberger, D., Weber, A. and Engel, K. (2008), “Influence of Blade Fillets on the Performance of a 15 Stage Gas Turbine Compressor”. ASME Turbo Expo 2008: Power for Land, Sea, and Air, Vol. 6: Turbomachinery, Parts A, B, and C, pp. 415-424, doi:10.1115/gt2008-50748.
- [2] Matteo, P. (2012), “Structural and Fluid-Dynamic Analysis of an Axial Compressor with Adjustable Inlet Guide Vanes”, Master of Science, Matriculation No. 1034265, Department of Industrial Engineering, Faculty for Engineering, University of Padova, Italy.
- [3] Meyer, R., Schulz, S., Liesner, K., Passrucker, H. and Wunderer, R. (2012), “A parameter study on the influence of fillets on the compressor cascade performance”. Journal of Theoretical and Applied Mechanics, Vol. 50, pp. 131-145.
- [4] Oh, J.J. (2016), “The Effects of Blade Fillets on Aerodynamic Performance of a High-Pressure Ratio Centrifugal Compressor”, International Compressor Engineering Conference, Paper 2396, available at: <https://docs.lib.purdue.edu/icec/2396/>.
- [5] Kanjirakkad, V. (2017), “Experimental study of endwall flow in a low-speed linear compressor cascade: effect of fillet radius”, International Journal of Turbines and Sustainable Energy, Vol. 1 (1), pp. 1-7, doi:10.4273/ijtse.1.1.01.
- [6] Vu, H.T., Vu, D.Q. and Dinh, C.T. (2018), “Aerodynamic Performances of a Transonic Axial Compressor with Rotor Hub Fillet”, ICFMAS 2018.
- [7] Lerche, A.H., Moore, J.J., White, N.M. and Hardin, J. (2012), “Dynamic Stress Prediction in Centrifugal Compressor Blades Using Fluid Structure Interaction”. Vol. 6: Oil and Gas Applications; Concentrating Solar Power Plants; Steam Turbines; Wind Energy, doi:10.1115/gt2012-69933.
- [8] Wang, Z.K., Tsai, G.C. and Chen, Y.B. (2014), “One Way Fluid-Structure Interaction Simulation of an Offshore Wind Turbine”, International Journal of Engineering and Technology Innovation, Vol. 4(3), pp. 127-137, available at: <https://ojs.imeti.org/index.php/IJETI/article/view/137>.
- [9] Chen, J., Wang, Q., Shen, W.Z., Pang, X., Li, S. and Guo, X. (2013). “Structural optimization study of composite wind turbine blade. Materials & Design”, Vol. 46, pp. 247-255, doi:10.1016/j.matdes.2012.10.036.
- [10] Song, Y.J., Kang, H.S. and Kim, Y. J. (2015), “Reliability evaluation of an axial compressor rotor using fluid-structural interaction analysis”, In: 3rd international conference on materials and reliability, Jeju island, South Korea.
- [11] Kang, H.S. and Kim, Y.J. (2016), “Optimal design of impeller for centrifugal compressor under the influence of one-way fluid-structure interaction”, Journal of Mechanical Science and Technology, Vol. 30(9), pp. 3953-3959, doi:10.1007/s12206-016-0807-0.
- [12] Dinh, C.T., Vu, D.Q. and Kim, K.Y. (2020), “Effects of Rotor Bleeding Airflow on Aerodynamic and Structural Performances of a Single Stage Transonic Axial Compressor”,

International Journal of Aeronautical and Space Sciences, Vol. 21, pp. 599-611, doi:10.1007/s42405-019-00239-5.

[13] Reid, L. and Moore, R. D. (1978), “Performance of single-stage axial-flow transonic compressor with rotor and stator aspect ratios of 1.63 and 1.78, respectively, and with design pressure ratio of 1.82”, NASA TP-1659, available at: <https://ntrs.nasa.gov/citations/19790001889>.

[14] Dunham, J. (1998), “CFD Validation for Propulsion System Components, AGARD-AR-355”, p. 11, p. 227, available at: <https://www.sto.nato.int/publications/AGARD/AGARD-AR-355/AGARD-AR-355.pdf>.

[15] ANSYS (2018), “ANSYS CFX-Solver Theory Guide”, ANSYS 19.1, ANSYS Inc.

[16] Weiler, W. (1981), “Compressor rotor wheel and Method of making same”, U.S. Patent, 4273512, available at:

<https://patentimages.storage.googleapis.com/0e/1d/76/dba12d9f8520ed/US4273512.pdf>.

[17] Ermachenko, A.G. and Kashaev, R.M. (2011), “Production of aircraft engine compressor rotor discs with desired service life in titanium alloys”, Materials Physics and Mechanics, Vol. 11, pp. 118–125.

[18] Linden, D.H. (2001), “Corrosion control in industrial axial flow compressor”, In: Proceeding of the 30th turbomachinery symposium, Texas A&M University. Turbomachinery Laboratories, pp. 115–120.

[19] Aziaka, D.S., Osigwe, E.O. and Lebele-Alawa, T. (2014), “Structural and conceptual design analysis of an axial compressor for a 100 MW industrial gas turbine (IND100)”, World Journal of Mechanics, Vol. 4, pp. 332–347, doi:10.4236/WJM.2014.411033.

[20] ANSYS (2018), “Mechanical User's Guide”, ANSYS 19.1, ANSYS Inc.

[21] Chen, C.J. and Jaw, S.Y. (1998), “Fundamentals of turbulence modeling”. Taylor & Francis, Washington, DC, USA.

[22] Dinh, C.T., Ma, S.B. and Kim, K.Y. (2017), “Effects of a Circumferential Feed-Back Channel on Aerodynamic Performance of a Single-Stage Transonic Axial Compressor”, In: Proceedings of the ASME Turbo Expo 2017: Turbomachinery Technical Conference and Exposition, Vol. 2A: Turbomachinery. Charlotte, North Carolina, USA, doi:10.1115/gt2017-63536.

[23] Vuong, T.D., Dinh, D.M., Dinh, C.T. and Bui, X.L. (2019), “Aerodynamic Performance of a Single-stage Transonic Axial Compressor using Recirculation-Bleeding Channels”, Journal of Science & Technology, Vol. 138, pp. 033-037.

[24] Dinh, C.T., Vuong, T.D., Le, X.T., Nguyen, T.M. and Nguyen, Q.H. (2020), “Aeromechanic performance of a single-stage transonic axial compressor with recirculation-bleeding channels”, Australian Journal of Mechanical Engineering, doi:10.1080/14484846.2020.1832727.

[25] Pham, K.Q., Nguyen, Q.H., Vuong, T.D. and Dinh, C.T. (2020), “Parametric Study on Aerodynamic Performance of a Single-stage Transonic Axial Compressor with Recirculation-bleeding Channels”, International Journal of Fluid Machinery and Systems, Vol. 13, No. 2, doi:10.5293/IJFMS.2020.13.2.348

Study on the Loading Redistribution during Braking Maneuver of a Tanker Semi-trailer – The Effect of the Configuration of the Baffles

Thong Duc Hong^{1,2,*}, Thien Phuoc Huynh³, Hieu Trung Le^{1,3}, and Thanh-Long Le^{2,4}

¹Department of Automotive Engineering, Faculty of Transportation Engineering, Ho Chi Minh City University of Technology (HCMUT), 268 Ly Thuong Kiet, District 10, Ho Chi Minh City, Vietnam

²Vietnam National University Ho Chi Minh City, Linh Trung Ward, Thu Duc District, Ho Chi Minh City, Vietnam

³Faculty of Automotive Engineering, Cao Thang Technical College, Ho Chi Minh City, Vietnam

⁴ Faculty of Mechanical Engineering, Ho Chi Minh City University of Technology (HCMUT), 268 Ly Thuong Kiet, District 10, Ho Chi Minh City, Vietnam

*Corresponding author. E-mail: hongducthong@hcmut.edu.vn

Abstract

In this study, the oscillations of liquid in the tanker of a semi-trailer, which cause load shifts on the kingpin and the rear axles, are simulated during braking maneuver with constant deceleration at different configurations of baffles and wave baffles; different heights and quantities of wave baffles; and different liquid filling levels in the tanker. A three-dimensional numerical model of a typical tanker is developed to study, and the transient multiphase fluid simulation is performed using the commercial finite volume package FLUENT 18.2. The results suggest that the load shifts on the kingpin decrease when replacing wave baffles with full baffles, increasing the height and quantity of the wave baffles. The height of the wave baffles has a stronger effect than their quantity in reducing the load shift on the kingpin. There is a liquid filling level for a given configuration of the tanker that produces the largest load shift on the kingpin. The optimal configuration of the tanker, which is considered for practical application, significantly depends on the liquid filling level. The results also show that when the tanker is filled with full liquid, Model 2 should be used to simplify the manufacturing process of the tanker. In the contrast, as the tanker is mostly used at a partial liquid filling level, Model 3 is considered for applying to obtain the reasonable load shifts on the kingpin.

Keywords: Liquid sloshing, lateral baffles, volume of fluid (VOF), numerical simulation, multiphase

Nomenclature

G_t	=	Cargo weight
G_{1t}	=	Load on kingpin
G_{2t}	=	Load on rear axles
L_0	=	Wheelbase of the semi-trailer
$\Delta x_{cg_tan\ ker}$	=	The change of the center of gravity due to sloshing
G'_{2t}	=	Load on the rear axles due to sloshing
V	=	(u_r, u_ϕ, u_z) : velocity field vector in the cylindrical coordinate
p	=	Pressure of the fluid

ρ	=	Density of the fluid
μ	=	Dynamic viscosity of the fluid
V_c	=	Volume of each cell in the mesh
M_c	=	The mass of fluid in each cell in the mesh
(x_c, y_c, z_c)	=	The cell's coordinate
(X_{cg}, Y_{cg}, Z_{cg})	=	The center of gravity of fluid in the tanker

1. Introduction

The oscillations of fluid in a partly filled tanker of a semi-trailer causes dynamic loads on the kingpin and the rear axles. A small excitation of the container, e.g. the accelerating, braking, turning may cause large excursion forces and moments. As a result, the stability and controllability of the vehicle could reduce. To prevent the growth of sloshing, the lateral baffles are usually inserted into the tanker structure.

Significant researches have been carried out to study the effect of the baffles to the sloshing of fluid in a tanker using both computational and experimental approach. Kandasamy et al. (Kandasamy T. et al., 2010) used the Volume of Fluid (VOF) method in the FLUENT environment to solve for multiple phases of transient flows in the partly-filled tank. The conventional transverse baffles and other baffle configurations are studied on their anti-slosh property while under braking maneuver with combined lateral and longitudinal acceleration excitations. Suyal (Suyal R., 2016), Xue-lian Zheng and coworkers (Zheng XL. et al., 2013) performed a transient numerical simulation using FLUENT to study the effectiveness in reducing dynamic fluid slosh forces and moments by making a different type of holes in the transverse baffles. Minho Ha et al. (Ha M. et al., 2012) experimented to validate the numerical simulation of liquid sloshing in a rectangular tank without baffle. Hong et al. (Hong D.T. et al., 2021) studied the effect of lateral wave baffles on the longitudinal stability of the fuel semi tanker during acceleration maneuver using the Computational Fluid Dynamics approach. Simulations were carried out on tanker models with different wave baffles configurations to find out the proper baffle model to resist the longitudinal sloshing.

Most of the published works are concerned with the shape and number of a typical baffle type. In this work, a study on combining full baffles and partial baffles (anti-wave baffles), in which the wave baffles were investigated with different heights, to damp the fluid slosh in a tanker is discussed. The quantity and the height of wave baffles and the various liquid filling levels in the tanker were also considered in this work. The FLUENT software running in the Visual Studio environment is used to solve the Navier-Stoke equation, the VOF technique is applied to track the free surface of the fluid in the tanker. The User-Defined-Function (UDF) is developed to control the acceleration excitation during the simulation. The objective of this study is to identify an appropriate model for the design of a tanker semi-trailer (1) to ensure the longitudinal stability of the vehicle during the braking process and (2) to simplify the fabrication technology of the tanker.

2. Physical Model & Stability Analysis

2.1 Physical Model

The physical model of the study is the tanker semi-trailer's model of KCT G43-BX40-02 made by Tan Thanh Trading & Mechanic Corporation, Vietnam (Tan Thanh, 2019). The tanker has an overall length of 10.500 mm with a uniform ellipse cross-section. The height and width of the tanker are 2.500 mm and 1.960 mm, respectively. Figure 1 shows the main components and

corresponding forces acting on the semi-trailer. The weights of the main components of the semi-trailer and the distributions of loads on kingpin and rear axles are described in Table I.

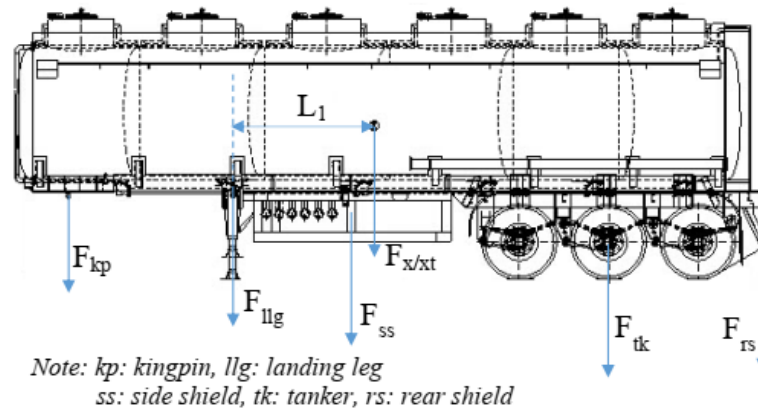


Figure 1. Main components and corresponding forces acting on the tanker semi-trailer

Table I. Distributions of loads on the kingpin and rear axles

No.	Components	Value (kg)	Load on kingpin (kg)	Load on rear axles (kg)
1	Plate to install kingpin	115	115	0
2	Landing leg	150	105	45
3	Side shield	80	40	40
4	Main beam & accessory	3870	0	3870
5	Rear shield & light sys.	150	-45	195
6	Tanker	5050	1960	3090
7	Curb weight	9415	2175	7240
8	Cargo weight (40 m ³ of gasoline)	29600	12840	16760
9	Gross weight at full load	39015	15015	24000

2.2 Static Stability Analysis

The analysis of the static stability of the tanker semi-trailer is obtained by counting the shifting of load on the kingpin and the rear axles as changing the level of the liquid in the tanker. The redistributions of loads are shown in Table II.

Table II. Distribution of load on the kingpin and rear axles at different fluid levels in the tanker

Filling level	G_t : Cargo weight (kg)	G_{1t} : Load on kingpin (kg)	G_{2t} : Load on rear axles (kg)
100%	29600	12840	16760
90%	29343	12729	16614
70%	27089	11751	15338
50%	14800	6420	8380

The distance from the center of gravity of the fluid in the tanker to the kingpin can be calculated by: $L_1 = L_0 G_{2t} / G_t$, in which $L_0 = 7930mm$ is the wheelbase of the semi-trailer.

2.3 Dynamic Stability Analysis

During the sloshing of fluid in the tanker, the fluid tends to oscillate. As a result, the center of gravity of the fluid will be changed, and a dynamic load shift on the kingpin and rear axles has occurred. To calculate these amounts of load shifts, it is necessary to calculate the center of gravity of the liquid carried in the tanker.

The dynamic stability of the semi-trailer is evaluated by estimating the load shift on the kingpin and the rear axles as sloshing occurred. Amount of applied load and load shift on the kingpin and the rear axles is estimated by:

Load and load shift on the kingpin:

$$\begin{aligned} G'_{1r} &= G_t \cdot (L_1 + \Delta x_{cg_tanker}) / L_0 \\ \Delta G_{1r} &= G'_{1r} - G_{1r} \end{aligned} \quad (1)$$

in which Δx_{cg_tanker} is the change of the center of gravity due to sloshing

Load and load shift on the rear axles:

$$\begin{aligned} G'_{2r} &= G_t - G'_{1r} \\ \Delta G_{2r} &= G'_{2r} - G_{2r} \end{aligned} \quad (2)$$

In order to calculate the change of the center of gravity due to sloshing Δx_{cg_tanker} , the computational approach combining the FLUENT and MS Excel is used. First of all, the geometry and meshing of the tanker are done by the Fluid Flow Module. Simulation is then performed to obtain the volume fraction of gasoline $vof(c)_{gas}$ of each cell in the computational domain. The mass of each cell is then calculated by:

$$M_c = \rho_{gas} \cdot V_c \cdot vof(c)_{gas} + \rho_{air} \cdot V_c \cdot (1 - vof(c)_{gas}) \quad (3)$$

in which V_c is the volume of cell in the mesh.

By knowing the cell's coordinates (x_c, y_c, z_c) , and assuming that the center of the fluid in the free surface cell is at the centroid of the cell, the center of gravity of fluid in the tanker can be obtained by:

$$X_{cg} = \frac{\sum x_c \cdot M_c}{\sum M_c}, Y_{cg} = \frac{\sum y_c \cdot M_c}{\sum M_c}, Z_{cg} = \frac{\sum z_c \cdot M_c}{\sum M_c} \quad (4)$$

3. Computational Analysis

3.1 Numerical Model

The simplification of the tanker without baffle is depicted in Figure 2. The fore and aft bulkheads of the tanker are assumed to be flat. The coordination system is located at the geometric center of the tanker; the x-axis is along the longitudinal axis of the tanker and points right; the y-axis is along the lateral axis of the tanker; the z-axis is in the vertical direction and points up.

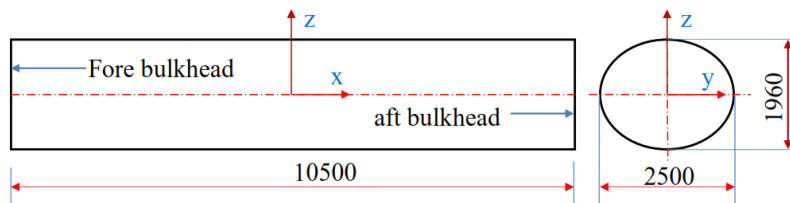


Figure 2. The simplified model of the tanker without baffle

There are two types of baffles used in the study, namely the full baffle and the partial baffle (wave baffle). The full baffle is extracted from the cross-section of the tanker. Hence, the shape and dimensions of the full baffle are the same as the tanker cross-section. Installed at an equal distance along the tanker’s longitudinal axis, the full baffles divide the tanker into small chambers. To ensure continuity in the computation, a small hole is made at the bottom of the full baffles. The detail of a full baffle is depicted in Figure 3a. The wave baffle is a modified version of the full baffle, by trimming the full baffle along the vertical axis. The wave baffles with a height of 30%, 40%, and 50% of the tanker height are respectively depicted in Figures 3b, 3c, and 3d.

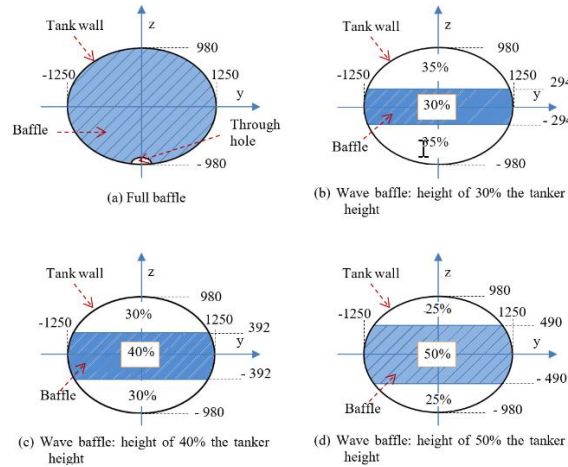


Figure 3. The shapes of full baffle and wave baffles

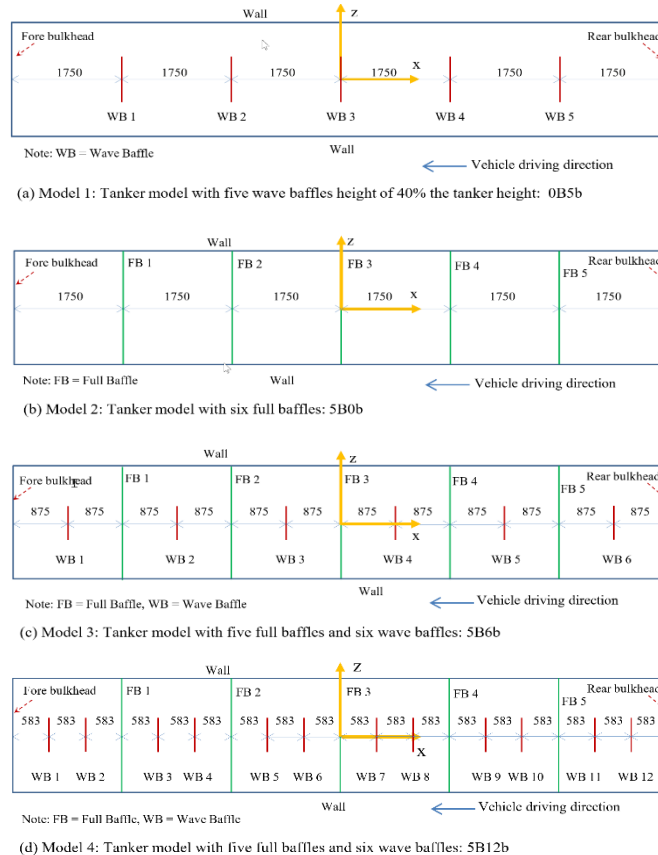


Figure 4. The four tanker models with different baffles and wave baffles using for study

Four tanker models equipped with different baffles and wave baffles are studied. In Model 1, five-wave baffles with a height of 40% of the tanker height are installed at an equal distance along the x-axis, and no full baffle is used. In Model 2, the wave baffles are replaced by full baffles. Models 3 and 4 combine full baffles and wave baffles into their structures. Six wave baffles are interleaved arranged with five full baffles in Model 3. In Model 4, five full baffles and twelve wave baffles are used. Three versions of the wave baffle with the height of 30%, 40%, and 50% of the tanker height are used in the Models 3 and 4. The arrangements of full baffles and wave baffles in four models are shown in Figure 4.

3.2 Motion of the Tanker

The tanker is subject to complete the braking maneuver at a constant deceleration of $a = 3 \text{ m/s}^2$ as shown in Figure 5. The velocity of the vehicle at the beginning of the braking is set at $V_0 = 40 \text{ km/h}$. The gravitational acceleration acting on the z-axis equals 9.81 m/s^2 . The filling level of the gasoline is 50%, 70%, and 90% of the tanker height. The summary of the cases that are considered for simulation on the tanker models is shown in Figure 6.

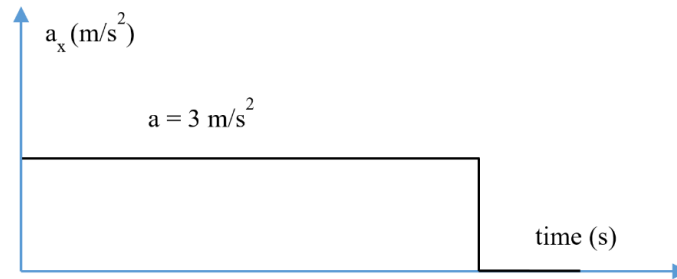


Figure 5. The time history of excitation deceleration along the x-axis

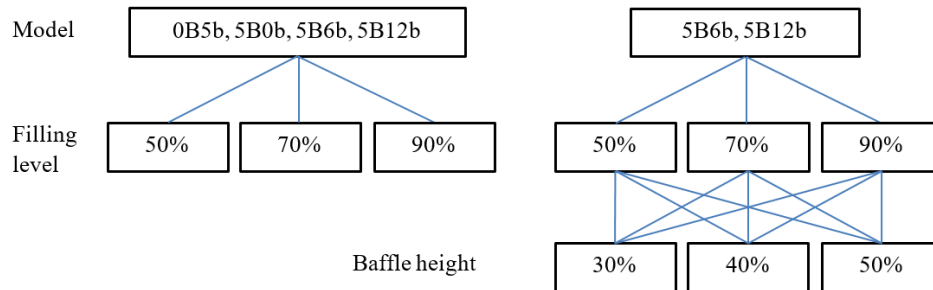


Figure 6. The scheme of simulation cases

Two sets of simulations are carried out. In the first set, the simulations are done in four models: 0B5b, 5B0b, 5B6b, 5B12b to investigate the effects of full baffles and wave baffles on the dynamic stability of the tanker. In the second set, the simulations are carried out for two models of 5B6b and 5B12b with different baffles' height to consider the effects of the heights and the quantities of the wave baffles on the dynamic stability of the tanker. The baffles' height is set to 30%, 40%, and 50% of the tanker height in the second set of simulations.

3.3 Mathematical Formulations

3.3.1 The governing equations for fluid motion and the Volume of Fluid technique

The sloshing of the fluid in a partly filled tanker is a complex phenomenon. There are two phases of fluid consisted of the tanker, i.e. the liquid phase (gasoline) and the gas phase (air), respectively. These two phases are immiscible, separated by a free surface. To formulate the

time-dependent motion of the multiple phases of fluid, the set of partial differential equations expressing Continuity equation, Navier-Stokes equation, and Multiphase governing equations including Momentum Conservation equations and Volume of Fluid (VOF) equations are used (Wang LS *et al.*, 2017, Suyal R., 2016):

- The Continuity equation represents that mass is conserved in a flow. For cylindrical coordinates, 3-Dimension, incompressible, unsteady, continuity equations are:

$$\begin{aligned} \frac{\partial \rho}{\partial t} + \nabla \cdot (\rho \mathbf{V}) &= 0 \\ \frac{\partial \rho}{\partial t} + \frac{1}{r} \frac{\partial}{\partial r} (r \rho u_r) + \frac{1}{r} \frac{\partial}{\partial \varphi} (\rho u_\varphi) + \frac{\partial}{\partial z} (\rho u_z) &= 0 \end{aligned} \quad (5)$$

In which $\mathbf{V} = (u_r, u_\varphi, u_z)$ is the velocity field vector in the cylindrical coordinate; p is the pressure; ρ is the mass density;

- The Navier-Stokes equations (Momentum equations) express conservation of momentum and conservation of mass for Newtonian fluids can be applied for both laminar and turbulent flow. In the cylindrical coordinate, (r, φ, z) , the Navier-Stokes equations of motion for an incompressible fluid of constant dynamic viscosity, μ , and density, ρ , are:

+ r – momentum equation:

$$\begin{aligned} \rho \left(\frac{\partial u_r}{\partial t} + u_r \frac{\partial u_r}{\partial r} + \frac{u_\varphi}{r} \frac{\partial u_r}{\partial \varphi} + u_z \frac{\partial u_r}{\partial z} - \frac{u_\varphi^2}{r} \right) \\ = - \frac{\partial p}{\partial r} + \mu \left[\frac{1}{r} \frac{\partial}{\partial r} \left(r \frac{\partial u_r}{\partial r} \right) + \frac{1}{r^2} \frac{\partial^2 u_r}{\partial \varphi^2} + \frac{\partial^2 u_r}{\partial z^2} - \frac{u_r}{r^2} - \frac{2}{r^2} \frac{\partial u_\varphi}{\partial \varphi} \right] + \rho g_r \end{aligned} \quad (6)$$

+ φ - momentum

$$\begin{aligned} \rho \left(\frac{\partial u_\varphi}{\partial t} + u_r \frac{\partial u_\varphi}{\partial r} + \frac{u_\varphi}{r} \frac{\partial u_\varphi}{\partial \varphi} + u_z \frac{\partial u_\varphi}{\partial z} + \frac{u_r u_\varphi}{r} \right) \\ = - \frac{1}{r} \frac{\partial p}{\partial \varphi} + \mu \left[\frac{1}{r} \frac{\partial}{\partial r} \left(r \frac{\partial u_\varphi}{\partial r} \right) + \frac{1}{r^2} \frac{\partial^2 u_\varphi}{\partial \varphi^2} + \frac{\partial^2 u_\varphi}{\partial z^2} - \frac{u_\varphi}{r^2} - \frac{2}{r^2} \frac{\partial u_r}{\partial \varphi} \right] + \rho g_\varphi \end{aligned} \quad (7)$$

+ z – momentum

$$\begin{aligned} \rho \left(\frac{\partial u_z}{\partial t} + u_r \frac{\partial u_z}{\partial r} + \frac{u_\varphi}{r} \frac{\partial u_z}{\partial \varphi} + u_z \frac{\partial u_z}{\partial z} \right) \\ = - \frac{\partial p}{\partial z} + \mu \left[\frac{1}{r} \frac{\partial}{\partial r} \left(r \frac{\partial u_z}{\partial r} \right) + \frac{1}{r^2} \frac{\partial^2 u_z}{\partial \varphi^2} + \frac{\partial^2 u_z}{\partial z^2} \right] + \rho g_z \end{aligned} \quad (8)$$

where μ is the dynamic viscosity; $\rho g_x, \rho g_y, \rho g_z$ are the body forces due to gravity.

- Momentum conservation equation gives the resulting velocity field shared among the phases:

$$\frac{\partial}{\partial t} (\rho \vec{V}) + \nabla \cdot (\rho \vec{V} \vec{V}) = -\nabla p + \nabla \cdot (\tau) + \rho g + F_s \quad (9)$$

where τ is the stress tensor, \vec{F}_s is the external body force (can be given as user defined source terms).

- Volume of Fluid equations

Equation (5-9) exposes limitation as a folded free surface occurs as in the case of fluid sloshing. To overcome this drawback, the concept of tracking the volume of liquid has been introduced. In the numerical based solution, the Volume of Fluid (VOF) technique has been proposed and widely used.

The VOF methodology introduces a new variable namely volume fraction. This variable represents the fraction volume of a cell occupied by a specified fluid. The unit value of F indicates a cell full of specified fluid, while a zero value of F indicates a cell contained no specified fluid. The air and gasoline phases can be defined by the value of F .

$$F(x, y, z, t) = \begin{cases} 0 & \text{air phase} \\ 0 < F < 1 & \text{free surface} \\ 1 & \text{gasoline phase} \end{cases} \quad (10)$$

The time dependence of F is governed by:

$$\frac{\partial F}{\partial t} + (V \cdot \nabla) F = 0 \quad (11)$$

The density and dynamic viscosity are calculated by (Wang LS *et al.*, 2017):

$$\rho = F\rho_{gas} + (1-F)\rho_{air} \quad \mu = F\mu_{gas} + (1-F)\mu_{air} \quad (12)$$

Substituting Eq.(12) into Eq.(6 - 9), the velocity and pressure could be obtained using the finite volume method.

3.3.2 Simulation solver setup

The model of the tanker and baffles is created by using the Fluid Flow (Fluent) module of Ansys Workbench. The unstructured mesh is used to capture the transition from the tanker wall to the baffles. The quality of the mesh is set to fine as doing automatic meshing. Table III shows the details of the four grid computing. A sample of mesh of the tanker model 3 (5B6b) is depicted in Figure 7.

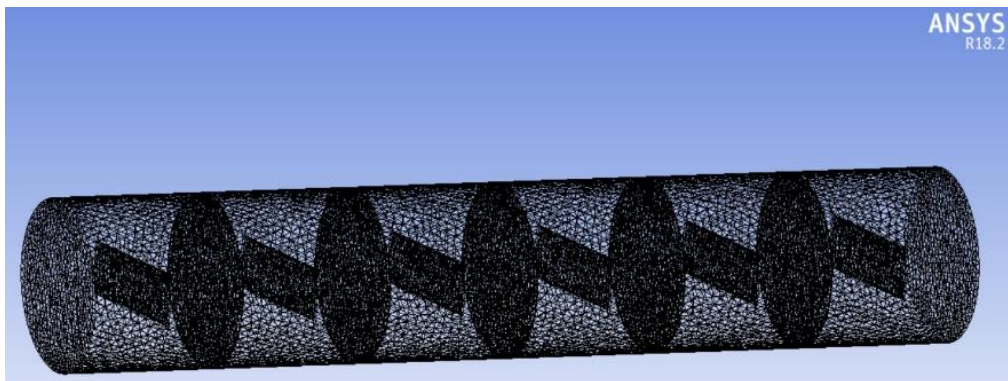


Figure 7. Details of the mesh of the tanker model 3 (5B6b)

Table III. Mesh details of the four grid computing

Quantity	Model 1	Model 2	Model 3	Model 4
Sizing function	Uniform	Uniform	Uniform	Uniform
Relevance center	Fine	Fine	Fine	Fine
Max face size	0.1m	0.1m	0.1m	0.1m
Defeature size	8e-04	8e-04	5e-04	5e-04
Smoothing	Medium	Medium	Medium	Medium
Node	11943	12743	46415	54257
Element	58316	59601	229657	267353

The ANSYS – FLUENT with activated VOF is used to numerical solve the multiple phases of fluid interaction in the tanker. The simulation is run in the Visual Studio environment to allow

the application of the User Defined Function (UDF) in setting up the time-varying acceleration excitation. The model and parameter settings for the solver are presented in Table IV.

Table IV. Solver model and parameter setting

Model and parameter	Setting
Solver type model	Pressure based multiple phase,
Number of Eulerian phases	2
Viscous model	Reliable $k - \varepsilon$
Near wall treatment	Scalable wall function
Pressure velocity coupling	SIMPLE
Tracking surface method	Geo – Reconstruct
Transient Formulation	First order implicit
Primary phase	Air
Secondary phase	Gasoline liquid
Air density (kg/m^3)	1.225
Air viscosity (kg/m-s)	1.7894e-05
Gasoline density (kg/m^3)	740
Gasoline viscosity (kg/m-s)	0.00332

4. Results and Discussion

4.1 Effect of Full Baffle and Wave Baffle on Dynamic Stability

In this case study, the simulation is performed on four baffle models, i.e. Model 1 (0B5b), Model 2 (5B0b), Model 3 (5B6b), Model 4 (5B12b). The initial braking velocity and acceleration are set of $V_0 = 40 \text{ km/h}$ and $a = 3 \text{ m/s}^2$, respectively. The liquid filling levels are set at 50%, 70%, and 90% of the tanker height. The absolute and percentage load shifts on the kingpin are presented in Table V.

Table V. Load shift on the kingpin at $V_0 = 40 \text{ km/h}$, $a = 3 \text{ m/s}^2$

Mode 1	Name	Filling level (50%)		Filling level (70%)		Filling level (90%)	
		ΔG (%)	ΔG (kg)	ΔG (%)	ΔG (kg)	ΔG (%)	ΔG (kg)
1	0B5b	19.6	1261	15.4	1383	6.4	742
2	5B0b	8.0	517	5.8	521	3.3	378
3	5B6b	2.9	188	1.7	149	0.8	94
4	5B12b	2.2	142	1.5	131	0.5	61

Figures 8 and 9 depict the absolute and the percentage, respectively, of load shifts on the kingpin of four tanker models due to sloshing of liquid in the tanker. Figures 10, 11, and 12 present the free surface during sloshing in Models 1, 2, 3, and 4 at filling levels of 50, 70, and 90% of the tanker height, respectively.

At the same liquid filling level in the tanker, the load shifts (both in absolute and percentage terms) on the kingpin decrease with the order of Model 1 - Model 2 - Model 3 - Model 4. The

load shifts on the kingpin of Model 1 are two times greater than that of Model 2, and Model 2 is twice as large as Model 3. Whereas Model 3 and Model 4 have very little difference in the load shifts on the kingpin.

When considering the same model, the absolute and percentage of load shifts on the kingpin of the liquid filling level of 90% of the tanker height are lowest for all four different models. It is easy to see from Figure 12 that there is not much free volume in the tanker, in which the liquid can oscillate.

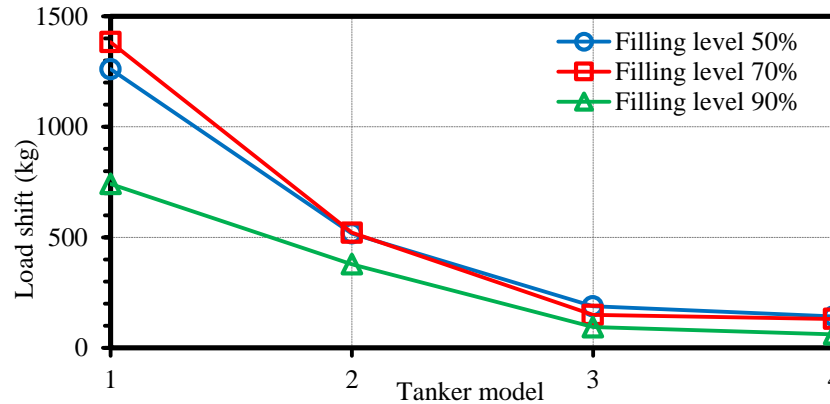


Figure 8. Absolute load shifts on kingpin of different baffle models on tanker

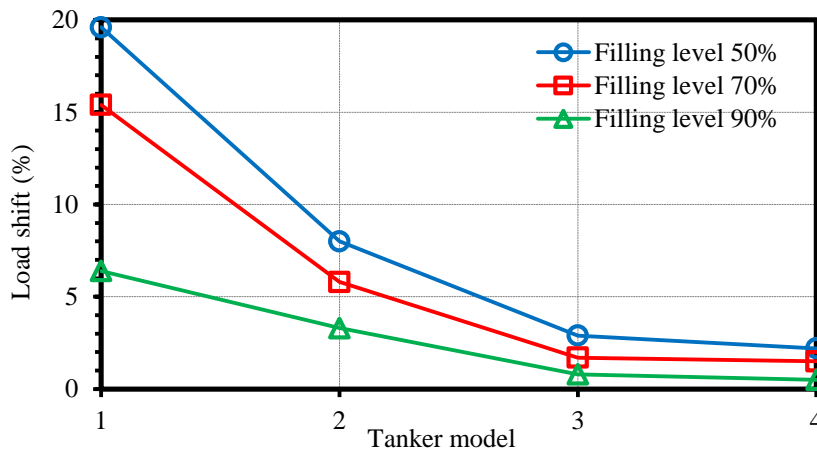


Figure 9. Percentage load shifts on kingpin of different baffle models on tanker

Figure 8 shows that the absolute load shift on the kingpin with the liquid filling level of 70% is higher than that of 50% for Model 1. While the absolute load shifts on the kingpin of Models 2, 3, and 4 have the same value between the liquid filling levels of 50 and 70% the tanker height. However, Figure 9 presents that the percentage load shifts on the kingpin at the liquid filling level of 50% are always higher than the liquid filling level of 70% for all four models. Based on Figures 10 and 11, it is explained that the lower the liquid filling level in the tanker, the more free volume space for the liquid to oscillate when braking occurs resulting in a large percentage of load shifts on the kingpin. However, due to the liquid filling level is low its weight is also proportionally low in the tanker leading to a small absolute load shift on the kingpin.

The results show that the liquid filling level and the configurations of the baffles and wave baffles in the tanker significantly influence the load shifts on the kingpin. The higher the liquid filling level, the smaller the load shifts on the kingpin because there is not much free space for the liquid to oscillate. The lower the liquid filling level, the higher percentage load shifts

obtained; but their absolute values may not be high because the volume contained in the tanker is small. It can conclude that with a given configuration of baffles, there is a liquid filling level in the tanker producing the maximum load shift on the kingpin.

In this case study, Model 2 and Model 3 could be reasonable options for practical applications. In applications when the liquid filling level of the tanker is always full, it is recommended to use Model 2, which has a load shift on the kingpin of about 380kg (approximately 3.3%), to simplify the fabrication process of the tanker. In the case that the tanker with a partial liquid filling level is used, Model 3 is considered for applying to obtain the reasonable load shifts on the kingpin.

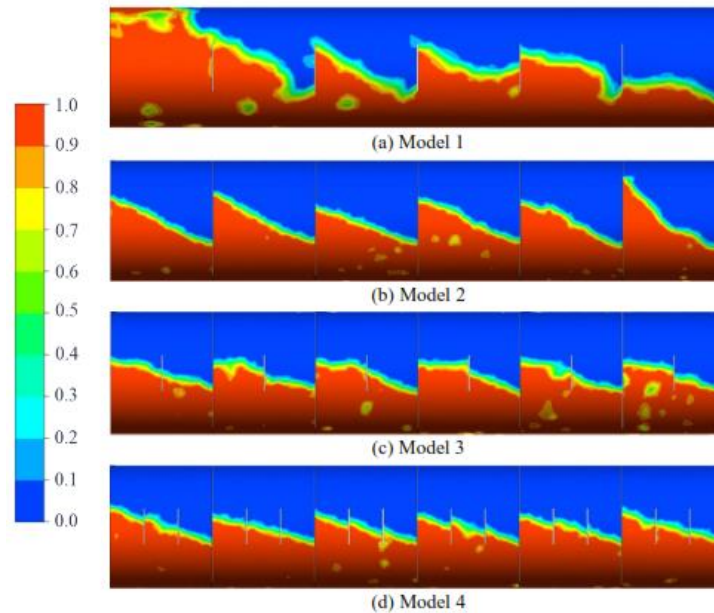


Figure 10. The free surfaces during sloshing on Models 1, 2, 3, and 4 at filling level of 50% of the tanker height

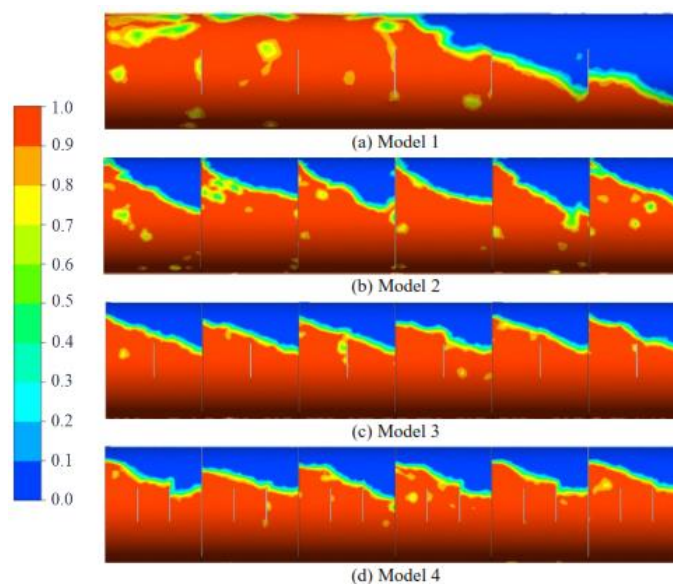


Figure 11. The free surfaces during sloshing on Models 1, 2, 3, and 4 at filling level of 70% of the tanker height

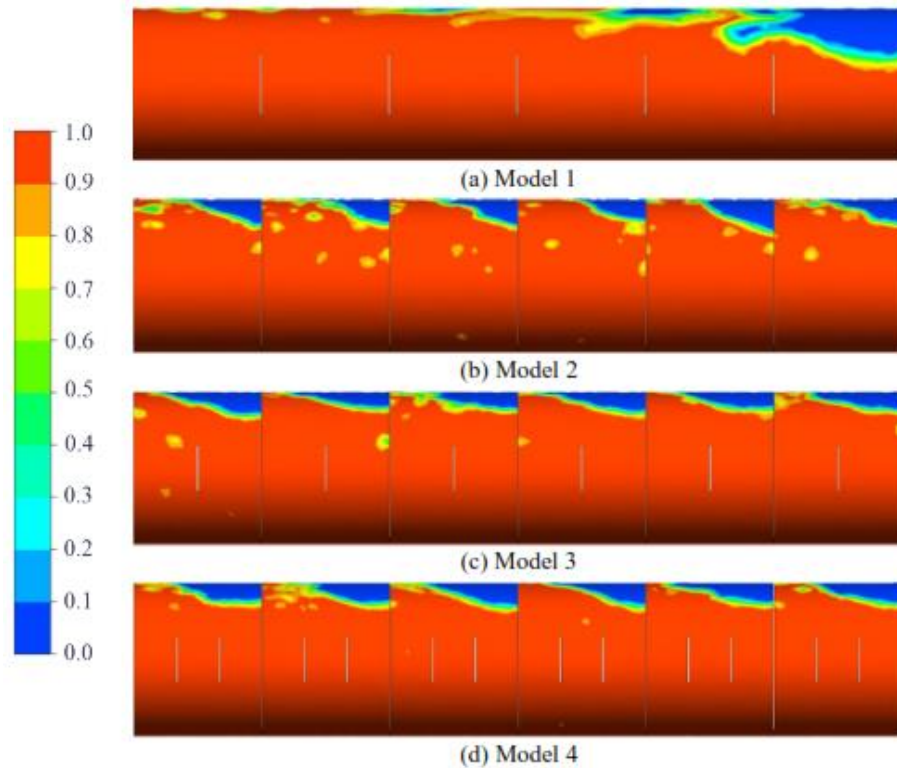


Figure 12. The free surfaces during sloshing on Models 1, 2, 3, and 4 at filling level of 90% of the tanker height

4.2 Effect of Quantity and the Height of Baffles on Dynamic Stability

The simulations are performed for Model 3 (which has five full baffles and six wave baffles) and Model 4 (which has five full baffles and twelve wave baffles) to evaluate the effects of the quantity and the height of wave baffles on the fluid sloshing inside the tanker. The heights of wave baffles vary from 30% to 40% and 50% of the tanker height with the same arrangement as shown in Figure 4. The initial braking velocity and the acceleration are set at $V_0 = 40$ km/h and $a = 3$ m/s² respectively. The absolute and percentage load shifts on the kingpin of Models 3 and 4 are shown in Tables VI and VII, respectively.

Table VI. Absolute load shifts on the kingpin of Models 3 and 4 as changing the heights and quantities of wave baffles

Parameters		Load shift on the kingpin (kg)					
		Model 3			Model 4		
Baffle height (%)		30	40	50	30	40	50
Filling level (%)	50	186.2	154.1	122.0	141.2	115.6	89.9
	70	152.8	116.8	89.9	134.8	107.9	89.9
	90	92.4	69.3	57.8	57.8	46.2	46.2

Table VII. The percentage load shifts on the kingpin of Models 3 and 4 as changing the heights and quantities of wave baffles

Parameters		Load shift on the kingpin (%)					
		Model 3			Model 4		
Baffle height (%)		30	40	50	30	40	50
Filling level (%)	50	2.90	2.40	1.90	2.20	1.80	1.40
	70	1.70	1.30	1.00	1.50	1.20	1.00
	90	0.80	0.60	0.50	0.50	0.40	0.40

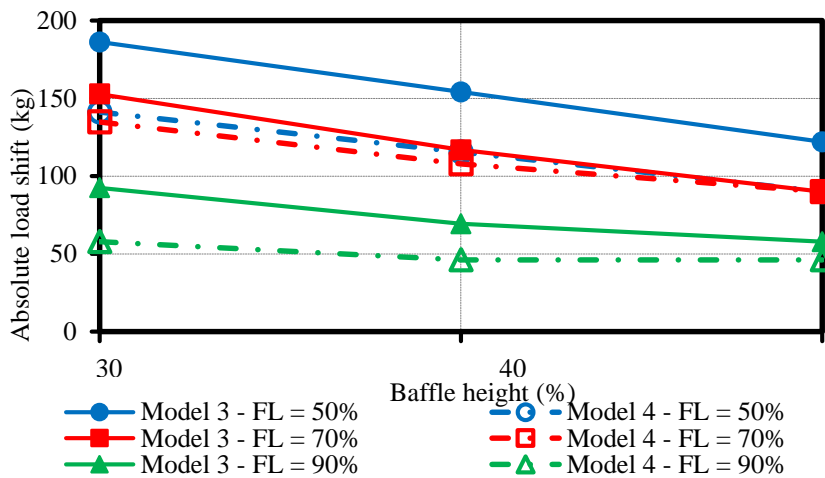


Figure 13. Absolute load shifts on the kingpin as changing the heights and quantities of wave baffles

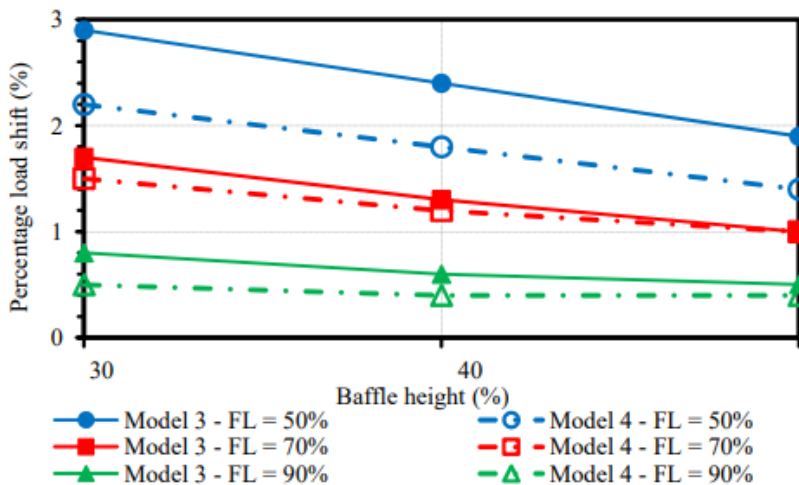


Figure 14. Percentage load shifts on the kingpin as changing the heights and quantities of wave baffles

Figures 13 and 14 show the absolute and percentage load shifts on the kingpin along with the heights and quantities of wave baffles. The free surfaces during sloshing as changing the heights of wave baffles of Model 3 are presented in Figures 15 – 17, and those of Model 4 are depicted in Figures 18 - 20. Figures 13 and 14 present that the load shifts on the kingpin of Model 4 are always higher than those of Model 3. The differences in the load shifts between Model 4 and Model 3 depend on the height of wave baffles and the liquid filling level in the tanker. With the same liquid filling level, the differences in the load shifts of Model 4 and Model 3 decrease when the height of wave baffles increase; meanwhile, at the same height of wave baffles, the differences in the load shifts between Model 4 and Model 3 gradually decrease when the liquid filling levels are at 50, 90 and 70% the tanker height. At the wave baffles' height of 50% and the liquid filling levels of 70% the tanker height, the load shift of Model 4 is equal to that of Model 3. Figures 13 and 14 also show the load shifts on the kingpin of Model 3 at the wave baffles' height of 50% are less than or equal to those of Model 4 at the wave baffles' height of 30% for all liquid filling levels in the tanker. We can gain a more specific understanding of this result by comparing the free surface profiles of the liquid in the tanker between the pairs of Figures 15c and 18a, Figures 16c and 19a, and Figures 17c and 20a, which correspond to the liquid filling levels at 50, 70, and 90% the tanker height. The results illustrate that the height of the wave baffles has a stronger effect than their quantity in reducing the load shift on the kingpin. Specifically, in this case of study, we can use Model 3, which has six wave baffles with their height of 50%, instead of Model 4, which has twelve wave baffles with their height of 30%, to have the same or better load shifts on the kingpin.

The load shifts on the kingpin at the liquid filling level of 70% the tanker height are higher than those of 90% the tanker height in both Model 3 (obtained from comparing the free surface profiles of liquid in the tanker between Figures 16 and 17.) and Model 4 (obtained from comparing the free surface profiles of liquid in tanker between Figures 19 and 20). However, the differences in the load shifts between Model 3 and Model 4 at the liquid filling level of 70% the tanker height are smaller than those of 90% the tanker height. It illustrates that the effect of the number of wave baffles is negligible when the height of the wave baffles is nearly equal to the height of the liquid filling level in the tanker. It is clearly shown through the similarity of the pairs of the corresponding free surface profiles of the liquid in Figures 16 and 19.

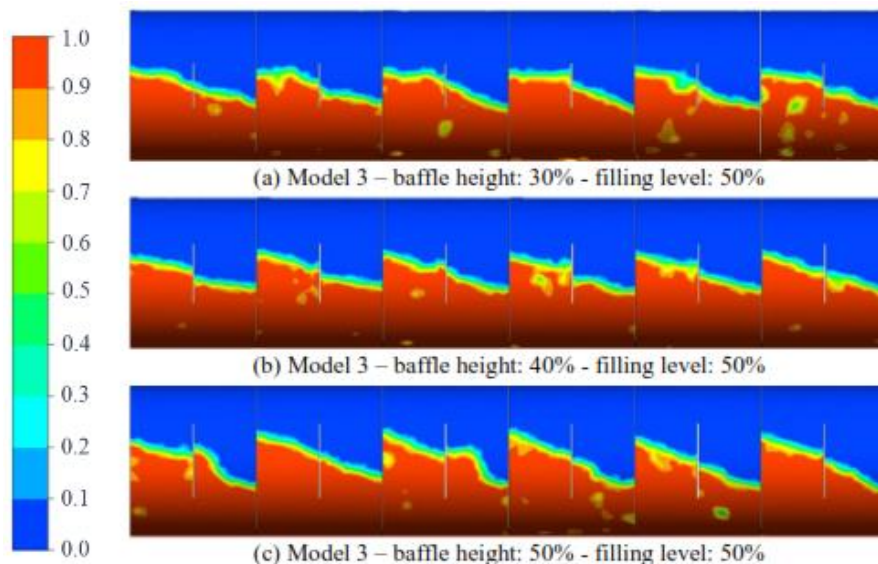


Figure 15. The free surfaces during sloshing on Model 3 with baffle heights of 30%, 40%, and 50%, at filling level of 50% of the tanker height

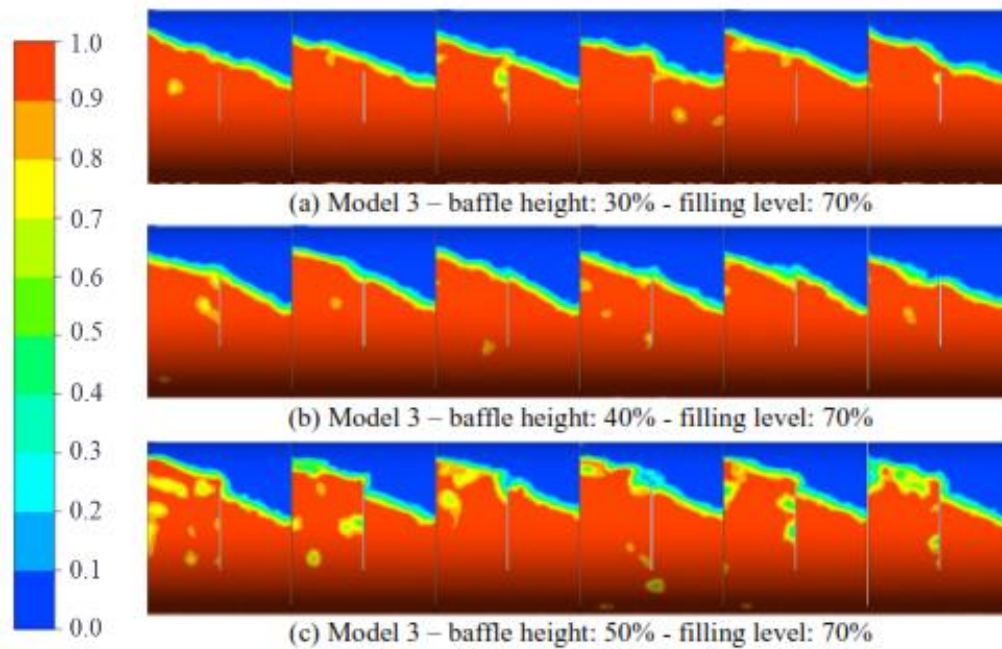


Figure 16. The free surfaces during sloshing on Model 3 with baffle heights of 30%, 40%, and 50%, at filling level of 70% of the tanker height

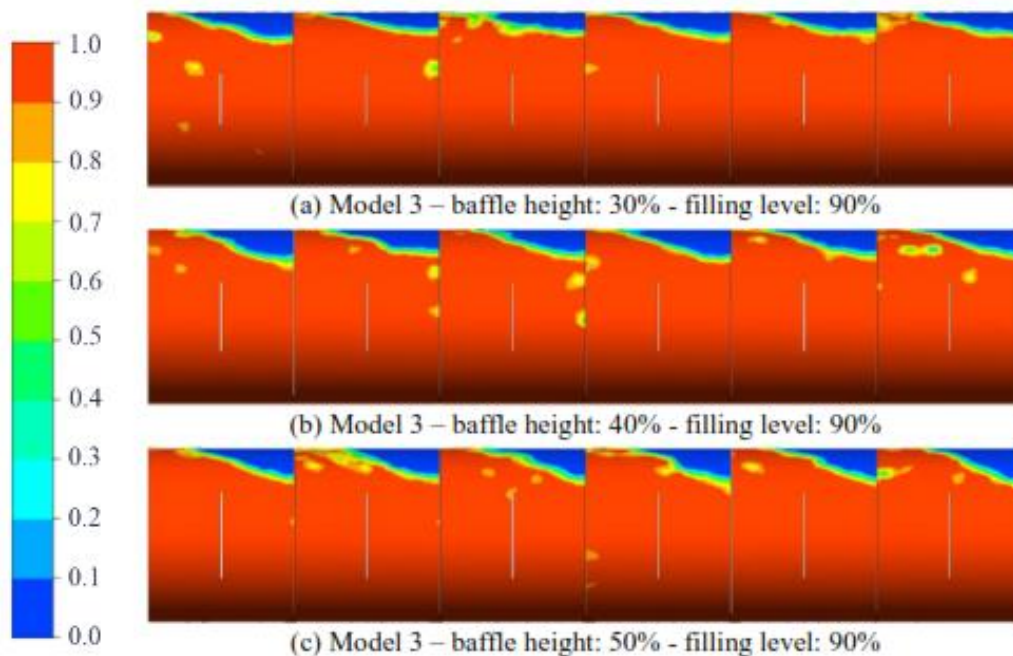


Figure 17. The free surfaces during sloshing on Model 3 with baffle heights of 30%, 40%, and 50%, at filling level of 90% of the tanker height

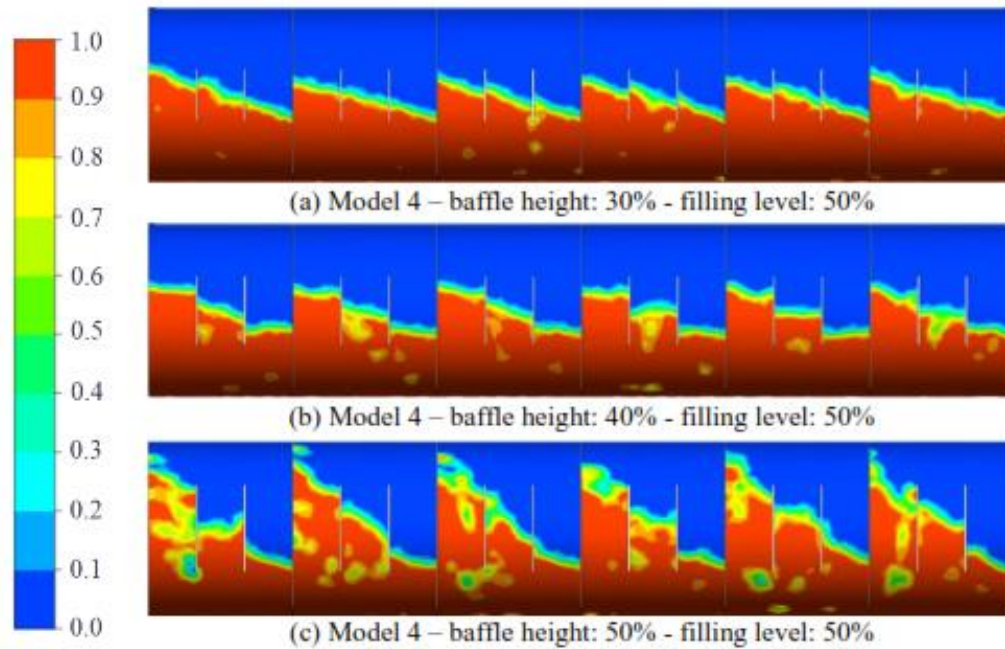


Figure 18. The free surfaces during sloshing on Model 4 with baffle heights of 30%, 40%, and 50%, at filling level of 50% of the tanker height.

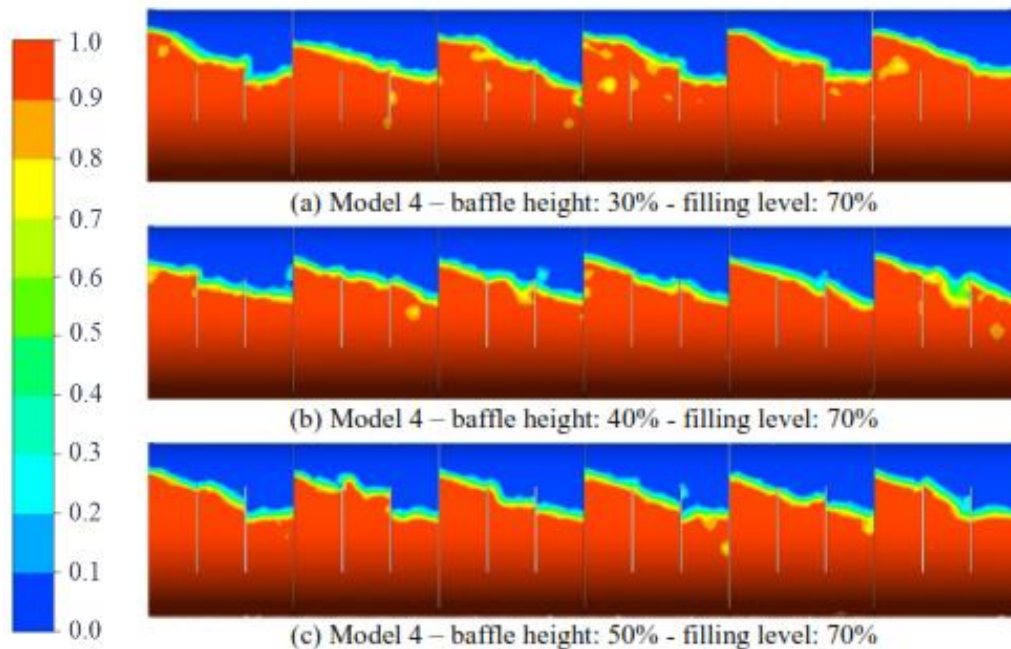


Figure 19. The free surfaces during sloshing on Model 4 with baffle heights of 30%, 40%, and 50%, at filling level of 70% of the tanker height.

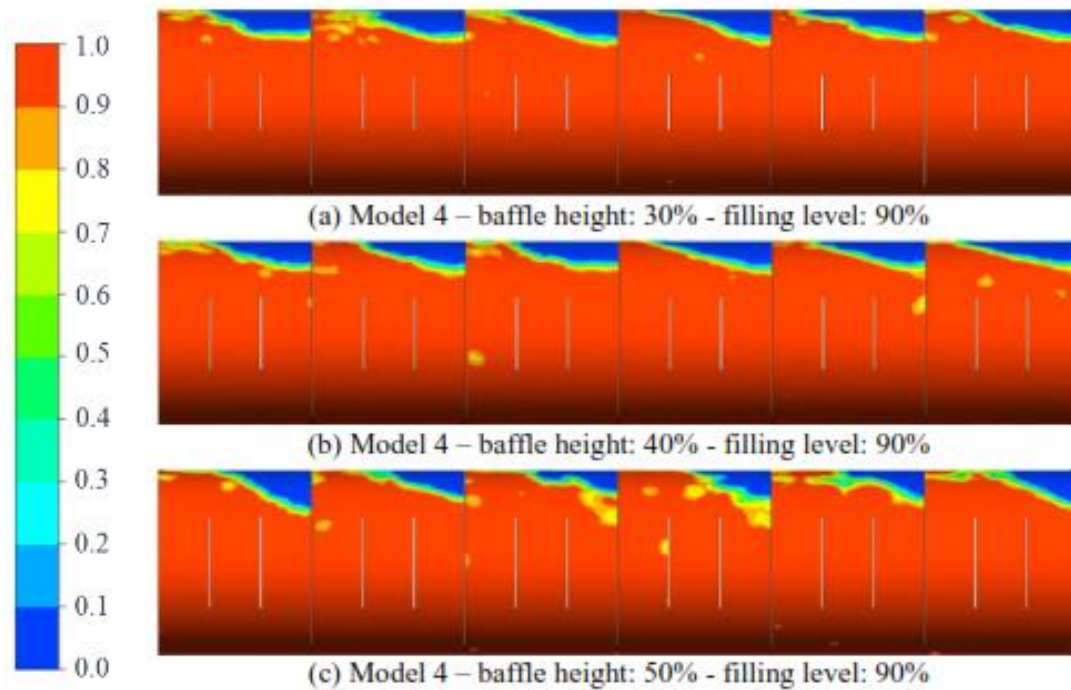


Figure 20. The free surfaces during sloshing on Model 4 with baffle heights of 30%, 40%, and 50%, at filling level of 90% of the tanker height

5. Conclusions

The study on the effects of adding the baffles and wave baffles into the gasoline tanker on the longitudinal stability of the semi-trailer has been investigated during the braking maneuver using the numerical simulation approach. The different configurations, heights, and quantities of baffles and wave baffles have been considered. The work results in the conclusions as follows:

- The anti-slosh ability of the tanker is improved by increasing the height and the quantity of wave baffles and replacing wave baffles with full baffles.
- The liquid filling level in the tanker significantly influences the load shifts on the kingpin. The results show that when the tanker is filled with full liquid, Model 2 should be used to simplify the manufacturing process of the tanker. In the case that the tanker with a partial liquid filling level is used, Model 3 is considered for applying to obtain the reasonable load shifts on the kingpin.
- The height of the wave baffles has a stronger effect than their quantity in reducing the load shift on the kingpin. From the result of this work, the load shift in the kingpin of Model 3, which has six wave baffles with the height of 50% the tanker height, is less than that of Model 4, which has twelve wave baffles with the height of 30% the tanker height.
- The higher the liquid filling level, the smaller the load shifts on the kingpin. The lower the liquid filling level, the higher percentage of load shifts obtained but their absolute values may not be large. With a given configuration of baffles, there is a liquid filling level in the tanker that producing the maximum load shift on the kingpin. In this study, the largest load shift on the kingpin is obtained at the liquid level is around 70% the tanker height.

Acknowledgments

We acknowledge the support of time and facilities from Ho Chi Minh City University (HCMUT), Vietnam National University Ho Chi Minh City (VNU-HCM) for this study.

References

- [1] Kandasamy T., Rakheja S., and Ahmed A.K.W. (2010), “An Analysis of Baffles Designs for Limiting Fluid Slosh in Partly Filled Tank Trucks”, *The Open Transportation Journal*, Vol. 4, pp. 23 - 32.
- [2] Suyal R. (2016), “CFD Analysis of Fuel Sloshing in A Cylindrical Tank with and without Baffles Under Linear Acceleration”, M.S. thesis, Department of Mechanical Engineering National Institute of Technology, Rourkela.
- [3] Zheng X.L., Li X.S., Ren Y.Y., Wang Y.N., and Ma J. (2013), “Effects of Transverse Baffle Design on Reducing Liquid Sloshing in Partially Filled Tank Vehicles”, *Mathematical Problems in Engineering*, Vol. 2, pp. 1-13, 10.1155/2013/130570.
- [4] Ha M.H., Kim D.H., Choi H.I., Cheong C.U., Kwon S.H. (2012), “Numerical and Experimental Investigations into Liquid Sloshing in A Rectangular Tank”, *The 2012 World Congress on Advances in Civil, Environmental, and Materials Research (ACEM’ 12)* Seoul, Korea, pp. 3546 – 3553.
- [5] Hong D.T., Tran M.T., Huynh. P.T. (2021). “Study of the effect of baffles on longitudinal stability of partly filled fuel tanker semi-trailer using CFD”. *Sci. Tech. Dev. J. – Engineering and Technology*; Vol. 3 (SI2), pp. SI13-SI23.
- [6] Tanthanh (2019), G43-BX40-02 tanker semi-trailer specification. Retrieved from: <https://tanthanhcontainer.com/wp-content/uploads/2018/06/G43-BX40-02-E.pdf>. (accessed 1st August 2019).
- [7] Wang L.S., Wang Z., Li Y.C. (2017), “Two-Dimensional Nonlinear Parametric Sloshing in The Irregular Tanks: Numerical Analysis and Experimental Investigation”. *Journal of Vibroengineering*, Vol. 3, No. 19, pp. 2153-2163.

Trajectory Tracking for Caterpillar Vehicles with Uncertain Parameters Using a Model Reference Adaptive Controller

Dae Hwan Kim^{1,2,*}, Hyun Jong Kim³ and Tan Tien Nguyen⁴

¹,State University of New York at Stony Brook, New York, USA, 11794

²Nsquare company, Busan, South Korea, 31040

³Institute for Advanced Engineering, Gyeonggi-do, South Korea, 17182

⁴Ho Chi Minh City University of Technology, Ho Chi Minh, Vietnam, 70000

*Corresponding author. E-mail: Daehwan.Kim@sunykorea.ac.kr

Abstract

This paper proposes trajectory tracking control of Caterpillar Vehicles (CVs) with uncertain parameters using a Model Reference Adaptive Control (MRAC) based on the backstepping method. To design the proposed controller, the followings are done. Firstly, a system modeling of the Caterpillar Vehicle is presented. Secondly, a backstepping control method is proposed based on the kinematic model for trajectory tracking of the Caterpillar Vehicle. Thirdly, to estimate uncertain parameters of the system modeling of the Caterpillar Vehicle, the MRAC based on the dynamic model is designed. Fourthly, by choosing candidate Lyapunov function, system stability is guaranteed and control laws can be obtained. Finally, to verify the effectiveness of the proposed controller, the simulation results of the proposed controller are shown and compared with the backstepping method proposed by P.S. Pratama in 2016. The simulation results are shown for the proposed controller to track the desired trajectory well.

Keywords: MIMO, MIP, LSID, Operator, Robust servo controller

1. Introduction

Recently, autonomous robots may act in place of human beings. The mobile robots are able to accomplish many tasks in dangerous places where humans cannot enter. These tasks may take place in unsafe environment, for example nuclear waste facilities, where harmful gases or high temperature present a hard environment for humans. There are several types of methods used to control a mobile robot. M. V. Gomes et al. [1] proposed a PID controller for trajectory tracking of the mobile robot. S. C. Yuan et al. [2] proposed another control method such, fuzzy control. Razvan Solea et al. [3] proposed the sliding mode controller design for trajectory tracking of a wheeled mobile robot in presence of uncertainties. P. S. Pratama et al. [4, 5] proposed a adaptive backstepping control method to track the trajectory. However, most of previous methods have slow response and are not robust due to the external disturbance as a friction and slip force. To solve the robust servo system design problem, S. B. Kim et al. [6] introduced a new design concept for the robust servo control system using the polynomial differential operator (PDO). D. H. Kim et al. [7] suggested a servo system design for speed control of AC induction motors using PDO. S.B. Kim et al. [8] developed this PDO design concept using a linear shift invariant differential (LSID) operator. However, these papers were not applied to Caterpillar Vehicles.

Therefore, this paper proposes a MIMO robust servo controller design for a Caterpillar Vehicle using the LSID operator. The main advantages of LSID are fast response and strong robustness against external disturbances. In order to verify the effectiveness of the proposed

MIMO robust servo controller, the simulation results are shown. These results are then compared to the adaptive backstepping control method proposed by P.S. Pratama in [4].

2. System Modeling

The Mobile robot Caterpillar Vehicle used in this paper is shown in Fig. 1. This Caterpillar Vehicles uses a differential drive wheeled configuration.

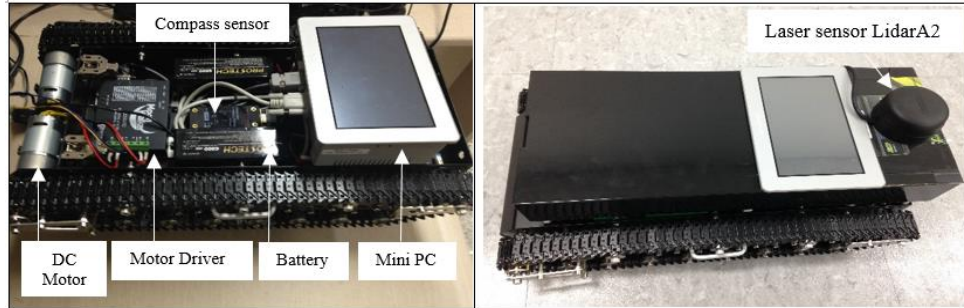


Figure 1. Structure of the Caterpillar Vehicle platform

Schematic modeling of a Caterpillar Vehicle is shown in Fig. 2. OXY is a global coordinate frame. Cxy is the moving coordinate frame attached on the Caterpillar Vehicle platform. This Caterpillar Vehicles has two driving standard wheels $W1$ and $W2$ with radius r , and $W3$ and $W4$ are passive wheels. (X_A, Y_A) is the Caterpillar Vehicle position vector in global coordinate OXY with orientation angle θ_A . The Caterpillar Vehicle moves with linear velocity v_A and angular velocity ω_A . v_R and v_L are the right and left wheel linear velocities, respectively, ϕ_R and ϕ_L are the right and left wheel angular velocities, respectively. b is a distance between wheels and Cx axis of the Caterpillar Vehicle. D is a mass center of the Caterpillar Vehicle. d is the distance between C and D .

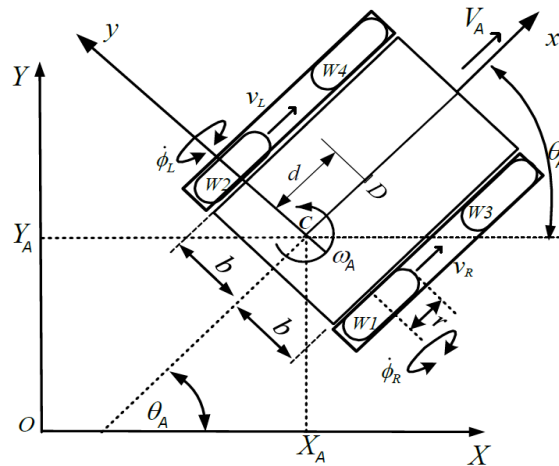


Figure 2. Schematic diagram of the Caterpillar Vehicle

The kinematic equation of the Caterpillar Vehicle as shown in Fig. 2 can be expressed as follows:

$$\dot{q} = H(q)z \quad (1)$$

$$\mathbf{q} = \begin{bmatrix} X_A \\ Y_A \\ \theta_A \end{bmatrix}, \mathbf{H}(\mathbf{q}) = \begin{bmatrix} \cos\theta_A & 0 \\ \sin\theta_A & 0 \\ 0 & 1 \end{bmatrix}, \mathbf{z} = \begin{bmatrix} V_A \\ \omega_A \end{bmatrix} \quad (2)$$

where \mathbf{q} is the posture vector of the Caterpillar Vehicle in global coordinate OXY , $\mathbf{H}(\mathbf{q})$ is full rank matrix, and \mathbf{z} is the velocity vector of the Caterpillar Vehicle.

Relation of the linear velocity v_A and angular velocity ω_A with the right and left wheel angular velocities ($\dot{\phi}_R, \dot{\phi}_L$) can be expressed as:

$$\mathbf{z} = \mathbf{T}\dot{\boldsymbol{\phi}} \text{ for } \mathbf{T} = \begin{bmatrix} \frac{r}{2} & \frac{r}{2} \\ \frac{r}{2b} & \frac{-r}{2b} \end{bmatrix}, \dot{\boldsymbol{\phi}} = \begin{bmatrix} \dot{\phi}_R \\ \dot{\phi}_L \end{bmatrix} \quad (3)$$

The dynamic equations of the Caterpillar Vehicle can be described by Euler-Lagrange formulation as follows [9]:

$$\overline{\mathbf{M}}\dot{\mathbf{z}} + \overline{\mathbf{V}}\mathbf{z} = \mathbf{u} \quad (4)$$

where

$$\overline{\mathbf{M}} = \begin{bmatrix} \frac{r^2}{4b^2}(m_t b^2 + I) + I_w & \frac{r^2}{4b^2}(m_t b^2 - I) \\ \frac{r^2}{4b^2}(m_t b^2 - I) & \frac{r^2}{4b^2}(m_t b^2 + I) + I_w \end{bmatrix}, \overline{\mathbf{V}} = \begin{bmatrix} 0 & \frac{r^2}{2b} m_c d \dot{\theta}_A \\ -\frac{r^2}{2b} m_c d \dot{\theta}_A & 0 \end{bmatrix},$$

$$I = m_c d^2 + 2m_w b^2 + I_c + 2I_m.$$

where $\mathbf{z} = [v_A \ \omega_A]^T$ is the velocity vector of the Caterpillar Vehicle, v_A is the linear velocity and ω_A is the angular velocity of the Caterpillar Vehicle, $\mathbf{u} = [\tau_R \ \tau_L] \in R^m (m=2)$ is the torque input vector applied to the two wheels of the Caterpillar Vehicle, $m_t = m_c + 2m_w$ is the total mass of the Caterpillar Vehicle, m_c is the mass of the body without driving wheels, m_w is the mass of each wheel, I_m is the moment of inertia of each motor, I_w is the moment of inertia of each wheel, and I_c is the moment of inertia of the body.

The Caterpillar Vehicle model can be described by the following MIMO linear model with a disturbance as:

$$\begin{cases} \dot{\mathbf{x}} = \mathbf{A}\mathbf{x} + \mathbf{B}\mathbf{u} + \boldsymbol{\varepsilon} \\ \mathbf{y} = \mathbf{C}\mathbf{x} \end{cases} \quad (5)$$

$$\mathbf{A} = \begin{bmatrix} L & 0 \\ I_2 & 0 \end{bmatrix}, \mathbf{B} = \begin{bmatrix} \mathbf{A} \\ \mathbf{0} \end{bmatrix}, \mathbf{I}_2 = \begin{bmatrix} I & 0 \\ 0 & I \end{bmatrix}, \mathbf{L} = (\overline{\mathbf{M}}\mathbf{T}^{-1})^{-1}\overline{\mathbf{V}}\mathbf{T}^{-1}, \mathbf{A} = (\overline{\mathbf{M}}\mathbf{T}^{-1})^{-1},$$

$$\mathbf{C} = \begin{bmatrix} 0 & 0 & 1 & 0 \\ 0 & 0 & 0 & 1 \end{bmatrix} = [\mathbf{c}_1^T \ \mathbf{c}_2^T \ \mathbf{c}_3^T \ \mathbf{c}_4^T]^T, \mathbf{x} = [V_A \ \omega_A \ l_A \ \theta_A]^T \in R^n (n=4)$$

where \mathbf{A} , \mathbf{B} and \mathbf{C} are parameter matrices for the Caterpillar Vehicle system, \mathbf{x} is the system state vector, l_A is linear displacement and θ_A is the orientation of the Caterpillar Vehicle, $\mathbf{y} = [l_A \ \theta_A]^T \in R^p$ ($p=2$) is the output vector of the Caterpillar Vehicle, and $\boldsymbol{\varepsilon} = [\varepsilon_1 \ \varepsilon_2 \ \varepsilon_3 \ \varepsilon_4]^T \in R^n$ is the disturbance vector.

3. MIMO Robust Servo Controller Design

An output error vector is defined as the difference between the output vector \mathbf{y} and reference input vector \mathbf{y}_r :

$$\mathbf{e} = [e_1 \ e_2]^T = \mathbf{y} - \mathbf{y}_r \in R^p \quad (6)$$

where $\mathbf{y}_r = [y_{r1} \ y_{r2}]^T \in R^p$ ($p=2$) is a reference input vector.

It is supposed that the following differential equation forms:

$$L_q(D)\mathbf{y}_r(t) = 0 \text{ and } L_q(D)\boldsymbol{\varepsilon}(t) = 0 \quad (7)$$

where $L_q(D)$ is a LSID operator for reference and disturbance signals.

A MIMO robust servo controller design method is implemented as follows [8]:

Firstly, to eliminate the effect of the disturbance in Eq. (5), operating a LSID operator $L_q(D)$ to both sides of Eq. (5) can be written as:

$$\frac{d}{dt}\{L_q(D)\mathbf{x}\} = \mathbf{A}L_q(D)\mathbf{x} + \mathbf{B}L_q(D)\mathbf{u} \quad (8)$$

$$L_q(D) = \prod_{i=1}^q (D - \beta_i I_d) = \prod_{i=1}^q P_{ai}(D) \quad (9)$$

where $P_{ai}(D)$ is the first order LSID operator of the i^{th} factorized term and $(D - \beta_i I_d)$ is the i^{th} factor of $L_q(D)$ with $\dim\{L_q(D)\} = q$, $\beta_i \in C$, $D = d/dt$ and I_d are derivative and identity operators, respectively.

The i^{th} output error can be obtained as follows:

$$e_i(t) = \boldsymbol{\gamma} L_q^{-1}(D) \mathbf{z}_i(t) \quad (10)$$

$$\boldsymbol{\gamma} = [\gamma_0 \ \gamma_1 \ \dots \ \gamma_{q-1}]^T, \gamma_0 = \prod_{i=1}^q \beta_i, \gamma_1 = \prod_{j \neq i, i=1}^q \beta_{ij}, \dots, \gamma_q = \sum_{i=1}^q \beta_i,$$

$$\mathbf{z}_i = [e_i \ e_i^{(1)} \ \dots \ e_i^{(q-1)}]^T \in R^q,$$

where $L_q^{-1}(D)$ is the inverse LSID operator.

Secondly, by operating $L_q(D)$ to Eq. (6), and combining with Eqs. (7)-(9), an extended system can be obtained as follows:

$$\dot{\mathbf{x}}_e = \mathbf{A}_e \mathbf{x}_e + \mathbf{B}_e \mathbf{v} \quad (11)$$

$$\mathbf{A}_e = \begin{bmatrix} \mathbf{A} & \mathbf{0} \\ \mathbf{M} & \text{diag}(\mathbf{N})_p \end{bmatrix} \in R^{(n+pq) \times (n+pq)}, \mathbf{B}_e = \begin{bmatrix} \mathbf{B} \\ \mathbf{0} \end{bmatrix} \in R^{(n+pq) \times m}, \mathbf{x}_e = \begin{bmatrix} L_q(D)\mathbf{x} \\ \mathbf{z} \end{bmatrix} \in R^{n+pq},$$

$$\mathbf{M} = [\mathbf{M}_1^T \quad \mathbf{M}_2^T \quad \cdots \quad \mathbf{M}_p^T]^T, \text{diag}(\mathbf{N})_p \in R^{pq \times pq}, \mathbf{z} = [\mathbf{z}_1^T \quad \mathbf{z}_2^T \quad \cdots \quad \mathbf{z}_p^T]^T \in R^{pq}.$$

$$\mathbf{N} = \begin{bmatrix} \mathbf{0} & & \mathbf{I}_{q-1} \\ \cdots & \cdots & \cdots \\ & & -\gamma^T \end{bmatrix} \in R^{q \times q}, \mathbf{M}_i = [\mathbf{0} \quad \cdots \quad \mathbf{c}_i^T]^T \in R^{q \times n}$$

where $\mathbf{x}_e \in R^{n+pq}$ is the extended system state variable vector, $\mathbf{v} \in R^m$ is a new control law for the extended system, $\mathbf{z} \in R^{pq}$ is an error variable vector for the extended system, and $\text{diag}(\mathbf{N})_p$ has p elements of matrix \mathbf{N} on the diagonal parts.

A new control law for the extended system is defined by the following form:

$$\mathbf{v} = L_q(D)\mathbf{u} = -\mathbf{F}\mathbf{x}_e \in R^m \quad \text{for } \mathbf{F} = [\mathbf{F}_x \quad \mathbf{F}_z] \in R^{m \times (n+pq)} \quad (12)$$

where $\mathbf{F}_x \in R^{m \times n}$ and $\mathbf{F}_z \in R^{m \times pq}$ are feedback control gain matrices for $L(D)\mathbf{x}$ and \mathbf{z} , respectively.

A new error variable vector for the extended system can be defined as:

$$\boldsymbol{\zeta} = L^{-1}(D)\mathbf{z} \quad \text{for } \boldsymbol{\zeta} = [\zeta_1^T \quad \zeta_2^T \quad \cdots \quad \zeta_p^T]^T \in R^{pq} \quad (13)$$

Using Eq. (12), the control law of Eq. (5) can be obtained as follows:

$$\mathbf{u} = L_q^{-1}(D)\mathbf{v} = -\mathbf{F}L_q^{-1}(D)\mathbf{x}_e = -\mathbf{F}\mathbf{x}_\zeta \quad (14)$$

where $\mathbf{x}_\zeta = L_q^{-1}(D)\mathbf{x}_e = [\mathbf{x}^T \quad \boldsymbol{\zeta}^T]^T \in R^{n+pq}$ is a new extended system variable vector.

From Eq. (11) and Eq. (12), a closed loop system is obtained as:

$$\dot{\mathbf{x}}_e = (\mathbf{A}_e - \mathbf{B}_e \mathbf{F})\mathbf{x}_e \quad (15)$$

Thirdly, by operating the inverse LSID operator $L_q^{-1}(D)$ for Eq. (11) and using the new input vector \mathbf{v} of Eq. (12), the following equations can be obtained:

$$\frac{d}{dt}\mathbf{x} = [\mathbf{A} - \mathbf{B}\mathbf{F}_x]\mathbf{x} - \mathbf{B}\mathbf{F}_z\boldsymbol{\zeta} + \boldsymbol{\varepsilon} \quad (16)$$

$$\frac{d\boldsymbol{\zeta}}{dt} = \mathbf{N}_z\boldsymbol{\zeta} + \mathbf{I}_\zeta \boldsymbol{\varepsilon} \quad \text{for } L_q(D)\boldsymbol{\varepsilon} = \mathbf{0} \quad (17)$$

where

$$\mathbf{N}_z = \begin{bmatrix} \mathbf{N} & \mathbf{0} & \cdots & \mathbf{0} \\ \mathbf{0} & \mathbf{N} & \cdots & \mathbf{0} \\ \vdots & \vdots & \ddots & \vdots \\ \mathbf{0} & \mathbf{0} & \cdots & \mathbf{N} \end{bmatrix} \in R^{pq \times pq}, \quad \mathbf{I}_\zeta = \begin{bmatrix} \lambda & \mathbf{0} & \cdots & \mathbf{0} \\ \mathbf{0} & \lambda & \cdots & \mathbf{0} \\ \vdots & \vdots & \ddots & \vdots \\ \mathbf{0} & \mathbf{0} & \cdots & \lambda \end{bmatrix} \in R^{pq \times n},$$

and $\lambda = [0 \ \dots \ 0 \ 1]^T \in R^q$.

The servo compensator of Eq. (17) includes the model of reference and disturbance signals since the matrix N_z is composed of the least common multiple model of two signals.

The configuration of the proposed MIMO robust servo controller under the disturbance can be described as in Fig. 3.

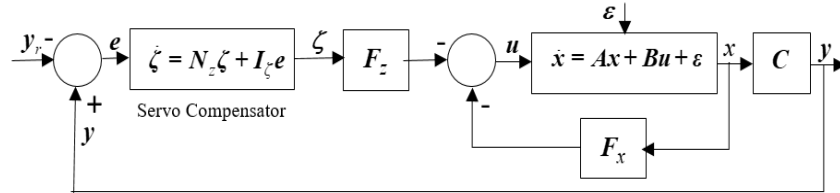


Figure 3. Configuration of the proposed MIMO robust servo controller

4. Simulation results

Simulations are done to verify the effectiveness of the proposed MIMO robust servo controller for a given Caterpillar Vehicle. This results are then compared to the adaptive backstepping control method proposed by P.S. Pratama in [4].

4.1 Proposed MIMO robust servo controller

The given MIMO system with $u = [u_1 \ u_2]^T$ is a torque input vector, and an output vector $y = [y_1 \ y_2]^T$ is the posture output vector of the Caterpillar Vehicle. The reference input vector consisting of linear displacement and orientation reference are chosen as follows: $y_r = [2.24\text{m} \ 0.46\text{rad}]^T$. It is assumed that the step type of disturbance vector is given as $\epsilon = [0.05\text{m/s} \ 0.01\text{rad/s} \ 0.1\text{m} \ 0.05\text{rad}]^T$.

Tables I-IV show parameters of the Caterpillar Vehicle, the matrices' values of MIMO system, the initial values and parameter values for the proposed controller.

Table I. Parameter values of Caterpillar Vehicle

Parameters	Values	Parameters	Values
b	0.12m	d	0m
r	0.04m	I_w	0.08kgm ²
m_w	1kg	I_m	0.48kgm ²
m_c	20kg	I_c	2.4kgm ²

Table II. Matrices' values of given MIMO system

Matrices	A	B	C
Values	$A = \begin{bmatrix} 0 & 0 & 0 & 0 \\ 0 & 0 & 0 & 0 \\ 1 & 0 & 0 & 0 \\ 0 & 1 & 0 & 0 \end{bmatrix}$	$B = \begin{bmatrix} 183.882 & 101.770 \\ 164.503 & 60.047 \\ 0 & 0 \\ 0 & 0 \end{bmatrix}$	$C = \begin{bmatrix} 0 & 0 & 1 & 0 \\ 0 & 0 & 0 & 1 \end{bmatrix}$ $= [c_1^T \ c_2^T \ c_3^T \ c_4^T]^T$

Table III. Initial values of the proposed MIMO robust servo controller

Initial values	$x(0)$	$\zeta(0)$
Values	$[0 \ 0 \ 0 \ 0]^T$	$[0 \ 0]^T$

Table IV. Matrices' values of the proposed MIMO robust servo controller

Matrices	Values
F_x, F_z	$F_x = \begin{bmatrix} -0.4469 & 0.6747 & -6.2026 & 8.4644 \\ 1.1796 & -1.2300 & 15.8669 & -15.5667 \end{bmatrix}, F_z = \begin{bmatrix} -28.1496 & 35.2550 \\ 70.1422 & -65.3878 \end{bmatrix}$
N_z, I_ζ	$N_z = \begin{bmatrix} 0 & 0 \\ 0 & 0 \end{bmatrix}, I_\zeta = \begin{bmatrix} 1 & 0 \\ 0 & 1 \end{bmatrix}$

4.2 Adaptive backstepping controller

The adaptive backstepping controller design for the Caterpillar Vehicle was described in [4]. It was designed based on Lyapunov stability theory and an adaptive backstepping control theory to track a desired trajectory. This backstepping controller is applied for the Caterpillar Vehicle with the parameters and gain values are shown in Table 5.

Table V. Parameter values of adaptive backstepping controller

Parameters	Values	Parameters	Values
b	0.12m	$X_A(0)$	0m
r	0.04m	$Y_A(0)$	0m
k_1	2	$\theta_A(0)$	0rad
k_2	5	$V_A(0)$	0m/s
k_3	21.5	$V_A(0)$	0rad/s

where k_1 , k_2 , and k_3 are positive constant values.

4.3. Simulation results

Simulation results using the step reference input vector y_r for both controllers are shown in Figs. 4-19. Figs. 4-5 show the control law vector using both controllers. The control laws u_1 and u_2 of the proposed MIMO robust servo controller converge to zero after 0.75 seconds, while the control laws u_1 and u_2 of the adaptive backstepping controller converge to zero after 3 seconds and 0.5 seconds, respectively. Figs. 6-7 show the output y_1 and y_2 of both controllers. Fig. 6 shows the output y_1 of both controllers track the step reference input y_{r1} well after about 0.75 second and 3 seconds, respectively. Fig. 7 shows the output y_2 of both controllers track the step reference input y_{r2} well after about 0.75 second and 0.5 seconds, respectively. Figs. 8-9 show the output X_A on the X axis and Y_A on the Y axis of both controllers. Fig. 8 shows the output X_A of both controllers converge to $X = 2$ m after about 0.75 second and 3 seconds, respectively. Fig. 9 shows the output Y_A of both controllers converge to $Y = 1$ m after about 0.75 second and 3 seconds, respectively.

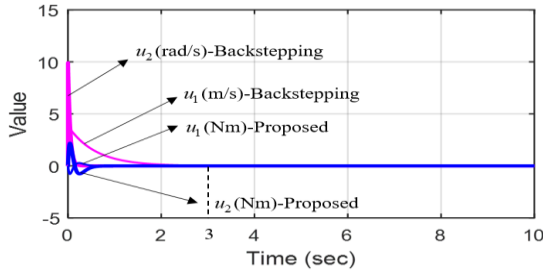


Figure. 4. Control law vector u

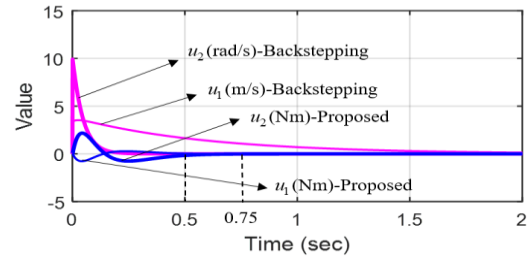


Figure. 5. Control law vector u at beginning

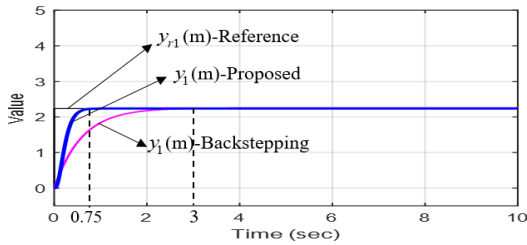


Figure. 6. Output y_1 for the step reference input

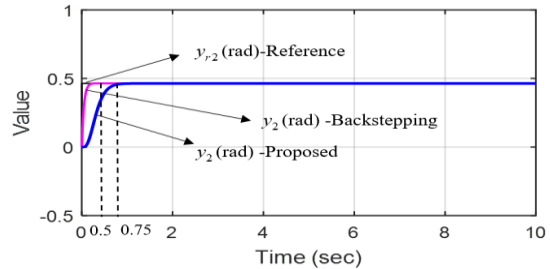


Figure. 7. Output y_2 for the step reference input

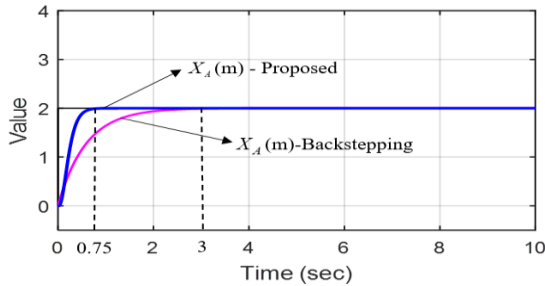


Figure. 8. Output X_A on the X axis of the Caterpillar Vehicle

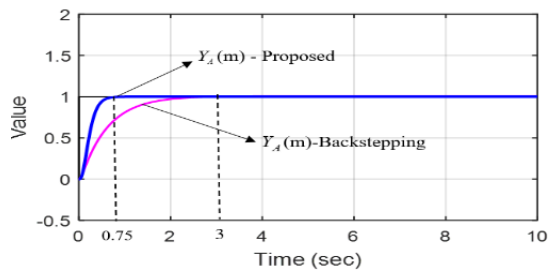


Figure. 9. Output Y_A on the Y axis of the Caterpillar Vehicle

5. Conclusions

A MIMO robust servo controller design for a Caterpillar Vehicle with the friction and slip force disturbance to track desired linear displacement and orientation references using a linear shift invariant differential (LSID) operator was proposed. The simulation results showed that the proposed controller had good tracking performance for a step type of reference input vector and a step type of disturbance vector. The output vector of the MIMO robust servo controller tracked the step type of the reference input vector well after about 0.75 seconds, while the output vector of the adaptive backstepping controller [4] tracked the step type of reference input vector after about 3 seconds. Therefore, the proposed MIMO robust servo controller showed the faster tracking performance than the adaptive backstepping controller [4].

Acknowledgments

This research was financially supported by the Ministry of Trade, Industry and Energy (MOTIE) and Korea Institute for Advancement of Technology (KIAT) through the International Cooperative R&D program. (Project No. P0004631)

References

- [1] Gomes, M. V., Bassora, L. A., Morandin, Jr. O., Vivaldini, K. C. T. (2016) "PID control applied on a line-follower AGV using a RGB camera", In: IEEE 19th International Conference on Intelligent Transportation Systems (ITSC), pp. 194-198
- [2] Solea, R., Filipescu, A., Nunes, U. (2009),) "Sliding-mode control for trajectory-tracking of a wheeled mobile robot in presence of uncertainties", In: 7th Asian Control Conference 2009, IEEE (2009).
- [3] Yuan, S. C., Yao, L. (2009) "Robust type-2 fuzzy control of an automatic guided vehicle for wall-following", In: Proceedings of International Conf. of Soft Computing and Pattern Recognition, pp. 172-177
- [4] Pratama, P. S., Luan, B. T., Tran, T. T., Kim, H. K., Kim, S. B.(2013), "Trajectory tracking algorithm for automatic guided vehicle based on adaptive backstepping control method", Lecture Notes in Electrical Engineering, vol. 282, pp. 535-544, Springer, Heidelberg
- [5] Pratama, P. S., Nguyen, T. H., Kim, H. K., Kim, D. H., Kim, S. B.(2016), "Positioning and obstacle avoidance of automatic guided vehicle in partially known environment", International Journal of Control, Automation and Systems, 14(6), 1572-1581
- [6] Kim, S. B., Kim, D. H., Pratama, P. S., Kim, J. W., Kim, H. K., Oh, S. J., Jung, Y. S.(2015), "MIMO robust servo controller design based on internal model principle using polynomial differential operator", Lecture Notes in Electric Engineering vol. 371, pp. 469-484, Springer, Switzerland
- [7] Kim, D. H., Nguyen, T. H., Pratama, P. S., Gulakari, A.V., Kim, H. K., Kim, S. B.(2017), "Servo system design for speed control of AC induction motors using polynomial differential operator", International Journal of Control, Automation, and Systems 15(3), 1207-1216
- [8] Kim, S. B., Nguyen, H. H., Kim, D. H., Kim, H. K.(2018), "Robust servo controller design for MIMO systems based on linear shift invariant differential operator", Journal of Institute of Control, Robotics and Systems 24(6), 501-511
- [9] Hung, N., Im, J. S., Jeong, S. K., Kim, H. K., Kim, S. B.(2010), "Design of a sliding mode controller for an automatic guided vehicle and its implementation", International Journal of Control, Automation, and Systems, 8(1), 81-90

Motion Control for Two Wheeled Mobile Inverted Pendulums Using a MIMO Robust Servo Controller Systems

Dae Hwan Kim^{1,2,*}, Huy Hung Nguyen³ and Sang Bong Kim⁴

¹,State University of New York at Stony Brook, New York, USA, 11794

²Nsquare company, Busan, South Korea, 31040

³Ho Chi Minh City University of Technology, Ho Chi Minh City, Vietnam, 70000

⁴Pukyong National University, Busan, South Korea, 48513

*Corresponding author. E-mail: Daehwan.Kim@sunykorea.ac.kr

Abstract

This paper proposes a MIMO robust servo controller design for two-wheeled Mobile Inverted Pendulums (MIPs) with an external disturbance to track desired linear displacement and orientation reference inputs using a linear shift invariant differential (LSID) operator. For this task, the followings are done. Firstly, based on Newton's 2nd law, the modeling of the two-wheeled MIP is presented. Secondly, by operating the LSID operator to the state space model and the output error vector, a new extended system and a new control law are obtained. Thirdly, a proposed MIMO robust servo controller for the given two-wheeled MIP is designed by using the pole assignment approach. Forthly, by operating the inverse LSID operator, a servo compensator for the MIMO system is obtained. Finally, in order to verify the effectiveness of the proposed MIMO robust servo controller, the simulation results are shown. The simulation results show the good tracking performance of the proposed MIMO robust servo controller under a step type of disturbance and the step linear displacement and angular reference signals.

Keywords: MIMO, MIP, LSID, Operator, Robust servo controller

1. Introduction

Recently, Mobile Inverted Pendulums (MIPs) with self-balancing capability have been regularly applied as mobile platforms for personal transporters, commuter vehicles, robotic wheelchairs and mobile manipulators. It also is used to test the complex control algorithms. The performance of MIPs depends heavily on the controller in use. Thus, there have been several control methods proposed for MIPs. E Silva et al. [1] proposed a PID control method for a coaxial two-wheeled mobile robot. P. Oryschuk et al. [2] proposed a linear quadratic regulator control method for experimental validation of an underactuated two-wheeled mobile robot. K. Pathak et al. [3] proposed a velocity and position control method of a wheeled inverted pendulum using feedback linearization. C. H. Huang et al. [4] proposed a fuzzy control method for a two-wheel inverted pendulum. However, these control methods are limited in keeping the posture stability. To improve this problem and increase the driving performance, Z. Li et al. [5] proposed a neural-adaptive output feedback control method for a wheeled inverted pendulum models. J. X. Xu et al. [6] proposed a sliding control method on an underactuated two-wheeled mobile robot. The main advantage of these control techniques is fast response. However, when the MIP is affected by intentional maneuvers or external disturbances, those algorithms are not robust. To solve the robust servo system design problem, S. B. Kim et al. [8] introduced a new design concept for the robust servo control system using the polynomial differential operator (PDO). D. H. Kim et al. [9] suggested a servo system design for speed control of AC induction motors using PDO. S. B. Kim et al. [10] developed perfectly this PDO design concept using a linear shift invariant differential (LSID) operator. However, these papers were not applied to two-wheeled MIPs.

Therefore, this paper proposed a MIMO robust servo controller design for two-wheeled MIP using a LSID operator when its mathematical model is designed. In order to verify the effectiveness of the proposed MIMO robust servo controller, the simulation results are shown. The simulation results demonstrate the efficiency of the proposed controller under a step type of external disturbance and step types of linear displacement and angular reference signals.

2. System Modeling

The configuration of a two-wheeled MIP platform use in this paper is shown in Fig 1.



Figure 1. Configuration of two-wheeled MIP platform

In this paper, the Caterpillar Vehicle uses a differential drive wheeled configuration. The schematic modeling of the system is shown in Fig. 1. In Fig. 1, OXY is a global coordinate frame. Cxy is the moving coordinate frame attached on the Caterpillar Vehicle (CV) platform. This CV has two driving standard wheels W1 and W2 with radius r , and W3 and W4 as passive wheels. (X_A, Y_A) is the CV position vector in global coordinate OXY with orientation angle θ_A . The CV moves with linear velocity V_A and angular velocity ω_A . v_R and v_L are the right and left wheel linear velocities, respectively. $\dot{\theta}_R$ and $\dot{\theta}_L$ are the right and left wheel angular velocities, respectively. b is a distance between wheels and Cx axis of the CV. D is a mass center of the CV. d is the distance between C and D.

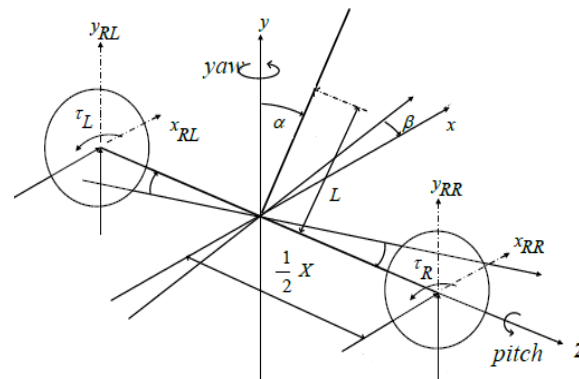


Figure 2. Schematic diagram of two-wheeled MIP

where α is the pitch angle of the MIP; β is the yaw angle of MIP; τ_R and τ_L are torque inputs for right wheel and left wheel, respectively; L is the distance between the wheel's center and the MIP's center of gravity; and X is the distance between the wheels.

The dynamic equation of two-wheeled MIP based on Newton's law can be described as follows[7]:

$$(2M_p R + \frac{2I_r}{R} + M_p R)\ddot{l} + M_p RL(\ddot{\alpha} \cos \alpha - \dot{\alpha}^2 \sin \alpha) = \tau_L + \tau_R \quad (1)$$

$$(I_p + M_p L^2)\ddot{\alpha} - M_p g L \sin \alpha + M_p L \cos \alpha \ddot{l} = 0 \quad (2)$$

where l is the moving displacement of the MIP.

By rearranging Eq. (1)-(3), dynamic equation of two-wheeled MIP can be represented as follows:

$$(M_p RL \cos \alpha - \phi_1 \phi_2 \sec \alpha)\ddot{\alpha} + \phi_1 g \tan \alpha - M_p RL \dot{\alpha}^2 \sin \alpha = \tau_L + \tau_R \quad (3)$$

The dynamic equations of the CV can be described as follows[3]:

$$\bar{M}\dot{z} + \bar{V}z = u \quad (4)$$

where u is a control input vector, and \bar{M}, \bar{V} are the parameters matrix of the given CV system :

$$\bar{M} = \begin{bmatrix} \frac{r^2}{4b^2}(m_t b^2 + I) + I_w & \frac{r^2}{4b^2}(m_t b^2 - I) \\ \frac{r^2}{4b^2}(m_t b^2 - I) & \frac{r^2}{4b^2}(m_t b^2 + I) + I_w \end{bmatrix}, \bar{V} = \begin{bmatrix} 0 & \frac{r^2}{2b} m_c d \dot{\theta}_A \\ -\frac{r^2}{2b} m_c d \dot{\theta}_A & 0 \end{bmatrix},$$

$$I = m_c d^2 + 2m_w b^2 + I_c + 2I_m.$$

where m is the total mass of the CV, m_t is the mass of the body without driving wheels, m_w is the mass of each wheel, I is the moment of inertia of each motor, I_w is the moment of inertia of each wheel, and I_c is the moment of inertia of the body.

The CV model can be described by the following state function as:

The Caterpillar Vehicle model can be described by the following MIMO linear model with a disturbance as:

$$\begin{cases} \dot{x} = Ax + Bu + \varepsilon \\ y = Cx \end{cases} \quad (5)$$

3. MIMO Robust Servo Controller Design

An output error vector is defined as the difference between the output vector y and reference input vector y_r :

$$e = [e_1 \ e_2 \ e_3]^T = y - y_r \in R^p \quad (6)$$

where $y_r = [y_{r1} \ y_{r2}]^T \in R^p$ ($p = 2$) is a reference input vector.

It is supposed that the following differential equation forms:

$$L_q(D)y_r(t) = 0 \text{ and } L_q(D)\varepsilon(t) = 0 \quad (7)$$

where $L_q(D)$ is a LSID operator for reference and disturbance signals.

A MIMO robust servo controller design method is implemented as follows [8]:

Firstly, to eliminate the effect of the disturbance in Eq. (5), apply a LSID operator $L_q(D)$ to both sides of Eq. (5). The equation can then be written as:

$$\frac{d}{dt}\{L_q(D)\mathbf{x}\} = \mathbf{A}L_q(D)\mathbf{x} + \mathbf{B}L_q(D)\mathbf{u} \quad (8)$$

$$L_q(D) = \prod_{i=1}^q (D - \beta_i I_d) = \prod_{i=1}^q P_{ai}(D) \quad (9)$$

where $P_{ai}(D)$ is the first order LSID operator of the i^{th} factorized term and $(D - \beta_i I_d)$ is the i^{th} factor of $L_q(D)$ with $\dim\{L_q(D)\} = q$, $\beta_i \in \mathbb{C}$, $D = d/dt$ and I_d are derivative and identity operators, respectively.

The i^{th} output error can be obtained as follows:

$$e_i(t) = \gamma L_q^{-1}(D)z_i(t) \quad (10)$$

$$\gamma = [\gamma_0 \quad \gamma_1 \quad \cdots \quad \gamma_{q-1}]^T, \gamma_0 = \prod_{i=1}^q \beta_i, \gamma_1 = \prod_{j \neq i, i=1}^q \beta_{ij}, \cdots, \gamma_q = \sum_{i=1}^q \beta_i,$$

$$\mathbf{z}_i = [e_i \quad e_i^{(1)} \quad \cdots \quad e_i^{(q-1)}]^T \in \mathbb{R}^q,$$

where $L_q^{-1}(D)$ is the inverse LSID operator.

Secondly, by applying $L_q(D)$ to Eq. (6), and combining with Eqs. (7)-(9), an extended system can be obtained as follows:

$$\dot{\mathbf{x}}_e = \mathbf{A}_e \mathbf{x}_e + \mathbf{B}_e \mathbf{v} \quad (11)$$

$$\mathbf{A}_e = \begin{bmatrix} \mathbf{A} & \mathbf{0} \\ \mathbf{M} & \text{diag}(\mathbf{N})_p \end{bmatrix} \in \mathbb{R}^{(n+pq) \times (n+pq)}, \mathbf{B}_e = \begin{bmatrix} \mathbf{B} \\ \mathbf{0} \end{bmatrix} \in \mathbb{R}^{(n+pq) \times m}, \mathbf{x}_e = \begin{bmatrix} L_q(D)\mathbf{x} \\ \mathbf{z} \end{bmatrix} \in \mathbb{R}^{n+pq},$$

$$\mathbf{M} = [\mathbf{M}_1^T \quad \mathbf{M}_2^T \quad \cdots \quad \mathbf{M}_p^T]^T, \text{diag}(\mathbf{N})_p \in \mathbb{R}^{pq \times pq}, \mathbf{z} = [z_1^T \quad z_2^T \quad \cdots \quad z_p^T]^T \in \mathbb{R}^{pq}.$$

$$\mathbf{N} = \begin{bmatrix} \mathbf{0} & & \mathbf{I}_{q-1} \\ \cdots & \cdots & \cdots \\ & & -\gamma^T \end{bmatrix} \in \mathbb{R}^{q \times q}, \mathbf{M}_i = [\mathbf{0} \quad \cdots \quad \mathbf{c}_i^T]^T \in \mathbb{R}^{q \times n}$$

where $\mathbf{x}_e \in \mathbb{R}^{n+pq}$ is the extended system state variable vector, $\mathbf{v} \in \mathbb{R}^m$ is a new control law for the extended system, $\mathbf{z} \in \mathbb{R}^{pq}$ is an error variable vector for the extended system, and $\text{diag}(\mathbf{N})_p$ has P elements of matrix \mathbf{N} on the diagonal parts.

A new control law for the extended system is defined by the following form:

$$v = L_q(D)u = -Fx_e \in R^m \quad \text{for } F = [F_x \quad F_z] \in R^{m \times (n+pq)} \quad (12)$$

where $F_x \in R^{m \times n}$ and $F_z \in R^{m \times pq}$ are feedback control gain matrices for $L(D)x$ and z , respectively.

A new error variable vector for the extended system can be defined as:

$$\zeta = L^{-1}(D)z \quad \text{for } \zeta = [\zeta_1^T \quad \zeta_2^T \quad \dots \quad \zeta_p^T]^T \in R^{pq} \quad (13)$$

Using Eq. (12), the control law of Eq. (5) can be obtained as follows:

$$u = L_q^{-1}(D)v = -FL_q^{-1}(D)x_e = -Fx_\zeta \quad (14)$$

where $x_\zeta = L_q^{-1}(D)x_e = [x^T \quad \zeta^T]^T \in R^{n+pq}$ is a new extended system variable vector.

From Eq. (11) and Eq. (12), a closed loop system is obtained as:

$$\dot{x}_e = (A_e - B_e F)x_e \quad (15)$$

Thirdly, by operating the inverse LSID operator $L_q^{-1}(D)$ for Eq. (11) and using the new input vector v of Eq. (12), the following equations can be obtained:

$$\frac{d}{dt}x = [A - BF_x]x - BF_z\zeta + \varepsilon \quad (16)$$

$$\frac{d\zeta}{dt} = N_z\zeta + I_\zeta e \quad \text{for } L_q(D)\varepsilon = 0 \quad (17)$$

where

$$N_z = \begin{bmatrix} N & 0 & \dots & 0 \\ 0 & N & \dots & 0 \\ \vdots & \vdots & \ddots & \vdots \\ 0 & 0 & \dots & N \end{bmatrix} \in R^{pq \times pq}, \quad I_\zeta = \begin{bmatrix} \lambda & 0 & \dots & 0 \\ 0 & 0 & \dots & 0 \\ \vdots & \vdots & \ddots & \vdots \\ 0 & 0 & \dots & \lambda \end{bmatrix} \in R^{pq \times n},$$

and $\lambda = [0 \quad \dots \quad 0 \quad 1]^T \in R^q$.

The servo compensator of Eq. (17) includes the model of reference and disturbance signals since the matrix N_z is composed of the least common multiple model of two signals.

The configuration of the proposed MIMO robust servo controller under the disturbance can be described as shown in Fig. 3.

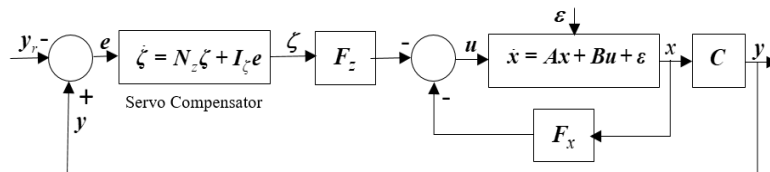


Figure 4. Configuration of the proposed MIMO robust servo controller

4. Simulation results

Simulations are done to verify the effectiveness of the proposed MIMO robust servo controller for a given Caterpillar Vehicle. This results of the proposed MIMO robust servo controller are compared with the adaptive backstepping control method proposed by P.S. Pratama in [4].

4.1 Proposed MIMO robust servo controller

The given MIMO system with $u = [u_1 \ u_2]^T$ is a torque input vector, and an output vector $y = [y_1 \ y_2]^T$ is the posture output vector of the Caterpillar Vehicle. The reference input vector consisting of linear displacement and orientation reference are chosen as: $y_r = [2.24m \ 0.46rad]^T$. It is assumed that the step type of disturbance vector is given as the following $\varepsilon = [0.05m/s \ 0.01rad/s \ 0.1m \ 0.05rad]^T$.

Tables I-IV show parameters of the Caterpillar Vehicle, the matrices' values of MIMO system, the initial values and parameter values for the proposed controller.

Table I. Parameter values of Caterpillar Vehicle

Parameters	Values	Parameters	Values
b	0.12m	d	0m
r	0.04m	I_w	0.08kgm ²
m_w	1kg	I_m	0.48kgm ²
m_c	20kg	I_c	2.4kgm ²

Table II. Matrices' values of given MIMO system

Matrices	A	B	C
Values	$A = \begin{bmatrix} 0 & 0 & 0 & 0 \\ 0 & 0 & 0 & 0 \\ 1 & 0 & 0 & 0 \\ 0 & 1 & 0 & 0 \end{bmatrix}$	$B = \begin{bmatrix} 183.882 & 101.770 \\ 164.503 & 60.047 \\ 0 & 0 \\ 0 & 0 \end{bmatrix}$	$C = \begin{bmatrix} 0 & 0 & 1 & 0 \\ 0 & 0 & 0 & 1 \end{bmatrix}$ $= [c_1^T \ c_2^T \ c_3^T \ c_4^T]^T$

Table III. Initial values of the proposed MIMO robust servo controller

Initial values	$x(0)$	$\zeta(0)$
Values	$[0 \ 0 \ 0 \ 0]^T$	$[0 \ 0]^T$

Table IV. Matrices' values of the proposed MIMO robust servo controller

Matrices	Values
F_x, F_z	$F_x = \begin{bmatrix} -0.4469 & 0.6747 & -6.2026 & 8.4644 \\ 1.1796 & -1.2300 & 15.8669 & -15.5667 \end{bmatrix}, F_z = \begin{bmatrix} -28.1496 & 35.2550 \\ 70.1422 & -65.3878 \end{bmatrix}$
N_z, I_ζ	$N_z = \begin{bmatrix} 0 & 0 \\ 0 & 0 \end{bmatrix}, I_\zeta = \begin{bmatrix} 1 & 0 \\ 0 & 1 \end{bmatrix}$

4.2 Adaptive backstepping controller

The adaptive backstepping controller design for the Caterpillar Vehicle was described in [4]. This adaptive backstepping controller was designed based on Lyapunov stability theory and an adaptive backstepping control theory to track a desired trajectory. This controller is applied for the Caterpillar Vehicle with the parameters and gain values are shown in Table 5.

Table V. Parameter values of adaptive backstepping controller

Parameters	Values	Parameters	Values
b	0.12m	$X_A(0)$	0m
r	0.04m	$Y_A(0)$	0m
k_1	2	$\theta_A(0)$	0rad
k_2	5	$V_A(0)$	0m/s
k_3	21.5	$\dot{\theta}_A(0)$	0rad/s

where k_1 , k_2 , and k_3 are positive constant values.

4.3 Simulation results

Simulation results using the step reference input vector y_r for both controllers are shown in Figs. 4-19. Figs. 4-5 show the control law vector using both controllers. The control laws u_1 and u_2 of the proposed MIMO robust servo controller converge to zero after 0.75 seconds, while the control laws u_1 and u_2 of the adaptive backstepping controller converge to zero after 3 seconds and 0.5 seconds, respectively. Figs. 6-7 show the output y_1 and y_2 of both controllers. Fig. 6 shows the output y_1 of both controllers track the step reference input y_{r1} well after about 0.75 second and 3 seconds, respectively. Fig. 7 shows the output y_2 of both controllers track the step reference input y_{r2} well after about 0.75 second and 0.5 seconds. Figs. 8-9 show that the output X_A on the X axis and Y_A on the Y axis of both controllers. Fig. 8 shows the output X_A of both controllers converge to $X = 2$ m after about 0.75 second and 3 seconds, respectively. Fig. 9 shows the output Y_A of both controllers converge to $Y = 1$ m after about 0.75 second and 3 seconds, respectively.

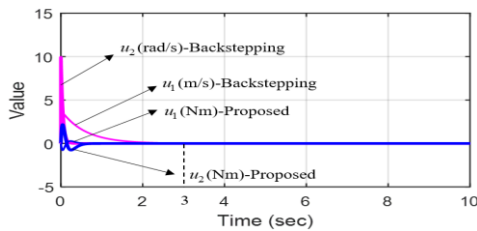


Figure 5. Control law vector u

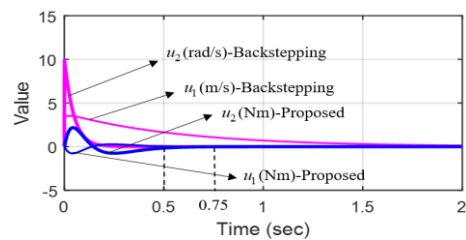


Figure 6. Control law vector u at beginning

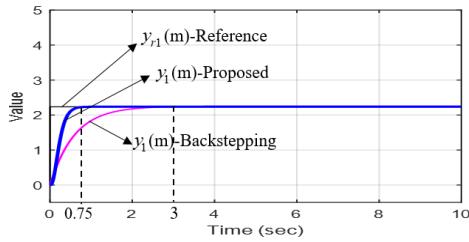


Figure 7. Output y_1 for the step reference input

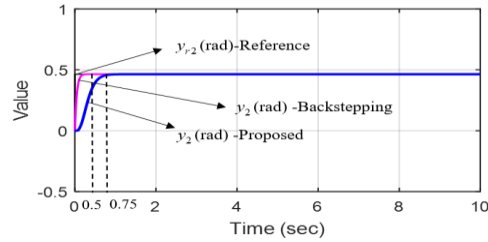


Figure 8. Output y_2 for the step reference input

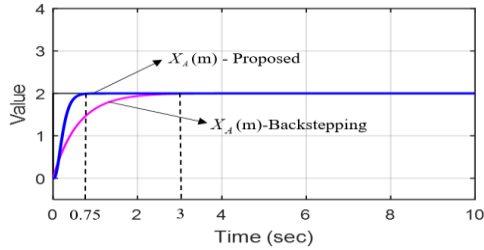


Figure 9. Output X_A on the X axis of the Caterpillar Vehicle

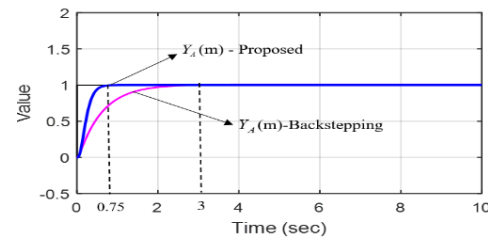


Figure 10. Output Y_A on the Y axis of the Caterpillar Vehicle

5. Conclusions

A MIMO robust servo controller design for a two-wheeled MIPs with a external disturbance to track desired reference inputs using a linear shift invariant differential (LSID) operator was proposed. The simulation results showed the proposed for a step type of reference input vector and a step type of disturbances vector. The output vector of the MIMO robust servo controller tracked the step type of the reference input vector well after about 1,2 seconds.

Acknowledgments

This research was financially supported by the Ministry of Trade, Industry and Energy (MOTIE) and Korea Institute for Advancement of Technology (KIAT) through the International Cooperative R&D program. (Project No. P0004631)

References

- [1] F. O. E Silva and L. H. De Carvalho Ferreira,(2013), “Design and implementation of a PID control system for a coaxial two-wheeled mobile robot,” In Industrial Electronics, 2013 IEEE International Symposium, pp. 1-6
- [2] P. Oryschuk, A. Salerno, A. M. Al-Husseini, and J. Angeles,(2009), “ Experimental validation of an underactuated two-wheeled mobile robot,” IEEE/ASME Transactions on Mechatronics, vol. 14, no. 2, pp. 252–257.
- [3] K. Pathak, J. Franch and S. K. Agrawal,(2005), “Velocity and position control of a wheeled inverted pendulum by partial feedback linearization,” IEEE Transactions on Robotics, vol. 21, no. 3, pp. 505–513.
- [4] C. H. Huang, W. J. Wang, and C. H. Chiu,(2011), “Design and implementation of fuzzy control on a two-wheel inverted pendulum,” IEEE Transactions on Industrial Electronics, vol. 58, no. 7, pp. 2988–3001.

- [5] Z. Li and C. Yang,(2012), “Neural-adaptive output feedback control of a class of transportation vehicles based on wheeled inverted pendulum models,” IEEE Transactions on Control Systems Technology, vol. 20, no. 6, pp. 1583–1591, Nov.
- [6] J. X. Xu, Z. Q. Guo, and T. H. Lee,(2014), “Design and implementation of integral sliding-mode control on an underactuated two-wheeled mobile robot,” IEEE Transactions on Industrial Electronics, vol. 61, no. 7, pp. 3671–3681.
- [7] P. Chetanraj,(2018), “PID back stepping controller design for motion control of segway vehicle,” International Journal of Innovative Research In Technology, vol 5, pp. 15-20.
- [8] Kim, S. B., Nguyen, H. H., Kim, D. H., Kim, H. K.(2018), "Robust servo controller design for MIMO systems based on linear shift invariant differential operator", Journal of Institute of Control, Robotics and Systems 24(6), 501-511.
- [9] S. -B. Kim, D. -H. Kim, P. S. Pratama, J. W. Kim, H. -K. Kim, S. -J. Oh, Y. -S. Jung,(2015) “MIMO robust servo controller design based on internal model principle using polynomial differential operator,” Lecture Notes in Electric Engineering, vol. 371, pp. 469-484.
- [10] D. -H. Kim, T. H. Nguyen, P. S. Pratama, A. V. Gulakari, H. -K. Kim, S. B. Kim,(2017), “Servo system design for speed control of AC induction motors using polynomial differential operator,” International Journal of Control, Automation, and Systems, vol. 15, no. 3, pp. 1207-1216.
- [11] S. -B. Kim, H. H. Nguyen, D. -H. Kim, H. -K. Kim,(2018), “Robust servo controller design for MIMO systems based on linear shift invariant differential operator,” Journal of Institute of Control, Robotics and Systems, vol. 24, no. 6, pp. 501-511.

Design, Analysis and Simulation of V-frame Octocopter

Tri Bien Minh^{1,*}, Hien Vo¹, Luan Hua Thanh²

¹Department of Electrical and Computer Engineering, Vietnamese German University, Binh Duong, Vietnam

²Research and Development Autonomous Robot, Robotlab, Binh Duong, Vietnam

*Corresponding author. E-mail: tri.bm@vgu.edu.vn

Abstract

Octocopter is one kind of multirotor vehicle (a rotorcraft with more than two rotors), that has lately gained a lot of attention in both the scientific and commercial sphere. With a greater number of rotors, the multirotor is very maneuverable and robust. Multi-copter makes an important contribution to the technological revolution in the military, industry, transportation, mapping, and especially agriculture. Nowadays, we are heading toward the fourth industrial revolution as well as new technological applications in the agricultural field such as precise agriculture, mapping, and surveillance. Due to recent advanced technology in sensors, electronics, 3D printing, battery with high performance, multi-copter can be manufactured at low cost. The main purpose of the study was mechanical designing, simulation, and manufacturing process for a new model of octocopter V-frame and achieve simple manufacturing with 3D printing technology. Moreover, the octocopter PID controller was simulated on the Simulink environment to get performance on the roll and pitch angle control. The V-frame octocopter was chosen in this paper as it has better performance scores including high redundancy rotors, high payload capability, and affordable cost compared to any other multi-copter family. The V-frame octocopter increasing freedom field of view of the camera was considered to place the camera position in the front of the drone.

Keywords: Octocopter, mechanical design, v-frame, multirotor vehicle, UAV

Nomenclature

FOV	= field of view	\dot{m}	= massflow
F_{Thrust}	= thrust force of each motor	v	= velocity of octocopter
E	= Young's modulus	S	= propeller surface area
σ_u	= ultimate tensile strength	P	= power
K_M	= torque constant	K_F	= thrust constant
ω_i	= rotation rate of rotor number		
iC	= drag coefficient		
ρ	= air density	A	= crossing area

1. Introduction

Remote sensing methods, such as digital photogrammetry or laser scanning, have recently been successfully applied to map terrain depth variability at local scales. However, in most countries, such data acquisition is costly if manned airplanes are involved. Another method to get map terrain depth distribution is using unmanned aerial systems (UASs) in combination with structure-from-motion photogrammetry (Bühler *et al.*, 2016), (Inês Gomes *et al.*, 2018). Many commercially available multi-copters have been used for mapping applications, but the most

common frame of the multi-copter family is a simple quadcopter (Quan, 2017). However, for mapping and surveillance applications, the multi-copter with a greater number of rotors is more maneuverable and robust compare with the simple quadcopter. Due to recent advanced technology in sensors, electronics, some open sources of autopilot controller, 3D printing, battery with high performance, multi-copter can manufacture at low cost (S. Weeks *et al.*, 2020). A multirotor aerial robot allows for different frame configurations. The main three types, quad, hex, and octocopter are the most popular and apparently well-known (Šolc *et al.*, 2012) (P. J. Speirs *et al.*, 2018) (He Zhu *et al.*, 2020). There were equipped with four, six, and eight brushless motors, respectively. Depending on frame configurations, the size of rotors, power of the motors, and the dimension of propellers could affect the payload and flight properties (Marcin Biczyski *et al.*, 2020). On the other hand, a number of factors should be considered when choosing a configuration for the multi-copter (M. Kim *et al.*, 2017). Table I shows the performance scores of multi-copter type affected by a variety of parameters: manufacturing complexity, thrust in failure situation (Michael Achtelik *et al.*, 2012), payload capability, and cost. These key factors must be considered to determine the suitable multi-copter configuration for a application. The scores are shown as low “+”, medium “++”, high “+++”.

Table I. Performance scores for each multi-copter type

Multi-copter UAV type	Number of rotors	Manufacturing complexity	Thrust in failure situation	Payload capability	Cost
Bi-copter	2	+++	None	+	+
Tri-copter	3	++	None	+	+
Quadcopter	4	+	None	+	+
Triangle hex-copter	6	++	50%	++	++
Hexagon hex-copter	6	++	66%	++	++
V-frame octo-copter	8	+++	62%	+++	++
Octagon octo-copter	8	+++	70-73 %	+++	+++

That is challenging to choose the correct configuration airframe of UAVs for mapping and surveillance applications. The V-frame octocopter has higher thrust in a failure situation, more payload capability than triangle hex-copter, and four, three, and two more rotors. Moreover, the manufacturing cost of V-frame octocopter is lower than that of the octagon octocopter, and the payload capability of V-frame is also higher than hexagon hex-copter. Thus, the octocopter was considered to carry a DSLR + Gimbal system with the ability to take photos at 360 degrees. For example, the UAV can take a picture with a different angle view from high or low positions such as under bridges, inside caves, or below 500 kV power wires. Generally, camera on the UAV is placed on the bottom of the airframe, reducing the field of view (FOV) of the octocopter, as shown in Figure 1 (a). Therefore, placing the camera in the front of the octocopter was considered to increase the FOV of the camera, as shown in Figure 1 (b). They could easily capture the objects located in the higher position of the airframe.

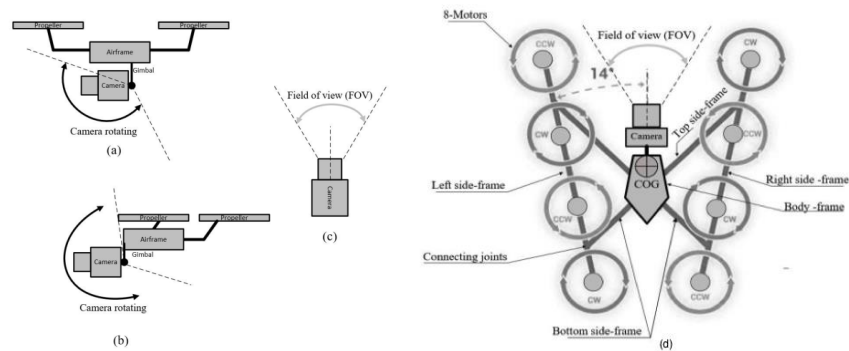


Figure 1. The camera position on the UAV Side view of the bottom position camera (a), side view of the front position camera (b), field of view of the mounted camera (c), conceptual drawing of the octocopter V-frame (d)

The hex and octo drone with triangle-frame, hexagon-frame, octagon-frame frequently place the camera position at the bottom of the multi-copter because it is close to the center of gravity (COG), which keeps the UAV more balanced, and makes it easier to control the roll, pitch, and yaw. Nevertheless, V-frame octocopter can place the camera on the front of the multi-copter's airframe, so that the drone can see 360 degrees in both horizontal and vertical directions (Michael Achtelik *et al.*, 2012). The V-frame octocopter is symmetric around the X-axis, making the octocopter more stable in roll control and highly dynamic in pitch control. In mapping applications, drone maneuverability and agility in pitch rotation can be an advantage when gathering the data. However, the disadvantage of the V-frame is lower stability in the air because the camera is placed far from the COG of the multi-copter, and the geometry of this UAV is only symmetric in the x-axis which means yaw and pitch control is the biggest challenge. It is clear that the open-angle from the centerline to the left side-frame is 140 degrees; the camera is placed in front and inside the airframe, as shown in Figure 1 (c).

Finally, the V-frame octocopter was chosen in this study based on the advantages of a completely free field of view for camera applications and better performance scores compared to any other kind of multi-copter. Figure 1 (d) illustrates the conceptual drawing, and Figure 2 shows a schematic view of the octocopter V-frame configuration.

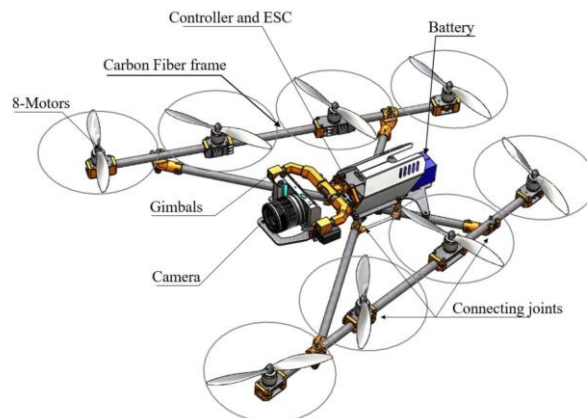


Figure 2. A schematic view of V-frame octocopter

2. The Octocopter Mechanical Design, Simulation and Manufacturing Process

2.1 Octocopter carbon air frame analysis

First, Figure 2 indicates the draft design of the octocopter V-frame airframe including the main airframe components: left, right, bottom, top side-frame, and body frame. A number of motors was fixed on the airframe, four motors along the left side frame and four motors along the right side frame. The airframe was connected using connecting joint, e.g. left side frame had a connecting joint with the bottom side frame, upper side frame connected with the bottom side frame.

The estimated weight of the airframe of the octocopter (including motors, electronic devices, batteries, and mechanical airframe) was 2.18 kg and can carry a DSLR camera and gimbal system with a payload of approximate 1 kg. Thus, the total estimated weight of the octocopter was 3.18 kg. Total thrust needed was generally taken to be twice the weight of octocopter (M. Kim *et al.*, 2017), (Marcin Biczyski *et al.*, 2020); if the thrust was too weak, the octocopter would be unresponsive; but if there was too much thrust, the octocopter would be too twitchy (Scaramuzza *et al.*, 2014). Therefore, the total thrust of 80N was decided, each propeller generating a thrust force of 10N. Normally, multi-copters use brushless motors, including wire coils in the core of the motor, there are rotary parts (rotor) and stationary parts which are the permanent magnet attached to housing of the motors (J. R. Hendershot *et al.*, 1995). The mechanical airframe of the UAV should be made by lightweight material so carbon fiber, ABS plastic 3D printing, and aluminum was chosen. The carbon hollow tube with the outside diameter of 16mm and thickness of 1mm, length of 500 mm and weighted only 33.2 g.

Before manufacturing the octocopter, the left-side and right-side frame of the robot should be analyzed and simulated with shear force and bending moment when the motor generated the thrust force on the carbon hollow tubes (Martinetti *et al.*, 2018). Figure 3 shows the beam diagram of thrust force exerting on carbon hollow beam, each point A, C, D, F generated by a thrust force F_{Thrust} of each brushless motor with Factor of Safety (FOS)=1.2 by the equation below:

$$F_{Thrust} = 10 \times FOS = 10 \times 1.2 = 12 N \quad (1)$$

On the carbon tube, two fixed points B and E were fixed to the top and bottom sides of the airframe. Firstly, the reaction force R_B and R_E was calculated by considering the entire beam as a free body.

$$R_B = R_E = 24 N \quad (2)$$

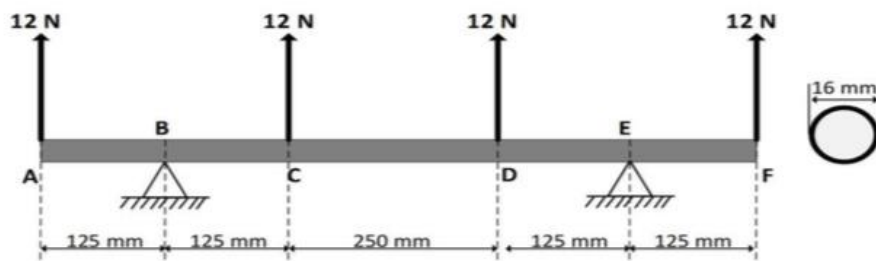


Figure 3. Beam diagram of thrust force and reaction forces exert on carbon hollow

The displacement, stress, shear and bending moment of the carbon beam was simulated by SOLIDWORKS Simulation. Table II shows the model information with standard iso carbon beam (Martinetti *et al.*, 2018).

Table II. Model information with standard iso carbon beam

Carbon beam mechanical properties	Value	Unit
Section area	47.1239	mm^2
Length	750	mm
Volume	5.89049e-006	m^3
Weight	49.8	g
Mass density	1600	kg/m^3
Young's modulus (E)	250	GPa
Ultimate tensile strength (σ_u)	1000	MPa
Poisson ratio (ν)	0.39	

The model beam simulation is shown in Figure 4, which is applied thrust forces of 12N (pink arrows) and the fixture of the model is 2 nodes (green arrows) whose fixture type is immovable (no translation). The carbon beam was analyzed using the finite element method (FEM) based on SOLIDWORKS software. The carbon beam meshed, with 119 nodes and 113 elements total. The FEM analysis was done with shear force diagram shown in Figure 5 (a), moment bending diagram is illustrated in Figure 5 (b), displacement and stress are shown in Figure 5 (c) and Figure 5 (d), respectively.

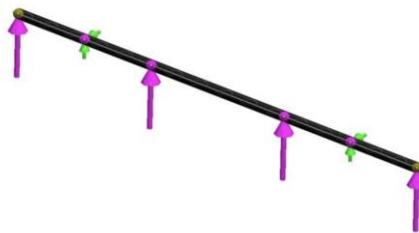


Figure 4. The model carbon beam simulation

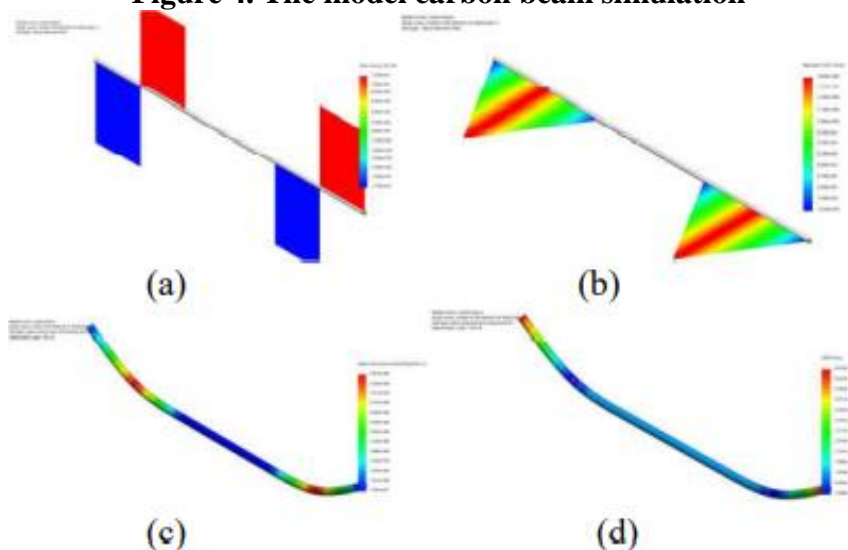


Figure 5. The model carbon beam simulation result, shear force diagram (a), moment bending diagram (b), stress diagram (c), displacement diagram (d)

The carbon beam shear force of ± 12 N at two fixed nodes, these nodes get the highest bending moment 1.5 N.m as shown in Figure 5 (a) and Figure 5 (b), respectively. The carbon fiber material has a tensile strength of 100 MPa, which is included in Table II. But in Figure 5 (c) the maximum stress of the carbon beam is only 9.01409 Mpa, well below the limit. Figure 5 (d) indicates the maximum displacement on the tip of carbon tube $6.423e-002$ mm. Therefore, the left and right side frames of the airframe structure were perfectly safe.

2.2 Design and simulation 3D printing connecting joints

Fused deposition modeling (FDM) is a 3D printing technology. This is an additive manufacturing technology commonly used for modeling, prototyping, and production applications. FDM begins with software that processes an STL file (stereolithographic file format), mathematically slicing and orienting the model for the building process. Designing the connecting joint was a challenge because all parts need a rigid and high-strength structure but the 3D Printer in the lab was easily broken with the FDM method by parameter setting or unsuitable printing. Each kind of plastic (ABS, PLA) needed another parameter for setting up printing, so finding the suitable parameter took a long time to try and test carefully each parameter (S. Weeks *et al.*, 2020). Designing connection joints for the Octocopter V-frame was quite challenging, the main components of a connecting joint between left side frame and top side frame include five main parts: 3D printing upper part and lower part, bolt M5 and M3, reducing damping rubber as illustrated in Figure 6 (a), (b). Moreover, the center holding part of the drone also used 3D printing manufacturing method as shown in Figure 7 (a), (b), which consists of four main parts: 3D printing center holding part, fixed-plate part, carbon tube with a diameter of 5 mm and four bolts M3.

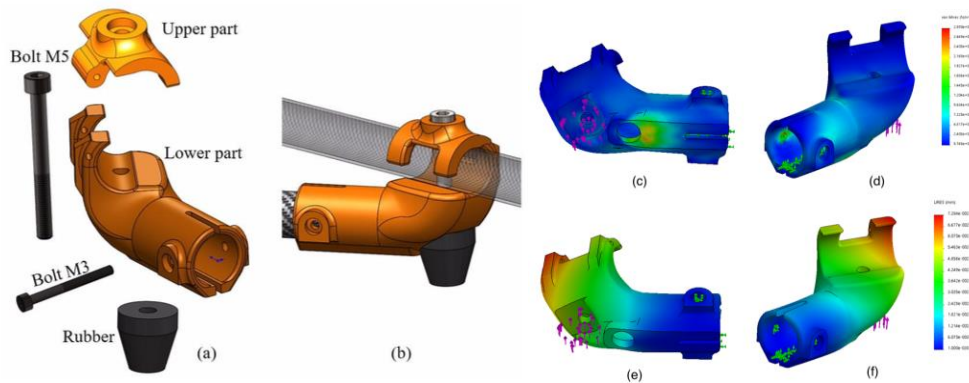


Figure 6. Connecting joint side frame (a), assembly side frame connecting joint (b), connecting joint stress analysis: bottom view (c), side view (d) and displacement analysis: bottom view (e), side view (f)

Before printing parts, the 3D printing of connecting joint with ABS Plastic material was analyzed by the FEM. The 3D model connecting joint was created by the Part environment in SOLIDWORKS, then went through Static Analysis by the Simulation Module in SOLIDWORKS. In Figure 6 (c) to (f), when a force of 24 N was applied (the purple arrows) and fixed face (the green arrows) on the model, the model was stressed and deformed. The maximum stress was $2.99e + 006$ N/m² but the tensile stress in ABS plastic was $3.0e+007$ N/m², ten times higher than the maximum stress on connecting joint. The maximum displacement in the tip of the part was only $7.28e-002$ mm. Base on the simulation, the side frame connecting the joint 3D printing part is completely safe.

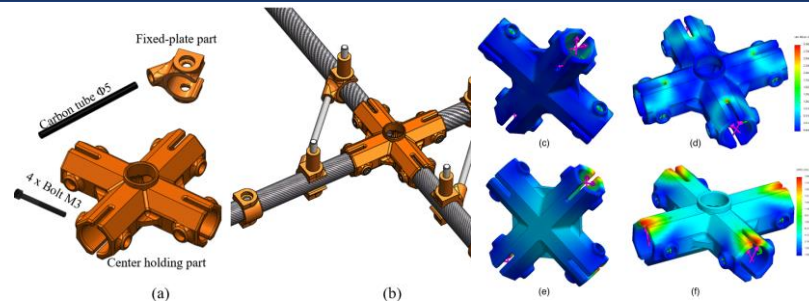


Figure 7. Center holding connecting joint p (a), assembly center holding joint (b), stress analysis: bottom view (c), side view (d) and displacement analysis: bottom view (e), side view (f)

In the same way as the simulation, the result of the center joint part stress analysis is shown in Figure 7 (c), (d) and displacement analysis is presented in Figure 7 (e), (f). The total force applied was 94 N, thus the maximum stress on the part was $3.005e + 006 \text{ N/m}^2$ and the maximum displacement was $1.895e - 002 \text{ mm}$. The center joint 3D printing part is completely safe.

2.3 Manufacturing process

The manufacturing process to build the octocopter V-frame from draft to final product followed several step Figure 8 (a). Step 1, design the 3D model from the sketching. The Octocopter was designed with over 80 parts then fixed together in SOLIDWORKS Assembly environment. Step 2, a simulation module was applied to simulate some critical parts like connecting joints and a center joint. Step 3, make the mechanical part of octocopter using 3D printing technology, over 30 mechanical parts were printed with ABS plastic, all of the mechanical printing parts in this study were manufactured at the Robotics Lab in Vietnamese German University (VGU) using the 3D printer MAKERBOT Replicator 2X. Step 4, other mechanical parts were manufactured by bending method with aluminum plate and CNC milling with carbon fiber plate. Step 5, all of the parts were assembled by hand with some power tools and measurement devices. Finally, the final air-frame octocopter was completed and ready to mount the electronics devices. The final air-frame (not including the electronic devices) of the Octocopter was created with a weight of 1151.5 g with gimbals frame is shown in Figure 8 (b).

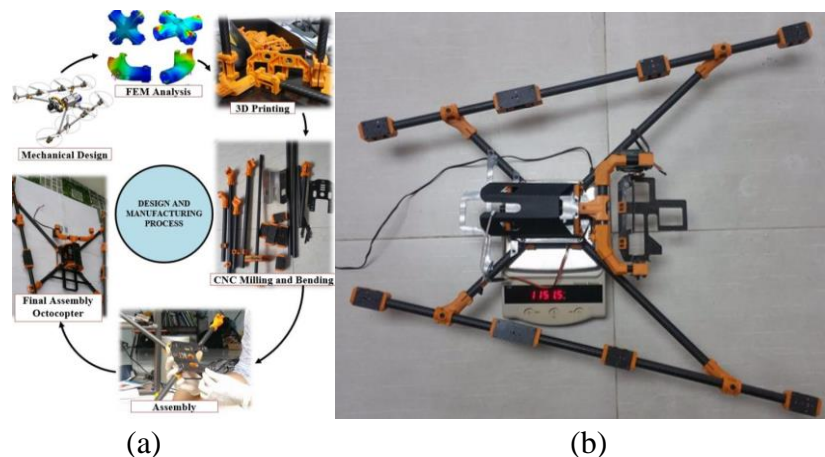


Figure 8. Octocopter V-frame manufacturing process (a), the final assembly octocopter model (b)

3. Octocopter Simulation

3.1 Octocopter Simulink model

The control system design and analysis were performed using computer simulation based on MATLAB Simulink (Mathworks, 2021). Figure 9 shows the diagram to build the V-frame octocopter simulation using the Simulink block diagram. Channel 1, 2, 3, and 4 are the roll, pitch, yaw, and thrust command, respectively. All the commands feed into the PID controller block. This PID control system has two main loops: the outer loop and the inner loop. Figure 10 indicates the block diagram of the octocopter simulation control. The outer loop using the PID algorithm controls the roll and pitch angle, the input of this control block is the simulation signal of the transmitter TX channel and the signal from the magnitude output a roll and a pitch angle of IMU simulation. The output of the outer loop was the rate of roll and pitch signals passing the inner loop. The inner loop used the PID controllers to maintain a set of angular velocities (roll, pitch, and yaw rate) and output signal to the Motor mixer block.

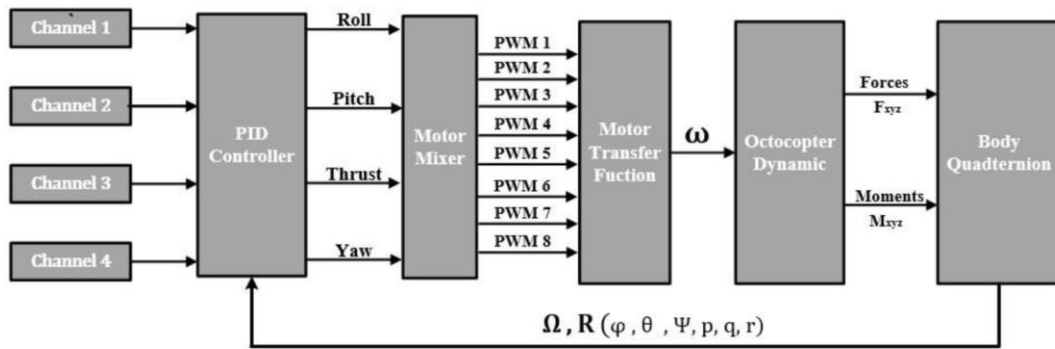


Figure 9. The hierarchical structure of Octocopter Simulation

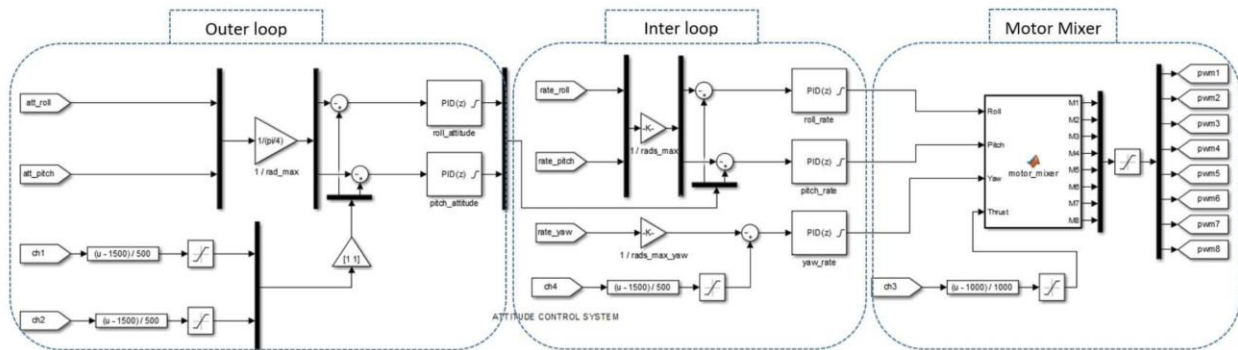


Figure 10. Block diagram of Octocopter Attitude Simulation Control

Figure 11 shows the Simulink block diagram of octocopter dynamic simulation. The output of the motor mixer was the PWM signal ranging from 1000us to 2000us. These signals were passed to the BLDC motor transfer function. The output of the motor transfer function was the angular velocity of motor unit rpm which was converted to the rad/s, then the signal was passed to the multi-copter dynamic block. The multi-copter dynamic block has the velocity, density, and rotor input, the output was body forces and moments. The multi-copter dynamic block was built with the MATLAB M-file. Inside the multi-copter, dynamic block built the algorithm to calculate the forces and moment based on the cross-section area, aircraft mass, motor distance, thrust forces, gravity force, and drag force.

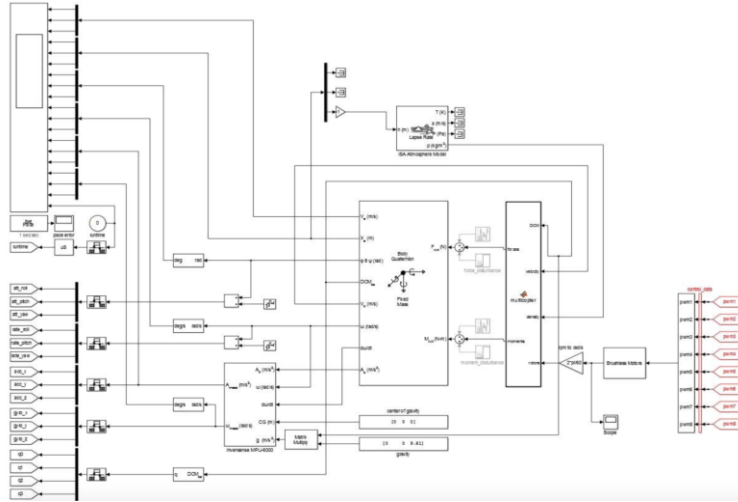


Figure 11. Block diagram of Octocopter Dynamic Simulation

3.2 Octocopter simulation results

This simulation focus on roll and pitch angle is controlled using the second Ziegler-Nichols method to find suitable parameters of the PID controller. When the roll command value is 1700 us (the corresponding angle is approximately 20°), the simulation results of the roll angle were shown when the critical value $K_{CR} = 0.267$ of the PID controller of the outer loop and inner loop of roll command was set, another PID controller parameters were deactivated. The roll response was oscillating with period $P_{CR} = 1.941$ (s), measured from point 1 to point 2 as shown in Figure 12. By the same method, the response signal of the pitch channel got oscillating with $K_{CR} = 0.333$, and the pitch angle response was oscillating with period $P_{CR} = 2.503$ (s).

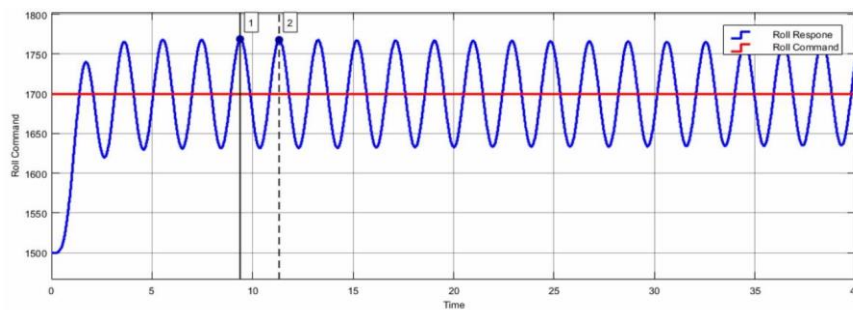


Figure 12. Roll step response when the critical value $K_{CR} = 0.267$

The second Ziegler-Nichols method was applied to find the PID parameters, shown in Table III.

Table III. PID parameters using second method Ziegler- Nichols tuning

PID controller parameters	K_P	K_I	K_D
	$0.6 K_{CR}$	$2K_P/P_{CR}$	$K_P * P_{CR}/8$
Roll angle	0.1602	0.164	0.064
Pitch angle	0.1998	0.159	0.0625

The step response and results of roll and pitch command are presented in Figure 13.

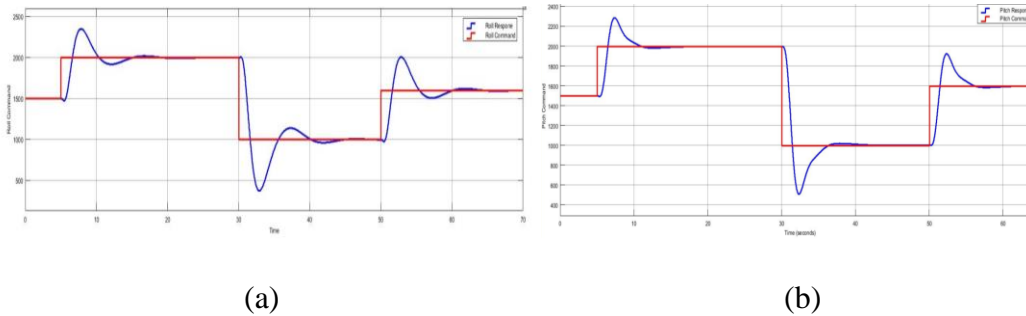


Figure 13. The step response of roll command (a) and pitch command (b) with the PID parameter using second method Ziegler- Nichols

Table IV. PID controller result using the second Ziegler- Nichols method of Roll and Pitch angle

	Raise time (s)	Settling time (s)	Overshoot (%)	Peak time (s)
Roll angle	0.5014	13.10	13.60	2.856
Pitch angle	0.5967	12.71	16.13	2.992

Table IV shows the roll and pitch angle obtained from flight simulation. The designed controller is tested with various step inputs with values from 1000 to 2000. The controller works very well with individual step inputs, but exhibits minor overshoot with 13% and 16% of roll and pitch angle, respectively. The detail of the roll angle result is as follows: raise time 0.5 (s), settling time 13.1 (s), and the peak time is 2.8 (s). Compared to the pitch angle result: raise time 0.59 (s), settling time 12.7 (s), and the peak time is 2.99 (s).

4. Conclusion

The study shows the new platform of the octocopter V-frame designed on the CAD software, with some important mechanical parts using FEM analysis to find the highest stress and displacement under high load applied, the result of all connecting the joints 3D printing part is completely safe. Mechanical parts were manufactured using 3D printing technology and CNC milling. Moreover, the study shows V-form octocopter simulation based on Simulink using the second Ziegler-Nichols method to find suitable parameters of the PID controller for roll and pitch angle. In conclusion, the new kind of octocopter V-frame made with a highly reliable structure using 3D printing technology works well under simulation environment. In the future, the mechanical structure of the octocopter could be improved using more advanced metal 3D printing to produce the aluminum or titan alloy materials for lighter and more rigid material compared to ABS, and finally the assembly to the real test.

Acknowledgments

We would like to extend our thanks to the engineer of the robotics laboratory of Vietnamese-German University and robotics community Robotlab.vn for their help in offering resources for this study.

References

[1] Šolc, R. B. (2012). "Modelling and control of a hexa-copter". (pp. 19-23). Proceedings of the 13th International Carpathian Control Conference (ICCC).

- [2] Bühler, Y. &. (2016). "Mapping snow depth in alpine terrain with unmanned aerial systems UASs: Potential and limitations.". *The Cryosphere*.
- [3] He Zhu, H. N. (2020). "Design and assessment of octocopter drones with improved aerodynamic efficiency and performance". *Aerospace Science and Technology*, 106.
- [4] Inês Gomes, L. P.-P.-J. (2018). "What's a picture really worth? On the use of drone aerial imagery to estimate intertidal rocky shore mussel demographic parameters". *Estuarine, Coastal and Shelf Science, Volume 213*, Pages 185-198.
- [5] J. R. Hendershot Jr., T. J. (1995). "Design of Brushless Permanent-Magnet Motors". Clarendon Press; 1st edition.
- [6] M. Kim, H. J. (2017). "Conceptual multicopter sizing and performance analysis via component database". (pp. 105-109). Ninth International Conference on Ubiquitous and Future Networks (ICUFN).
- [7] Marcin Biczyski, R. S. (2020). Multicopter Sizing Methodology with Flight Time Estimation. *Journal of Advanced Transportation*.
- [8] Martinetti, A. &. (2018). "Simulating mechanical stress on a micro Unmanned Aerial Vehicle (UAV) body frame for selecting maintenance actions". *7th International Conference on Through-life Engineering Services*. Procedia Manufacturing.
- [9] Mathworks. (2021). Retrieved from Matlab Simulink:
<https://www.mathworks.com/products/simulink.html>
- [10] Michael Achtelik, K.-M. D. (August 2012). "Design of a Multi Rotor MAV with regard to Efficiency, Dynamics and Redundancy," . *AIAA Guidance, Navigation, and Control Conference* . (pp. AIAA 2012-4779).
- [11] P. J. Speirs, A. S. (2018). "Comparisons Between Simulated and Measured X-band Signatures of Quad-, Hexa- and Octocopters". *15th European Radar Conference (EuRAD)*, (pp. 325-328).
- [12] Quan, Q. (2017). *"Introduction to Multicopter Design and Control"*. Singapore: Springer Nature.
- [13] S. Weeks, R. M. (2020). "Additive Manufacturing Drone Design Challenge" . *2020 Intermountain Engineering, Technology and Computing (IETC)*, (pp. 1-6).
- [14] Scaramuzza, D. (2014). "Vision-Controlled Micro Flying Robots: From System Design to Autonomous Navigation and Mapping in GPS-Denied Environments". *IEEE Robotics & Automation Magazine*, 21, 26-40.

Hybrid Transmission Line Kite Thread Removal Robot

Katherine Carlos, Nickita Chen, Fida Hussain, Wenzheng Liu, Sheryl Mourin, Rini Akmeliawati*, Lei Chen

School of Mechanical Engineering, The University of Adelaide, Adelaide, Australia, SA 5005

*Corresponding author. E-mail: rini.akmeliawati@adelaide.edu.au

Abstract

Robotic maintenance of high voltage transmission lines is becoming an increasingly feasible solution in providing a safer and more reliable alternative to manual maintenance. In particular, in areas of Indonesia, a significant majority of electrical faults are attributed to kite thread entanglements, and if not swiftly resolved, may cause significant power disruptions and blackouts. Due to the hazards associated with traditional manual removal methods, the paper proposes the preliminary design of a hybrid robot capable of remotely traversing the transmission lines and removing kite thread entanglements. A top-down system engineering approach is utilized in designing and building the robot. Furthermore, a functional analysis was performed to identify the user and system requirements of the robot that leads to the identification of its subsystems. A transmission line maintenance robot, equipped with a unique removal system with blades designed to fit onto varying transmission line sizes, has been designed and built for removing kite threads using a remotely-controlled drone. The proposed hybrid robot with its novel cutting mechanism provides an efficient and safe solution to remove kite threads entangled on transmission lines as it rolls along the lines.

Keywords: Hybrid movement system, Transmission lines, Maintenance robot, Drone, Cutting mechanism

1. Introduction

Transmission lines are keys to the continued operations of a modern city, and prolonged periods of disruptions can bring significant inconveniences and dangers to the inhabitants. Among the common causes of transmission line disruptions across the world, entanglement of foreign objects remains one of the most prevalent [1]. In Indonesia, due to the widespread popularity of competitive kite flying [2], kite threads have become a significant contributor to blackouts, with 94% of all blackouts in Pontianak in 2019 being attributed to kite thread entanglements [3]. Traditionally, the removal of such entangled kite threads is done through manual efforts, involving utility personnel who will climb onto the transmission lines and remove the threads using bamboo poles. This method remains inefficient and hazardous. In this paper, we propose a robot capable of removing kite threads from transmission lines.

Autonomous robotic inspections of transmission lines are becoming increasingly prominent. Among the many challenges and ongoing developments is the complexity in the movement of robots onto and along transmission lines. Similar problems regarding transmission line maintenance have been explored across various other solutions, featuring a range of functions from repair and monitor to debris removal. However, due to the unpredictable nature of thread entanglements, and the uncommon material compositions ranging from synthetics such as Kevlar to special glass-coated cotton threads, existing robots are often ill-fitted and inefficient for the task. According to [4], power line inspection robots can be predominantly classified into two groups: flying or climbing robots. For example, a climbing robot that has been commercialized is the LineRanger. The LineRanger uses four wheels to travel on the power line [5]. However,

hybridizing the flying and climbing robot for transmission line inspection is gaining popularity as well and is deemed to be an excellent approach [6]. Though flying robots are easy to operate and have advantages of maneuverability compared to climbing robot, its challenges are cost, regulation, coming in contact with live, energized wires and consequent high risk of accidents [7]. The climbing robot is more effective due to its proximity to the power line, but it is often complex and challenging to deploy as it is slowed down by the obstacles along the transmission lines [8]. Hybrid robots, having the advantages of both flying and climbing, can improve efficiency, accuracy, cost and overall performance. This type of robots, with better mobility, can avoid obstacles, thus one can deploy the robot on the power line with ease. Additionally, the robot can monitor the transmission lines from a closer proximity, providing greater accuracy [6]. However, due to the nature of the hybrid design and the need for electromagnetic field (EMF) shielding, the weight and powering the robot are some of the limiting factors [8]. Though there are numerous existing flying and climbing robots for high voltage power line maintenance, the emerging hybrid robots are proving to be a more effective solution. Regardless, among the existing transmission line robot designs, analyzing the benefits and drawbacks of a variety of locomotion systems such as climbing and flying can provide the foundation for establishing a stable traversal system, while a much more novel design will be required for the specialized task of removing tangled kite threads.

In this paper, we propose a remote-controlled transmission line maintenance robot composed of a hybrid drone equipped with the novel bladed removal system and line traversal system, capable of flying onto the transmission line before traversing along the line via rollers while removing any entangled kite threads. Section 2 describes the overall design of the robot followed by Section 3, which elaborates on the design of the kite-thread removal system. Section 4 describes the roller-based line traversal system. Section 5 details the drone used for deployment. The paper concludes by presenting the future goals and implications of the robot in Section 6.

2. The Proposed HV Maintenance Robot

The proposed hybrid robot consists of a drone, which is equipped with a kite-thread removal system and a line transversal system, which allows the robot to move along the transmission line on which it is deployed. The functional flow block diagram of the robot and its subsystems is shown in Figure 1. The functional analysis was performed to identify keys subsystems and requirements of the robot. The key subsystems are the kite-thread removal system, line transversal system and the deployment system, which is a remote controlled quadrotor.

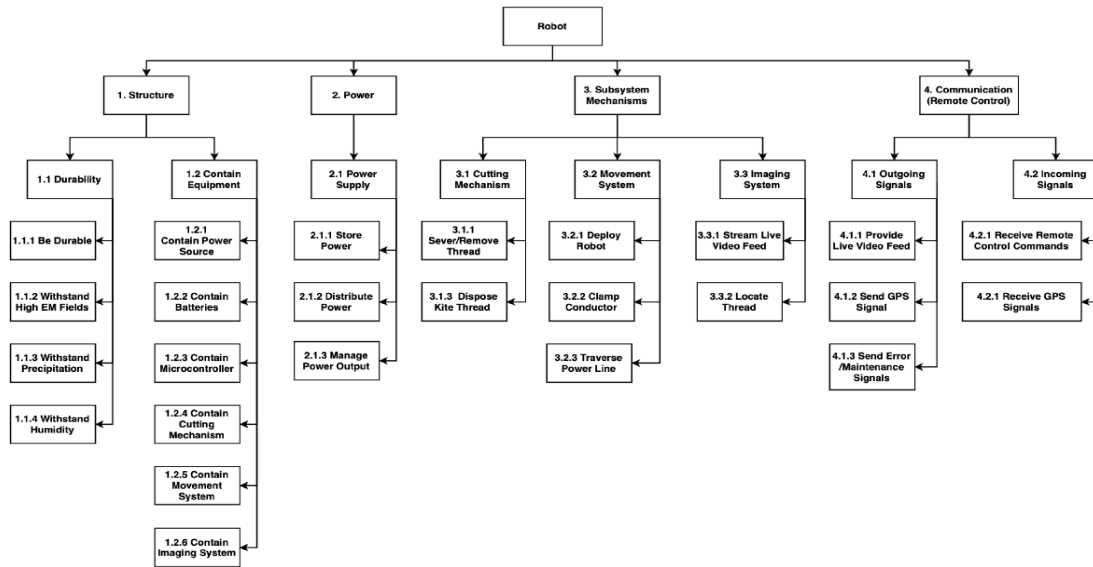


Figure 1. Functional Flow Block Diagram of the Proposed Robot

3. Kite Thread Removal System

In Indonesia, the kites that frequently entangle power lines and cause blackouts are known as *manjha* kites, which are made of cotton threads with a thin layer of glass coating. As the glass layer is extremely thin and brittle, the kite thread can be effectively treated as a cotton thread for the purpose of removal.

Heat and lasers were considered potential solutions; however, they are held back by the difficulty of its implementation and energy consumption. The proposed solution utilizes blades integrated into a clamp that fits onto the transmission lines, with blades positioned perpendicular to the transmission line to sever kite threads as the robot traverses along the lines. This solution serves not only as a cutting mechanism but also as a clamp to further ensure the stability of the traversal system, fitting onto the bottom of the transmission line while the grooved wheels fit onto the top. As shown in Figure 3, the blades are lodged into three plates that serve as the clamp, connected via hinges to allow a degree of freedom, enabling the clamp to fit onto a range of different diameters. The plates are attached to a stationary base through a set of springs that serve to constantly the blades against the transmission line, providing enough force to sever tangled threads without damaging the transmission lines.

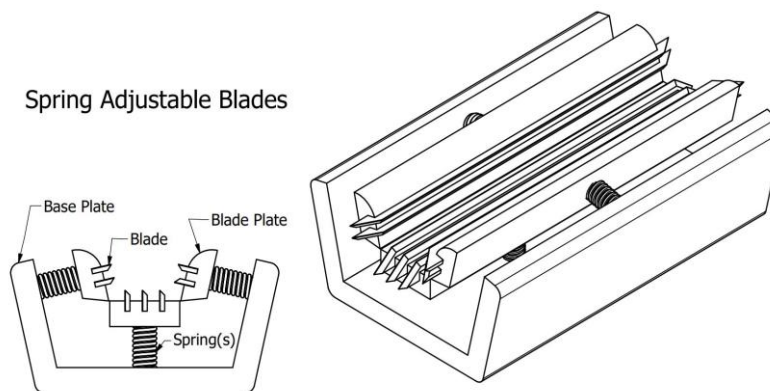


Figure 2. Spring-loaded Blade Clamp Design

In addition to the spring-loaded bladed clamps, an abrasive burr removal system was also devised to deal with a wider variety of situations. Using a pair of abrasive burrs positioned on opposite sides and rotate in opposite directions, the robot is able to tear loose threads through tension and friction. The burrs are able to change their distance from the transmission line, allowing the system to deal with threads loosely wound around the lines, unlike the spring-loaded blades, which are only capable of severing threads tightly wound around the transmission line. Each burr will be powered by a DC motor, and the overall modular nature of the design enables it to be integrated onto the robot easily.

4. Line Traversal System

To move the robot and its removal system along the transmission lines, a separate traversal system along the transmission lines was developed. This novel design adopts a roller-based traversal system, where two sets of grooved wheels are deployed through a gear system that rotates the wheels on top of the transmission line, with the wheels settling onto the lines, and the grooves helping centre the wheels to maintain stability. As shown in Figure 3, combined with the removal system, the transmission line is securely encapsulated by the rollers, ensuring stable movement and effective thread removal. The wheels are installed onto motors, which are controlled by the core microcontroller providing control of movement to the operator.

Due to the traversal system's close proximity to the live conductors, the wheels must be coated in a light, flexible, non-conductive material capable of gripping onto the transmission line.

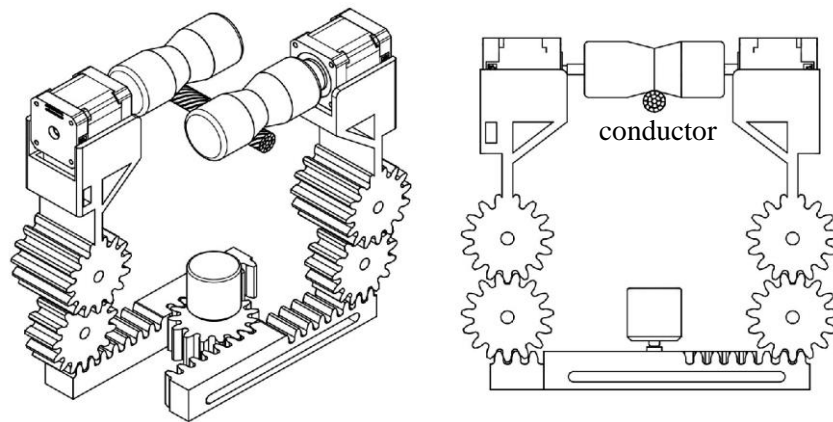


Figure 3. Traversal System

Both the traversal and removal systems are mounted on a custom-made connecting bracket, which allows both systems to be placed on the quadrotor as shown in Figure 4. The bracket is made of Magnesium alloy. Its optimized geometry based on finite element analysis is shown in Figure 5.

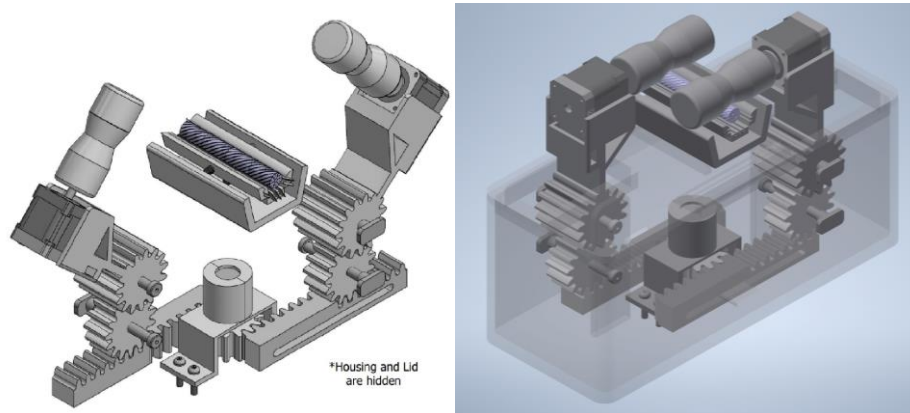


Figure 4. CAD of Line Traversal System and Spring-loaded Blade Clamp Design

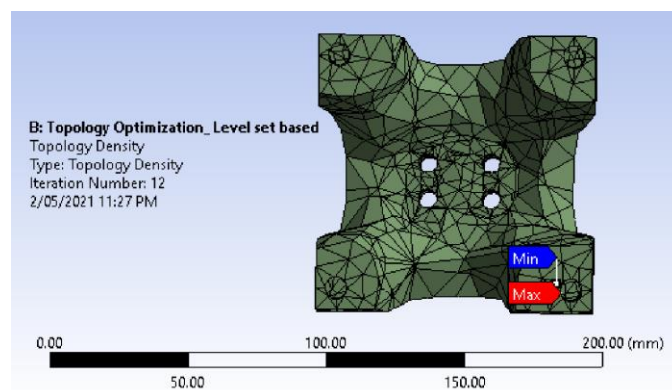


Figure 5. Mounting Bracket

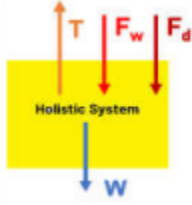
5. Deployment System

Considering the height of typical high voltage transmission lines, a drone was selected as the preferred deployment method as it provides a more practical and safe way to bring the kite-thread removal system to latch onto the conductors. A quadrotor system is selected with greater customisability of the frame for additions as well as stability. To aid in the operator's accurate deployment, cameras, infrared and ultrasonic sensors are installed at the top surface of the drone, to provide the drone position and orientation to the operator.

Two cameras will be used; one will be installed facing the conductor, so that the latching process can be controlled based on the camera feed and an ultrasonic sensor, and another camera, which has a greater field of view will be installed facing downward to provide the feed of the surroundings. Other sensors include inertial measurement unit (IMU), global positioning system (GPS) and infrared sensor (to measure and detect infrared radiation around the overall system). Additionally, to protect the electronics from electromagnetic interference from the HV conductors, a shield is used.

5.1 Required Motor Thrust

In this context, the required motor thrust is calculated based on the setup of the HV transmission lines in Pontianak, Indonesia. For simplification, we use the free-body diagram (FBD) shown in Figure 6.



In the figure, T is the thrust produced by the drone, F_w is the wind load, F_d is the drag force and W is the weight of the overall system. To design a durable system, the worst-case scenario will be considered for environmental wind loads. As such, though it will be unlikely, the wind load is assumed to be normally downwards as illustrated. This will be the direction that will result in the largest net force opposing the vertically upwards flight of the system. The wind load can be described through the following equation.

$$F_w = p_d A = \frac{1}{2} \rho v^2 A \quad (1)$$

where A is the surface area (m^2), p_d is the dynamic pressure (Pa), ρ is the density of air (kg/m^3), v is the wind speed (m/s).

The drag force (F_d) can be calculated via:

$$F_d = c_d \frac{1}{2} \rho v^2 A \quad (2)$$

where c_d is the drag coefficient, ρ is the density of the air, v is the relative speed of the system to the air and A is the cross-sectional area of the system (which has been modelled as a cuboid).

The total thrust force required then, for this simplified model is:

$$T = F_w + F_d + W \quad (3)$$

In Pontianak, Indonesia, at 10 meters above the ground, the windiest time of the year has recorded average wind speeds of more than 4.5 kilometers per hour [9]. Allowing for a safety factor of 1.5, this will be adjusted to 6.75 kilometers per hour, or 1.875 meters per second. In the current design, assuming a box-shaped body to simplify calculations, the system has a limit surface area of approximately $0.02125 m^2$ (0.25 m by 0.085 m). Hence, using the standard air density, the wind load is evaluates to be:

$$F_w = \frac{1}{2} (1.2) (1.875^2) (0.02125) = 0.0448 N \quad (4)$$

The weight of the entire system can be assumed to be 0.5kg. Similarly adjusting for a safety factor of 1.5, the weight considered is 0.75kg.

$$W = 0.75 \times 9.81 = 7.3575 N \quad (5)$$

Assuming a high drag coefficient of a non-streamlined cube body, $c_d = 1.05$, and a flight speed of 2 m/s, the drag force is:

$$F_d = 1.05 \left(\frac{1}{2}\right) (1.2) (2^2) (0.02125) = 0.05355 N \quad (6)$$

Therefore, the required thrust is:

$$T = 0.0448 + 0.05355 + 7.3575 \approx 7.45585 N \quad (7)$$

As such, the total required thrust is 7.5 N. For a quadcopter, the thrust required per motor is 1.9 N. In terms of thrust in kilograms, per motor, this is approximately 18.6 kg. To ensure added effective maneuverability during flight, a 2:1 thrust-to-weight ratio is assumed. Hence, the required thrust for efficient and effective flight per motor is 37.3 kg.

The overall architecture of the proposed HV maintenance robot with the capability to remove kite thread is shown in Figure 6.

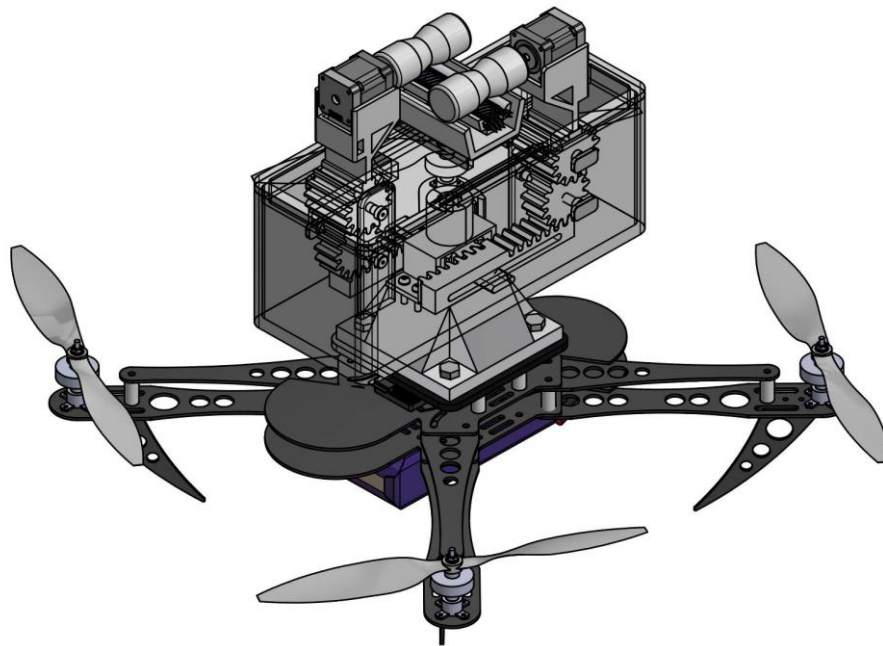


Figure 6. CAD of Final Assembly Mounted on the Deployment Drone

6. Conclusion

In this paper, the design for a remote-controlled transmission-line kite-thread removal robot is proposed and discussed. The novelty of the proposed solution lies in the kite-thread removal and the line traversal systems. The kite-thread removal system is separated into two subsystems: the spring-loaded blade clamp, which further supports the stability of the wheels while severing any tightly wound kite threads that the robot encounters with, and a pair of adjustable burrs designed to remove any loose threads through tension and friction. The novel line traversal system allows the thread removal system to traverse along the transmission line while removing the kite thread. To reach the transmission lines, a remote-controlled drone is chosen for deployment, equipped with cameras, infrared and ultrasonic sensors to provide feedback to the operator while navigating and orienting the robot. Upon reaching the transmission lines, the robot transitions into a roller-based locomotion system, locking onto the transmission lines and maintaining stability by the grooved wheels, and depowering the propellers to conserve energy. While the robot is custom designed to resolve a major issue experienced due to entanglement of kite threads, a successful implementation can significantly reduce the hazards experienced by transmission-line maintenance workers, and may serve as a design that can be adapted to autonomously remove a broader range of debris in future work.

Acknowledgments

The authors would like to thank The University of Adelaide - Australia, Telkom University and the Indonesian National Electricity Company (PLN), Indonesia for providing financial support and expert advice.

References

- [1] Prajapat D. (2021), “Faults and Effects in Electrical Power System”, The Department of Electrical Engineering, Madhav University.
- [2] Sydney Morning Herald (SMH) (2004), “Children at the cutting edge of kite fighting”, 10 April.
- [3] Mulyana, C. (2019), “Wire Kites Cause 94% of Electricity Downs in Pontianak”, Media
- [4] Dian, S., *et al.* (2012), “Development of a self-balance dual-arm robot for inspection of high-voltage power transmission lines”, 2012 IEEE International Conference on Mechatronics and Automation, Chengdu, China.
- [5] Pierre, R., *et al.* (2019), “LineRanger: Analysis and Field Testing of an Innovative Robot for Efficient Assessment of Bundled High-Voltage Powerlines”, 2019 International Conference on Robotics and Automation (ICRA), Palals des congres de Montreal, Canada, pp. 20-24.
- [6] Ahmad, A., *et al.* (2020), “Power Transmission Line, Trends and Challenges for Future Research”, International Journal of Electrical Power Energy Systems, vol. 118, pp. 11.
- [7] Jaka, K., *et al.* (2010), “A Climbing-Flying Robot for Power Line Inspection”, Climbing and Walking Robots, pp. 95-110.
- [8] Luis, F., *et al.* (2014) “Power Line Inspection Via an Unmanned Aerial System Based on the Quadrotor Helicopter”, 17th IEEE Mediterranean Electrotechnical Conference, Beirut, Lebanon, pp. 393-397.
- [9] WeatherSpark (2016), “Average Weather in Pontianak, Indonesia, Year Round”, available at <https://weatherspark.com/y/120717/Average-Weather-in-Pontianak-Indonesia-Year-Round>, accessed on 14 June 2021.

Experimental Study of the Thrust Generation Performance of the Tapered Biomimetic Fin with Cupping Effect

Arie Sukma Jaya^{1,*} and Muljo Widodo Kartidjo²

¹Universitas Pertahanan Republik Indonesia, Sentul, Indonesia, 16810

²Intitut Teknologi Bandung, Bandung, Indonesia, 40132

*Corresponding author. E-mail: arie.jaya@idu.ac.id

Abstract

Biomimetic fin is one of the potential propulsion mechanisms for an efficient Autonomous Underwater Vehicle (AUV). Most recent developments of the biomimetic fin mimic the natural caudal fin of fish as the main thrust generator. This study involved a scaled AUV model with a fixed body and a moving biomimetic fin. A membrane-like tapered cupping fin replicated a cupping effect of the caudal fin of fish without flexible rays. An instrument of the three-component dynamometer measured net values of forces and torque of the model in static and dynamic conditions. Static performance determined the ability of the fins in a no-flow state, which consisted of the average net thrust, $\overline{F_{XNet}}$, and the ratio of thrust to the required power, Thrust to Power Ratio (*TPR*). The results showed that the cupping fin could produce a maximum thrust of four times higher than the rigid fin. Likewise, the maximum *TPR* value of the cupping fin was three times greater than the rigid fin. Biomimetic cupping fin could achieve estimated cruising speed, V_{cr} , up to twice as fast as the rigid fin. The experimental results showed that, for tapered fins, the cupping effect introduces higher effectiveness and efficiency in generating thrust for the static and dynamic states than the rigid fin.

Keywords: Biomimetic, Fin, Cupping, Static, Efficiency, Thrust, Propulsion, AUV

Nomenclature

A	=	fin area
AR	=	aspect ratio
b_0	=	fin breadth at root
b_c	=	cupping fin thickness
b_L	=	fin breadth at tip
D	=	drag
E	=	modulus of elasticity
f	=	fin frequency
$\overline{F_{XNet}}$	=	average net force
h_L	=	maximum height of the fin
L	=	fin length
N	=	neutral
O_I	=	fin origin
TPR	=	thrust to power ratio
T	=	thrust
V_{cr}	=	estimated cruising speed
V_N	=	normal velocity

- V_T = tangential velocity
 θ = fin amplitude
 ρ = density
 ω = fin angular velocity

1. Introduction

The development of the unmanned systems has become a global trend (Rojko, 2017). Unmanned underwater vehicle is a newly emerging technology in many maritime countries, especially the non-tethered Autonomous Underwater Vehicle (AUV) (Kartidjo et al., 2006; Kartidjo and Nugroho, 2007; Kartidjo et al., 2009). The AUV is facing a growing field of application such as finding new sources of energy and minerals (Fish and Kocak, 2011). One of the limitations of AUVs is the range of operation, which depends on the power utilization of the vehicle (Fernandes et al., 2002). To perform a successful underwater operation, the AUV should be energy efficient. A propulsion system required a large portion of power to generate thrust (Bellingham, 2001). The propulsion power of a sea glider typically comprises 60%-85% of the mean power (Furlong et al., 2007). Therefore, the efficiency of the propulsion system should be the primary concern to support the high-performance biomimetic AUV (Scaradozzi et al., 2017; Sahoo et al., 2019).

The propeller system is the most common thrust generation system in the AUV. However, a propeller has low efficiency for a small vehicle at a low speed (Mohammadshahi et al., 2008; Rufo and Smithers, 2011; Masoomi et al., 2013). AUV is generally small compared to a manned underwater vehicle. Furthermore, many operational tasks of the AUV requires the AUV to locomote in low-speed regimes (Christ and Wernli, 2013). The underwater missions of the AUV require a speed of less than 3.0 m/s (Aguirre et al., 2017), and it operates at a low speed, so an alternative approach is needed to increase the efficiency of the thrust generation system of the AUV. A potential approach is a biomimetic approach that mimics mechanisms in nature and is based on natural evolution which has produced a mechanism with a high level of efficiency and effectiveness (Cohen, 2006). In the underwater region, the fin propulsion mechanism could be considered the primary alternative mechanism to enhance the propulsion efficiency of the AUV (Lauder et al., 2007; Liu and Hu, 2010; Low et al., 2010; Fish, 2013; Lauder, 2015). Furthermore, the performance evaluation of the mechanism should involve a relatively simple robotic device to simplify the control of motion parameters that occurs naturally with natural creature such as fishes (Lauder et al., 2007; Lauder, 2015).

An experimental study by Esposito et al. (2012) identified the effect of cupping shape in the thrust of the biomimetic fin. The preliminary numerical study of this research by Alamsjah et al. (2015) also indicated a similar advantage of the cupping shape in the thrust generation. However, there were rarely discussions about the significance the cupping effect on the efficiency performance. In the present experimental study, the ratio of thrust to the required power (Thrust to Power Ratio, *TPR*) characterized the cupping effect on the efficiency of the tapered biomimetic fin. The *TPR*, together with the average net force $\overline{F_{XNet}}$ represents the static performance of the fins. Furthermore, this study includes the dynamic performance of the tapered cupping fin using the estimated cruising speed, V_{cr} . The results of this study should be valuable in designing a highly effective and efficient biomimetic AUV.

2. Experimental Setup

This study utilized a circular water tunnel facility at the Research and Innovation Building of Institut Teknologi Bandung. The water tunnel has the test section of $300\text{ mm} \times 300\text{ mm} \times 1200$

mm. The setup is similar to the previous investigation in Jaya and Kartidjo (2019). Figure 1 shows a biomimetic AUV model in the water tunnel test section. The streamlined body covers the submerged kinematic mechanism to avoid excessive drag by the kinematic structures in the flowing water. A tapered fin mimics the caudal fin of fishes that generates thrust by oscillating motion. There were two tapered fin types in the present experimental evaluation: flat rigid fin and cupping fin. Figure 2 shows the three-dimensional model of the fins. Unlike the cupping effect by the fin with flexible rays in Esposito et al. (2012), the cupping fin in the present study is mainly a modified rigid fin with a uniform thickness of the membrane-like surface. The configuration of the cupping fin should provide a flexibility effect on the lateral and longitudinal direction of the fins that create a cupping effect. Table I lists the geometry and material of the fins. A four-bar linkage mechanism within the body drives the fin motion. This mechanism supports the adjustable amplitude and frequency of the fin motion.

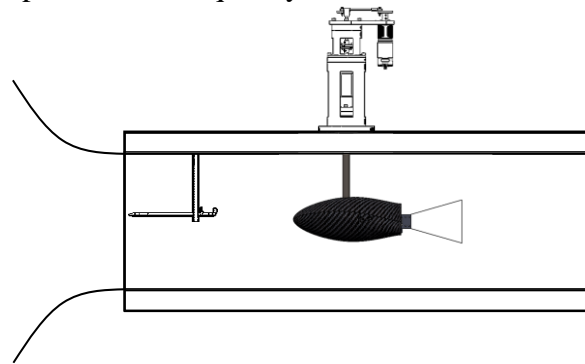


Figure 1.A scaled biomimetic AUV model in the water tunnel test section

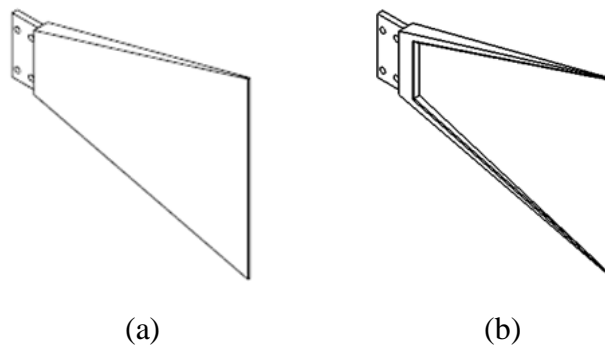


Figure 2.Biomimetic fins (a) Rigid fin, (b) Cupping fin

Tabel I. Geometrical parameter of the biomimetic fin

Fin Type and Material	Thickness [mm]	Common Parameters
Rigid	$b_0 = 8$ $b_L = 0,5$	Nylon 6,6 $E = 8,97 \text{ GPa}$
Cupping	$b_0 = 8$ $b_L = 0,5$ $b_c = 0,5$	$\rho = 1426 \text{ kg/m}^3$ $A = 0,008 \text{ m}^2$ $h_L = 0,1 \text{ m}$ $AR = 1,2$ $L = 0,125 \text{ m}$

A four-bar linkage mechanism within the body drives the fin motion. This mechanism supports the adjustable amplitude and frequency of the fin motion. The fin amplitude, θ , was limited to 40° , while the fin frequencies were varied from 0.5 Hz to 1.5 Hz with an interval of 0.1 Hz . The limitation is mainly to keep the reliability of the dynamometers during measurement. The three-component dynamometers measured net forces and net torque by the fin motion. The dynamometer has a sensitivity of $1 \times 10^{-2} \text{ N}$ for measuring forces and $1 \times 10^{-3} \text{ Nm}$ for measuring torque (Jaya et al., 2018). The water tunnel experiments consist of a static or no-flow condition and a dynamic condition with a flowing stream. The static performance parameters for thrust generation were the average net force $\overline{F_{XNet}}$ and the ratio between the average net thrust to the required power, Thrust to Power Ratio (TPR). The dynamic performance was identified by estimated cruising speed, V_{cr} , which correlated with a linearly interpolated flow speed at which the $\overline{F_{XNet}}$ due to the fin motion is zero. The water flow velocity ranged from 0.16 m/s to 0.4 m/s with an interval of 0.04 m/s , to represent the low-speed regime. The initial evaluation was data recording and analysis of the static and dynamic parameters for rigid fin. The next evaluation was for the cupping fin. The data of the two fin types were compared to obtain the quantitative analysis of the cupping effect.

3. Results and Discussion

Figure 3 shows the performance comparison of the rigid and cupping fins. The graph in Figure 3(a) shows the effectiveness of the fins in generating thrust in static conditions. The rigid fin begins to produce a positive value of $\overline{F_{XNet}}$ at $f = 1.3 \text{ Hz}$. The values of $\overline{F_{XNet}}$ of the rigid fin increases with the increasing fin frequency and generates 0.1 N of $\overline{F_{XNet}}$ at the maximum tested fin frequency. On the other hand, the cupping fin starts to produce a positive $\overline{F_{XNet}}$ at $f = 0.9 \text{ Hz}$. The values of $\overline{F_{XNet}}$ of the cupping fin show an increasing trend at a higher value of fin frequencies. The increasing trend of $\overline{F_{XNet}}$ of the cupping fin, especially at high fin frequency, is more significant than the rigid fin. The result of $\overline{F_{XNet}}$ indicates that the cupping fin, compared to the rigid fin, has a wider effective fin frequency range and four times the maximum $\overline{F_{XNet}}$ at the maximum tested fin frequency. The range of effective fin frequency of the cupping fin indicates that the fin is more effective to generate thrust at the accelerating stage with less power required than the rigid fin. The significant increase in the value of $\overline{F_{XNet}}$ of the cupping fin also has an advantage for the acceleration movement compared to the rigid fin. The results of $\overline{F_{XNet}}$ indicate that the cupping effect enhances the effectiveness of the fins in generating maximum thrust at a low-speed regime.

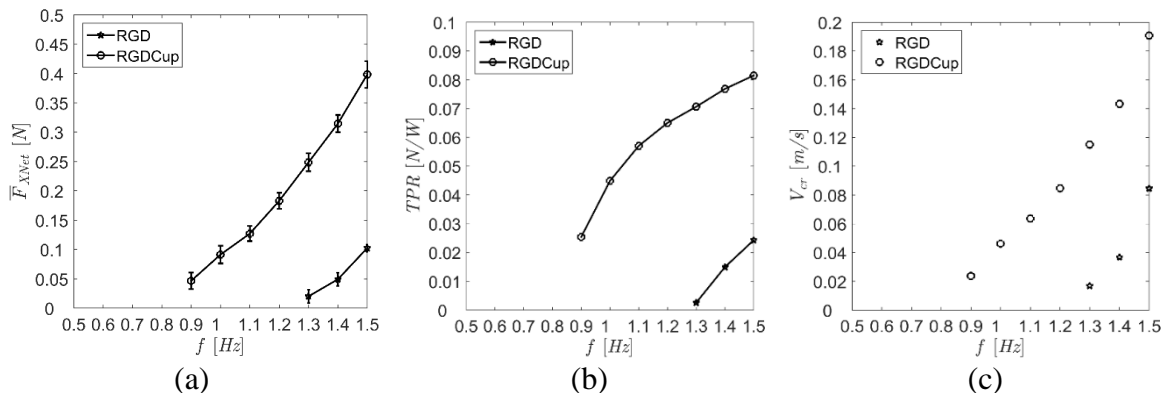


Figure 3. Fin performance (a) $\overline{F_{XNet}}$, (b) TPR , (c) V_{cr} (RGD: Rigid fin, RGDCup: Cupping fin)

Figure 3(b) presents the comparison of the TPR parameter of the biomimetic fins. The effective fin frequencies for the fins are similar to the previous result in $\overline{F_{XNet}}$. In the figure, TPR values increase at a higher fin frequency. As can be observed from the results of the cupping fin, there is a decreasing trend in the positive slope of the TPR curve. The decreasing trend indicates that fin frequency could limit the efficiency of the fin. The present experimental setup could not obtain the maximum TPR values due to limitations in the force measurement setup. However, the results indicate that at the maximum tested fin frequency, the TPR value of the cupping fin is three times higher than of the rigid fin. Thus, the cupping effect could increase the efficiency of the fin in generating maximum thrust. Figure 3(c) presents the estimated cruising speed, V_{cr} , of the fins. The figure shows a similar range of effective fin frequency range to the static performance. Following the static performance, the cupping fin maintains its superiority in dynamic performance. The values of V_{cr} increase at higher values of fin frequencies with a relatively constant slope. At the maximum tested fin frequency, the cupping fin could provide a forward motion twice as fast as the rigid fin. The rigid fin must oscillate at $f = 1.5 \text{ Hz}$ to achieve a cruising speed of 0.08 m/s , while the cupping fin only needs $f = 1.2 \text{ Hz}$. At fin frequency $f = 1.5 \text{ Hz}$, the cupping fin achieves cruising speed of 0.19 m/s . Hence, the graph shows a practical efficiency enhancement by the cupping effect during a constant forward motion. The results support the superior performance of cupping fins compared to rigid fins in Esposito et al. (2012) and Alamsjah et al. (2015).

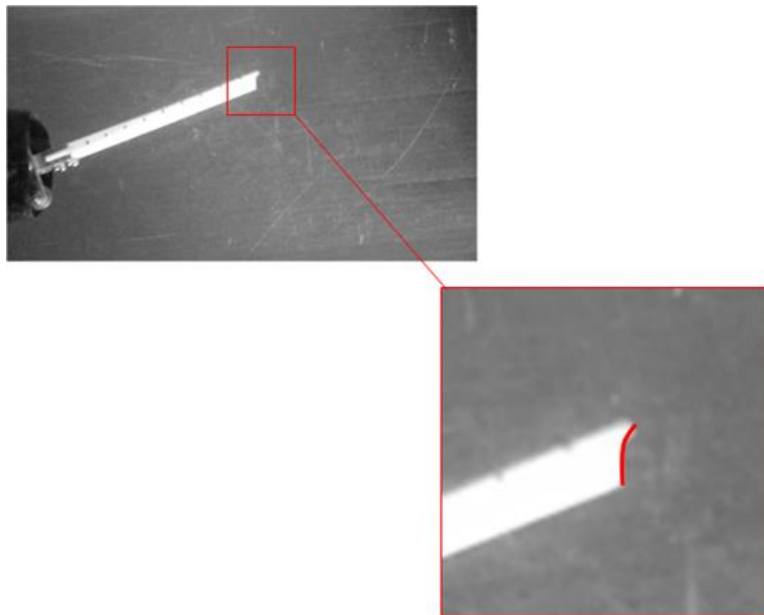


Figure 4. Formation of cupping effect during fin motion (clockwise motion, $\theta = 40^\circ$, $f = 1.5 \text{ Hz}$)

Figure 4 shows the formation of the cupping effect at maximum acceleration stage in a clockwise direction. As shown in the figure, the deflection at the fin tip indicates a cupping shape during the fin motion. Following the motion of the fin in a clockwise direction, Figure 5 compares the configuration of the rigid and cupping fins when the driving mechanism is at the middle position. The rigid fin in Figure 5(a) does not experience a deflection while the cupping fin in Figure 5(b) deflected almost half of the length of the fins. The figures indicate that the cupping effect occurs along with the height and the length of the fin. Thus, the cupping fin introduces the flexibility effect to enhance the performance of the rigid fin.

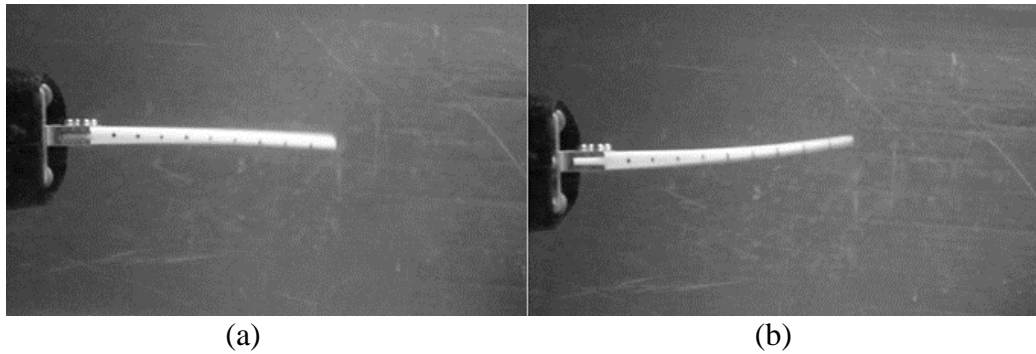


Figure 5. Fin orientation at the middle position during fin motion (a) Rigid fin, (b) Cupping fin (clockwise motion, $\theta = 40^\circ$, $f = 1.5 \text{ Hz}$)

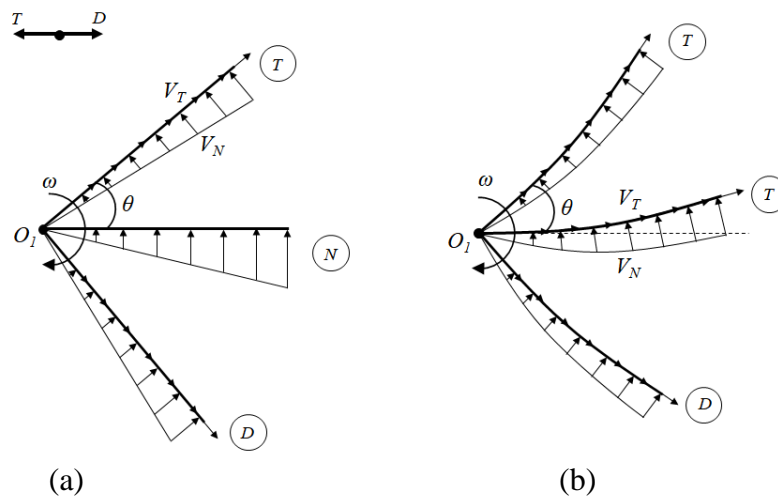


Figure 6. Vector composition analysis at midline (a) Rigid fin, (b) Cupping fin (O_I : Fin origin, ω : Fin angular velocity, θ : Fin amplitude, V_N : Normal velocity, V_T : Tangential velocity, T : Thrust, D : Drag, N : Neutral)

For practical consideration, a simple analysis using the vector composition method at the midline of the fin could be presented to support the thrust generation enhancement by the cupping fin. The comparison of the vector composition analysis for the rigid and cupping fins can be seen in Figure 6. In a condition without external flow velocity, the fluid velocity around the surface of the fin is proportional to the velocity of the fin. In the figure, the fin moves in a clockwise direction with three vector compositions: just after reaching the maximum amplitude at the top, the middle position, and just before reaching the maximum amplitude at the bottom. There are normal velocity vectors and tangential velocity vectors. The direction of the velocity vector represents the reactive force to the fin surface, if the direction of the resultant vector is to the left of the image (towards the front of the fin), then the fin generates thrust (T), while the opposite direction represents the generation of drag. Vector composition analysis for rigid fins is shown in Figure 6(a), while cupping fins is in Figure 6(b). The cupping effect introduces a deflection along the length of the fin, thus a curvy vector distribution along the midline. The figures indicate a significant difference in vector compositions of the two fins at the middle position. The deflection of the cupping fin generates thrust by directing the resultant velocity vector in the thrust direction. Thus, the deflection in the flexible fin could be a driving factor to direct more vectors in the thrust direction. This vector analysis indicates that by optimizing the

deflection characteristics of the fin with a flexibility effect, such as the cupping fin, the biomimetic fin propulsion could have a high performance of thrust generation efficiency and effectiveness.

4. Conclusion

The present study evaluated the effect of cupping shape on the thrust and efficiency performance of the tapered biomimetic fin. A modified rigid fin with a membrane-like fin surface successfully forms the cupping shape. The cupping fin provides a wider range of effective fin frequency than the rigid fin. Static performance shows that the cupping fin introduces an enhancement in the maximum and efficiency of the thrust generation. Furthermore, the dynamic performance indicates that the cupping fin moves forward faster than the rigid fin. The deflection at the tip and middle position of the cupping fin shows a role of flexibility in performance enhancement. The vector composition method could be a useful tool to simplify the analysis of the performance enhancement by the cupping fin. The main role of the flexibility in the biomimetic fin is to direct more vectors in the thrust direction. Further optimization of the deflection characteristics, such as modification of the thickness of the fin surface and fin material properties, of the cupping fin could provide an efficient underwater biomimetic fin propulsion in a low-speed regime.

Acknowledgments

The authors acknowledge research supports of Universitas Pertahanan Republik Indonesia (Unhan RI) and the Center for Unmanned System Studies (Centrums) ITB.

References

- [1] Aguirre, F., Vargas, S., Valdés, D., & Tornero, J. (2017), “State of the Art of Parameters for Mechanical Design of an Autonomous Underwater Vehicle”, *International Journal of Oceans and Oceanography* ISSN, 11(1).
- [2] Alamsjah, J., Jaya, A.S., and Kartidjo, M.W. (2015), “Performance analysis on biomimetic fin with cupping base and cupping ratio variation”, *Progress and Communication in Science*, 2, 2.
- [3] Bellingham, J. (2001), “Autonomous underwater vehicles (AUVs)”, *Encyclopedia of Ocean Sciences*. Edited by H. Steele. San Diego: Academic Press. (doi: 10.1006/rwos.2001.0303)
- [4] Christ, R. D., & Wernli, R. L. (2013), “The ROV Manual: A User Guide for Remotely Operated Vehicles: Second Edition”, In *The ROV Manual: A User Guide for Remotely Operated Vehicles: Second Edition*. <https://doi.org/10.1016/C2011-0-07796-7>
- [5] Cohen, Y.B. (2006), “Biomimetics using nature to inspire human innovation”, *Bioinspiration and biomimetics*, 1, pp. 1-12.
- [6] Esposito, C. J., Tangorra, J.L., Flammang, B.E., and Lauder, G.V. (2012), “A robotic fish caudal fin: effects of stiffness and motor program on locomotor performance”, *Journal of Experimental Biology*, 215, pp. 56-67.
- [7] Fernandes, P. G., Stevenson, P., & Brierley, A. S. (2002), “AUVs as research vessels: The pros and cons”, *Ices Cm*, 2002 J.
- [8] Fish, F.E. (2013), “Advantages of natural propulsive systems”, *Marine Technology Society Journal*, 47, pp. 37-44.
- [9] Fish, F.E. and Kocak, D.M. (2011), “Biomimetics and marine technology: An introduction”, *Marine Technology Society Journal*, 45, pp. 8-13.

- [10] Furlong, M. E., McPhail, S. D. and Stevenson, P. (2007), “A concept design for an ultra-long-range survey class AUV”, Proceedings of OCEANS 2007 Europe, pp. 568–575.
- [11] Gafurov, S. A. and Klochkov, E. V. (2015), “Autonomous Unmanned Underwater Vehicles Development Tendencies”, in *Procedia Engineering*. doi: 10.1016/j.proeng.2015.06.017.
- [12] Jaya, A. S. and Kartidjo, M. W. (2019), “Performance Evaluation of the Shape and Flexibility Combination of the Underwater Biomimetic Fin Propulsion”, in *Proceeding of the 15th International Conference on Intelligent Unmanned Systems, ICIUS 2019*.
- [13] Jaya, A.S., Kartidjo, M.W., Zuhul, L.R., and Brodjonegoro, I.S. (2018), “Evaluation of force and torque measurement uncertainties of the three component dynamometer of the biomimetic fin propulsion system”, Proceeding of SNTTM XVII, pp. 185-190.
- [14] Kartidjo, M.W., Jenie, S.D., Budiyo, A., and Nugroho, S.A. (2006), “Design, development and testing of underwater vehicles: ITB experience”, Proceedings of the International Conference on Underwater System Technology: Theory and Application.
- [15] Kartidjo, M.W. and Nugroho, S.A. (2007), “Heading Lock Maneuver Testing of Autonomous Underwater Vehicle: Sotong ITB”, Proceedings of the 3rd International Conference on Intelligent Unmanned Systems.
- [16] Kartidjo, M.W., Nugroho, S.A., Prayogo, N., and Budiyo, A. (2009), “Design and Testing of Underwater Thruster for SHRIMP ROV-ITB”, Indian J. Mar. Sci., Vol. 38, No. 3, pp. 338-345.
- [17] Lauder, G.V. (2015), “Fish locomotion: recent advances and new directions”, Annual Review of Marine Science, 7, pp. 521-545.
- [18] Lauder, G.V., Anderson, E.J, Tangorra, J., and Madden, P.G.A. (2007), “Fish biorobotics: kinematics and hydrodynamics of self-propulsion”, Journal of Experimental Biology, 210, 2767-2780.
- [19] Liu, J. and Hu, H. (2010), “Biological Inspiration: From Carangiform Fish to Multi-Joint Robotic Fish”, Journal of Bionic Engineering, 7, pp. 35–48.
- [20] Low, K.H., Chong, C.W., and Zhou, C. (2010), “Performance study of a fish robot propelled by a flexible caudal fin”, IEEE International Conference on Robotics and Automation.
- [21] Masoomi, S.F., Gutschmidt, S., Chen, X.Q., and Sellier, M. (2013), “The Kinematics and Dynamics of Undulatory Motion of a Tuna-mimetic Robot”, Int. J. Adv. Robot Syst., 12, 83, pp. 1-11, doi: 10.5772/60059.
- [22] Mohammadshahi, D., Yousefi-koma, A., Bahmanyar, S., and Maleki, H. (2008), “Design, fabrication and hydrodynamic analysis of a biomimetic robot fish”, Proceedings of the 10th World Scientific and Engineering Academy and Society Int. Conf. on Automatic Control, modelling & Simulation.
- [23] Rojko, A. (2017), “Industry 4.0 Concept: Background and Overview”, International Journal of Interactive Mobile Technologies, Vol. 11, No. 5, doi: 10.3991/ijim.v11i5.7072.
- [24] Rufo, M. and Smithers, M. (2011), “Applying biomimetics to underwater robotics for achievement of tactical relevance”, Marine Technology Society Journal, 45, pp. 24-30.
- [25] Sahoo, A., Dwivedy, S. K. and Robi, P. S. (2019), “Advancements in the field of autonomous underwater vehicle”, *Ocean Engineering*. doi: 10.1016/j.oceaneng.2019.04.011.
- [26] Scaradozzi, D. *et al.* (2017), “BCF swimming locomotion for autonomous underwater robots: a review and a novel solution to improve control and efficiency”, *Ocean Engineering*, 130. doi: 10.1016/j.oceaneng.2016.11.055.

A Numerical Study on the Design of a Cold Heat Storage Device in a Liquefied Air Energy Storage System (LAES)

Hyunjong Kim^{1*}, Juyeol Ryu¹, Kwansu Kim¹, Jungtae Kim¹, Dae Hwan Kim² and Jongpo Park¹

¹ Institute for advanced engineering, Gyeonggi-do, Republic of Korea, 17180

²State University of New York at Stony Brook, New York, USA, 11794

*Corresponding author. E-mail: kimhj@iae.re.kr

Abstract

As the demand for eco-friendly energy generation increases, research to overcome intermittent and irregularly generated energy through energy storage devices are being conducted actively. Among many energy storage devices, the liquefied air energy storage device is an eco-friendly energy storage system that stores energy in a power-rich situation and enables power supply when power demand increases. The liquefied air energy storage device is currently in the commercialization stage. The cold energy storage facility in this system has a key influence on the efficiency of the liquefied air energy storage system, and requires low pressure drop characteristics and excellent heat exchange performance. In order to optimize the cold energy storage facilities, performance analysis on various variables using a validated numerical model are required, but demonstration cases are very limited. Therefore, numerical analysis was performed using the mathematical modeling of the porous medium region – in which porosity was considered for the cold heat storage device with a pellet-shaped filling material. The verified numerical model will be applied and used for an optimal design.

Keywords: Liquefied Air Energy Storage, Cold heat storage device, Numerical analysis

Nomenclature

a	=	Specific density area, m^{-1}
C_p	=	Specific heat, $J/kg \cdot K$
D	=	Diameter of the cold energy storage device, m
D_p	=	Diameter of the pellet, m
ε	=	Porosity
F	=	Inertia coefficient
f	=	Fluid phase
h	=	Heat transfer coefficient
J	=	Unit vector oriented along the pore velocity vector
K	=	Permeability, m^2
k	=	Thermal conductivity, $W/m \cdot K$
μ	=	Dynamic viscosity, $N \cdot m/s^2$
Nu	=	Nusselt number
ρ	=	Density, kg/m^3
Re	=	Reynolds number
s	=	Solid phase
t	=	time, s
\vec{V}	=	Velocity vector

1. Introduction

As the demand for eco-friendly energy generation increases, research to overcome intermittent and irregular energy through energy storage devices is being actively conducted [1]. Among many energy storage devices, the liquefied air energy storage (LAES) facility has been in the commercialization stage since 2015 [2], and an eco-friendly energy storage system that stores energy in a situation where electricity is plentiful and enables power supply when demand for electricity rises. However, the LAES technology is reported to have a charge-discharge efficiency of 50% [1] despite its commercialization stage, and research is needed to improve the low charge-discharge efficiency to promote technology dissemination.

The cold heat storage device in the LAES is a facility that has a key influence on the charge/discharge efficiency of the liquefied air energy storage system, and requires low pressure drop characteristics and excellent heat exchange performance. It can be seen that the structure of this cold heat storage device in the LAES is used by filling a cylindrical tank with quartz beads to have a large surface area and high heat capacity in order to effectively store and utilize cold heat [1]. Previous studies related to the facility can be easily found in heat transfer studies of porous media in the field of chemical engineering that mainly utilizes a packed bed reactor.

Representatively, the Wakao N and Kaguei S [3] described the empirical correlations for heat and mass transfer for this packed bed shape, and is evaluated to bring reliable results for the heat transfer coefficient and analysis method [4]. Furthermore, Achenbach, E. [5] conducted a study on the Reynolds number dependency for heat transfer in a packed bed with a high Reynolds number, and suggested a heat transfer correlation that can be used in a wider operating range. Also, for analyzing the cold heat storage device, it is important to understand physical phenomena in the facility and selecting an appropriate analysis approach. Kaviani, M. [6] carried out that the assumption of one energy equation approach is not reasonable because the solid and fluid phases are regarded as no thermal equilibrium due to significantly large temperature differences.

This means that when the heat capacity and conductivity of the solid phase and the fluid phase are significantly different, it is appropriate to analysis the local heat transfer using the two-energy equations for each phase. Therefore, in the LAES cold heat storage device, since the initial temperature difference between the fluid and the solid is about 160K [1], the use of a numerical model based on the two energy equations is suitable for the analysis.

In order to optimize these cold and heat storage devices, it is necessary to try and analyze various design parameters using a validated numerical model, but empirical examples and information disclosure are very limited. Therefore, the numerical verification study was conducted using the mathematical modeling of the porous medium region considering the porosity for the cold heat storage device with the pellet-shaped filling material, the verified numerical model will be used when the designing the 10kW/10kWh LAES test facility.

2. The Liquefied Air Energy Storage System

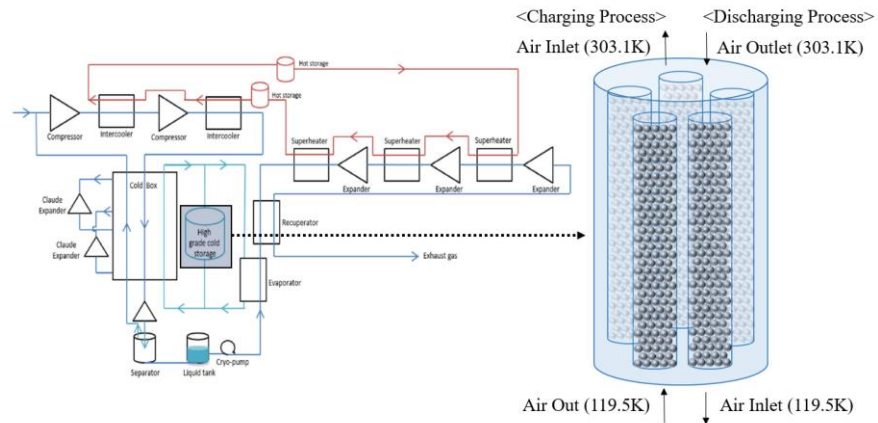


Figure 1. Block Diagram of LAES system and Schematic of high-grade cold storage facility^(1,7)

A block diagram to better understand the process flow of the LAES is shown in Fig. 1 [1,7]. The LAES process can be divided into a charging process for liquefied air and a discharging process that generates power by expanding air using a heat source such as waste heat. In the charging process, the air compressor compresses ambient air, the air temperature increases. Then, the compressed air passes through the intercooler, the air temperature reached near ambient temperature, as it passes through the cold box which has a Claude cycle and high-grade cold storage stage, the air temperature reaches the temperature of liquefaction. As shown in Figure 1, a ‘High grade cold storage’ device is used for cold heat storage and utilization. This cylindrical device has filled by quartz pellets to maximize heat transfer surfaces and to store cold heat using high heat capacity of the pellets by its volume.

3. Numerical analysis for the cold heat storage device in LAES

3.1 Numerical modeling for the cold heat storage device

The numerical analysis for the cold heat storage device was conducted by ANSYS CFX, a commercial code, an axial symmetry model which is the 1/16 of a cylinder was considered. The mesh field and boundary conditions are shown in Fig. 2. The cold heat storage device was simulated using a porous media approach method, and about 7800 nodes were used. The dimensions and the physical properties for this numerical verification work are shown in Table 1, the initial temperature of the cold heat storage device is 0°C. The mass flow rate at the inlet of the cold heat storage device is 0.3725 kg/s, and the temperature of the air flow is -160°C.

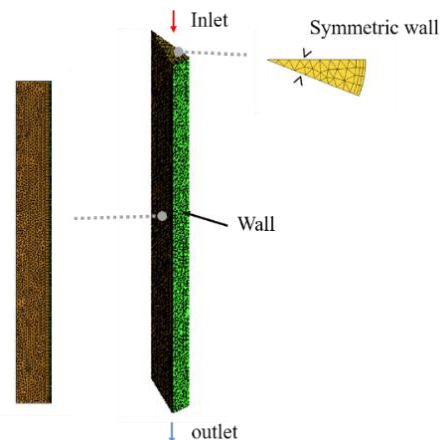


Figure 2. Mesh field and boundary conditions of the cold heat storage device

Table I. Dimensions and material properties for the numerical model

Parameter	Unit	Value
D	m	0.7
D _p	m	0.015
y	m	3.2
ρ _s	kg/m ³	2,560
k _s	W/m-K	8.99
C _{p,s}	kJ/kg-K	541

3.2 Governing equations

In terms of heat transfer, when the temperature difference between phases is large, it is difficult to assume that the heat transfer phenomena in each phase is homogeneous. Therefore, it is required to define the physical properties of the variables contributing to heat transfer for each phase and a numerical approach based on the 2-energy equation [8]. In addition, since actual physical phenomena such as microscopic flows between spherical particles cannot be reflected in the process of assuming the bead-shaped filler as a porous medium, suitable experimental correlations [3,4,5] needs to be used. Based on these prior studies, the micro flows of channels between the spherical particles approach incompressible flow, and an unsteady state analysis was conducted to implement internal temperature changes with time increases presented in the result of Sciacovelli et. al. [1]. The radiation effect can be negligible because the device has a high mass flow rate and extremely small distances between each pellet, the convective and conductive heat transfers appear the dominantly. Since this thermal storage device is vacuum insulated, the effect on heat loss is not considered, and the outer wall defines adiabatic wall conditions. These approaches also can be found in the previous studies [8, 11], thus the governing equation can be expressed as follows.

Mass conservation equation:

$$\nabla \cdot (\vec{V}) = 0 \quad (1)$$

Momentum equation:

$$\frac{\rho_f}{\varepsilon} \left[\frac{\partial(\vec{V})}{\partial t} + \{(\vec{V} \cdot \nabla)\vec{V}\} \right] = \frac{k_f(\vec{V})}{K} - \frac{\rho_f F \varepsilon}{\sqrt{K}} [(\vec{V}) \cdot (\vec{V})]J + \frac{\mu_f}{\varepsilon} \nabla^2(\vec{V}) - \nabla(P)^f \quad (2)$$

Energy conservation equation – a fluid domain:

$$\begin{aligned} \varepsilon(\rho_f)^f C_{p,f} \frac{\partial(T_f)^f}{\partial t} + (\rho_f)^f C_{p,f}(\vec{V}) \cdot \nabla(T_f)^f \\ = \nabla \cdot [k_f \cdot \nabla(T_f)^f] + h_{sf} a_{sf} [(T_s)^s - (T_f)^f] \end{aligned} \quad (3)$$

Energy conservation equation – a solid domain:

$$(1 - \varepsilon)\rho_s C_{p,s} \frac{\partial (T_s)^s}{\partial t} = \nabla \cdot [k_s \cdot \nabla (T_s)^s] + h_{sf} a_{sf} [(T_s)^s - (T_f)^f] \quad (4)$$

The permeability can be determined by:

$$K = \frac{\varepsilon^3 D_p^2}{150(1 - \varepsilon)^2} \quad (5)$$

And the inertia coefficient, F function in momentum conservation term [9], is given by:

$$F = \frac{1.75}{\sqrt{150\varepsilon^3}} \quad (6)$$

The specific surface area can be expressed as follows [10]:

$$a_{sf} = \frac{(1 - \varepsilon) y}{D_p} \quad (7)$$

The porosity of the packed bed in a cold tank is calculated by the equations [1,12]:

$$\varepsilon = 0.375 + 0.17 \frac{D_p}{D} + 0.39 \left(\frac{D_p}{D}\right)^2 \quad (8)$$

The heat transfer for the packed bed is empirically suggested by [5]:

$$Nu = [(1.18Re^{0.58})^4 + (0.23Re_h^{0.75})^4]^{0.25} \quad (9)$$

where Re_h is defined as follows with hydraulic diameter (D_h) and porosity:

$$Re_h = \frac{1}{1 - \varepsilon} Re \quad (10)$$

3.3 Results and discussion

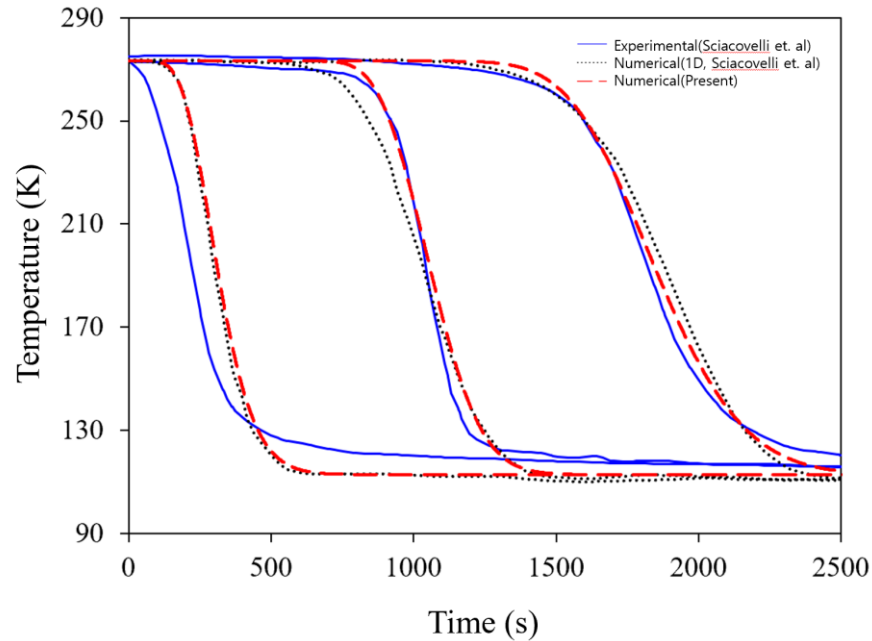


Figure 3. Numerical validation for cold heat storage device

Figure 3 shows the calculated result the temperature variations with time increases in the cold heat storage device. The data were acquired at the points presented in by Sciakovelli et al. [1], 0.27 m, 1.7 m, and 3.13 m, respectively, the results depending on the flow direction started from the inlet. The blue solid lines indicate experimental data [1], the black dotted lines indicate one-dimensional numerical analysis results [1], and the red dotted lines show numerical analysis results performed in present study. The result at 0.27 m showed almost the same as the numerical analysis model of the previous study, and at the middle and near outlet points, 1.7 m and 3.13 m, the slope of the temperature change showed a tendency to reflect the experimental results better than the numerical analysis model of previous studies.

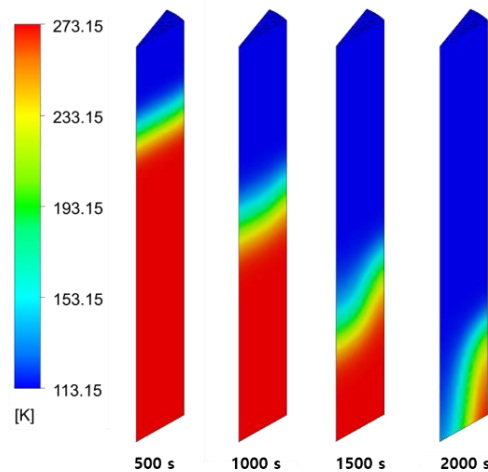


Figure 4. Visualization in a cold heat storage device with time increases

The reason why the present results of the numerical interpretation better reflect the experimental values is that the wall effect cannot be reflected in the one-dimensional numerical

model. Figure 4 shows the data that visualizes the temperature distribution at a particular time. Due to the effect of uniform flow by boundary conditions, the temperature contour in the radial direction is initially obtained almost identically, but as time goes by, the temperature distribution between the wall and the center becomes larger due to the wall effect, and it can be seen that the center cools the fastest. When determining the value of h , the heat transfer coefficient, the correlation developed under high Re as in the equation (9) is applied. The heat transfer coefficient used in this study was about $41 \text{ W/m}^2 \cdot \text{K}$, and Nu was about 1607. The Ranz and Marshall correlation [13] used in the previous paper and patent [1,12] is a model suitable for laminar flow, and Nu number is obtained approximately 2.5 times lower than this study.

Conclusion

In order to promote the LAES technology as an eco-friendly energy storage system, improvement of charging and discharging efficiency is required. In this study, numerical verification was performed on the cold heat storage device in the LAES. By applying the empirical correlation to the packed bed and using the porous media approach, it was possible to obtain more accurate results than the previous study. In the future, this numerical analysis model will be applied to optimum design of the cold heat storage device with various storage capacity. The lab scale LAES (10kW / 10kWh) test facility is currently being built and this facility will be used to ensure reliability of the cold energy (sensible and latent heat) storage device and its various materials.

Acknowledgments

This work was supported by the Korea Institute of Energy Technology Evaluation and Planning (KETEP) granted financial resource from the Ministry of Trade, Industry & Energy, Republic of Korea (No. 20188550000200).

References

- [1] Sciacovelli, A., Vecchi, A., and Ding, Y., (2017), "Liquid air energy storage (LAES) with packed bed cold thermal storage–From component to system level performance through dynamic modelling", *Applied energy*, Vol 190, pp. 84-98.
- [2] Morgan, R., Nelmes, S., Gibson, E., and Brett, G., (2015), "Liquid air energy storage–analysis and first results from a pilot scale demonstration plant", *Applied energy*, Vol 137, pp. 845-853.
- [3] Wakao N and Kaguei S, (1982), "Heat and mass transfer in packed beds", Gordon and Breach Science, New York
- [4] Nakayama, A., Ando, K., Yang, C., Sano, Y., Kuwahara, F., and Liu, J. (2009), " A study on interstitial heat transfer in consolidated and unconsolidated porous media", *Heat and Mass Transfer*, 45(11), 1365-1372.
- [5] Achenbach, E. (1995), "Heat and flow characteristics of packed beds", *Experimental thermal and fluid science*, 10(1), 17-27.
- [6] Kaviany, M. (2012), "Principles of heat transfer in porous media", Springer Science & Business Media.
- [7] Damak, C., Leducq, D., Hoang, H. M., Negro, D., and Delahaye, A., (2020), "Liquid Air Energy Storage (LAES) as a large-scale storage technology for renewable energy integration–A

review of investigation studies and near perspectives of LAES”, International Journal of Refrigeration, Vol 110, pp. 208-218.

[8] Da Silva, R. M., de Lima, A. G. B., Pereira, A. S., Machado, M. C. N., and Santos, R. S. (2018), "Unsteady state heat transfer in packed-bed elliptic cylindrical reactor: theory, advanced modeling and applications", In Transport Phenomena in Multiphase Systems, Springer, Cham., pp. 139-179.

[9] Ergun, S. (1952), " Fluid flow through packed columns", J. Chem. Eng. Prog. 48(2), 89–94.

[10] Dullien, F.A.L. (1992), "Porous Media—Fluid Transport and Pore Structure", 2nd, p. 574. Academic Press Inc, San Diego, USA

[11] Ljung, A. L., Lundström, T. S., and Tano, K. (2006), "Simulation of heat transfer and fluid flow in a porous bed of iron ore pellets during up-draught drying", SIMULATION, 13, 15.

[12] Morgan R, Dearman M, inventors; Highview Enterprises Limited, assignee. Method and apparatus for storing thermal energy. US 2013/0240171 A1.

[13] Ranz, W. E., Marshall, W. R. (1952), "Evaporation from Drops", Chem. Eng. Prog, pp. 141-146.

Computational Fluid Dynamics Based Propeller Design Improvement for High Altitude Long Endurance (HALE) UAV

Mochammad Agoes Moelyadi¹, Fatwa Azam Maulana^{2*}, Ema Amalia³

^{1,2,3} Bandung Institute of Technology

e-mail: ¹moelyadi@ftmd.itb.ac.id, ²fatwaazam669@gmail.com, ³ema@ftmd.itb.ac.id

Abstract

High Altitude Long Endurance Unmanned Aerial Vehicle (HALE UAV) driven by a hybrid power between battery and solar panel have attracted the attention of many researchers and engineers. The HALE UAV developed at Bandung Institute of Technology has a design requirements of a 63 kg MTOW with a cruise velocity of 22.1 m/s at an altitude of 60,000 ft propelled by two propellers. The main problems that arise with the propellers gained from the market are that these propellers cannot operate properly at the cruise phase due to the less air density and low Reynolds number value which impact inadequate thrust and high drag value. The Larrabee method is used to design this propeller geometry with an output in the form of a chord and twist distribution. The CFD approach method is used to improve the design resulting from the Larrabee method. The further off-design process is done to get the performance characteristics propeller and analyse its ability in various mission profiles. This study shows that the inputted thrust value of the propeller designed using the Larrabee method is always higher than the thrust value resulted from the CFD simulation with a difference of around 20% so that a design improvement process using CFD is required. The analysis of propeller implementation in various mission profiles shows that this propeller can operate fully from the climbing flight phase at sea level to cruising flight at an altitude of 60,000 ft.

Keywords: Propeller, HALE UAV, Larrabee Method, CFD, Design Improvement

Nomenclature

α	= Angle of Attack (°)	D/L	= Drag/ Lift
ζ	= Ratio between axial velocity increment and freestream axial velocity [-]	$\frac{dT_c}{d\xi}$	= Infinitesimal thrust per span from BET [N/-]
η	= Efficiency [-]	et	= Error thrust [N]
θ/R	= Twist distribution [°/m]	F	= Prandtl's Tip Loss Factor [-]
ξ	= Pointed radius/ prop radius [-]	J	= Advance ratio [-]
ϕ_a	= Angle between axial and rotational velocity [°]	P	= Power [W]
x	= Ratio between rotational velocity and freestream axial velocity [-]	Re	= Reynolds number [-]
a	= Axial interference factor [-]	T_{Lar}	= Thrust calculated by Larrabee method [N]
a'	= Rotational interference factor [-]	T_{CFD}	= Thrust calculated by CFD simulation [N]
c/R	= Chord distribution [-]	$T_{analytic}$	= Thrust by analytic calculation [N]
C_L	= Lift coefficient [-]	T_{target}	= Thrust targeted [N]
C_D	= Drag coefficient [-]	V_o	= Freestream axial velocity [m/s]

C_T = Thrust coefficient [-] W = Resultant velocity [m/s] C_P = Power coefficient [-]

1. Introduction

The advent of high altitude, low speed aircraft for reconnaissance or atmospheric research had brought about a renewed interest in the topic of propeller design for efficiency at high altitudes [1]. The main problem related to high altitude operation is low density of air, which results in less thrust generated by the propeller. The second problem is the low Reynolds number value of airstream along the propeller span, which tend to increase the drag force. To solve these problem, Larrabee Method [2] accompanied by CFD improved design method will be used to design a propeller which suits the propeller operating condition.

This paper focus on the preliminary design and performance analysis of propeller for HALE ITB v.4 [3] using Larrabee method along with some parameter variation to gain more optimum result. CFD analysis is also conducted to improve the designed propeller to match the generated thrust to the desired one. This paper will be organized as follows: UAV specification and flight condition, propeller design process and improvement, propeller characteristics performance and implementation method in various UAV mission profile will be in Section 2. The result and discussion of chord and twist distribution for both by Larrabee Method and improved geometry by CFD, propeller performance characteristics, and propeller implementation in UAV will be in Section 3. The conclusion will be in Section 4. At the end, the acknowledgment and reference will close this paper.

2. Design Methodology

2.1 UAV Specification and Flight Condition

The main points of specifications related to propeller design and additional general view is shown in Table 1.

Table I. UAV specification [3]

UAV Specification				UAV Cruise Flight Condition	
MTOW	63 kg	Max Power	3000-Watt x 2	Altitude	60,000 ft
W/S	2.17 kg/m ²	Max Motor Speed	3400	Throttle	100%
CD0	0.012	Prop Diameter	34 inches	Speed	22.1 m/s
Max L/D	31.5			T_{target}	22.1 N

The UAV model can be seen in Figure 1 [3] with general specification as length front of 12 m and length rear wing of 15 m, triple boom each with 4.5 m length, and vertical tail of 0.5 m. The two propellers are mounted in joint between rear wing to right-vertical tail and rear wing to left-vertical tail.

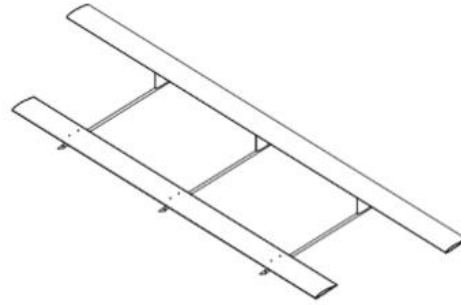


Figure 1. HALE UAV ITB v.4 Model

2.2 Design Process Using Larrabee Method

Larrabee sought a way of achieving for the propeller this ideal of minimum induced loss to maximize the efficiency for a given power input [2]. For simplicity, the Larrabee design method is shown in Figure 2 which then an Excel design code can be made.

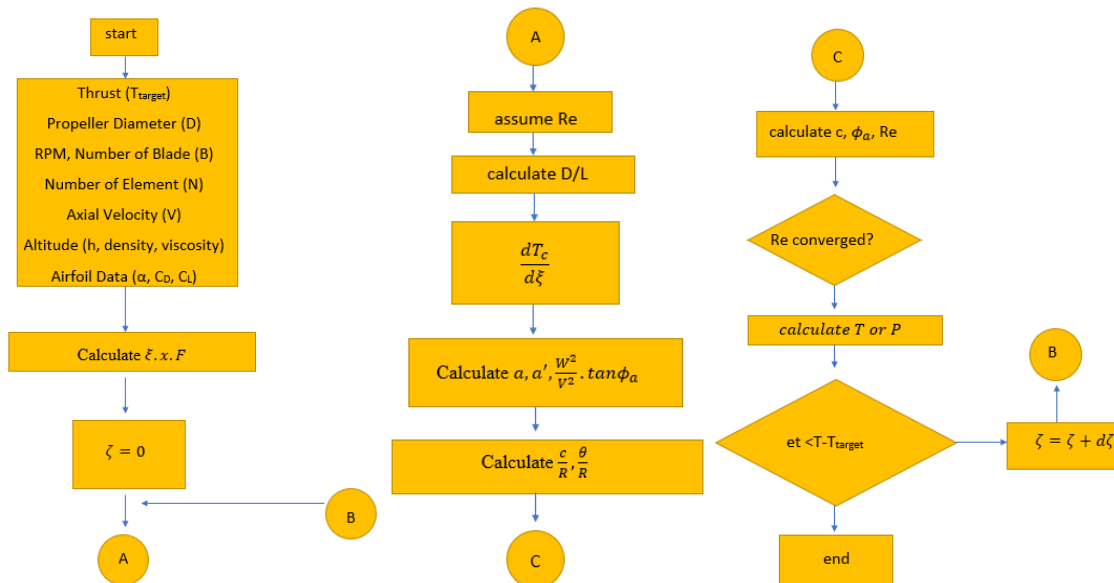


Figure 2. Larrabee Method Flowchart

In the initial analysis, Clark-Y as initial airfoil is used to find the distribution of Reynolds number along the span [1] which the authors then gained the value of $Re = 70,000$ at $r/R = 0.75$. The study is carried out by creating selections among approximately 119 airfoils listed in summary of low Reynolds number airfoil which is set of airfoils specially designed for low Reynolds number [4,5,6,7,8,9]. To filter the airfoil quickly, the authors use XFLR software to find the 5 best airfoil candidates in terms of aerodynamic efficiency, then continued by CFD 2D airfoil analysis to select the best airfoil. The CFD analysis result is shown in Figure 3.

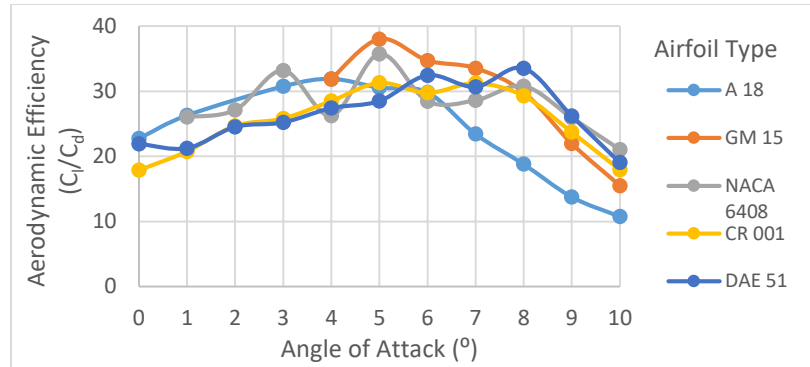


Figure 3. Curve of Airfoil Efficiency vs Angle of Attack Using CFD for 5 airfoils candidate

From Figure 3, the author chooses the DAE 51 airfoil for the next propeller design step due to its high C_L/C_D value (compared to CR 001 and A 18), the simulation result also always converges (compared to the GM 15) and the C_L/C_D graph is relatively stable (compared to the fluctuating NACA 6408 graphs). To get a more efficient propeller performance, angle of attack variation is made in linear and parabolic distribution along the span [11] which can be seen in Figure 4.

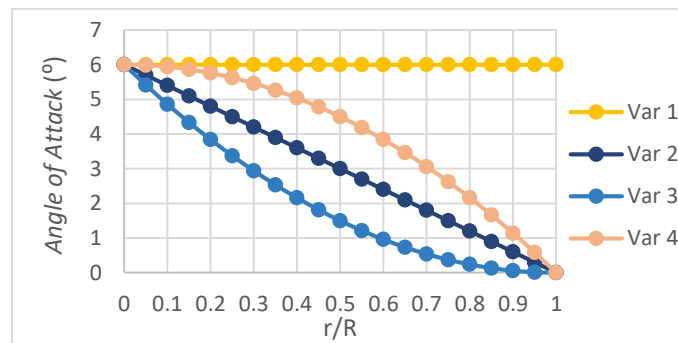


Figure 4. Linear and Parabolic Curve for Various Angle of Attack Distribution Along the Span

Executing the Excel design code, the most efficient propeller is found from the 2nd angle of attack variation. From the previous discussion, all parameters needed to design a propeller using Larrabee method have been fulfilled. The Larrabee Method calculation was performed by inputting the thrust target value $T_{target} = 22.1 N$ in Excel design code ($T_{Lar} = 22.1 N$). The generated geometry is then analyzed using CFD simulation and shows that the thrust is only $T_{CFD} = 17.61 N$, which yields a 20.34% difference compared to the desired T_{target} , hence the improved design using CFD simulation is needed.

2.3 Improvement Design Using CFD

The author creates 5 variations of input thrust using Larrabee Method (T_{Lar}) and looks for the relationship to the CFD simulation thrust result (T_{CFD}). The resulting 3D geometry from Larrabee Method can be seen in Figure 5 (left). CFD analysis is carried out using ANSYS using Multiple Reference Frame (MRF) method. The fluid domain is divided into rotating domain and stationary domain which can be seen in Figure 5.

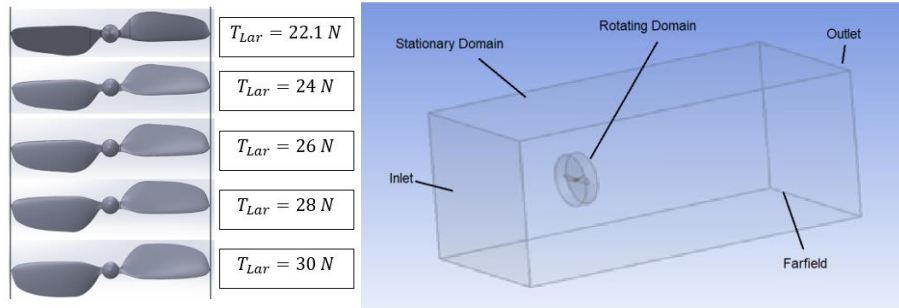


Figure 5. 3D Prop Model Geometry (left), CFD Simulation Domain (right)

The meshing process was done using ANSYS meshing, resulting in unstructured mesh. Face sizing is applied for the propeller face for about 2-4 mm (adjusted for each thrust variation) and for the outer stationary domain for 100 mm. The turbulence intensity is set to 0.1% for Transition SST adjusted to the cruise flight condition [11] [4]. The thrust inputted in Larrabee method calculation accompanied by their correlative CFD simulation are graphed in Figure 6.

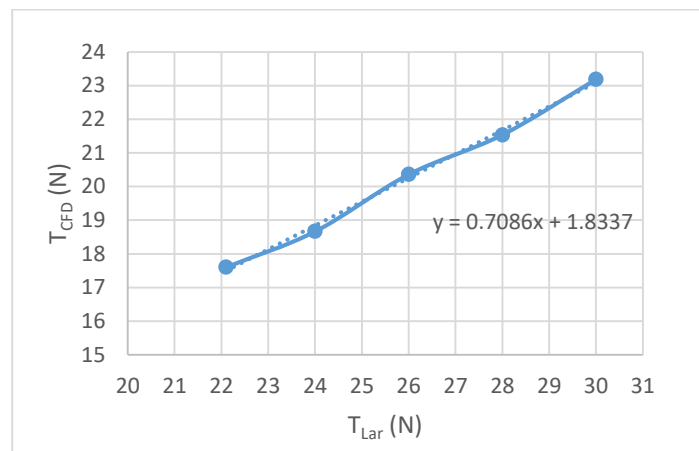


Figure 6. Thrust CFD Simulation vs Thrust Larrabee Method

Using the trendline in Figure 6, for the desired $T_{CFD} = 22.1 N$ the thrust input in Larrabee method should be $T_{Lar} = 28.6 N$. The geometry result for this improved design will be explained further in Section 3.

2.4 Propeller Performance Characteristics

A propeller performance characteristic is usually identified or stated as its efficiency performance, power coefficient, and thrust coefficient in terms of its advance ratio (η vs J , C_P vs J , and C_T vs J)[1]. CFD simulation is carried out in cruise altitude to get the thrust and torque of the propeller in various freestream velocity and RPM conditions.

2.5 Propeller Implementation in Various UAV Mission Profile

The HALE UAV ITB v.4 mission profile for both cruise and climb phase can be seen in Table II [3]. For various altitude, the required throttle, UAV velocity, and thrust by analytical calculation can differ for each case.

Table II. Cruise and Climb Performance by Analytic Calculation [3]

CRUISE PERFORMANCE					CLIMB PERFORMANCE				
Case	Altitude (ft)	Throttle	V_o (m/s)	$T_{analytic}$ (N)	Case	Altitude (ft)	Throttle	V_o (m/s)	$T_{analytic}$ (N)
1	60,000	100%	22.1	22.1	6	0	100%	10.7	307.4
2	50,000	76%	17.5	22.1	7	10,000	100%	12.5	234.9
3	40,000	59%	14	22.1	8	20,000	100%	13.1	165.8
4	30,000	50%	11.3	22.1	9	30,000	100%	13.9	114.4
5	20,000	50%	14.7	38.5	10	40,000	100%	15.3	63.6
					11	50,000	91%	17.5	31
					12	60,000	100%	22.1	22

To convert the throttle percentage to related RPM value, the performance graph for U13 Motor is used [3][12][13]. Knowing the propeller operating condition from Table II, CFD simulation can be carried out to evaluate the thrust and torque for each phase in the UAV mission profile, which then is plotted in averaged propeller performance characteristics chart from Section 2.4. Some unconverged situations may happen in simulation process related to low or high advance ratio value such as in cases 6 and 7.

3. Result and Discussion

The calculation of Larrabee method in Section 2.1 and 2.2 resulted in chord distribution and twist distribution as in Figure 7. To recap the previous discussion, the blue line (indicates the design by Larrabee method) is generated by inputting $T_{Lar} = 22.1 N$ in Excel design code, whereas the green line (indicates the improved design) is generated by inputting $T_{Lar} = 28.6 N$ in Excel design code. The improved design using CFD graph can be modelled as 3D model as in Figure 7 (right).

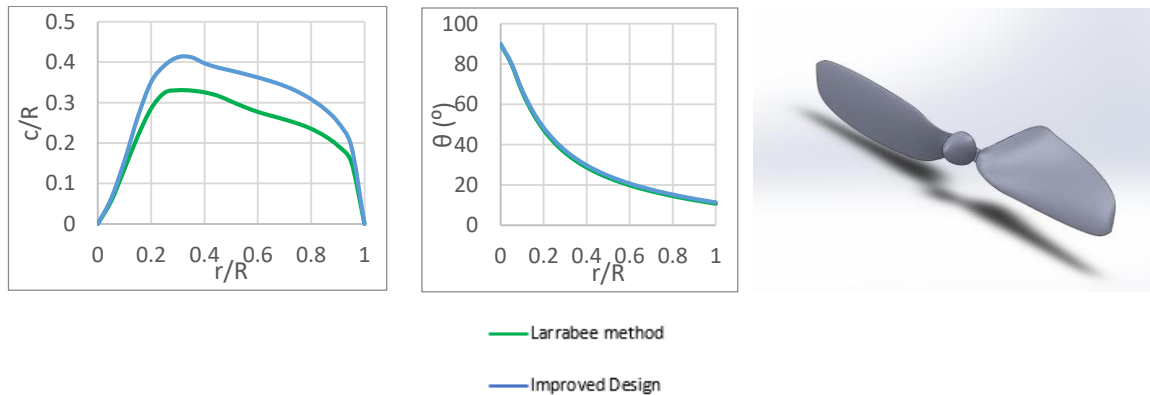


Figure 7. Chord Distribution (left), Twist Distribution (middle) using Larrabee Method and Improved Design, and 3D Propeller Model using Improved Design

It showed that Larrabee method geometry model (green line) produces thrust as high as $T_{CFD} = 17.61 N$ after running the geometry in CFD simulation, whereas the improved design geometry model (blue line) produces thrust as high as $T_{CFD} = 22.2 N$. Compared to the targeted thrust $T_{target} = 22.1 N$, the differences produced are 20.34% and 0.45% for Larrabee method geometry and improved design geometry respectively, which shows that the improved geometry using trendline equation can predict the thrust result close to the targeted thrust. Some aspects

yields this error are the 3D geometry model sacrifice the $r/R = 0$ to $r/R = 0.15$ section for the spinner whereas in Larrabee Method that section is composed by airfoils which may produce thrust, the CFD simulation carried out to collect the aerodynamics database for DAE 51 airfoils may not be too accurate due to low Reynolds number condition, and the Larrabee method uses the combined theory among momentum theory, blade element theory, and vortex theory which in each individual theory some assumption in parameters also used. The propeller performance characteristics charts for the improved design are shown in Figure 8, accompanied by the 12 cases of propeller performance in cruising and climbing phase.

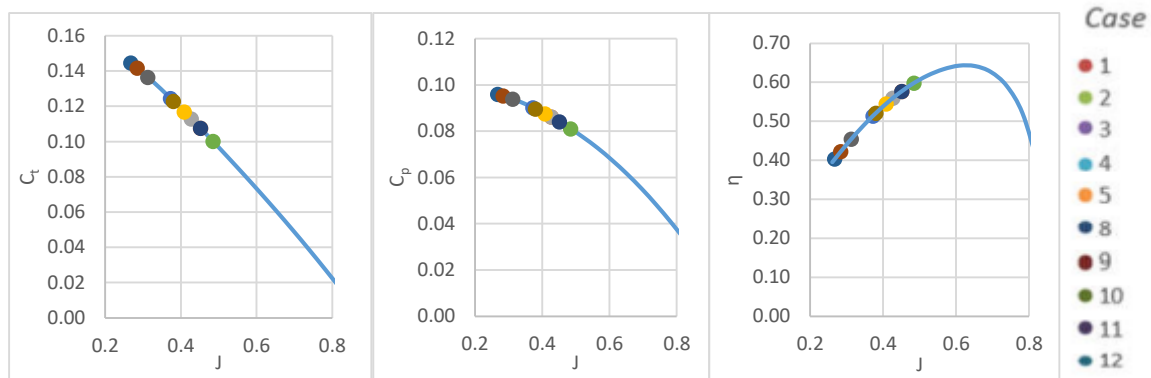


Figure 8. Thrust Coefficient (left), Power Coefficient (middle), and Efficiency(right) Plot in Propeller Performance Characteristics Chart for Each Case

Figure 8 (left) shows that the high thrust coefficient value correlating with the low advance ratio value is clearly used in the climbing flight phase from sea level to an altitude of 40,000 ft (cases 6,7,8,9, and 10), because these flight phase requires the ability of propeller to generate a large thrust to perform climbing. This is of course also accompanied by large power consumption. From Figure 8 (middle), it shows that the largest power consumption is used to perform a climbing motion from sea level to an altitude of 40,000 ft. Based on Figure 8 (right), each phase of the vehicle's flight has different efficiency values because there is a compromise between the thrust requirements required to undergo the mission profile and the power consumption used. The CFD simulation also shows that the thrust generated by propeller is always higher than the analytical calculation showed in Table II, making it fulfill the requirement to bring the vehicle from sea level to cruise altitude.

4. Conclusion

The propeller design and analysis has been conducted and shows that the results of thrust inputted in Larrabee Method is always higher compared to its CFD simulation with the thrust error value around 20%. Improvement geometry is also conducted to match the desired thrust to the CFD simulation thrust and succeeds to meet the specified requirement for the UAV to climb from sea level until cruising at 60,000 ft altitude without exceeding the maximum torque supplied by the motor. From the CFD off-design analysis, it is showed that the propeller is not operating at its peak efficiency value as the result of trade-off between thrust required and consumed power. To make good analysis and understanding about the thrust and torque characteristics, further steps such as experimental validation is required for future work.

Acknowledgement

The author would like to thank the Indonesia Endowment Fund for Education (LPDP), who support research funding, and the HALE UAV ITB research team which support this research project this year.

References

- [1] Monk, John Steven (2010). A Propeller Design and Analysis Capability Evaluation for High Altitude Application.
- [2] Larrabee, E. E. (1979). Practical design of minimum induced loss propellers. SAE Technical Paper Series. doi:10.4271/790585
- [3] Moelyadi, Mochammad Agoes et al. (2021). HALE UAV ITB perpetual flight. IOP Conf. Ser.: Mater. Sci. Eng. 1109.
- [4] Park, Donghun & Lee, Yunggyo & Cho, Th & Kim, Cheolwan. (2018). Design and Performance Evaluation of Propeller for Solar-Powered High-Altitude Long-Endurance Unmanned Aerial Vehicle. International Journal of Aerospace Engineering. 2018. 1-23. 10.1155/2018/5782017.
- [5] Selig, M. S. (1995). *Summary of low speed airfoil data*. Virginia Beach, VA: SoarTech Publ.
- [6] Selig, M. S. (1996). *Summary of low speed airfoil data*. Virginia Beach, VA: SoarTech Publ.
- [7] Selig, M. S. (2004). *Summary of low speed airfoil data*. Virginia Beach, VA: SoarTech Publ.
- [8] Lyon, C. A. (1997). *Summary of low speed airfoil data*. Virginia Beach, VA: SoarTech Publ.
- [9] Williamson, G.A (2012). *Summary of low speed airfoil data*. Virginia Beach, VA: SoarTech Publ.
- [10] Haidar, M. D., Moelyadi, M. A., & Hartono, F. (2019). Design and performance analysis of low reynolds number propeller using analytical methods by varying blades alpha design. *IOP Conference Series: Materials Science and Engineering*, 645, 012021. doi:10.1088/1757-899x/645/1/012021
- [11] Ahmed, Hairuniza & Rajendran, Parvathy. (2017). 3D CFD Simulation and Experimental Validation of Small APC Slow Flyer Propeller Blade. *Aerospace*. 4. 10.3390/aerospace4010010.
- [12] Moelyadi, Mochammad Agoes et al. (2020). High Altitude Long Endurance UAV ITB Concept: Pas and Future, The 2020 International Seminar on Aerospace Science and Technology
- [13] Moelyadi, Mochammad Agoes et al. (2020). High Altitude Long Endurance UAV ITB Solar Panel Conceptual Design, The Second International Conferences Aero Space Aviation 2020.

Determination of Longitudinal Dynamic Derivatives of High-altitude Long Endurance UAV Using Computational Fluid Dynamics

Mochammad Agoes Moelyadi¹, Rais Fadillah^{2*}, Ema Amalia³

¹The Professor, Faculty of Mechanical and Aerospace Engineering, Bandung Institute of Technology (E-mail: moelyadi@ftmd.itb.ac.id).

²The BSc Student, Faculty of Mechanical and Aerospace Engineering, Bandung Institute of Technology (E-mail: raisfadillah99@gmail.com).

³The Junior Lecturer, Faculty of Mechanical and Aerospace Engineering, Bandung Institute of Technology (E-mail: ema@ftmd.itb.ac.id)

Abstract

This paper deals with the determination of longitudinal dynamic derivatives for High Altitude Long Endurance UAV. The UAV is designed as a configuration of twin wings (front and rear) connected by triple booms and three vertical stabilizers. This complex configuration has unique vehicle response rates to aerodynamic forces and moments, called dynamic derivatives, that will be needed for flight control system design. They can be determined using Computational Fluid Dynamics (CFD) by solving unsteady aerodynamic force and moments around configurations and analyzing using Harmonic Fourier method. The given oscillatory motion models of the HALE UAV including small amplitude sinusoidal pitch oscillations, sinusoidal heaving, or both combinations of them are generated. The unsteady flow solution around the UAV motion is obtained by solving unsteady Reynolds Averaged Navier Stokes Equations with the dynamic grids. The static derivatives which were obtained from the CFD simulations agree with wind tunnel data.

Keywords: Computational Fluid Dynamics, Dynamic Derivatives, Unsteady Aerodynamics, High Altitude Long Endurance UAV, Fourier Analysis

1. Introduction

Dynamic derivatives are parameters indicating the tendency of the amplitude of vehicle motion, after being disturbed, to decrease to zero or to a new steady state, after some time, on its own, after the disturbance stop. Static and dynamic derivatives have important roles in aircraft performance analysis and flight control system design [1,2]. The stability or aerodynamic derivatives was first proposed by Bryan [3] in 1991 based on linearity assumptions. This concept is still applied in flight dynamics today.

HALE UAV operates commonly in the stratosphere (17-25 km). It can provide a great potential platform equipped with sensors to support a range of military and civilian surveillance applications [4, 5], such as security surveillance, telecommunication, monitoring area, etc. HALE UAV also operates for several days, even months. Thus, HALE UAV requires an adequate control system and good flight dynamics analysis, so that it can carry out the flight missions safely and successfully. Dynamic derivatives are one of key parameters in designing control system and analyzing flight dynamic performance.

Dynamic derivatives have been calculated using some approaches, such as the approximation based on linear theory, semi-empirical method (e.g., DATCOM [6]), experimental method [7-9], and Computational Fluid Dynamics method. With the progress of the CFD method, it has become the most economic and promising method in determining stability derivatives for various

advanced aircraft design. Recently, various numerical techniques have been used to determine dynamic derivatives based on CFD. Ronch *et al.* [10] used an unsteady time-domain CFD solver to predict longitudinal combined dynamic derivatives for aircraft full configuration. They used the Fourier integral and least square solution to calculate the dynamic derivatives of the Standard Dynamic Model (SDM) and the Transonic Cruiser (TCR). They also investigated the influence of applied motion parameters and flight conditions on the dynamic derivatives. Numerical results obtained from both methods have good agreement with experimental data. Moelyadi and Sachs [11] presented results on the dynamic yaw stability derivatives of a bird. They modelled simple harmonic motions and the dynamic derivatives were calculated using Fourier analysis. With the same kinds of motion models and numerical technique, Moelyadi *et al.* [12] performed the determination of longitudinal stability derivatives of the twin booms UAV by CFD. Mi *et al.* [13] studied the longitudinal and longitudinal-lateral coupling force and moment coefficients with small amplitude sinusoidal pitch oscillation based on CFD and rigid dynamic mesh techniques. They also investigated the effects of different types of battle damage on the dynamic derivatives.

In this paper, the numerical method for determining the dynamic derivatives of HALE UAV is studied in detail. The unsteady simulations of forced pitch oscillating and heaving (translational) motion are presented. The results of unsteady aerodynamic force and moment are analyzed using Fourier analysis to calculate the dynamic derivatives. The HALE UAV designed by Bandung Institute of Technology research team (HALE UAV ITB) is taken as a computational model. The static derivatives obtained from the CFD simulations show good agreement with wind-tunnel testing data.

2. Computational Fluid Dynamics Formulation

The unsteady Euler equations is written in non-dimensional conservative form in body fitted coordinates as:

$$\frac{\partial Q}{\partial \tau} + \frac{\partial(F^i + F^v)}{\partial \xi} + \frac{\partial(G^i + G^v)}{\partial \eta} + \frac{\partial(H^i + H^v)}{\partial \zeta} = 0 \quad (1)$$

where Q is the vector of conservative variables times the Jacobian transformation. The superscripts (i) and (v) denote the inviscid and viscous components of the conservative flux vectors with respect to the ξ, η , and ζ directions. The inviscid flux vectors, F^i, G^i , and H^i are given by:

$$\begin{aligned} F^i &= (\rho u, \rho u^2 + p, \rho u v, \rho u w, u(\rho E + p))^T \\ G^i &= (\rho v, \rho v u, \rho v^2 + p, \rho v w, v(\rho E + p))^T \\ H^i &= (\rho w, \rho w u, \rho w v, \rho w^2 + p, w(\rho E + p))^T \end{aligned} \quad (2)$$

while the viscous flux vectors, F^v, G^v , and H^v can represented by:

$$\begin{aligned} F^v &= \frac{1}{Re} (0, \tau_{xx}, \tau_{xy}, \tau_{xz}, u \tau_{xx} + v \tau_{xy} + w \tau_{xz} + q_x)^T \\ G^v &= \frac{1}{Re} (0, \tau_{xy}, \tau_{yy}, \tau_{yz}, u \tau_{xy} + v \tau_{yy} + w \tau_{yz} + q_y)^T \\ H^v &= \frac{1}{Re} (0, \tau_{xz}, \tau_{yz}, \tau_{zz}, u \tau_{xz} + v \tau_{yz} + w \tau_{zz} + q_z)^T \end{aligned} \quad (3)$$

The viscous flux vectors contain terms of the heat flux vectors, q_i , and viscous forces exerted on the body (stress tensor), τ_{ij} . The dual time-stepping methods proposed by Jameson [14] is used to solve the unsteady flow. This method employs a pseudo-time to achieve convergence and redefine the unsteady flow problem to steady problem, with the physical time derivative included in the discretized equations.

3. The Calculation Method of Dynamic Derivatives

The aerodynamic forces and moments of the vehicle are influenced by some factors. We assume that the flight state in this study is steady, symmetric, and straight with small amplitude. The aerodynamic forces and moments can be described using the Taylor expansions as

$$C_j(t) = C_{j0} + \Delta\alpha(t) C_{j\alpha} + \Delta\hat{\alpha}(t) C_{j\dot{\alpha}} + \hat{q}(t) C_{jq} + \hat{\ddot{q}}(t) C_{j\ddot{q}} + \dots \quad (4)$$

where, $\Delta\hat{\alpha}$, \hat{q} , and $\hat{\ddot{q}}$ are dimensionless parameters of the rate of angle of attack, the pitch angular velocity, and the pitch angular acceleration, respectively. The subscript (j) denote the aerodynamic forces and moments.

3.1 Static Stability Derivatives, $C_{j\alpha}$, and Dynamic Stability Derivatives, $C_{j\dot{\alpha}}$, from Heaving Motion

The static and dynamic derivatives can be calculated with simple harmonic heaving or translation (up/down) method. By forcing the aircraft to move upward and downward with simple harmonic motion as shown in Figure 1, the unsteady aerodynamic solutions calculated with CFD tools can be used to get the dynamic stability derivatives. The heaving motion can be formulated as:

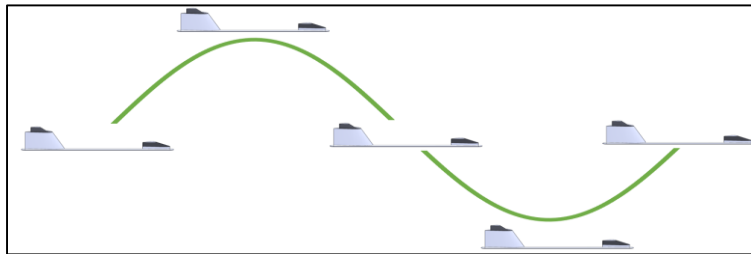


Figure 1. Heaving motion illustration

$$z = z_m \sin(\omega t) \quad (5)$$

where, z is the displacement in the vertical motion that depends on the time, and z_{max} is the amplitude of the motion. When the vehicle moves upward, there is local air going downward, and vice versa. This phenomenon generates induced angle of attack at every time step of the movement, $\alpha(t)$. These variables can be expressed as

$$\alpha = \frac{\dot{z}}{V_\infty} = \frac{z_m \omega}{V_\infty} \cos(\omega t) = \alpha_m \cos(\omega t) \quad (6)$$

$$\dot{\alpha} = \frac{\ddot{z}}{V_\infty} = -\frac{z_m \omega^2}{V_\infty} \sin(\omega t) = -\alpha_m \omega \sin(\omega t) \quad (7)$$

The aerodynamic forces and moments can be assumed to be linear or weakly nonlinear at small angles of attack, so the higher order can be neglected. Substituting Eq. (6) and Eq. (7) to Eq. (4), we can get:

$$C_j(t) = C_{j0} + (\alpha_0 - \alpha_m \cos k \sin(\omega t)) C_{j\alpha} + (\dot{\alpha}_0 - (-\alpha_m k \sin(\omega t))) C_{j\dot{\alpha}} \quad (8)$$

where, α_0 is the mean value of angle of attack, $\dot{\alpha}_0$ denotes the mean value of rate of angle of attack, and $k = l \omega / V_\infty$ indicates the non-dimensional reduced frequency of the applied motion. l is a characteristic length, given as $l = \bar{c} / 2$. The non-dimensional reduced frequency represents the degree of unsteadiness of the flow behavior around moving vehicle [11].

The static and dynamic stability derivatives can be computed taking the first Fourier Coefficients of time history of C_j over n_c cycles.

$$C_{j\alpha} = \frac{2}{(\alpha_0 - \alpha_m) n_c T} \int_0^{n_c T} C_j(t) \cos(\omega t) dt \quad (9)$$

$$C_{j\dot{\alpha}} = \frac{2}{k (\alpha_0 - \alpha_m) n_c T} \int_0^{n_c T} C_j(t) \sin(\omega t) dt \quad (10)$$

where, $T = 2\pi / \omega$ denotes the period of one cycle of motion.

3.2 Dynamic Stability Derivatives from Pitch Oscillating Motion, $C_{j\dot{\alpha}} + C_{jq}$



Figure 2. Pitch Oscillating Motion Illustration

The other dynamic derivatives are calculated with simple harmonic pitching oscillation method. By forcing the aircraft rotating around its center of gravity with harmonic motion as shown in Figure 2, the unsteady aerodynamic solutions calculated with CFD tools can be used to get the dynamic derivatives. This rotating motion can be formulated with Eq. (6). Similarly, in heaving motion, then dynamic derivatives from Pitch Oscillating Motion can be computed taking the first Fourier Coefficients of time history of $C_{j\dot{\alpha}} + C_{jq}$ over n_c cycles.

4. CFD Modeling

4.1 Computational Model

The computational model in this study is a HALE UAV which have been developed by research team from Bandung Institute of Technology. HALE UAV ITB has been designed as a configuration of tandem wings connected by triple booms and three vertical stabilizers. The mean aerodynamic chord is $\bar{c} = 0.83$ m, and the main wing area is $s = 12.75$ m². The main wingspan is $b = 15.83$ m, and the total length is 4.5 m. The center of gravity is located along the symmetry line of model at 1.96 m from leading edge front wing. This complex configuration will

have unique vehicle response rates on aerodynamic forces and moments, called dynamic derivatives. The geometry of this model created using SolidWorks 2019 is shown in Figure 3.

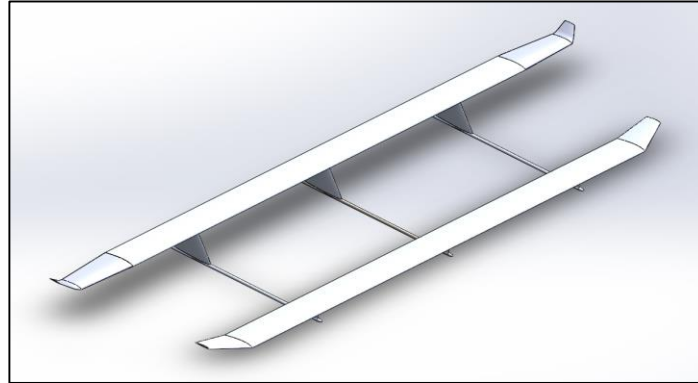


Figure 3. HALE UAV ITB geometry

4.2 Grid Generation

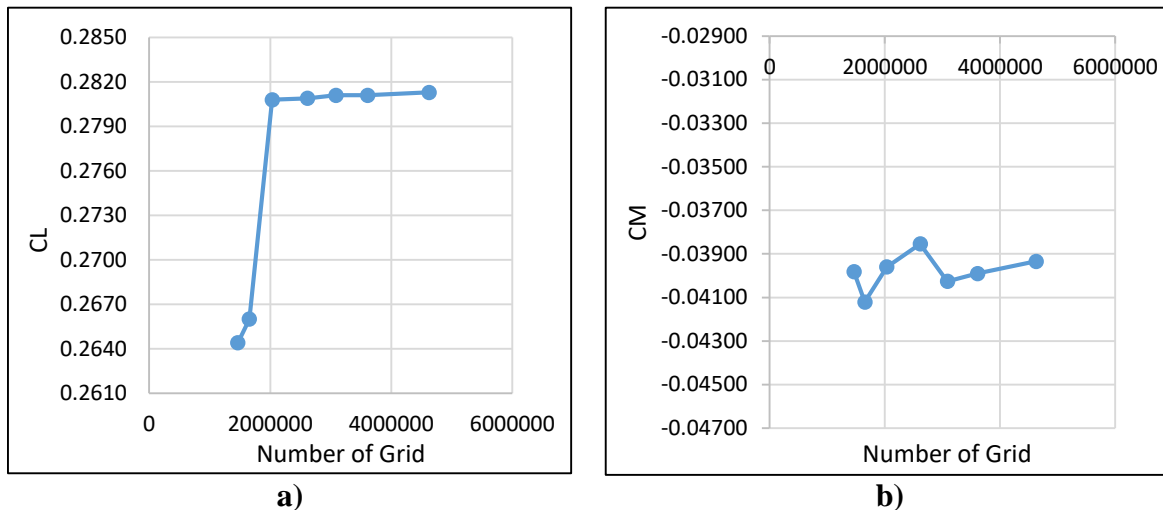


Figure 4. Grid Independence Test, a) Coefficient of Lift, b) Coefficient of Moment

The computational domain or topology and grid are generated using the ANSYS MESHING. There are two rectangular domains (inner and outer domain) generated in this simulation which aims to prevent the folded grids. The length size for outer domain is 20 times the length of the model, the width size is 3.3 times the length of rear wingspan, and the height size is 4.5 times the length of rear wingspan. Meanwhile, the length size for inner domain is 2.5 times the length of the model, the width size is 1.5 times the length of rear wingspan, and the height size is 1.4 times the length of the model. The outer domain is fixed (cannot move) and the inner one is moving depend on the time. The unstructured grids are generated in this simulation because the complexity of the geometry. Two different types of mesh are applied in this simulation, which consist of surface and volume meshes. The inner domain uses dependent surface meshes and the outer domain uses independent surface meshes. Prism mesh is applied to capture the boundary layer phenomenon around the wall and the near-wall spacing is set in such a way that $y^+ = 1$ in the wall-adjacent cells. The mesh density is also adjusted around the model. The final number of grids for this simulation have 3 million grid elements considering the required CPU time and have the convergence solutions, as shown Fig. 4.

5. Numerical Results

The fluid defined in this simulation is viscous, turbulent, incompressible, and isothermal flow. The SST (Shear Stress Transport) turbulence model is employed to evaluate the effect of viscous in this simulation. A Reynolds number of 1.67×10^5 , based on the mean aerodynamic chord and freestream speed of 25 m/s, is used. In the pitch oscillating motion, the amplitude of oscillation is set to 2 degrees while for the heaving motion the maximum of induced angle of attack is set to 2 degree. For both motions, constant reduced frequencies, $k = 0.05$ and 0.09 , are applied and the mean angle of attack is 0 degree. The moment reference point or the center of oscillatory motion coincide with the center of gravity.

5.1 Result Validation

The static derivatives are obtained by simulating the heaving motion using CFD transient method. Only the static derivatives of the numerical method were compared with wind-tunnel testing data for validation. Dynamic test is still not possible due to wind tunnel limitations and costs. Wind tunnel tests use a 1:10 scaled model. The tests are run at two flight conditions. The first test is run at a value of freestream speed of 20 m/s, which corresponds to a Reynolds number of 1.08×10^5 , based on the mean aerodynamic chord of the wind tunnel model. The second test is run at a value of freestream speed of 30 m/s, which corresponds to a Reynolds number of 1.63×10^5 , based on the mean aerodynamic chord of the wind tunnel model.

Table I shows the comparison of static derivatives obtained from CFD transient method and wind-tunnel testing. The agreement of the CFD results with wind-tunnel test data is good.

Table I. Comparison of results between CFD and Wind Tunnel test

Static Derivative	Reduced Frequency, k	CFD transient	Wind tunnel test at $Re = 1.08 \times 10^5$	Error (%)	Wind tunnel test at $Re = 1.63 \times 10^5$	Error (%)
$C_{L\alpha}$	0.05	4.70	4.64	1.29	4.72	0.42
	0.09	4.65		0.22		1.48

5.2 Static and Dynamic Derivatives from Heaving Motion Model

The static and dynamic derivatives can be obtained by simulating the heaving motion. The results of unsteady aerodynamic forces and moments are extracted using Fourier analysis to calculate the static and dynamic derivatives.

Figure 5 shows the loop of lift and pitch moment coefficient for heaving motion. Using the Fourier analysis in Eq. (9) and Eq. (10), the dynamic derivatives can be calculated, as shown in Table II. The negative values for $C_{M\alpha}$ indicate the HALE UAV ITB is statically stable in the longitudinal motion.

Table II. The static and dynamic derivatives from heaving motion for several reduced frequencies

k	Static Derivatives		Dynamic Derivatives	
	$C_{L\alpha}$	$C_{M\alpha}$	$C_{L\dot{\alpha}}$	$C_{M\dot{\alpha}}$
0.05	4.698	-0.086	8.324	6.619
0.09	4.650	-0.496	3.563	10.477

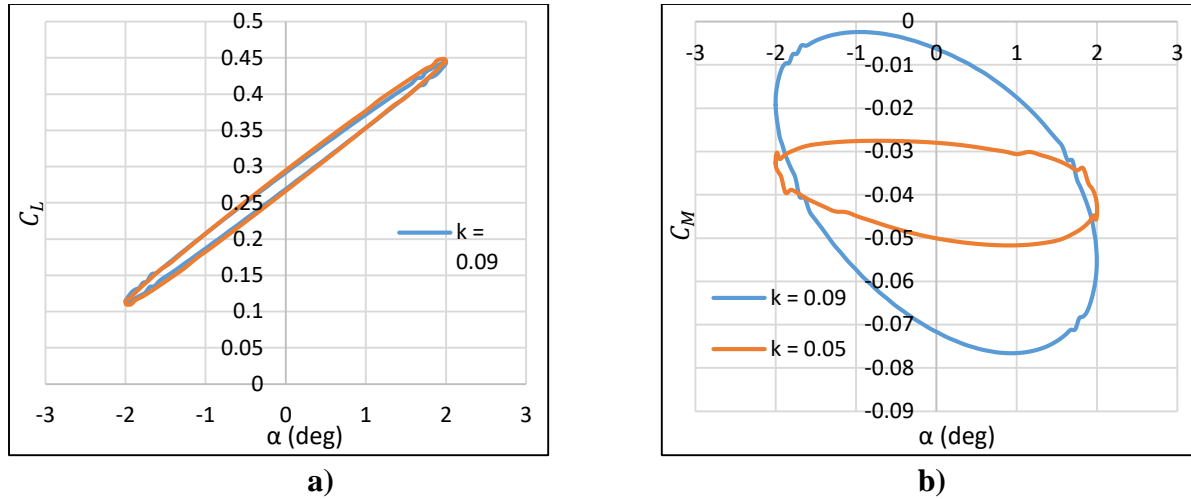


Figure 5. Unsteady lift, a) and pitch moment, b) coefficient loops of heaving motion for several reduced frequencies

3.1 Dynamic Derivatives from Pitch Oscillating Motion Model

The other dynamic derivatives are obtained by simulating the pitch oscillating motion. The results of unsteady aerodynamic forces and moments are extracted using Fourier analysis to calculate the dynamic derivatives.

Figure 6 shows the loop of lift and pitch moment coefficient for pitch oscillating motion. The moment response of this vehicle to the angle of attack and pitch rate at $k = 0.09$ are greater than the moment response of this vehicle at $k = 0.05$ as shown Figure 5 b). Using the Fourier analysis, the dynamic derivatives can be calculated, as shown in Table III.

Table III. The dynamic derivatives from pitch oscillation motion for several reduced frequencies

k	$C_{L\dot{\alpha}} + C_{Lq}$	$C_{M\dot{\alpha}} + C_{Mq}$
0.05	5.971	-68.648
0.09	6.870	-65.418

With the data from Table II and Table III, the dynamic derivatives of pitch rate (C_{Mq}) can be obtained. At $k = 0.05$, $C_{Mq} = -75.267$. At $k = 0.09$, $C_{Mq} = -75.895$. These negative values indicate the HALE UAV ITB is dynamically stable due to the disturbance in pitch.

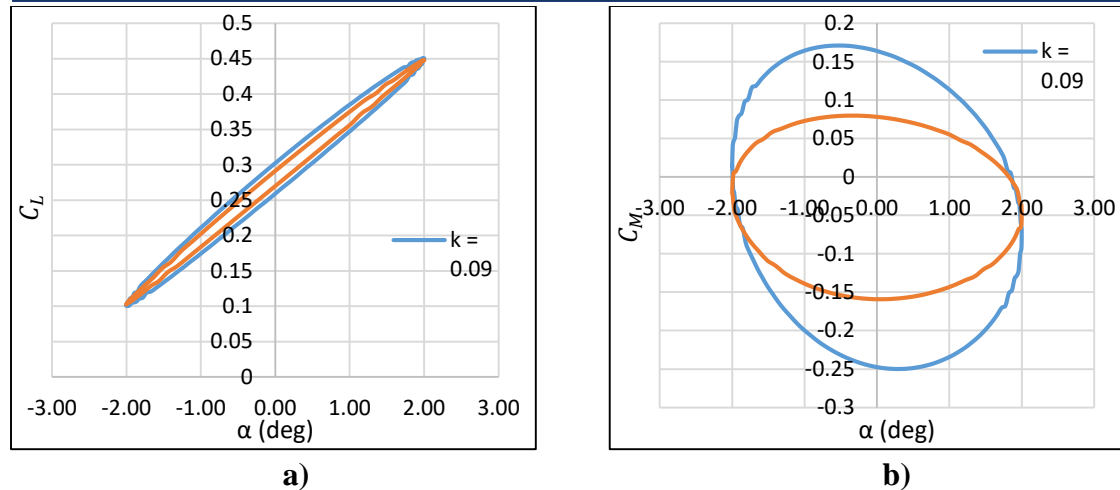


Figure 6. Unsteady lift, a) and pitch moment, b) coefficient loops of pitch oscillating motion for several reduced frequencies

4. Conclusion

The CFD method is used for the determination of longitudinal dynamic derivatives of HALE UAV ITB. Two different motion models are simulated, which consist of heaving and pitch oscillating motion, and Fourier analysis technique is used for calculating dynamic derivatives from instantaneous force and moment data. The static derivatives from numerical method show good agreement with experimental data. The longitudinal dynamic derivatives indicate that the HALE UAV ITB is stable statically and dynamically.

References

- [1] Stalnaker, J. (2012), "Rapid computation of dynamic stability derivatives", 42nd AIAA Aerospace Sciences Meeting and Exhibit, AIAA 2004-210, Reno.
- [2] Boyd, T.J.M. (2011), "One hundred years of G. H. Bryan's stability in aviation", Journal of Aeronautical History, No. 2011/4, pp.97-115.
- [3] Bryan, G.H. (1991), Stability in aviation, MacMillan, London, UK.
- [4] Alsahlani, A.A. *et al.* (2017), "Design of a high-altitude long endurance flying-wing solar-powered unmanned aerial vehicle", Progress in Flight Physics 9, Vol. 9, pp.3-24.
- [5] Moelyadi, M.A. *et al.* (2018), "Preliminary design and analysis of hybrid solar powered high altitude long endurance UAV", paper presented at the International Conference on Intelligent Unmanned System (ICIUS 2018), 2018, Jeju, South Korea, available at: https://www.researchgate.net/publication/327573528_Preliminary_Design_and_Analysis_of_Hybrid_Solar_Powered_High_Altitude_Long_Endurance_UAV (accessed 26 June 2021).
- [6] Williams, J. E., and S. R. Vukelich, The USAF Stability and Control Digital DATCOM, Technical Report, AFFDL-TR-79-3032-VOLUME I-III.
- [7] Kramer, B. (2002), "Experimental evaluation of superposition techniques applied to dynamic aerodynamics", 40th AIAA Aerospace Sciences Meeting & Exhibit, AIAA 2002-0700, Reno.
- [8] Greenwell, Douglas I. (1998), "Frequency effects on dynamic stability derivatives obtained from small-amplitude oscillatory testing", Journal of Aircraft, Vol. 35 No. 5, pp.776-783.

[9] Vicroy, Dan D. *et al.* (2014). “Low-speed dynamic wind tunnel test analysis of a generic 530 swept UCAV configuration”, 32nd AIAA Applied Aerodynamics Conference, AIAA 2014-2003, Atlanta.

[10] Da Ronch, A. *et al.* (2010), “Computation of dynamic derivatives using CFD”, 28th AIAA Applied Aerodynamic Conference, AIAA, Chicago, IL.

[11] Moelyadi, M.A., and Sachs, G. (2007), “Simulations of dynamic yaw stability derivatives of a bird using CFD”, International Conference on Intelligent Unmanned System (ICIUS 2007), Bali, Indonesia.

[12] Moelyadi, M A. *et al.* (2019), “CFD based determination of longitudinal static and dynamic stability derivatives of twin boom UAV”, Journal of Applied Science and Engineering, Vol. 22 No. 2, pp.259-266.

[13] Mi, B.G. *et al.* (2021), “Simulation on the dynamic stability derivatives of battle-structure-damaged aircrafts”, Defence Technology, Vol. 17 Issue 3, pp.987-1001.

[14] Jameson, A. (2012), “Time Dependent Calculations Using Multigrid, with Applications to Unsteady Flows Past Airfoils and Wings”, 10th Computational Fluid Dynamics Conference, AIAA, Honolulu, pp.91-1596.

Drone Detection and Localization Using Omnidirectional Cameras

Kieren Chua¹, Loh Yu Kang^{2*} and Sutthiphong Srigrarom³

¹ National University of Singapore, 5A Engineering Drive 1, Singapore 117411
e0322754@u.nus.edu

² National University of Singapore, 5A Engineering Drive 1, Singapore 117411
e0325508@u.nus.edu

³ National University of Singapore, 5A Engineering Drive 1, Singapore 117411
spot.srigrarom@nus.edu.sg

Abstract

The purpose of this study is to prove that drone detection and localization can be done using omnidirectional cameras in an indoor setting. By capturing images on two separate cameras, disparity maps are processed through a computer vision algorithm (YOLOv5) to detect and generate a bounding box around the drone. Thereafter, cylindrical coordinates were converted into spherical coordinates from static equirectangular images, allowing object localization, therefore determine the depth of an object in the image. We have demonstrated that it is possible for drones to be detected and localised using omnidirectional cameras and object detection algorithms that are both open source and capable of running with limited hardware requirements.

Keywords: Drone detection, Drone localisation, Omnidirectional cameras, Fisheye lens, YOLOv5

1. Introduction

Conventional cameras are widely used to obtain a stereo image pair which allows us to estimate the depth of an object in image by placing two cameras at a distance apart from each other [1]. However, conventional cameras have a limited field of vision, and thus a limited range of vision-based applications. To overcome the hardware limitations of conventional cameras, this study aims to replace conventional cameras with omnidirectional cameras, to improve the field of view while preserving the desired level of accuracy for drone detection and localisation. The motivation of this study stems from the rapid improvements in camera technology which translates to better affordability and image resolution for omnidirectional cameras. Omnidirectional cameras remove the need for multiple cameras to obtain a snapshot of the surroundings, further enhancing the value of exploring this relatively untapped field of application for such cameras.

While the use of omnidirectional cameras come with the benefit of a full field of vision in a single image, images captured by omnidirectional cameras are subjected to a degree of distortion, widely known as the ‘barrel distortion’, which produces a warped image. In other words, straight lines are subjected to inward warping, where objects located near the centre of the image remain undistorted and the degree of warping increases with distance from the centre. Figure 1 illustrates the effect of barrel distortion on a checkerboard image. ‘Dewarping’ functions are readily available in both post-processing and programming software, but do not allow for real-time image processing. Disparity mapping for ‘dewarped’ images cannot be used as the features of the images have been altered, hence distance and disparity information have also been lost in image processing. Hence, the key deliverable of this study is to integrate

computer vision and disparity mapping with the intention to design a model that can perform both drone detection and localisation respectively using real-time 3D images.

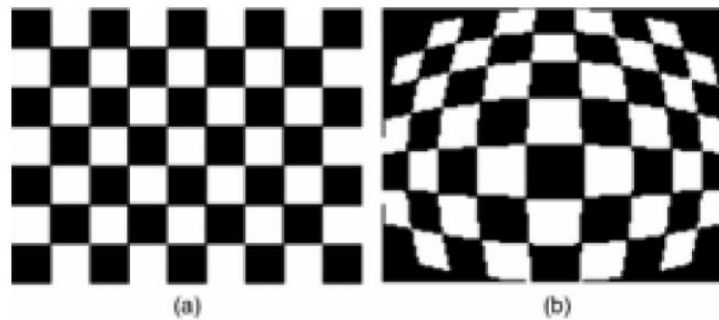


Figure 1. Checkerboard images that are subjected to (a) no distortion and (b) barrel distortion [2]

In determining the optimal choice of computer vision models for drone detection, two object detection methods were considered: ‘one-stage approach’ and ‘two-stage approach’. It was found that one-stage detectors have a much faster computational and detection speed due to its simple architecture, while two-stage detectors trade-off speed to produce highly accurate results i.e. bounding boxes with high accuracy [3]. While detection accuracy is certainly a desirable output, it was found that even the fastest two-stage detector, that is, Faster-RCNN, can only operate at 7 frames-per-second (FPS)[4], which is grossly insufficient for real-time detection. In the context of drone detection where movements can be swift and sudden, drone detection speed is the primary determining factor for our choice of object detection algorithms. YOLOv5, a single convolutional neural network was selected due to its low latency, fast processing and higher mean average precision compared to other real-time systems [5]. With a frame rate of up to 140 FPS [6], YOLOv5 also operates at a much faster frame rate compared to its one-stage detector counterparts. Related works within the field of drone detection involve the use of both ‘one-stage’ detectors, namely SSD [7] and YOLOv2 [8], for quadcopter drone detection, as well as ‘two-stage’ detectors, namely Faster-RCNN, for detecting drones in long-range surveillance videos [9].

2. Disparity Mapping

2.1 2D Disparity Mapping

With the use of a stereo-camera pair, one can easily determine the depth of an object in image via disparity mapping, provided that the focal length of cameras f , baseline or distance between cameras b and disparity d is given. This is done by comparing the shifts in pixels between the left and right images. With the use of similar triangles, the following equation can be derived:

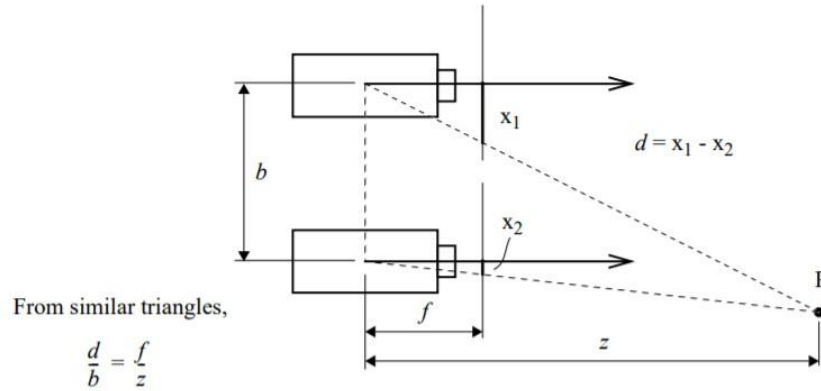


Figure 2. Relationship between baseline b , disparity d , focal length f and depth z [10]

2.2 3D Disparity Mapping

Our experimental set-up resembles that of a horizontally aligned omnistereo, where two omnidirectional cameras, represented by O_1 and O_2 , are placed at equal height. This is illustrated in the right diagram in Figure 3. The drone, represented by P , is hovered along the same horizontal plane as the cameras to maintain a horizontally aligned omnistereo, allowing us to neglect the relative differences in vertical height between the drone and the cameras. The goal of the preliminary experiment is to illustrate a proof of concept that the depth of object in image can be obtained using triangulation, hence justifying the simplicity of the set-up.

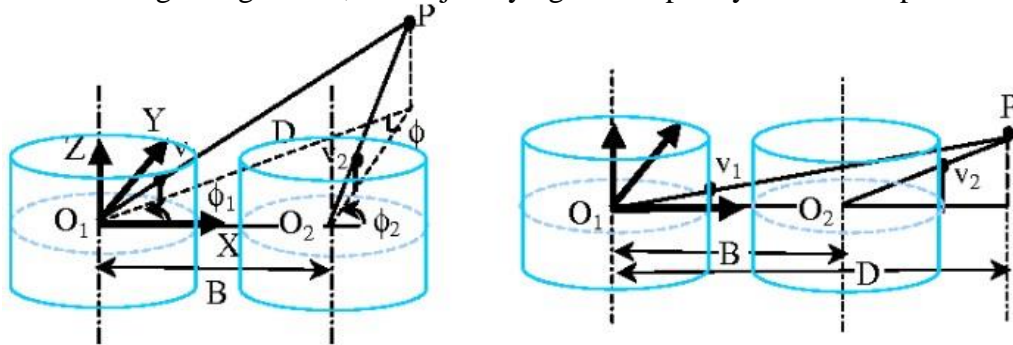


Figure 3. Horizontally aligned omnistereo: object P displaced upwards from x - y plane (left), object P kept along x - y plane (right) [11]

The image points can be obtained from the cameras respectively. However, as the image is distorted due to the nature of the fisheye lens, the image points cannot be used as an accurate reference. Hence, even though the experimental set-up can be visualized as a 2D diagram, a new formula needs to be derived to account for the warping effect. Equirectangular projections preserve the angles of each point from the centre of the screen, resulting in linear representations of points as angles from the camera in the image plane. Using similar triangles, we can find the depth of object in a fish-eye image using an angulation approach. With reference to Figure 3, we can derive the following equations:

$$D = B \frac{\sin\phi}{\sin\phi_2 - \sin\phi_1} \quad (1)$$

$$D = B \frac{B}{\tan\phi_2 - \tan\phi_1} \quad (2)$$



Figure 4. Preliminary Experimental Set-up in Vicon Room

3. Disparity Mapping

3.1 Methodology

Test flights were conducted using DJI Mavic Minis as drone samples to be detected and tracked. The DJI Mavic Mini drones are shown in Figure 5. The tests were conducted in a closed controlled environment with a 6 x 6m grid as seen in Figure 6. This was to ensure that there were no external factors such as lighting that could affect the detection of the drone. The grid markings provided the necessary measurements that could be used to compare the depth calculated by the disparity. Each of the grids were evenly spaced at 1m distance apart from each other. Two Ricoh Theta S omnidirectional cameras were placed 2m apart, represented by the blue spheres in Figure 5. The orange spheres represent the 14 different locations of our test object, which was a cylinder that was marked with two crosses. The two crosses were located away from the central xy plane, where the camera lenses were aligned, at +0.22m and -0.225m respectively along the z-axis i.e. positive z-direction points out of the page towards the viewer. It is noted that the cylinder had a diameter of 0.3m and this is accounted for when determining the actual depth of the object in image.



Figure 5. Two DJI Mavic Mini Drones used for tracking

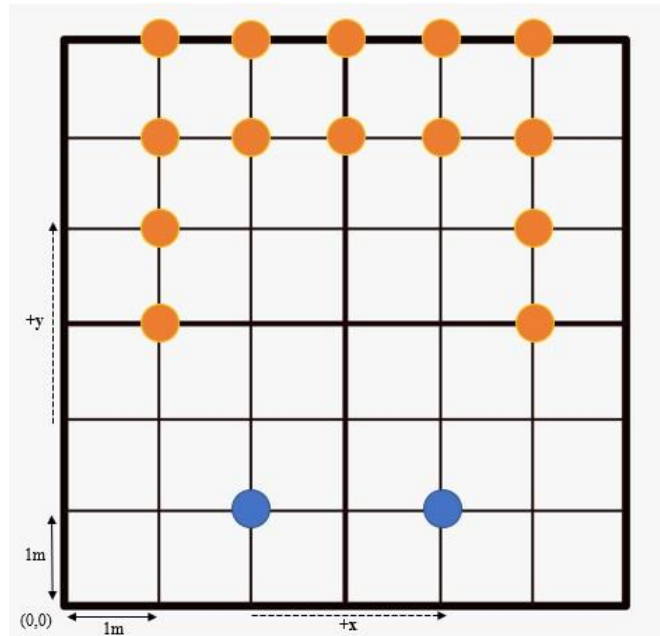


Figure 6. Experimental Set-up (Floor Plan)

3.2 Specifications

Ricoh Theta S: 14 Effective Megapixels, F2 Lens with 1/2.3 CMOS sensor.

Still Image Resolution: L: 5376 x 2688, M: 2048 x 1024

The large still image resolution was used to retain image features and keep the drone visible enough for human annotation of drone images. The inbuilt conversion software in the Ricoh Theta took the two fisheye images (front and back) and converts them into a single equirectangular format through image stitching.

3.3 Disparity Calculations

By comparing the azimuth and polar angle obtained from both cameras and inputting the values into Equation (2) above, we were able to obtain the calculated depth of object in image. A root mean error was then obtained by comparing the difference between the calculated depth and actual measured depth.

4. Model Architecture

YOLOv5 is an object detection framework that uses the “You Only Look Once” method of object detection, where the image is segmented into grids and object detection is done in each of those grids. This format allows parallelization during inference and training, making both faster and more accurate results without many images, as based on the model, the inferences are drawn from images of different scales and compared to each other in the loss function, effectively some augmentation inside. YOLOv5 was also selected due to its higher average precision as compared to other learning models. A comparison of YOLOv5 with respect to other detections models can be seen in Figure 7.

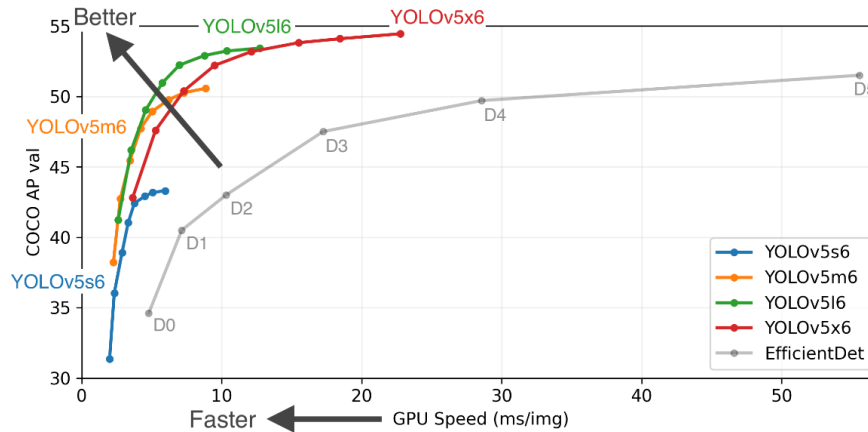


Figure 7. YOLO v5 comparison with EfficientDet [12]

Model Training

1) Cropping and brightness variance were the main image augmentations that were implemented. Cropping adjustments were made so that the image could fit within the model. YOLOv5 only accepts input images of 416 x 416 pixels, hence image preprocessing is required as our original images are of 5376 x 2688 pixels. By utilizing Roboflow, the original images were resized via center cropping, which maintains the aspect ratio of the image. While source image data is lost through cropping, it was determined that this does not affect the quality of the results. The resized image represented an ideal region of interest that caters to the small size of our drone in image. Similarly, processing smaller size images also contributes to faster computational and training speed. For brightness variance, the brightness of the image was adjusted within the $\pm 30\%$ range. We chose to augment the brightness to introduce some other form of noise within the image, as we managed to manually input other forms of noise while collecting data, such as positioning the drone in front of complicated background patterns and backgrounds of the same colour, with the intent of increasing the difficulty of training. Image reduction has already introduced pixel noise into the image, and to prevent further loss of features, we chose brightness augmentation as a conservative form of augmentation without further degrading the image.

2) Losses: Cross-entropy loss was used as a gauge to find the item due to its popular use as a classification tool in image classification. YOLOv5 employs cross-entropy loss to 3 metrics to calculate total loss, namely Generalized Intersection over Union, Objectiveness and Mean Average Precision

3) Epochs: Models were trained with 2 different values of epochs, 500-1500. Training with 500 epochs shown signs of underfitting, while at 1500 epochs, the model was beginning to overfit. Due to the relatively small size of data, the training epochs was kept at 1500 to reduce overfitting.

5. Results

A total of 82 samples, which sums up to 198 samples after including augmentation samples, were gathered for the dataset. 70.7% of the dataset was used for model training while 19.5% and 9.8% of the dataset was used for validation and testing respectively. All samples were preprocessed via center cropping for YOLOv5 compatibility. Figure 8 illustrates the mAP, precision and recall curves for 500 Epochs and 1500 Epochs models, respectively. It can be observed that the 1500 Epochs achieved a recall of close to 1, that is, there were close to 0 false

negative cases based on a 0.5 IoU threshold, while the 500 Epochs model fell short of attaining the desired recall of 1. Figure 9 illustrates the training and validation losses for the 500 Epochs model, while Figure 10 illustrates the training and validation losses for the 1500 Epochs model. In general, both training and validation loss curves converges in a similar downward trendline. The trendline indicates that the model possesses a good learning rate. It is to be noted that as fisheye lenses were used in omnidirectional cameras, all source images were subjected to distortion. When the drone was distorted in the image, the heavy loss of features made it difficult for the YOLOv5 algorithm to detect and classify the drone. This problem was particularly prominent for drones that are found along the edges of the source image. However, drone shots near the centre horizon line of the image were not affected as heavily by distortion, and the YOLOv5 algorithm was effective in detecting drones in that region. The output images of both Epoch models can be viewed in Figure 11.

It is to be noted that there could be slight over-fitting in the 1500 Epochs model as there were multiple false detection when the drone was placed very close to the camera. This error can be seen in Figure 12. To rectify this issue, a larger data set could be obtained, ideally with different types of drones. By capturing more images of different drones, we could possibly minimize data generalization and model over-fitting. Conversely, underfitting could be an issue for the 500 Epochs model as there were false negative cases in the model. An example of such a case can be seen in Figure 13, where the model failed to detect the drone at the bottom right edge of the image.

The calculated RMS error was around 11% for distances ranging from 2m – 5m. Compared to the accuracy of other comparable stereo cameras, such as the ZED stereo camera by Stereolabs where the error ranged from 2-4%, the Ricoh Theta S cameras did not perform as well in this scenario. However, a positive systematic error was identified after examining the calculated errors. This suggests that there were other factors to consider when accounting for distance, such as lens distortion. When lens distortion is present, additional calibration methods will need to be introduced to conduct disparity mapping with omnidirectional cameras, where the centroid of objects was used to map the disparity rather than pixel points in traditional disparity mapping. Having a smaller baseline might also reduce the error in calculating the depth of object in image as the large baseline results in a larger 3D effect and thus warping effect, which would contribute to increased error.

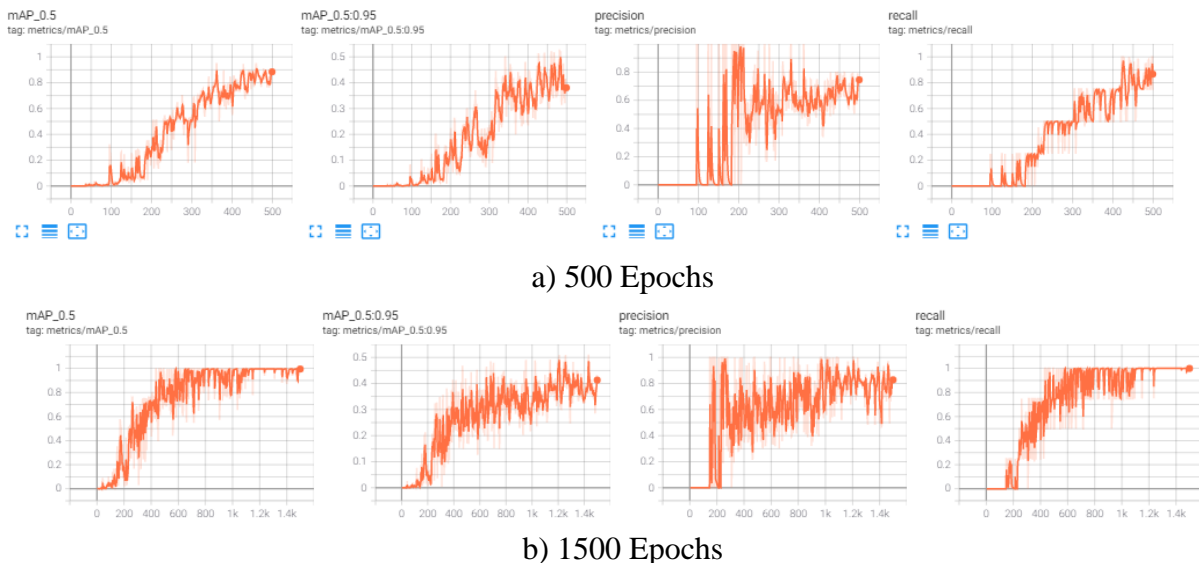


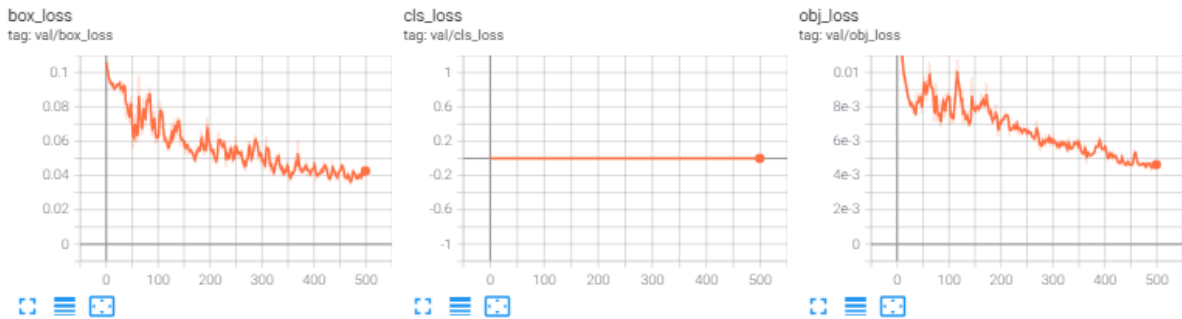
Figure. 8. mAP, Precision and Recall Curves

train



a) Training Loss

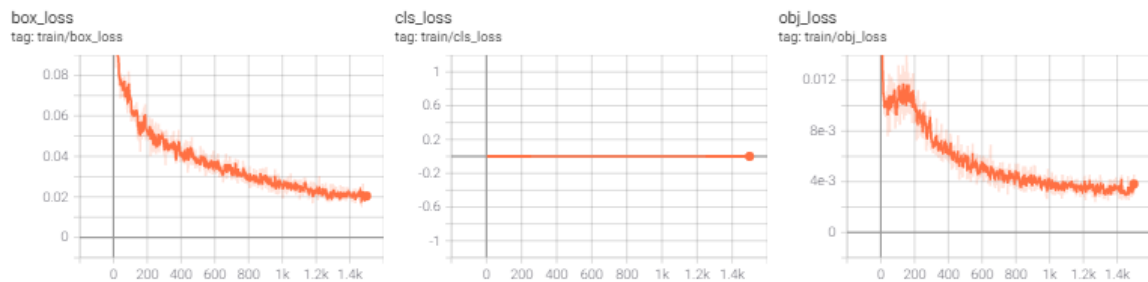
val



b) Validation Loss

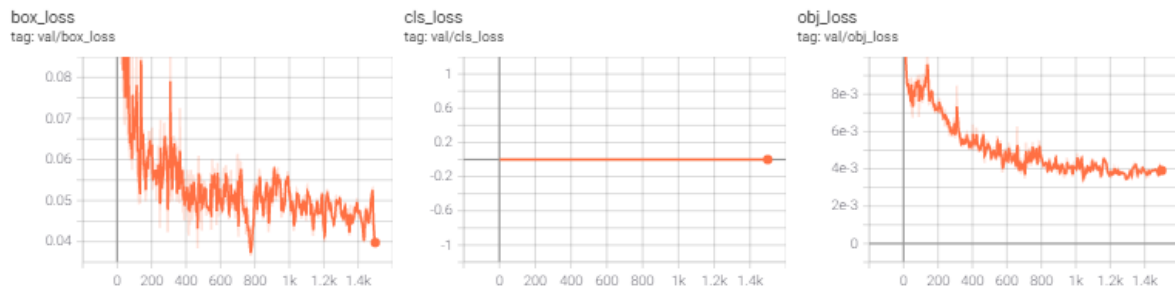
Figure. 9. Loss Curves at 500 Epoch

train



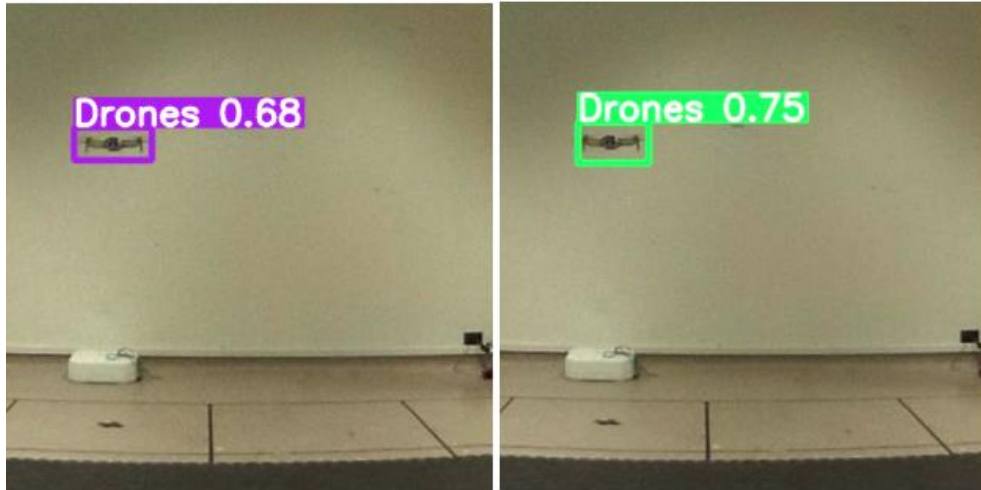
a) Training Loss

val



b) Validation Loss

Figure. 10. Loss Curves at 1500 Epoch



a) 500 Epoch

b) 1500 Epoch

Figure 11. Bounding Box Detection

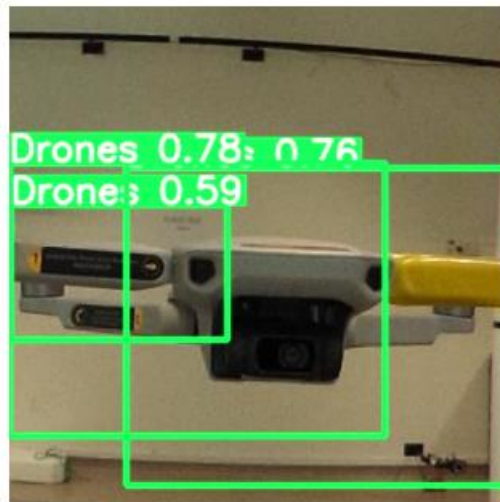


Figure 12. False positive detection, 1500 Epoch



Figure 13. False negative detection, 500 Epoch

6. Discussion

6.1 Observations

Due to the short focal length of the Ricoh Theta S cameras, the size of the drone in image was very small when located far away from the camera. There were difficulties faced during the annotation of data as it was challenging to search for the drone in image using the human eye. However, when processing the images with the YOLOv5 algorithm, the model took significantly less time to locate the drone in image with fewer errors as it processed the entire image. This observation enhances the value of this study as it that object detection algorithms are more capable in locating objects within a 3D space as compared to humans due to its faster inference time, especially when the objects are small.

6.2 Limitations

1) *Large Image Sizes*

360-degree images require a significantly larger amount of storage space due to the amount of visual information stored in them. As a result, training object detection models with 360-degree images is both time-consuming and prone to error as conventional models work with smaller, square images while 360-degree images are way larger and have a 2:1 aspect ratio.

2) *Hardware Limitations*

The small shot size of the drone in image is due to the small focal length used in the Ricoh Theta S cameras. Short focal lengths allow the camera to capture a wide field of view, which is a requirement for omnidirectional cameras. This makes objects appear further than they seem, which causes the drone, which was already small, to appear even smaller in image. When the drone was located 5-6m away from the camera (which is the furthest distance of the test area), there was a significant loss in feature, and it is almost impossible for the model to detect any distinguishable features. This hardware limitation cannot be rectified using larger sensor or lenses with larger focal length as the size of the lens would be very big and difficult to manufacture.

3) *Compatibility Issues*

The YOLOv5s model is not suitable for processing large images. YOLOv5s is only suitable for smaller images like COCO & Imagenet, which was what the original model was trained on. This is due to the 416 x 416 pixels restriction imposed by YOLOv5. Hence, image pre-processing (center cropping) was done for the original YOLOv5 model. However, when dealing with large data sets, manual image cropping will not be feasible as it would require too much time to complete. Even though large data sets can be processed through automated scripts, it may not always be the optimal solution as there is possibility for error such as the loss of key features and failure to detect the region of interest. Thus, a potential solution would be to process the source image uncropped, which would eliminate the lengthy process of image pre-processing. A test was conducted to test this hypothesis, where the source image is fitted into the 416 x 416 format while maintaining its aspect ratio, to test if the YOLOv5 model is able to detect the drone in image. The results were compared with a separate training model on Datature [13] which is an end-to-end AI Vision Platform, where there was no need for image pre-processing. A Faster-RCNN Inception V2 training model was implemented with Datature's platform to process uncropped source images and the model was able to detect warped features confidently as seen in Figure 14. This highlighted that image pre-processing was not a requirement for drone detection in 360-degree images. However, while the output from the Faster-RCNN model is desirable, it is to be noted that the Faster-RCNN model tradesoff speed for accuracy and that the Faster-RCNN model has a significantly longer computational speed compared to YOLOv5. In

contrast, the compression of images for YOLOv5 has resulted in an image with indistinguishable features where the model is unable to detect the drone, as seen in Figure 15.



(a) 0.74 Confidence Score Detection



(b) 0.86 Confidence Score Detection

Figure 14. Faster-RCNN Inception V2 on Datature, Source Image used



Figure 15. YOLOv5 with fitted image, 1500 Epochs

7. Potential Applications and Use Cases

While object detection and localisation may be challenging for real life applications due to aforementioned limitations, this study has demonstrated that the usage of omnidirectional cameras in stereo vision could still be effective. Image disparity between two omnidirectional cameras can be calculated without the use of focal length while maintaining reasonable accuracy. Even though object detection rates greatly diminish with increased distance from the camera, the model performed reasonably well within closer distance i.e. 3m from the camera. With improvements to existing hardware, the object detection effective range within an indoor setting can certainly be improved.

8. Conclusion

This study has successfully demonstrated a proof-of-concept, that it is possible for drones to be detected and located using omnidirectional cameras and object detection algorithms that are both open source and capable of running with limited hardware requirements. The untapped potential for higher-end omnidirectional cameras to be used for drone localisation should be further explored as omnidirectional cameras possess a distinct advantage over the directional vision offered by traditional cameras. Future work can be conducted with better cameras with more suitable lens and sensors for stereo imaging, thus improving the accuracy of our results. To enhance the applicability of this study for real-life usage, future datasets should also include multiple drone types and possibly even other object classes such as birds and other flying objects for differentiation purposes. Larger data sets with larger Epochs should also be experimented to find the most accurate results.

Acknowledgement

The research is supported in part by the Defence Science and Technology Agency (DSTA).

References

- [1] N. Raajan, M. Ramkumar, B. Monisha, C. Jaiseeli et al., “Disparity estimation from stereo images,” *Procedia engineering*, vol. 38, pp. 462–472, 2012.
- [2] S. Qureshi, “Lens distortion correction,” Feb 2020.[Online]. Available: <https://www.edge-ai-vision.com/2011/05/lens-distortion-correction-2/>
- [3] X. Lu, Q. Li, B. Li, and J. Yan, “Mimicdet: Bridging the gap between one-stage and two-stage object detection,” *arXiv preprint arXiv:2009.11528*, 2020.
- [4] W. Liu, D. Anguelov, D. Erhan, C. Szegedy, S. Reed, C.-Y. Fu, and A. C. Berg, “Ssd: Single shot multibox detector,” in *European conference on computer vision*. Springer, 2016, pp. 21–37.
- [5] J. Redmon, S. Divvala, R. Girshick, and A. Farhadi, “You only look once: Unified, real-time object detection,” in *Proceedings of the IEEE conference on computer vision and pattern recognition*, 2016, pp. 779–788.
- [6] H. Wang, X. Tong, and F. Lu, “Deep learning based target detection algorithm for motion capture applications,” in *Journal of Physics: Conference Series*, vol. 1682, no. 1. IOP Publishing, 2020, p. 012032.
- [7] W. Budiharto, A. A. Gunawan, J. S. Suroso, A. Chowanda, A. Patrik, and G. Utama, “Fast object detection for quadcopter drone using deep learning,” in *2018 3rd International Conference on Computer and Communication Systems (ICCCS)*. IEEE, 2018, pp. 192–195.

[8] C. Aker and S. Kalkan, “Using deep networks for drone detection,” in 2017 14th IEEE International Conference on Advanced Video and Signal Based Surveillance (AVSS). IEEE, 2017, pp. 1–6.

[9] M. Nalamati, A. Kapoor, M. Saqib, N. Sharma, and M. Blumenstein, “Drone detection in long-range surveillance videos,” in 2019 16th IEEE International Conference on Advanced Video and Signal Based Surveillance (AVSS). IEEE, 2019, pp. 1–6.

[10] S. B. Kang, J. Webb, C. L. Zitnick, and T. Kanade, “An active multibaseline stereo system with real-time image acquisition,” CARNEGIE-MELLON UNIV PITTSBURGH PA SCHOOL OF COMPUTER SCIENCE, Tech. Rep., 1994.

[11] Z. Zhu, “Omnidirectional stereo vision,” in Proceedings of the Workshop on Omnidirectional Vision, Budapest, Hungary, 2001.

[12] Ultralytics, “YOLOv5,” GitHub. [Online]. Available: <https://github.com/ultralytics/yolov5>. [Accessed: 20-Jun-2021].

[13] Datature | transform datasets to computer vision models. [Online]. Available: <https://www.datature.io/>

Design and Implementation of a Hardware-in-the-Loop UAV System for Forest Fire Monitoring

Hossein Jamshidi¹, Youmin Zhang^{2*}

^{1,2} Department of Mechanical, Industrial and Aerospace Engineering, Concordia University,
Montreal, Quebec H3G 1M8, Canada

*Corresponding author. E-mail: youmin.zhang@concordia.ca

Abstract

The purpose of this study is to design a unique Hardware-in-the-loop (HIL) simulation architecture to test fire-detection drones, mainly focusing on the search and locating algorithm and simulating thermal cameras to test computer vision techniques. We simulated a thermal camera with a raw image provider which is similar to the actual hardware output and a fire-making system in a forest-like environment that can randomly set fire to the simulated forest's specific location. We used a game engine to implement the 3D graphics and utilized the built-in Nvidia PhysX to solve the rigid-body equations. The simulator transfers data to the ground control station (GCS) using a UDP port. The GCS exchanges data with autopilot hardware using a serial port. We implement multitasking in most of the simulation systems and the GCS to achieve real-time simulation performance. We integrated the HIL system in our designed Autopilot (APOne), tested some flight and search algorithms using thermal camera image processing, and analyzed the results to confirm the designed hardware and software architecture. Finally, the outcome of the system exhibited a good agreement with the autopilot as well as the guidance and navigation system in terms of the fire detection and positioning algorithms.

1. Introduction

As climate change consequences are getting more devastating (IPCC, 2019), the world needs to take some serious measures. In this paper, the focus is on designing intelligence systems such as aerial systems to fly over the forest, monitor the signature, and search for any possible threats. For this purpose, we implement a hardware-in-the-loop (HIL) simulation to test small UAV behaviors and their computer vision algorithms. The HIL is capable of simulating multiple aerial systems in the forest area. Throughout the implementation process we address many challenges, including real-time and concurrency issues, data communication, and sensor simulation whereby the simulation is executed in a game-like 3D environment. Since our requirement for simulating a thermal camera image is not a part of any game engine, it is necessary to implement a method to simulate the data input to the computer vision algorithms. In other words, the contribution of this study is the development of a HIL simulator designed solely for the purpose of fire detection.

2. Target Hardware and control software

For the purpose of this research, an autopilot named APOne is designed using a powerful STM32F7 with ARM Cortex M7 core as the microcontroller (STMicroelectronics, 2020). It has a 9-DOF IMU sensor (InvenSense, 2016) with a three-axis accelerometer, three-axis rate gyroscopes, and a three-axis magnetometer capable of detecting heading and attitude with a barometric pressure sensor for detecting altitude (Bosch Sensortec, 2020). It can calculate the AHRS sensor fusion algorithm (Madgwick *et al.*, 2011) for more than 1 kHz. To detect the platform location, it utilizes a GNSS module that is able to use GPS and GLONASS signals

concurrently to achieve 10Hz of positioning data with an accuracy of approximately 2.5 meters (u-blox, 2020). In addition, it has a 512K EEPROM to save the controller’s settings and waypoints where it stores other data like flight path or sensors’ raw data in a removable external SD card with 16GB. The autopilot software is written in C++ using the STM32CubeIDE. To achieve the lowest communication latency possible, it uses a dedicative UART port with DMA access for the HITL interface. Finally, it has eight output channels configured to control eight different actuators with different control signals, such as PWM or DShot (“DShot ESCs”, 2021). If the actuator supports the DShot protocol, the command refresh rate could be more than 37,500 Hz.

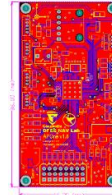


Figure 1. Autopilot board Figure 2. Autopilot PCB layout

A ground control station (GCS) is a software that communicates with the autopilot using a wireless data modem. It sends and receives configurations, commands, the system status. Figure 3 shows some screenshots of the software. In our implementation, the GCS also controls the HIL simulation. In short, the GCS is a bridge between the simulator and the autopilot.

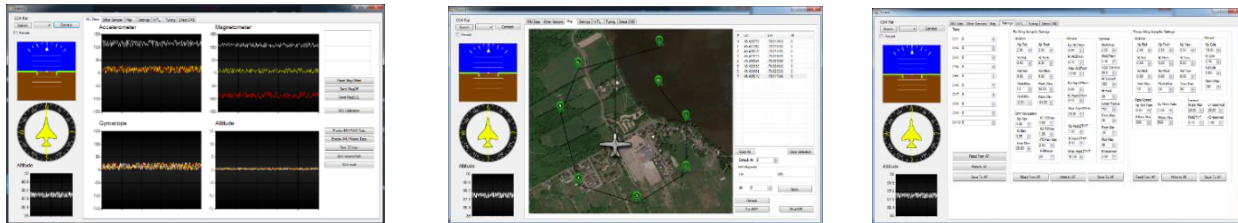


Figure 3. GCS software

One of the main challenges in designing such a software is to use multi-threading and concurrency in the software to achieve real-time capability (Trahay *et al.*, 2009). The GCS has to run the UDP server (Simulator to GCS), the UART (GCS to Autopilot), and the user interface (Drawing indicators, etc.) on separate threads to achieve real-time capability.

3. Simulation and Visualization Environment

Achieving an excellent real-time visual interface provides the user with a better insight into the system’s behavior. A 3D interface that shows the system’s behavior in a forest-like environment in real-time is therefore required. Such a 3D environment with sophisticated visual features like forest and fire (shown in Figure 4) requires a complete 3D engine. The Unity game engine (Wikipedia, 2020) is chosen to implement the 3D environment because of the ease of use (especially for prototyping), more resources on the internet, and better online community. The Unity engine benefits from C# as the intermediate language.

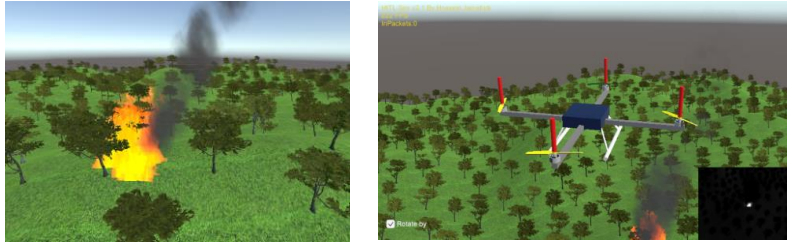


Figure 4. Fire and forest-like environment

In this paper, the drones are presumed as rigid-body; therefore, in order to predict the system behavior and fulfill the flight dynamic model, a rigid-body solver is needed. There are many well-known implementations of flight dynamic models, especially for quadcopters (Mahony *et al.*, 2012). For this study, we chose to apply a confirmed out-of-the-shelf solver so that we can focus more on the other aspects, such as interfaces and real-time capability. Consequently, the generic rigid-body dynamic solver built in the Unity engine is adopted. The Unity physics engine is an integration of the Nvidia PhysX engine (Unity, 2021a; Fingas, 2018). The first step is to define the rigid-body object characteristics such as weight, mass, and inertia. Next is to apply the corresponding forces and moments according to the object defined as the drone (quadcopter, hexacopter, rover, any other object) and eventually let the 6DOF solver estimate the motion and the corresponding reactions. Besides estimating the 6DOF dynamics, the implemented simulator can handle object collision (Unity, 2021b), whether it is the behavior of the ground colliders (landing gears) or the reactions between the flying objects (mid-air collisions), which is one of the key benefits of our design and implementation.

An instance of an implemented model is the quadcopter model that is used for the case study. Figure 5 outlines the assumptions behind the design of the drone's rigid body. The green arrow specifies the actual rigid-body weight distribution. Figure 6 depicts the corresponding force and moments of the actuators on the quadcopter used as a test case.

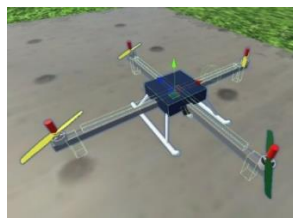


Figure 5. Drone rigid body and weight distribution

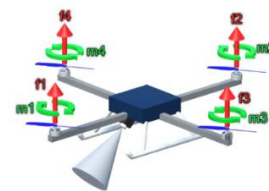


Figure 6. Force and moments

To simulate a fire detection system, one needs to implement fire in the simulation environment. Since the focus is not on investigating the fire behavior itself, it seems advantageous to simulate as much details as needed for the sake of computational cost. Simulating the fire behavior in detail will require larger processing power, which in turn will lead to the occupation of the CPU and GPU by non-related tasks to the HIL that is unfavorable. As such, the fire system is modeled as an animation captured from a real fire. This fire system is provided by the Unity as part of its particle system (Unity, 2021c). It provides total control over the fire behavior, including random or programmed position, growing or diminishing, emitting smoke or not. A random fire position enables us to find any possible corner or edge cases in our algorithms. Since our approach is to use a thermal camera, we simulate the camera with a

greyscale output format in which the high-temperature objects (the fires) get a brighter value and keep the output similar to the original format of the real camera on our platform.

The image data structure and the pixel format are similar to an 8-bit (0-255) greyscale image. The image formats for the thermal cameras have been illustrated in Table I (FLIR, 2021). In this study, the White Hot format is chosen because it is easier to process and has a smaller image size. In this image format, the absolute black is 0 (coldest), and the absolute white is 255 (warmest). To test some basic computer vision algorithms, the simulated camera image should be sent to the flight controller to check if the image processing algorithms are practical.

Table I. Thermal image formats

Format	Color pallet	Image sample
White Hot		
Iron Bow		

4. Test Scenarios

To confirm the methods, a simple case study is designed to test overall system’s integrity and consistency. It starts with a takeoff and then moving toward the fire and uses an algorithm to detect and report the fire coordination. To perform the search mission, first, the platform needs to be stabilized. The method used to stabilize the platform is a well-tuned PID controller. The PID gains are tuned manually by observing the system’s behavior. It is started with some reasonable guesses for the values of PID controller gains K_p , K_i , and K_d , and then tried to find an acceptable step by step combination. The procedure for tuning the roll and yaw axis is illustrated in Figure 7. Since the platform is symmetrical on the roll and pitch axis, it exhibits the same behavior on the pitch axis as that of the roll axis.

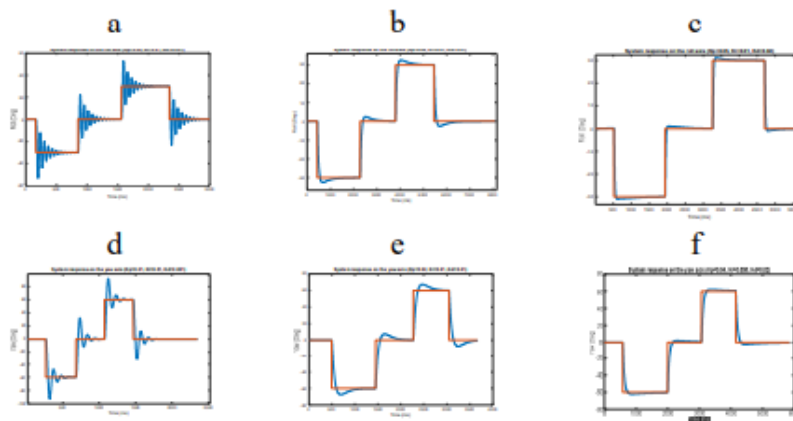


Figure 7. The system behavior and responses

After following the same procedure for altitude and navigation controllers with the same PID structures as the other channels, it can navigate to a specific location. The next step is to test the image processing system’s functionality that was discussed in Section 4.

Our approach for detecting the fire location is to use the raw image from the simulated thermal camera and calculate the centroid of high-temperature areas (the white pixels). Figure 8 shows the image that is perceived and processed by the flight controller.

Suppose the centroid is off-center, based on the deviation, dy , dx (depicted in Figure 8), camera mounting angle, and the camera field of view, the algorithm estimates the fire location relative to the drone and reports it to the GCS. Given the slight roll angle during a normal flight, the enormous size of the fire, the low camera field of view, and assuming a flat terrain, the equation can be simplified with the least compromise in the accuracy as follows,

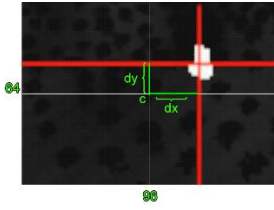


Figure 8. High-temperature area's centroid

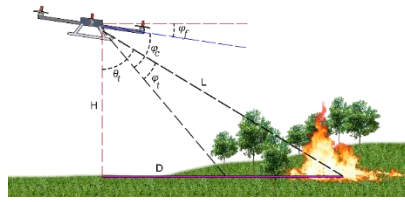


Figure 9. Side view

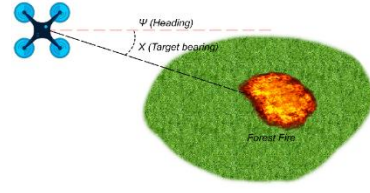


Figure 10. Top view

For a $96H \times 64V$ pixel image and $75^\circ H \times 60^\circ V$ field of view, we have:

$$X_c = \frac{1}{n} \sum_{i=1}^n x_i \quad (1)$$

$$dx = \frac{96}{2} - X_c \quad (3)$$

$$X_t = dx * \frac{75}{96} \quad (5)$$

$$\varphi_t = dy * \frac{60}{64} \quad (7)$$

$$D_t = H_{GPS} * \tan \theta_t \quad (9)$$

$$Y_c = \frac{1}{n} \sum_{i=1}^n y_i \quad (2)$$

$$dy = \frac{64}{2} - Y_c \quad (4)$$

$$\omega_t = \omega_{GPS} + X_t \quad (6)$$

$$\theta_t = 90 - (\varphi_f + \varphi_c) + \varphi_t \quad (8)$$

Then we have X_t and θ_t , we can further use this equation (Veness, 2002) to calculate the fire location:

$$Lat_t = \arcsin(\sin(Lat_{gps}) * \cos\left(\frac{D_t}{R}\right) + \cos(Lat_{gps}) * \sin\left(\frac{D_t}{R}\right) * \cos\omega_t) \quad (10)$$

$$Lon_t = Lon_{GPS} + \text{Atan2}(\sin\omega_t * \sin\left(\frac{D_t}{R}\right) * \cos(Lat_{GPS}), \cos\left(\frac{D_t}{R}\right) - \sin(Lat_{GPS}) * \sin(Lat_t)) \quad (11)$$

where

x_i, y_i : x, y location of each pixel representing high temperature zone, respectively

n : Number of total pixels in the high temperature zone

ω_t : Absolute target bearing

D_t : Estimated target ground distance from the drone (Meter)

Lat_{gps} : The drone Latitude from GPS

Lon_{gps} : The drone Longitude from GPS

R : Mean Earth radius ($6371 * 10^3$ meter)

After detecting the fire location, the drone performs a loiter maneuver around the fire while keeping the camera (the platform heading) pointed toward the fire. It calculates the target direction using the fire position from Eq. (10) and Eq. (11) and the current platform position from the GPS (simulated) and sends it to the YAW controller as the set point. Furthermore, the distance from the fire location is calculated and controlled simultaneously. The result is exhibited in Figure 11.

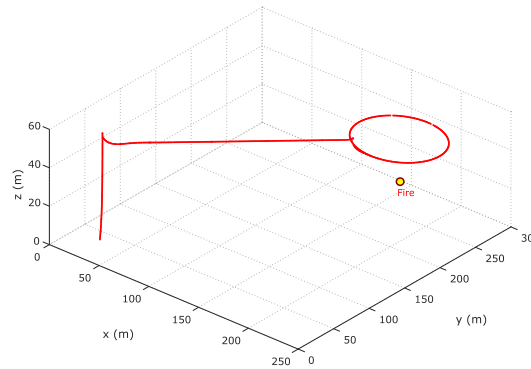


Figure 11. Flight path of the mission

The results suggest that the system has a high consistency where the guidance and navigation algorithms and the simulated image processing system perform satisfactory. Several other tests with different fire locations are carried out where the reported location error is calculated. The results are shown in Table . Since the terrain elevation is not provided to the system, the area is assumed to be a flat surface, so only the x and y are calculated, and z is considered 0.

Table II. Fire location estimation accuracy

Attempt	Actual location (x,y,z)	Detected location (x,y,z)	Error
#1	195, 219, 21	197.3, 231.4, 0	12.6m
#2	150, 100, 10	153.1, 107.3, 0	7.9m
#3	100, 100, 10	103.9, 106.1, 0	7.2m

5. Conclusion

In this paper, the implementation of a complete HIL system was discussed. The main goal of the system is to examine the fire detection of the aerial platform. A full 3D forest-like simulation environment was designed and integrated with the developed autopilot hardware and the GCS software. The PID controller is used for implementing the control and navigation algorithms of the platform and performed simple navigation maneuvers. A computer vision playground is designed and tested by simulating thermal image sensor output using the in-game camera. The image is transferred to the autopilot and a simple image processing algorithm is performed to detect the fire location. Finally, a case study is introduced to confirm the system's

functionality, performance, and integrity. The main contribution of this research is the development of a functional simulator that can be adapted to the existing autopilots to assess fire detection algorithms, eliminating the necessity of experimenting with real fire forest. In future work, consideration and implementation of scenarios with multiple drones using multiple autopilot hardware will be carried out.

References

- [1] Bosch Sensortec. (2020), BMP280 Technical Specification, available at: www.bosch-sensortec.com (accessed 25 May 2021).
- [2] “DShot ESCs”. (2021), , available at: <https://docs.px4.io/master/en/peripherals/dshot.html> (accessed 23 May 2021).
- [3] Fingas, J. (2018), “NVIDIA’s physics simulation engine”, available at: <https://www.engadget.com/2018-12-03-nvidia-physx-open-source.html> (accessed 21 May 2021).
- [4] FLIR. (2021), “Your Perfect Palette | FLIR Systems”, available at: <https://www.flir.com/discover/ots/outdoor/your-perfect-palette/> (accessed 19 April 2021).
- [5] InvenSense. (2016), MPU-9250 Product Specification Revision 1.1.
- [6] IPCC. (2019), “IPCC SR: Climate Change and Land”, An IPCC Special Report on Climate Change, Desertification, Land Degradation, Sustainable Land Management, Food Security, and Greenhouse Gas Fluxes in Terrestrial Ecosystems.
- [7] Madgwick, S.O.H., Harrison, A.J.L. and Vaidyanathan, R. (2011), “Estimation of IMU and MARG orientation using a gradient descent algorithm”, IEEE International Conference on Rehabilitation Robotics, available at: <https://doi.org/10.1109/ICORR.2011.5975346>.
- [8] Mahony, R., Kumar, V. and Corke, P. (2012), “Multirotor aerial vehicles: Modeling, estimation, and control of quadrotor”, IEEE Robotics and Automation Magazine, Vol. 19 No. 3, pp. 20–32.
- [9] STMicroelectronics. (2020), STM32F722xx Datasheet, available at: www.st.com (accessed 25 May 2021).
- [10] Trahay, F., Brunet, É. and Denis, A. (2009), “An analysis of the impact of multi-threading on communication performance”, IPDPS 2009 - Proceedings of the 2009 IEEE International Parallel and Distributed Processing Symposium, available at: <https://doi.org/10.1109/IPDPS.2009.5160893>.
- [11] u-blox. (2020), SAM-M8Q Easy-to-Use u-Blox M8 GNSS Antenna Module Data Sheet Document Information Title SAM-M8Q Subtitle Easy-to-Use u-Blox M8 GNSS Antenna Module Document Type Data Sheet Document Number This Document Applies to the Following Products: Product Name Type Number ROM/FLASH Version PCN Reference, available at: www.u-blox.com (accessed 31 May 2021).
- [12] Unity. (2021a), “Rigidbody overview”, available at: <https://docs.unity3d.com/Manual/RigidbodiesOverview.html> (accessed 21 May 2021).
- [13] Unity. (2021b), “Continuous collision detection (CCD)”, available at: <https://docs.unity3d.com/Manual/ContinuousCollisionDetection.html> (accessed 21 May 2021).
- [14] Unity. (2021c), “Introduction to Particle Systems - Unity Learn”, available at: <https://learn.unity.com/tutorial/introduction-to-particle-systems> (accessed 23 May 2021).
- [15] Veness, C. (2002), “Calculate Distance and Bearing between Two Latitude/Longitude Points Using Haversine Formula in JavaScript”, MIT Open Source.
- [16] Wikipedia. (2020), “Unity (game engine)”, available at: [https://en.wikipedia.org/wiki/Unity_\(game_engine\)](https://en.wikipedia.org/wiki/Unity_(game_engine)) (accessed 23 May 2021).

Developing CMOS MEMS Flow Sensors on a Flapping Wing Surface

Lung-Jieh Yang^{1*}, Reshmi Waikhom¹, and Horng-Yuan Shih²

¹Department of Mechanical and Electromechanical Engg., Tamkang University, Tamsui, Taiwan, 251301

²Department of Electrical and Computer Engg., Tamkang University, Tamsui, Taiwan, 251301

*Corresponding author. E-mail: ljyang@mail.tku.edu.tw

Abstract

A flapping wing micro air vehicle (FWMAV) demands high lift and thrust generation to achieve good flight maneuverability. Researches regarding the FWMAV improvement need the on-site lift information and measurement. In this case, microelectromechanical systems (MEMS) flow sensors on a flapping wing can be helpful in detecting real-time downwash and lift. The conventional MEMS flow sensor design is composed of a floating plate with resistive temperature detectors (RTDs) heated by another side heater, both made by polysilicon. We herein used 0.18 μm -linewidth complementary-metal-oxide-semiconductor (CMOS) IC foundry with MEMS post processing provided by UMC/TSRI Taiwan to implement the new sensor chips. We adopt the self-heating of the RTD half-bridge with the area of $300 \times 250 \mu\text{m}^2$ for sensor functionality and omit the heater aside. The schematic and the fabricated chip are shown in Fig.1. This new sensor generates a normalized output sensitivity of $138 \mu\text{V/V}/(\text{m/s})/\text{mW}$ within the speed range of 0-15 m/s in a low-speed wind tunnel. The dummy specimen test and the orientation-free test in the wind tunnel were also done. As an interdisciplinary study, COMSOL Multiphysics simulation is to check the sensor performance. Very small chip size of flow sensors is beneficial to integrate the sensor on flapping wing surface. The future work of this new flow sensor is on the packaging issue of the sensor-wing integration and its corresponding testing.

Keywords: MEMS flow sensor, self-heating, polysilicon, UMC 0.18 μm CMOS foundry

Nomenclature

- R_0 = design resistance value ($\text{K}\Omega$)
- R_1 = resistor on the substrate ($\text{K}\Omega$)
- R_2 = resistor on the MEMS cavity ($\text{K}\Omega$)
- ΔT_0 = rise of self-heating Temperature ($^\circ\text{C}$)
- ΔT_1 = rise of temperature across R_1 ($^\circ\text{C}$)
- ΔT_2 = rise of temperature across R_2 ($^\circ\text{C}$)
- V_0 = bias voltage (V)
- V_{out} = voltage output (V)

1. Introduction

Through more than 2 decades of research, the flapping wing micro air vehicles (FWMAVs) has made great progress recently by the control of the tailless configuration. The “Delfly Nimble” [1] and the “Konkuk Beetle” [2] are two successful examples that could perform hovering flight and some distinguished maneuvers. However, based on the flapping wing design improvement by the conventional wind tunnel testing, the forward flight and the level cruising of

FWMAVs are still the most primary flapping flight under investigation [3-5]. How to measure the lift and downwash values during cruising to achieve long-term flight endurance is very crucial to the development of FWMAVs [6-7]. This paper reports a new design of thermal flow sensor by a standard UMC 0.18 μm CMOS MEMS foundry. Our intelligible yet coherent design has the self-heating of RTDs half-bridge circuit with the size of $300 \times 250 \mu\text{m}^2$. Self-heating of RTD bridge circuit is originally a noise and a shortcoming to the thermal flow sensors [8-10]. We conventionally need to eliminate this noise by ways of reducing excitation (sensing) current or using pulse measurements. Our work is different from other conventional design by including a floating plate with resistive temperature detectors (RTDs) heated by a side heater [11, 12].

2. Fabrication Using CMOS MEMS Foundry

Taiwan Semiconductor Research Center (TSRI; old name CIC- Chip Implementation Center) provided low-price or even free CMOS foundry to academic researchers in Taiwan since 1992. The CMOS MEMS foundry was started in the 2000s, but the post process should be done by the applicants at that time. The high-quality foundry services provided by TSMC and UMC were highly welcomed over the past years. In 2019, UMC 0.18 μm process provided post processing of the fabricated chips with chip size of $1.5\text{mm} \times 1.5\text{mm}$. This CMOS MEMS foundry is of course the best candidate to implement the new flow sensor design in this work.

2.1 UMC 0.18 μm process

Based on the 0.18 μm standard CMOS foundry with MEMS post etching in UMC shown in Fig. 1(a) (this new service was announced and call-for designs in 2019), people can easily design and implement the capacitive sensors and actuators like comb-drives by the freestanding multiple metal layers M1-M6. However, the process flow of Fig. 1(a) is not directly suited for MEMS device with polysilicon sensing elements which will be damage during the isotropic undercut etching in the final step of the post process. The gate oxide thickness is probably 4 nm and hard to protect the polysilicon gate/sensor from the final undercut etching. Herein the authors propose using the much thicker shallow-trench-isolation (STI) oxide to protect polysilicon during the final undercut etching, shown in Fig. 1(b). Placing the polysilicon patterns above STI is a violation to the design rule check (DRC) initially. The authors received the understanding permission from TSRI, but this DRC violation is only available in the MEMS region rather than the IC region.

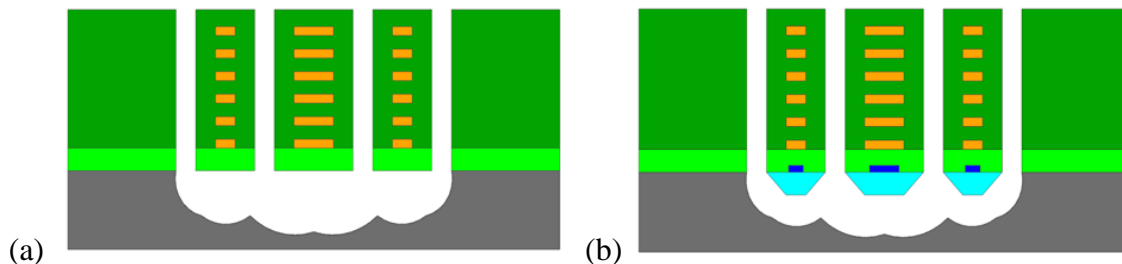


Figure 1. (a) UMC 0.18 μm standard process, the MEMS post process including the anisotropic deep trench etching and the isotropic undercut etching; (b) Proposed new layout of using STI (shallow trench isolation; light-blue color) to protect polysilicon (dark-blue color) during the isotropic undercut etching

3. Principle of operation

We purposely increase the self-heating power of the RTDs and turn off the heater aside the RTDs. We only adopt a half-bridge composing of 2 RTDs in series. One is on the substrate and the other is on the MEMS cavity or the floating plate region which provides a good thermal isolation. If the RTD half bridge in Fig. 2 is small enough, the temperature rise due to the self-heating should be apparent for thermal detection [13].

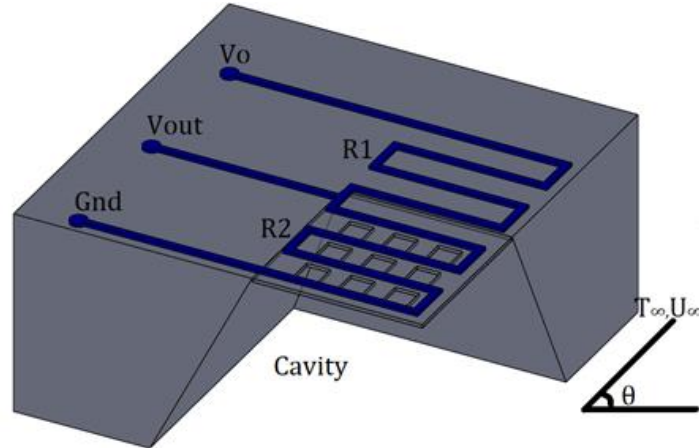


Figure 2. The self-heating RTDs with the configuration of half-bridge for measuring wind speed

3.1 Convert self-heating noise into useful signal

Assume R_0 is the design resistance value ($1k\Omega$) of one RTD with temperature coefficient of resistance TCR. Due to the self-heating of the bias voltage V_0 for both R_1 and R_2 in Fig. 1 under zero wind velocity, the self-heating temperature rise is assumed as ΔT_0 for both R_1 and R_2 .

$$R_1 = R_2 = R_0[1 + (TCR)(\Delta T_0)] \quad (1)$$

As the wind velocity increases across the biased RTDs, both RTDs experience temperature drop, but the cooling effect of R_1 on the silicon substrate is better than that of R_2 on the MEMS cavity, the thermal isolated area. So, the rise of temperature ΔT_2 of R_2 is greater than ΔT_1 of R_1 . ($(\Delta T_2 - \Delta T_1) > 0$.) R_1 and R_2 are shown as below.

$$R_2 = R_0[1 + (TCR)(\Delta T_0 - \Delta T_2)] \quad (2)$$

$$R_1 = R_0[1 + (TCR)(\Delta T_0 - \Delta T_1)] \quad (3)$$

The output voltage of the half-bridge in Fig. 1 due to the temperature difference between ΔT_2 and ΔT_1 is a function of wind velocity and can be measured as:

$$V_{out}/V_0 = (0.5)[1 + (TCR)(0.5)(\Delta T_2 - \Delta T_1)] \quad (4)$$

We can observe that the output voltage V_{out} is not explicitly expressed with the self-heating temperature rise ΔT_0 . However, ΔT_0 still locates a ceiling limit for the two cooling drops ΔT_2 and ΔT_1 to reach gradually. By the one-dimensional, steady state thermal resistance analysis of heat conduction about Fig.1 configuration, the output voltage change due to the temperature difference $\Delta T_2 - \Delta T_1$ in Eq. (4) can be calculated and plotted in Fig. 2 even though the R_1 and R_2

resistors are very close to each other in the real CMOS MEMS fabrication. From Eq. (4), the output voltage change is first estimated as 0.125-0.5 mV by 1 V DC bias per 1 m/s velocity change if the TCR values are 500-2000 ppm/K [14].

The function which describes the relation between the velocity and the temperature of the RTD is shown in Eq. (5). The flapping frequency is very low and considered as in steady state.

$$N_u = 0.664 \times (Re^{1/2}) \times (Pr^{1/3}) \quad (5)$$

3.2 Transfer block of flow sensor

The primary level of strategy implementation is shown below in Fig. 3. The design depiction of the sensor is first calculated theoretically by setting up the desired values, which is the conception and construction of the framework that underpins the major operation plan and its subsequent execution. It decreases the resistance value when the velocity is gradually increased, thereby creating an unbalance voltage output.

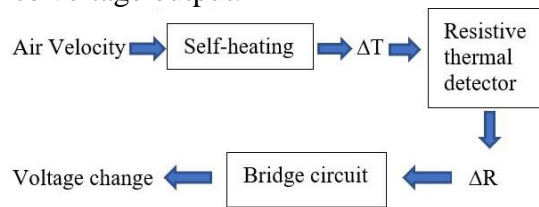


Figure 3. Transfer block for the flow sensor operation

3.3 Layout Design in CADENCE

The total chip area for applying a free service from TSRI is 1.5 mm × 1.5 mm, which is much larger than our need for the flow sensor design. Therefore, the authors added some additional devices for further verification and investigation of the flow sensor design. The MEMS sensor layout designed by Cadence software is shown in Fig. 4(a), and the white color metal-mesh area is filled with several MEMS open area filled with MEMS cavity holes with hole size of 8 μm as shown in Fig. 4(b).

The MEMS area includes the center heater and two (upstream and downstream) RTDs whose resistance are changed with wind speed. The center resistor is designed as 10 KΩ and the RTD's resistance is 1 KΩ for each. An identical flow sensor pattern on the upper half of Fig. 4(a) is the dummy device without MEMS cavity underneath.

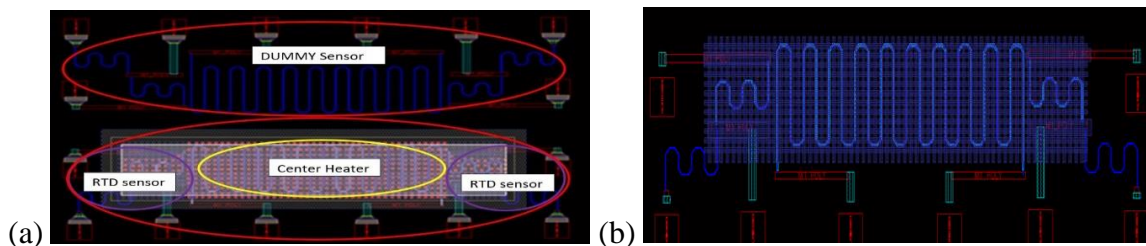


Figure 4. (a) Cadence layout of the flow sensor; (b) MEMS open area filled with many cavity holes of (8 μm)²

3.4 Microscopic observation

After the CMOS MEMS foundry, the microscopic observation of the received chips from TSRI are shown in Fig. 5. The resistance error between the design values and the measured values after the foundry is found to be 4-6.8%.

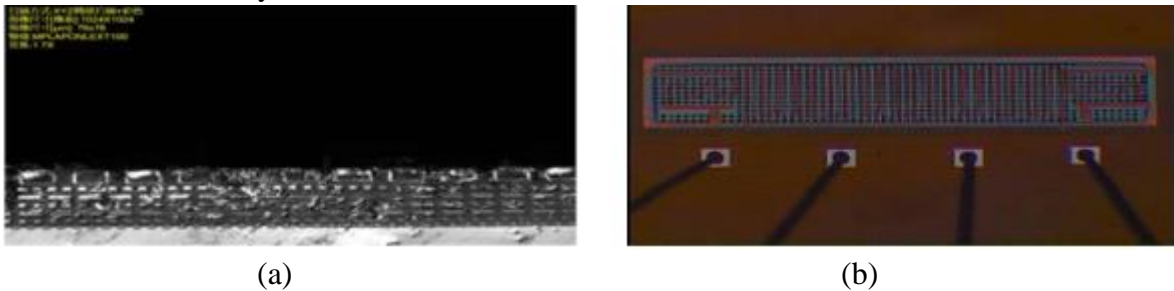


Figure 5. CMOS MEMS flow sensor chips of the design in Fig. 4. (a) Confocal microscope (cross section view); (b) Optical microscope (top view)

3.5 18 pin packaging style of TSRI

The MEMS area includes the center heater and two (upstream and downstream) RTDs whose resistance are changed with wind speed. The center resistor is designed as 10 K Ω and the RTD's resistance is 1 K Ω for each. An identical flow sensor pattern on the upper half of Fig. 4(a) is the dummy device without MEMS cavity underneath. The MEMS sensor chip packaging herein is shown in Fig. 6 and is also provided by TSRI.

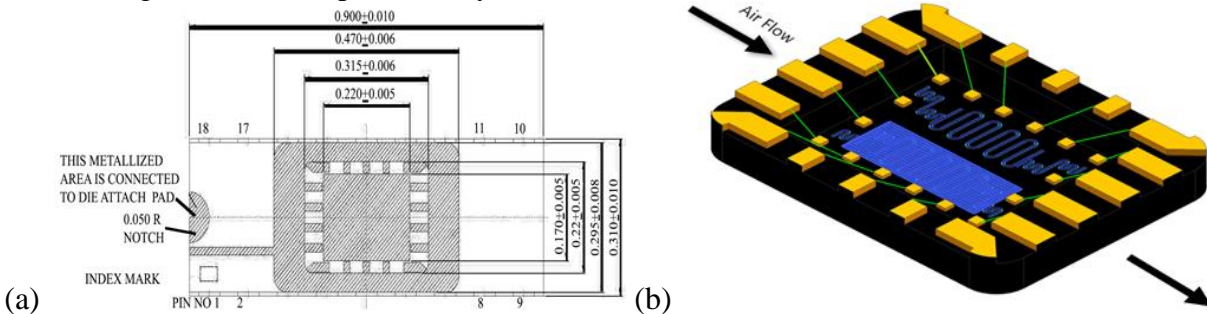


Figure 6. (a) 18-pin packaging design provided by TSRI; (b) CMOS MEMS flow sensor with package

4. Wind tunnel testing

Of many flow sensing method, thermal flow sensors have simple and easy to implement structure. The design was made using CADENCE software. The designed, fabricated CMOS MEMS flow sensor of Figs. 4 and 6 after packaging is validated by keeping the sensor packaged chip in a low-speed wind tunnel, and calibration is done for the wind speed ranging from 0-15 m/s. The flow sensor setup in Fig. 7(a) is apparently output signal changed with wind velocity under the inclined angle more than 60°. As temperature changes, its resistance value changes. When the velocity increases, resistance value decreases, thus, it generates an unbalance voltage output.

With application of the bias voltage of 1.8 V for the half bridge RTDs (1 K Ω each) and the center heater (10 K Ω), the overall self-heating power is 1.62 mW from the RTDs themselves. The nearby center heater dissipates only 0.324 mW and has almost no thermo-fluidic effect on the flow sensor temperature change. Figure 7(b) presenting the two output voltages vs. wind velocity of the upstream (left) and downstream (right) half-bridged RTDs. Both self-heating flow sensors have the same normalized sensitivity of 138 $\mu\text{V/V}/(\text{m/s})/\text{mW}$ if counting only one RTD

dissipating power of 0.81 mW. Compared to the claimed resolution towards micrometer per second and the normalized sensitivity of $155 \mu\text{V}/\text{V}/(\text{m/s})/\text{mW}$ of Lee's work in MEMS'20, our design without any signal filtering and amplification herein achieved 89% of Ref. [15]. The output performance variation denotes the intrinsic influence by the packaging issue of flow sensors [16, 17].

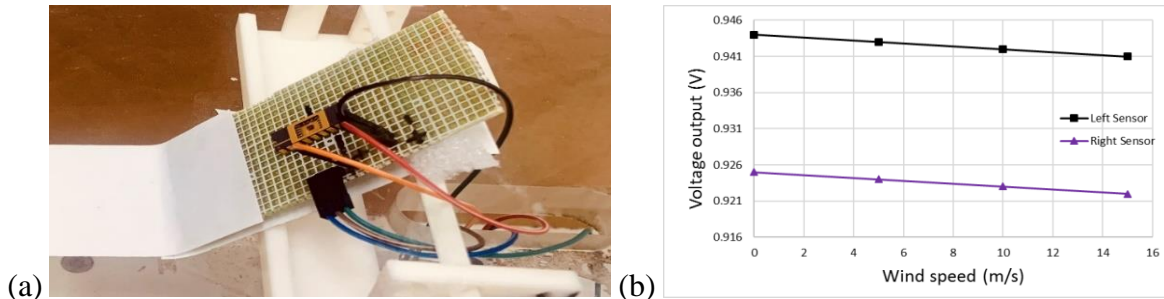


Figure 7.(a) Sensor board on an inclined stage in the wind tunnel; (b) Output signals of the two half-bridged (upstream and downstream) RTDs with the same sensitivity value of $138 \mu\text{V}/\text{V}/(\text{m/s})/\text{mW}$

5. Applications

Researches regarding the FWMAV improvement need the on-site lift information and measurement. In this case, microelectromechanical systems (MEMS) flow sensors on a flapping wing can be helpful in detecting real-time downwash and lift. Furthermore, this type of CMOS-MEMS flow sensor will be promising flow measuring device for various range of wind speed and different kind of applications [18, 19], it became utmost important for this type of flow sensors to emerge its design in applications for on-site lift measurement in micro air vehicles (MAVs), wind turbines, biomedical purpose, and so on. Lift data can be gathered from the downstroke and upstroke motions of a full flapping cycle. There are several ways for lift improvement, for instance, by increasing the wing foil thickness and the camber [20], by adding wing corrugation [21], by enlarging the stroke angle [22], using wing rotation mechanisms [23], using morphing wings [24-26], by changing the wing materials [27-29], or by adjusting the wing stiffness along the chord-wise/ span-wise direction [30]. Fig. 8(a) and (b) shows the sensor application on wing membrane to measure the lift during downstroke and upstroke.

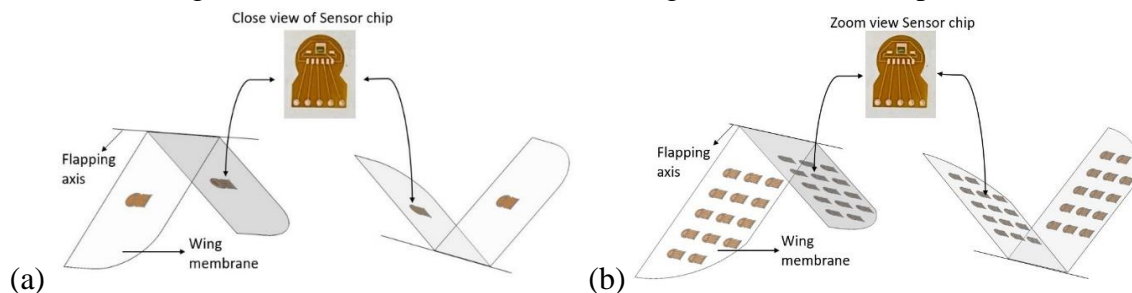


Figure 8. (a) Downstroke flapping and upstroke flapping with single sensor mounted on the wing surface; (b) Downstroke flapping and upstroke flapping with multiple sensors mounted on the wing surface

6. Conclusion

The CMOS sensor design is made using U18MEMS process, which combines UMC $0.18\mu\text{m}$ 1P6M process along with MEMS post process. The measured sensitivities of the CMOS

flow sensor are close to the 1st estimation by the thermal resistance analysis in the initial stage design. Three main findings are as follows:

(1) A new design concept of self-heating half-bridges RTDs is proposed. It successfully converts the role of self-heating from a noise to a useful sensor driving.

(2) The sensor size is as small as $300 \times 250 \mu\text{m}^2$ size and asked for the CMOS MEMS foundry service of UMC 0.18 μm standard process with MEMS post etching process. Polysilicon is assigned as the RTD material and STI is used as the protection layer during the post etching process.

(3) A normalized sensitivity of $138 \mu\text{V/V}/(\text{m/s})/\text{mW}$ within the wind velocity range of 0-15 m/s was measured in a wind tunnel. This sensitivity is 89% of Y.-K. Lee's work in IEEE MEMS 2020 [15]. The dummy specimen test and the orientation-free test in the wind tunnel were also done.

Currently, the CMOS MEMS flow sensor design is made without any instrumentational amplifier, hence, in future work our research team is planning to add an amplifier to give a better output result.

Acknowledgments

This work is financially support by Ministry of Sci. and Tech. of Taiwan with the project number of MOST 109-2221-E-032-001-MY3. The CMOS MEMS foundry service provided by TSRI is highly appreciated.

References

- [1] Narásek, M. *et al.* (2018), "A Tailless Aerial Robotic Flapper Reveals that Flies Use Torque Coupling in Rapid Baked Turns", *Science*, Vol. 361, pp. 1089–1094.
- [2] Phan, H. V. and Park, H. C. (2020), "Mechanisms of Collision Recovery in Flying Beetles and Flapping-Wing Robots", *Science*, Vol. 370, pp. 1214-1219.
- [3] Yang, L. J. *et al.* (2012), "Wing Stiffness on Light Flapping Micro Aerial Vehicles", *Journal of Aircraft*, Vol. 49(2), pp. 423-431.
- [4] Yang, L.J. *et al.* (2020), "Inertial Effect on the Time-Averaged Lift of Flapping Wings", *Journal of Applied Science and Engineering*, Vol. 23, pp. 357-359.
- [5] Yang, L.J. *et al.* (2021), "Check-Valve Design in Enhancing Aerodynamic Performance of Flapping Wings" *Applied Sciences*, Vol. 11(8), p.3416.
- [6] Bronz, M. *et al.* (2009), "Towards a Long Endurance MAV", *International Journal of Micro Air Vehicles* 2009, Vol. 1(4), pp. 241-254.
- [7] Nguyen, Q.V. *et al.*, (2010), "Measurement of Force Produced by an Insect-Mimicking Flapping-Wing System", *Journal of Bionic Engineering*, Vol. 7, pp. S94-S102.
- [8] Kuo, J. T. *et al.* (2012), "Micromachined thermal flow sensors—A review", *Micromachines*, vol. 3, pp. 550-573.
- [9] Xu, W. *et al.* (2019), "A CMOS-MEMS Thermoresistive Micro Calorimetric Flow Sensor with Temperature Compensation", *J. Microelectromech. Syst.*, vol. 28, no. 5, pp. 841-849.
- [10] Hagleitner, C. *et al.* (2001), "Smart single-chip gas sensor microsystem", *Nature*, vol. 414, pp. 293-296.
- [11] Bruschi, P., *et al.* (2009), "A single chip, double channel thermal flow meter", *Microsyst.*

Technol., vol. 15, pp. 1179-1186.

[12] Ahmed, M. *et al.* (2019), “Fully Integrated Bidirectional CMOS-MEMS Flow Sensor with Low Power Pulse Operation”, *IEEE Sens. J.*, vol. 19, pp. 3415-3424.

[13] Kovacs, G. T. A. (2000), “Micromachined Transducers Sourcebook”, McGraw-Hill, p. 565, 2000.

[14] Chuang, H. M. *et al.* (2003), “Temperature-dependent characteristics of polysilicon and diffused resistors”, *IEEE Transactions on electron devices*, Vol. 50(5), 1413-1415.

[15] Xu, W. *et al.* (2020), “An Integrated CMOS MEMS Gas Flow Sensor with Detection Limit towards Micrometer Per Second”, in *Proc. of IEEE MEMS Conference*, Vancouver, Canada, Jan. 18-22, pp. 200-203.

[16] Xu, W. *et al.* (2017), “Systematic Study of Packaging Designs on the Performance of CMOS Thermoresistive Micro Calorimetric Flow Sensors”, *Journal of Micromechanics and Microengineering*, vol. 27, p.085001.

[17] Dumstorff, G. *et al.* (2015), “Investigations into Packaging Technology for Membrane-Based Thermal Flow Sensors”, *Journal of Sensors and Sensor Systems*, vol. 4, no. 1, pp. 45-52.

[18] Ejeian, F. *et al.* (2019), “Design and Applications of MEMS Flow Sensors: A Review”, *Sensors and Actuators A: Physical*, vol. 295, pp. 483-502.

[19] Silvestri S. and Schena E., (2012), “Micromachined flow sensors in biomedical applications”, *Micromachines*, Vol. 3(2), pp. 225-243.

[20] Ashraf, *et al.* (2011), “Reynolds Number, Thickness, and Camber Effects on Flapping Airfoil Propulsion”, *Journal of Fluids and Structures*, Vol. 27, pp. 145-160.

[21] Yang, L. J., *et al.*, (2021), “Fabrication, Aerodynamic Measurement and Performance Evaluation of Corrugated Flapping Wings”, *Journal of Aeronautics, Astronautics and Aviation*, Vol. 53(1), pp. 83-94.

[22] Keennon, M. *et al.* (2012), “Tailless Flapping Wing Propulsion and Control Development for the Nano Humming Bird Micro Air Vehicle”, *American Helicopter Society Future Vertical Aircraft Design Conference*, SanFrancisco, California, USA, Jan. 18-20.

[23] Dickinson, M. D. *et al.* (1999), “Wing Rotation and the Aerodynamic Basis of Insect Flight”, *Science*, Volume 284, pp. 1954-1960.

[24] Ismail, N. I. *et al.* (2014), “Optimization of Aerodynamic Efficiency for Twist Morphing MAV Wing. *Chinese Journal of Aeronautics*, Vol. 27(3), pp. 475-487.

[25] Chang, E. *et al.* (2020), “Soft Biohybrid Morphing Wings with Feathers Underactuated by Wrist and Finger Motion”, *Science Robotics*, Vol. 5(38).

[26] Matloff, L. Y. *et al.* (2020), “How Flight Feathers Stick together to Form a Continuous Morphing Wing” *Science*, Vol. 367(6475), pp. 293–297.

[27] Nguyen, Q.V. *et al.* (2010), “Measurement of Force Produced by an Insect-Mimicking Flapping-Wing System”, *Journal of Bionic Engineering*, Vol. 7, pp. S94-S102.

[28] Yang, L.J. and Suseendar, M. (2015), “Acoustic Comparison of PET and Latex Wings for Flapping Micro-Air-Vehicles”, *Proc. of the 10th IEEE International Conference on Nano/Micro Engineered and Molecular Systems (IEEE-NEMS)*, Xi’an, China, 7-11 Apr, pp. 172-174.

[29] Wei, G. *et al.* (2018), “Self-Powered Hybrid Flexible Nanogenerator and Its Application in Bionic Micro Aerial Vehicles” *Nano Energy*, Vol. 54, pp. 10-16.

[30] Combes, S. A. and Daniel, T. L. (2003), “Flexural Stiffness in Insect Wings I. Scaling and the Influence of Wing Venation”, *Journal of Experimental Biology*, Vol. 206(17), pp. 2979-2987.

Characteristic of Paddle Squeezing Angle and AMBU Bag Air Volume in Bag Valve Mask Ventilator

Cong Toai Truong³, Kim Hieu Huynh³, Van Tu Duong^{1,2,3*}, Huy Hung Nguyen^{3,4}, Le An Pham⁵, and Tan Tien Nguyen^{1,2,3*}

¹Faculty of Mechanical Engineering, Ho Chi Minh City University of Technology (HCMUT), 268 Ly Thuong Kiet, District 10, Ho Chi Minh City, Vietnam

²Vietnam National University Ho Chi Minh City, Linh Trung Ward, Thu Duc District, Ho Chi Minh City, Vietnam

³National Key Laboratory of Digital Control and System Engineering (DCSELab), HCMUT, 268 Ly Thuong Kiet, District 10, Ho Chi Minh City, Vietnam

⁴Faculty of Electronics and Telecommunication, Saigon University, Vietnam

⁵Grant and Innovation Center (GIC), University of Medicine and Pharmacy at Ho Chi Minh City

*Corresponding author: dvtu@hcmut.edu.vn, nttien@hcmut.edu.vn

Abstract

In the COVID-19 period, the number of deaths increases every day around the world. The pandemic has impacted life and economy. There is a shortage in medical service, including a lack of technology, facility and equipment. Among those, ventilator is an essential equipment that hospital does not have enough. A ventilator is an essential unit in hospitals because it seems to be the first step to protect the life of the patient. Some low-income countries aim to make a simple ventilator using locally available and low-cost materials for primary care and palliative care. One simple principle of ventilators is to adopt an artificial manual breath unit (AMBU) bag with paddles. Unfortunately, the squeezing angle of paddles is not proportional to the exhaust air volume from the AMBU bag. This paper analyzes the character of the squeezing angle of the paddles and the exhaust air volume of the adult AMBU bag through experiments. The result can be used to control the squeezing angle through a DC motor mounted with paddles to obtain the desired air volume.

Keywords: simple ventilator, AMBU bag, Covid19, bag valve mask

1. Introduction

The coronavirus (COVID-19) pandemic is very complicating and multi-staged. Currently, COVID-19 has many dangerous strains and has not shown signs of decreasing around the world. Besides that, COVID-19 patients must be treated with ventilators which have many higher functional requirements in Intensive Care Unit, but also need a simple assist ventilator in primary, palliative care, and safety transportation. Thus, the number of modern-ventilator is a big challenge for the health (Ercole *et al.*, 2009; P Smetanin, D Stiff, A Kumar, P Kobak, R Zarychanski, N Simonsen, 2009; Stiff *et al.*, 2011; Wiederhold and Riva, 2013), especially in developing countries (Fisher and Heymann, 2020; The Lancet, 2020; WHO, 2020). Several attempts have been made to create low-cost ventilators (Russell and Slutsky, 1999; Fang *et al.*, 2020). In particular, there are machines operating using grippers (Kwon *et al.*, 2020) to deal with the overload of COVID-19 cases. Medically, although some studies showed that the two-handed mask-face technique is prone to be better than one-handed mask-face technique (Jesudian *et al.*, 1985; Wheatley *et al.*, 1997; Davidovic, LaCovey and Pitetti, 2005; Joffe, Hetzel and Liew, 2010), in some emergency situations, the one-handed technique is still applied due to the lack of AMBU compression which can be conducted by the ventilator using the grippers. Therefore, this type of ventilator is very essential which has the advantages of easy manufacturing and

assembly, low cost, easy-to-find materials and control volume adjustment according to the angle of the paddles. However, the biggest difficulty when developing the BVM ventilator is that it is quite difficult to identify the mathematical model of the AMBU bag, making the control process complicated. To be more specific, during the development the BVM ventilator, the most important device is the AMBU bag (not only standard in ER, but also very popular in primary care), defining the characteristic correlation between the squeezing angle of the ventilator and the volume exiting the AMBU bag contributes to the development of controllers that allows the ventilator to achieve better controlling performance in volume-controlled mode. Therefore, this paper studies BVM ventilators in order to investigate the characteristic of the grippers angle of the BVM ventilator and the air volume exiting the AMBU bag. To achieve the result, the experiment was conducted by controlling the gripper to rotate at a random angle in each cycle, within the limitation of the paddles' angle before reaching the safety limit switch. The obtained data includes the squeezing angle measured from the motor encoder and the volume exiting the AMBU bag calculated from the flow value read from the flow sensor. The flow sensor has been calibrated to zero in normal condition, and the air volume calculation is conducted by integrating the flow value slices along time from the beginning of the inhalation to the beginning of the exhalation. The interpolation function is determined from the least squares regression method and the acceptability of the interpolation function is evaluated from the correlation coefficient, root mean square error, sum square error and mean absolute error value. Through analyzing and building characteristics based on simulation and experiment, this research finds out the relationship between the paddles and the AMBU bag (for adults), and the mathematical model of the relationship between grippers angle and exhausted air volume is obtained.

2. Materials and Methods

2.1 Overall system description

Breath circuit is depicted in Figure 1 with the usage of bag valve mask ventilation system. At the inspiration phase, two paddles squeeze the artificial manual breath unit (AMBU) bag, which allows oxygen to move from the air mixer through the humidifier and the HEPA filter into the patient's lungs. Following this is the spontaneous exhaling of the patient into the external environment due to the elasticity of the lungs and the operation of the one-way valve. The positive end-expiratory pressure (PEEP) valve should be placed closed to the patient wearing a mask in order to avoid exceed pressure in the lung. The working principle of PEEP van is that the patient exhales against a spring, and PEEP valve is used to keep up the pressure higher than an adjustable value that keeps the alveoli from collapsing in the expiration phase. Air mixture is humidified and warmed before ventilating by the humidifier. HEPA filter is used for removing harmful elements in the air such as dust, pet dander, etc. Besides, for the purpose of avoiding barotrauma, a relief valve is placed close to the patient which prevents overpressure during the breath.

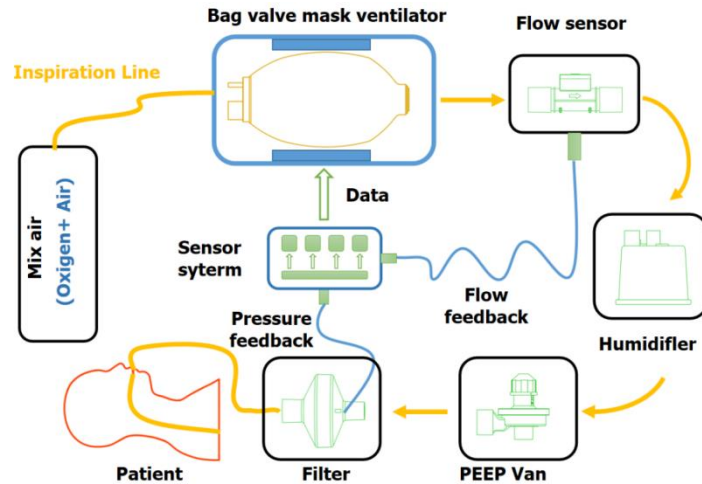


Figure 1. The operating system of bag valve mask ventilator

2.2 Bag Valve Mask Ventilator

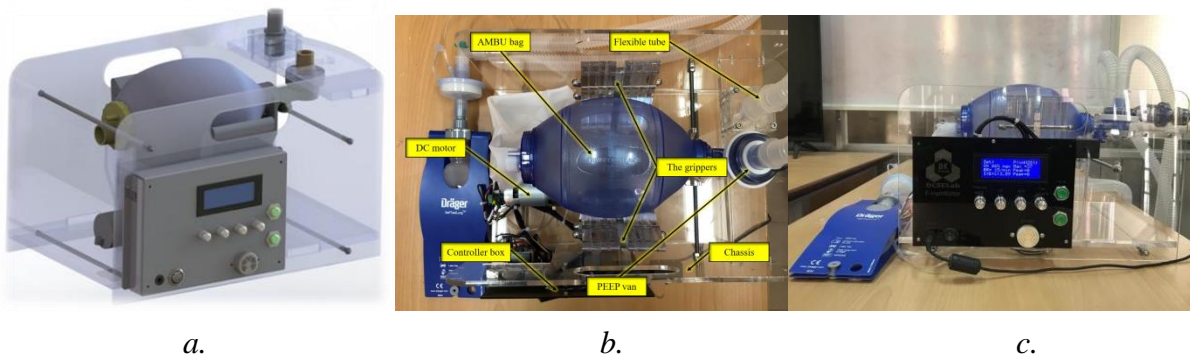


Figure 2. The modeling to show the relationship between the grippers and AMBU bag

Figure 2a shows a 3D model of a ventilator operating based on BVM system. Figures 2 b, c shows the experimental model of the machine with the listed components, including AMBU bag, flexible tube, PEEP valve, the grippers, DC motor, and controller box. The operation of the BVM ventilator is started by pressing the Start/Home button in order to return the two clamps to its home position by sensing the signal from a limit switch. After the homing process, the clinicians can vary the parameters displayed on the ventilator's LCD, including V_T , $I:E$, RR , PIP . In addition, there are two other parameters displayed on the ventilator, the PEEP value and the current pressure on the breath circuit. After the initial setting, the clinicians can press the Start/Home button again to confirm the parameter change and allow for the machine to operate. Following this is the squeezing of the two paddles at regular cycle. The BVM might generate a warning in the following cases: the current pressure exceeds the PEEP and PIP limit range; the doctor set the parameters without pressing Start/Home button to confirm; the squeezing angle of the paddles exceeds the limitation large and reaches the safety limit switch.

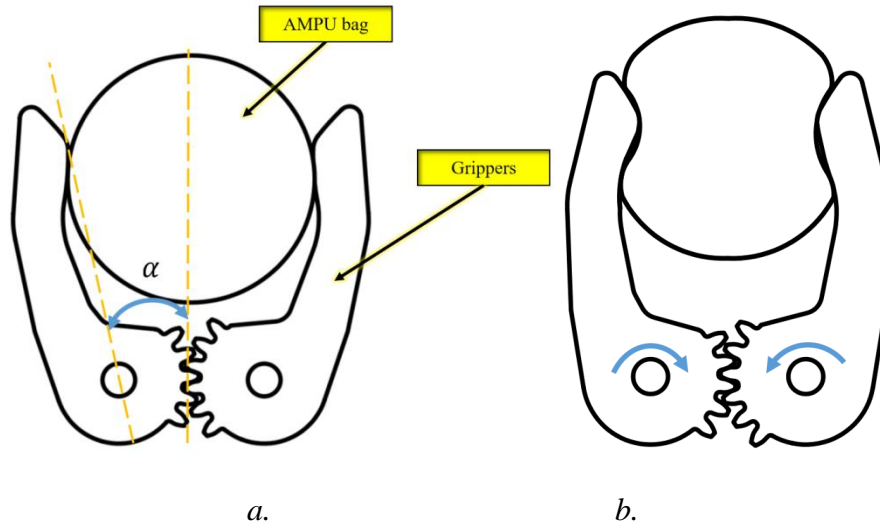


Figure 3. Determination between grippers and AMBU bag

Figure 3 shows the angle (α) and grippers of projection directly in the front view of the BVM. Figure 3a shows the state of grippers and AMBU bag in the homing position. In this initial position, the gripper touches the AMBU bag. In this position, α is conceptualized as the initial angle of the system, which is adjusted based on the position sensor to ensure the BVM start position. When the BVM is operating, the motor providing torque to the grippers by the gear transmission. The grippers of BVM impact the AMBU bag causing the bag to deform without a fixed shape as shown in Figure 3b. Therefore, the squeezing angle causes the exhausted air volume to change nonlinearly, which make it difficult to determine the tidal volume of air traveling into the patient's lungs. In particular, the silicon mechanical properties of AMBU bags makes determining the exhausted air volume more difficult. Thus, to solve this issue, the calculation of the α and the volume of the AMBU are carried out as a basis for the controller studies in the next section.

2.3 Theoretical basis

The AMBU bag adopted for this research is adult unit. Thus, the specification on the AMBU bag is referred to (UW Health, 2019) and shown in Table I.

Table I. Manual-Resuscitator of AMBU Adult

Body weight	> 40kg
Stoke volume	800 ml
Resuscitator volume	1650 ml
Dimensions (Length x Diameter)	212x131 mm
Bag reservoir volume	2000 ml

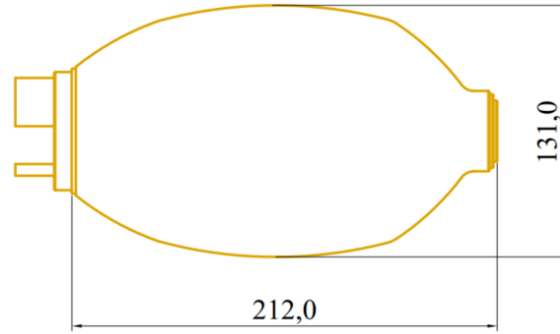


Figure 4. Dimension 2D of AMBU bag

Due to the circular shape, the volume of the AMBU bag is approximated by the following integral:

$$V = \pi \int_{\alpha}^{\beta} f(x)^2 dx \quad (1)$$

Where, $(\alpha, \beta) = [-106; 106]$; $f(x)$ is the AMBU contour curve equation. According to Table 1, the AMBU's volume provided by the manufacturer is equal to 1650ml. Eq. (1) becomes:

$$\pi \int_{\alpha}^{\beta} [f(x)]^2 dx = 1650 \quad (2)$$

$$\Leftrightarrow \int_{-110}^{110} [f(x)]^2 dx = \frac{1650}{\pi} \quad (3)$$

Solving Eq. ((3)) for $f(x)$ is very complicated, therefore, we approximate $f(x)$ as a quadratic function satisfying the following conditions (Otten *et al.*, 2014) :

$$f(x = -106) = f(x = 106) = 0 \quad (4)$$

$$f(x = 0) = 65.5 \quad (5)$$

$$f(x) = ax^2 + bx + c \quad (6)$$

By substituting Eq. (4) – (5) into Eq.(6)(3), $f(x)$ becomes:

$$f(x) = -0.00583x^2 + 65.5 \quad (7)$$

Substitute Eq. (7) (8) into Eq. (3) , it yields:

$$V = \pi \int_{\alpha}^{\beta} [f(x)]^2 dx = \frac{\pi}{1000} \int_{-106}^{106} (-0.00583x^2 + 65.5)^2 dx \approx 1523.87 \text{ (ml)} \quad (8)$$

The approximate contour equation of the AMBU bag gives the bag's volume error of 7.6% compared to the volume value provided by the manufacturer.

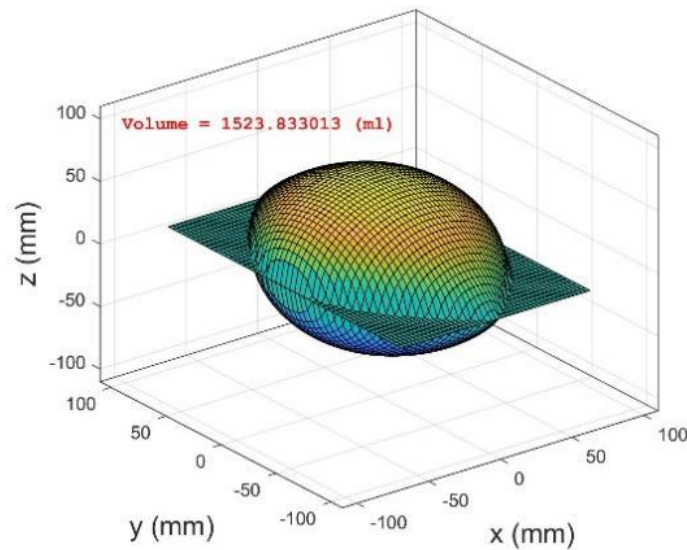


Figure 5. Simulation of AMBU bag by linear interpolation method

When it comes to simulation, the volume result of AMBU bag calculated by linear interpolation is approximately 1523.87 ml . Approximating the squeezing process with the exhaust air from the AMBU bag being outside the $x = -d$ and $x = d$ planes. Assuming $d = 30 \text{ mm}$, the remaining volume of the AMBU bag is calculated by the following simulation.

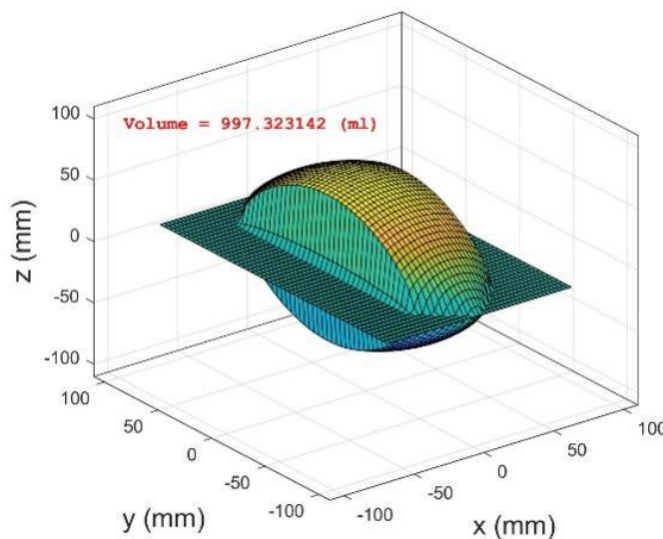


Figure 6. Simulation of AMBU bag at $d = 30 \text{ mm}$

According to Figure 6, the remaining air volume in the AMBU bag is $\approx 997.32 \text{ (ml)}$, the exhaust air volume is therefore calculated as $\approx 526.51 \text{ (ml)}$. Given the increasing of α from 0° (home position) to 32° , we determine the graph of the characteristic of the grippers angle α and the exhaust air volume V_T :

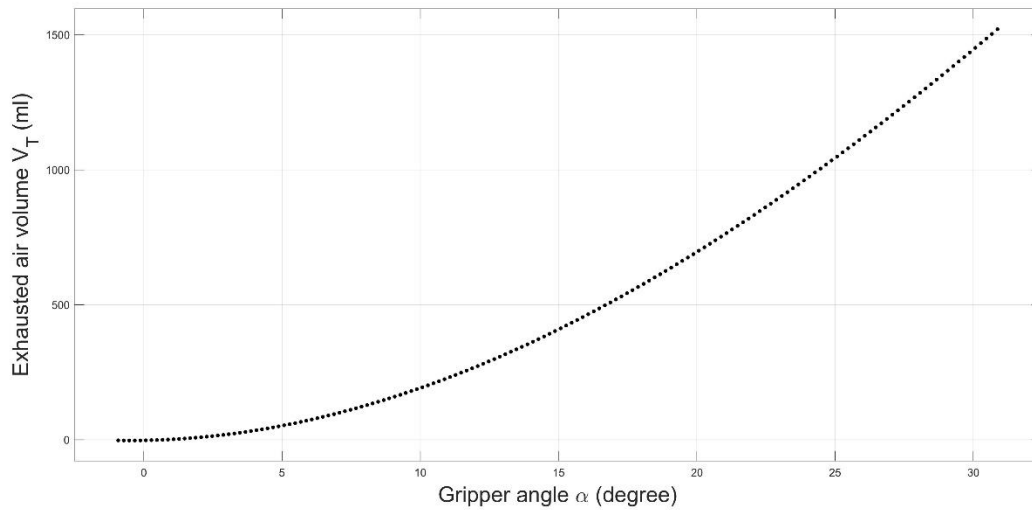


Figure 7. The characteristic of grippers angle and exhaust air volume from AMBU bag

The characteristic showed in Figure 7 is determined to be nonlinear. However, within the operation of the BVM ventilator, V_T has a range of 350ml to 700ml. Figure 8 displays the characteristic showed in Figure with V_T being within the required range.

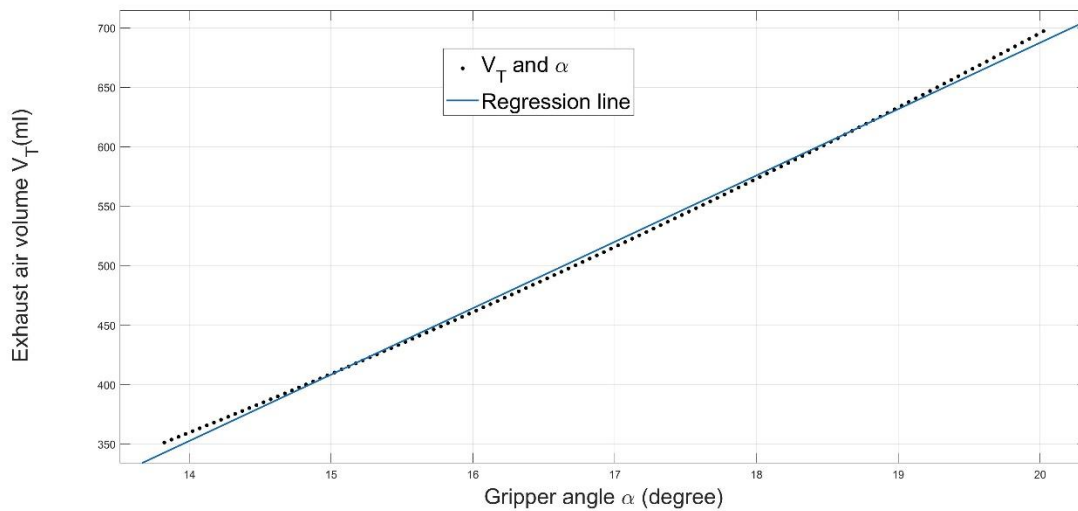


Figure 8. The characteristic of grippers angle and exhaust air volume from AMBU bag within the exhausted air volume range from 350ml to 700ml

The theoretical characteristic between grippers angle α (degree) and exhaust air volume V_T (ml) can be approximated as linear with the correlation coefficient $R \approx 0.9985$. The equation showing the relationship can be written as follow:

$$V_T(t) = 55.81 \times \alpha(t) - 428.6 \quad (9)$$

3. Experimental Result

To evaluate the theory, an experiment on the actual BVM ventilator model was conducted, the obtained data including grippers angle calculated from motor encoder and exhaust air volume calculated from flow sensor.

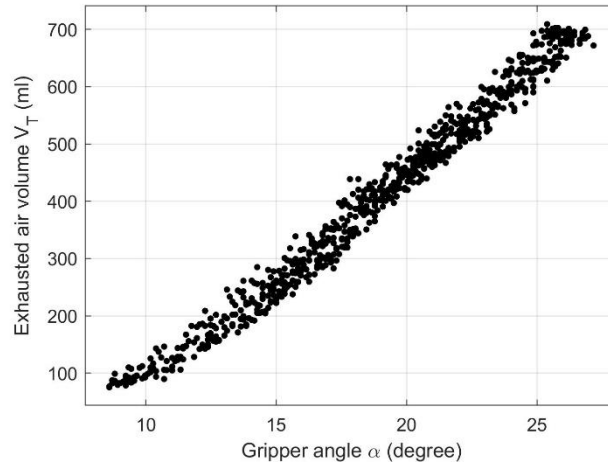


Figure 9. The experimental characteristic of grippers angle and exhaust air volume from AMBU bag

The nonlinearity of the characteristic shown in Figure 9 has been identified. It can be seen that the shape of the theoretical characteristic curve presented in Figure 7 is similar to the experimental one in Figure 9. Figure 10 shows the same feature as Figure 9, but with V_T inside the the operating range of the BVM ventilator ($350ml \div 700ml$).

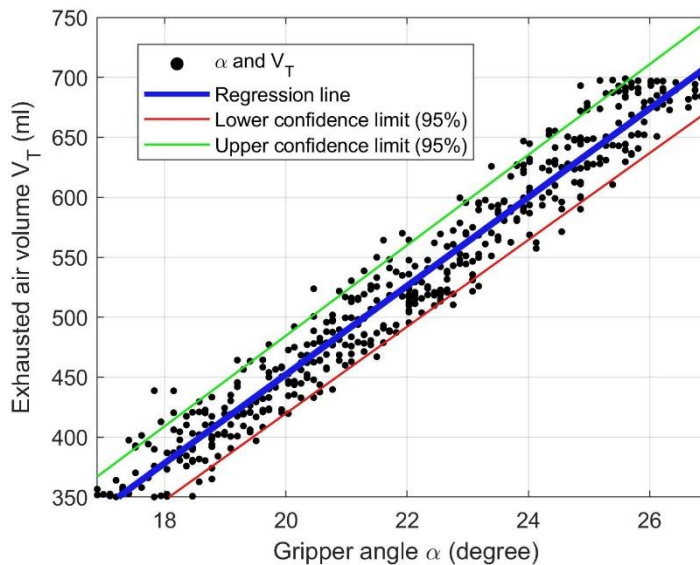


Figure 10. The experimental characteristic of grippers angle and exhaust air volume from AMBU bag with the exhaust air volume range from 350ml to 700ml

The experimental characteristic of the two variables V_T and α can be approximated as a linear function with the fitting properties presented in Table II.

Table II. Regression properties of experimental characteristic presented in Figure 10

Linear model Poly1	$V_T(t) = p_1 \times \alpha(t) + p_2$
Coefficients	$p_1 = 36.96 (36.19, 37.73)$
(95% confidence bounds)	$p_2 = -287.1 (-304.1, -270.1)$
Goodness of fit:	Sum square error (SSE): 22900(ml²) Coefficient of determination (R-square): 0.9505 Adjusted R-square: 0.9504 Root mean square error (RMSE): 22.17(ml)

The interpolation function has coefficient of determination of 0.9505. The sum square error is 22900(ml²) and root-mean-square error is 22.17(ml). In general, the actual and the theoretical equation has the same form of function, but the coefficients are different because the AMBU bag is dilated during squeezing, which make the exhausted air volume in the simulated model smaller than the actual model. In other word, the exhaust air volume AMBU in the simulation model is lower than that of the actual model with the same value of grippers angle. In short, V_T is approximated by two components, the linear component $\alpha(t)$ with slope $p_1 = 36.36$ and the constant component with the value of $p_2 = -287.1$.

$$V_T(t) = V_{T,1} + V_{T,2} = 36.96 \times \alpha(t) - 287.1 \quad (10)$$

In order to evaluate the regression result of the Eq. (10), another experiment was conducted. The scenario of the experiment consists of carrying out several times squeezing with fixed input gripper angles, the output exhausted air volume is obtained. The evaluation result is shown in Figure 11.

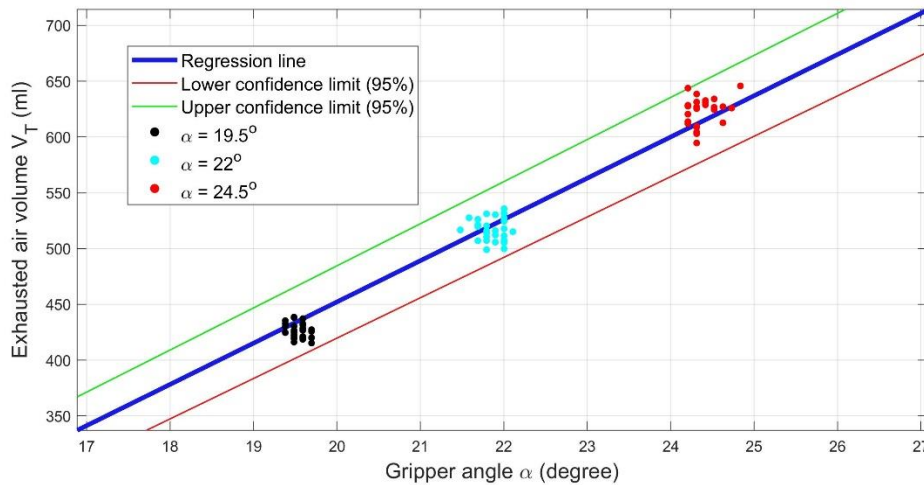


Figure 11. Evaluation of the regression line presented in Figure 10

It can be seen that the obtained exhausted air volumes are within the confidence limit lines. In a clearer way, at α equal to 19.5°, 22°, 24.5°, we calculate root mean square error values

(RMSE) and mean absolute error values (MAE) of the obtained exhausted air volume with respect to volume values calculated from the regression line. The results are shown in Table III for the purpose of evaluating the operating error of the ventilator compared to the regression line.

Table III. Operating error of the ventilator at fixed gripper angles compared to the regression line

Gripper angle	RMSE	MAE
$\alpha = 19.5^\circ$	9.9138 (ml)	6.1409 (ml)
$\alpha = 22.5^\circ$	11.6461 (ml)	9.6960 (ml)
$\alpha = 24.5^\circ$	13.9763 (ml)	10.1799 (ml)

4. Conclusions

As mentioned in Section 1, the correlation between the AMBU bag and the grippers angle is the most critical factor of the BVM ventilator, since the ventilation results depends mainly on the grippers' controlling results and the behaviors of the AMBU bag. Thus, determining the characteristic between the ventilator's gripper angle and the exhausted air volume of the AMBU bag plays an important role in improving the BVM ventilator controlling performance. Our research could have potential applications in the future when it comes to the production and the control of ventilators based on the BVM system. It can be seen that there were errors in the BVM ventilator modeling process. More specifically, although the coefficients of the simulated correlation equation between the gripper angle and the exhausted air volume are different compared to the experimental correlation, the simulated correlation equation and the experimental correlation equation still have the same form within the confidence limit. In short, based on the presented BVM ventilator modeling process, the result of this research make effort to reduce errors in future studies.

Acknowledgments

This research is supported by DCSELAB and funded by Vietnam National University Ho Chi Minh City (VNU-HCM) under grant number TX2021-20b-01. We acknowledge the support of time and facilities from Ho Chi Minh City University of Technology (HCMUT), VNU-HCM for this study. This research is also funded by Department of Science and Technology under grant number 58/2020/HĐ-QPTKHCN.

References

- [1] Davidovic, L., LaCovey, D. and Pitetti, R. D. (2005) 'Comparison of 1- versus 2-person bag-valve-mask techniques for manikin ventilation of infants and children', *Annals of Emergency Medicine*, 46(1), pp. 37–42. doi: 10.1016/j.annemergmed.2005.02.005.
- [2] Ercole, A. *et al.* (2009) 'Modelling the impact of an influenza A/H1N1 pandemic on critical care demand from early pathogenicity data: The case for sentinel reporting', *Anaesthesia*, 64(9), pp. 937–941. doi: 10.1111/j.1365-2044.2009.06070.x.

- [3] Fang, Z. *et al.* (2020) ‘AmbuBox: A Fast-Deployable Low-Cost Ventilator for COVID-19 Emergent Care’, *SLAS Technology*, 25(6), pp. 573–584. doi: 10.1177/2472630320953801.
- [4] Fisher, D. and Heymann, D. (2020) ‘Q&A: The novel coronavirus outbreak causing COVID-19’, *BMC Medicine*, 18(1), pp. 18–20. doi: 10.1186/s12916-020-01533-w.
- [5] Jesudian, M. C. S. *et al.* (1985) ‘Bag-valve-mask ventilation; two rescuers are better than one: Preliminary report’, *Critical Care Medicine*, pp. 122–123. doi: 10.1097/00003246-198502000-00015.
- [6] Joffe, A. M., Hetzel, S. and Liew, E. C. (2010) ‘A two-handed jaw-thrust technique is superior to the one-handed “EC-clamp” technique for mask ventilation in the apneic unconscious person’, *Anesthesiology*, 113(4), pp. 873–879. doi: 10.1097/ALN.0b013e3181ec6414.
- [7] Kwon, A. H. *et al.* (2020) ‘Rapidly scalable mechanical ventilator for the COVID-19 pandemic’, *Intensive Care Medicine*, 46(8), pp. 1642–1644. doi: 10.1007/s00134-020-06113-3.
- [8] Otten, D. *et al.* (2014) ‘Comparison of bag-valve-mask hand-sealing techniques in a simulated model’, *Annals of Emergency Medicine*, 63(1), pp. 6-12.e3. doi: 10.1016/j.annemergmed.2013.07.014.
- [9] P Smetanin, D Stiff, A Kumar, P Kobak, R Zarychanski, N Simonsen, F. P. (2009) ‘Potential intensive care unit ventilator demand / Canada’, *Journal of Infectious Diseases*, The, 20(4), pp. 115–123.
- [10] Russell, J. and Slutsky, A. (1999) ‘International consensus conferences in intensive care medicine: Ventilator-associated lung injury in ARDS’, *American Journal of Respiratory and Critical Care Medicine*, 160(6), pp. 2118–2124. doi: 10.1164/ajrccm.160.6.ats16060.
- [11] Stiff, D. *et al.* (2011) ‘Potential pediatric intensive care unit demand/capacity mismatch due to novel pH1N1 in Canada’, *Pediatric Critical Care Medicine*, 12(2), pp. 51–57. doi: 10.1097/PCC.0b013e3181e2a4fe.
- [12] The Lancet (2020) ‘COVID-19: too little, too late?’, *The Lancet*, 395(10226), p. 755. doi: 10.1016/S0140-6736(20)30522-5.
- [13] UW Health (2019) ‘Manual Resuscitator Bag’, *Department of Nursing*. Available at: <https://www.uwhealth.org/healthfacts/respiratory/7820.pdf>.
- [14] Wheatley, S. *et al.* (1997) ‘A comparison of three methods of bag valve mask ventilation’, *Resuscitation*, 33(3), pp. 207–210. doi: 10.1016/S0300-9572(96)01024-6.
- [15] WHO (2020) ‘Critical preparedness, readiness and response actions for COVID-19: WHO/2019-nCoV/Community_Actions/2020.3’, (March), pp. 1–3. Available at: <https://www.who.int/publications-detail/critical-preparedness-readiness-and-response-actions-for-covid-19>.
- [16] Wiederhold, B. K. and Riva, G. (2013) ‘Original research’, *Annual Review of CyberTherapy and Telemedicine*, 11, p. 63. doi: 10.1097/01.naj.0000529715.93343.b0.

Tracking of High-speed and Aggressively-maneuvered Aerial Targets by Kalman-Kernelized and Kalman-Discriminative Correlation Filters (K-KCF & K-DCF)

Shao Xuan Seah¹, Niven Junliang Sie² and Sutthiphong Srigrarom^{3,*}

¹Shao Xuan Seah is with National University of Singapore, 5A Engineering Drive 1, Singapore, 117411

Email: seahshaoxuan@u.nus.edu

²Niven Sie is with National University of Singapore, 5A Engineering Drive 1, Singapore, 117411

Email: e0201647@u.nus.edu

³S. Srigrarom is with National University of Singapore, 5A Engineering Drive 1, Singapore, 117411

Email: spot.srigrarom@nus.edu.sg

Abstract

In this work, we present an integrated target tracking method that combined the fast Kalman Filter for tracking initialization and the effective Kernelized Correlation Filter (K-KCF) and Discriminative Correlation Filter (K-DCF) for tracking continuation. Both K-KCF and K-DCF are able to track multiple high-speed and aggressively maneuvered aerial targets, especially drones, even if the target may cross-path with each other in camera view, in comparison to normal Kalman Filter (KF). We conducted test cases and compare the results from individual KF, KCF and DCF, together with K-KCF and K-DCF combinations. Our initial results show both K-KCF and K-DCF perform better than those individual filters. For long term tracking, together with varying target (drone) sizes, K-DCF performs better as it can handle and track the drone more continuously with less discontinuities compared to K-KCF. Hence, K-DCF is the preferred choice for tracking of fast and aggressively moving aerial targets.

1. Introduction

Over the years, small aircraft such as drones are becoming more accessible and affordable. This increases the importance of detection and tracking of aerial targets, especially drones, due to the cases of drones intruding areas such as airports and military bases. With the advancement of computer vision, aerial target detection using vision is preferable, as this technique is able to recognize the moving object more quickly and effectively at low cost comparing to other techniques [1].

In aerial target tracking, the tracking of small fast and aggressively maneuvered aerial targets (especially drones) have been of great interest nowadays, because the conventional tracking methods will not be able to track effectively. For example, Kalman Filter (KF) assumes either constant velocity or constant acceleration motion models. Similarly, Extended Kalman Filter (EKF) expects the target to follow certain smooth moving patterns [2]. While both models can track most common target motions well, they cannot track highly maneuvered drone, especially if those drones make high-speed sharp turn or U-turn. The example of such case of is shown in this Youtube link <https://youtu.be/GcJtVqOBXOs> and snap shot is shown in figure 1.



Fig 1. Example of small, fast and aggressively maneuvered drone flights

In this work, we proposed to combine Kalman-Kernelized Correlations Filter (K-KCF) as well as Kalman-Discriminative Correlation Filter (K-DCF) as a tool for tracking the small, fast and aggressively maneuvered aerial target. The Kalman filter with constant velocity is used for initializing the detection, whereas KCF or DCF is used for subsequent continuous tracking. The block diagram of the proposed K-KCF and K-DCF schemes for tracking aerial target is shown in Figure 2.

These subsequent sections explain the individual KF, KCF, DCF and our proposed K-KCF and K-DCF models.

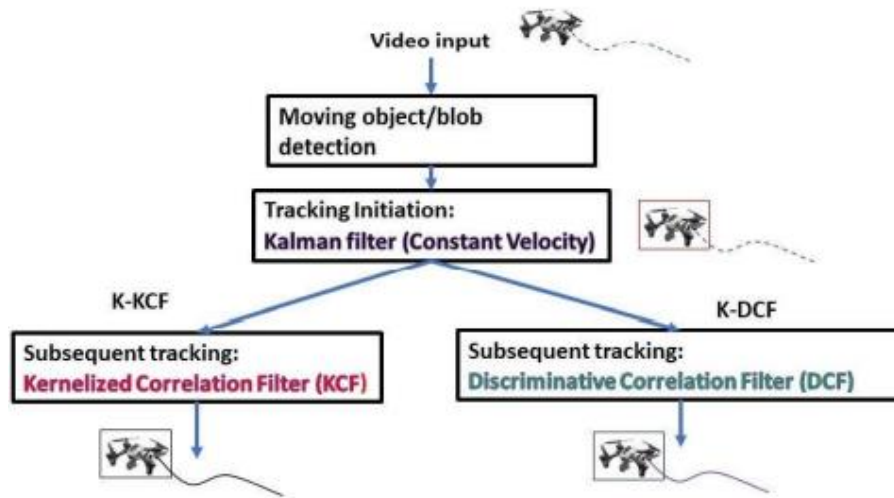


Fig 2. Block Diagram of K-KCF and K-DCF

2. Filter Models

2.1 Kalman Filter (KF)

The Kalman Filter (KF) is a well-known algorithm that estimates an unknown state of the system with given measurement over time. The algorithm consists of 2 stages: prediction and update [3].

Prediction:

$$X_k^- = FX_{k-1}^+ \quad (1)$$

$$P_k^- = FP_{k-1}^+ F^T + Q \quad (2)$$

Update:

$$K_k = P_k^- H^T (R + HP_k^- H^T)^{-1} \quad (3)$$

$$X_k = X_k^- + K_k (z_k - HX_k^-) \quad (4)$$

$$P_k^+ = (1 - K_k H) P_k^- \quad (5)$$

where subscript - and + denoted predicted prior to and post estimates. Here, we use KF with constant velocity (CV) motion model to predict the prior state estimate and update the Kalman Gain to obtain the state of the system for the current state.

The Constant Velocity (CV) model is used to model object traveling in constant velocity. The state is modeled by 4 states, $[x, y, v_x, v_y]$. The state transition matrix is as follow:

$$F_{CV} = \begin{bmatrix} 1 & dT & 0 & 0 \\ 0 & 1 & 0 & 0 \\ 0 & 0 & 1 & dT \\ 0 & 0 & 0 & 1 \end{bmatrix} \quad (6)$$

2.2 Kernelized Correlation Filter (KCF)

Proposed in [4], the kernelized correlation filter tracks in frequency domain and the maximum response of the filter gives the new location of the target on the correlation map.

The correlation filter w is learnt through Ridge Regression, i.e. solving the regularized least squared problem given as:

$$w^* = \arg \min_w \{ \sum_i \| w^T X_i - y_i \|^2 + \lambda \| w \|^2 \} \quad (7)$$

where $\lambda > 0$ is a regularization parameter, X_i is a circulant matrix of the feature map and y_i denotes regression target.

The correlation filter can be written in frequency domain as

$$W_d = \frac{Y \odot X_d^*}{\sum_i^D X_i \odot X_i^* + \lambda} \quad (8)$$

where $d \in \{1, \dots, D\}$, D denotes number of color channels (red, green and blue), and Y is the Fourier transformation of y_i . More details can be found in [5].

KCF allows non-linear regression functions using "kernel trick", that is mapping the input data with a non-linear function and expressing the solution as linear combination of the samples. Though this comes with growing complexity of the regression function with the size of samples, KCF avoid this by assuming the kernel matrix as a circulant matrix which allows diagonalization of the solution to the kernelized Ridge Regression. KCF is valid for Radial Basis Function kernels, dot-product kernels and additive kernels.

2.3 Discriminative Correlation Filter (DCF)

Discriminative correlation filter (DCF) based trackers have shown great performance. This paper in particular uses discriminative correlation filter with channel and spatial reliability (CSR-DCF). CSR-DCF is a novel approach to DCF tracking proposed by Lukežič et al. (2018) [6].

The correlation filter w is obtained by minimizing the output ridge loss, in the same manner as equation (9):[7]

$$w^* = \arg \min_w \{ \sum_i \| w^T X_i - y_i \|^2 + \lambda \sum_i^D \| w \|^2 \} \quad (9)$$

The tracking algorithm consists of localization step and update step. In localization, the object is localized through the responses of the learnt correlation filters weighted by channel reliability scores. In the update step, foreground/background histograms are extracted, and the spatial reliability map is constructed. The spatial reliability map restricts the correlation filter to the parts suitable for tracking. CSR-DCF uses standard HOG and Colornames feature channels in its correlation filters and HSV foreground/background histograms in reliability map estimation.

2.4 K-KCF and K-DCF Combinations

The key contribution of this work is the combinations of KF and KCF (KF+KCF, labelled as K-KCF) or DCF filters (KF+DCF, labelled as K-DCF) for tracking high-speed drones. The Kalman filter with constant velocity is used for initializing the detection, whereas KCF or DCF is used for subsequent continuous tracking. Figure 2 shows the block diagram of K-KCF and K-DCF.

3. Experimental Results

We conducted test flight to verify the idea. Two DJI Mavic Mini drones as shown in Figure 3 were used. We flew two (2) DJI Mavic Mini drones manually and independently. The motions of the two drones were recorded by a Logitech Web camera connected to a laptop. The two drones flew at high speed around 5-10m/s at 10-20m distance from the camera. From time to time, they may cross path each other. They do make sudden turns and U-turns along their courses. The tracking algorithm is supposed to track them at all time with less interruption.

The example test clip is shown in this Youtube link <https://youtu.be/GcJtVqOBXOs> and snap shot is shown in Figure 1. The same video clip is further post-processed with different filter models (tracking schemes). Here, we present the result from 1) KF only, 2) KCF only, 3) DCF only, 4) KF+KCF (labelled as K-KCF) and 5) KF+DCF (labelled as K-DCF).



Fig 3. Two DJI Mavic Mini drones used for tracking

The tracking results are examined in terms of: (1) accuracy, (2) continuity (lower number of drop detections) and (3) noise (error tracks).



Fig 4. The snapshot of the KF tracking result from the video footage at 00:15

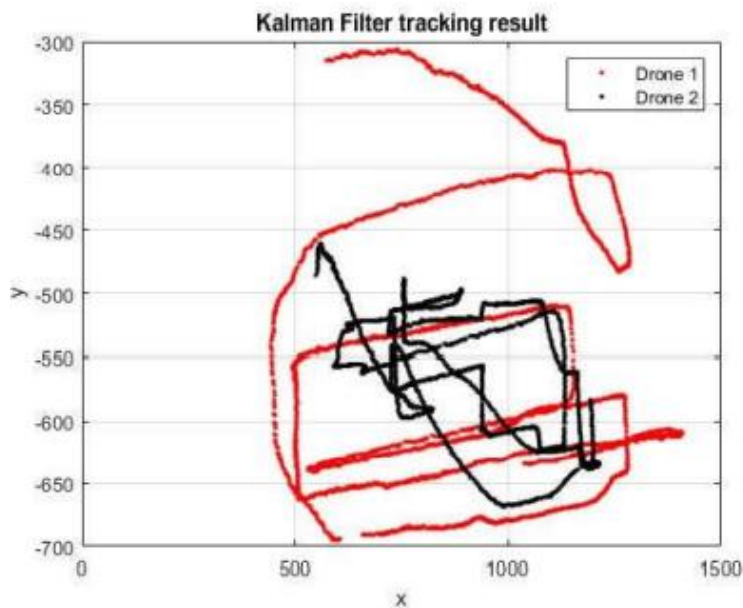


Fig 5. The snapshot of result from Kalman Filter with constant velocity (KF) tracking schemeKalman Filter (KF) result

3.1 Kalman Filter (KF) result

The result from Kalman Filter (KF) with constant velocity tracking scheme can be seen at this Youtube link: <https://youtu.be/KHZU9kbi9SU>.

The snapshot of the KF tracking result from the video footage at 00:15 is shown in Figure 4. The colorful rainbow-like lines represent the two tracked drones. Figure 5 shows the trajectories of the two tracked drones based on this KF. Figure 6 shows the trajectories of all the tracks obtained by this KF, representing the noisy data error tracks, on the left; and the time history of the two track drones' elevation, representing continuity of tracking, on the right.

In this result, we can observe that this KF model can track the two drones most of the time. However, there are a lot of noises on the ground as shown in Figures 4 and 6. At the turns, KF are not captured well as the corners are smoothed out.

3.2 Kernelized Correlation Filter (KCF) only result

The result from Kernelized Correlation Filter (KCF) only tracking scheme can be seen at this Youtube link: https://youtu.be/MWPSC_Le5Lg.

The snapshot of the KCF tracking result from the video footage at 00:15 is shown in Figure 7. The two blue and red lines represent the two tracked drones. Figure 8 shows the trajectories of all the tracks obtained by this KCF, representing no noisy data error tracks, on the left, and the time history of the two track drones' elevation, representing continuity of tracking but partially, on the right.

In this result, we can observe that this KCF can track the two drones just part of the time, and it needs initiation. However, there is no noise on the ground as shown in Figures 7 and 8.

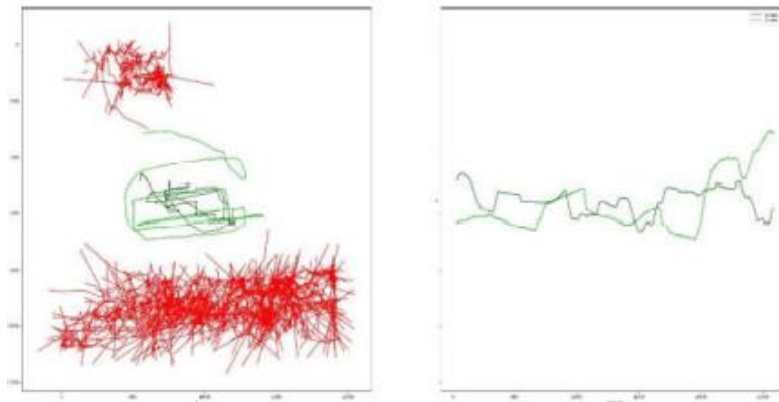


Fig 6. (Left) Trajectories of all the tracks obtained by this KF, representing the noisy data error tracks, and (Right) the time history of the two track drones' elevation, representing continuity of tracking



Fig 7. The snapshot of the Kernelized Correlation Filter (KCF) only tracking result from the video footage at 00:15

3.3 Discriminative Correlation Filter (DCF) only result

The result from Discriminative Correlation Filter (DCF) only tracking scheme can be seen at this Youtube link: <https://youtu.be/LAD09YDjBYU>.

The snapshot of the DCF tracking result from the video footage at 00:15 is shown in Figure 9. The two blue and red lines represent the two tracked drones. Figure 10 shows the trajectories of all the tracks obtained by this DCF, representing no noisy data error tracks, on the left, and the time history of the two track drones' elevation, representing continuity of tracking fully, on the right.

In this result, we can observe that this DCF can track the two drones at all time, although it needs initiation. There is no noise on the ground as shown in Figures 4 and 10.

3.4 KF+KCF combination (K-KCF) result

The result from KF+KCF combination (K-KCF) tracking scheme can be seen at this Youtube link: <https://youtu.be/F3Fsaty1leA>.

The snapshot of the K-KCF tracking result from the video footage at 00:15 is shown in Figure 11. The colorful rainbow-like lines represent the two tracked drones. Figure 12 shows the trajectories of all the tracks obtained by this K-KCF, representing the noisy data error tracks, on the left, and the time history of the two tracked drones' elevation, representing continuity of tracking, on the right.

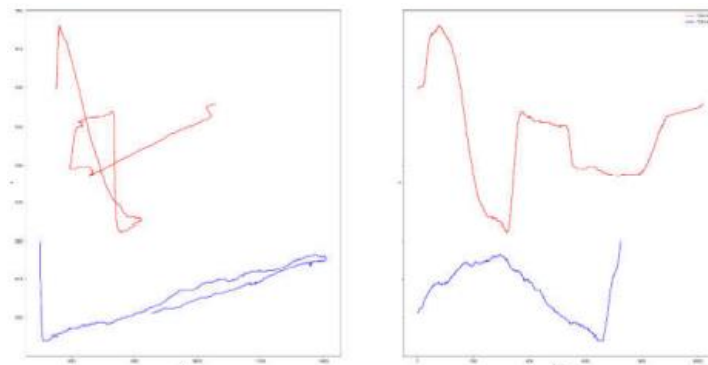


Fig 8. (Left) Trajectories of all the tracks obtained by this Kernelized Correlation Filter (KCF) only tracking, representing no noisy data nor error tracks, and (Right) the time history of the two track drones' elevation, representing continuity of tracking but partially



Fig 9. The snapshot of the Discriminative Correlation Filter (DCF) only tracking result from the video footage at 00:15

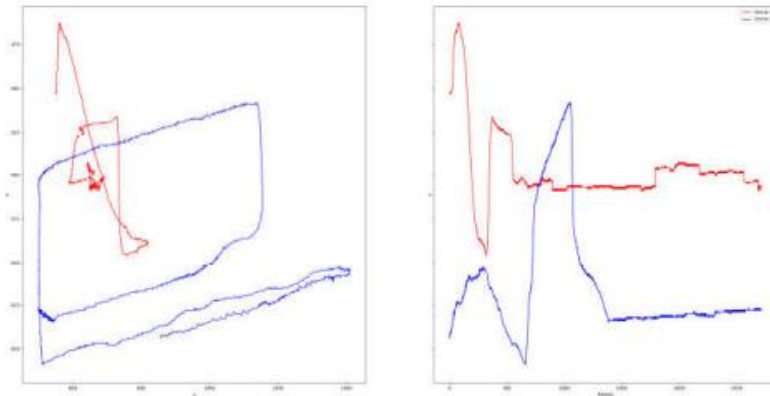


Fig 10. (Left) Trajectories of all the tracks obtained by this Discriminative Correlation Filter (DCF) only tracking, representing no noisy data nor error tracks, and (Right) the time history of the two track drones' elevation, representing continuity of tracking but partially



Fig 11. The snapshot of the KF+KCF combination (K-KCF) tracking result from the video footage at 00:15

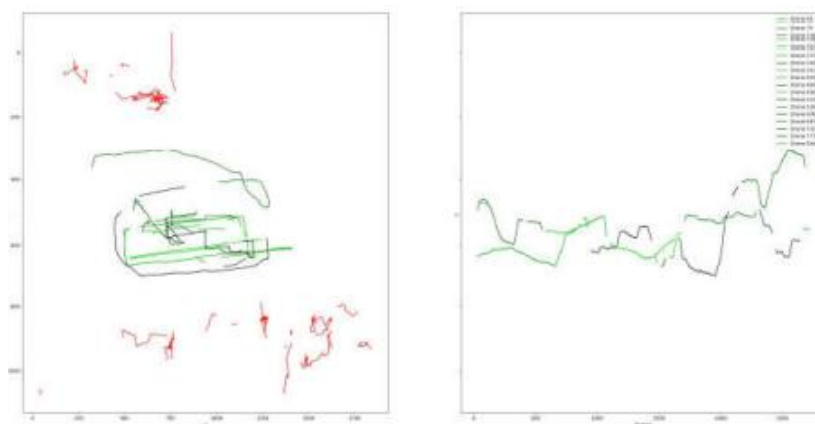


Fig 12. (Left) Trajectories of all the tracks obtained by this K-KCF, representing the noisy data error tracks, and (Right) the time history of the two track drones' elevation, representing continuity of tracking

In this result, we can observe that this KF+KCF combination (K-KCF) model have less noise compared to KF, but can only track the two drones part of the time. There are a lot of interrupted tracking as shown in Figures 11 and 12.

3.5 KF+DCF combination (K-DCF) result

The result from KF+DCF combination (K-DCF) tracking scheme can be seen at this Youtube link: <https://youtu.be/gqd6qkwUvQI>.

The snapshot of the K-DCF tracking result from the video footage at 00:15 is shown in Figure 13. The colorful rainbow-like lines represent the two tracked drones. Figure 14 shows the trajectories of the two tracked drones based on this K-DCF. Figure 15 shows the trajectories of all the tracks obtained by this K-DCF, representing the noisy data error tracks, on the left, and the time history of the two track drones' elevation, representing continuity of tracking, on the right.

In this result, we can observe that this K-DCF model can track the two drones most of the time. However, there are a lot of noises on the ground as shown in Figures 13 and 15. At the turns, K-DCF are not captured well as the corners are smoothed out.

4. Discussion and Future Research

From the results shown in the previous section, the comparable tracking schemes are KF and K-DCF results, whereas K-KCF has discontinuity issues. Figures 16 and 17 show direct comparisons. In terms of accuracy, both KF and K-DCF could track the two drones well as shown in Figure 16. However, K-DCF has significantly less noise and less error tracks as shown in Figure 17. These results show that the combined Kalman-Discriminative Correlation Filters (K-DCF) can be a good low-cost position estimator for small, fast and aggressively maneuvering aerial target, especially drone. The trajectory of the DJI Mavic Minis might be too linear due to its build-in stability control, however, their sudden turns make their flight non-linear, and that, conventional filters fail to track. Therefore, we deduce from our existing results that the K-DCF model is the suitable and preferred choice. The next step of the research is to find more test cases and compare the performance and efficiency of the other different models for vision-based drone tracking.



Fig 13. The snapshot of the KF+DCF combination (K-DCF) tracking result from the video footage at 00:15

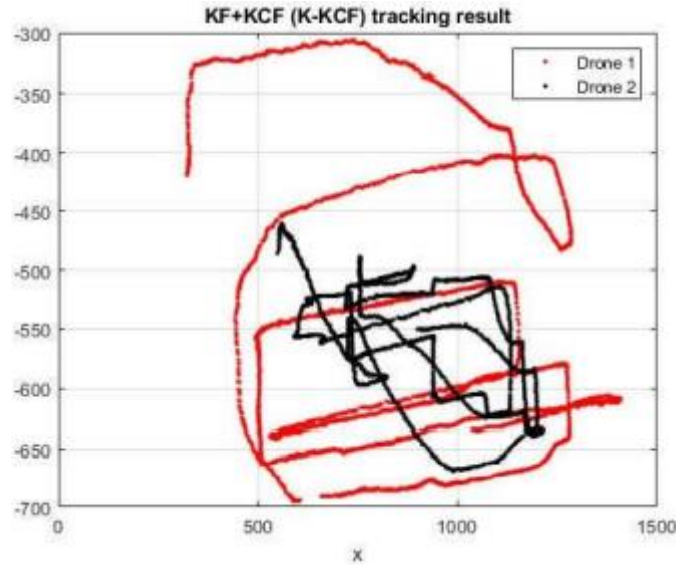


Fig 14. The snapshot of result from KF+DCF combination (K-DCF) tracking scheme

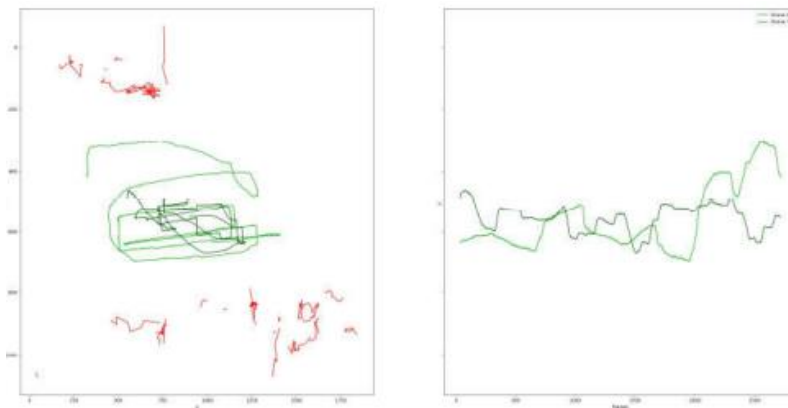


Fig 15. (Left) Trajectories of all the tracks obtained by this K-DCF, representing the noisy data error tracks, and (Right) the time history of the two track drones' elevation, representing continuity of tracking

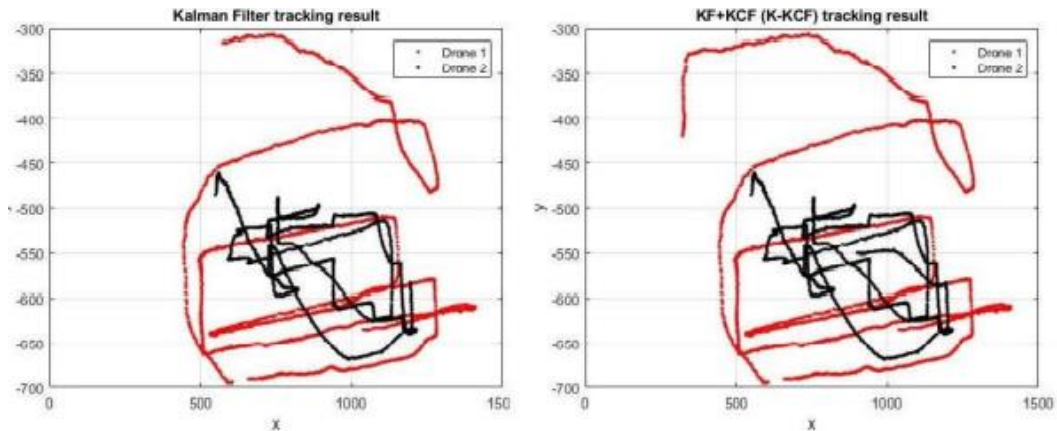


Fig 16. Side-by-side comparison of drones trajectories from KF and K-DCF tracking schemes

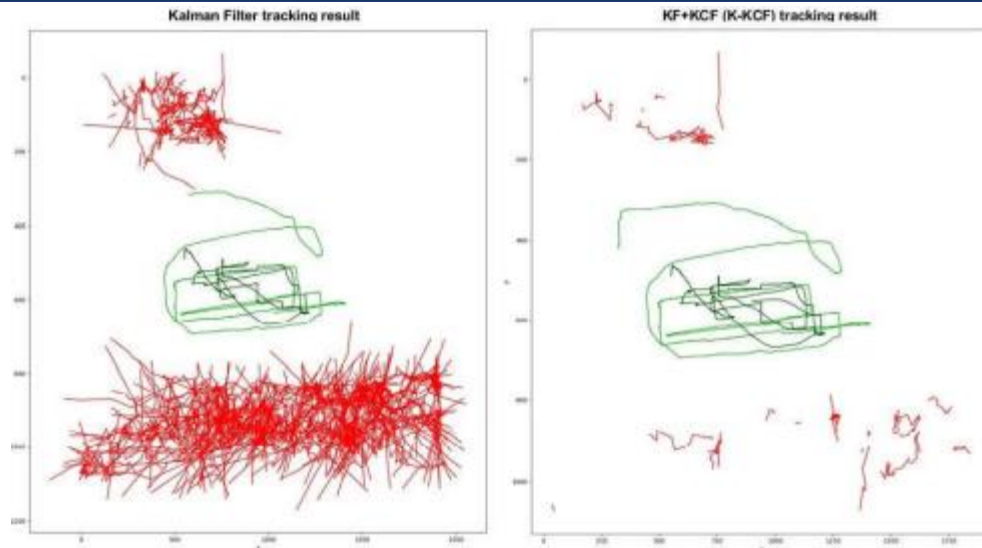


Fig 17. Side-by-side comparison of all trajectories (inclusive of noises and error tracks) from KF and K-DCF tracking schemes

Acknowledgement

The research is supported in part by Civil Aviation Authority of Singapore (CAAS) and Defense Science and Technology Agency (DSTA@71).

References

- [1] S. Srigrarom and K. H. Chew, “Hybrid motion-based object detection for detecting and tracking of small and fast moving drones,” in *International Conference on Unmanned Aircraft Systems 2020*. IEEE Robotics and Automation, Athens, Greece, 2020.
- [2] M. Hoshiya and E. Saito, “Structural identification by extended kalman filter,” *Journal of Engineering Mechanics*, vol. 110, no. 12, pp.1757–1770, 1984.
- [3] Y. Kim and H. Bang, *Introduction to Kalman Filter and Its Applications*, 11 2018.
- [4] J. F. Henriques, R. Caseiro, P. Martins, and J. Batista, “High-speed tracking with kernelized correlation filters,” *IEEE transactions on pattern analysis and machine intelligence*, vol. 37, no. 3, pp. 583–596, 2014.
- [5] K. Chaudhary, M. Zhao, F. Shi, X. Chen, K. Okada, and M. Inaba, “Robust real-time visual tracking using dual-frame deep comparison network integrated with correlation filters,” in *2017 IEEE/RSJ International Conference on Intelligent Robots and Systems (IROS)*. IEEE, 2017, pp. 6837–6842.
- [6] A. Lukežič, T. Vojšič, L. Čehovin Zajc, J. Matas, and M. Kristan, “Discriminative correlation filter tracker with channel and spatial reliability,” *International Journal of Computer Vision*, 2018.
- [7] Q. Wang, J. Gao, J. Xing, M. Zhang, and W. Hu, “Defnet: Discriminant correlation filters network for visual tracking,” *arXiv preprint arXiv:1704.04057*, 2017.

Wing Rotation Mechanism to Enhance Flapping Lift

Lung. J. Yang¹, Vivek. J. Joseph^{1*}, Saravana Kompala¹ and Neethish. K. Unnam²

^{1,2}Tamkang University, Tamsui, Taiwan, 25137

*Corresponding author. E-mail: vivekjabarajwork@gmail.com

Abstract

This paper presents an active wing rotation mechanism for FWMAVs. New types of servo based flapping mechanisms were developed and added with set of differential gears to achieve wing rotation. The mechanisms were designed and assembled in such a way that the wing rotation occurs only at pronation and supination, and mechanical stoppers were added in servo-based mechanisms in order to control the over rotation. The flapping mechanisms are expected to produce average lift as FWMAVs flight performance rely on it. Characteristics of various flapping mechanism based on servo and DC motor are discussed in detail. A rapid 3D printing of these mechanisms was developed and assembled with the body and polyethylene terephthalate (PET) wing. The wing rotation flapping mechanism's aerodynamic performances were tested using a low-speed wind tunnel. Lift and net thrust signal data are extracted and compared with well-known Dickinson's work. By adding the active wing rotation technique using the servo, it is observed that the maximum average lift increases by 45% compared to the pure FBL mechanism, and cruising lift to weight ratio increases by 32%. Cruising condition for flight in each mechanism is assessed and discussed in detail. The various 3D printed mechanisms were well suited for detailed comparative evaluation as it didn't affect the flapping frequency and performance much by adding more weight into it. and their flight parameters are estimated.

Keywords: Flapping mechanism, FWMAV – Flapping Wing Micro Aerial Vehicle, bevel gears, wing rotation, 3D printing, lift, net thrust, FBL- Four bar linkage

Nomenclature

V = Volt

Re = Reynolds number

C_L = Lift coefficient

Hz = Hertz

gf = Gram force

L = Lift

Γ = Circulation

1. Introduction

There are many work in literature that dealt with flapping mechanisms with wing rotation [2-4], collision recovery [5-10], hummingbird hovering [11-13], flapping-wing using artificial muscle [14], morphing wing [15], and fly's banked turn [16]. However, Dickinson et al. [1] conducted a systematic study about the wing rotation lift. Due to difficulty in measuring insect's or birds' aerodynamic characteristics in a wind tunnel setup [17-18], they developed a robot model to mimic the flapping motion of fruit-flies. The total flapping lift includes the main contribution from the translational lift called delayed stall and the additional peaks corresponding to wing rotation.

Kutta-Joukowski law states that positive lift L is generated when (clockwise) circulation Γ is combined with relative freestream velocity V_∞ . Taking account of a baseball with Kutta-

Joukowski law, velocity is increased in the upper regime of the ball compared to the lower regime. Flow attachment and detachment at the entry and exit is seen.

Similar to the baseball, insect's horizontal Figure-of-8 motion has two-stroke reversals called pronation and supination at both sides [19]. The wing rotation motion of supination at the end of the downstroke is the same as the clockwise circulation. The flow field just before the supination naturally creates additional lift. Similarly, regarding the flow field just before the pronation or at the end of the upstroke, the velocity direction is negative. Also, the wing rotation has a counterclockwise direction with negative circulation attained. Therefore, the generated lift is still positive due to the rotation circulation. The developed wing rotation is one of the categories proposed by Dickinson. Moreover, there are symmetric and delayed wing rotations occurring in insects.

Before the stroke reversal due to advanced wing rotation, the flow field already generates an additional positive lift. The active wing rotation motion needs extra power, which can be produced through the actuation of servo motors or a special mechanism.

Symmetric wing-rotation lift generation is similar to the advanced wing rotation, except the wing rotation moment happens exactly at the stroke reversal. In hovering flight, the first and last half of the wing rotation is supposed to increase and decrease the lift characteristics without forward speed. As we know, the air drag, and power dissipation increase with lift. However, during the symmetric wing rotation, power consumption is less than in the case of advanced wing rotation. In other words, higher frequency symmetric wing rotation may be a more efficient way to perform a low-speed hovering or forward flight.

Delayed wing rotation happens after the stroke reversal and creates a negative V_∞ which leads to a negative lift. The delayed wing rotation is shown in the oblique Figure-of-8 of *Golden-Snitch* of Ref. [20]. It is generated naturally and passively due to the fluid-structural interaction between the wing frame and the unsteady flow field. It is not contributed to enhancing the lift characteristics of flapping wings. Some of the recent wing rotation mechanisms are categorized in Table 1.

Table 1. Recent researches in wing rotation mechanisms

Former Work	Remarks
Conn et. al., [21], 2007	Parallel crank-rocker (PCR) mechanism
Balta et. al., [22], 2017	Parallel crank-rocker (PCR) mechanism
Zhou et. al., [23], 2018	Crank slider and double pendulum control mechanism
Wu et. al., [24], 2010	Crank slider mechanism
Yang et. al., [25], 2017	FBL
Wang et. al., [26], 2018	Planar FBL
Nguyen et. at., [29], 2010	Scotch Yoke mechanism and linkage mechanism
Moses et. al., [30], 2018	Scotch Yoke mechanism
Jeon et. al., [31], 2017	Six bar linkages with FBL and crank slider mechanism
Wu et. al., [32], 2012	Flapping rotary wings is used as mechanism
Roshanbin et. al., [33], 2017	Leading edge bars and trailing edge bars motion for mechanism
Cheng et. al., [34], 2019	Single-slider-double-rocker mechanism
Kok et. al., [35], 2016	Combination of solenoids and bearings
Hassanalain et. al., [36], 2016	2- six bar mechanism

Gong et. al., [37], 2018

Trailing edge control mechanism with six strings

Jang et. al., [38], 2018

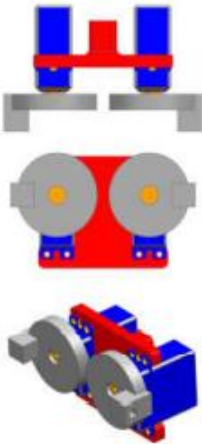
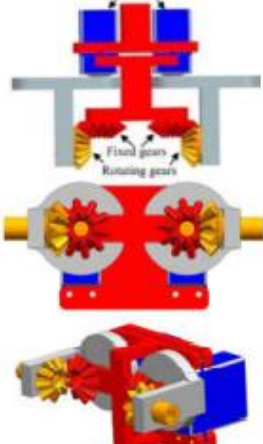
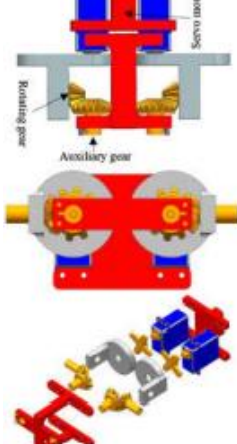
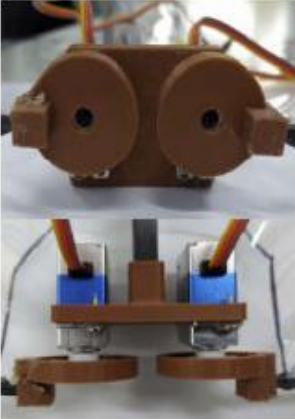
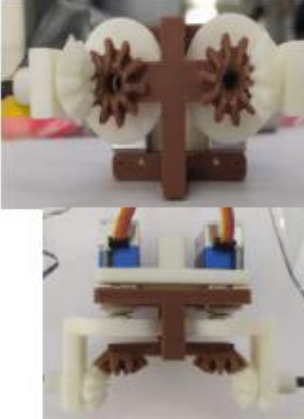
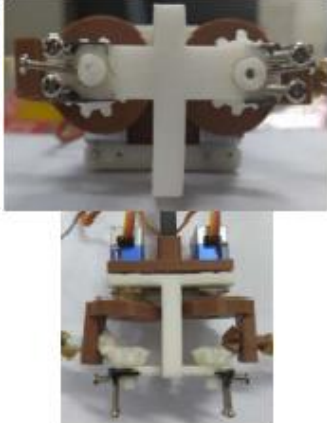
Slide crank mechanism with 3- bar linkage mechanism

Although Dickinson claimed that the horizontal wing rotation, including the rotational circulation and wake capture, could provide an extra 35% lift relative to the flapping lift without wing rotation, we need to evaluate whether the advanced (or symmetric) wing rotation can provide it. The following section addresses this issue.

2. Materials and Methods

In an attempt to achieve active wing rotation, the authors surveyed various flapping mechanisms that can actively rotate their wings along with the flapping motion [21-39]. Most of them focused on the flapping mechanism design with multiple degree-of-freedom and not dealt with aerodynamic force measurement for the case of flapping with wing rotation. Henceforth, several flapping mechanisms are designed and are mentioned in Table 2. For comparison, type A1 (normal servo) and Golden Snitch FBL are for no active wing rotation. The different configuration features are briefly stated, and their performances are discussed further in sections.

Table 2. Flapping Mechanisms for Investigating Wing-Rotation Effect [40, 41]

Mechanism types	Type-A 2 servos	Type-B 2 servos+bevel gear	Type-B1 2 servos+bevel gear+stopper
CAD			
Fabrication: 3D printing			

	Wing area 1,407 cm ²	Wing area 1,474 cm ²	Wing area 1,407 cm ²
	Total weight 80.9 gf	Total weight 88.1 gf	Total weight 93 gf
Best condition	Inclined 25°	Inclined 35°	Inclined 35°
	Cruise speed 3 m/s	Cruise speed 1.5 m/s	Cruise speed 3 m/s
	Cruise lift 63.2 gf	Cruise lift 51.1 gf	Cruise lift 84 gf
Flight test	NA	NA	NA
	(Cruise lift < total weight)	(Cruise lift << total weight)	(Cruise lift < total weight)

Type-A1 mechanism uses 2 servo motors for up and down flapping motion, and has no wing rotation. The overall weight of FWMAV is 80.9 g, the cruise lift is 63.2 gf, and Type-A1 cannot withstand the total weight for real flight. The lift and net thrust signal data are shown in Figure 1. Cruising point is important in analyzing the FWMAV performance and can predict the MAV can fly or not. We find a point where the FWMAV has zero net thrust and maximum average lift; by seeing the data acquired, we can predict whether the MAV can withstand its own weight.

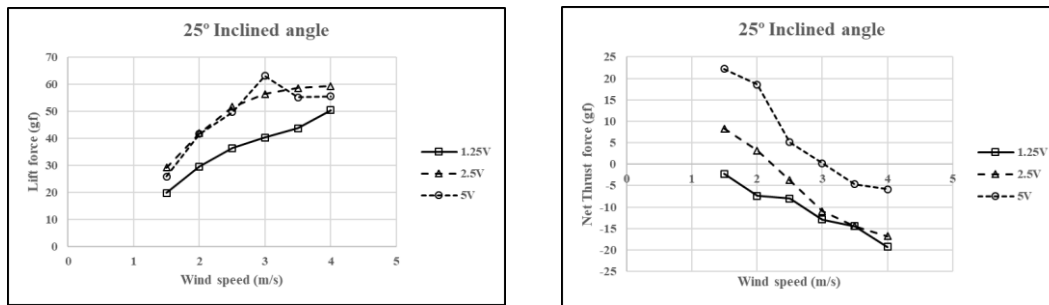


Figure 1. Lift and net thrust by Type-A1 at 25° inclined angle

Type-B mechanism uses 2 servos for flapping and a pair of bevel gears for “continuous” wing rotation. The total weight increased to 88.1 g and simultaneously the cruise lift decreased to 51.1 gf. Cruise speed decreases due to smaller thrust. From the lift and net thrust signals from Table 1, we can observe that the high peak parts disappear compared to the case of Type-A1, and the lift and net thrust are shown in Figure 2.

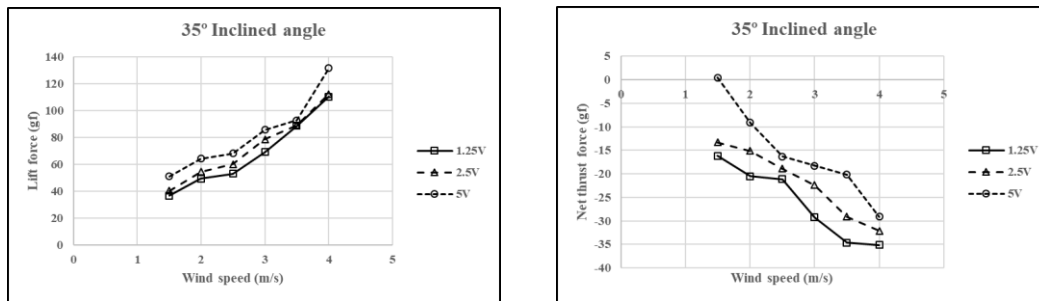


Figure 2. Lift and net thrust by Type-B mechanism at 35° inclined angle

It is observed from the insect flapping motion that “continuous” wing rotation is not necessary. Wing rotation happens only at stroke reversal. Therefore, Type-B mechanism is novelly modified into Type-B1 mechanism which has rotary switchable bevel gear controlled by two pin stoppers shown in Table 1. For the angle position between two stopper pins, there is no wing rotation involved. The total weight is quite larger, but this mechanism also produces larger

cruise lift of 84 gf, the largest among the three mechanisms in Table 1. Lift and net thrust data for cruising condition is shown in Figure 3.

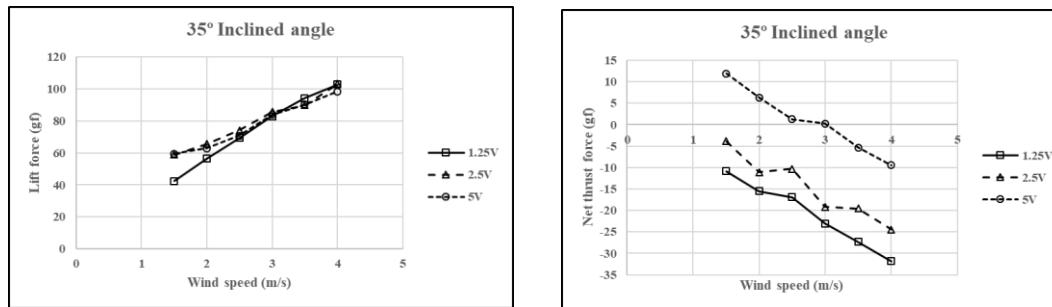


Figure 3. Lift and net thrust by Type-B1 mechanism at 35° inclined angle

3. Results and Discussions

The 3D printed mechanisms were assembled and tested using a wind tunnel. The FWMAV assembly was set to different inclined angles and tested with varying wind velocities. The lift and net thrust data were collected and averaged. The best condition for each mechanism were identified using a cruising point idea. The cruising point depicts that the maximum lift is generated when the net thrust is zero, which infers that the MAV can withstand its own weight and can fly in that particular cruising condition. The lift performances were compared to Dickinson's wing rotation experiment [1], which tells that the 35% lift enhancement is due to the wing rotation phenomena and the results from this study explains that the wing rotation effect is almost same.

4. Conclusion

After the successful fabrication and assembly of all the servo mechanisms, wind tunnel experiments were conducted for the MAV's of 70cm wingspan to obtain the aerodynamic forces at different inclined angles of 10° to 35° and by varying the wind speed of 1.5m/s to 4m/s also with voltages of 1.25V, 2.5V, and 5V. The obtained data points of aerodynamic forces are successfully plotted, compared and studied. From all the servo mechanisms mentioned, the Type-B1 mechanism have higher aerodynamic performances of 84gf at the cruising speed of 3m/s at 35° inclined angle, which is 32.9% higher than the Type-A1 mechanism having a maximum lift of 63.17gf at the cruising speed of 3m/s and 68% higher than the Type-B mechanism having a maximum lift of ~50gf at the cruising speed of 2m/s.

Acknowledgments

Financial support from MOST of Taiwan with the project number 109-2221-E-032-002-MY2. Wind tunnel testing facility from Civil Engineering, Tamkang University.

References

- [1] Dickinson, M. D., *et al.* (1999), "Wing rotation and the aerodynamic basis of insect flight", *Science*, 284, 1954-1960.
- [2] Banala, S. K. and Agrawal, S. K. (2005), "Design and optimization of a mechanism for out-of-plane insect wing like motion with twist", *Journal of Mechanical Design/ Transactions of the ASME*, 127(4), 841-844.
- [3] Galin'ski, C., Żbikowski, R. (2005), "Insect-like flapping wing mechanism based on a double spherical Scotch yoke", *Journal of Royal Society Interface*, 2(3), 223-235.

- [4] McIntosh, S. H., *et al.* (2006), “Design of a mechanism for biaxial of a wing for a hovering vehicle”, *IEEE/ASME Transactions on Mechatronics*, 11(2), 145-153.
- [5] Phan, H. V. and Park, H. C. (2020), “Mechanisms of collision recovery in flying beetles and flapping-wing robots”, *Science*, 370, 1214-1219.
- [6] Phan, H. V. and Park, H.C. (2019), “Insect-inspired, tailless, hover-capable flapping-wing robots: recent progress, challenges, and future directions”, *Progress in Aerospace Sciences*, 111, 100573.
- [7] Phan, H.V., *et al.* (2020), “Towards the long-endurance flight of an insect-inspired, tailless, two-winged, flapping-wing flying robot”, *IEEE Robot. Autom. Lett.* 5(4), 5059–5066.
- [8] Briod, A., *et al.* (2014), “A collision-resilient flying robot”, *J. Field Robot.* 31, 496–509.
- [9] Sareh, P., *et al.* (2018), “Rotorigami: a rotary origami protective system for robotic rotorcraft”, *Sci. Robot.* 3, eaah5228.
- [10] Mountcastle, A. M., *et al.* (2019), “An insect-inspired collapsible wing hinge dampens collision-induced body rotation rates in a microrobot”, *J. R. Soc. Interface* 16, 20180618.
- [11] Keennon, M. T., *et al.* (2012), “Development of the Nano Hummingbird: a tailless flapping wing micro air vehicle”, paper presented at the 50th AIAA Aerospace Sciences Meeting, Nashville, TN, USA.
- [12] Tu, Z., *et al.* (2020), “Untethered flight of an at-scale dual-motor hummingbird robot with bio-inspired decoupled wings”, *IEEE Robot. Autom. Lett.* 5, 4194–4201.
- [13] Nguyen, Q. V., Chan, W. L. (2018), “Development and flight performance of a biologically-inspired tailless flapping-wing micro air vehicle with wing stroke plane modulation”, *Bioinspir. Biomim.* 14, 016015.
- [14] Chen, Y. *et al.* (2019), “Controlled flight of a microrobot powered by soft artificial muscles”, *Nature*, 575, 324–329.
- [15] Stowers, A. K., Lentink, D. (2015), “Folding in and out: passive morphing in flapping wings”, *Bioinspir. Biomim.* 10, 025001.
- [16] Narásek, M., *et al.* (2018), “A tailless aerial robotic flapper reveals that flies use torque coupling in rapid baked turns”, *Science* 361, 1089–1094.
- [17] Ellington, C. P. (1996), “Leading-edge vortices in insect flight”, *Nature*, 384, 626-630.
- [18] R.J. Bomphrey, R. J. (2006), “Insects in flight: direct visualization and flow measurements”, *Bioinspiration and Biomimetics*, 1, s1-s9.
- [19] Sane, S. P. (2003), “The aerodynamics of insect flight”, *The Journal of Experimental Biology*, 206, 4191-4208.
- [20] Yang, L. J. (2012), “The micro-air-vehicle *Golden-Snitch* and its Figure-of-8 flapping”, *Journal of Applied Science and Engineering*, 15(3), 197-212.
- [21] Conn, A. T., *et al.* (2007), “Design of a parallel crank-rocker flapping mechanism for insect-inspired micro air vehicles”, *Proceedings of the Institution of Mechanical Engineers, Part C: Journal of Mechanical Engineering Science*, 221(10), 1211-1222.
- [22] Balta, M., *et al.* (2017), “Design and manufacturing of flapping wing mechanisms for micro air vehicles”, In 58th AIAA/ASCE/AHS/ASC Structures, Structural Dynamics, and Materials Conference (p. 0509).

[23] Wu, P., *et al.* (2010, April), “Active Rotation and Vibration During the Flapping Stroke of a Micro Elastic Wing for Thrust Production”, In 51st AIAA/ASME/ASCE/AHS/ASC Structures, Structural Dynamics, and Materials Conference 18th AIAA/ASME/AHS Adaptive Structures Conference 12th (p. 2885).

[24] Yang, W., *et al.* (2018), “Dove: A biomimetic flapping-wing micro air vehicle”, *International Journal of Micro Air Vehicles*, 10(1), 70-84.

[25] Wang, P. L., *et al.* (2018), “Design of a flapping wing mechanism to coordinate both wing swing and wing pitch”, *Journal of Mechanisms and Robotics*, 10(2).

[26] Phan, H. V., & Park, H. C. (2016), “Generation of control moments in an insect-like tailless flapping-wing micro air vehicle by changing the stroke-plane angle”, *Journal of Bionic Engineering*, 13(3), 449-457.

[27] Phan, H. V., *et al.* (2017, February), “Controlled hovering flight of an insect-like tailless flapping-wing micro air vehicle”, In 2017 IEEE International Conference on Mechatronics (ICM) (pp. 74-78). IEEE.

[28] Phan, H. V., *et al.* (2019), “KUBeetle-S: An insect-like, tailless, hover-capable robot that can fly with a low-torque control mechanism”, *International Journal of Micro Air Vehicles*, 11, 1756829319861371.

[29] Nguyen, Q. V., *et al.* (2010), “Characteristics of a beetle's free flight and a flapping-wing system that mimics beetle flight”, *Journal of Bionic Engineering*, 7(1), 77-86.

[30] Moses, K. C., *et al.* (2018, July), “Simulating flapping wing mechanisms inspired by the *Manduca sexta* hawkmoth”, In Conference on Biomimetic and Biohybrid Systems (pp. 326-337). Springer, Cham.

[31] Jeon, J., *et al.* (2017), “Design and analysis of the link mechanism for the flapping wing MAV using flexible multi-body dynamic analysis”, *International Journal of Micro Air Vehicles*, 9(4), 253-269.

[32] Wu, J. H., *et al.* (2012), “A novel design in micro-air-vehicle: flapping rotary wings”, In *Applied Mechanics and Materials* (Vol. 232, pp. 189-193). Trans Tech Publications Ltd.

[33] Roshanbin, A., *et al.* (2017), “COLIBRI: A hovering flapping twin-wing robot”, *International Journal of Micro Air Vehicles*, 9(4), 270-282.

[34] Cheng, H., *et al.* (2019, July), “Mechanism Design and Kinematics Analysis of a Bio-Inspired Flexible Flapping Wing”, In IFToMM World Congress on Mechanism and Machine Science (pp. 209-218). Springer, Cham.

[35] Kok, J. M., & Chahl, J. (2016), “Design and manufacture of a self-learning flapping wing-actuation system for a dragonfly-inspired MAV”, In 54th aiaa aerospace sciences meeting (p. 1744).

[36] Hassanalian, M., & Abdelkefi, A. (2016), “Effective design of flapping wing actuation mechanisms: theory and experiments”, In 54th AIAA aerospace sciences meeting (p. 1745).

[37] Gong, D., *et al.* (2018), “Design and Experiment of String-based Flapping Mechanism and Modulized Trailing Edge Control System for Insect-like FWMAV”, In 2018 AIAA Information Systems-AIAA Infotech@ Aerospace (p. 0987).

[38] Jang, J. H., & Yang, G. H. (2018), “Design of wing root rotation mechanism for dragonfly-inspired micro air vehicle”, *Applied Sciences*, 8(10), 1868.

[39] Fenelon, M. A. and Furukawa, T. (2010), “Design of an active flapping wing mechanism and a micro aerial vehicle using a rotary actuator”, *Mechanism and Machine Theory*, 45, 137-146.

[40] Panchal, N. (2019), “Wing Rotation Effect on an Ornithopter Using Servo Control”, Master Thesis, Department of Mechanical and Electromechanical Engineering, Tamkang University, Taiwan.

[41] Kompala, S. (2020), “Wing Rotation Mechanisms Using Bevel Gears for Ornithopters”, Master Thesis, Department of Mechanical and Electromechanical Engineering, Tamkang University, Taiwan.

Development of Communication System for Amphibious Multicopter

Yuta Motoki¹ and Masafumi Miwa^{2,*}

^{1,2}Tokushima University, Tokushima, Japan

*Corresponding author. E-mail: mokigorilla@gmail.com

Abstract

In recent years, the number of aging dams is increasing. In Japan, more than 3,000 dams are exist, and cracks are generated in some of these dams. Dam's investigation is needed to maintain safety. The methods for detection of crack for the dam are visual check with rope action and diving, laser measuring from the ground, etc. These methods have been performed for a long time, and sometimes have a risk of investigating at a high altitude. Therefore, we present an underwater multirotor helicopter as the underwater-investigable tool for the underwater wall surface. The use of our proposed underwater multirotor helicopter has the advantages of cutting the investigation time and making the cost of investigation cheap, improving safety in air and water. However, a radio control system (72MHz radio controller) used in the previous research could only communicate up to 0.3 m under the sea. In order to operate the underwater multirotor helicopter in deeper water, it is necessary to develop a new communication system. This research uses a buoy equipped with an access point. The purpose of the present research is to develop a system that connects the DTRU-KAI and the buoy with a wired LAN and communicates between the ground station and the buoy with a wireless LAN.

Keywords: UAV, Infrastructure inspection, Local network, localization, Amphibious multicopter

1. Introduction

In Japan, the aging of social infrastructure development created during the period of high economic growth is considered a problem. Under such circumstances, dams have been aging in recent years. Although the number of dams constructed peaked in the 1960s and has been on a downward trend, the total number of dams has been on an increasing trend. There are 3000 dams in Japan in total, and many cracks due to aging have been confirmed on the downstream surface of these dams [1]. In addition, there is a problem with dam sedimentation on the upstream side of the dam. Therefore, maintenance work such as confirmation of sediment status and dredging is required. The current wall surface survey of dams mainly uses visual analysis or image analysis from the ground surface with a camera. These are often done by the human eye, and the accuracy varies. Moreover, these investigations are very time consuming and very inefficient. In addition, special survey methods such as rope crafting and diving surveys are used to survey the walls of high places and upstream surfaces. Compared to the former method, this takes longer to prepare and is more dangerous. These problems exist not only in dams but also in road retaining walls adjacent to bridges and reservoirs.

To address these problems, it is effective to use the amphibious multicopter. Using an amphibious multicopter, we can investigate the wall of the downstream surface by aerial photography by flight. Next, we can investigate the wall of the upstream surface by underwater photography by diving. Thus, safety of work will be improved, the work facilitated, the inspection cost reduced, and the results made uniform.

In a previous study, it was confirmed that the DTRU (Diving Tilt Rotor UAV) developed can move in water by thrust vectoring without changing the attitude using the Tilt mechanism [2]. It

was also found that by changing the shape of the aircraft, problems such as attitude disturbance when starting underwater and failure to take off from the water surface could be solved. However, DTRU has problems. One problem is that there is no way to check camera image real-time during operation. Another problem is that wireless communication with the ground is immediately interrupted in seawater, making it impossible to dive.

Figure 1 shows the relationship between the frequency of radio waves and the transmission distance in the water. From the graph, it can be seen that the transmission distance becomes shorter as the frequency of radio waves increases. The DTRU communication in the previous study was performed wirelessly by a radio control transmitter / receiver in the 72 MHz band. Therefore, the area where wireless communication can reach is extremely small, and the operating area of DTRU is limited. From the above viewpoint, it is necessary to construct a communication system for DTRU so that communication is not interrupted even at a certain depth of water.

In order to solve this problem, this research examines the system in which a communication relay buoy is mounted on the airframe. The purpose of this study is to develop a system that enables DTRU to be operated even at a water depth of 3 m or more.

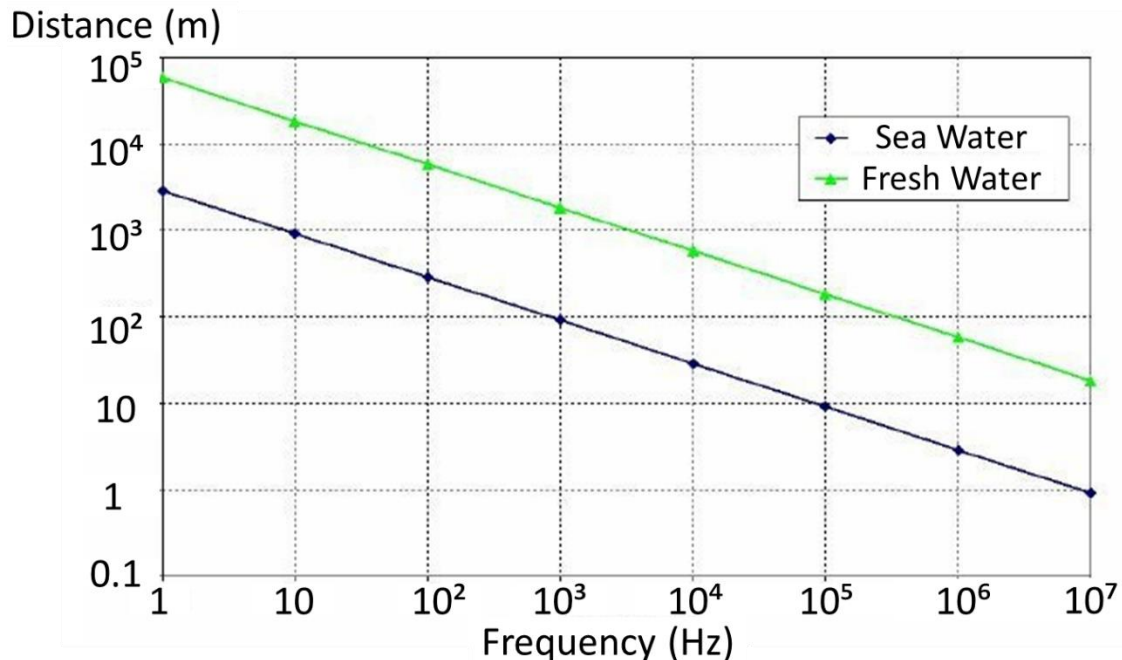


Figure 1. Relationship between radio frequency and transmission distance in water [3]

2. System configuration

2.1 Traditional communication system

Figure 2 shows the configuration of the device in the previous research. The communication of the experimental aircraft was carried out between the transmitter controlled by the operator and the receiver mounted on the aircraft. In addition, the aircraft was connected to a PC using telemetry, and information such as the attitude of the aircraft was acquired via the ground station software installed in advance on the PC. However, the frequency band of the transmitter / receiver used at that time was 72 MHz, and communication was interrupted at the depth of 0.3 m. Furthermore, previous research has revealed that communication on the telemetry side was interrupted immediately after landing on the water.

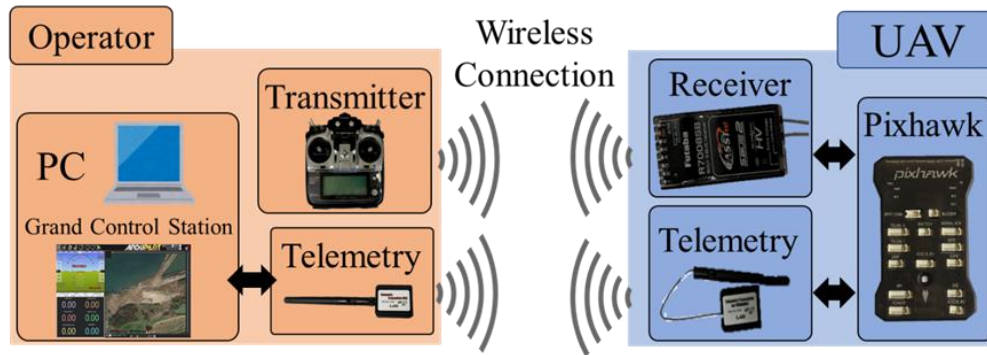


Figure 2. Conventional system configuration

2.2 The new communication system of this research

In this research, a relay buoy equipped with an access point was mounted on the DTRU, and a system was constructed in which the relay buoy and the aircraft were always connected by wire. First, the radio control transmitter and PC were connected by a simulator cable as an input device (controller). As a result, the input of the transmitter will be incorporated into the connection with Mavlink, and the aircraft can be operated without the need for a receiver for normal radio control. Next, the PC and the wireless LAN board were connected by Wi-Fi. The access point and two Raspberry Pi 4s are connected to the switching hub with LAN cables, and information can be sent and received via wired connections. The Raspberry Pi 4 in the DTRU was connected to the flight controller by UART. In addition, the USB camera was connected to the Raspberry Pi 4 via USB, and the video image was transmitted to the browser of the operator's PC via the access point of the relay buoy. Furthermore, a GPS module was connected to the Raspberry Pi 4 on the relay buoy side, GPS information was received, and data was transmitted to the Raspberry Pi 4 of DTRU. Then, the Raspberry Pi 4 on the DTRU side was connected to the GPS port of the flight controller via UART, and GPS data was transmitted. Figure 3 shows the configuration of the device in the previous research.

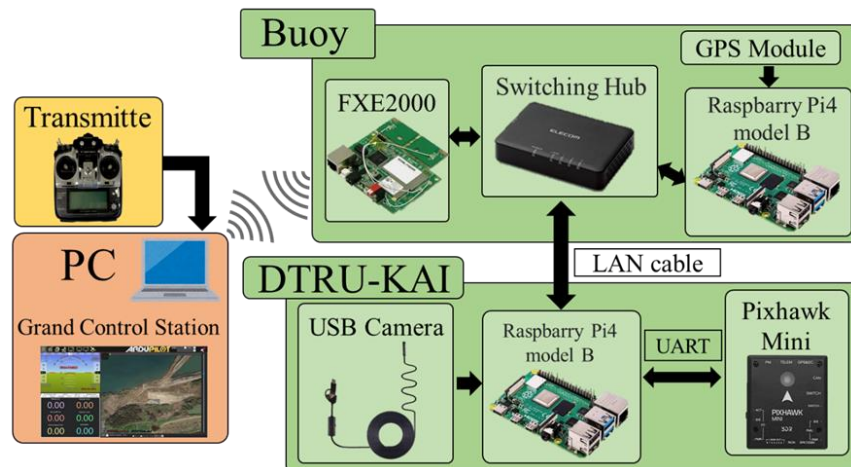


Figure 3. System configuration of this research

2.3 How to operate the communication system

In the previous study, the DTRU was operated using the signal of the R / C transmitter, and it was possible to communicate up to a depth of about 0.3 m. However, when maneuvering underwater, it is necessary to visually operate the aircraft, but it is more difficult to determine the orientation and depth of the aircraft than when maneuvering in the air. Therefore, to operate

while checking the video in real time, we tried video communication using the relay buoy produced in this research. The usage image is shown in Figure 4. The operation flow is explained below. First, the communication equipment is mounted on the relay buoy and connected to the aircraft with a wired LAN cable. After taking off with the relay buoy mounted on the upper part of the aircraft, it will land on the water surface. After landing, the relay buoy is left on the water surface, and only the aircraft dives. When the aircraft returns to the water surface, it floats while winding the cable and mounts the relay buoy on the aircraft again. After that, it takes off and returns to the starting point.

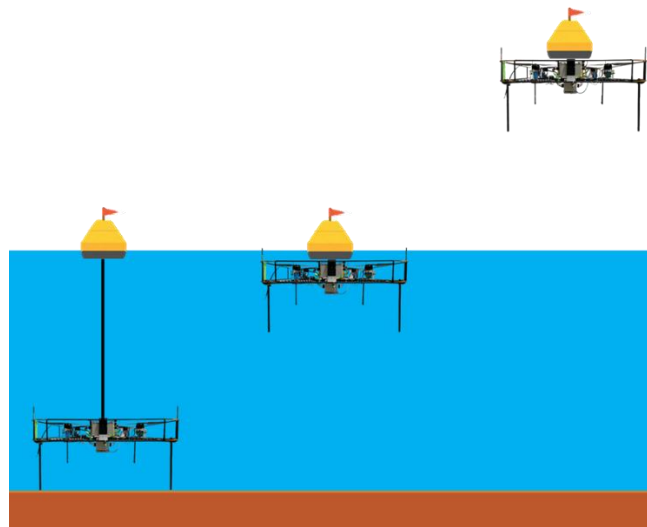


Figure 4. Image of the relay buoy system

3. Experimental

3.1 Experimental aircraft

In present research, DTRU-KAI, which is an improved version of DTRU manufactured in the previous research, is used as an experimental aircraft. The difference from the previous version is that the entire aircraft has been enlarged. By making the propeller and frame one size larger, it was possible to fly with a buoy. We also changed the waterproof case to a larger one. This is to protect the microcomputers such as Raspberry Pi and flight controller in the aircraft and to secure the buoyancy of the aircraft. Figure 5 shows the appearance of DTRU-KAI.

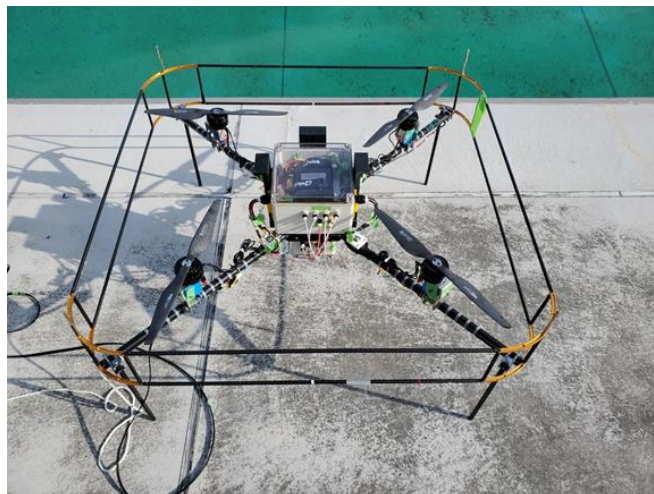


Figure 5. DTRU-KAI

3.2 Experimental method

In the experiment, a buoy is floated on the water surface and a diving experiment is conducted at a depth of up to 3 m. The experiment was conducted in a 25m pool (water depth 3m) at the water rescue training facility of the Tokushima Prefectural Fire School. Figure 6 shows the state of the diving experiment. In the diving experiment, DTRU-KAI is submerged in water, and then a buoy is floated in to check underwater maneuverability, communication stability, and camera images. This time, in order to avoid applying excessive stress to the LAN cable connecting the buoy and DTRU-KAI, a wire shorter than the LAN cable is stretched. As soon as the stability of communication is confirmed, the LAN cable and wire are collected by the winding mechanism inside the buoy, and after mounting the buoy on the aircraft, it is confirmed whether the water can be separated.

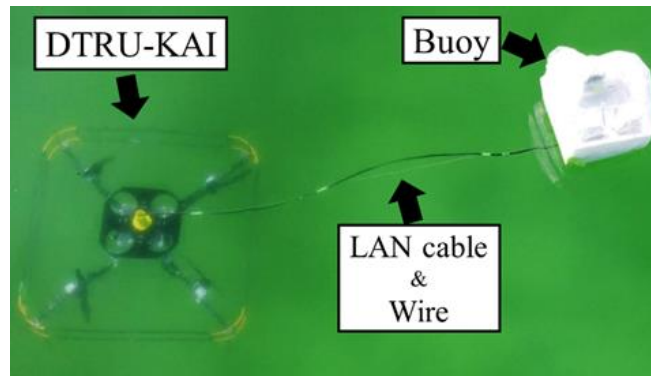


Figure 6. The state of experimentation

3.3 Experimental result

In the experiment, DTRU-KAI was able to perform diving maneuvers by input from the transmitter. In addition, the telemetry log was consistently preserved during the experiment. In addition, it was confirmed that real-time underwater images were sent from the USB camera attached to the aircraft. Furthermore, the GPS module in the buoy acquired the position information and was able to transmit the position information data to the underwater aircraft. Figure 7 shows an example of an image taken from the underwater camera.

From the above, it was found that the communication system constructed in this study is functioning normally. However, since the controller that operates the take-up mechanism was separated from the one for operating the aircraft, it was a burden on the operator, and it was not possible to check the operation of the take-up mechanism. In addition, because the size of the buoy itself was large and the weight was too heavy, it was not possible to confirm the separation of water with the buoy mounted.

3.4 Consideration

Since it was confirmed in the experiment that the aircraft could be operated from the transmitter on the ground, it can be said that the signal from the transmitter was transmitted into the flight controller by wireless and wired communication. Since the telemetry log data could be acquired accurately, it can be said that stable communication was possible without interruption of the connection between the aircraft and the ground during the experiment. It was also found that real-time video from the USB camera was sent to the operator. As a result, the aircraft could only be operated visually during underwater maneuvering, but the disadvantages could be eliminated by transmitting real-time underwater images to the operator. Since the position information from the GPS module could be acquired on the Mission Planner, it can be said that the position information acquired by the GPS module in the buoy could be communicated to the flight controller in the underwater aircraft.

However, the problems were that the size and weight of the buoy were too large and that there needed to be a winding mechanism that did not burden the operator. In the future, it will be necessary to improve the winding mechanism in addition to reducing the size and weight of the entire buoy. Specifically, we will consider mounting a depth sensor on the underwater fuselage side and controlling the length of the cable according to the depth of the diving water by the motor of the take-up mechanism.

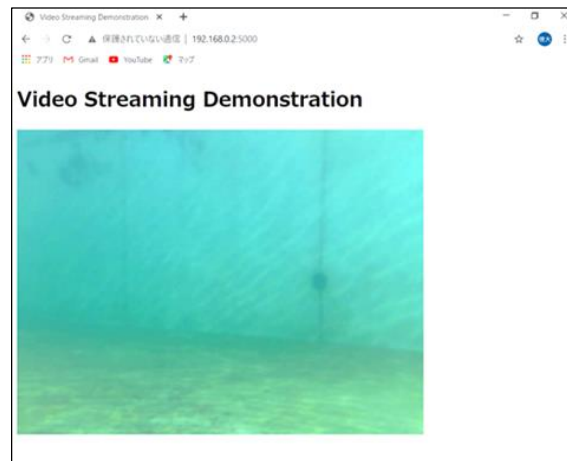


Figure 7. Underwater camera image screen

4. Conclusion

In the present research, we developed a system that communicates between a buoy equipped with an access point and the aircraft via a wired LAN, and between a terrestrial transmitter and a buoy via a wireless LAN. In the experiment, it was confirmed that the underwater aircraft could be operated from the ground and that the flight controller of the aircraft could exchange data and transfer images with the GCS on the ground. With this system, the operational area of DTRU underwater can be increased, and the operator can acquire real-time underwater images. In the experiment, it was not possible to dive to a place with a water depth of 3 m or more, but it was thought that it could be operated at a place with a water depth of 3 m or more depending on the length of the cable, and the operable area of DTRU-KAI could be expanded.

In the future, we will reduce the weight of the buoy and improve the winding mechanism, aiming to realize flight and water separation with the buoy mounted.

Acknowledgments

We would like to express our gratitude to Maxell Co., Ltd. for providing the battery and assistance for the experiment, and to Tokushima Prefecture Fire School for providing the experiment location.

References

- [1] National Institute for Land and Infrastructure Management, Project research report, available at: <http://www.nilim.go.jp/lab/bcg/siryoku/kpr/prn0004pdf/kp0004100.pdf> (accessed 20 May 2020)
- [2] Yuto Takigawa Miwa Masafumi "Development of Diving Tilt Rotor UAV", ICIUS 2019, Paper 0068f
- [3] Tetsuo Nozawa, Nikkei Electronics (2009) "Wireless communication is possible even underwater," ask WFS, the company that developed it", Nikkei XTECH, available at: (accessed 20 May 2020)

Design of Robust Controller Applied for Series Elastic Actuators in Controlling Humanoid's Joint

Anh Khoa Lanh Luu³, Van Tu Duong^{1,2,3}, Huy Hung Nguyen^{3,4}, Sang Bong Kim⁵ and Tan Tien Nguyen^{1,2,3,*}

¹Faculty of Mechanical Engineering, Ho Chi Minh City University of Technology (HCMUT), 268 Ly Thuong Kiet, District 10, Ho Chi Minh City, Vietnam

²Vietnam National University Ho Chi Minh City, Linh Trung Ward, Thu Duc District, Ho Chi Minh City, Vietnam

³National Key Laboratory of Digital Control and System Engineering (DCSELab), HCMUT, 268 Ly Thuong Kiet, District 10, Ho Chi Minh City, Vietnam

⁴Faculty of Electronics and Telecommunication, Saigon University, Vietnam

⁵Pukyong National University, Busan, Republic of Korea

*Corresponding author. E-mail: nttien@hcmut.edu.vn

Abstract

Although the application of Series elastic actuators (SEAs) in the biomechatronic field has proved its appropriation in many aspects so far, the problems of maintaining the stability for the SEAs still remains. This paper proposes a robust controller to overcome the drawbacks of the previous research. Firstly, a mathematical model considering both the SEAs and the hip joint of humanoid UXA-90 is obtained. Secondly, a reference input of the proposed controller achieved from desired hip joint's angle in a walking cycle is utilized. Then, a backstepping based sliding mode force control approach is employed to ensure the precise movement of robot's link as well as meeting the requirement of robustness for the whole system, which is significant for the task of walking of a humanoid. Finally, some simulations are carried out to verify the quality and effectiveness of the proposed controller.

Keywords: Series elastic actuators (SEAs), UXA-90, backstepping based sliding mode control

1. Introduction

Actuators are essential components in most modern robots since they provide the motive power for the robots. Electromagnetic, hydraulic and pneumatic actuators have been widely utilized in industry applications. With the advantages such as high precision, high torque and easy to control, electromagnetic actuators are used extensively in industrial robot that involve welding, painting, assembling and other repeatable tasks. Hydraulic actuators offer very high force/torque and speed characteristic which can outperform current electromagnetic actuators.

These types of actuators are commonly used in humanoid robots. DC Motors are used in the KHR series, HRP series, Humanoid Robot series from HONDA (Park, I. W. *et al.*, 2004) (Park, I. W. *et al.*, 2007) (Kaneko, K. *et al.*, 2002) (Akachi, K. *et al.*, 2005) (Kazuo, H *et al.*, 1988) (Sakagami, Y. *et al.*, 2002). Atlas from Boston Dynamic utilized hydraulic actuators for its lower limbs, torso and upper arms, while the forearms and wrists are electrically powered (Banerjee, N. *et al.*, 2015). TaeMu's humanoid robot (Hyon, S. H. *et al.*, 2017) has fifteen active joints driven by hydraulic servo cylinders. Hydra humanoid robot (Ko, T. *et al.*, 2018) utilized Electro-Hydrostatic Actuator (EHA) to simultaneously realize both of the back drivability and high control bandwidth. Pneumatic actuator are often used in robot hands and artificial muscle (Kim,

K. R. *et al.*, 2018) (Li, S. *et al.*, 2019) (Bierbaum, A *et al.*, 2009) (Nishino, S. *et al.*, 2007) since they cannot generate large force or torque like electromagnetic and hydraulic actuators.

However, the advantageous stiffness in these actuators could cause devastating effect on the robot's system themselves. Humanoid robots are expected to work in dangerous environment and cooperate with human in various condition working space, thus they are subjected to numerous external impact forces which could damage the motor through transmission elements. Various solutions to overcome this drawback have been proposed in literature so far. One approach is to use compliance control using torque feedback. Another method is impedance control, it was introduced by Neville Hogan (Hogan, N., 1985) and was adopted in various researches for controlling rigid or flexible joints, *e.g* (Suarez, A *et al.*, 2018) (Zhu, H *et al.*, 2017) (Jiang, Z. H. *et al.*, 2019,) (Hirayama, K. *et al.*, 2019). Nevertheless, this control strategy is limited when controlling interaction force with the environment. Therefore, compliant actuator has received considerable attention.

The compliant actuator involves integrating an elastic element into a stiffness actuator. With proper design, this technique not only protects the entire system against impact, storing energy in the compliant element, but also offers additional information about force/torque in joints of the robot. This design has been developed in various humanoid robot such as M2V2 (Pratt, J *et al.*, 2012), ESCHER (Knabe, C *et al.*, 2015), COMAN (Ajoudani, A *et al.*, 2015), WALK-MAN (Tsagarakis, N. G. *et al.*, 2017).

In our previous studies, the commercial humanoid robot UXA-90 can only walk straight on a perfectly flat ground with a pre-calculated trajectory. The humanoid robot suffered significant impact force when walking, causing vibrations in the whole system. The impact force also causes great wear in the actuator's transmission gear over time. Therefore, it is crucial to implement the compliant actuator into UXA-90's legs since it will ease the impact force, eliminating vibration on the humanoid robot.

Since we have already succeeded in designing the SEA actuator for humanoid robot (Truong, K. D. *et al.*, 2020) (Truong, K. D. *et al.*, 2020). In this paper, SEA actuators are used for two legs instead of the original DC servo actuators. First, a dynamic model is deduced for one leg of the humanoid as well for the SEA. Secondly, a novel backstepping based sliding mode force control approach is employed to build the controller for each joint of the leg. Finally, some simulations are carried out to evaluate the effectiveness of the controller and the SEA mechanism.

2. System Modelling

2.1 Overall system modelling

The overall system is modelled as in Figure 1. The lower limb of humanoid is simplified to an L-shape link (E-D-C) which rotates about the hip joint (denoted as point E). The whole mass distribution of the limb is concentrated into one point (F) with the amplitude of m . The SEA has one end rotating about point B and the other end connecting to point C of the limb. Thus, the prismatic movement and linear force of the SEAs results in the rotation movement and external torque acting on the robot link.

Since B and τ_D are the system's uncertainties, in order to achieve the control objective, an integral sliding mode control (ISMC) is implemented to guarantee the robustness of the whole system despite the uncertainty parameters and external disturbances.

2.2 SEA modelling

For the mechanical aspect of the actuator, the dynamic equation of the output point C is:

$$\ddot{X}_C + \frac{k}{m}X_C = \frac{k}{m}X_0 - \frac{F_R}{m} \quad (8)$$

in which k is the stiffness coefficient of the spring used in the SEAs, and X_C and X_0 are the displacements of the SEA's end effector and the ball screw's nut, respectively.

For the electrical aspect of the actuator, the characteristic of an ideal DC motor can be expressed by:

$$V_{IN} = IR + V_{EMF} + L \frac{dI}{dt} \quad (9)$$

where V_{IN} is the DC motor's applied voltage, I is the armature current, R is the motor's internal resistance, L is the inductance.

The back-EMF voltage defined as $V_{EMF} = K_{EMF}\omega_M$ (K_{EMF} is the back-EMF constant) and the electrical torque defined as $T_M = K_T I$ (K_T is the torque constant), Eq. (9) can be rewritten as:

$$V_{IN} = IR + K_{EMF}\omega_M + \frac{L}{K_T} \frac{dT_M}{dt} \quad (10)$$

By applying Newton - Euler equation for the motor's rotor, the dynamics of the rigid part can be written as:

$$J_M \dot{\omega}_M = T_M - \frac{1}{n\eta_1} \left(J_s \dot{\omega}_s + \frac{l}{2\pi\eta_2} (m_0 \dot{v}_0 + F_L) \right) - B_M \omega_M \quad (11)$$

where J_M , ω_M and J_s , ω_s are the moment of inertia and the angular velocity of the motor and ball screw respectively, m_0 and v_0 are the mass and velocity of the ball screw's nut together with the spring base, B_M is the viscous friction coefficient, n is the gearbox transmission ratio, l is the lead of ball screw, η_1 and η_2 are the efficiency coefficients of the gearbox and the ball screw respectively, and F_L is the reaction force from the load.

For simplicity, define the equivalent moment of inertia of the whole SEA-system J_{eq} , which includes the moment of inertia of motor, ball screw, ball screw nut and spring base:

$$J_{eq} = J_M + \frac{1}{n^2\eta_1} J_s + \frac{l^2}{4\pi^2 n^2 \eta_1 \eta_2} m_0 \quad (12)$$

Moreover, the torque acted on the load (which is also the reaction torque from the load) can be calculated from load force as:

$$T_L = \frac{l}{2\pi n \eta_1 \eta_2} F_L \quad (13)$$

Substituting Eq. (12) and Eq. (13) into Eq. (11), and recall that $\omega_M = v_0 \frac{2\pi n}{l}$, the mechanical equation of the rigid part can be represented as:

$$J_{eq} \frac{2\pi n}{l} \dot{v}_0 = T_M - T_L - B_M v_0 \frac{2\pi n}{l} \quad (14)$$

By substituting Eq. (14) into Eq. (10), the differential equation describes the system can be written as:

$$V_{IN} = \frac{T_M}{K_T} R + K_{EMF} \frac{n2\pi}{l} v_0 + \frac{L}{K_T} \frac{dT_M}{dt} \quad (15)$$

Expand the Eq. (15), it yields:

$$V_{IN} - \frac{RT_L - L\dot{T}_L}{K_T} = \frac{2\pi n}{lK_T} (LJ_{eq}\ddot{v}_0 + (RJ_{eq} + LB_M)\dot{v}_0 + (B_MR + K_{EMF}K_T)v_0) \quad (16)$$

U_v^* is defined as:

$$U_v^* = V_{IN} - \frac{RT_L - L\dot{T}_L}{K_T} \quad (17)$$

Hence the dynamic equation of the SEAs is expressed as:

$$U_v^* = \frac{2\pi n}{lK_T} (LJ_{eq}\ddot{v}_0 + (RJ_{eq} + LB_M)\dot{v}_0 + (B_MR + K_{EMF}K_T)v_0) \quad (18)$$

The unknown parameters are determined by examining the step signal response in no-load state of the DC motor used in our project. The characteristic equation of just only the motor is:

$$V_{IN} = \frac{LJ_M\ddot{\omega}_M + (RJ_M + LJ_M)\dot{\omega}_M + (RB_M + K_{EMF}K_T)\omega_M}{K_T} \quad (19)$$

The System Identification toolbox and Simulink toolbox of MATLAB are utilized for this task. The results are: $R = 5,56 \Omega$, $B_M = 16,5 \times 10^{-5} Nms/rad$, $J_M = 1,57 \times 10^{-4} Kgm^2$, $K_T = K_{EMF} = 0,202 Nm/A$, $L = 4,6 mH$.

The equivalent moment is then calculated as:

$$J_{eq} = J_M + \frac{1}{n^2\eta_1} J_G + \frac{l^2}{4\pi^2 n^2 \eta_1 \eta_2} m_0 = 1,574 \times 10^{-4} (Kgm^2) \quad (20)$$

Then, Eq. (18) becomes:

$$U_v^* = (4.69 \times 10^{-3})\ddot{v}_0 + 5.68\dot{v}_0 + 270v_0 \quad (21)$$

Since the coefficient of \ddot{v}_0 is relatively small compared to others, it can be neglected to simplify the equation, which leads to:

$$U_v^* = 5,68\dot{v}_0 + 270v_0 \quad (22)$$

Let $U_v = U_v^*/5.68$, it yields:

$$U_v = \dot{v}_0 + 47,535v_0 = \ddot{X}_0 + 47,535\dot{X}_0 \quad (23)$$

Combine Eq. (8) and Eq. (23), the dynamic equation of the SEA is obtained as:

$$(\ddot{X}_C - \ddot{X}_0) = -\frac{k}{m}(X_C - X_0) - \frac{F_R}{m} + 48\dot{X}_0 - U_v \quad (24)$$

Let $[\Delta] = X_C - X_0$, $\omega = \sqrt{\frac{k}{m}}$, $U_{eq} = 48\dot{X}_0 - U_v$, Eq. (24) becomes:

$$[\ddot{\Delta}] + \omega^2[\Delta] = U_{eq} - \frac{F_R}{m} \quad (25)$$

3. Controller Design

3.1 Sliding mode approach

First, the torque created by the SEA is calculated as:

$$\tau_{SEA} = F_{SEA} \frac{d_6 d_7 \sin\left(\varphi + \sigma + \frac{\pi}{2} - \alpha\right)}{L(\varphi)} = -[\Delta] \frac{k d_6 d_7 \sin\left(\varphi + \sigma + \frac{\pi}{2} - \alpha\right)}{L(\varphi)} \quad (26)$$

where $F_{SEA} = -k[\Delta]$ is the output force of the SEA, k is the total stiffness coefficient of the springs inside the SEA. Then, Eq. (7) is rewritten as:

$$\ddot{\varphi} = \frac{-mgd_3 \sin \varphi - B\dot{\varphi} + \tau_D}{md_3^2} - [\Delta] \frac{k d_6 d_7 \sin\left(x_1 + \sigma + \frac{\pi}{2} - \alpha\right)}{md_3^2 L(x_1)} \quad (27)$$

From Eq. (27), the system state variables can be defined as follow:

$$\begin{aligned} x_1 &= \varphi \\ \dot{x}_1 &= x_2 \\ \dot{x}_2 &= u \cdot g(x_1) + f(x_1, x_2, \tau_D) \end{aligned} \quad (28)$$

in which $u \triangleq [\Delta]$, $f(x_1, x_2, \tau_D) \triangleq -\frac{Bx_2 + mgd_3 \sin x_1 - \tau_D}{md_3^2}$, $g(x_1) \triangleq -\frac{k d_6 d_7 \sin\left(x_1 + \sigma + \frac{\pi}{2} - \alpha\right)}{md_3^2 L(x_1)}$

The first error variable is defined as the differences between the desired and response rotation angle while the second one is between the desired and response angular velocity. They are shown as:

$$\begin{aligned} e_1 &= \varphi_d - \varphi \\ e_2 &= \dot{e}_1 \end{aligned} \quad (29)$$

The sliding function is determined as:

$$\sigma = e_2 + c e_1, \quad c > 0 \quad (30)$$

The first time-derivative of sliding function yields:

$$\dot{\sigma} = \dot{e}_2 + c \dot{e}_1 = \ddot{\varphi}_d - g(x_1)u - f(x_1, x_2, \tau_D) + c(\dot{\varphi}_d - \dot{\varphi}) \quad (31)$$

The Candidate Lyapunov Function is chosen as:

$$V_x = \frac{1}{2} \sigma^2 \quad (32)$$

Take the first time-derivative of CLF, it yields:

$$\dot{V}_x = \sigma \dot{\sigma} = \sigma [\ddot{\varphi}_d - u \cdot g(x_1) - f(x_1, x_2, \tau_D) + c(\dot{\varphi}_d - \dot{\varphi})] \quad (33)$$

To ensure the stabilization of the system, the following condition must be met $\dot{V}_x \leq 0$. For that requirement, the control signal u must be determined as:

$$u = \frac{1}{g(x_1)} [\rho \operatorname{sign}(\sigma) + \ddot{\varphi}_d - f(x_1, x_2, \tau_D) + c(\dot{\varphi}_d - \dot{\varphi})] \quad (34)$$

where ρ is a positive constant. The time-derivative of CLF becomes:

$$\dot{V}_x = -\rho \sigma \operatorname{sign}(\sigma) = -\rho |\sigma| \leq 0 \quad (35)$$

This leads to the fact that \dot{V}_x and σ are bounded. Moreover, \dot{V}_x is an absolute function so that it is uniform continuity. Hence, $\dot{V}_x \rightarrow 0$ when $t \rightarrow \infty$ and σ is proven to converge to zero.

3.2 Backstepping algorithm

In this section, the dynamic system in Eq. (27) is combined with Eq. (25) to determine the function of input voltage U_{eq} which is the primary control variable.

First, Eq. (27) is express in the state space form as follow:

$$\dot{X} = f_x(X) + g_x(X)u \quad (36)$$

where $X \triangleq [x_1 \quad x_2]$, $f_x(X) \triangleq \left[-\frac{Bx_2 + mgd_3 \sin x_1 - \tau_D}{md_3^2} \right]$, $g_x(X) \triangleq \left[\begin{array}{c} 0 \\ -\frac{kd_6 d_7 \sin(x_1 + \sigma + \frac{\pi}{2} - \alpha)}{md_3^2 L(x_1)} \end{array} \right]$

Consider the first augmented dynamic system:

$$\begin{cases} \dot{X} = f_x(X) + g_x(X)z_1 \\ \dot{z}_1 = u_1 \end{cases} \quad (37)$$

In the previous section, an adaptive control law $u_x = u$ is proven to be able to ensure the stability of the X-system. The control goal now is to make z_1 follow the desired value of u_x . The augmented Lyapunov function is:

$$V_1 = V_x + \frac{1}{2}(u_x - z_1)^2 = \frac{1}{2}\sigma^2 + \frac{1}{2}(u_x - z_1)^2 \quad (38)$$

The first time-derivative of V_1 yields:

$$\dot{V}_1 = \sigma[\dot{\varphi}_d - z_1 g(x_1) - f(x_1, x_2, \tau_D) + c(\dot{\varphi}_d - \dot{\varphi})] + (u_x - z_1)(\dot{u}_x - \dot{u}_1) \quad (39)$$

By adding and subtracting the term $\sigma g(x_1)u_x$, Eq. (39) becomes:

$$\begin{aligned} \dot{V}_1 = & \sigma[\dot{\varphi}_d - u_x g(x_1) - f(x_1, x_2, \tau_D) + c(\dot{\varphi}_d - \dot{\varphi})] + \sigma g(x_1)(u_x - z_1) \\ & + (u_x - z_1)(\dot{u}_x - \dot{u}_1) \end{aligned} \quad (40)$$

To stabilize the proposed extended system, the pseudo-control law is:

$$u_1 = k_1(u_x - z_1) + \dot{u}_x + \sigma g(x_1) \quad (k_1 > 0) \quad (41)$$

Continue the back-stepping algorithm, the second augmented system is proposed as:

$$\begin{cases} \dot{X}_1 = f_1(X_1) + g_1(X_1)z_2 \\ \dot{z}_2 = f_2(X_2) + g_2(X_2)U_{eq} \end{cases} \quad (42)$$

in which: $X_1 \triangleq \begin{bmatrix} X \\ z_1 \end{bmatrix}$, $f_1(X_1) \triangleq \begin{bmatrix} f_x(X) + g_x(X)z_1 \\ 0 \end{bmatrix}$, $g_1(X_1) \triangleq \begin{bmatrix} 0 \\ 1 \end{bmatrix}$, $X_2 \triangleq \begin{bmatrix} X_1 \\ z_2 \end{bmatrix}$, $f_2(X_2) \triangleq -\omega^2 z_1 - \frac{FR}{m}$, $g_2(X_2) \triangleq 1$

The X_1 -system is assumed to be stable by the control law u_1 . The goal is to make z_2 reach the value of u_1 . The 2nd augmented Lyapunov function:

$$V_2 = V_1 + \frac{1}{2}(u_1 - z_2)^2 \quad (43)$$

Take the first time-derivative of Eq. (43), it yields:

$$\begin{aligned} \dot{V}_2 = & \sigma[\dot{\varphi}_d - u_x g(x_1) + f(x_1, x_2, \tau_D) + c(\dot{\varphi}_d - \dot{\varphi})] + \sigma g(x_1)(u_x - z_1) \\ & + (u_x - z_1)(\dot{u}_x - \dot{z}_2) + (u_1 - z_2)[\dot{u}_1 - f_2(X_2) - g_2(X_2)U_{eq}] \end{aligned} \quad (44)$$

By adding and subtracting the term $(u_x - z_1)u_1$, Eq. (44) becomes:

$$\begin{aligned} \dot{V}_2 = & \sigma[\dot{\varphi}_d - u_x g(x_1) + f(x_1, x_2, \tau_D) + c(\dot{\varphi}_d - \dot{\varphi})] + \sigma g(x_1)(u_x - z_1) \\ & + (u_x - z_1)(\dot{u}_x - u_1) + (u_x - z_1)(u_1 - z_2) + (u_1 - z_2)[\dot{u}_1 \\ & - f_2(X_2) - g_2(X_2)U_{eq}] \end{aligned} \quad (45)$$

Then, control input for the second augmented system, which is the input voltage, is obtained as:

$$\begin{aligned} U_{eq} = & \frac{1}{g_2(X_2)} [-f_2(X_2) + k_2(u_1 - z_2) + \dot{u}_1 \\ & + (u_x - z_1)] \quad (k_2 > 0) \end{aligned} \quad (46)$$

4. Simulation and Analyzing

The simulation is carried out to evaluate the capability of the control algorithm. The physical and geometric parameters of the system are given in Table I.

Table I. Simulation parameters

Physical parameters	
Mass, m (kg)	2
Viscous friction coefficient, B (Nms)	0.5
Stiffness coefficient, k (N/m)	20000
Geometric parameters	
d_1 (m)	0.0280
d_2 (m)	0.0525
d_3 (m)	0.0525
d_4 (m)	0.0350
d_5 (m)	0.1180

The referenced signal used is the rotation angle at the hip joint of humanoid UXA-90 in a walking cycle, which is inferred from (Nguyen, X. T. *et al.*, 2020).

First, the sliding mode and back-stepping controller are designed with the initial gain values chosen as: $c = 10$, $\rho = 3$, $k_1 = 1$, $k_2 = 5$. The results are shown in Figure 2.

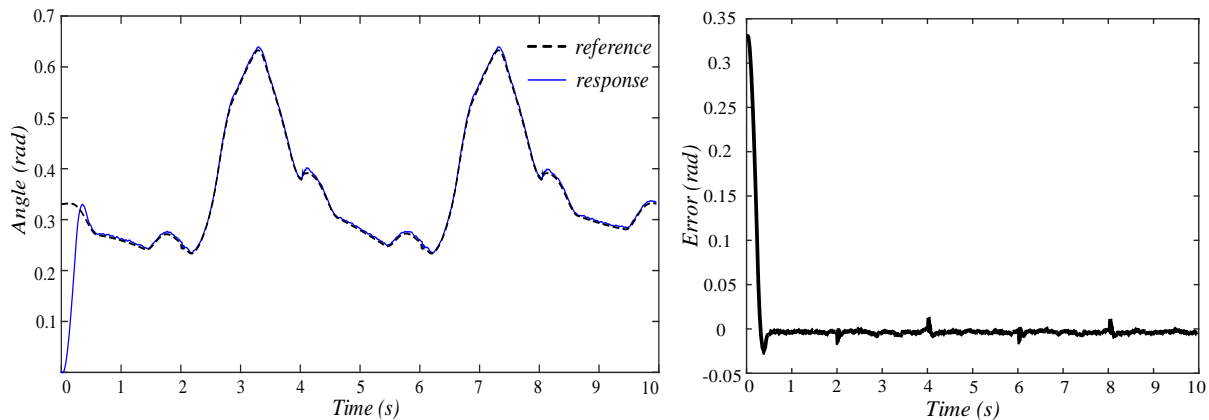


Figure 2. The simulated response in comparison with the referenced signal (left) and the angle tracking error (right)

Overall, the output response of the system can track the referenced angle trajectory with relatively small error. In specific, except for the initial error during the transient phase, the highest absolute error is approximate 0.02 rad , which is less than 10% compared to the tracking value in every instant during the whole cycle. The disturbances mainly appear at the peak of the graph since it is the moment when the joint reverses its rotating direction rapidly.

Next, the influence of each gain coefficients in the sliding mode based backstepping control law is examined. Figure 3 illustrates the simulated responses of the system in different sets of gain values. In each case, each coefficients is modified respectively while the others are kept unchanged. Based on the obtained results in Figure 3, the impact of c, ρ, k_1, k_2 can be summarized. First, the increases of k_1, k_2 and ρ reduce the transient time and changing-phase instant of the system while the increase of c causes a contrast effect. However, the higher the value of c , the lower the steady-state error. Besides, high values of k_1 and k_2 lead to the overshoot of the response, which can make the system become unstable. The increase of ρ hardly create overshoot phenomenon like k_1 and k_2 . However, a control law with high value of ρ will make the system stay at high steady-state error.

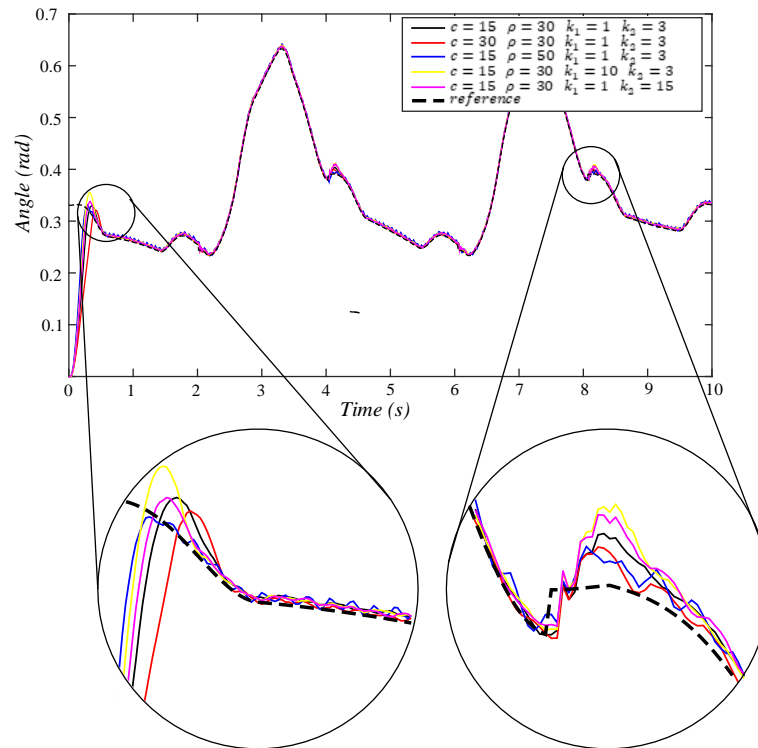


Figure 3. The simulated response in different sets of gain value in the control law

The reasons for those impacts mainly rely on the positions and roles of each coefficients in the proposed equations. Coefficient c is defined in the sliding function in Eq. (30) and can be considered as a pole of the error system (e_1, e_2) , which explains why the increase in c leads to the stabilization with low overshoot of the output variable φ of the system. Meanwhile, ρ appears as the coefficient of term $sign(\sigma)$ in the control law u . Since the output values of this term only vary among definite numbers (-1; 0 and 1), ρ has no impact to the variation of σ except when it changes sign, which means ρ just assures the bounded error for the system with the same recovery speed (equal to ρ itself). However, due to the constant recovery speed at every error value, the high value of ρ will make the system's response oscillates in the steady-state about the zero-error point, and with a high enough value, it would lead to the unstable response. On the other hand, k_1 and k_2 are the proportion coefficients which influence the errors of z_1 and z_2 respectively. For that reason, they perform just like the K_p coefficient in a standard PID controller. Specifically, the higher values of them will make the system rapidly recover whenever the error occurs, however it may also cause huge overshoot and make the system unstable if assigned by too high values.

5. Conclusion

In conclusion, the sliding mode based back-stepping control algorithm is proven to be appropriate for this application. The effectiveness and quality of the controller rely on the selections of gain values, which can cause both positive and negative impact to the stability of the system. Moreover, although the simulation shown good results in this process, the real response of the system in practice might be different due to the incorrect measurements of the uncertainties parameters. In the future, more experiments will be carried out to further evaluate the capability of this control algorithm to the humanoid field.

Acknowledgments

This research is supported by DCSELab and funded by Vietnam National University HoChiMinh City (VNU-HCM) under grant number B2019-20-09 and TX2021-20b-01. We acknowledge the support of time and facilities from Ho Chi Minh City University of Technology (HCMUT), VNU-HCM for this study.

References

- [1] Ajoudani, A *et al.*, 2015. *A manipulation framework for compliant humanoid COMAN: Application to a valve turning task*. Madrid, Spain, IEEE-RAS International Conference on Humanoid Robots, p. 664–670.
- [2] Akachi, K. *et al.*, 2005. *Development of humanoid robot HRP-3P*. Tsukuba, Japan, 5th IEEE-RAS International Conference on Humanoid Robots, p. 50–55.
- [3] Banerjee, N. *et al.*, 2015. *Human-supervised control of the ATLAS humanoid robot for traversing doors*. Seoul, South Korea, IEEE-RAS International Conference on Humanoid Robots, p. 722–729.
- [4] Bierbaum, A *et al.*, 2009. *Force position control for a pneumatic anthropomorphic hand*. Paris, France, 9th IEEE-RAS International Conference on Humanoid Robots, p. 21–27.
- [5] Hirayama, K. *et al.*, 2019. *Passivity-Based Compliant Walking on Torque-Controlled Hydraulic Biped Robot*. Beijing, China, IEEE-RAS International Conference on Humanoid Robots, p. 552–557.
- [6] Hogan, N., 1985. Impedance Control: an Approach To Manipulation: Part I - Theory. *Journal of Dynamic Systems, Measurement and Control, Transactions of the ASME*, Volume 107, p. 1–7.
- [7] Hyon, S. H. *et al.*, 2017. Design and Experimental Evaluation of a Fast Torque-Controlled Hydraulic Humanoid Robot. *IEEE/ASME Transactions on Mechatronics*, Volume 22, p. 623–634.
- [8] Jiang, Z. H. *et al.*, 2019,. *Impedance Control of Flexible Joint Robots Based on Singular Perturbation Method*. Bangkok, Thailand, Proceedings of the IEEE 2019 9th International Conference on Cybernetics and Intelligent Systems and Robotics, Automation and Mechatronics, CIS and RAM 2019, p. 548–552.
- [9] Kaneko, K. *et al.*, 2002. *Design of prototype humanoid robotics platform for HRP*. Lausanne, Switzerland, IEEE International Conference on Intelligent Robots and Systems, p. 2431–2436.
- [10] Kazuo, H *et al.*, 1988. *The Development of Honda Humanoid Robot*. Leuven, Belgium, IEEE International Conference on Robotics & Automation, p. 1321–1326.

- [11] Kim, K. R. *et al.*, 2018. Design of Robot Hand with Pneumatic Dual-Mode Actuation Mechanism Powered by Chemical Gas Generation Method. *IEEE Robotics and Automation Letters*, Volume 3, p. 4193–4200.
- [12] Knabe, C *et al.*, 2015. *Design of a series elastic humanoid for the DARPA Robotics Challenge*. Seoul, South Korea , IEEE-RAS International Conference on Humanoid Robots, p. 738–743.
- [13] Ko, T. *et al.*, 2018. *Compliant Biped Locomotion of Hydra, an Electro-Hydrostatically Driven Humanoid*. Beijing, China, 2018 IEEE-RAS 18th International Conference on Humanoid Robots (Humanoids), p. 587–592.
- [14] Li, S. *et al.*, 2019. Intuitive Control of a Robotic Arm and Hand System with Pneumatic Haptic Feedback. *IEEE Robotics and Automation Letters*, Volume 4, p. 4424–4430.
- [15] Nguyen, X. T. *et al.*, 2020. *Controlling Center of Mass in Humanoid Robot using Sliding Mode Control*. Hanoi, Vietnam, International Conference on Advanced Mechatronic Systems 20, pp. 17 - 22.
- [16] Nishino, S. *et al.*, 2007. *Development of robot hand with pneumatic actuator and construct of master-slave system*. Lyon, France, Annual International Conference of the IEEE Engineering in Medicine and Biology - Proceedings, p. 3027–3030.
- [17] Park, I. W. *et al.*, 2004. *Development of humanoid robot platform KHR-2 (KAIST humanoid robot - 2)*. Santa Monica, CA, USA, 4th IEEE-RAS International Conference on Humanoid Robots, p. 292–309.
- [18] Park, I. W. *et al.*, 2007. Mechanical design of the humanoid robot platform, HUBO. *Advanced Robotics*, Volume 21, p. 1305–1322.
- [19] Pratt, J *et al.*, 2012. Capturability-based analysis and control of legged locomotion, Part 2: Application to M2V2, a lower-body humanoid. *International Journal of Robotics Research*, Volume 31, p. 1117–1133.
- [20] Sakagami, Y. *et al.*, 2002. *The intelligent ASIMO: System overview and integration*. Lausanne, Switzerland, IEEE International Conference on Intelligent Robots and Systems, p. 2478–2483.
- [21] Suarez, A *et al.*, 2018. Physical-Virtual Impedance Control in Ultralightweight and Compliant Dual-Arm Aerial Manipulators. *IEEE Robotics and Automation Letters*, Volume 3, p. 2553–2560.
- [22] Truong, K. D. *et al.*, 2020. *A Study on Series Elastic Actuator Applied for Human-Interactive Robot*. Hanoi, Vietnam, International Conference on Advanced Mechatronic Systems, p. 7–12.
- [23] Truong, K. D. *et al.*, 2020. *Design of Series Elastic Actuator Applied for Humanoid*. Hanoi, Vietnam, International Conference on Advanced Mechatronic Systems, ICAMechS, p. 23–28.
- [24] Tsagarakis, N. G. *et al.*, 2017. WALK-MAN: A High-Performance Humanoid Platform for Realistic Environments. *Journal of Field Robotics*, Volume 34, p. 1225–1259.
- [25] Zhu, H *et al.*, 2017. *Design and validation of a torque dense, highly backdrivable powered knee-ankle orthosis*. Singapore, Proceedings - IEEE International Conference on Robotics and Automation, p. 504–510.

Simulate Deformation and Stress of 3-Axis CNC Milling Machine Body in Outsoles Mold Machining

Thanh Luan Bui¹, Vinh Tuong Vuong³, Duc Dat Do² and Tan Tien Nguyen² *

¹Industrial Maintenance Training Center, HCMUT, VNU-HCM

²National Key Laboratory of Digital Control and System Engineering, HCMUT, VNU-HCM

³Institute of Engineering, Hutech University

*Corresponding author. E-mail: nttien@dcselab.edu.vn

Abstract

The leather footwear manufacturing industry is very developed today. Molds to produce outsoles are in high demand and necessitate quick delivery time. To meet these requirements, manufacturers need CNC milling machines to process molds quickly and accurately. In this paper, a simulation of forces and stresses is presented on the body of a 3-axis computer numerical control (CNC) milling machine designed for outsole mold machining. A simulation is performed by ANSYS Workbench software with tetrahedral meshing method on the structural blocks of the machine body using FCD370 cast iron. The simulation is performed with roughing milling and in 5 different machining positions on the same workpiece with a mass of 700 kg. The simulation results provide the deformations and stresses on the parts of the machine body when machining and demonstrate the response to the requirements of the machine body under the effect of machining force.

Keywords: CNC milling machines, 3-axis, FCD370 cast iron, outsole mold, ANSYS Workbench

1. Introduction

The design and development of CNC machine tools have always been an important topic in industrial production. The machine design calculation purposes are to create machines with high durability and long life. The simulation, deformation, and stress on the machine tool will help to design the overall structure of the machine tool with good results. Simulation of forces acting on the overall structure of the machine will help the designer foresee the fields of deformation, impact stress, making the design faster and with better results. In machining, the machine body is affected by external forces, including friction, so there are many studies and simulations on CNC milling machines. Study on the effect of friction on static and dynamic characteristics on the durability and service life of CNC machine tools [1]. There is also a study on the error of guide geometry of milling machines based on modeling by finite element method [2]. Besides, there is also a deeper study of the tool head positioning error to help better milling machine design. This study provided a good solution to reduce the tooltip position error [3]. B. M. Swami et al. [4] selected a bed machine to analyze the static and dynamic loads acting on the machine, then reduce the weight of the machine without reducing the rigidity of the structure and the accuracy of the machine tool by adding ribs at suitable locations. C. C. Hong et al. [5] also relies on CAE software to analyze the linear structure, stress, and deformation in order to reduce the weight of the CNC machine while maintaining enough stress to resist the external load. In addition, there is also a research on the design and manufacture of the body based on the configuration principle of the biological skeleton to improve the static and dynamic structural performances of high-speed machine tools [6]. The above studies have been done with simulations of forces acting on the

CNC machine body but have not given specific cases of these forces during machining. Therefore, this paper will present a simulation of deformation and stress acting on the body of a CNC milling machine from 5 machining positions with the largest cutting force when roughing with facemilling diameter $D = 90\text{mm}$.

With the requirement of outsole mold thickness of $\pm 0.01\text{mm}$, the body design must have a deformation within 0.001mm and stress must be less than 40Mpa . Simulations will be performed using software by ANSYS Workbench. Maximum deformation and stress values are provided for reference and evaluation with design requirements.

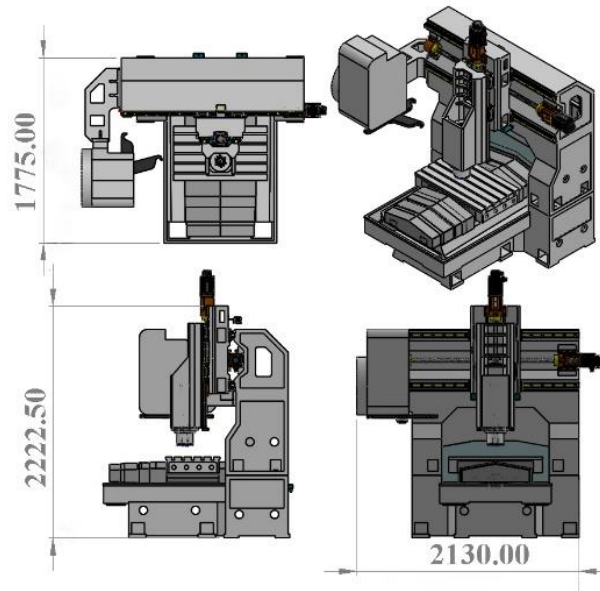


Figure 1. Three axis CNC milling machine assembling 3D parts

2. Method and simulation

2.1 Parameters of 3 Axis CNC Milling Machine

The CNC milling machine shown in Figure 1 has a width of 2130 mm , a length of 1775 mm , a height of 2222.5mm and a mass of 7018 kg . The weight of the workpiece placed on the machine table is 700 kg and the material is C45 steel. Parameters of the machining process are: Facemilling $D = 90\text{mm}$, number of teeth: $Z = 5$, breaking strength of C45 steel $\sigma_B = 610\text{MPa}$, spindle rotation $n = 700\text{ rpm}$, depth of cut $t = 2.5\text{ mm}$.

$$\text{The main cutting force [7]: } P_z = \frac{10 \cdot C_p \cdot t^x \cdot S_z^y \cdot B^u \cdot Z}{D^q \cdot n^w} \cdot k_{MP} \quad (1)$$

where: S_z^y : feedrate, B^u : milling width, k_{MP} : adjustment coefficient, C_p : coefficient depends on machining condition [7], t : width of the blade, D : milling cutter diameter, n : number of revolutions of the tool, the exponents x, y, z, q, w, u are the coefficients calculated according to the cutting mode.

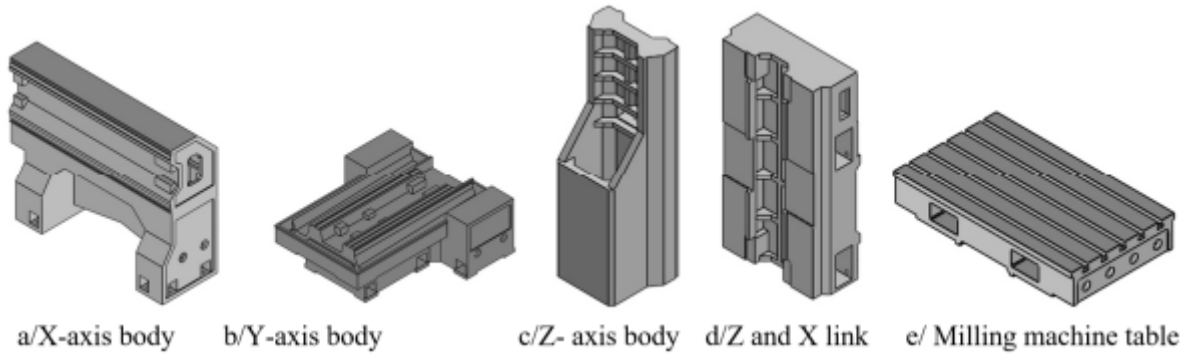


Figure 2. Three axis CNC milling machine 3D parts

Figure 2 shows the 3D parts of CNC milling machine body. The components of the machine are: X-axis body weighs 3084 kg, Y-axis body weighs 2694 kg, Z-axis body weighs 306 kg, Z and X link weighs 424 kg, milling machine table weighs 390 kg, spindle weighs 120 kg. Total weight is 7018kg.

2.2 Simulated Positions and Applied Forces

2.2.1 Five Positions of Workpiece Cutting Points on The Machine Table

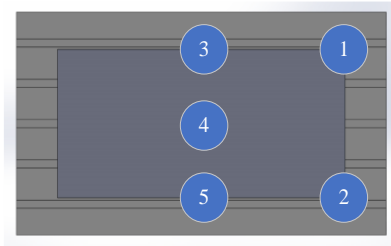


Figure 3. Five positions of workpiece cutting points on the machine table

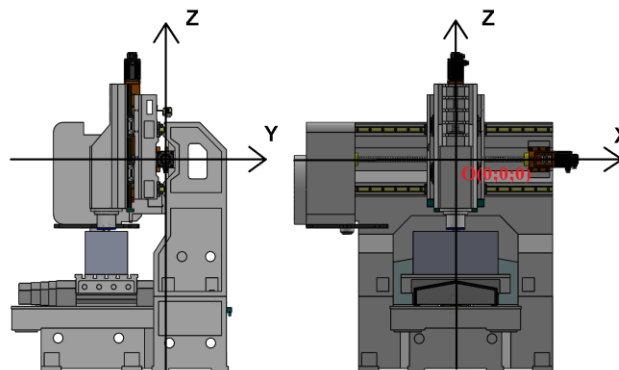


Figure 4. Origin machine coordinates

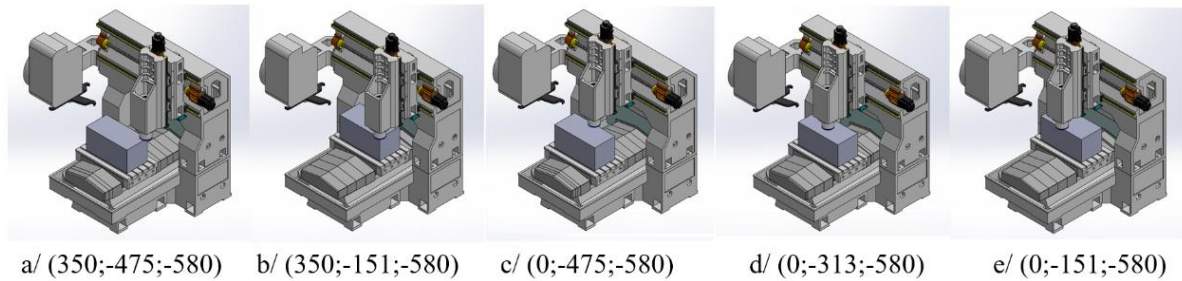


Figure 5. Position of the machining points

Figure 3 shows five positions of workpiece cutting points on the table. Figure 4 shows the machine's origin position. Figure 5 shows the five machining points of the machine.

2.2.2 Cutting force acting at the machining point

Cutting force acting at the machining point [7]: $F_x = 0.7P_z$, $F_y = 0.65P_z$, $F_z = 0.5P_z$. Parameters of the machining process: Facemilling $D = 90$ mm, number of teeth: $Z = 5$, breaking strength of C45 steel $\sigma_B = 610$ MPa, spindle rotation $n = 700$ rpm, depth of cut $t = 2.5$ mm, $B = 72$, $s_z = 0,15$.

Based on the input parameters with facemilling and the workpiece is steel C45 [7], we have the coefficients: $C_p = 825$, $x = 1$, $y = 0.75$, $u = 1.1$, $q = 1.3$, $w = 0.2$, $k_{MP} = 0.94$.

From the above coefficients into equation (1) we can obtain:

$$P_z = \frac{10.825 \cdot 2,5^1 \cdot 0,15^{0,75} \cdot 72^{1,5}}{90^{1,3} \cdot 700^{0,2}} \cdot 0.94 = 2004.89(N)$$

From the machining parameters will be calculated: $F_x = 0.7P_z = 1403.423(N)$,
 $F_y = 0.65P_z = 1303.178(N)$, $F_z = 0.5P_z = 1002.445(N)$.

3. Simulations and Results

3.1 Simulation of Deformation and Stress with the X-axis Body

3.1.1 Machining position one (350;-475;-580)

- A: Force applied point from Z axis and motor spindle: 4177.6 N.
- B: Force applied point from the linkage plate between the X and Z axes: 4158 N.
- C: Gravity moment converted: 2499.3 N.m.
- D: The part adjacent to the Y shaft body.
- E: The impact of cutting force components when roughing: 2161.7 N.
- F: Impact torque from machining position 1: 1641.8 N.m.

X-axis body will be simulated by Finite Element Method with ANSYS Workbench for milling machine strength analysis with X-axis body: Element size 100 mm, nodes: 26167 and elements: 13507.

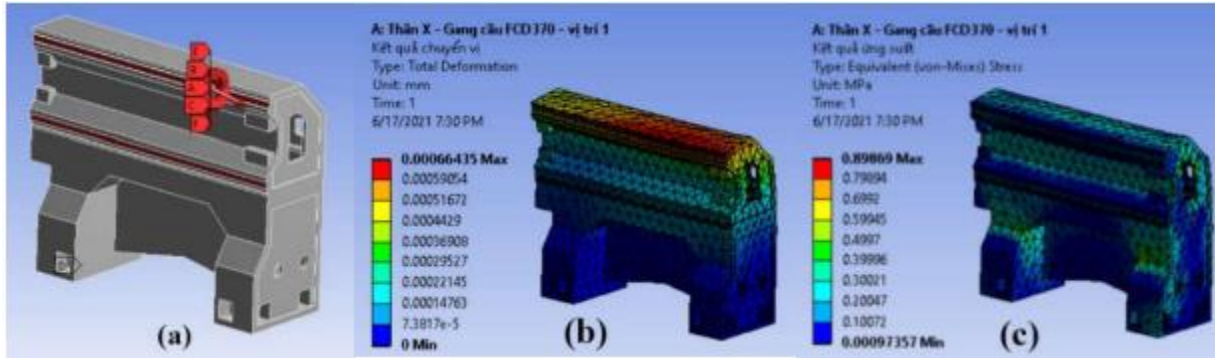


Figure 6. Simulation of deformation and stress with the X-axis body at machining position one

Figure 6 (a) shows the forces and moments acting on the X-axis at position one. Figure 6 (b) shows the maximum deformation on the X-axis body from simulation as 0.00066435 mm. Figure 6 (c) shows the maximum stress on the X-axis body from simulation as 0.89869 MPa.

3.1.2 Machining position two (350;-151;-580)

In this position, components A, B, C, D, E are the same, only F is changed.

F: Impact torque from machining position 2: 1472.6 N.m.

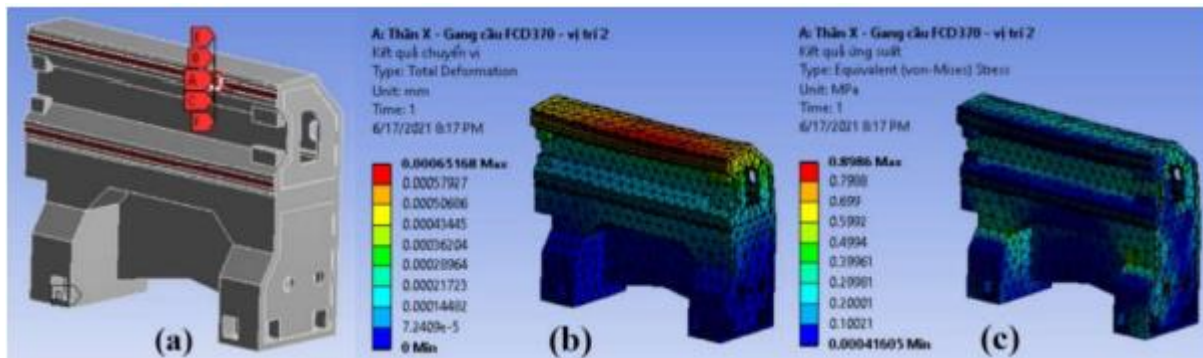


Figure 7. Simulation of deformation and stress with the X-axis body at machining position two

Figure 7 (a) shows the sum of forces and moments acting on the X-axis at position two. Figure 7 (b) shows the maximum deformation on the X-axis body from simulation as 0.00065168 mm. Figure 7 (c) shows the maximum stress on the X-axis body from simulation as 0.8986 MPa.

3.1.3 Machining position three (0;-475;-580)

In this position, components A, B, C, D, E are the same, only F is changed.

F: Impact torque from machining position 3: 1088.7 N.m

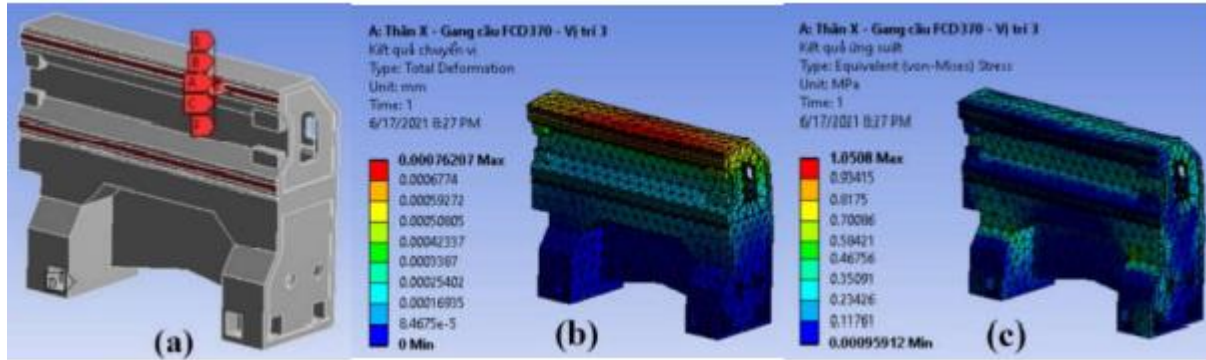


Figure 8. Simulation of deformation and stress with the X-axis body at machining position three

Figure 8 (a) shows the sum of forces and moments acting on the X-axis at position three. Figure 8 (b) shows the maximum deformation on the X-axis body from simulation as 0.00076207 mm. Figure 8 (c) shows the maximum stress on the X-axis body from simulation as 1.0508 MPa.

3.1.4 Machining position four (0;-313;-580).

In this position, components A, B, C, D, E are the same, only F is changed.

F: Impact torque from machining position 4: 1025.2 N.m.

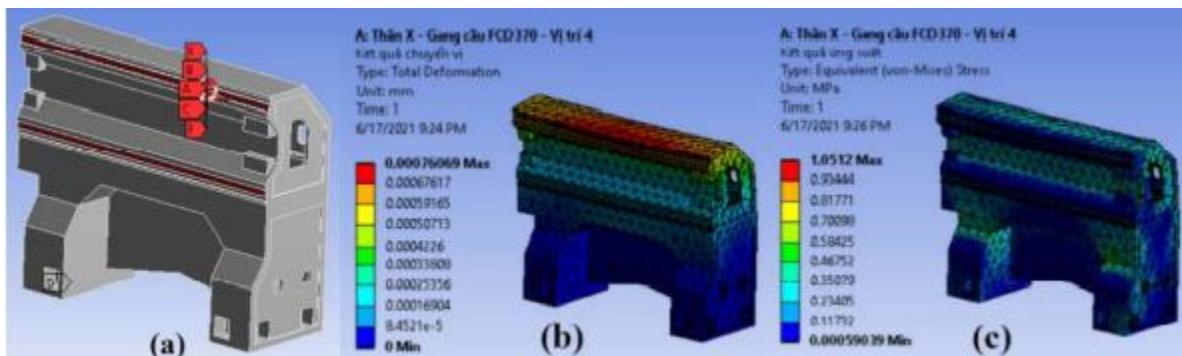


Figure 9. Simulation of deformation and stress with the X-axis body at machining position four

Figure 9 (a) shows the sum of forces and moments acting on the X-axis at position four. Figure 9 (b) shows the maximum deformation on the X-axis body from simulation as 0.00076069 mm. Figure 9 (c) shows the maximum stress on the X-axis body from simulation as 1.0512 MPa.

3.1.5 Machining position five (0;-151;-580).

In this position, components A, B, C, D, E are the same, only F is changed.

F: Impact torque from machining position 5: 1035.8 N.m.

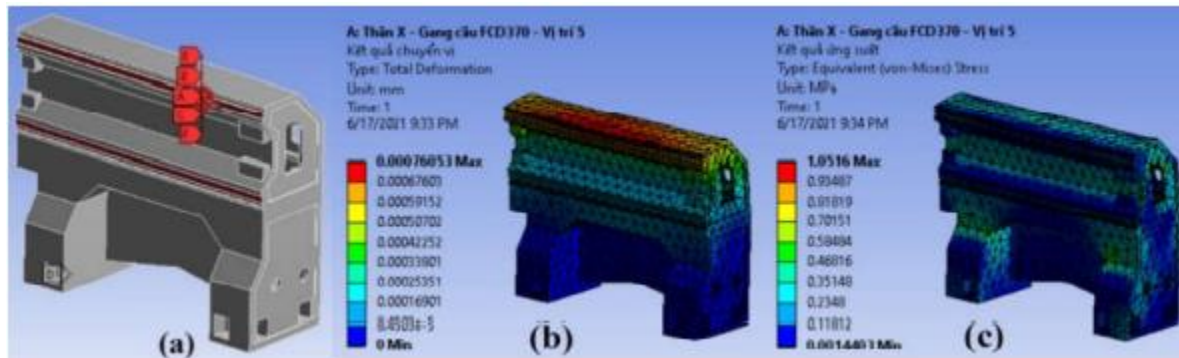


Figure 10. Simulation of deformation and stress with the X-axis body at machining position five

Figure 10 (a) shows the sum of forces and moments acting on the X-axis at position five. Figure 10 (b) shows the maximum deformation on the X-axis body from simulation is 0.00076053 mm. Figure 10 (c) shows the maximum stress on the X-axis body from simulation is 1.0516 MPa.

From Figure 6 to Figure 10, the maximum deformation at five machining positions. The maximum deformation changes from: 0.00065168 mm to 0.00076207 mm, this change is very small. The maximum stress changes from 0.8986 MPa to 1.0516 MPa, this change is also very small. From the simulation results, the X-axis body is designed to ensure rigidity.

3.2 Simulation of Deformation and Stress with the Y-axis Body

3.2.1 Machining position one (350;-475;-580)

A: Force applied point from X and Z axis: 38579 N.

B: Point of force applied from the table: 3824.6 N.

C: Force applied from workpiece: 6864.7 N.

E: The impact of cutting force components when roughing: 2161.7 N.

F: Impact torque from machining position 1: 771.81 N.m.

Y-axis body will be simulated by Finite Element Method with ANSYS Workbench for milling machine strength analysis with Y-axis body: Element size 100 mm, nodes: 26812 and elements: 14095.

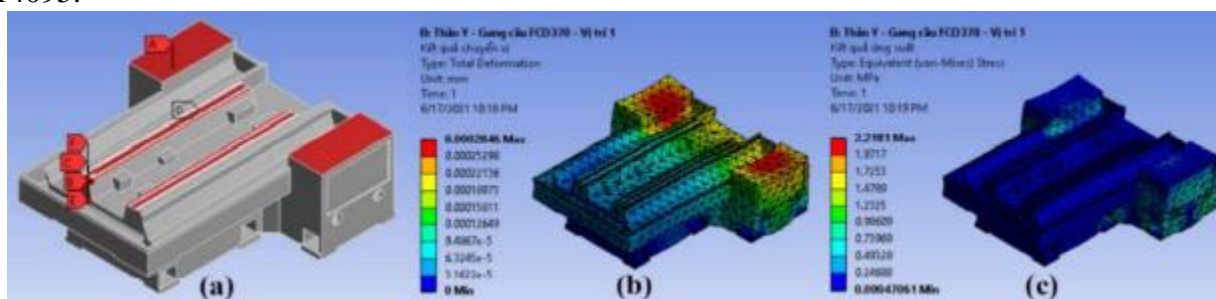


Figure 11. Simulation of deformation and stress with the Y-axis body at machining position one

Figure 11 (a) shows the sum of forces and moments acting on the Y-axis at position one. Figure 11 (b) shows the maximum deformation on the Y-axis body from simulation as 0.0002846 mm. Figure 11 (c) shows the maximum stress on the Y-axis body from simulation as 2.2181 MPa.

3.2.2 Machining position two (350;-151;-580)

In this position, components A, B, C, E are the same, only F is changed.

F: Impact torque from machining position 2: 1254.7 N.m.

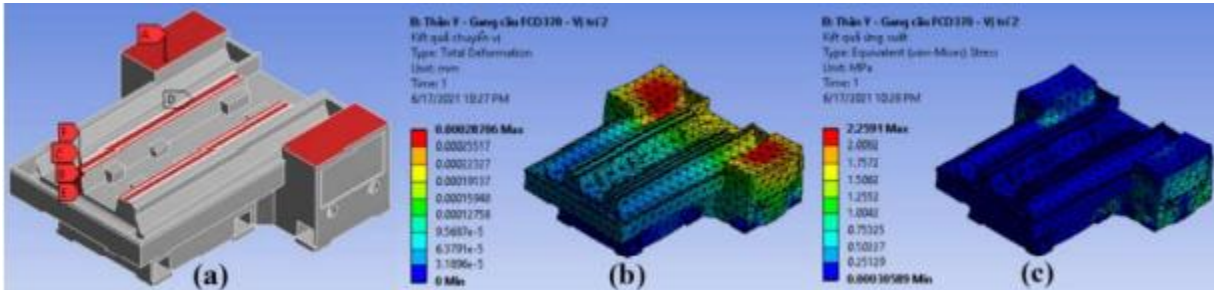


Figure 12. Simulation of deformation and stress with the Y-axis body at machining position two

Figure 12 (a) shows the sum of forces and moments acting on the Y-axis at position two. Figure 12 (b) shows the maximum deformation on the Y-axis body from simulation as 0.00028706 mm. Figure 12 (c) shows the maximum stress on the Y-axis body from simulation as 2.2591 MPa.

3.2.3 Machining position three (0;-475;-580)

In this position, components A, B, C, E are the same, only F is changed.

F: Impact torque from machining position 3: 1029.5 N.m.

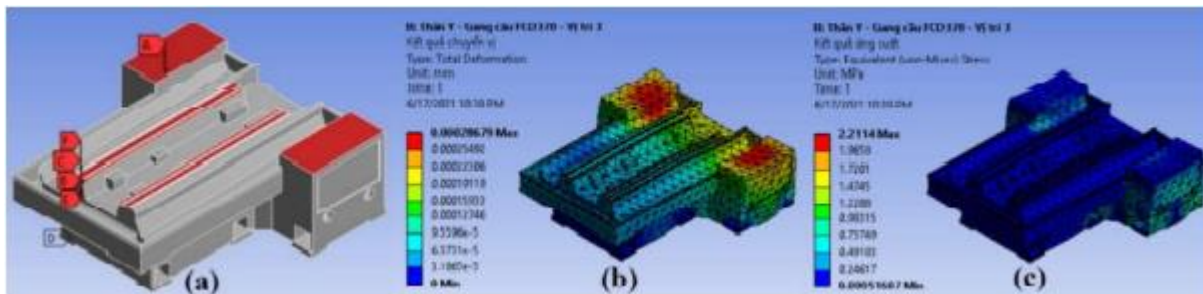


Figure 13. Simulation of deformation and stress with the Y-axis body at machining position three

Figure 13 (a) shows the sum of forces and moments acting on the Y-axis at position three. Figure 13 (b) shows the maximum deformation on the Y-axis from simulation as 0.00028679 mm. Figure 13 (c) shows the maximum stress on the Y-axis body from simulation as 2.2114 MPa.

3.2.4 Machining position four (0;-313;-580).

In this position, components A, B, C, E are the same, only F is changed.

F: Impact torque from machining position 4: 1110.8 N.m.

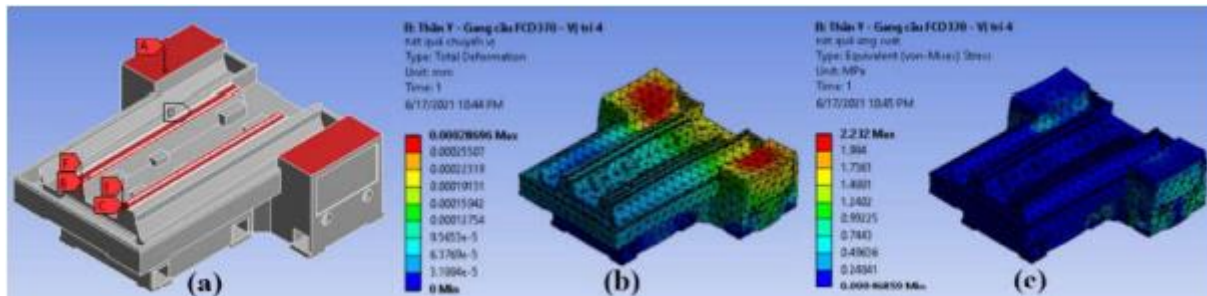


Figure 14. Simulation of deformation and stress with the Y-axis body at machining position four

Figure 14 (a) shows the sum of forces and moments acting on the Y-axis at position four. Figure 14 (b) shows the maximum deformation on the Y-axis body from simulation as 0.00028696 mm. Figure 14 (c) shows the maximum stress on the X-axis body from simulation as 2.232 MPa.

3.2.5 Machining position five (0;-151;-580).

In this position, components A, B, C, E are the same, only F is changed
 F: Impact torque from machining position 5: 1261 N.m

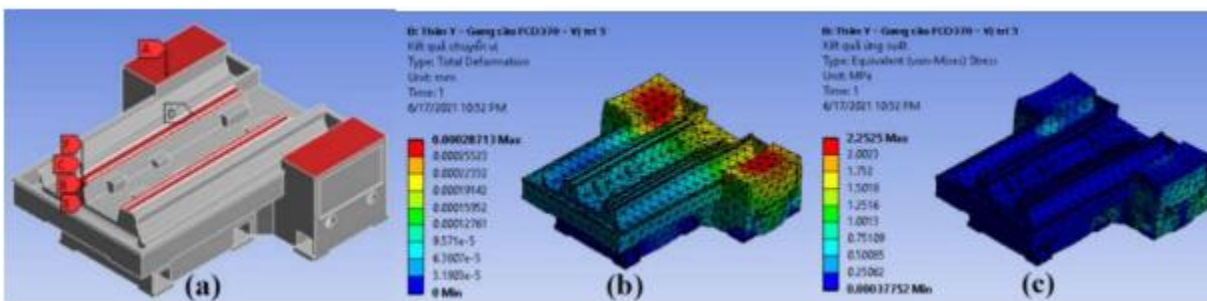


Figure 15. Simulation of deformation and stress with the Y-axis body at machining position five

Figure 15 (a) shows the sum of forces and moments acting on the Y-axis at position five. Figure 15 (b) shows the maximum deformation on the Y-axis body from simulation as 0.00028713 mm. Figure 15 (c) shows the maximum stress on the Y-axis body from simulation as 2.2525 MPa.

From Figure 11 to Figure 15, the maximum deformation at 5 machining positions. The maximum deformation changes from: 0.0002846 mm to 0.00028713 mm, this change is very small. The maximum stress changes from 2.2114 MPa to 2.2591 MPa, this change is also very small. From the simulation results, the Y-axis body is designed to ensure rigidity.

3.3 Simulation of Deformation and Stress with the Z-axis Body

- A: Force applied point from the spindle motor: 1176.8 N
- B: The spindle motor gravity torque is converted: 230.65 N.m
- C: The contact plate between the X and Z axes.
- D: Components of cutting force acting in roughing: 2161.7 N.

Z-axis body will be simulated by Finite Element Method with ANSYS Workbench for milling machine strength analysis with Z-axis body: Element size 100 mm, nodes: 3507 and elements: 1836.

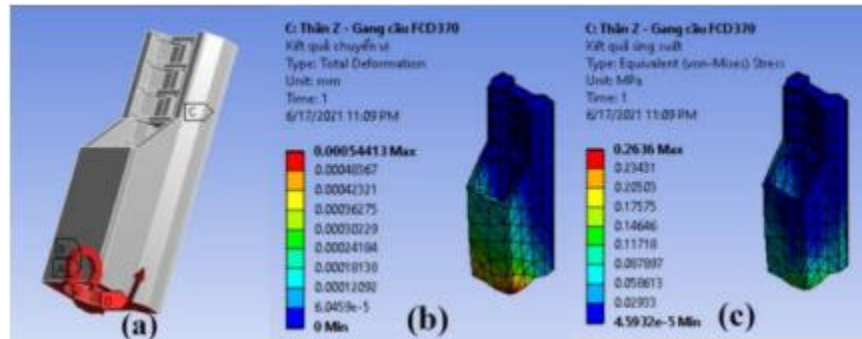


Figure 16. Simulation of deformation and stress with the Z-axis body

Figure 16 (a), shows the sum of forces and moments acting on the Z-axis. Figure 16 (b) shows the maximum deformation on the Z-axis body from simulation as 0.00054413 mm. Figure 16 (c) shows the maximum stress on the Z-axis body from simulation as 0.2636 MPa. This displacement and stress are small, so the Z axis has been designed to ensure accuracy.

4. Conclusion

In this paper, the deformation and stress of the body components at 5 machining positions are simulated by ANSYS Workbench software. It is desirable to know that the machine body after being designed is good enough to resist static loads and impact loads during machining. The maximum values of deformation and stress due to impact are small, with CNC milling machine can be considered to ensure accuracy for thick outsole mold machining.

Acknowledgments

This research is supported by DCSELAB and funded by Department of Science and Technology under grant number 74/2019/HĐ-QPTKHCN

References

- [1] Y. L. Hwang and T. N. Ta (2018), “The friction effects for contact force analysis of three-axes CNC machine tool”, *Industrial Lubrication and Tribology*, Vol. 70 No. 8, pp. 1527-1535.
- [2] P. Majda, G. Szwengier and R. Jastrzebski (2013), “New approach to modeling geometric errors in precision manufacturing machines”, *Advances in Manufacturing Science and Technology*, Vol. 37, No. 3, pp. 33 - 44.
- [3] A. Afkhamifar, D. Antonelli and P. Chiabert. (2016), “Variational analysis for CNC milling process”, 14th CIRP Conference on Computer Aided Tolerancing (CAT), CIRP 43 pp.118-123.
- [4] B. M. Swami and K. S. R. Kumar (2012), “Design and structural analysis of CNC milling machine bed with composite material”, *International Journal of Advanced Engineering Technology*, Vol-2, Issue-12, pp. 97-100.
- [5] C. C. Hong, C. L. Chang and C. Y. Lin (2016), “Static structural analysis of great five-axis turning–milling complex CNC machine”, *Engineering Science and Technology, an International Journal*, Volume 19, Issue 4, pp. 1971-1984.
- [6] L. Zhao, W. Chen, J. Ma and Y. Yang (2008), “Structural bionic design and experimental verification of a machine tool column”, *Journal of Bionic Engineering Suppl*, Volume 5, pp. 46–52.
- [7] D. L. Nguyen, V. T. Le, D. T. Ninh and X. V. Tran, (2010), *Handbook of machine building technology*, Volume 2, Science and Technology, Hanoi, Vietnam.

Study on Designing of Coaxial BLDC Applied for Underwater Vehicle

Thien Phuc Tran^{1,2}, Cuong Quoc Thai Lam³, Ngoc Quan Duong³, Huy Hung Nguyen^{3,4}
and Tan Tien Nguyen^{1,2,3,*}

¹Faculty of Mechanical Engineering, Ho Chi Minh City University of Technology (HCMUT),
268 Ly Thuong Kiet, District 10, Ho Chi Minh City, Vietnam

²Vietnam National University Ho Chi Minh City, Linh Trung Ward, Thu Duc District, Ho Chi
Minh City, Vietnam

³National Key Laboratory of Digital Control and System Engineering (DCSELab), HCMUT, 268
Ly Thuong Kiet, District 10, Ho Chi Minh City, Vietnam

⁴Faculty of Electronics and Telecommunication, Saigon University, Vietnam

*Corresponding author. E-mail: nttien@hcmut.edu.vn

Abstract

This study presents a design of coaxial BLDC motor that are consistent with the counter-rotating propeller of underwater vehicles. Coaxial BLDC motor consists of two co-centric shafts driven by the outer separate rotor pairs and the inner common intermediate stator fixed with the enclosure frame. This topology of coaxial BLDC is design base on a theoretical calculation of geometrical parameters and accuracy verification by analysis software through flux density, rated torque, rated power, and speed evaluation. The parameters of the coaxial BLDC prototype are performed to evaluate the feasibility of applying for the underwater vehicles.

Keywords: BLDC motor, dual-rotor, coaxial motor, underwater vehicle

Nomenclature

A_g	=	airgap flux area, mm ²
B_g	=	airgap flux density, T
B_r	=	remanence of residual induction, T
B_t	=	tooth flux density, T (Maximum threshold $B_t=30\%B_g$)
B_{ry}	=	rotor yoke flux density, T (Maximum threshold $B_{ry}=50\%B_g$)
B_{sy}	=	stator yoke flux density, T (Maximum threshold $B_{sy}=50\%B_g$)
C_ϕ	=	flux concentration factor, $C_\phi \leq 1$
D_g	=	diameter of gap, mm
D_{ro}	=	rotor outer diameter, mm
D_{si}	=	stator inner diameter, mm
D_{so}	=	stator outer diameter, mm
E_{2ph}	=	2 nd phase back EMF amplitude (to output into torque), V ($E_{2ph}=2E_b$)
E_b	=	1 st phase back EMF amplitude, V
g	=	air gap, mm
I	=	input DC current, A
K_{st}	=	lamination stacking factor, $K_{st}=0.0425\delta_{la}+0.6032 \tan^{-1}(108.16\delta_{la})$
K_l	=	leakage factor, $K_l=0.9\div 1$
K_r	=	reluctance factor, $K_r=1\div 1.2$
l_m	=	magnet length, mm
L_{rotor}	=	rotor axial stack length, mm

L_{stator}	= stator axial stack length, mm
N	= number of turns/coil
n	= speed of one shaft BLDC motor
N_m	= number of poles
N_{ph}	= number of phases
N_s	= number of slots
P	= power of coaxial BLDC motor
P_{ds}	= designed power of BLDC motor
P_c	= permeance coefficient, $P_c=4\div 6$
T	= output torque
U	= voltage source, V
w_{ry}	= rotor yoke width, mm
w_{sy}	= stator yoke thickness, mm
w_{tb}	= teeth width, mm
μ_R	= recoil permeability (H/m)
ω_m	= mechanical rotation, rpm

1. Introduction

Many studies of coaxial motor have been conducted upon the high-efficiency propulsion capability to applying underwater vehicle when compared to the single shaft motor. In recent years, many authors have been attracted to BLDC motors (Uygun, 2015; Ravi Kumar and Siva Kumar, 2017; Tran *et al.*, 2020) owing to their higher efficiency, operational flexibility, higher torque/weight ratio and higher power density characteristics to perform the analysis and evaluation of the novel topologies to further improve performance and be suitable for each specific application (Brando *et al.*, 2015; Bondyra *et al.*, 2016; Dalal and Kumar, 2018). In a recent BLDC motor study for the marine thruster (Uygun *et al.*, 2015), Durmus introduced a new topology with two separate BLDC motor bodies nesting together, whose effectiveness of structure and design procedure were verified through finite element method. In (Cheng, Pan and Mao, 2019), and torque ripple reducing with the axial flux configuration study was presented through the simulation analysis results with the 3.7% electromagnetic torque improving and torque ripple coefficient is 5.1%.

In the practical underwater vehicle application, the most important condition in the control is that the velocities of the two output shafts are equal in magnitude for the best propulsion efficiency. Therefore, in the process of mechanical design, it is necessary to ensure that the parameters such as moment of inertia, size, mass, magnetic force of two shaft are equal. In existing literature, it is difficult to achieve the torque balance of two rotors due to the outer rotor being larger than the inner rotor, which result in differences of masses and distributions of the permanent magnets between two rotors. Therefore, this paper proposes a coaxial BLDC with the two separate rotors serial associating configuration to apply for the underwater vehicle. The designing procedure of coaxial BLDC motor is validated through the result of theoretical and is verified by simulation in section 2. The prototype of coaxial BLDC motor is made, and its experiment data are presented in section 3. In section 4, the conclusion presents the achievements of this study.

2. Coaxial BLDC Motor Designing

2.1 Designing Method

The proposed topology involves twin rotors, which is coaxial adjacent assembly, the designing of geometrical parameters of stator and rotor, winding diagram, electromagnetic for one rotor is conducted and then deduced the other one equivalently. Two rotors have the same operating power and the total power of coaxial BLDC motor $P=1.2$ (kW), speed of each axial $n=6000$ (rpm). Therefore, the BLDC motor is designed with the following power:

$$P_{ds} = \frac{P}{2} \tag{1}$$

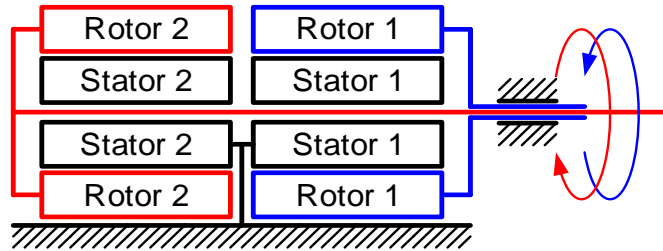


Figure 1. Principle diagram of coaxial BLDC motor

2.2 Designing process

The calculation process of the one rotor is shown in Figure 2. The design parameters and selected parameters summarized in Table I. The formulas below are used to calculate the external rotor BLDC motor magnet to the surface according to (Hanselman, 1994, 2003).

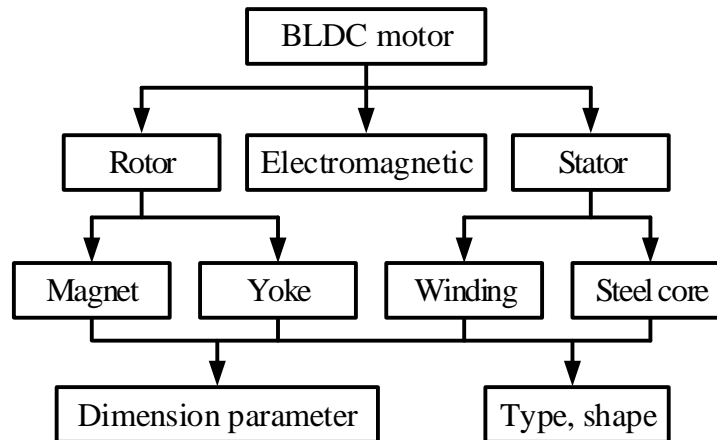


Figure 2. Designing process of BLDC motor

Table I. The required parameters of BLDC motor

Parameters	Value	Parameters	Value
P_{ds}	600 W	T	0.9 N
U	30 V	Type	Magnet surface-mounted, outer rotor
n	6000 rpm	Winding	Lap, double layer

2.3 Designing Calculation

The coaxial BLDC motor torque is expressed in Eq. (2), which depends on the two-phase back EMF amplitude. And the back-EMF single-phase depends on the basic geometrical

parameters of the BLDC motor, by choosing unknown parameters to calculate the remaining parameters, a set of motor parameters are gathered suitable for design requirements as shown in Table II.

Moment of motor:

$$T=9.55 \times 10^3 \frac{E_{2ph} I}{\omega_m} \quad (2)$$

Back EMF of single phase:

$$E_b = \frac{\pi \times N_m N B_g L_{rotor} D_{ro} \omega_m}{30 \times 10^6} \quad (3)$$

Table II. The basic parameters of BLDC motor

Parameters	Value	Parameters	Value
N_s	1.2 kW	B_g	0.4 T
N_m	8	L_{rotor}	40 mm
N_{ph}	3	D_{ro}	100 mm
N	15		

2.3.1 The rotor design of BLDC motor

The two main components of rotor are magnets and yoke. The permanent magnets are fixed to the yoke rotor in a Halbach array manner, the yoke rotor is assembled to the shaft via a flange, and the ball bearing is mounted on the shaft which is nested in the steel core of the stator to enable rotation. From the basic parameters, the geometrical and electromagnetic parameters of the rotor are calculated by following equations:

Rotor yoke width:

$$w_{ry} = \frac{\pi D_{ro} B_g}{2 N_m K_{st} B_{ry}} \quad (4)$$

Air gap:

$$g \geq 0.2 + 0.003 \sqrt{\frac{D_g L_{rotor}}{2}} \quad (5)$$

Airgap flux density:

$$B_g = \frac{K_l C_\phi}{1 + K_r \frac{\mu_R}{P_c}} B_r \quad (6)$$

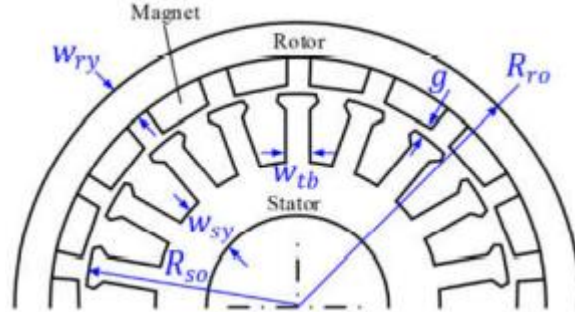


Figure 3. The geometrical parameters of BLDC motor

2.3.2 The stator design of BLDC motor

The stator is composed of a steel core which is formed by many electrical engineering steel laminations. They insulate each other and their shape have many teeth, which are used to wrap wire. Two stators are associated by four bolts which are mounted through a steel core and fixed to the outer motor frame. The geometrical parameters are expressed by following equations:

Teeth width:

$$w_{tb} = \frac{\pi D_{ro} B_g}{N_s K_{st} B_t} \quad (7)$$

Stator yoke thickness:

$$w_{sy} = \frac{\pi D_{ro} B_g}{2 N_m K_{st} B_{sy}} \quad (8)$$

To select the conductor cross-section, the maximum current can be calculated based on the standard evaluation system of logarithmic wire. Then, the result is compared with the amperage in the BLDC motor when reaching the maximum power. Thus, it can design the cross section of wire suitable for the given parameters and with a wiring diagram as shown in Figure 4.

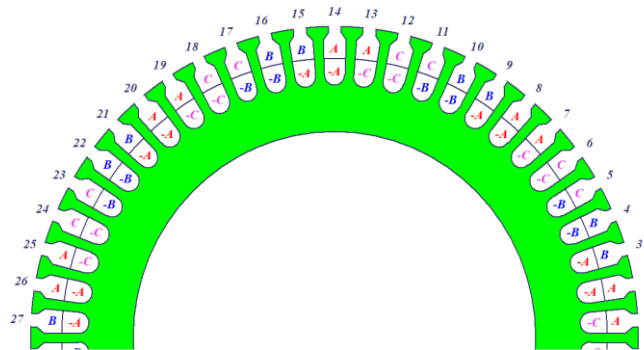


Figure 4. Lap type, two-layer winding diagram on stator of BLDC motor

2.3.3 The 3D model of coaxial BLDC motor

The results of the above geometric parameters calculation are presented in Table III and cross section 3D model as Figure 5.

Table III. The geometrical parameters of BLDC motor

Parameters	Value	Parameters	Value	Parameters	Value
D_{so}	80 mm	l_m	6 mm	w_{ry}	12 mm
D_{si}	40 mm	g	1 mm	B_t	0.24 T
D_{ro}	104 mm	K_{st}	0.9	B_{sy}	0.4 T
L_{rotor}	40 mm	w_{tb}	1.7 mm	B_{ry}	0.4 T
L_{stator}	50 mm	w_{sy}	12.5 mm	B_g	0.8 T

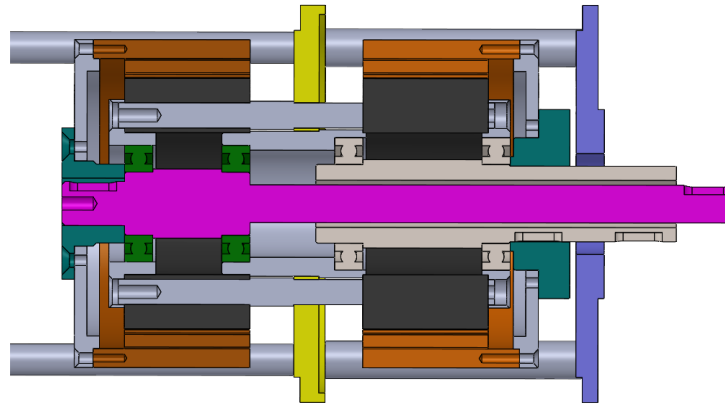


Figure 5. The cross section of coaxial BLDC motor

Through mass properties tool in Solidworks, the mass and moments of inertia at the axis of rotation of rotor linked with inner shaft have parameters are 1.43 kg and 2.4 g/m² respectively, and 1.59 kg and 2.5 g/m² for the rotor linked with outer shaft. The difference between these two sets of numbers is small, about 0.16 kg and 0.1 g/m². Thus, the requirements of mechanical design have been met.

2.4 Simulation of Electromagnetic

The simulation results of electromagnetic in BLDC motor are shown in Figures 6 and 7 with input voltage 30V, windage loss 10w, fraction loss 15w.

Table IV. The coaxial BLDC motor performance evaluation results

Parameter	Value	Parameter	Value
Specific electric loading	8411 A/m	Efficiency	90 %
Output power	626 W	Current density	17 A/mm ²
Rated speed	6100 rpm	Rated torque	0.97 Nm

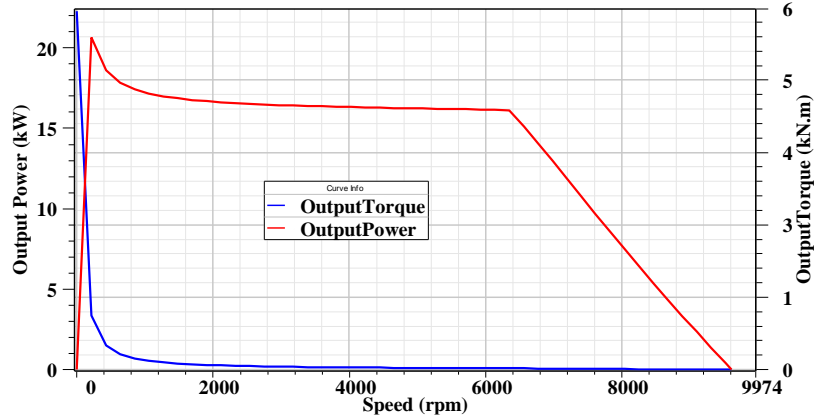


Figure 6. The correlation of efficiency, output torque and output power with speed

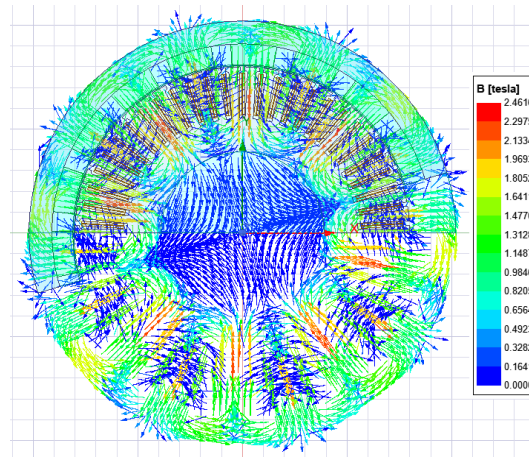


Figure 7. The flux density distribution in BLDC motor

In Figure 6, the efficiency is approximately 90% with a speed of 6100 rpm, the rotor speed is higher than the design parameters. This can be explained by the common magnet arrangement in the simulation while the design is arranged by Halbach array type. In Figure 7, the average flux density has the magnitude of about 1.4 T, the minimum value is in the core of the rotor (about 0.2 T) and the maximum uneven flux density distribution is up to 2.4 T when the teeth are in the middle position of the magnet. On the yoke, the max flux density magnitude is 1.8 T and decreases gradually when they move to the sides. The maximum permissible flux density value of the existing material is about 2.4 T; therefore, it is possible to manufacture the coaxial BLDC motor.

3. Experiment

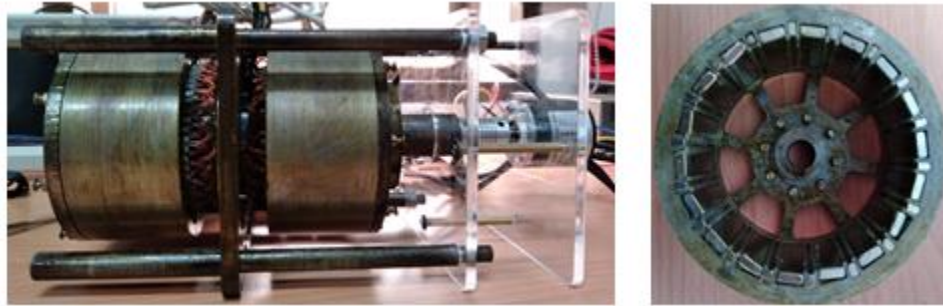


Figure 8. The coaxial BLDC motor prototype (left) and the Halbach array arrangement of permanent magnet on rotor (right)

The prototype of the coaxial BLDC motor is implemented as shown in Figure 8. Experimental data are obtained by setting up an oscilloscope to measure single phase voltage when connecting one pin to GND of DC source and the other one to anyone phase. Rotational speed is obtained by transmitting pulse value of encoder to MCU to estimate. The results are expressed in Figure 9:

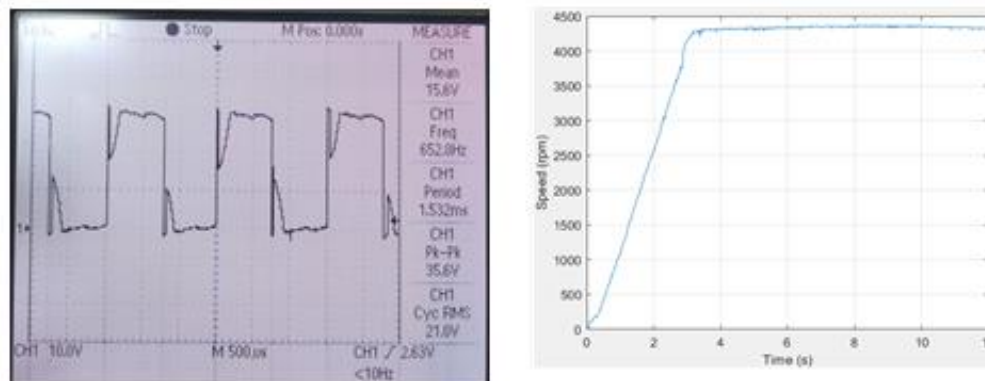


Figure 9. The voltage on one phase (left) and the speed responds with 30V voltage over time of outer rotor (right)

After about 3s, the rotor speed reached its maximum value and gradually stabilized at 4300 rpm. In this moment, the excitation frequency of single phases can be measured 652 Hz with a trapezoidal pulse shape, and the voltage value between the two peak is 35.6 V. The rotational speed from experiment data does not reach the design speed because the precision of machining and mechanical assembly is not high. Thus, the concentricity between the rotor and the stator does not meet the design requirements, leading to deviations. The speed of the rotor is affected by the center of gravity of the engine, the direction of the magnetic force and the collision induced friction.

4. Conclusion

In this study, the design of the coaxial BLDC motor is expressed and the theoretical computations results that have been verified by the specialized software, and a coaxial gearbox has presented in terms of the principle of operation as well as the mechanical structure. Through experiment with the prototype of coaxial BLDC motor, several reasons have been presented for failure to achieve designed speed. However, the rotor speed achieved more than 70% of the

design requirements, the dimensions and mass of two rotor are equal and designed parameters are validated. Hence, it can also achieve the designed speed when these reasons are solved. Therefore, this is a viable solution to replace conventional motors to apply for underwater vehicles.

Acknowledgments

This research is supported by DCSELAB and funded by Vietnam National University Ho Chi Minh City (VNU-HCM) under grant number B2019-20-09 and TX2021-20b-01. We acknowledge the support of time and facilities from Ho Chi Minh City University of Technology (HCMUT), VNU-HCM for this study.

References

- [1] Bondyra, A. *et al.* (2016) ‘Performance of coaxial propulsion in design of multi-rotor UAVs’, *Advances in Intelligent Systems and Computing*, 440, pp. 523–531. doi: 10.1007/978-3-319-29357-8_46.
- [2] Brando, G. *et al.* (2015) ‘A direct drive solution for contra-rotating propellers in electric unmanned aerial vehicle’, *Electrical Systems for Aircraft, Railway and Ship Propulsion, ESARS*, 2015-May. doi: 10.1109/ESARS.2015.7101428.
- [3] Cheng, B., Pan, G. and Mao, Z. (2019) ‘An Axial Flux Double-Rotor Counter-Rotating Permanent Magnet Machine for Underwater Vehicles’, *APAP 2019 - 8th IEEE International Conference on Advanced Power System Automation and Protection*, pp. 1304–1308. doi: 10.1109/APAP47170.2019.9224769.
- [4] Dalal, A. and Kumar, P. (2018) ‘Design, Prototyping, and Testing of a Dual-Rotor Motor for Electric Vehicle Application’, *IEEE Transactions on Industrial Electronics*, 65(9), pp. 7185–7192. doi: 10.1109/TIE.2018.2795586.
- [5] Hanselman, D. (2003) *Brushless permanent magnet motor design*. Available at: http://digitalcommons.library.umaine.edu/fac_monographs/231/.
- [6] Hanselman, D. C. (1994) *Brushless Motor Design, New York*.
- [7] Ravi Kumar, B. V. and Siva Kumar, K. (2017) ‘Design of a new dual rotor radial flux BLDC motor with halbach array magnets for an electric vehicle’, *IEEE International Conference on Power Electronics, Drives and Energy Systems, PEDES 2016*, 2016-Janua, pp. 1–5. doi: 10.1109/PEDES.2016.7914552.
- [8] Tran, T. P. *et al.* (2020) ‘Study on Designing and Manufacturing Coaxial Brushless DC Motor’, *International Conference on Advanced Mechatronic Systems, ICAMechS*, 2020-Decem, pp. 113–117. doi: 10.1109/ICAMechS49982.2020.9310082.
- [9] Uygun, D. *et al.* (2015) ‘A new topology for dual rotor/stator BLDC motors applied to marine thrusters’, *International Conference on Power Engineering, Energy and Electrical Drives*, 2015-Sept(113), pp. 353–359. doi: 10.1109/PowerEng.2015.7266342.
- [10] Uygun, D. (2015) ‘Dual Stator / Rotor Brushless DC Motors: A Review of Comprehensive Modelling Based on Parametric Approach and Coupled Circuit Model’, pp. 635–641.

Effectiveness Evaluation of Vacuum Pressure as Contributing Factor to Lightweight Seasoning Packets Distribution System

Tuan Huynh Thanh³, Nhat Nguyen Le Minh³, Van Tu Duong^{1,2,3}, and Tan Tien Nguyen^{1,2,3,*}

¹Faculty of Mechanical Engineering, Ho Chi Minh City University of Technology (HCMUT),
268 Ly Thuong Kiet, District 10, Ho Chi Minh City, Vietnam

²Vietnam National University Ho Chi Minh City, Linh Trung Ward, Thu Duc District, Ho Chi Minh City, Vietnam

³National Key Laboratory of Digital Control and System Engineering (DCSELab), HCMUT,
268 Ly Thuong Kiet, District 10, Ho Chi Minh City, Vietnam

*Corresponding author. E-mail: nttien@hcmut.edu.vn

Abstract

Instant noodle is a fast-growing product and has become a notable feature in Asian countries market. With the increase of living standard, the quality of instant noodles should be improved. Therefore, the workers are substituted by the automatic lightweight seasoning packets distribution system in the production line. This paper evaluates the vacuum pressure as a contributing factor to the pick-place system for distributing the seasoning packets in the instant noodles production line. Some scenarios are carried out to validate the vacuum pressure through the experiments. The experimental results show that the proposed method is suitable for job production of instant noodle package line.

Keywords: seasoning packets, instant noodle industry, vacuum pressure, contributing factor

1. Introduction

A typical instant noodles sachet mainly contains: a block of noodles, satay oil, soup and dried vegetable sealed in sachets that are specialized for food. The process of making instant noodles can be described in the Figure 1:

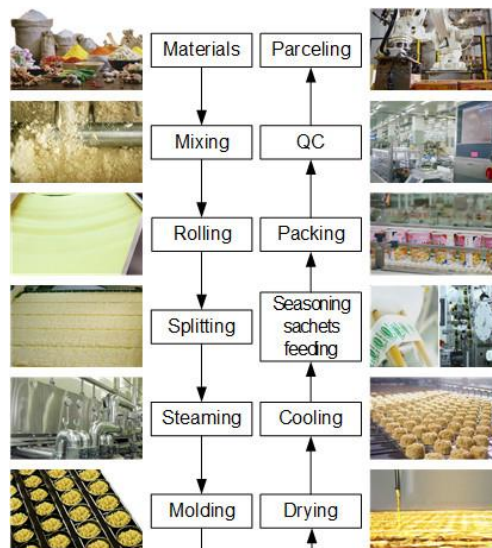


Figure 1. Process of making instant noodles

1. Prepare materials;
2. Mixing: wheat flour, turmeric solution and spices are mixed together;
3. Rolling: wheat flour is gradually flattened into sheets of dough until it meets the requirements

for toughness and thickness based on the specifications of each product; 4. Splitting: the noodles are split into strips with wavy-shape; 5. Steaming: noodles are steamed in a steam oven; 6. Quantitative cutting and mold serving: the noodles are cut shorter, falling into a frying mold. The molds are square or round to make the corresponding shape; 7. Dehydration: the noodles will go through the frying or drying system to reduce the moisture in the noodles to the required level; 8. Cooling: the noodles are cooled with air; 9. Seasoning sachets feeding: seasoning sachets are supplied manually or automatically; 10. Packing: after having all the ingredients based on the specifications of each product, the noodles will be packed in a cup or a bag; 11. Quality inspection: metal detector, weighing machines and an extraneous detector; and 12. Parceling: print the date of production, storage and check the quality by the QC department before distributing to the market.

2. Problem Setting

In step 9 - supplying the seasoning sachets, depending on the types of sachets, there are two different ways of supplying the sachet known as automatic feeding (Gulia, Dhaka and Khatkar, 2014) and manual feeding (Peng, Wang and Yang, 2012). The way of feeding depends on how the seasoning sachets are made. In the automatic feeding system, the seasoning is quantified, packed at the same time as the production line. Most automatic instant noodle package lines adopt this approach (Dissanayake and Jayawardena, 2016) (Liu *et al.*, 2019). For job production, the package process of the seasoning sachets is performed individual due to the availability of the materials or the limitation of facilities; sachets are fed to the line separately. If the weight of the seasoning sachets is relatively large, the feeding of seasoning sachets into package line is quite simple. For lightweight seasoning sachets, the automatic feeding of seasoning sachets is a difficult problem. This study proposes a novel solution for feeding seasoning sachets in the instant food production line. Characteristic of a seasoning sachet used in this research is specified as cut separately; stored in a disorder condition; weighted $0.6g$; dimension: $52 \times 47mm$; thickness $8 \div 9mm$; density: around $0.49kN/m^3$; three types of surfaces: smooth, hollow, vertical.

3. Solution Proposals

For mass production, the seasoning sachets are packed but not cut separately and stored in rolls. When it is necessary to use in noodles or congee packing stage, the seasoning sachets rolls is discharged and cut into sachets one by one; thus, the issue of controlling the seasoning sachet is not difficult.

For job production, which is considered in this study, an automatic feeding solution that is suitable for the separate seasoning sachet is required. The separate products are usually fed automatically by the vibration feeders (Boothroyd, 2006). These feeders are used with most electronic and mechanical products, details and components and so on but not always applicable to all products. There are 3 factors affecting the working ability of the vibration feeding funnel: size, shape and density of products.

The feeding products are completely symmetrical in shape or too large in size, making it difficult or impossible to classify. Feeders with a vibrational method of transporting the products make poor transport for products with density less than (Yuan-yuan, 2010) $1.5kN/m^3$. Therefore, the option of vibration feeder is not suitable for the case study.

A possible option in this case is to use a vacuum suction to suck each seasoning sachet and move it to the area where the operation is required. Seasoning sachets are contained in funnel 1 with a smaller bottom to put the sachet in position between the hopper, and the vacuum cup is in the waiting position as shown in *Figure 2*.

The activity includes the following steps: 1. When there is a request signal, the seasoning sachet that is waiting in funnel 4 will be dropped to the area to be manipulated; 2. Vacuum sensing 2 moves vertically down the storage hopper, when the suction cup collides with the spice sachet, stop moving and start vacuuming; 3. Draw the vacuum to bring the seasoning sachet; 4. When there is a request signal, the seasoning sachet that is waiting in funnel 4 will be dropped to the area to be manipulated; 6. Vacuum sensing 2 moves vertically down the storage hopper, when the suction cup collides with the spice sachet, stop moving and start vacuuming; 7. Draw the vacuum to bring the seasoning sachet; 8. Identify the sorbent status of a packet from the sensor data obtained during retraction; 9. Transport the seasoning sachet horizontally to the drop-off area or return to the beginning if the sachet does not stick; 10. Drop the seasoning sachet into the hopper and back the cylinder to standby position 3 ready for the new cycle; 11. In step 2, the suction cup goes down and contacts randomly with the seasoning sachets in the hopper. The result of this process may be 1 sachet, 2 sachets, or no sachets. This result is influenced by factors such as: type of suction angle, contact position of the suction sensor, and vacuum pressure.

The suction cup used in the paper is DP-6 with 2 layers, with a diameter of 6mm.

The contact position can be divided into 12 characteristic regions based on the characteristics of the seasoning sachet surface and the mouthpiece diameter as shown in *Figure 3*.

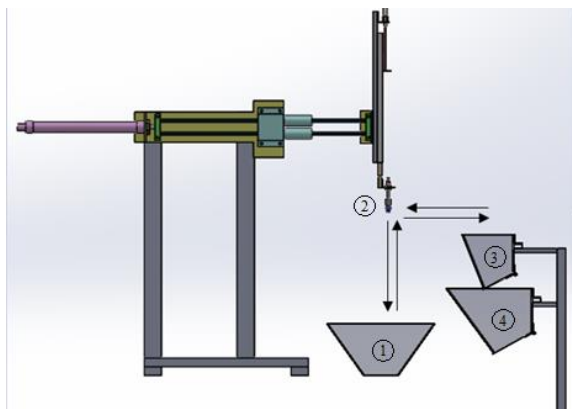


Figure 2. A feeder machine using vacuum pressure

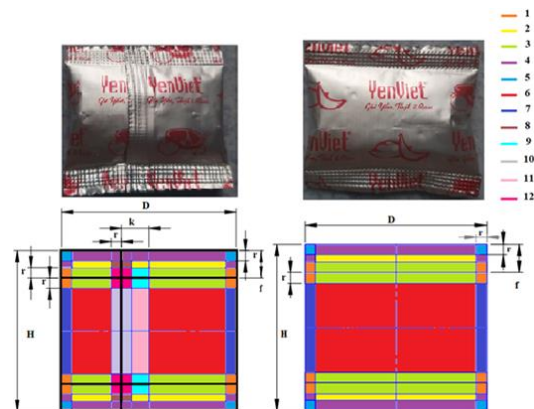


Figure 3. Characteristic surface of a sachet

During the random collision between the suction cup and the spice sachets, it is possible to randomly contact one of the 12 characteristic regions with a probability equal to the ratio of the surface area shown in *Table 1*. This could be non-stick, stick one-pack, stick two-pack, or stick more than two sachets.

Two-sachet sticky suction occurs when the suction cup comes into contact with an area located at the edge of the seasoning sachet such as VT1, VT4, VT5, VT7. The suction senses then come into contact with the edge of this spice pack and a random area of another seasoning sachet to allow two packets or non-stick suction. Probability of these combinations is shown in *Table 2*.

In the case of single-sachet stick, the suction cup touches the areas completely inside the seasoning sachets such as VT2, VT3, VT6, VT8, VT9, VT10, VT11, VT12.

In the case of sticking more than two sachets in one suction experiment, it did not appear in the preliminary survey, so it was not mentioned in the article.

Table 1. Specific area and ratio for vacuum suction cup with diameter of 6mm

Region	Area (mm^2)	Ratio (%)
VT1	144	2.95
VT2	516	10.56
VT3	984	20.13
VT4	624	12.77
VT5	72	1.47
VT6	1886	38.58
VT7	276	5.65
VT8	36	0.74
VT9	48	0.98
VT10	138	2.82
VT11	92	1.88
VT12	72	1.47

Table 2. Ratio of occurring combination of two specific area with suction cup diameter of 6mm

Combination	VT1 (%)	VT4 (%)	VT5 (%)	VT7 (%)
VT1	0.09	0.38	0.04	0.17
VT2	0.31	1.35	0.16	0.60
VT3	0.59	2.57	0.30	1.14
VT4	0.38	1.63	0.19	0.72
VT5	0.04	0.19	0.02	0.08
VT6	1.14	4.93	0.57	2.18
VT7	0.17	0.72	0.08	0.32
VT8	0.02	0.09	0.01	0.04
VT9	0.03	0.13	0.01	0.06
VT10	0.08	0.36	0.04	0.16
VT11	0.06	0.24	0.03	0.11
VT12	0.04	0.19	0.02	0.08

In addition to the effect of the suction type and the contact position, the vacuum pressure level greatly affects the rate of suction per pack in one random suction. The more negative the vacuum pressure, the higher the binding force between the suction cup and the seasoning sachet. This strong bonding force reduces the chance of falling when smoking one sachet, but also increases the ability to attract two sachets and the surfaces will be pressed closer together. This reduces the difference between one-pack and two-pack suction, making the process of identifying the condition more difficult. In addition, to create a negative vacuum pressure, the energy consumption will rise, so choosing the right pressure level is important.

To support that problem, in this study we conducted some surveys:

- The effect of the vacuum pressure level on the vertical transportation of the seasoning sachets.
- The effect of the vacuum pressure level on the horizontal transportation of the seasoning sachets.

4. Analysis

The survey model was built experimentally consisting of a 2-cylinder system to move the suction cup vertically and horizontally and a vacuum pressure control system arranged as shown in *Figure 4*.



Figure 4. An experimental model

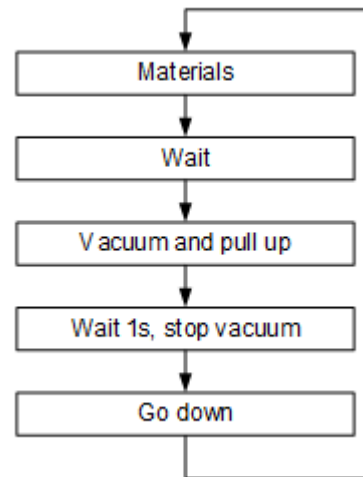


Figure 5. Survey process of how the vacuum level affects the vertical transport ability of sachets

Model parameters: Moving speed of the sachet in the vertical direction: $0.67m/s$; Horizontal sachet transport speed: $0.67m/s$; Moving distance of the sachet in the vertical direction $200mm$.

Investigation of the effect of vacuum pressure on the vertical transport of the seasoning sachet

Recommended pressure levels (psi): -90 , -85 , -80 and -75 use DP-6 suction cup with four pressure levels; 8 positions to investigate the ability to stick with 1 pack; 48 combinations of sites for investigating the ability to absorb 2 sachets; and 10 suction per case.

A total of 2240 vacuum aspirations were performed for the results of the number of stick aspirations and one pack of seasoning in the 10 vertical transport surveys shown in *Table 3*, the number of suction times and two holding times. Seasoning sachets at the pressure levels are shown in *Tables 4, 5, 6, and 7*.

Table 3. Successful suction and holding times of seasoning sachets in 10 vertical transportation experiments

	Vacuum pressure (psi)			
	-75	-80	-85	-90
VT2	10	10	10	10
VT3	9	10	10	10
VT6	10	10	10	10
VT8	9	10	9	9
VT9	10	10	10	10
VT10	6	5	10	9
VT11	10	10	10	10
VT12	6	8	9	8

Table 4. Successful suction and holding times of seasoning sachets in 10 vertical transportation experiments at -90 psi

	Times			
	VT1	VT4	VT5	VT7
VT1	0	0	0	0
VT2	2	0	3	10
VT3	3	5	4	10
VT4	0	0	0	0
VT5	0	0	0	0
VT6	5	8	1	2
VT7	0	0	0	0
VT8	0	0	0	8
VT9	6	5	7	10
VT10	5	2	7	1
VT11	6	8	9	2
VT12	0	0	2	8

Table 5. Successful suction and holding times of seasoning sachets in 10 vertical transportation experiments at -85psi

	Times			
	VT1	VT4	VT5	VT7
VT1	0	0	0	0
VT2	0	1	0	4
VT3	0	1	0	5
VT4	0	0	0	0
VT5	0	0	0	0
VT6	7	1	0	0
VT7	0	0	0	0
VT8	0	0	0	7
VT9	8	10	9	5
VT10	7	0	2	0
VT11	3	5	6	0
VT12	0	0	4	8

Table 6. Successful suction and holding times of seasoning sachets in 10 vertical transportation experiments at -80psi

	Times			
	VT1	VT4	VT5	VT7
VT1	0	0	0	0
VT2	0	0	0	5
VT3	0	0	0	4
VT4	0	0	0	0
VT5	0	0	0	0
VT6	5	0	0	0
VT7	0	0	0	0
VT8	0	0	0	8
VT9	6	8	6	10
VT10	0	0	0	0
VT11	5	0	2	0
VT12	0	0	3	7

Table 7. Successful suction and holding times of seasoning sachets in 10 vertical transportation experiments at -75psi

	Times			
	VT1	VT4	VT5	VT7
VT1	0	0	0	0
VT2	0	0	0	7
VT3	0	1	0	8
VT4	0	0	0	0
VT5	0	0	0	0
VT6	4	3	1	0
VT7	0	0	0	0
VT8	0	0	0	7
VT9	6	9	7	10
VT10	0	0	3	0
VT11	5	3	10	0
VT12	0	0	7	3

Aspiration rate and holding of 1-, 2- sachet and non-stick during vertical transport:

$$P_{vc_td_1(i)} = \frac{N_{vc_td_1(i)}}{N_{vc_td}}, P_{vc_td_2(i)} = \frac{N_{vc_td_2(i)}}{N_{vc_td}}, P_{vc_td_0(i)} = \frac{N_{vc_td_0(i)}}{N_{vc_td}}$$

where, $P_{vc_td_1(i)}$, $P_{vc_td_2(i)}$, $P_{vc_td_0(i)}$: suction and holding rates were 1, 2 packs and non-stick in vertical transport at each test site

$N_{vc_td_1(i)}$, $N_{vc_td_2(i)}$, $N_{vc_td_0(i)}$: the number of aspirations and holding of one pack, two sachets and non-stick when transported vertically at each test site

N_{vc_td} : the number of aspirations at the test site

Probability of non-stickiness and holding of one pack, two sachets, and non-stick during the vertical transport of the sachet at the test site:

$$P_{xhvc_td_1(i)} = P_{VT(i)} \times P_{vc_td_1(i)}, P_{xhvc_td_2(i)} = P_{VT(i)} \times P_{vc_td_2(i)}, P_{xhvc_td_0(i)} = P_{VT(i)} \times P_{vc_td_0(i)}$$

where, $P_{xhvc_td_1(i)}, P_{xhvc_td_2(i)}, P_{xhvc_td_0(i)}$: probability of occurrence of non-sticky and holding of one pack, two packs and non-stick

$P_{VT(i)}$: probability of appearing test position in 1 random aspiration

The probability of suction and holding a sachet during vertical transport during a random suction is equal to the total probability of having suction and holding two sachets during vertical transport at the test site. The same is true for two sachets and not sticking during the vertical transport of the sachet in one random suction. This result is shown in Table 8 below.

Table 8. Probability of successfully holding 2 seasoning sachets, 1 sachet and no sachet in vertical transportation experiments corresponding to testing pressure levels

Pressure P (psi)	Ratio stick 2 sachets (%)	Ratio stick 1 sachet (%)	Ratio non-stick (%)
-75	3.98	73.36	22.66
-80	1.63	75.46	22.90
-85	3.00	76.95	20.05
-90	8.98	76.52	14.50

Investigation of the effect of vacuum pressure on the horizontal transport of the seasoning sachets

Investigation Pressure Levels (psi): -90, -85, -80 and -75 use DP-6 suction cups with 4 pressure levels; 8 positions for investigating the ability to stick with 1 pack; and 10 suction per case.

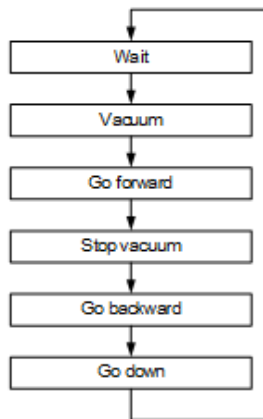


Figure 6. Survey process of how the vacuum level affects the horizontal transportation ability of sachets

Table 9. Successful suction and holding times of seasoning sachets in 10 horizontal transportation experiments

	Vacuum pressure (psi)			
	-75	-80	-85	-90
VT2	6	5	10	10
VT3	10	10	10	10
VT6	10	8	10	10
VT8	7	6	7	10
VT9	10	10	10	10
VT10	5	6	4	5
VT11	10	10	10	9
VT12	7	8	3	10

The lateral transport takes place after the identification phase to detect one-pack suction, so only one-pack suction continues to enter the process. Therefore, surveying the process of transporting sachets in the horizontal direction only investigates the positions where one sachet can be absorbed, such as: VT2, VT3, VT6, VT8, VT9, VT10, VT11, VT12.

Percentage of suction and one-pack, two-pack and non-stick holding during horizontal sachet transport:

$$P_{vc_ng_1(i)} = \frac{N_{vc_ng_1(i)}}{N_{vc_ng}}, P_{vc_ng_2(i)} = \frac{N_{vc_ng_2(i)}}{N_{vc_ng}}, P_{vc_ng_0(i)} = \frac{N_{vc_td_0(i)}}{N_{vc_ng}}$$

where, $P_{vc_ng_1(i)}$, $P_{vc_ng_2(i)}$, $P_{vc_ng_0(i)}$: 1-pack, two-pack and non-stick holding rates when transported horizontally at each test site

$N_{vc_ng_1(i)}$, $N_{vc_ng_2(i)}$, $N_{vc_ng_0(i)}$: siphon and retain one sachet, two sachets and non-stick when transported horizontally at each test site

N_{vc_ng} : number of aspirations at the test site

Probability of adsorption and holding of a sachet after transport at test site

$$P_{vc(i)} = P_{xhvc_td_1(i)} \times P_{vc_ng_1(i)}$$

Probability of suction and holding of a sachet after transport at pressures is equal to the sum of the probabilities of adhesion and holding of a sachet after transport at locations within the same test pressure level, resulting in are shown in *Table 10*.

Table 10. Successful suction and holding times of 1 sachet in horizontal and vertical experiments

Pressure (<i>psi</i>)	Probability of successfully holding 1 sachet in vertical and horizontal transportation (%)
-75	67.83
-80	61.37
-85	74.13
-90	75.06

From experimental results, it shows that the vacuum feeding plan is a possible option for the bulk, small volume seasoning sachet with initial confusion with the mentioned spice pack parameters. in the article. The vacuum pressure directly affects the efficiency of this feeding process.

The results shown in *Table 8* show that the highest rate of absorption and holding of one pack during the vertical transport of seasoning sachets at $-85psi$ pressure with $-85psi$ and 3% of stick suction and holding two packs. At $-90psi$, there is also an adhesive rate and keep a pack of approximately $-85psi$ but the 2-pack suction ratio is almost 3 times. Hence the $-85psi$ pressure level is effective for vertical transport of the seasoning sachets. The probability of suction and holding a sachet after vertical and horizontal transport is presented in *Table 10*, which shows that the deeper the vacuum pressure, the higher the rate of successful adhesion and transport, where the suction rate is. Stick and keep a pack of $-85psi$ pressure close to that of an adhesive rate and keep a $-90psi$ pack. According to *Table 3* and *Table 9*, at positions VT2, VT3, VT6, VT9, VT11 when transported vertically and VT3, VT6, VT9, VT11 when transported horizontally, there is a stable rate of sucking successfully one sachet, with little change in all 4 vacuum pressure levels that are analyzed in the article. Thereby, it shows that these positions are less affected by the vacuum pressure levels. Therefore, if the seasoning sachets are not in a messy condition as in the article and they are arranged, or there is a solution to point the vacuum

into these positions of the seasoning sachets, then is also possible to achieve high efficiency and save energy with not too low vacuum pressure.

5. Conclusion

The paper presents research on the effects of vacuum pressure on feeding separate and light weight seasoning sachets in the instant noodles production line. The above experimental data are used as the basis for designing and manufacturing a seasoning sachet feeding system. The research has been continued at DCSELab.

Acknowledgments

This research is supported by DCSELAB and funded by Vietnam National University Ho Chi Minh City (VNU-HCM) under grant number TX2021-20b-01. We acknowledge the support of time and facilities from Ho Chi Minh City University of Technology (HCMUT), VNU-HCM for this study.

References

- [1] Boothroyd, G. (2006) ‘Assembly Automation and Product Design, second edition (Manufacturing Engineering and Materials Processing)’, *Emerald Group Publishing Limited*, 26(4). doi: 10.1108/aa.2006.03326dae.001.
- [2] Dissanayake, B. D. M. P. B. and Jayawardena, H. S. (2016) ‘Development of a Method for Manufacturing Noodles from Finger Millet’, *Procedia Food Science*, 6, pp. 293–297. doi: 10.1016/j.profoo.2016.02.058.
- [3] Gulia, N., Dhaka, V. and Khatkar, B. S. (2014) ‘Instant Noodles: Processing, Quality, and Nutritional Aspects’, *Critical Reviews in Food Science and Nutrition*. Taylor and Francis Inc., pp. 1386–1399. doi: 10.1080/10408398.2011.638227.
- [4] Liu, Z. *et al.* (2019) ‘Packaged food detection method based on the generalized Gaussian model for line-scan Raman scattering images’, *Journal of Food Engineering*, 258, pp. 9–17. doi: 10.1016/j.jfoodeng.2019.04.005.
- [5] Peng, K., Wang, T. C. and Yang, Z. Q. (2012) ‘Research of image processing in instant noodle packets auto-inspection system’, *Proceedings of the 2nd International Conference on Electronic and Mechanical Engineering and Information Technology, EMEIT 2012*, pp. 1509–1512. doi: 10.2991/emeit.2012.334.
- [6] Yuan-yuan, R. (2010) ‘Current situation, problems and prospect of instant noodle industry in China’, *Business*.

Active Door Preventing Infectious Air of Hospital Isolation Room

Vo Nhat Quang Mo³, Duy Anh Nguyen^{1,2}, Tan Huy Nguyen³, Phuc Long Duong³, Dae Hwan Kim^{5,6}, Le An Pham⁴, and Tan Tien Nguyen^{1,2,3,*}

¹Faculty of Mechanical Engineering, Ho Chi Minh City University of Technology (HCMUT), 268 Ly Thuong Kiet, District 10, Ho Chi Minh City, Vietnam

²Vietnam National University Ho Chi Minh City, Linh Trung Ward, Thu Duc District, Ho Chi Minh City, Vietnam

³National Key Laboratory of Digital Control and System Engineering (DCSELab), HCMUT, 268 Ly Thuong Kiet, District 10, Ho Chi Minh City, Vietnam

⁴GIC, University of Medicine and Pharmacy at Hochiminh City

⁵State University of New York at Stony Brook, New York, USA, 11794

⁶Nsquare company, Busan, South Korea, 31040

Corresponding Email: nttien@hcmut.edu.vn

Abstract

This paper presents a design and control of automatic sliding door used for isolation room in the medical field using sliding mode control. Therefore, the article includes the design of a mechanical and control systems for the sliding door and its characteristic to serve medical purposes, especially for isolation rooms using container modules during epidemic periods. Simulations and experiments are attached to compare the differences between the ideal door and the actual door.

Keywords: isolation room, automatic sliding door, sliding mode control, air-sealing, antimicrobial door, epidemic solution

1. Introduction

From December 2019, the COVID 19 outbreak has rapidly spread throughout all over the world and become a fatal epidemic. Some nations have been dealing with the lack of quarantine areas, hospital space and especially medical equipment, which leads to millions of deaths and sometimes even the collapse of a whole medical system. In order to solve the given challenging problem, the authors introduce an isolation room using container modules solution.

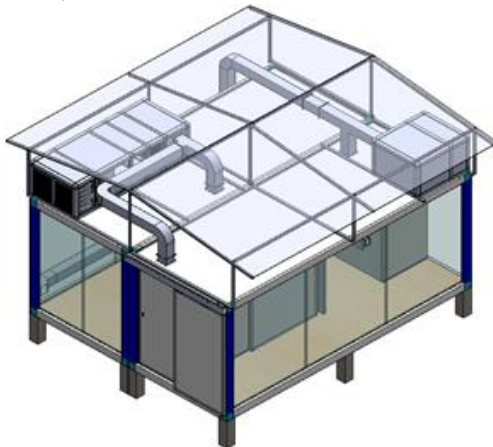


Figure 1. Isolation room module

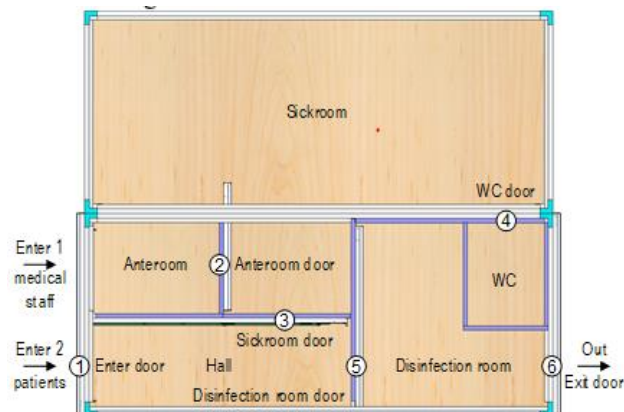


Figure 2. Door arrangement inside the module

The isolation chamber is the combination of 2 connected container designed to have negative pressure value to keep the airflow one-way in and out through special ventilating system keeping

all bacteria and pathogens isolated inside the chamber for curing the infected and preventing the pandemic from spreading into the community. All areas must be airtight to each other and to the outside atmosphere. On the other hand, the following room is used in tough conditions of the front line of the epidemic, so it needs to endure continuous weather condition change and the restriction of replacing materials. Four areas are called anteroom for medical staff handling sanitary issues, hall area for inserting patients, sickroom for curing the infected, and finally bathroom. Anteroom has the highest pressure in the whole modules to keep the airflow move from outside into the healing room. Therefore, the sickroom would have a lower negative pressure value than the above areas, keeping the airflow circulate inside, then pump air outside through special filters. Last but not least, the bathroom is where all bacteria would be trapped in and eliminated by the UV light system. The overall design of the whole container is shown in Figure 1.

Separating the 4 areas of the isolation room are the combination of panel walls for fixed separation and automatic doors for temporary isolating the walk way inside the model, both of which are specially designed for medical uses. The authors using 2 types of doors for the whole container modules: hinged doors and automatic sliding doors. In the restricted content of this article, only automatic sliding doors are introduced. What makes these automatic sliding doors unique are the abilities of air-sealing, non-touching opening and closing as well as anti-microbial surface. Each door has a different length and journey as well as opening types according to the its function, the sliding door's arrangements inside the module are shown in Figure 2.

Key specifications: Prevent the air from flowing outside the module and anti-microbial to kill all the bacteria on the wall; control all doors in the container module, overcome the disturbance created from frictional force and anything else; automatically open when the infrared sensor is activated (when there are someone that want to get through the door), automatically close after $3 \div 6s$ and reopen when there are obstacle on the door's closing journey; approximate operation life of 24 hours after having unwilling accident causing the collapse of the whole electric system.

2. Mechanical Design

2.1 Design of the sliding door

The use of panel door

Researches have shown that through sneezes, COVID 19 virus is able to exist for many hours up to 72hours on plastic and steel walls. Therefore, the concept of *automatic* door instead of manual door which must be touched to open is formed. As mentioned in the introduction, the doors in the system must meet 3 requirements: non-touching, anti-microbial, airtightness, and one more optional demand is fast response. Fast response means that there is risk of impact at the end of door journey. So, glass material could not be used, and the panel door should be the best choice. Two walls outside are made of 0.6 mm alloy steel that prevent oxidation, corrosion and antimicrobial. For heat and sound insulation, the inside wall is made of polyurethane foam. The walls are hard enough to ensure there is no trouble for closing and opening. Since the area of isolation room is limit, to test door, we use the 50mm panel. Figure 3 and Figure 4 present the assembly of the automatic sliding door in 3D model.

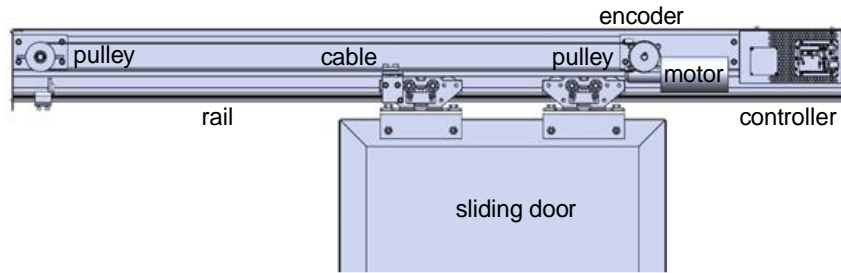


Figure 3. Automatic sliding door 3D sketch

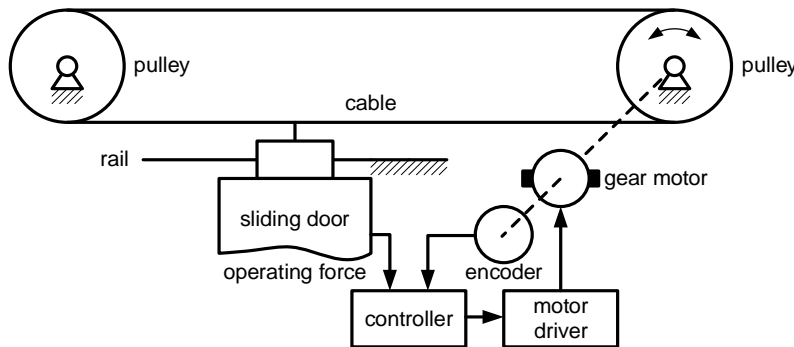


Figure 4. Control diagram for sliding door

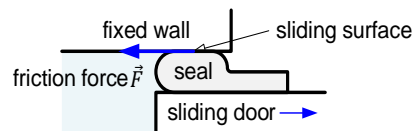


Figure 5. Sealing demonstration

2.2 Design of drive system

Motor parameters

Since the motor shaft is not coaxial with the pulley itself, the need of using a worm-gearbox in order to change the outer shaft into a perpendicular direction and enhance the torque pulling the panel door to win the enormous friction from the rubber sealing. Thus, the transmission ratio of the gearbox and belt should be chosen at 15 to calculate the essential power and speed of the motor, assuming the against force from the door is applied all the journal time. The total force applies to the motor is the combination of the kinetic and static friction force from the seal and the rolling frictional force.

Backup plan for emergency situation

There are two situations that we should considered for the problems of automatic sliding door.

Firstly, blackout. The motor system uses worm gear to reduce speed so that the door cannot be opened when it is blackout due to the self-braking ability of worm gear system. The problem can be solved with the backup battery which be placed outside the drive system. Since the estimated power of motor is 24V, 100W, the backup battery has to be the same type. The DCSE battery can last for 24 hours and is enough for logistic to repair the power system.

Secondly, the impact of fast-moving objects such as stretcher with patients and door could be dangerous since the door must operate continuously when outbreak occur and the gap time for fixing these doors can be many hours. So, the concept of the problem creates a demand for fast response sensor. The faster the sensor gets signal, the better response the system has and the less possibility for impact to occurs. For this experience, the authors choose the Kerui P819 Bluetooth sensor. This sensor can detect the existence of people at the range of $3 \div 5m$, that is enough to prevent any moving creature from touching the panel door. Besides, P819 uses an adapter (220V to 5V) to maintain the power supply, which is better than lots of sensors when they are out of battery. Beside, to ensure the operation of the door, the authors choose 2 more sensors called M204G and E18-D80NK.

3. Controller System Design

The problem of the isolation room is the overall control law for all automatic sliding doors used inside. All of them have the same function and categories, but different dimensions and parameters such as mass (m) and frictional coefficient (μ), both of which nonlinearly vary over time base on door panels. According to the door's size, which changes depending on the use of doors named in Figure 2, the sealing method and the door's mass would be different. The sealing method decides how large the frictional coefficient would be as well as the door mass, both of which affect the results of controlling these doors dramatically. Therefore, it is obvious that with two varying parameters μ and m , the choice of model reference sliding mode control for this system is applied with the disturbance of around 10% of the control signal as one of the most suitable solutions to deal with these problems.

Consider the plant model for a sliding door shown in Figure 4. On one side of the rail, we could place a DC motor that can control the traction force of the belt through teeth pulleys. The travel distance is x . When the door stands still, there is static frictional force applied to the seal, F_s . When the door moving, there are dynamic frictional force applied to the seal and roller, named F_{ds} and F_{dr} respectively. To sum up, the authors define these frictional force by using equivalent coefficient. The concept of sliding mode control and the followed block diagram could be described in Figure 6.

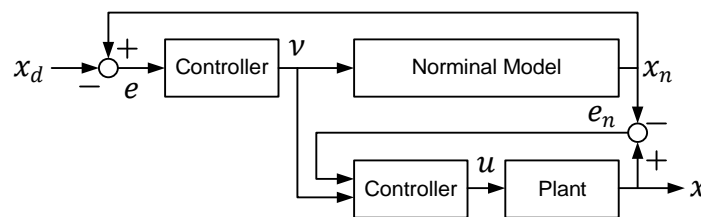


Figure 6. Automatic sliding door control block diagram

Ignoring the stiffness, the system can be presented in the following forms

$$m\ddot{x} + \mu_e\dot{x} + d = u \quad (1)$$

where, m : the mass of the door, kg

x : the position of the door, m

μ_e : the equivalent viscous friction coefficient

d : disturbance of the system

Let the nominal model be:

$$m_n \ddot{x}_n + \mu_n \dot{x}_n = v, m_n > 0, \mu_n > 0 \quad (2)$$

where, m_n : the nominal moment of mass, kg

$$m_n = (m_m + m_M)/2, m_m \leq m \leq m_M$$

x_n : the nominal position of the door, m

μ_n : the nominal friction coefficient

$$\mu_n = (\mu_m + \mu_M)/2, \mu_m \leq \mu_e \leq \mu_M$$

v : the nominal control input

The controller for the nominal model is

$$v = m_n[-h_1 e - h_2 \dot{e} + (\mu_n/m_n)\dot{x}_d + \ddot{x}_d] \quad (3)$$

with, $h_1 = k^2$, $h_2 = 2k - \mu_n/m_n$, $e = x_n - x_d$

The controller for the plant is

$$u = -Ks - h \operatorname{sgn}(s) + m_n(v/m_n - \lambda \dot{x}) + \mu_n \dot{x}, K > 0 \quad (4)$$

with, $e_n = x - x_n$, $s = \dot{e}_n + \lambda e_n$

$$h = d_M + \frac{1}{2}(m_M - m_m) \left| \frac{1}{m_n} v - \lambda \dot{x} \right| + \frac{1}{2}(\mu_M - \mu_m) |\dot{x}|$$

$$\lambda = \mu_n/m_n, |d| \leq d_M$$

4. Simulation Results

The design above has been executed at DCSELab, all parameters used in this paper are drawn from the previous research, “Power Assist for Slide Door”, listed in the reference [1]. According to our design and the referred researches, the mass and the frictional coefficient of the doors can be described as follow:

$$\begin{cases} 45 < m < 60 \\ 18 < \mu_e < 22 \\ d = 0.1u \end{cases}$$

Thus, the authors choose one sample door’s specification throughout 6 doors in Figure 2. The parameters showed in Table I presents the specifications of one of the panel doors inserted inside the module about the mass and its corresponding frictional force is used for choosing and calculating the drive and control system later.

Table I. Door specification

Mass	52.5 <i>kg</i>
Kinetic frictional coefficient	0.4
Kinetic frictional force	29 N
Static frictional coefficient	0,7
Maximum static frictional force	29 N
Roller frictional coefficient	0.002
Roller frictional force	1.18 N

The 100W-24VDC motor is chosen to drive the whole automatic sliding door system about the motor, which have the parameters shown in table II.

Table II Motor’s parameters

Motor parameter	Value
Motor speed	250 rpm
Motor torque	4 Nm
Motor inertia	$4.5 \times 10^{-5} \text{ kgm}^2\text{w}$
Torque constant	$3.2 \times 10^{-2} \text{ Nm/A}$
Inductance of amateur circuit	$1.2 \times 10^{-3} \text{ H}$
Convert coefficient from θ to X	$7.7 \times 10^{-4} \text{ m/rad}$

Using the above numerical values, the system is in the form

$$\ddot{x} + 1.356\dot{x} + 6.307x = 20.24u + d \quad (5)$$

and the controllers

$$v = 0.05[5.24e - 0.66\dot{e} + 0.33\dot{x}_d + \ddot{x}_d] \quad (6)$$

$$u = -10s - hsgn(s) + 52.5\left(\frac{\mu}{0.05} - 1.34\dot{x}\right) + 20\dot{x} \quad (7)$$

with $k = 1, h_1 = -5.24, h_2 = 0.66, \lambda = 1.34, K = 10$

To ensure for the above calculation, simulation of the door movement is made using MATLAB tools. In the following results, the authors want to show the response of the door’s movement within 2 control functions (switch function and saturated function). In addition, the response when using 2 modes of the door, which are step input mode (present for one time opening and closing use) and sin input mode (present for repeated opening and closing use), are tested.

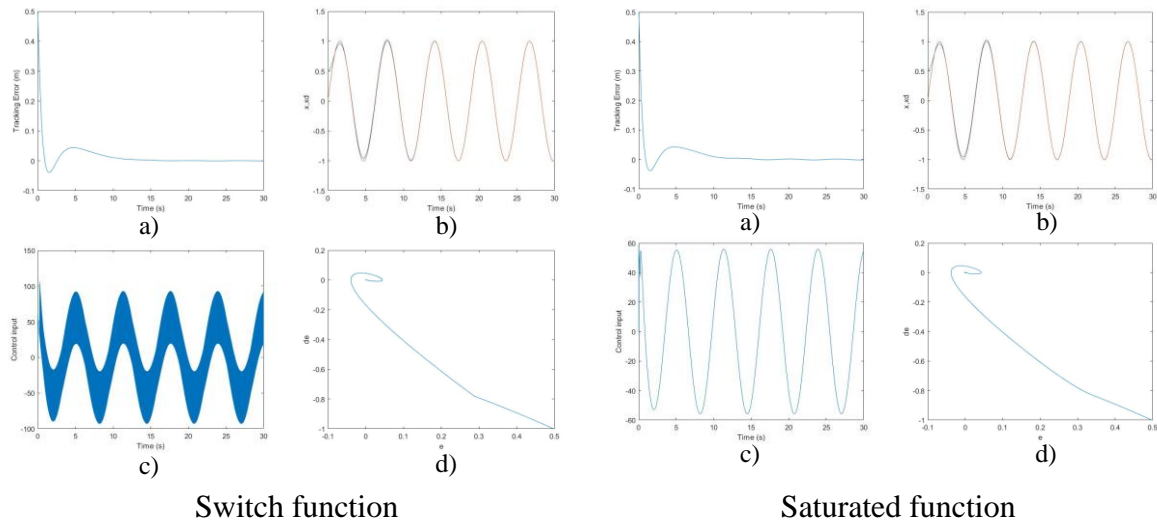


Figure 7 & 8. Control sin input

a) Tracking error b) Position tracking c) Control input d) Phase trajectory

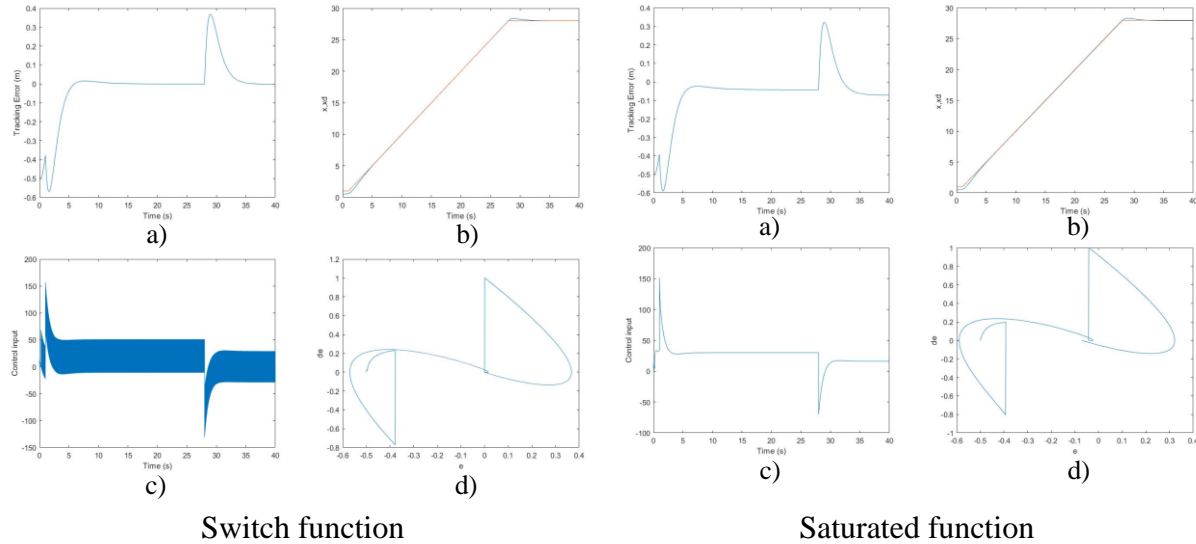


Figure 9 & 10. Control step input

a) Tracking error b) Position tracking c) Control input d) Phase trajectory

From the simulation above, it is obvious that the sliding mode control is able to resolve all of the disturbance caused by the frictional force of the rubber seal and the door's mass. It has a fast and stable response using saturated function. On the other hand, the responses of the switch function in both step input and sin input are critically interfered. Overall, simulations have shown that model reference sliding mode control is able to deal with the massive nonlinear change of frictional coefficient and door's mass, created a transient and stable response with saturated function.

5. Conclusion

It has been proved that the sliding mode control method for controlling automatic sliding door can achieve accurate door position adjustments. Furthermore, it can obtain more comfort thanks to the resolve of the varying frictional coefficient and the door's mass which lead to the reduction of noise and the smooth of door's movement. The given design has simplicity for assemble and manufacturing, and it is easy to adjust the door's parameter as well as the coefficient of the controller. The impact on the real door can be modify through the nominal plant so the door length is adjustable. For further research, the authors plan to discuss the controller design which reduce the power consumption and enhance the sealing method.

Acknowledgments

This research is supported by DCSELAB and funded by Vietnam National University Ho Chi Minh City (VNU-HCM) under grant number TX2021-20b-01. We acknowledge the support of time and facilities from Ho Chi Minh City University of Technology (HCMUT), VNU-HCM for this study. This research is also funded by Department of Science and Technology under grant number 59/2020/HĐ-QPTKHCN.

References

- [1] Kalpak Shah, Hong Tae Kang and Upendra Deshmukh, "Design of Dual Sliding Door for

a Small-size Car and Its Validation Using CAE Tools”, University of Michigan, Dearborn, July 28th, 2018.

[2] Kensuke Osamura, Shinya Kobayashi, Mitsuo Hirata and Hitoshi Okamoto, “Power Assist for Slide Door”, Utsunomiya University, Tochigi, Japan, September 17th-20th, 2007.

[3] Hisato Kobayashi, “A Control of Sliding Doors For Realizing Well-Being Livings”, Hosei University, Fujimi, Chiyoda, Tokyo, Japan, 2015.

[4] Gabriela Mamani, Jonathan Becedas, Vicente Feliu Batlle, “Robust Position Control of a DC Motor by Sliding Mode”, United Kingdom, 2010.

[5] Jinkun Liu, Xinhua Wang, Advanced Sliding Mode Control for Mechanical Systems, Tsinghua University Press, 2012.

[6] Tan Tien Nguyen, Sliding Mode Control Slides, Hochiminh City University of Technology, April 6th 2019.

Design of Powered Air Purifying Respirator Used for Healthcare Workers

An Thanh Vo Ta³, Thanh Long Le^{1,2,3,*}, Ngoc Dang Tran⁴, Le An Pham⁴, Hoang Long Phan^{1,2}, and Tan Tien Nguyen^{1,2,3}

¹Faculty of Mechanical Engineering, Ho Chi Minh City University of Technology (HCMUT),
268 Ly Thuong Kiet, District 10, Ho Chi Minh City, Vietnam

²Vietnam National University Ho Chi Minh City, Linh Trung Ward, Thu Duc District, Ho Chi Minh City, Vietnam

³National Key Laboratory of Digital Control and System Engineering (DCSELab), HCMUT,
268 Ly Thuong Kiet, District 10, Ho Chi Minh City, Vietnam

⁴GIC, University of Medicine and Pharmacy at Hochiminh City

*Corresponding author. Email: ltlong@hcmut.edu.vn

Abstract

During the outbreak of COVID-19, preventive measures including facemasks and respirators may be the only available protection for health care providers when no drugs or vaccines are promising. Facemasks are recommended for diseases transmitted through droplets and respirators for respiratory aerosols. This paper presents a design and control of Powered Air Purifying Respirator (PAPR) used for Vietnamese healthcare workers in preventing COVID-19 infection. The system controls the air flow by adjusting the speed of a centrifugal blower provide to a mask. This air flow is cleaned by particle filters and ultraviolet germicidal light. In particular, in case of an emergency, it can be connected to commercially available masks through a connector hose and a respiratory hose. This Vietnamese design of PAPR can protect the health of healthcare workers during work, and can also be used for other purposes such as protecting people in polluted environment, toxic chemical environments and other viruses.

Keywords: Clean air, Dual filtration, Ultraviolet germicidal light, Preventing of Covid infection

1. Introduction

During the outbreak of COVID-19, preventive measures including facemasks and respirators may be the only available protection for health care providers when no drugs or vaccines are promising. Facemasks are recommended for diseases transmitted through droplets and respirators for respiratory aerosols. To health care workers, evidence suggests that respirators offer superior protection to facemasks. During pandemics and outbreaks, these form a part of a suite of protection offered to frontline workers to ensure occupational health and safety. Respirators are also preferable when the disease is severe, with a high case fatality rate, and no available drug treatment or vaccine such as COVID-19. Powered air purifying respirators (PAPR) (Cook, 2020) use a battery powered blower to filter out contaminants and provide the user with a continuous flow of clean air, usually through a loose-fitting hood or helmet. PAPRs likely offer greater protection and do not generally require fit testing, making them particularly desirable during rapid rollout conditions. The burgeoning need for respiratory personal protection equipment (PPE) precipitated major challenges to supply chains as need for PPE exceeded the capacity of suppliers and strategic reserves. In the United States, shortages triggered contingency and crisis standards of practice which deviated from conventional and accepted best practices. This type of air purifying respirator is specialized for the medical sector, it removes particles (dust, smoke, mist, virus) and toxic chemical in the atmosphere using

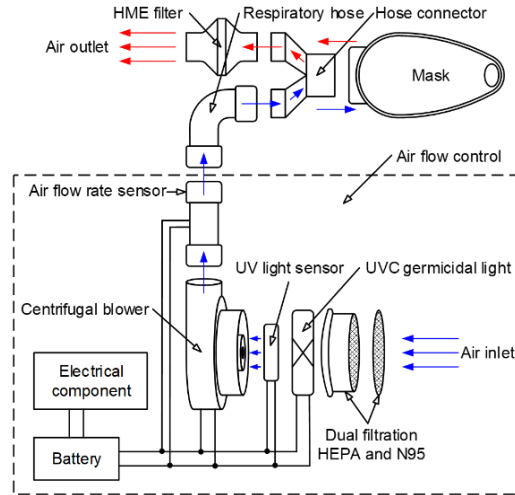


Figure 2. Principle diagram of the system

2.2 Design a mechanical of PAPR

To achieve the required air flow, the centrifugal blower must provide more than 115 liters per minute with a tight-fitting. During use, there are many factors that may cause a decrease in the air flow such as reduced performance of filter after a period of use, or due to the difference in air pressure. Therefore, centrifugal blower with max air flow more than doubled the standard of tight-fitting used for this system, brushless DC blower model WS7040-12-X200 is chosen to provide air flow as requested above.

For dual filtration system, a 3M Particulate Filter according to N95 standards [2] is installed at the air inlet and a HEPA Filter according to HEPA standards [3] is installed immediately behind it, these particle filters are used to arrest very fine particles effectively, but they do not filter out gasses and odor molecules. Hence must be additional UVC germicidal light to clean air, based on the UV dose in mJ/cm^2 needed to inactivate virus Corona [4], the UV power can be calculated to choose the suitable UVC germicidal light. The formula is as follows [5]

$$UV \text{ Dose} = E \times t = \frac{P}{A} \times t \quad (1)$$

where E : UV intensity, mW/cm^2

t : time, s

P : UV power, mW

A : contact area, cm^2

From the calculation as above, two UVC germicidal light bulbs model GTL3 254nm can achieve the desired UV dose inactivate virus Corona up to 99%.

3. Control system Design

3.1 Mathematical model

Consider the following model for PAPR. Centrifugal blower is controlled through driver to achieve the desired speed. Based on air flow sensor, the measured flow is x (l/min). When the system works, obtain the nonlinear relationship between pwm duty cycle and air flow. In addition, there are factors that disturb the air flow such as dusty filter and air resistance, so using sliding mode control (SMC) based on linearization feedback control is a common approach in controlling these nonlinear systems. To describe the mathematical model, block diagram of SMC system shown in Figure 3.

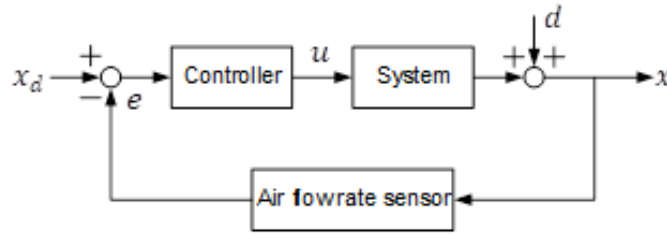


Figure 3. Block diagram of SMC system

3.2 Calculate the control system

Consider the following second-order SISO uncertain nonlinear system

$$\ddot{x} = f(x, t) + g(x, t)u + d(t) \quad (2)$$

where x : state variable

f, g : known nonlinear functions

d : uncertainty due to disturbance

The system (2) will be determined from measured experimental data and given in part 4 of this paper.

Let the desired trajectory be x_d , the tracking error e

$$\mathbf{e} = \mathbf{x} - \mathbf{x}_d = [e \quad \dot{e}]^T \quad (3)$$

Sliding variable s is selected as

$$s(x, t) = \mathbf{c}\mathbf{e} \quad (4)$$

where $\mathbf{c} = [c \quad 1]$ and $\mathbf{e} = [e \quad \dot{e}]^T$

Based on linearization feedback technique, the sliding mode controller is designed as

$$u = \frac{v - f(x, t)}{g(x, t)} \quad (5)$$

$$v = \ddot{x}_d - c\dot{e} - \eta \operatorname{sgn}(s), \eta > D \quad (6)$$

where \mathbf{u} : the control input

v : the auxiliary controller

sgn : the signum function defined by

$$\operatorname{sgn}(s) = \begin{cases} -1 & \text{if } s < 0 \\ 0 & \text{if } s = 0 \\ 1 & \text{if } s > 0 \end{cases} \quad (7)$$

The discontinuity in the feedback control creates a special dynamic behavior in the environment of the surface called chattering. Chattering is the main obstacle for sliding mode control implementation, the most simple and popular solution is the so-called boundary layer approach in which the signum function is replaced by the saturation function [6]

$$\text{sat}(s) = \begin{cases} -1 & \text{if } s \leq \beta \\ s/\beta & \text{if } -\beta < s \leq \beta \\ 1 & \text{if } \beta < s \end{cases} \quad (8)$$

4. Electrical Design

After supplying power to PAPR, the system will be controlled in 3 air flow modes – 120/140/160 liters per minute by pressing a button. Besides, two UVC germicidal light bulbs can be turned on or turned off by holding a button for 3 seconds depending on the purpose of use. Block diagram of electrical system is shown in Figure 4.

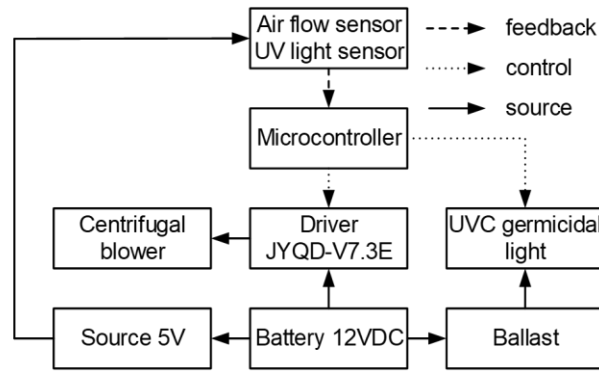


Figure 4. Block diagram of electrical system

4.1 Air flow sensor

PAPR detects output air flow with the help of SFM3020 Sensirion flow sensor, then sensor feedbacks the signal to microcontroller. Then, according to the output given by sensors, microcontroller drives the motors. The air flow sensor works through a thin film mounted on the sensor head, the air will pass through the film to create vibrations, then this sensor generates the corresponding signal through the jump. Therefore, the sensor is used to identify air flow mode, keep the systems providing the desired constant air flow. According to the manufacturer's datasheet, equation for converting from analog signal to air flow of SFM3020 Sensirion is shown below

$$Q = 212.5 \times \left(\frac{A_{out}}{V_{DD}} - 0,1 \right) - 10 \quad (9)$$

where, Q : air flow, l/min

A_{out} : linear analog voltage output, V

V_{DD} : voltage supply, V

4.2 UV light sensor

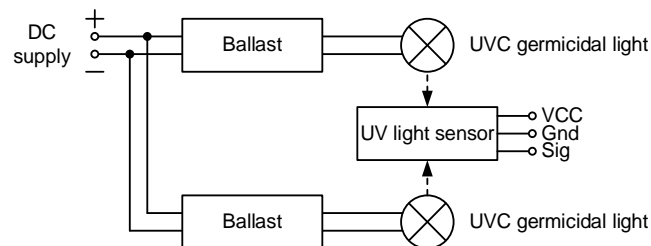


Figure 5. Measurement diagram of UV light sensor

UV light sensor GUVA-S12SD is sensitive to light from $240nm \div 370nm$, and helps to monitor and measure UV-C light intensity [7]. UV intensity measurement diagram of sensor is shown in Figure 5, place sensor 2cm away from UVC germicidal lamp, then convert output voltage to UV intensity using the following formulas

$$I_D = \frac{V_{out}}{G \times R_G} \quad (10)$$

where I_D : current from diode, A

V_{out} : output voltage, V

G : voltage gain

R_G : transimpedance gain, Ω

Convert the current from diode to total power on diode

$$P_D = \frac{I_D}{Re} \quad (11)$$

where P_D : total power on diode, W

Re : responsivity at $254nm$, A/W

Divide the total power by the excitable active area of the diode to get UV intensity E

$$E = \frac{10^3 \times P_D}{S_a} \quad (12)$$

where S_a : **active area**, cm^2

UV intensity through above calculation and UV intensity is inferred as in Eq. (1). When UV intensity drops below the specified level, the buzzer will be active, letting users know they need to maintain the system.

5. Simulation and Experimental Results

The system is set up at DCSELab as shown in Figure 6



Figure 6. Experimental system set up

From the measured data, the model of the experimental system is given by

$$\ddot{x} = -6.267\dot{x} - 31.08x + 98.9u + d \quad (13)$$

And the controller is given as follows:

$$u = \frac{v + 6.267\dot{x} + 31.08x}{98.9} \quad (14)$$

5.1 Simulation sliding mode control

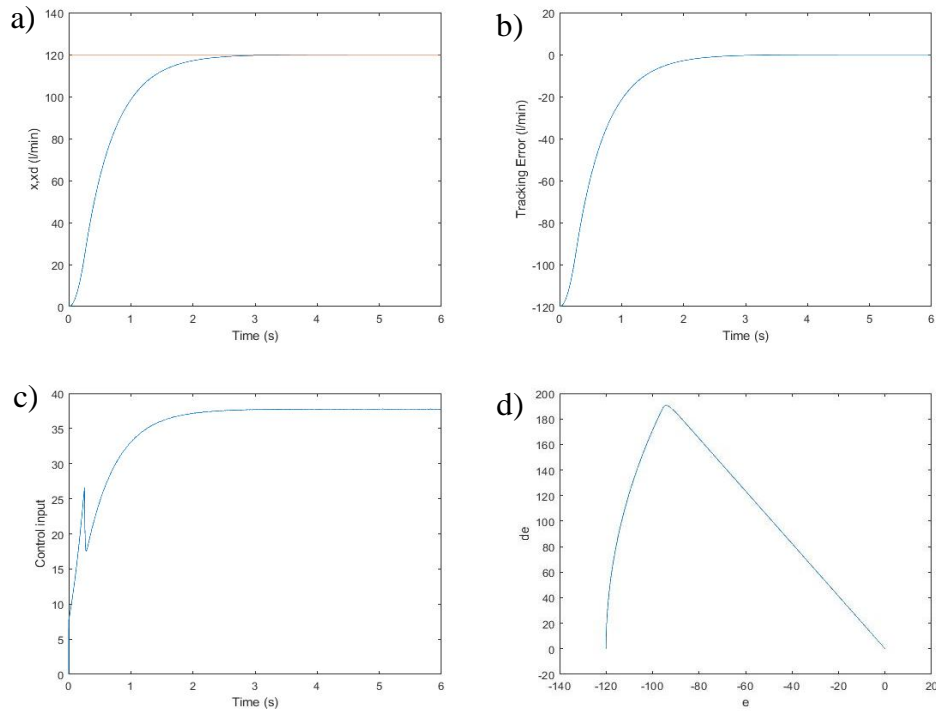


Figure 7. Simulation of the controller with a saturation function, a) Tracking error, b) Airflow tracking, c) Control input, d) Phase trajectory

To ensure the system control calculation, simulation using MATLAB tools is conducted. The response of the controller with a saturation function shown in Figure 7. Where desired airflow is $x_d = 120$ (l/min). Other desired airflows such as 140 and 160 liters per minute are simulated similarly, where initial state = 0 (l/min), controller parameters $c = 2$, $\eta = 530$, disturbance data $d = 12$ (l/min), saturation function parameter $\beta = 1$.

5.2 Experimental air flow

With the system set up as shown in Figure 6, conduct air flow experiment to compare between desired air flow and measured air flow, experimental results for the controller are shown in Fig. 8.

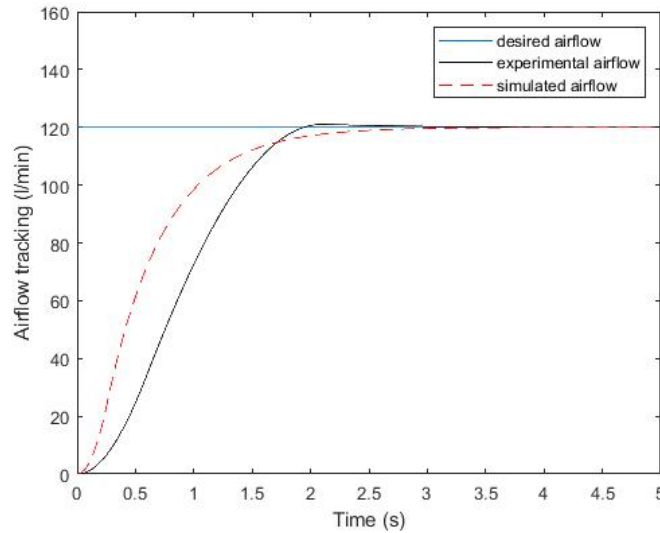


Figure 8. Experiment of the controller with a saturation function

Experimental results for the controller show a little overshoot but then have a shorter settling time than simulation results.

5.3 Experimental UV intensity

Feedback signal of UV light sensor must ensure that UV intensity achieves the desired inactivation of Corona virus at maximum air flow, because based on Eq. (1), when the air flow increases then UV exposure time decreases, making UV dose also decrease.

From the datasheet of sensor, we have $G = 4.3$, $R_G = 10^7 \Omega$, $Re = 0.04 A/W$, and $S_a = 0.00076 \text{ cm}^2$

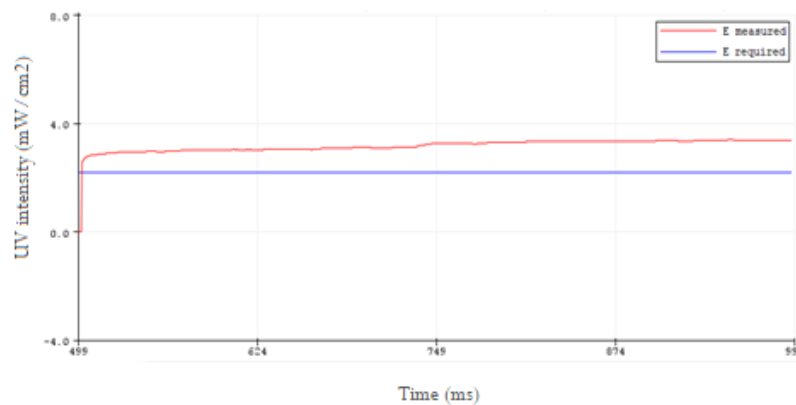


Figure 9. Response of sensor to the UV intensity

Figure 9 shows measured UV intensity of UV light sensor increasing over time and higher than required UV intensity, experiment results are surveyed at a distance of 2cm from UVC germicidal light.

6. Conclusion

This paper presents the mechanical design, electrical design, simulation and experiment to control PAPR used for healthcare workers in case of preventing of COVID-19 infection. With a compact design, PAPR can be worn by the user's hip, comfortable during work, use in case of

emergency, lack of medical supplies and equipment. Feedback signals from sensors will help users monitor and control the system effectively. However, this research has not yet examined viral inactivation, more intensive research can test and increase UV dose inactivate virus Corona than 99%.

Acknowledgments

This research is supported by DCSELAB and funded by Vietnam National University Ho Chi Minh City (VNU-HCM) under grant number TX2021-20b-01. We acknowledge the support of time and facilities from Ho Chi Minh City University of Technology (HCMUT), VNU-HCM for this study. This research is also funded by Department of Science and Technology under grant number 61/2020/HĐ-QPTKHCN.

References

- [1] E.-C. (2020) *42 CFR Part 84 Respiratory Protective Devices | NPPTL | NIOSH | CDC*. Available at: <https://www.cdc.gov/niosh/npptl/topics/respirators/pt84abs2.html> (Accessed: 17 June 2021).
- [2] Al., J. et (2015) *The Use and Effectiveness of Powered Air Purifying Respirators in Health Care, The Use and Effectiveness of Powered Air Purifying Respirators in Health Care*. National Academies Press. doi: 10.17226/18990.
- [3] Chung, T. L. et al. (2004) ‘Sliding mode control of two-wheeled welding mobile robot for tracking smooth curved welding path’, *KSME International Journal*, 18(7), pp. 1094–1106. doi: 10.1007/BF02983284.
- [4] Cook, T. M. (2020) ‘Personal protective equipment during the coronavirus disease (COVID) 2019 pandemic – a narrative review’, *Anaesthesia*. Blackwell Publishing Ltd, pp. 920–927. doi: 10.1111/anae.15071.
- [5] Guyon, L. et al. (2012) ‘Photodiagnosis and photodynamic therapy of peritoneal metastasis of ovarian cancer’, *Photodiagnosis and Photodynamic Therapy*, pp. 16–31. doi: 10.1016/j.pdpdt.2011.08.003.
- [6] Hunter et al. (no date) *EP3024503A4 - Air sterilization and disinfection apparatus and method - Google Patents*. Available at: <https://patents.google.com/patent/EP3024503A4/en> (Accessed: 17 June 2021).
- [7] Japuntich et al. (1994) *Face mask that has a filtered exhalation valve*.
- [8] Nguyen, X. T. et al. (2020) ‘Controlling Center of Mass in Humanoid Robot using Sliding Mode Control’, in *International Conference on Advanced Mechatronic Systems, ICAMechS*. IEEE Computer Society, pp. 17–22. doi: 10.1109/ICAMechS49982.2020.9310088.
- [9] Pope, A. K. (2016) ‘Chapter 19 Risk management in clean room assisted reproductive units’, in *Clean Room Technology in ART Clinics*. CRC Press, pp. 257–310. doi: 10.1201/9781315372464-20.
- [10] Tilley et al. (no date) *US20100224190A1 - Modular powered air purifying respirator - Google Patents*. Available at: <https://patents.google.com/patent/US20100224190> (Accessed: 17 June 2021).
- [11] Tompkins, B. M. and Kerchberger, J. P. (2010) ‘Personal protective equipment for care of pandemic influenza patients: A training workshop for the powered air purifying respirator’, *Anesthesia and Analgesia*, 111(4), pp. 933–945. doi: 10.1213/ANE.0b013e3181e780f8.

Design and Implementation of Upper Limb Rehabilitation Exoskeleton for Post-Stroke Patients

Binh Vo Dang Phuong³, Xuan Thang Nguyen⁴, Van Tu Duong^{1,2,3}, Huy Hung Nguyen^{3,5},
and Tan Tien Nguyen^{1,2,3,*}

¹Faculty of Mechanical Engineering, Ho Chi Minh City University of Technology (HCMUT),
268 Ly Thuong Kiet, District 10, Ho Chi Minh City, Vietnam

²Vietnam National University Ho Chi Minh City, Linh Trung Ward, Thu Duc District, Ho Chi
Minh City, Vietnam

³National Key Laboratory of Digital Control and System Engineering (DCSELab), HCMUT,
268 Ly Thuong Kiet, District 10, Ho Chi Minh City, Vietnam

⁴115 Hospital, Hochiminh City, Vietnam

⁵Faculty of Electronics and Telecommunication, Saigon University, Vietnam

*Corresponding author. E-mail: nttien@hcmut.edu.vn

Abstract

In the modern world, stroke is one of the leading causes of adult disability. Post-stroke patients need to perform exercises to recover the upper limb's function through treatment with clinician support. This paper works on designing and implementing a device known as an exoskeleton for upper limb rehabilitation of post-stroke patients. The proposed exoskeleton must be low-cost, portable, and straightforward, so that patients' relatives can operate it. The proposed exoskeleton enables the recovery of the elbow and wrist of post-stroke patients and uses high torque servo motors.

Keywords: post-stroke patient, rehabilitation, upper limb, artificial muscle

1. Introduction

According to the Ministry of Health's statistic (2017), catastrophic diseases and movement disorders are serious mainstream problems (1.7% -2.5 % in the middle age and the elderly) (Pennati *et al.*, 2020). The number of people who have a stroke every year are increasing (Frimpong *et al.*, 2014). Stroke is the most often occurring diseases which leads to disability (Thrift *et al.*, 2017). (French *et al.*, 2016) showed that robotic devices can recover walking function for post-stroke patients through the method called repetitive task training. The assistance of the robotic devices is to keep the therapists out of physical burden (Moucheboeuf *et al.*, 2020). Several studies have been investigated the effect of automatic mechanism of robot assisted gait training (Zhou *et al.*, 2018; Mane *et al.*, 2019; Niu *et al.*, 2019; Foong *et al.*, 2020). Robotic assisted recover function plays a key role in rehabilitation of stroke patients. However, during the COVID19 pandemic (Park, 2021), rehabilitation function in patients is facing many difficulties such as shortage of equipment and medical operators, patients encounter difficulties in accessing medical centers and lack of specified treatment regimen for each patient. Therefore, a portable device which can be used in homecare for stroke patients is required. Earlier, several studies about assisted robots intended for function recover have been presented (Ab Patar, Komeda and Mahmud, 2014; Yurkewich *et al.*, 2019; Pennati *et al.*, 2020). However, these studies are not suitable for home use.

This paper proposes a portable upper limb rehabilitation exoskeleton for post-stroke patients which is intended for home use. The proposed robot device assists the stroke patient in recovering function of upper limbs. In order for ease of use, the proposed robot device is constructed with locally available material and components of low-cost and lightweight. The proposed robot device is controlled by a local controller equipped on the unit and a remote controller implemented on a computer. To validate the effectiveness, a prototype of the proposed robot device is employed to achieve experimental results.

2. Medical Backgrounds

The passive upper limb rehabilitation equipment, as shown in Figure 1(a), cannot fully move limbs but can prevent movements in the wrong direction. The active type of upper limb rehabilitation equipment can only be used to rehabilitate a patient who can still move a part of his limbs. This active equipment, as shown in Figure 1(b), is capable of transmitting limbs. The active equipment is usually a combination of actuators and controllers; thus, this equipment is large and heavy. It can be applied to people with severe paralysis. Figure 1(c) shows that the interactive upper limb rehabilitation equipment interacts with the patient's touch. Usually, the equipment is attached with many motion sensors to create supporting forces. However, the force generated is usually miniature. Interactive equipment is often used in rehabilitation in conjunction with a virtual reality environment. As shown in Figure 1(d), the training of upper limb rehabilitation equipment neither supports nor resists motion. The equipment merely monitors movement and measures the anthropometric parameters of a patient. As interactive equipment, training equipment is also commonly used in virtual reality environments.

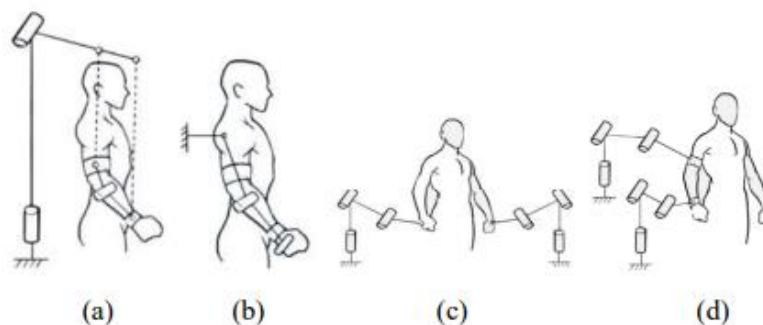


Figure 1. Type upper limb rehabilitation equipment

2.1 The structure and physical parameters of human upper limb

The upper limb of the human body comprises of bones and surrounding musculature shown in Figure 2 can be categorized into three main joints called shoulder joint, elbow joint, and wrist joint, as well as upper arm bone, forearm bone, and hand bone combination.

Anatomically, the upper limb can be simplified into a simple muscle system of 7 degrees of freedom:

- The upper arm connects to the shoulder through the shoulder joint.
- The upper arm is attached to the forearm through the elbow joint.
- The forearm connects to the hand through the wrist joint.

These joints are regarded as rotary joints, and connecting parts are regarded as linkage bars.

Our research is based on anthropometric statistics from the Ministry of Health in 2017 in people between the ages of 50 and 70. This age group is considered the age group at high risk of stroke.

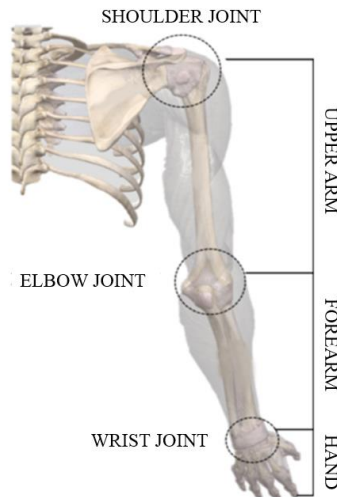


Figure 2. Structure of human upper limb

Table 1. Bar parameters of human upper limb

	Width (cm)	Length (cm)
Hand	9.29 ± 0.3	17.52 ± 0.63
Forearm	8.17 ± 0.32	44.1 ± 3.9
Upper arm	8.35 ± 0.76	33.1 ± 4

2.2 Exercise mode

Our research refers to the most popular applicable Bobath method (Kollen et al., 2009). This method focuses on relative positions of the body – joints – muscle to facilitate muscles, joints to work, avoid bad post-stroke posture due to sclerosis of joints and muscle. During the experimental phase, the research built a training exercise in which the patient is passive while the device actively moved limbs (joints) following scripted settings.

Exercise duration: about 3 hours a day. This exercise duration is the best condition for reorganizing the brain, and movements are familiar to avoid muscular atrophy and subchondral sclerosis.

The research team aims at an exoskeleton that can flex and extend both joints (elbow joint and wrist joint). The exercise intensity and mode are presented in Table 2.

Table 2. Recommend input for each exercise

	Wrist	Elbow
Torque (Nm)	8.5	23.35
Low level (°)	0 ÷ 10	-20 ÷ 15
Medium Level (°)	0 ÷ 25	-50 ÷ 45
Hard Level (°)	0 ÷ 50	-80 ÷ 65
Period (cycle/sec)	30	25

3. Design and Modeling

3.1 System description

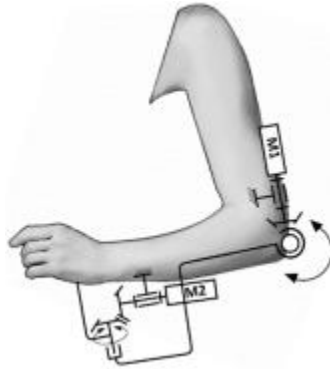


Figure 3. Mechanical network of exoskeleton

The exoskeleton this research is aiming for is a kind of active training equipment. The exoskeleton is a combination of linkage bars and armbands that are fixed to the patient's arm, servomotors, and bevel gear transmissions.

Based on the kinematic diagram in Figure 3, the research builds up the exercise procedure shown in Figure 4. During each exercise, the operator can power up the power supply and connect the control box to the computer that has installed the control software. Then, the operator selects a suitable training method and duration and processes to start an exercise.

The embedded computer controls the servomotors via the servo drivers to control each cycle's flexion and extension phase during an entire exercise. In addition, the encoder can track servomotor position and send that data to the embedded computer via UART protocol.

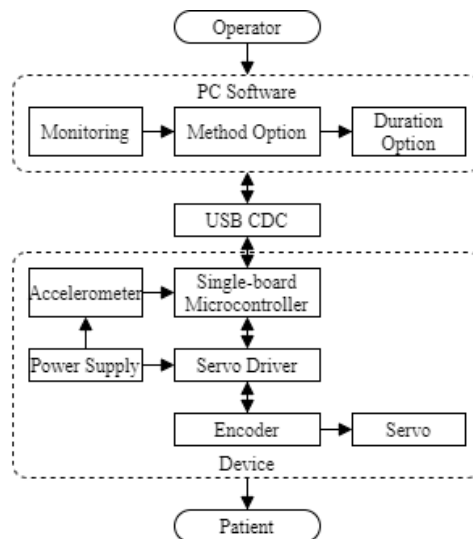


Figure 4. Schematic of selection process for exoskeleton

In addition, to prevent any accident during exercise, the research team built three safety mechanisms:

- Emergency stop button on a control box.
- Virtual button to stop the training process in control software.
- Background function analyzes abnormal signals from the embedded computer (collected data from encoders and accelerometers). This function can send a request to force servomotors to return to their initial position.

3.2 Mechanical model

The exoskeleton is designed for movement rehabilitation of the patient's upper limb, aiming to simplify the operation and mobility. In addition, the equipment can be used in both right and left hands.

The design was inspired by a multi-functional fitness chair - used in gymnasiums, with joints connected via expandable bars to customize their length so the exoskeleton will be fit with any patient's arm.



Figure 5. 3D mechanical design of exoskeleton

3.3 Controller design

The embedded computer that controls the exoskeleton is simulated on MATLAB Simulink. All servomotor parameters are collected to build an electromechanical model. Due to the muscle stiffness in post-stroke patients, the exoskeleton needs to perform from low-intensity to high-intensity exercises. The research team has written a specific algorithm to modify the servomotor's velocity and accelerator over time. The control parameters are calibrated with the Root Locus method to find the optimal training duration for each exercise method. The operator can evaluate a patient's condition and select a suitable method from the available recommended methods. Each joint is built with a specified model to meet different requirements. The time step in simulation is ten milliseconds (0.01s).

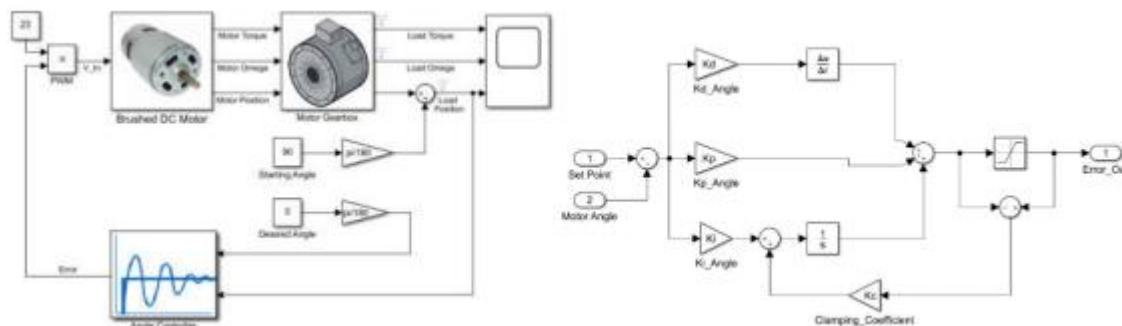


Figure 6. Modeling of servo motor control system in MATLAB Simulink

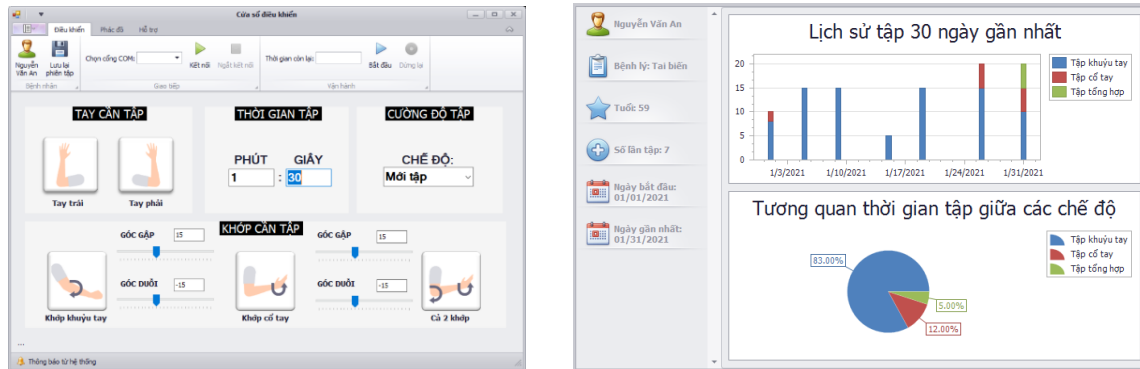


Figure 7. Several user interfaces of control software

The exoskeleton can be controlled via a GUI program installed on the computer. For each exercise, the exoskeleton needs to be assigned to a designated patient. During exercise, the operator can choose the exercise mode, training duration, intensity and save the current session to adjust the treatment regimen.

Software is written on .NET Core library to run on all Windows and Linux operating systems (Debian kernel). Data from the encoder and accelerometer will be sent back to the embedded computer. The embedded computer will give these feedback data to the software via the USB-CDC protocol. The exercise data is recorded in the software directory and can be backed up or shared with other computers using XML format.

4. Experiment Results

The experimental setup is done with some members ($N = 5$), using data from the accelerometers to compare with the estimated angle programmed to be sent to the embedded computer during the exercise.

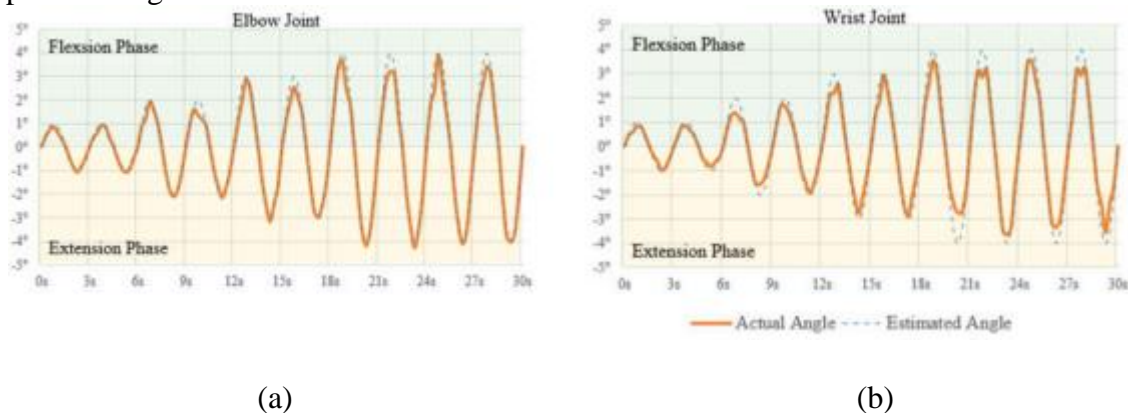


Figure 8. Estimated angle versus actual angle for elbow joint and wrist joint in Experiment, (a) elbow joint, (b) wrist joint

The equipment responds well to specified training angles. During the flexion phase, the elbow joint, as shown in Figure 8(a), has not reached the desired angle partly due to inertia from the weight of the exoskeleton (less than 89.61% of the estimated angle). Figure 8(b) shows that the actual angle approximately reached 92.25% of the estimated angle at the wrist joint.

Components and modules are stably working under long-term training conditions lasting more than 3 hours, with no software hanging or suddenly stopping equipment.



Figure 9. A prototype of the exoskeleton developed

5. Conclusion

This paper presents the design of the upper limb rehabilitation exoskeleton for post-stroke patients, which is receiving much social attention. Research in this field partly improves the quality of life for patients, creates a downright domestic product, and somewhat helps hospitals no longer depend on purchasing – importing medical equipment from abroad.

This design is the first step in designing home-based rehabilitation equipment. The design of the exoskeleton, which is compact, simple, easy to wear, low-cost but functions well, is achieved. The exoskeleton is undergoing evaluation and clinical trials to demonstrate the feasibility of the solution proposed in this paper.

Future work seeks to determine the efficiency of exoskeleton uses on rehabilitation therapies over conventional therapies. That will be the base for various combinations of proximal and training modes for the best rehabilitation practice.

Acknowledgments

This research is supported by DCSELAB and funded by Vietnam National University Ho Chi Minh City (VNU-HCM) under grant number TX2021-20b-01. We acknowledge the support of time and facilities from Ho Chi Minh City University of Technology (HCMUT), VNU-HCM for this study.

References

- [1] Ab Patar, M. N. A. Bin, Komeda, T. and Mahmud, J. (2014) ‘Force assisted hand and finger device for rehabilitation’, in *ISTMET 2014 - 1st International Symposium on Technology Management and Emerging Technologies, Proceedings*. Institute of Electrical and Electronics Engineers Inc., pp. 133–138. doi: 10.1109/ISTMET.2014.6936493.
- [2] Foong, R. *et al.* (2020) ‘Assessment of the Efficacy of EEG-Based MI-BCI with Visual Feedback and EEG Correlates of Mental Fatigue for Upper-Limb Stroke Rehabilitation’, *IEEE Transactions on Biomedical Engineering*, 67(3), pp. 786–795. doi: 10.1109/TBME.2019.2921198.
- [3] French, B. *et al.* (2016) ‘Repetitive task training for improving functional ability after stroke’, *Cochrane Database of Systematic Reviews*. John Wiley and Sons Ltd. doi: 10.1002/14651858.CD006073.pub3.
- [4] Frimpong, E. *et al.* (2014) ‘Task-oriented circuit training improves ambulatory functions in acute stroke: a randomized controlled trial’, *Journal of Medicine and Medical Sciences*, 5(8), pp. 169–175. Available at: <https://pdfs.semanticscholar.org/109b/06ebd94e1f0544127c345c53a9f7b781e6ec.pdf>.

- [5] Kollen, B. J. *et al.* (2009) ‘The effectiveness of the bobath concept in stroke rehabilitation what is the evidence?’, *Stroke*. Lippincott Williams & Wilkins. doi: 10.1161/STROKEAHA.108.533828.
- [6] Mane, R. *et al.* (2019) ‘Prognostic and monitory EEG-biomarkers for BCI upper-limb stroke rehabilitation’, *IEEE Transactions on Neural Systems and Rehabilitation Engineering*, 27(8), pp. 1654–1664. doi: 10.1109/TNSRE.2019.2924742.
- [7] Moucheboeuf, G. *et al.* (2020) ‘Effects of robotic gait training after stroke: A meta-analysis’, *Annals of Physical and Rehabilitation Medicine*, 63(6), pp. 518–534. doi: 10.1016/j.rehab.2020.02.008.
- [8] Niu, C. M. *et al.* (2019) ‘Synergy-Based FES for Post-Stroke Rehabilitation of Upper-Limb Motor Functions’, *IEEE Transactions on Neural Systems and Rehabilitation Engineering*, 27(2), pp. 256–264. doi: 10.1109/TNSRE.2019.2891004.
- [9] Park, W. (2021) ‘The Comparison for Epidemiological Investigation of Corona Virus-19 Pandemic’, in *International Conference on Advanced Communication Technology, ICACT*. Institute of Electrical and Electronics Engineers Inc., pp. 446–448. doi: 10.23919/ICACT51234.2021.9370522.
- [10] Pennati, G. V. *et al.* (2020) ‘Recovery and prediction of dynamic precision grip force control after stroke’, *Stroke*, pp. 944–951. doi: 10.1161/STROKEAHA.119.026205.
- [11] Thrift, A. G. *et al.* (2017) ‘Global stroke statistics’, *International Journal of Stroke*. SAGE Publications Inc., pp. 13–32. doi: 10.1177/1747493016676285.
- [12] Yurkewich, A. *et al.* (2019) ‘Hand extension robot orthosis (hero) glove: Development and testing with stroke survivors with severe hand impairment’, *IEEE Transactions on Neural Systems and Rehabilitation Engineering*, 27(5), pp. 916–926. doi: 10.1109/TNSRE.2019.2910011.
- [13] Zhou, M. *et al.* (2018) ‘Modeling of Return Strokes with Their Initiation Processes under Consideration’, *IEEE Transactions on Magnetics*, 54(3). doi: 10.1109/TMAG.2017.2771322.

Optimal Oil Lubrication for Ball Slide-guide of CNC Milling Machine Using Taguchi Method

Huy Hung Nguyen^{3,4}, Quoc Dat Le³, Hoang Long Phan^{1,2,3}, Van Tu Duong^{1,2,3}, and Tan Tien Nguyen^{1,2,3*}

¹Faculty of Mechanical Engineering, Ho Chi Minh City University of Technology (HCMUT), 268 Ly Thuong Kiet, District 10, Ho Chi Minh City, Vietnam

²Vietnam National University Ho Chi Minh City, Linh Trung Ward, Thu Duc District, Ho Chi Minh City, Vietnam

³National Key Laboratory of Digital Control and System Engineering (DCSELab), HCMUT, 268 Ly Thuong Kiet, District 10, Ho Chi Minh City, Vietnam

⁴Faculty of Electronics and Telecommunication, Saigon University, Vietnam

*Corresponding author. E-mail: nttien@hcmut.edu.vn

Abstract

Ball slide-guide has been widely used to guide and carry a payload in linear motion of the precise machine tools. Because of carrying the main payload, a surface deformation may result in the processing accuracy and lifetime of the CNC machine. Therefore, oil lubrication is introduced as a key factor in the design of machinery. Lubricants are usually used for modern CNC machines thanks to the fact that the volume and flow of lubricants can be monitored easily. Since it is difficult to obtain a mathematical model for estimating the leakage of lubricants, this paper studies the Taguchi method to evaluate factors that affect the time-variant friction force on the ball slide-guide such as the oil amount of feed oil, feed cycle, load, slide-guide installation. The distribution of this paper to carry out a useful tool for designing a lubrication system for precise ball slide-guide.

Keywords: Oil lubrication, Taguchi method, optimization, ball slide-guide, modular CNC machine

1. Introduction

CNC (computerized numerical control) has become increasingly popular in manufacturing all around the world. To keep CNC machine working with low vibration, high performance and high precision, many factors should be considered, one of which is lubrication for the ball slide guide of 3 axes. There are two well know lubricants in the industry for ball rails known as grease and oil (Hiwin Technologies Corp., 2018). The clear benefit of grease is hard to leak, therefore the system does not need to be re-lubricated frequently; beside, it has sealing properties which protects bearing surfaces from dust, chemistry and water. However, the grease is difficult to clean and limit a cooling ability (Doyle, 2020). Contrary to grease, oil is easily leaked and requires lubricating periodically, but it includes many advantages such as: providing better cooling properties, the ability to control the accuracy amount needed to lubricate, easy to clean and maintain the system.

This paper first provides factors that affect the lubrication ability of oil in rail-guideways systems. Then, an experiment that investigates the influence of each factor on the effectiveness of lubrication is performed. Base on the experimental results, this paper proposes the optimal lubrication method to bring high performance of slide guide movement. The main purpose of lubrication process is reducing the friction factor between guideways and slide rail, protecting the slide surface by oxidation, and prevent harmful object from getting into contact surface.

Thus, this leads to lower friction force for slide guide movement. Therefore, in this experiment, we measure the friction force of four slide units in different cases to survey the effect of factors on this force. There are many independent factors suspected of influencing an output. Having more factors and more levels of each factor can create a considerable amount of time and cost to finish experiment. The Taguchi method can be applied on this case to lower the number of experiments. Many studies have indicated that the Taguchi method can be used for academic research, as well as for production applications (Montgomery, 2017). The advantage of the Taguchi method in designing parameters model is to cut off many experiments, thus lowering the price and performance time but still gives a reliable result to help optimize the design.

2. Experimental procedure

This section describes the process of conducting the experiment, collecting data as well as method to evaluate the results.

2.1 Experimental setup

Figure 1 (a) illustrates the mechanism of the experiment used in this study. The surveying ball slide-guide include two HIWIN HGR45R1000C ball rail is arranged in parallel, each rail has 2 guideway units (HIWIN HGW45CBZ0C+SH) on it. These 4 guideway units are fixed on steel plate, which is pushed by screw nut through loadcell sensor. The movement of screw nut is made by turning of screw which is connected to 86HS85 stepping motor by timing belt.

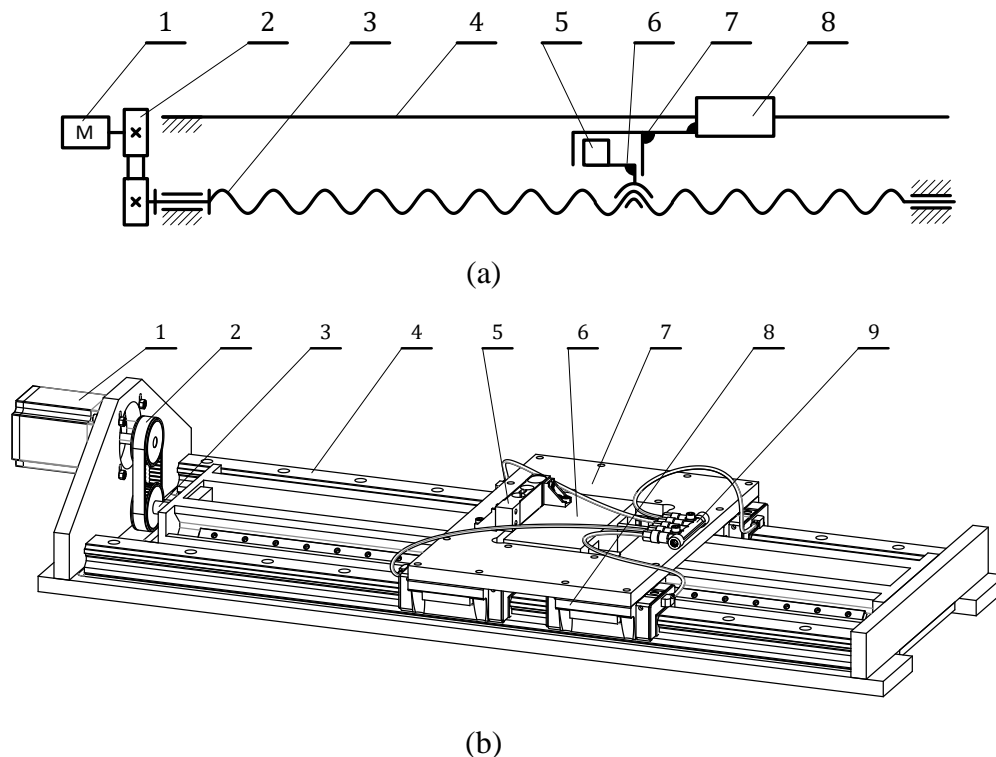


Figure 1. (a) Experiment mechanism (b) 3D model

1: Stepping motor, 2: Timing belt, 3: Ball screw, 4: Ball rail, 5: Sensor, 6: Ball nut, 7: Steel plate, 8: Guideway, 9: Oil distributor

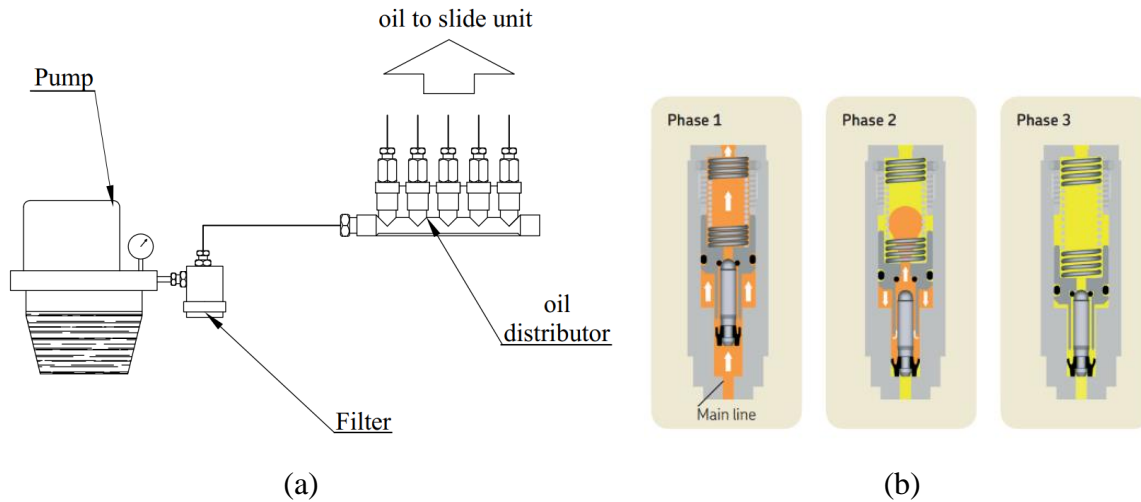


Figure 2. (a) Lubrication system (b) working principle of oil distributor

Each guideway unit connect to multi-output oil distributor by soft plastic line, the oil is supplied from high pressure pump, get into filter before going straight to the distributor. The oil connection is present in Figure 2(a).

The working principle of a high-pressure oil distributor is shown in Figure 2 (b) when the high-pressure pump is activated; the oil from the oil tank travels to the oil pump through the pipeline; the oil pressure generates the push force to compress the spring in the directional valve to push oil in the discharge chamber to the valve out; when the oil pump is disconnected, the oil loses the high pressure so the spring returns to its original position and pushes the oil from the storage chamber into the discharge chamber in preparation for the next delivery. Thus, in one pulse of the oil pump, the volume of oil gone out of the distributor at each time is equal to the discharge chamber volume (Callahan, 1981). This feature of distributor guarantees the amount of oil distribute to each slide guide block is the same, independent of the time operation pump of each cycle and length of connection pipe from pump to each distributor block.

2.2 Data collection process

In this experiment, a EGQ7–Q9VP loadcell is used to measure force coming from the ball screw to the steel plate. The oil is fed one time at the start of each experiment, the stepping motor runs periodic to move the steel plate laterally. In one cycle of moving mentioned, the loadcell just measures compression force. The motion profile of the stepping motor is defined with acceleration and to reducing the force of inertia of mass. The acquisition data of loadcell is sampled at specified points in the whole travel where the steel plate run with constant speed.

The oil leakage affects the pushing force of ball screw to steel plate during moving operation. The data acquisition and the motion control are implemented on the ESP32 microcontroller, meanwhile the data received by loadcell is stored in microSD card and transferred to PC at the end of experiment period. There are one limit switches inserted to the terminal of slide rail. The feedback signal of the limit switch is captured to reset the starting sampling position in all period.

Many factors affect lubrication efficiency as well as leaking of oil. These factors lead to the varying of the push force to move unit slideway on rail. Some factors can be recognized and controlled by CNC processor such as oil volume per cycle, re-lubrication cycle time, sum of

travel distance on one cycle. Some factors change slowly in time or are difficult to be sensed by CNC processor like temperature and moisture of atmosphere, oil viscosity, load on slideway unit.

Oil viscosity

Oil viscosity or oil thickness determines the lubricant's film strength. If the oil viscosity is too high, the isolating coefficient between slide surface and harmful object is better, the time for oil leakage is longer, but high viscosity is also an obstacle to movement and cause the machine to work harder. Conversely, if the oil viscosity is too low, the film created by oil may not be thick enough to prevent friction. The oil viscosity for slideway lubrication is usually limited from 30cSt to 150cSt (Hiwin Technologies Corp., 2018). The oil used in this paper has a viscosity of 50cSt.

Load on slideway

The data of loadcell is sampled at a constant velocity of slideway unit, at this point, the main force active in loadcell is rolling friction. This force is proportional to a coefficient of rolling friction and the weight of the load on the slide unit. High friction force leads to the increase of rail temperature, which may affects oil leakage. However, in the CNC machine, the fixed load which is the weight of the machine table always impacts slideway while either at rest or in motion, while the weight of the manufacturing product is small compare with the load of the table. The weight as a load put on four slide unit for this research is limited to 70kg.

The atmosphere conditions

The temperature and moisture of air in a factory may cause the evaporation of lubricant. However, oil evaporation is only significant when the temperature higher than 100°C. Thus, oil evaporation is not considered as an effect object to lubrication efficiency.

Oil volume per cycle

The oil volume which is fed on one lubrication cycle affects lubrication efficiency directly. Small volume may be insufficient for creating oil film; in contrast, too much oil can waste lubricant. Almost all modern CNC machines use a one-line lubrication system to distribute oil to 3 axes. The one-line lubrication system has used the distributor which supplies a constant volume of oil, independent of the length of the connection pipeline from the pump to the distributor. The distributor which is used for our experiment is SKF MonoFlex 450 with 0.1cm³ metered quantity at 1 bar of relief pressure (Callahan, 1981).

Re-lubrication cycle time

The lubricant is not necessary to be fed continuously during the operation of the CNC machine, the continuous running of lubrication is harmful to the oil pump as well as wastes power and oil. In most CNC machines, the oil is fed periodically at a constant time, the lubrication cycle time installed in the CNC controller relates directly to oil leakage time. The re-lubrication cycle time is not long enough to evaporate the oil, but it may cause leaking oil off the rail by oil gravity. This is an essential factor that needs to be investigated to find the reasonable cycle time value for lubrication controllers.

Speed of slide unit

The lubricant does not make the film on the rail surface immediately. When the oil is fed to the slideway, it is stored in slideway unit slots and distributed on rail when the slideway unit runs on it. Different speeds of slideway lead to different travel distances on the rail in one lubrication cycle. This travel distance may affect the quantity of the oil that goes off from the storage slot of

the slideway unit to the rail. In this paper, we perform the experiments with 3 levels of speed of the stepping motor.

2.3 Taguchi parameters

Before applying the Taguchi analysis, the parameters and number of levels for each parameter must be established. Taguchi method shows that 3 levels for each parameter are suitable for finding optimum design values. As mentioned above, the Taguchi parameters are the oil volume per cycle, the re-lubrication cycle, and the speed of the slideway.

With some pre-experiment, we conclude that the change of friction force is only significant when the volume of the oil reaches 1/30 of the amount referred to slide guide manufacturer (Hiwin Technologies Corp., 2018). Therefore, this experiment is performed with 0.1cm³, 0.2cm³ and 0.3cm³ volume of feed oil on start of lubrication cycle. The reference re-lubrication cycle from another CNC machines is 8 hours. Thus, our experiment investigates 3 levels of the cycle time, which are 8 hours, 16 hours, and 24 hours. The speed of one axis fluctuates during the operation of the CNC machine, depending on the machining mode. In a high rigidity machine, the tool feed rate can reach 1000mm/min. In the limit of this experiment, the tool feed rate is utilized respectively with 300mm/min, 400mm/min, and 500mm/min. Table I lists the parameters and levels of each parameter is validated in this experiment.

Table I. Factors and levels for oil lubrication experiments

Parameters	Level 1	Level 2	Level 3
Oil volume per cycle (cm ³)	0.1	0.2	0.3
Re-lubrication cycle (hour/cycle)	8	16	24
Speed (mm/min)	300	400	500

At the beginning of each experiment, the same initial conditions are made such as drying the oil on the rail, running the slide unit until getting the same initial force with another experiment. For each experiment, the load-cell value is collected at three specified points. Then, the difference between the collected values at the beginning and the ending are used the getting value for the Taguchi method. One measured value from load-cell at one point before and after filtering is illustrated in Fig 3.

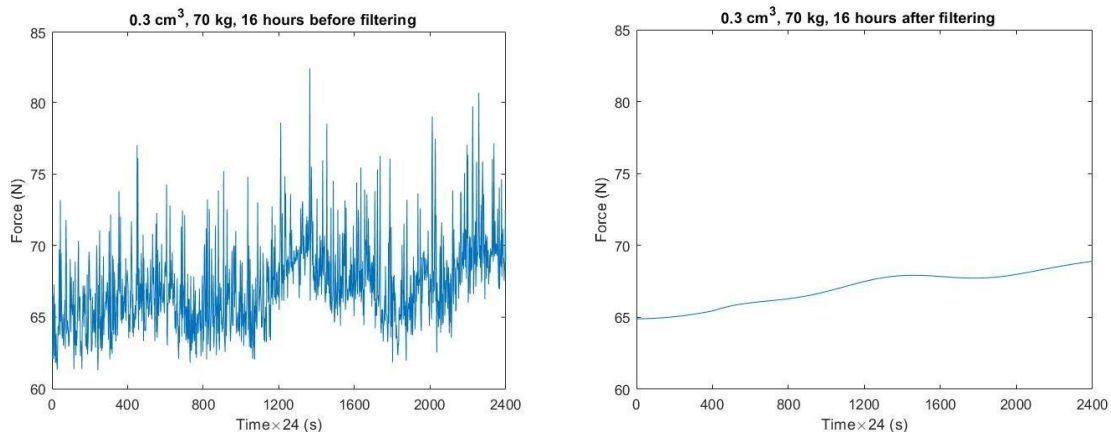


Figure 3. The force measurement in one lubrication cycle at one point

In Taguchi method, the S/N (signal-to-noise) ratio is transformed from loss function:

$$L = k(y - m)^2 \quad (2)$$

Where L is the loss due to error from the deviation of received value y compared to the desired value m , k is a constant. The S/N ratio is built and converted to calculate for three main cases:

- Received value y should be “the larger the better”.
- Received value y should be “the smaller the better”.
- Received value y should be “best rating”.

Each case has their own applied formula, in this experiment measured value is friction force change, The S/N ratio needs to be “the smaller the better” because more friction force means more leakage of lubricant (having same load on), the S/N ratio in this case is calculated using this formula (Mori, 2001):

$$SN_s = -10 \log \left(\frac{1}{n} \sum_{i=1}^n y_i^2 \right) \quad (3)$$

In which SN_s is the ratio for “smaller the better”, n number of data, y_i is a change of measured friction force by the time. When all SN_s ratio is calculated, the medium value of each parameter be achieved, ranking of the parameters as well as efficiency of oil lubrication can be shown. From the SN_s ratios, the optimum parameters can be found and the experiment’s goal is obtained.

3. Experimental result

After all data were collected, the Taguchi analysis was carried out to determine the effect of parameters on friction force change. The statistical analysis was performed by using Minitab software. The SN_s ratios are obtained from Eq. (3) and the results of friction force change is shown in Table III. Since an L_9 orthogonal array is used to perform the test, there are 9 experiments in total.

Table III. Friction force change results and SN_s ratio

No.	Lubrication Cycle (hour)	Oil volume (cm ³)	Speed (mm/min)	Force change point 1 (N)	Force change point 2 (N)	Force change point 3 (N)	SN_s ratio
1	8	0.1	300	0.672	0.65	0.672	3.546865
2	8	0.2	400	0.683	0.661	0.696	3.347862
3	8	0.3	500	0.722	0.703	0.739	2.835476
4	16	0.1	400	0.732	0.691	0.738	2.84568
5	16	0.2	500	0.848	0.829	0.862	1.448062
6	16	0.3	300	0.681	0.663	0.697	3.343756
7	24	0.1	500	0.902	0.884	0.909	0.930653
8	24	0.2	300	0.767	0.745	0.785	2.317224
9	24	0.3	400	0.874	0.853	0.886	1.198572

The mean of S/N response for friction force change of each level of parameters is shown in Table III and Figure 4. From the result of Taguchi analysis, we can realize that the significant factors that affect lubrication efficiency are the re-lubrication cycle and speed of the slide unit, while the parameter with the least impact is oil volume per cycle. Base on the Delta of each parameter, the affecting percentage to lubrication efficiency of re-lubrication, oil volume per cycle, and speed are 50%, 6%, and 40.6%, respectively.

As shown in Figure 4, between the three levels of the re-lubrication cycle, 8 hours is the optimal period time for the lubrication, while slideway unit speed also seriously affects the efficiency of the lubrication process. The volumes of oil fed at the beginning of the cycle almost no difference between 0.1cm³, 0.2cm³, and 0.3cm³.

Table IV. Response Table for Signal to Noise Ratios

Level	Re-lubrication	Oil volume per cycle	Speed
1	3.243	2.441	3.069
2	2.546	2.371	2.464
3	1.482	2.459	1.738
Delta	1.761	0.088	1.331
Rank	1	3	2

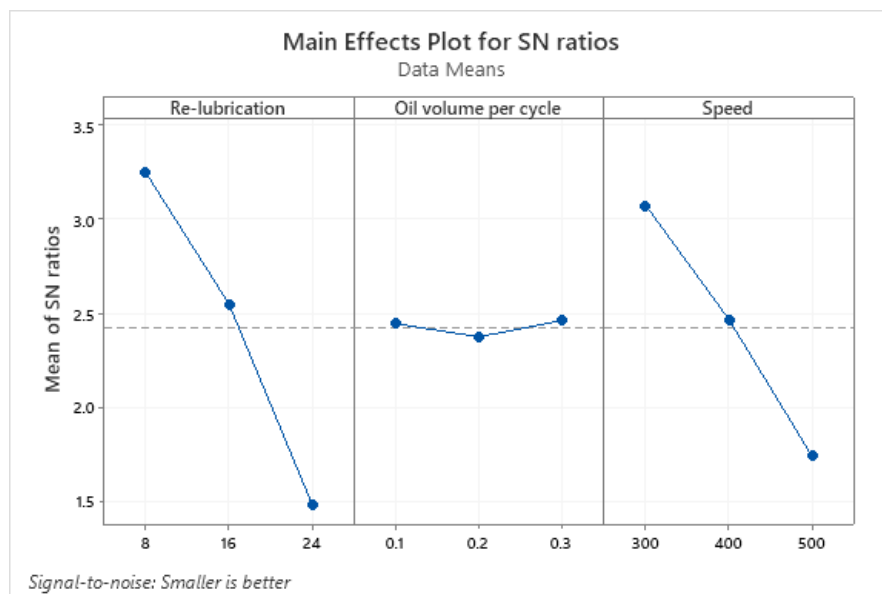


Figure 4. The effect of S/N ratios on the measured force

4. Conclusion

From the experiment result set of optimum parameters for re-lubrication is achieved. Within the experiment, the Taguchi method is proved to be a robust technique for optimal lubrication method. Three parameters are validated, and the result provides insight in designing an oil lubrication system. In these parameters, the oil volume and the period time of one cycle

can be controlled, while the speed of the machinery table can be monitored by the CNC controller. Using the result above to proposing the new algorithm for lubrication will make the CNC machine getting smarter, saving the oil for lubrication, while still protecting the slideway surface.

For the operation of CNC machine in practical, there are other factors which affect to lubrication efficiency such as how slideway is covered, how is the angle of rail relative to the horizontal plane, and how is the vibration of machine during cutting process. This paper presents an overview of the main factors that are easily controlled and directly affect to lubrication process. Our experimental results will inspire the next experiments with more factors as well as providing data for a smarter control algorithm for the lubrication process.

Acknowledgement

This research is supported by DCSELAB and funded by Vietnam National University Ho Chi Minh City (VNU-HCM) under grant number TX2021-20b-01. We acknowledge the support of time and facilities from Ho Chi Minh City University of Technology (HCMUT), VNU-HCM for this study. This research is also funded by Department of Science and Technology under grant number 21/2019/HĐ-QPTKHCN.

References

- [1] Callahan, J. J. (1981) ‘Centralized Lubrication Systems.’, Plant Engineering (Barrington, Illinois), 35(11).
- [2] Doyle, D. (2020) Grease Lubrication versus Oil Lubrication, ALS Tribology. Available at: <https://www.alsglobal.com/%2Fen%2Fnews%2Farticles%2F2020%2F01%2Fesource-123-grease-lubrication-versus-oil-lubrication> (Accessed: 31 May 2021).
- [3] Hiwin Technologies Corp. (2018) ‘Linear Guideway’, p. 211.
- [4] Montgomery, D. C. (2017) Design and Analysis of Experiments, Mycological Research.
- [5] Mori, T. (2001) ‘Taguchi Methods Benefits, Impacts, Mathematics, Statistics, and Applications’, NIR news, 12(1), pp. 8–9.

An Optimal Method for Distributing Tolerance of Milling Spindle's Components

Xuan Quang Ngo², Van Tu Duong^{1,2,4}, Thanh Luan Bui^{2,3,4}, Huy Hung Nguyen^{2,5}, and Tan Tien Nguyen^{1,2,4,*}

¹Faculty of Mechanical Engineering, Ho Chi Minh City University of Technology (HCMUT),
268 Ly Thuong Kiet, District 10, Ho Chi Minh City, Vietnam

²National Key Laboratory of Digital Control and System Engineering (DCSELab), HCMUT, 268
Ly Thuong Kiet, District 10, Ho Chi Minh City, Vietnam

³Industrial Maintenance Training Center, HCMUT, VNU-HCM

⁴Vietnam National University Ho Chi Minh City, Linh Trung Ward, Thu Duc City, Ho Chi Minh
City, Vietnam

⁵Faculty of Electronics and Telecommunication, Saigon University, Vietnam

*Corresponding author. E-mail: nttien@hcmut.edu.vn

Abstract

In CNC milling machine, the motorized spindle is a crucial part on which cutting tools are mounted to shape the workpiece into the desired form during cutting process. Therefore, the milling accuracy and surface quality of the cutting process are directly affected by tolerances for milling spindles. The spindle's assembly tolerance is formed from components' tolerances which depend on the process and manufacturing cost of parts. The easiest way to ensure that the assembly process is under control is to process the components with high accuracy. This would result in higher production costs and a longer time for processing. This paper estimates the accumulation of individual tolerances on the assembly dimension, then redistributes the assembly tolerance judiciously among the individual dimensions in the relevant dimension chain by considering the relation of part's tolerance with manufacturing cost. The final approach is to reach the required assembly tolerance with reasonable cost.

Keywords: CNC Milling machine, Motorized spindle, Assembly tolerance, Individual tolerance, Accumulated tolerance

1. Introduction

Milling machine is one of the most fundamental machinery in the manufacturing industry. One important factor associated with development of milling machine is machining accuracy. Therefore, the motorized spindle which influences the machining accuracy of a component directly is required strictly by accuracy and reliability.

Requirements for accuracy as well as the working ability of the motorized spindle determine its assembly tolerance. Since the motorized spindle is composed of many parts, the spindle assembly tolerance is affected by the tolerance of each spindle's component, also known as the accumulated tolerance. The more component forming the motorized spindle, the less the whole spindle's precision is. Therefore, in order to meet the required accumulated tolerance for this case, distributing of individual tolerances has to be strictly considered.

The tolerance analysis process is the evaluation of the accumulated tolerance in each assembly dimension with all given individual tolerances. This is a very important step in designs for the tolerances. The accumulated tolerance resulting from the tolerance analysis process shall be equal to or less than the corresponding assembly tolerance which is determined by the designer, based on the assembly and functional requirements of the machine. There are a variety of

methods for determining the accumulated tolerance in the dimensional chain such as the worst-case or the method of extremes and the root sum square (RSS) or the statistical model. Both models have pros and cons (Singh *et al.*, 2009a). Allocated tolerances using the worst-case model tend to be tighter than necessary and lead to higher manufacturing costs. The statistical model ignores dimensions with very low probability, so it is called incomplete interchangeability, meaning that defective products occur.

Once the accumulated tolerance has been evaluated, if the assembly tolerance exceeds the target tolerance, there will be a problem leading to unexpected performances. There have been many researchers solving this issue by applying cost-tolerance design methods to specific machines such as Yue Wang for an overrunning clutch assembly (Wang *et al.*, 2019) and Jhy-Cherng Tsai for a spindle head (Tsai and Wu, 2013). This paper applies one optimal tolerance design approach for minimum cost to redistribute the target tolerance for each part when the assembly tolerances exceed the target tolerances. This design approach not only ensures suitable accumulated tolerances but also controls the production cost. In section 2, optimal tolerance design methods are presented for minimizing cost. Section 3 will solve the tolerance problem of the motorized spindle by applying the method presented in section 2.

2. An optimal tolerance design method

As mentioned, when the assembly tolerance of the product exceeds the specified limit, it should be judiciously redistributed to the product's components. The cost and quality of the product depend on the machining process used to manufacture its constituent parts. Many methods have been proposed to try to optimize cost-tolerance such as the Peter approach (Peter, 1970) which solves the problem with the graphical technique, making it easy for the designer to judge, but it should only apply for assemblies consisting of two components. However, we can expand it by considering subassemblies which include two parts. Wilde-Prentice approach for exponential cost functions under worst-case stack-up criteria (Wilde and Prentice, 1975). This paper uses the Lagrange multiplier-based approach because it enables designers to avoid multiple-parameter iterative solutions, use either worst-case or statistical model and use alternative cost models.

The worst-case method for calculating the accumulated tolerance (Singh *et al.*, 2009a):

$$\Delta Y = \sum_{i=1}^n T_i \quad (1)$$

The statistical (RRS) method for calculating the accumulated tolerance (Singh *et al.*, 2009a):

$$\Delta Y = \sqrt{\sum_{i=1}^n T_i^2} \quad (2)$$

where n is number of constituent dimensions in the dimension chain, and T_i is the tolerance associated with each dimension.

Table 1. Proposed cost-tolerance model

Cost Model	Function	Author
Reciprocal Squared	$C(T) = A + B/T^2$	Spotts (Spotts, 1972)
Reciprocal	$C(T) = A + B/T$	Chase and Greenwood (Chase and Greenwood, 1988)
Reciprocal Power	$C(T) = A + B/T^k$	Chase (Chase <i>et al.</i> , 1990)
Exponential	$C(T) = Ae^{-BT}$	Speckhart (Speckhart, 1971)

where $C(T)$ is the cost function; A is the coefficient represents fixed cost including setup cost, tooling, material, etc.; B is the coefficient determines the cost of producing a component corresponding to a specified tolerance; and k is the coefficient describes how sensitive the process cost is to change in tolerance specifications.

The coefficient A , B and k depend on the machining condition, the machining method, the quality of the machine, etc. Therefore, there are few documents going into determining these cost curves. and data about production costs are public by manufacturers. It is possible to refer to these curves for different machining processes in the reference (Drake, 1999).

The following points should be notable when using Lagrange multiplier-based approach (Singh, Jain and Jain, 2009b). Each constraint corresponds to each Lagrange multiplier λ , so we have to solve a set of equation of multipliers to get these λ . When the value of λ is achieved, optimal tolerances of parts can easily be calculated. Tolerances gotten from this method can not be suitable for the selected process ability such as milling, grinding, etc., so designers have to guarantee calculated results which range in the tolerance limit.

The set of equations of multipliers can be represented in the form (Singh *et al.*, 2009b):

$$\frac{\partial}{\partial T_i} [C(T)] + \lambda_j \frac{\partial}{\partial T_i} [g_j(T)] = 0, \quad i = 1, 2, \dots, n \quad (3)$$

where $g_j(T)$ is the j th constraint; and λ_j is the coefficient corresponding to each constraint $g_j(T)$.

Assuming there is only one assembly tolerance requirement, that is, there is only one multiplier λ . Combining the mathematical model of reciprocal power of Chase as shown in Table 1 and the worst-case model Eq.(1), the Eq.(3) becomes:

$$\frac{\partial}{\partial T_i} \left(\sum \left(A_i + \frac{B_i}{T_i^{k_i}} \right) \right) + \lambda \frac{\partial}{\partial T_i} \left(\sum T_i - T_{ASM} \right) = 0, \quad i = 1, 2, \dots, n \quad (4)$$

where T_{ASM} is the specified assembly tolerance.

From Eq.(4), solving for λ , it can be obtained as:

$$\lambda = \frac{B_i k_i}{T_i^{k_i+1}}, \quad i = 1, 2, \dots, n \quad (5)$$

Solving Eq.(5) for T_i , it can be obtained:

$$T_i = \left(\frac{B_i k_i}{B_1 k_1} \right)^{\frac{1}{k_i+1}} T_1^{\frac{k_1+1}{k_i+1}}, \quad i = 1, 2, \dots, n \quad (6)$$

Substituting Eq.(6) into Eq.(1), we get the assembly tolerance:

$$T_{ASM} = T_1 + \sum_{i=2}^n \left(\frac{B_i k_i}{B_1 k_1} \right)^{\frac{1}{k_i+1}} T_1^{\frac{k_1+1}{k_i+1}} \quad (7)$$

With the same manner for the statistical model of Eq.(2), it can be achieved the assembly tolerance as follows:

$$T_{ASM}^2 = T_1^2 + \sum_{i=2}^n \left(\frac{k_i B_i}{k_1 B_1} \right)^{\frac{2}{k_i+2}} T_1^{\frac{2(k_1+2)}{k_i+2}} \quad (8)$$

3. A case study

In this section, the Lagrange multiplier-based approach for designing cost-tolerance presented in section 2 is used to solve the spindle assembly tolerance problem discussed in section 1.

The spindle tolerance design procedure includes the steps shown in Figure 1, which is the iterative process until the designer's requirements are met.

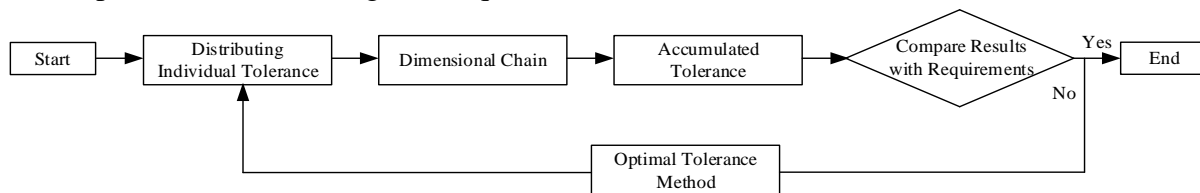


Figure 1. The procedure for designing the spindle tolerance

By applying the above procedure, we calculate the assembly tolerance of the motorized spindle, namely the clearance between part 10 (ring) and part 11 (bearing) as shown in Figure 2, for choosing a suitable bearing to compensate errors in the system, i.e. manufacturing error, accumulated error, thermal expansion error, etc.

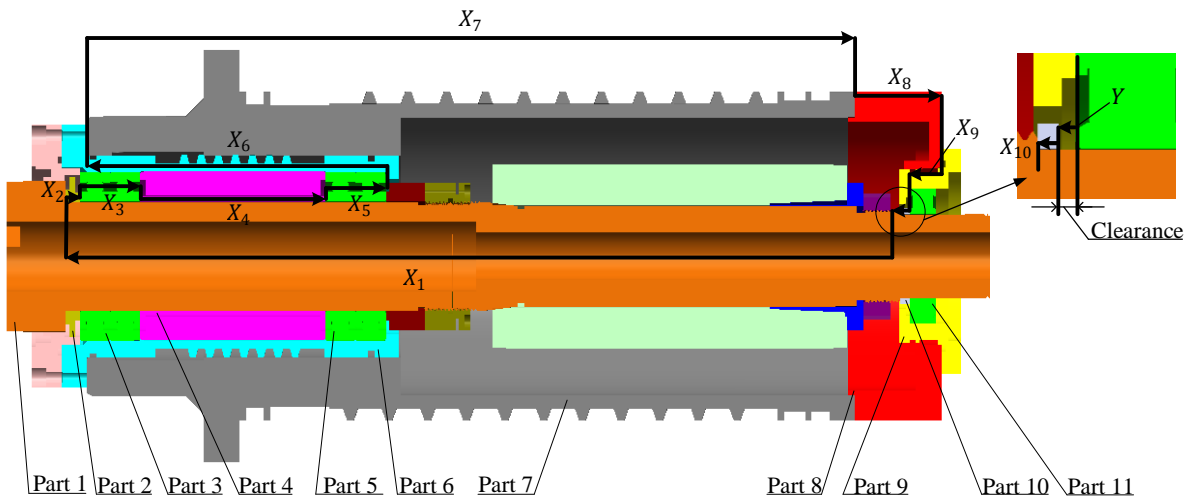


Figure 2. The dimensional chain of the motorized spindle

Step 1. Distributing individual tolerances based on part designs, standards, experience, etc.

The bearings (part 3 and part 5) are vender-supplied, thus their tolerances are fixed and have no effect on the optimal cost-tolerance design. The bearing (part 11) do not participate in the dimensional chain, therefore we do not mention its tolerance. The remaining parts are assumed to be machined by turning, hence the initial values of the parts 1,2,4,6,7,8,9 and 10 are referenced based on the instruction of the document (Drake, 1999).

Table 2. Initial tolerance specifications

Part	Name	Nominal Dimension (mm)	Initial Tolerance (mm)	Process Tolerance Limits	
				Min	Max
1	Spindle shaft	496.5	0.35	0.1	0.6
2	Cover	8.4	0.06	0.02	0.1
3*	Bearing	36	0.25*	*	*
4	Spacer	110	0.18	0.05	0.3
5*	Bearing	36	0.25*	*	*
6	Sleeve	178	0.2	0.065	0.35
7	Spindle housing	457	0.35	0.1	0.6
8	Rear housing	51.5	0.15	0.04	0.25
9	Bearing holder	19	0.09	0.03	0.15
10	Retaining ring	5.4	0.06	0.02	0.1

Note: *fixed tolerance (using angular contact ball bearing of SKF manufacturer, (SKF Super-Precision Bearing, 2016))

Step 2. Constructing the dimensional chain.

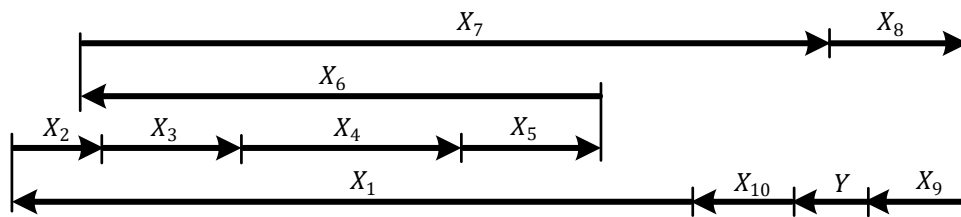


Figure 3. Modeling the dimensional chain

From the dimensional chain (Figure 3), we achieve the following dimensional chain equation:

$$Y = -X_1 + X_2 + X_3 + X_4 + X_5 - X_6 + X_7 + X_8 - X_9 - X_{10} \quad (9)$$

Where X_i is individual dimension ($i = 1,2, \dots, 10$); Y is assembly dimension.

Step 3. Calculating the accumulated tolerance.

Solving the dimensional chain equation Eq. (9) with the specifications shown in Table 2 for the nominal dimension of the clearance, we have $Y = 0 \text{ mm}$.

The clearance tolerance is the accumulated tolerance of the assembly process, determined by the corresponding dimensional chain. We use the worst-case method Eq.(1) and the initial tolerances of the parts as shown in Table 2 in order to calculate the accumulated tolerance of the clearance. As a result, we have $\Delta Y = T_Y = 1.94 \text{ mm}$.

Step 4. Compare the accumulated tolerance and the production cost with the required assembly tolerance and the desired production cost, respectively.

We choose the assembly tolerance of the clearance having value of 1.2 mm , because the sum of the errors, which includes maximum axial displacement of a single row cylindrical roller bearing of SKF manufacturer as shown in Figure 4 with the bore diameter 50 mm is $1,5\text{ mm}$ (SKF General Catalogue, 2008) and axial displacement of spindle shaft resulting from the heat generation in the motorized spindle with speed of 12000 rpm is about 0.09 mm (Fan *et al.*, 2018), is 1.59 mm .

Since the accumulated tolerance of the clearance $T_Y = 1.94\text{ mm}$ calculated in step 3 exceeds the specified assembly tolerance $T_{ASM} = 1.2\text{ mm}$, redistributing the tolerance to each part should be carried out.

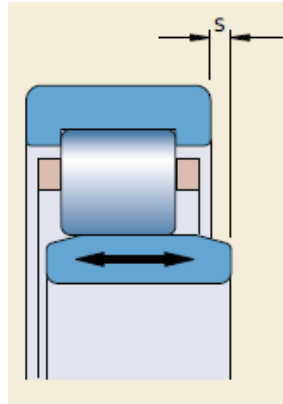


Figure 4. Axial displacement of single row cylindrical roller bearings

Step 5. Applying the optimal cost-tolerance design method.

In order to apply the optimal tolerance equation Eq.(7), the fixed tolerances must be removed, namely part 3 and part 5:

$$\begin{aligned}
 T'_{ASM} &= T_{ASM} - T_3 - T_5 \\
 &= T_1 + \left(\frac{k_2 B_2}{k_1 B_1}\right)^{\frac{1}{k_2+1}} T_1^{\frac{k_1+1}{k_2+1}} + \left(\frac{k_4 B_4}{k_1 B_1}\right)^{\frac{1}{k_4+1}} T_1^{\frac{k_1+1}{k_4+1}} + \left(\frac{k_6 B_6}{k_1 B_1}\right)^{\frac{1}{k_6+1}} T_1^{\frac{k_1+1}{k_6+1}} \\
 &\quad + \left(\frac{k_7 B_7}{k_1 B_1}\right)^{\frac{1}{k_7+1}} T_1^{\frac{k_1+1}{k_7+1}} \\
 &\quad + \left(\frac{k_8 B_8}{k_1 B_1}\right)^{\frac{1}{k_8+1}} T_1^{\frac{k_1+1}{k_8+1}} + \left(\frac{k_9 B_9}{k_1 B_1}\right)^{\frac{1}{k_9+1}} T_1^{\frac{k_1+1}{k_9+1}} + \left(\frac{k_{10} B_{10}}{k_1 B_1}\right)^{\frac{1}{k_{10}+1}} T_1^{\frac{k_1+1}{k_{10}+1}}
 \end{aligned} \tag{10}$$

Values of the coefficient k_i and B_i in Table 3 of the cost-tolerance function for each dimension depend on the machining method and the part's dimension, which can be referenced according to (Drake, 1999).

Table 3. Coefficient k_i and B_i of cost-tolerance function

Part	k_i	B_i
1	0.46823	0.15301
2	0.46823	0.07202
3	*	*
4	0.45747	0.11805
5	*	*
6	0.46537	0.12576
7	0.46823	0.15301
8	0.43899	0.11800
9	0.45747	0.08597
10	0.46823	0.07202

Note: *vendor-supplied

Solving Eq.(10) based on the figures in Table 3 for the optimal tolerance of part 1, we have $T_1 = 0.11 \text{ mm}$.

Inserting T_1 into Eq.(6) to calculate other tolerances, we have $T_2 = 0.07 \text{ mm}$; $T_4 = 0.09 \text{ mm}$; $T_6 = 0.1 \text{ mm}$; $T_7 = 0.11 \text{ mm}$; $T_8 = 0.08 \text{ mm}$; $T_9 = 0.07 \text{ mm}$; $T_{10} = 0.07 \text{ mm}$.

Table 4. Minimum cost tolerance allocation

Part	Tolerance Cost Data			Initial Tolerance (mm)	Allocated Tolerance (mm)	
	A_i	B_i	k_i		Worst-Case	RRS
1	\$1.00	0.15301	0.46823	0.35	0.11	0.47
2	\$1.00	0.07202	0.46823	0.06	0.07	0.35
3		*	*	0.25*	0.25*	0.25*
4	\$1.00	0.11805	0.45747	0.18	0.09	0.42
5		*	*	0.25*	0.25*	0.25*
6	\$1.00	0.12576	0.46537	0.2	0.1	0.43
7	\$1.00	0.15301	0.46823	0.35	0.11	0.47
8	\$1.00	0.11800	0.43899	0.15	0.08	0.41
9	\$1.00	0.08597	0.45747	0.09	0.07	0.37
10	\$1.00	0.07202	0.46823	0.06	0.07	0.35
Accumulated Tolerance				1.94	1.2	1.2
Assembly Cost				\$17.31	\$20.16	\$13.98
Acceptable Fraction					100%	99.73%
True Cost					\$20.67	\$14.02

The setup cost which is coefficient A in the cost function does not affect the optimization, so we assign the cost of \$1.00 per part in order to compare the production costs before and after using the optimal method.

The allocated tolerances satisfy the process tolerance limits shown in Table 2, so this set of tolerances can be used. In case of exceeding the process tolerance limits, other coefficients and other machining methods should be re-selected, or we can use the max limit of the selected process.

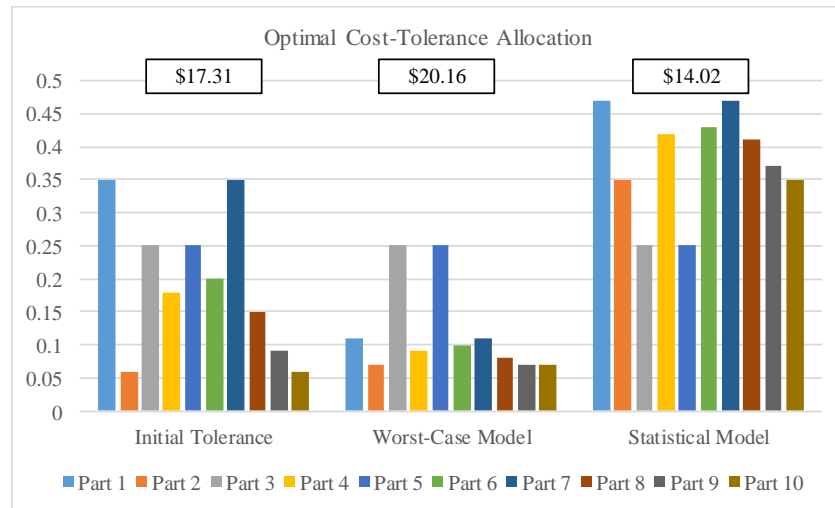


Figure 5. Comparison of optimal cost-tolerance allocation results

4. Conclusion

This paper proposes the Lagrange multiplier-based cost-tolerance design approach with reciprocal power cost model to solve the motorized spindle tolerance problem. The method establishes a relationship between the product design and the manufacture of the motorized spindle so that a set of tolerances that satisfies both assembly tolerance requirements and production costs can be given. In a case study, the optimal cost-tolerance design procedure for the motorized spindle as shown in Figure 1 is performed step- -step with both worst-case and statistical models. When using the worst-case model, to ensure the complete interchangeability, that is, 100% of parts are successful, leads to the tighten tolerance requirements and the higher production cost than the statistical model as shown in Figure 5. The original tolerances, when summed by the worst-case model, give an assembly tolerance of 1.94 mm . This exceeds the specified assembly tolerance limit of 1.2 mm . Thus, the component tolerances have to be tightened, driving up the cost to \$20.16. When using the statistical model, the accumulated tolerance is only 0.69 mm , which is less than the specification limit of 1.2 mm . Then, the allocation algorithm increases component tolerances and lower the cost to \$14.02. The single row cylindrical roller bearing NU 2210 ECP of SKF bearing manufacturer having maximum axial displacement of 1.5 mm is chosen to design the motorized spindle (SKF General Catalogue, 2008).

Acknowledgement

This research is supported by DCSELAB and funded by Vietnam National University Ho Chi Minh City (VNU-HCM) under grant number TX2021-20b-01. We acknowledge the support of time and facilities from Ho Chi Minh City University of Technology (HCMUT), VNU-HCM for this study. This research is also funded by Department of Science and Technology under grant number 75/2019/HĐ-QPTKHCN.

References

- [1] Chase, Kenneth W., Greenwood William H., Loosli, Bruce G., Hauglund, Loren F. (1990), "Least cost tolerance allocation for mechanical assemblies with automated process selection", *Manufacturing review*, Vol 3 No. 1, pp. 49–59.
- [2] Chase, K. W. and Greenwood, W. H. (1988), "Design Issues in Mechanical Tolerance

Analysis", *Manuf Rev*, Vol 1 No 1, pp. 50–59.

[3] Fan, L T; Jing, X R; Zhang, L X; Li, D (2018), "Hybrid modelling for thermal deformation prediction of high speed motorized spindle", *IOP Conference Series: Materials Science and Engineering*, 399(1).

[4] Peter, J. (1970), "Tolerancing the components of an assembly for minimum cost", *Journal of Engineering for Industry*, Vol 93 No2, pp. 677-682.

[5] Singh, P. K., Jain, P. K. and Jain, S. C. (2009a), "Important issues in tolerance design of mechanical assemblies. Part 1: Tolerance analysis", *Proceedings of the Institution of Mechanical Engineers, Part B: Journal of Engineering Manufacture*, 223(10), pp. 1225–1247.

[6] Singh, P. K., Jain, P. K. and Jain, S. C. (2009b), "Important issues in tolerance design of mechanical assemblies. Part 2: Tolerance synthesis", *Proceedings of the Institution of Mechanical Engineers, Part B: Journal of Engineering Manufacture*, 223(10), pp. 1249–1287.

[7] Speckhart, F.H. (1971), "Calculation of tolerance based on a minimum cost approach", *Journal of Engineering for Industry*, Vol 3 No 1, pp. 447–453.

[8] Drake, Paul J. (1999), "Dimensioning and Tolerancing", *the United States of America*.

[9] Spotts, M. F. (1972), "Allocation of Tolerances To Minimize Cost of Assembly", *Journal of Engineering for Industry*, Vol 95 No 3, pp. 762-764.

[10] Tsai, J. C. and Wu, S. R. (2013), "Tolerance analysis and re-distribution of a machine tool spindle by negative tolerancing", *Procedia CIRP*, Vol 10, pp. 267–270.

[11] Wang, Yue; Li, Lei; Hartman, Nathan W.; Sutherland, John W. (2019), "Allocation of assembly tolerances to minimize costs", *CIRP Annals*, Vol 68 No 1, pp. 13–16.

[12] Wilde, D.; Prentice, E. (1975), "Minimum Exponential Cost Allocation of Sure-Fit Tolerances", *Journal of Engineering for Industry*, Vol 97 No. 4, pp. 1395-1398.

[13] SKF (2008) "SKF General Catalogue".

[14] SKF (2016), "SKF Super-Precision Bearing".

Design of Three Axes of CNC Milling Machine Using Lucas Design for Assembly

Viet Toan Vu³, Van Tu Duong^{1,2,3,*}, Thanh Luan Bui^{2,5}, Huy Hung Nguyen^{3,4}, and Tan Tien Nguyen^{1,2,3,*}

¹Faculty of Mechanical Engineering, Ho Chi Minh City University of Technology (HCMUT), 268 Ly Thuong Kiet, District 10, Ho Chi Minh City, Vietnam

²Vietnam National University Ho Chi Minh City, Linh Trung Ward, Thu Duc District, Ho Chi Minh City, Vietnam

³National Key Laboratory of Digital Control and System Engineering (DCSELab), HCMUT, 268 Ly Thuong Kiet, District 10, Ho Chi Minh City, Vietnam

⁴Faculty of Electronics and Telecommunication, Saigon University, Vietnam

⁵Industrial Maintenance Training Center, HCMUT, VNU-HCM

*Corresponding author. E-mail: dvtu@hcmut.edu.vn, nttien@hcmut.edu.vn

Abstract

Lucas Design for assembly (DFA) is a product redesign method which involves assigning and summing penalty factors associated with potential design problems. The penalty factors are manipulated into three indices. These indices of the redesign are compared to thresholds or values established for previous designs. Lucas DFA method minimizes the number of parts. This paper uses the Lucas DFA method to analyze each component to determine three assembly ability indices of the design of three axes X, Y, Z, and their redesign. Firstly, the functional analysis is carried out to determine whether it is essential and cannot be eliminated. Secondly, the handling analysis is performed to determine a handling index that relates to using the tools to assemble the part. Thirdly, the paper carries out the fitting analysis. This is used to determine values for every possible operation during assembling. Finally, the assembly sequence chart for the redesign of the machine's three linear axes is illustrated.

Keywords: CNC Milling machine, Motorized spindle, Assembly tolerance, Individual tolerance, Accumulated tolerance

1. Introduction

Product design quality has a significant impact on manufacturing cost and assembly cost. Several methods have been used by engineer. Two such methods are Design or Assembly and Design for Manufacture (DFA/DFM) (Miles, 1989; Leaney and Wittenberg, 1992; Dalgleish, Jared and Swift, 2000). These are formal analysis for the evaluation of design suitability for manufacture and assembly, brought together to identify possible solutions. This method can claim success with many industrial applications.

The Lucas DFA method is the product of cooperation between the Lucas organization and the University of Hull. Due to the successful use of the paper-based version, the first commercial computer version was launched in October 1989.

Lucas DFA brings many benefits when it is used for minimum part-count, ease of handling, ease of inserting and fixing, minimizing operations that do not add value (e.g., reorientations, adjustments). In order to achieve these goals, we have to follow following guidelines: reduce the part-count and types; modularize the design, strive to eliminate adjustments, especially blink adjustments; design parts for ease of feeding or handling (from bulk); design parts to be self-aligning and self-locating; ensure adequate access and unrestricted vision; design parts so that

they cannot be installed incorrectly; use efficient fastening or fixing techniques; minimize handling and reorientation; utilize gravity; maximize part-symmetry; strive for detail design that facilitates assembling (Sarmiento *et al.*, 2011; Dochibhatla, Bhattacharya and Morkos, 2017).

The Lucas DFA method provides scope for Functional Analysis of parts and the generation of Assembly Sequence Diagrams to reduce the number of components and identify assembly issues. These analyses require detailed knowledge of component geometry and function. However, the approach has no real provision for the proactive analysis of the product as the design progresses. Enabling earlier DFA investigations would alert designers to possible assembly before detailed designs are produced.

The first implementations of DFA took the form of paper-based methodologies that required much laborious, subjective form-filling to complete the analysis. This was often viewed as unnecessarily, time and resource consuming, and with many opportunities for errors. To overcome these issues, several computer-based versions are now available. These systems are stand-alone computer implementations of the manual methods, but again, are only proficient when implemented on detailed design solutions. Embedding DFA/DFM techniques within a CAD environment would support interactive early design evaluation. First indications of success with this approach were reported by (Mitzner, 2007; Sarmiento *et al.*, 2011; Alfadhilani *et al.*, 2018). This work indicated that 72% of the DFA interrogations necessary could be extracted from enhanced solid models. In this way, less emphasis is placed upon user interaction and more data is reasoned from a geometric model (Barnes *et al.*, 1997).

The importance of generating an assembly sequence within the DFA analysis has been overlooked by many researchers. Little detailed construction assistance is available to the designer in any of the DFA methodologies. This is in spite of the implications for the results if an inappropriate assembly sequence is used. The assembly plan was only considered in detail when the design was essentially fixed. It is clear, therefore, that within industry there is a need for an effective CAD-based tool to construct assembly sequences and proactively assess assemblability. Using the assembly sequence flow chart as a central theme, this paper outlines the designs of axes of milling CNC machine. The relationship between a suitable assembly sequence and the DFA analysis is considered.

2. Lucas DFA approach for axes of milling CNC machine

The method uses penalty factors corresponding to potential design problems for assessing handling as well as fitting. The penalty factors include three indices: “design efficiency”, “handling ratio” and “fitting ratio”. These indices of the new design are compared to the ones of previous designs. A functional analysis which is described below is used to analyze handling and fitting, and then all information is entered on the ASF. The ASF includes five columns, component number in the first column, the component number, namely the component description, quantity of each component, a functional analysis and a handling analysis, and the assembly flowchart which represents the assembling sequence and is built up elsewhere on the form by various symbols for many assembling operations.

The functional analysis addresses each component in turn and establishes whether it exists for fundamental reasons. Every part is assigned as an essential “A” part or a non-essential “B” part, and these symbols are entered on the ASF. Almost all of the components can be categorized in a way analogous to Boothroyd’s method. For example, the parts, which move relative to all other parts already assembled, made of a different material to those already assembled, separated so as to allow assembling or disassembling of parts already assembled, are called “A” parts, and the others are called “B” parts. The advantage of performing this functional analysis on all parts before undertaking the handling and fitting analysis is that, if the design efficiency lowers below

the specified, the current design should be reconsidered before moving on a more detailed analysis. The design efficiency, which is defined as: essential “A” parts divided by all parts and should not be less than 60% (Leaney and Wittenberg, 1992).

$$\text{Design efficiency} = \frac{\text{quantity component A}}{\text{quantity component A} + \text{quantity component B}} \quad (2)$$

The handling analysis helps designers know what components in respect of handling should be improved if the handling ratio is greater than the suggested value, which is usually 1.5. The more abrasive and tendentious to nest the components are, the higher the handling index is.

The fitting analysis is conducted after the handling analysis was completed. This process allows designers to determine values entered on the ASF for every possible operation during assembling. The processes include: inserting and fixing by riveting, screwing, bending; non-assembling operations (e.g., adjustments) or reorientations (e.g., turnover); work-holding (e.g., placing a temporary part to act as a guide to insertion).

Fitting indices is recommended for the threshold of 1,5 except for the gripping index, which has a threshold of 0. If these value of any operation or process escape these thresholds, the designers should seek improvements. Finally, the overall results could be assessed by perusing the design efficiency, the handling ratio and the fitting ratio.

$$\text{Handling ratio} = \frac{\text{feeding index total}}{\text{number of essential component}} \quad (\text{Threshold } 2, 5) \quad (3)$$

$$\text{Fitting ratio} = \frac{\text{fitting index total}}{\text{number of essential component}} \quad (\text{Threshold } 2, 5) \quad (4)$$

(Leaney and Wittenberg, 1992)

These values of performance can be used to estimate the product with regard to assembling. The feeding ratio threshold of 2.5 happens to be equal to all feeding indices at 1.5 (the threshold) for a design efficiency of 60% (the threshold). Having the fitting ratio threshold at 2.5 implies that the average fitting index should be below 1.5. Establishing the Lucas DFA by following steps:

Step 1: Specification

Step 2: Design

Step 3: Functional analysis (This is the first Lucas analysis)

In this step, the components of the product are reviewed only for their function. The components are divided into two groups, essential parts of the product in group A and non-essential parts of the product in group B. The functions of components in group B is mainly for fastening, locating, etc. Loop back to step 2 if the analysis yields problems.

Step 4: Handling analysis (This is the second Lucas analysis)

The part handling and insertion times are examined here. In step 4, the problems associated with the handling of the part are scored.

Step 5: Fitting analysis (This is the third Lucas analysis)

Step 6: Manufacturing Analysis (This is the fourth Lucas analysis)

The last part of the Lucas method is to calculate the cost of manufacturing each component. This cost can influence the choice of material and the process by which the part is made. Although not a true "costing" of the part, this method still guides designers by giving a relative

measure of manufacturing cost. But in this paper, we don't recommend this step because it is very complicated and take a lot of time to calculate the cost.

Step 7: Assessment (Possibly return to step 2 if the analyses identify problems.).

3. Case study

In this section, we carry out steps 1, 2, 3, 4, 5, 7 mentioned to find a better design for the three axes group X, Y, Z. The basic diagram of the three axes CNC milling machine is shown in Figure 1.

Step 1: Specification

We need to design three axes of milling CNC machine that has the travel of X-axis (table) is 750mm, travel of Y-axis (saddle) is 400mm and travel of Z-axis (spindle) is 400mm. The table size is 800x450 (mm).

There are some components which are important in axes of a milling CNC machine as follow: Table (where mounting workpiece), Saddle (link X axis and Z axis), Body (mount X axis and Y axis), Spindle housing (where mounting spindle), Linear guides (guide group in the X, Y, Z direction of milling CNC machine), Axis drive group (provide movement to axes group), counterweight component (steering for Z-axis drive group).

The drive groups of X-axis, Y-axis, Z-axis group are different in dimension but have the same structure, so they are designed separately to be viewed without difficulty.

Step 2: Built the design for X, Y, Z axes groups and their axis drive group.

Step 3, 4, 5: Perform functional analysis, handling analysis, and fitting analysis for the original design.

Step 6: Specify the enable improvements and built other design to deal with these.

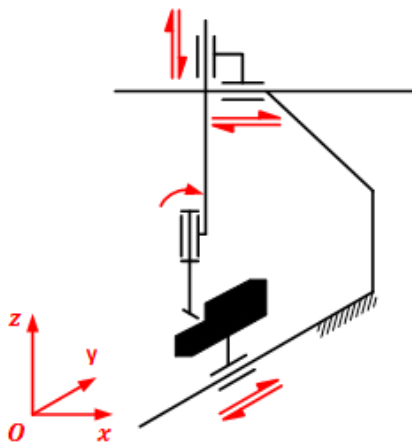


Figure 1. Basic diagram of 3 axes Milling CNC Machine

After building the design of X-axis, Y-axis, Z-axis groups, and their drive group, we can calculate the design efficiency, handling ratio, fitting ratio of them.

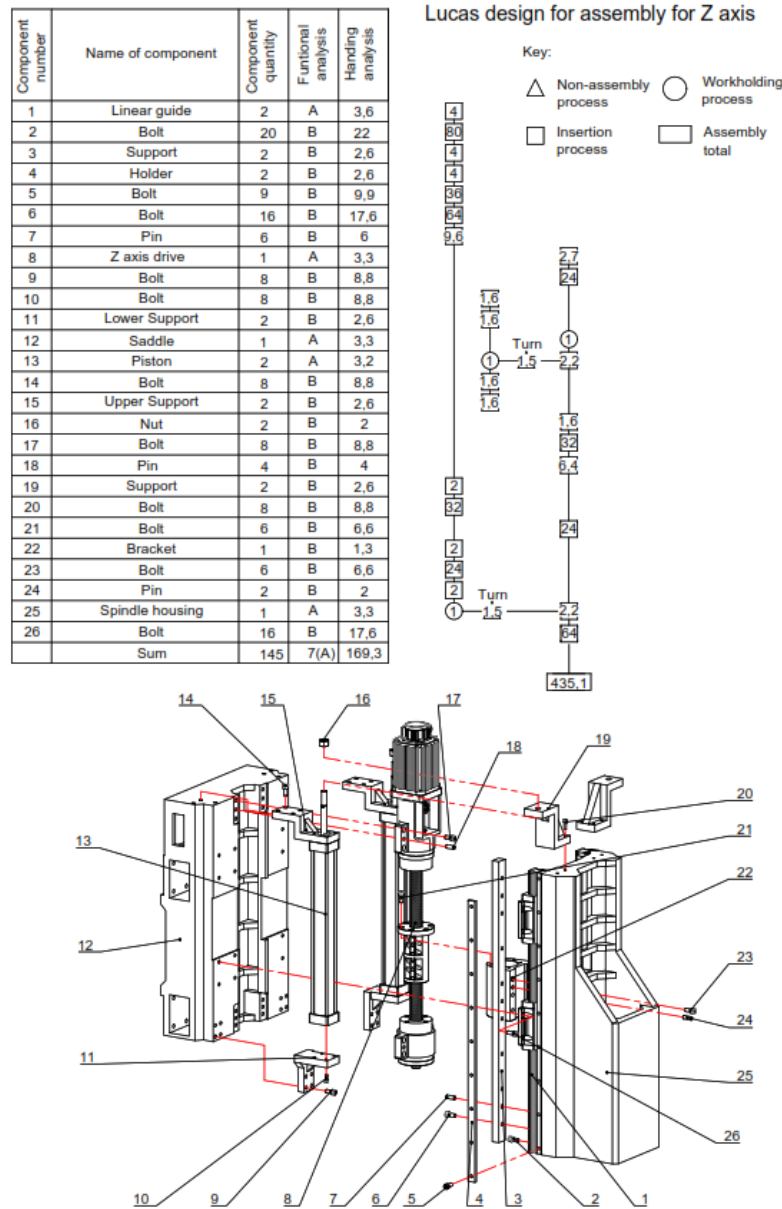


Figure 4. Analysis Z axis design using Lucas DFA Method

Using equations (2), (3), (4) we calculate three indices: Design efficiency, Handling ratio, Fitting ratio of Y axis group

$$1. \text{ Design efficiency} = \frac{7}{145} = 4,83\% < 60\%$$

$$2. \text{ Design efficiency} = \frac{7}{145} = 4,83\% > 2,5$$

$$3. \text{ Fitting ratio} = \frac{435,1}{7} = 62,16 > 2,5$$

We see that these values are higher than the threshold values, so a new design of Z axis group is necessary.

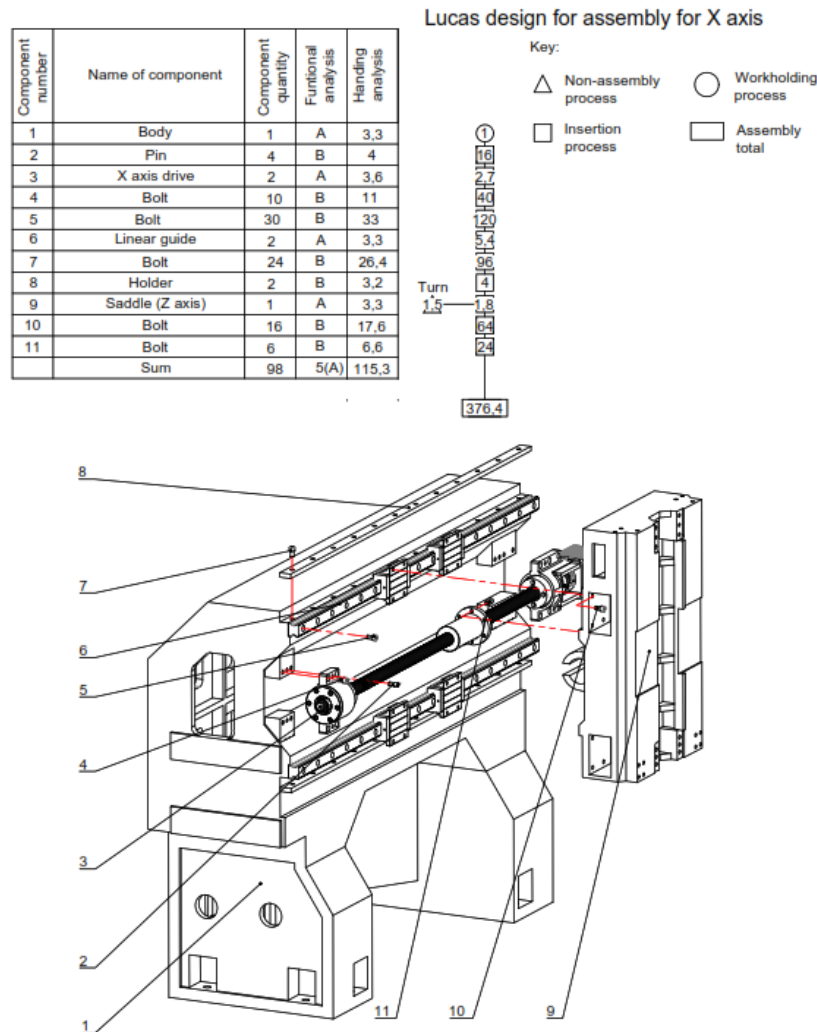


Figure 6. Analysis X axis new design using Lucas DFA Method

The first modification (in X axis group) as shown in Figure 2 consists of integrating the components bracket (component 14) and four plates (component 15) and saddle (component 17) to become single component 9 as shown in Figure 6.

The second modification (in X axis group) as shown in Figure 2 consists of integrating the components two supports (component 4) and the body (component 1) to become single component as shown in Figure 6. The new design of X axis group is shown in Figure 6. The new designs of X, Y, Z axis groups and axis drive group have the design efficiency, handling ratio, fitting ratio as below:

$$1. \text{ Design efficiency} = \frac{5}{98} = 5,1\%;$$

$$2. \text{ Handling ratio} = \frac{115,3}{5} = 20,06;$$

$$3. \text{ Fitting ratio} = \frac{376,4}{5} = 75,28$$

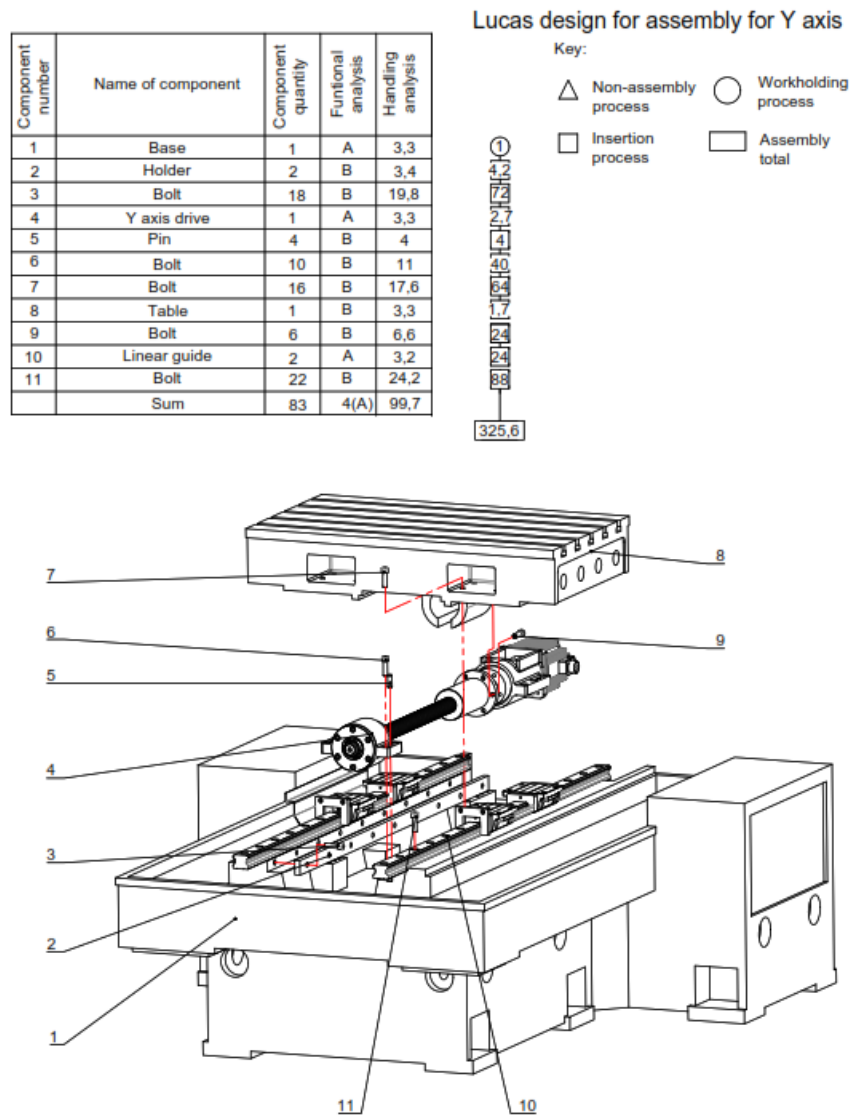


Figure 7. Analysis Y axis new design using Lucas DFA Method

The third modification (in Y axis group), the components 9,12,13 in Figure 3 can be merged with component 8 to become a single component, as shown in Figure 7

The fourth modification (in Y axis group) consists of integrating the components 14,16 and component 1 to become single component as show in Figure 3. The new design of Y group is illustrated in Figure 7.

The new designs of Y axis groups have the design efficiency, handling ratio, fitting ratio as below:

1. Design efficiency = $\frac{4}{83} = 4,82\%$
2. Handling ratio = $\frac{99,7}{4} = 24,925$
3. Fitting ratio = $\frac{323,9}{4} = 80,975$

4. Result

The design illustrated in Figures 1 and Figure 5 shows the evaluation of a manually assembled X axis. The redesign contains 98 components compared to 132 components in the original design. This represents a design efficiency improvement from 3,79 percent to 5,1 percent as well as significant improvements in the handling ratio, from 32,2 to 20,06, and in the fitting ratio, from 93,6 to 75,28.

The design illustrated in Figures 2 and Figure 6 shows the evaluation of a manually assembled Y axis. The redesign contains 98 components compared to 132 components in the original design. This represents a design efficiency improvement from 3,57 percent to 4,82 percent as well as significant improvements in the handling ratio, from 30,6 to 24,925, and in the fitting ratio, from 99,375 to 80,375.

The design illustrated in Figures 3 and Figure 7 shows the evaluation of a manually assembled Z axis. The redesign contains 105 components compared to 145 components in the original design. This represents a design efficiency improvement from 4,83 percent to 6,67 percent as well as significant improvements in the handling ratio, from 24,19 to 17,84, and in the fitting ratio, from 62,16 to 47,39.

The design illustrated in Figures 4 and Figure 8 shows the evaluation of a manually assembled axis drive. The redesign contains 36 components compared to 49 components in the original design. This represents a design efficiency improvement from 12,24 percent to 16,67 percent as well as significant improvements in the handling ratio, from 9,23 to 6,28, and in the fitting ratio, from 23,95 to 17,27.

5. Conclusion

Applying the Lucas DFA method to the design of axes in CNC milling machines yields great results. Three indices Design efficiency, Handling ratio, Fitting ratio are all improved, so it helps to reduce the number of parts, thereby reducing assembly time. Since the structure of the CNC machine is very complicated as well as limited in manufacturing technology, it is understandable that the mounting indicators cannot be achieved as the original goal of the Lucas method mentioned in chapter 1 is understandable, so the improvement of the indicators as presented in this article meet the requirements of CNC machines well. Assembly time is reduced because the total number of parts is reduced from 438 to 322; in addition, reducing number of components reduces management, storage, and transportation costs. Step 7 of the Lucas DFA method will be done by computer later.

Acknowledgement

This research is supported by DCSELAB and funded by Vietnam National University Ho Chi Minh City (VNU-HCM) under grant number TX2021-20b-01. We acknowledge the support of time and facilities from Ho Chi Minh City University of Technology (HCMUT), VNU-HCM for this study. This research is also funded by Department of Science and Technology under grant number 22/2019/HĐ-QPTKHCN.

References

- [1] Alfadhilani *et al.* (2018) ‘A Framework for the Development of Automatic DFA Method to Minimize the Number of Components and Assembly Reorientations’, *IOP Conference Series: Materials Science and Engineering*, 319(1). doi: 10.1088/1757-899X/319/1/012083.
- [2] Barnes, C. J. *et al.* (1997) ‘Assembly sequence structures in design for assembly’, in *Proceedings of the IEEE International Symposium on Assembly and Task Planning*. IEEE, pp. 164–169. doi: 10.1109/isatp.1997.615402.

[3] Dalglish, G. F., Jared, G. E. M. and Swift, K. G. (2000) ‘Design for assembly: Influencing the design process’, *Journal of Engineering Design*, 11(1), pp. 17–29. doi: 10.1080/095448200261162.

[4] Dochibhatla, S. V. S., Bhattacharya, M. and Morkos, B. (2017) ‘Evaluating assembly design efficiency: A comparison between lucas and boothroyd-dewhurst methods’, in *Proceedings of the ASME Design Engineering Technical Conference*. American Society of Mechanical Engineers (ASME). doi: 10.1115/DETC2017-68126.

[5] Leaney, P. G. and Wittenberg, G. (1992) ‘Design for assembling’, *Assembly Automation*. MCB UP Ltd, pp. 8–17. doi: 10.1108/eb004359.

[6] Miles, B. L. (1989) ‘Design for assembly - a key element within design for manufacture’, *Proceedings of the Institution of Mechanical Engineers. Part D, Transport engineering*, 203(1), pp. 29–38. doi: 10.1243/pime_proc_1989_203_145_02.

[7] Mitzner, K. (2007) ‘Introduction to Design for Manufacturing’, *Complete PCB Design Using OrCad Capture and Layout*, pp. 79–107. doi: 10.1016/b978-075068214-5/50006-8.

[8] Sarmiento, A. *et al.* (2011) ‘Design for assembly study case: Automotive fuel intake cover’, in *SAE Technical Papers*. SAE International. doi: 10.4271/2011-36-0046.

One-leg Stance of Humanoid Robot Using Active Balance Control

Tri Duc Tran³, Anh Khoa Lanh Luu³, Van Tu Duong^{1,2,3}, Huy Hung Nguyen^{3,4} and Tan Tien Nguyen^{1,2,3*}

¹Faculty of Mechanical Engineering, Ho Chi Minh City University of Technology (HCMUT),
268 Ly Thuong Kiet, District 10, Ho Chi Minh City, Vietnam

²Vietnam National University Ho Chi Minh City, Linh Trung Ward, Thu Duc District, Ho Chi Minh City, Vietnam

³National Key Laboratory of Digital Control and System Engineering (DCSELab), HCMUT,
268 Ly Thuong Kiet, District 10, Ho Chi Minh City, Vietnam

⁴Faculty of Electronics and Telecommunication, Saigon University, Vietnam

*Corresponding author. E-mail: nttien@hcmut.edu.vn

Abstract

The task of self-balancing is one of the most important tasks when developing humanoid robots. This paper proposes a novel external balance mechanism for humanoid robot to maintain sideway balance. First, a dynamic model of the humanoid robot with balance mechanism and its simplified model are introduced. Secondly, a backstepping-based control method is utilized to split the system into two sub-systems. Then, a minimum observer-based controller is used to control the first sub-system. Since the second sub-system has unknown parameters, a model reference adaptive controller (MRAC) is used to control it. The proposed design divides walking and balancing into two separated tasks, allowing the walking control to be executed independently of the balancing control. Furthermore, the use of the balance mechanism ensures the humanoid robot's hip movement does not exceed the threshold of a human when walking, thus making the overall pose of the humanoid robot looks more natural. An experiment is carried out on a commercial humanoid robot known as UXA-90 to evaluate the effectiveness of the proposed method.

Keywords: Humanoid robot, Adaptive controller, sideway balancing, Observer-based controller, One-leg stance

1. Introduction

Ever since ancient times, man has always been yearned for a replica of himself to serve in daily life. The idea of creating humanoid robots came to many great historical figures' minds. Leonardo da Vinci was believed to be the first man to have drawn a humanoid mechanism. At the beginning of the 20th century, Elektro humanoid robot was made by the Westinghouse society (Chevallereau *et al.*, 2010). But it was not until the 1970s that an actual humanoid robot started to appear. Ichiro Kato from Waseda University successfully built WABOT-1 – the first recognized humanoid robot in the world. Untill now, many researchers have succeeded in developing their own humanoid robot with great capabilities (Kagami *et al.*, 2001; Sakagami *et al.*, 2002; Akachi *et al.*, 2005; Park *et al.*, 2007; Banerjee *et al.*, 2015; Tsagarakis *et al.*, 2017; Ko *et al.*, 2019). Despite that, the task of keeping balance on one leg is nowhere near good enough.

There have been many approaches to solve the problem, but it can be summarized into three strategies: ankle strategy, hip strategy and taking a step strategy (Stephens, 2007). The ankle strategy involves the adjustment of ankle torque to avoid falling. For example, Jun-Ho Oh et. al. (Kim, Park and Oh, 2007) utilized the inertial sensor feedback to adjust the ankle torque to make the humanoid robot staying upright. On the other hand, the hip strategy requires movements of different joints other than the ankle, which creates moment in the center of mass (CoM). Goswami et. al. (Goswami and Kallem, 2004) utilized a method similar strategy to the hip strategy to keep the robot stable. The third strategy includes taking a step forward, backward, or sideway to maintain balance. Pratt et. al. (Pratt *et al.*, 2012) derived a velocity-based formulation and “Linear Inverted Pendulum Plus Flywheel Model” to formulate a “capture region”, where the robot has to step to avoid falling. Hoffman (Hofmann, 2006) also studied balancing task in humanoid robot in his thesis, and argued that the control of horizontal motion of the CoM is effective in balancing the robot and analyzed the three strategies to accomplish this.

Another unique approach is to use an external mass to keep balance. Jo et. al. (Jo and Mir-Nasiri, 2013) utilized three masses, two major static masses and one minor movable mass. However, the use of too many masses is redundant and makes the humanoid robot heavier. Also, the controller for the movable mass is the traditional PID, and although this method is easy to implement, it does not guarantee robustness.

In our previous studies (Nguyen *et al.*, 2017; Van Tien *et al.*, 2017), UXA-90 is assumed to work in a perfect environment, which means the ground is perfectly flat without external forces and disturbances. While it can walk slowly with pre-computed trajectories, the humanoid robot lacks many features, one of them is the ability to stand on one leg.

In this paper, an external balance mechanism is built and crafted onto the humanoid robot’s back. This mechanism allows sideway balancing for the humanoid robot while standing on one leg. First, a simplified model for the humanoid robot with an external balance mechanism is derived. Second, a backstepping-based controller is implemented to decompose the aforementioned system into two sub-systems, then two controllers are proposed to control them. Since one role of the external balance mechanism is to separate the walking task and the balancing task, a simple control method for the balance mechanism is crucial to reduce the computation load of the processor. For that reason, pole placement method is implemented. This method only is not simple but also guarantees the closed-loop stability. However, because the pole placement method requires knowledge of all state variables, which is impossible to achieve, an observer to estimate the state variable is required. Therefore, the first controller is an observer-based method. The second controller is an MRAC based method due to the unknown parameters in the second sub-system. Finally, a simulation is carried out in MATLAB to evaluate the effectiveness of the proposed mechanism.

2. Humanoid robot and movable mass model

2.1 Full one-leg stance model

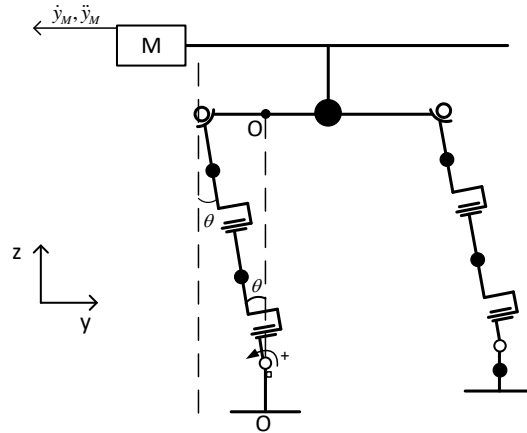


Figure 1. Model of humanoid robot with balance mechanism

The one-leg stance model for the robot with the balance mechanism attached to its back is shown in Fig. 1.

When moving or standing on one leg, man tends to rotate his hip and ankle slightly to shift his CoM toward the supporting feet, thus keeping balance. According to some research (Chumanov, Wall-Scheffler and Heiderscheit, 2008; S., J. and B., 2019), when walking normally, the maximum value of hip adduction is 8.5° in women and 6.1° in men. To mimic this behavior naturally, the balance mechanism is mounted onto the back of UXA-90 to reduce its hip adduction when walking or standing on one leg.

We constrained the acceptable range for hip adduction at $6^\circ \sim 8.5^\circ$. Thus, the range of the moving mass to keep the system balance is calculated to be $6.24\text{cm} \rightarrow 10\text{cm}$.

2.2 Simplified one-leg stance model

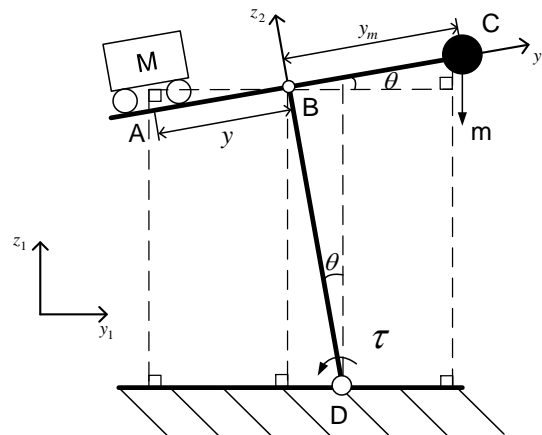


Figure 2. Simplified one-leg stance model

The simplified model for humanoid robot lifting one leg is shown in Fig. 2.

In this model, the stance leg is BD and assumed to be massless. The mass of the body and swinging leg are simplified as point mass m at point C. The cart with mass M moves horizontally along AC to balance the humanoid robot. The position of the cart and the simplified point mass are determined with respect to $z_2 B y_2$ axis, where B is the origin of this coordinate frame. The objective is to control the cart such that θ is as close to zero as possible.

First, we derive a mathematical model for the cart-table model in Fig. 2.

By applying Euler-Lagrange, the dynamic equation for the one-leg stance is expressed as follows:

$$\tau = M\ddot{y}L - mg(y_m \cos \theta - L \sin \theta) + Mg(y \cos \theta + L \sin \theta) \quad (1)$$

where

M is the external movable mass.

y is the position of the external movable mass with respect to z_2By_2 axis.

m is the total mass of the body and swing leg.

y_m is the position of simplified mass point with respect to z_2By_2 axis.

θ is the tilting angle formed by the stance leg and the z_1 axis.

L is the length of the stance leg.

The relationship between torque and moment of inertia is expressed as follows:

$$\tau = \ddot{\theta}(I_M + \sum I_m) \quad (2)$$

where

τ is the torque acting on point D.

I_M is the movable mass's moment of inertia.

I_m is the simplified mass's moment of inertia.

Substituting Eq. (2) into Eq. (1), it yields:

$$\ddot{\theta} = \frac{M\ddot{y}L - mg(y_m \cos \theta - L \sin \theta) + Mg(y \cos \theta + L \sin \theta)}{[M(L^2 + y^2) + m(L^2 + y_m^2)]} \quad (3)$$

The equilibrium point of Eq. (3) is reached when the following conditions are satisfied:

$$\theta = 0^\circ, \dot{\theta} = 0, \ddot{\theta} = 0^\circ, \dot{y} = 0, \ddot{y} = 0 \quad (4)$$

Recall in the previous section that the range of the movable mass y is constrained to be $6.24cm \rightarrow 10cm$. Since the $L = 0.42m$ is the length of the humanoid robot's leg, we have $L^2 \gg y^2$, the y^2 term in Eq. (3) can be ignored. Thus, Eq. (3) can be rewritten as:

$$\ddot{\theta} = \frac{M\ddot{y}L - mg(y_m - L\theta) + Mg(y + L\theta)}{[ML^2 + m(L^2 + y_m^2)]} \quad (5)$$

By defining $\delta = [ML^2 + m(L^2 + y_m^2)]$, Eq. (5) becomes:

$$\ddot{\theta} = \frac{gL}{\delta}(M + m)\theta - \frac{mgy_m}{\delta} + \frac{Mg}{\delta}y + \frac{ML}{\delta}\ddot{y} \quad (6)$$

Substituting Eq. (4) into Eq. (6) yields:

$$\frac{Mg}{\delta}y - \frac{mgy_m}{\delta} = 0 \quad (7)$$

Eq. (7) shows the position relationship between the moving mass and the body's simplified mass when the humanoid robot is standing upright on one leg.

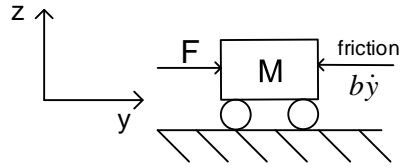


Figure 3. The moving cart model

To control the moving cart, a model of the moving cart shown in Fig. 3 is derived. According to Newton’s second law, we have:

$$\ddot{y} = \frac{u_c}{M} - \frac{b}{M}\dot{y} \quad (8)$$

where

$u_c = F$ is the force applied to the cart.

b is the friction coefficient.

Combining Eq. (7) and Eq. (8), it yields:

$$\begin{cases} \ddot{\theta} = \frac{gL}{\delta}(M+m)\theta - \frac{mgy_m}{\delta} + \frac{Mg}{\delta}y + \frac{ML}{\delta}\dot{y} \\ \ddot{y} = \frac{u_c}{M} - \frac{b}{M}\dot{y} \end{cases} \quad (9)$$

Eq. (9) introduces the system modeling of the overall system with the combination of two subsystems, one-leg stance, and external balancing mechanism. In order to obtain the objective control, the proposed controller for the overall system is performed in two steps. First, the terms y and \dot{y} are considered as the virtual control input of the first system in Eq. (9) to drive θ to zero. Then y and \dot{y} are used as reference input for the second system of Eq. (9). Therefore, a backstepping technique is employed to build the proposed controller for the recursive structure system of Eq. (9).

3. Controller design

The block diagram of the overall control system is shown in Fig. 4.

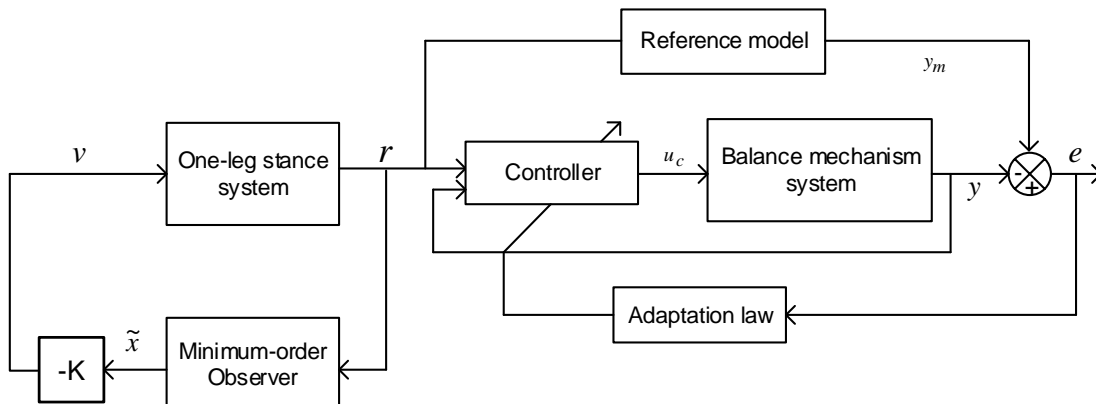


Figure 4. Overall control system.

By defining the virtual control input $v = \frac{Mg}{\delta}y - \frac{mgy_m}{\delta}$, the first system of Eq. (9) becomes:

$$\ddot{\theta} = \frac{gL}{\delta}(M+m)\theta + v + \frac{L}{g}\ddot{v} \quad (10)$$

To eliminate the 2nd derivative of the virtual control input v , let us define:

$$X_1 = \theta - \frac{L}{g}v, X_2 = \dot{\theta} - \frac{L}{g}\dot{v}, a = -\frac{gL}{\delta}(M+m), b = 1 + \frac{L^2}{\delta}(M+m) \quad (11)$$

Eq. (10) can be expressed in the state space:

$$\begin{aligned} \begin{bmatrix} \dot{X}_1 \\ \dot{X}_2 \end{bmatrix} &= \begin{bmatrix} 0 & 1 \\ -a & 0 \end{bmatrix} \begin{bmatrix} X_1 \\ X_2 \end{bmatrix} + \begin{bmatrix} 0 \\ b \end{bmatrix} v \\ Y &= [1 \quad 0] \begin{bmatrix} X_1 \\ X_2 \end{bmatrix} + \frac{L}{g}v \end{aligned} \quad (12)$$

With $X_1 = \theta - \frac{L}{g}v$, recall Eq. (7) shows that $v \rightarrow 0$ as $t \rightarrow \infty$ when the system is at equilibrium state. Therefore, to drive the angle θ to zero, X_1 needs to converge to zero as t tends to infinity.

Since only X_1 can be calculated through the measurement of θ , X_2 needs to be estimated. Therefore, a Regulator System with Minimum-Order Observers is proposed to control the system.

Step 1: Regulator with Minimum-order Observers design for the first system

The first step in designing the Minimum-Order Observers is to divide the state vector of Eq. (12) into two parts, the measurable and unmeasurable state variable. The partitioned state of Eq. (12) is as follows:

$$\begin{aligned} \begin{bmatrix} \dot{x}_a \\ \dot{x}_b \end{bmatrix} &= \begin{bmatrix} A_{aa} & A_{ab} \\ A_{ba} & A_{bb} \end{bmatrix} \begin{bmatrix} x_a \\ x_b \end{bmatrix} + \begin{bmatrix} B_a \\ B_b \end{bmatrix} v \\ Y &= [1 \quad 0] \begin{bmatrix} x_a \\ x_b \end{bmatrix} + \frac{L}{g}v \end{aligned} \quad (13)$$

where $A_{aa} = 0, A_{ab} = 1, A_{ba} = -a, A_{bb} = 0, B_a = 0, B_b = 1$.

$x_a = X_1$ is measurable and $x_b = X_2$ is unmeasurable.

The plant and error for Minimum-Order Observers are given as (Ogata and Brewer, 1971):

$$\begin{aligned} \dot{\tilde{x}}_b &= (A_{bb} - K_e A_{ab})\tilde{x}_b + A_{ba}x_a + B_b u \\ &\quad + K_e A_{ab}x_b \\ \dot{e} &= (A_{bb} - K_e A_{ab})x_b - \tilde{x}_b \end{aligned} \quad (14)$$

where x_b is the unmeasurable state variable.

\tilde{x}_b is the estimated unmeasurable state variable.

$\dot{\tilde{x}}_b$ is the first derivative of the estimated unmeasurable state variable.

Substituting the value of $A_{aa}, A_{ab}, A_{ba}, A_{bb}, x_a, x_b$ into Eq. (14) it yields:

$$\begin{aligned}\dot{\tilde{X}}_2 &= -K_e \tilde{X}_2 - aX_1 + u + K_e X_2 \\ \dot{e} &= -K_e X_2 - \tilde{X}_2\end{aligned}\quad (15)$$

where K_e is the observer gain.

Assuming the control signal v to be:

$$v = -K\tilde{x} \quad (16)$$

where K is the state feedback gain matrix.

The system with observed state feedback is shown in Fig. 5.

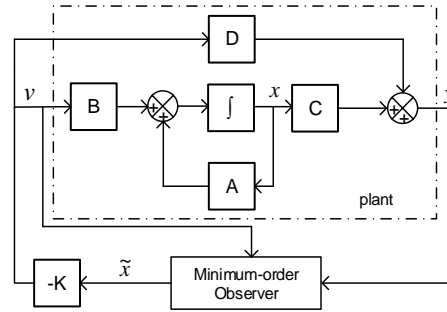


Figure 5. Minimum-order Observer graph

Step 2: Adaptive control design for the second system

Since only the friction coefficient b is unknown, an MRAC is derived to control the second system in Eq. (9).

By defining $X = [y \quad \dot{y}]^T$, $A = \begin{bmatrix} 0 & 1 \\ 0 & \frac{-b}{M} \end{bmatrix}$, $B = \begin{bmatrix} 0 \\ \frac{1}{M} \end{bmatrix}$, $\Lambda = [1]$, the second system of Eq. (9) can be rewritten as follows:

$$\dot{X} = AX + B\Lambda u_c \quad (17)$$

Consider a reference model as below:

$$\dot{X}_m = A_m X_m + B_m r \quad (18)$$

where

$$A_m = \begin{bmatrix} 0 & 1 \\ -1 & \frac{-b}{M} \end{bmatrix} \text{ is stable matrix.}$$

$$B_m = \begin{bmatrix} 0 \\ \frac{-b}{M} \end{bmatrix}.$$

r is bounded reference input vector.

The ideal control input and the tracking control input for the system in Eq. (17) is as follows:

$$u_{ideal} = K_x^T X + K_r r \quad (19)$$

$$u_c = \hat{K}_x^T X + \hat{K}_r r \quad (20)$$

where

$\mathbf{K}_x \in \mathcal{R}^{2 \times 1}$ is ideal feedback gain matrix.

K_r is ideal feedforward gain parameter.

$\widehat{\mathbf{K}}_x \in \mathcal{R}^{2 \times 1}$ is estimated feedback gain matrix.

\widehat{K}_r is estimated feedforward gain parameter.

Substituting Eq. (19) and Eq. (20) to Eq. (17), it yields:

$$\dot{\mathbf{X}} = (\mathbf{A} + \mathbf{B}\Lambda\mathbf{K}_x^T)\mathbf{X} + \mathbf{B}\Lambda K_r r \quad (21)$$

$$\dot{\mathbf{X}} = (\mathbf{A} + \mathbf{B}\Lambda\widehat{\mathbf{K}}_x^T)\mathbf{X} + \mathbf{B}\Lambda\widehat{K}_r r \quad (22)$$

Comparing Eq. (21) and the reference model in Eq. (18), the ideal gain \mathbf{K}_x and K_r must satisfy the matching condition:

$$\begin{cases} \mathbf{A} + \mathbf{B}\Lambda\mathbf{K}_x^T = \mathbf{A}_m \\ \mathbf{B}\Lambda K_r = \mathbf{B}_m \end{cases} \quad (23)$$

Using the matching condition in Eq. (23), Eq. (22) becomes:

$$\dot{\mathbf{X}} = \mathbf{A}_m\mathbf{X} + \mathbf{B}_m r + \mathbf{B}\Lambda(\widehat{\mathbf{K}}_x - \mathbf{K}_x)^T \mathbf{X} + \mathbf{B}\Lambda(\widehat{K}_r - K_r)r \quad (24)$$

The difference between the state of reference model in Eq. (18) and the state of the system in Eq. (17) is defined as:

$$\mathbf{e} = \mathbf{X} - \mathbf{X}_m \quad (25)$$

Taking the 1st derivative of Eq. (25), it yields:

$$\dot{\mathbf{e}} = \dot{\mathbf{X}} - \dot{\mathbf{X}}_m \quad (26)$$

Substituting Eq. (18) and Eq. (24) into Eq. (26), we have:

$$\dot{\mathbf{e}} = \mathbf{A}_m(\mathbf{X} - \mathbf{X}_m) + \mathbf{B}\Lambda(\widehat{\mathbf{K}}_x - \mathbf{K}_x)^T \mathbf{X} + \mathbf{B}\Lambda(\widehat{K}_r - K_r)r \quad (27)$$

Define the parameter estimation errors as follows:

$$\begin{aligned} \Delta\mathbf{K}_x &= \widehat{\mathbf{K}}_x - \mathbf{K}_x \\ \Delta K_r &= \widehat{K}_r - K_r \end{aligned} \quad (28)$$

With Eq. (25) and Eq. (28), the error dynamic in Eq. (27) can be rewritten as:

$$\dot{\mathbf{e}} = \mathbf{A}_m\mathbf{e} + \mathbf{B}\Lambda(\Delta\mathbf{K}_x^T\mathbf{X} + \Delta K_r r) \quad (29)$$

Consider the Lyapunov function candidate for Eq. (29):

$$V(\mathbf{e}, \Delta\mathbf{K}_x, \Delta K_r) = \mathbf{e}^T \mathbf{P} \mathbf{e} + \text{tr}(\Delta\mathbf{K}_x^T \Gamma_x^{-1} \Delta\mathbf{K}_x \Lambda) + \Gamma_r^{-1} \Delta K_r^2 \Lambda \quad (30)$$

where

$$\Gamma_x = \Gamma_x^T > 0$$

$$\Gamma_r > 0$$

$\mathbf{P} = \mathbf{P}^T > \mathbf{0}$ and must satisfy the following algebraic Lyapunov equation:

$$\mathbf{P}\mathbf{A}_m + \mathbf{A}_m^T \mathbf{P} = -\mathbf{Q} \quad (31)$$

where \mathbf{Q} is any symmetric positive definite matrix.

Taking the 1st derivative of Eq. (30) gives:

$$\dot{V}(\mathbf{e}, \Delta \mathbf{K}_x, \Delta K_r) = \dot{\mathbf{e}}^T \mathbf{P} \mathbf{e} + \mathbf{e}^T \mathbf{P} \dot{\mathbf{e}} + 2tr \left(\Delta \mathbf{K}_x^T \Gamma_x^{-1} \dot{\hat{\mathbf{K}}}_x \Lambda \right) + 2\Gamma_r^{-1} \Delta K_r \dot{\hat{K}}_r \Lambda \quad (32)$$

Using Eq. (29), Eq. (32) can be rewritten as:

$$\begin{aligned} \dot{V}(\mathbf{e}, \Delta \mathbf{K}_x, \Delta K_r) & \\ &= \mathbf{e}^T (\mathbf{A}_m^T \mathbf{P} + \mathbf{P} \mathbf{A}_m) \mathbf{e} + 2\mathbf{e}^T \mathbf{P} \mathbf{B} \Lambda (\Delta \mathbf{K}_x^T \mathbf{X} + \Delta K_r r) + 2tr \left(\Delta \mathbf{K}_x^T \Gamma_x^{-1} \dot{\hat{\mathbf{K}}}_x \Lambda \right) \\ & \quad + 2\Gamma_r^{-1} \Delta K_r \dot{\hat{K}}_r \Lambda \end{aligned} \quad (33)$$

Substituting Eq. (31) into Eq. (33), it yields:

$$\begin{aligned} \dot{V}(\mathbf{e}, \Delta \mathbf{K}_x, \Delta K_r) & \\ &= -\mathbf{e}^T \mathbf{Q} \mathbf{e} + \left[2\mathbf{e}^T \mathbf{P} \mathbf{B} \Lambda \Delta \mathbf{K}_x^T \mathbf{X} + 2tr \left(\Delta \mathbf{K}_x^T \Gamma_x^{-1} \dot{\hat{\mathbf{K}}}_x \Lambda \right) \right] \\ & \quad + \left(2\mathbf{e}^T \mathbf{P} \mathbf{B} \Lambda \Delta K_r r + 2\Gamma_r^{-1} \Delta K_r \dot{\hat{K}}_r \Lambda \right) \end{aligned} \quad (34)$$

Using the trace identity, we get:

$$\mathbf{e}^T \mathbf{P} \mathbf{B} \Lambda \Delta \mathbf{K}_x^T \mathbf{X} = tr(\Delta \mathbf{K}_x^T \mathbf{X} \mathbf{e}^T \mathbf{P} \mathbf{B} \Lambda) \quad (35)$$

Substituting Eq. (35) into Eq. (34) yields:

$$\begin{aligned} \dot{V}(\mathbf{e}, \Delta \mathbf{K}_x, \Delta K_r) & \\ &= -\mathbf{e}^T \mathbf{Q} \mathbf{e} + 2tr \left[\Delta \mathbf{K}_x^T \left(\mathbf{X} \mathbf{e}^T \mathbf{P} \mathbf{B} + \Gamma_x^{-1} \dot{\hat{\mathbf{K}}}_x \right) \Lambda \right] + 2\Lambda \Delta K_r \left(\mathbf{e}^T \mathbf{P} \mathbf{B} r + \Gamma_r^{-1} \dot{\hat{K}}_r \right) \end{aligned} \quad (36)$$

The adaptive laws are chosen as follows:

$$\begin{aligned} \dot{\hat{\mathbf{K}}}_x &= -\Gamma_x \mathbf{X} \mathbf{e}^T \mathbf{P} \mathbf{B} \\ \dot{\hat{K}}_r &= -\Gamma_r \mathbf{e}^T \mathbf{P} \mathbf{B} r \end{aligned} \quad (37)$$

With Eq. (37), Eq. (36) becomes:

$$\dot{V}(\mathbf{e}, \Delta \mathbf{K}_x, \Delta K_r) = -\mathbf{e}^T \mathbf{Q} \mathbf{e} \leq 0 \quad (38)$$

Hence, the tracking error \mathbf{e} and the parameter estimation errors $\Delta \mathbf{K}_x$, ΔK_r are bounded.

Taking the 2nd derivative of Eq. (38), we have:

$$\ddot{V}(\mathbf{e}, \Delta \mathbf{K}_x, \Delta K_r) = -2\mathbf{e}^T \mathbf{Q} \dot{\mathbf{e}} \quad (39)$$

Eq. (39) showed that $\ddot{V}(t)$ is bounded, which means $\dot{V}(t)$ is uniformly continuous. According to Barbalat's Lemma, we have:

$$\lim_{t \rightarrow \infty} \dot{V}(t) = 0 \quad (40)$$

Thus the tracking error \mathbf{e} will converge to zero as t tends to infinity.

4. Simulations and results

The physical parameters for the model in Fig. 2 are given by Table I.

Table I. Physical parameters for simplified one-leg stance model

Name	Length
BD	$0.42m$
AB	y
BC	y_m

Since the response of the system depends on the initial condition, the chosen observer poles and controller poles, multiple simulations are carried out in MATLAB to analyze the system's response. First, by regulating θ to zero in the first system of Eq. (9), the trajectory of the moving mass is obtained. The aforementioned trajectory is then used as reference for the second system. The sampling time is 0.01 second.

- **Scenario 1: The hip adduction of humanoid robot is 6° , the position of the simplified point mass is calculated to be $y_m \approx 0.049$.**

The two closed-loop poles and observer pole are $\mu_1 = -4.5, \mu_2 = -4.5, s = -10$ respectively.

The adaptive gains are chosen as follows:

$$\Gamma_x = \begin{bmatrix} 10000 & 0 \\ 0 & 2000 \end{bmatrix}$$

$$\Gamma_r = 10$$

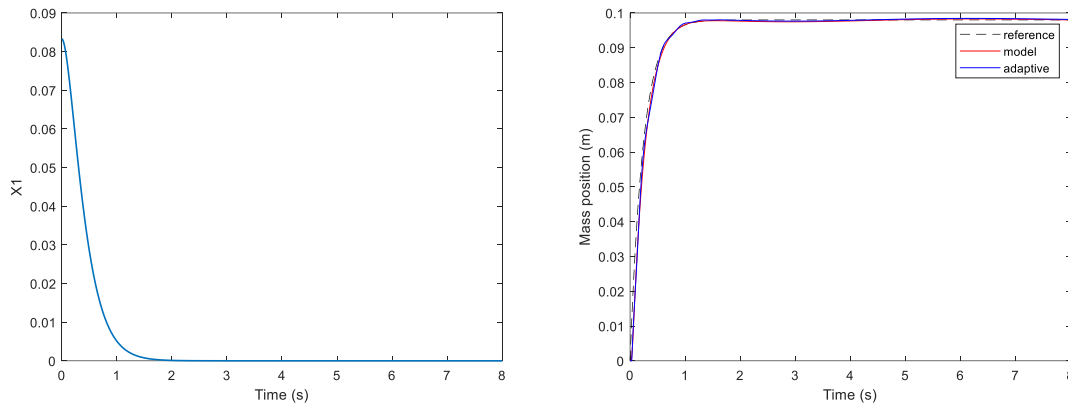


Figure 6. X_1 response and the tracking of the position of movable mass when $y_m = 0.049m$

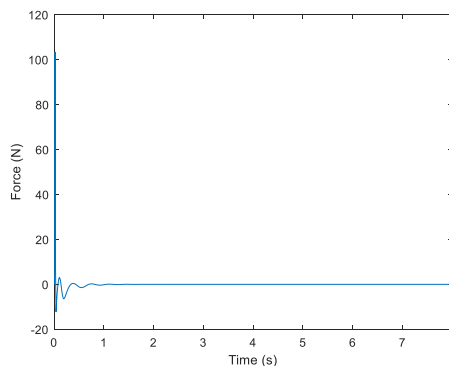


Figure 7. Control signal u_c for the movable mass

- **Scenario 2: The hip adduction of humanoid robot is 7.3° , the position of the simplified point mass is calculated to be $y_m \approx 0.04$.**

The two closed-loop poles and observer pole are $\mu_1 = -4.5, \mu_2 = -4.5, s = -10$ respectively.

The adaptive gains are chosen as follows:

$$\Gamma_x = \begin{bmatrix} 5000 & 0 \\ 0 & 4000 \end{bmatrix}$$

$$\Gamma_r = 14$$

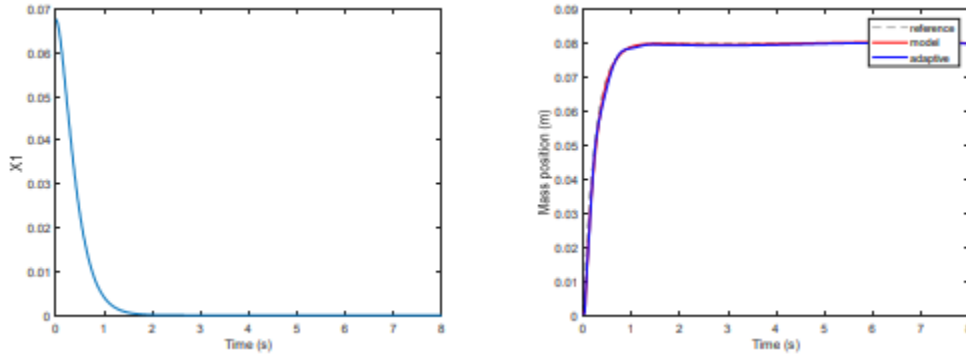


Figure 8. X_1 response and the tracking of the position of movable mass when $y_m = 0.04m$

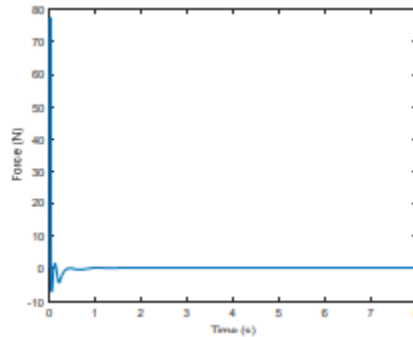


Figure 9. Control signal u_c for the movable mass

- **Scenario 3: The hip adduction of humanoid robot is 8° , the position of the simplified point mass is calculated to be $y_m \approx 0.035m$**

The two closed-loop poles and observer pole are $\mu_1 = -7, \mu_2 = -7, s = -14$ respectively.

The adaptive gains are chosen as follows:

$$\Gamma_x = \begin{bmatrix} 7000 & 0 \\ 0 & 700 \end{bmatrix}$$

$$\Gamma_r = 6.3$$

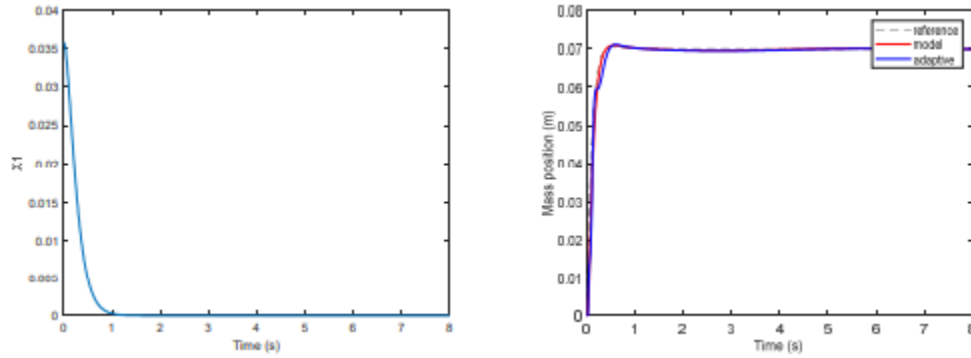


Figure 10. X_1 response and the tracking of the position of movable mass when $y_m = 0.035m$

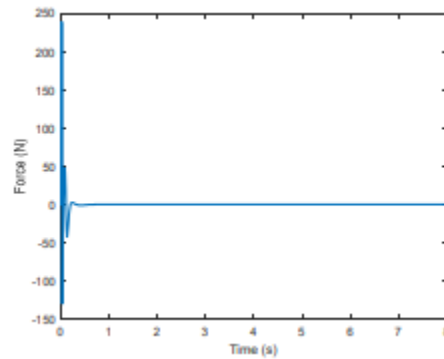


Figure 11. Control signal u_c for the movable mass

- **Scenario 4:** The hip adduction of humanoid robot is 8.5° , the position of the simplified point mass is calculated to be $y_m \approx 0.03m$

The two closed-loop poles and observer pole are $\mu_1 = -2, \mu_2 = -2, s = -4$ respectively.

The adaptive gains are chosen as follows:

$$\Gamma_x = \begin{bmatrix} 7000 & 0 \\ 0 & 5000 \end{bmatrix}$$

$$\Gamma_r = 100$$

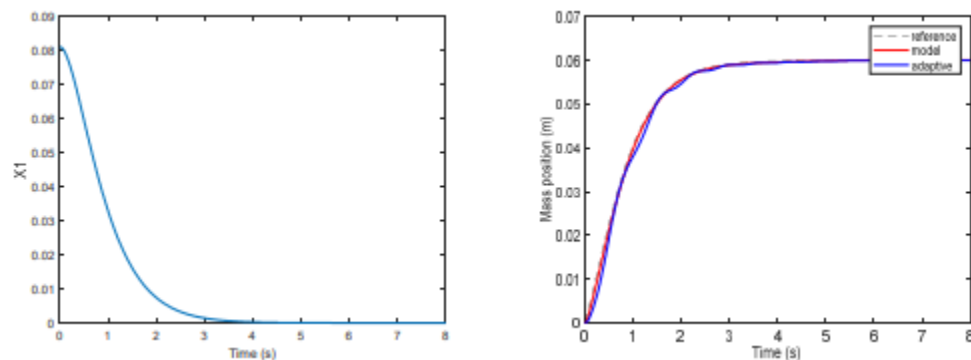


Figure 12. X_1 response and the tracking of the position of movable mass when $y_m = 0.03m$

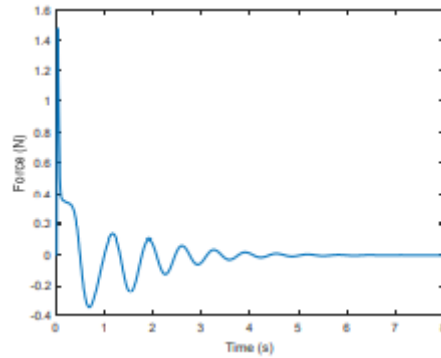


Figure 13. Control signal u_c for the movable mass

In general, the controller drove the state variable $X_1(t)$ in the one-leg stance system (first system) to zero in every simulation, as shown in the first image of Fig 6, 8, 10, 12, which means θ was regulated to zero. The movable mass system (second system) also tracked the desired position closely as shown in the second image. Thus, the controller satisfies the goal.

The simulations show that the choice of the adaptive gains Γ_x , Γ_r varies with different positions of y_m and the poles. The further the poles are placed, the faster the θ in the first system is regulated to zero. However, because the response time of the first system decreases, the second system suffers from a slight overshoot as shown in the second image in Fig. 10. Since the adaptive gain Γ_r is affected directly by the reference input of the second system, if the first system responds too fast, the second system will be extremely sensitive to any slight change in Γ_r , making it difficult to tune the controller.

5. Conclusions

This paper proposed a novel external balancing mechanism for humanoid robot to maintain sideway balance when standing on one leg. The backstepping method is employed to split the system into two subsystems, then a minimum-order observer controller and MRAC are utilized to control the two subsystems. The MRAC guarantees the system stability even when subjected to unknown parameters. The simulation results show that the MRAC successfully tracked the desired mass trajectory and the θ is driven to zero, satisfying the control objective. In the future, experiment will be made on humanoid robot UXA-90 to evaluate the effectiveness of the proposed method. Furthermore, UXA-90 is still subjected to disturbances when walking or standing still. Therefore, a new controller utilizing the external balance mechanism to reject disturbances will be researched in depth.

Acknowledgments

This research is supported by DCSELAB and funded by Vietnam National University Ho Chi Minh City (VNU-HCM) under grant number B2019-20-10 and TX2021-20b-01. We acknowledge the support of time and facilities from Ho Chi Minh City University of Technology (HCMUT), VNU-HCM for this study.

References

- [1] Akachi, K. *et al.* (2005) ‘Development of humanoid robot HRP-3P’, *Proceedings of 2005 5th IEEE-RAS International Conference on Humanoid Robots*, 2005, pp. 50–55. doi: 10.1109/ICHR.2005.1573544.
- [2] Banerjee, N. *et al.* (2015) ‘Human-supervised control of the ATLAS humanoid robot for traversing doors’, *IEEE-RAS International Conference on Humanoid Robots*, 2015-Decem, pp.

722–729. doi: 10.1109/HUMANOIDS.2015.7363442.

[3] Chevallereau, C. *et al.* (2010) *Bipedal Robots: Modeling, Design and Walking Synthesis*, *Bipedal Robots: Modeling, Design and Walking Synthesis*. doi: 10.1002/9780470611623.

[4] Chumanov, E. S., Wall-Scheffler, C. and Heiderscheit, B. C. (2008) ‘Gender differences in walking and running on level and inclined surfaces’, *Clinical Biomechanics*, 23(10), pp. 1260–1268. doi: 10.1016/j.clinbiomech.2008.07.011.

[5] Goswami, A. and Kallem, V. (2004) ‘Rate of change of angular momentum and balance maintenance of biped robots’, *Proceedings - IEEE International Conference on Robotics and Automation*, 2004(4), pp. 3785–3790. doi: 10.1109/robot.2004.1308858.

[6] Hofmann, A. G. (2006) ‘Robust Execution of Bipedal Walking Tasks From Biomechanical Principles’, p.407. Available at:
<http://citeseerx.ist.psu.edu/viewdoc/download?doi=10.1.1.73.4060&rep=rep1&type=pdf>.

[7] Jo, H. S. and Mir-Nasiri, N. (2013) ‘Development of minimalist bipedal walking robot with flexible ankle and split-mass balancing systems’, *International Journal of Automation and Computing*, 10(5), pp. 425–437. doi: 10.1007/s11633-013-0739-4.

[8] Kagami, S. *et al.* (2001) ‘Design and implementation of software research platform for humanoid robotics: H6’, in *Proceedings - IEEE International Conference on Robotics and Automation*, pp. 2431–2436. doi: 10.1109/ROBOT.2001.932986.

[9] Kim, J. Y., Park, I. W. and Oh, J. H. (2007) ‘Walking control algorithm of biped humanoid robot on uneven and inclined floor’, *Journal of Intelligent and Robotic Systems: Theory and Applications*, 48(4), pp. 457–484. doi: 10.1007/s10846-006-9107-8.

[10] Ko, T. *et al.* (2019) ‘Compliant Biped Locomotion of Hydra, an Electro-Hydrostatically Driven Humanoid’, *IEEE-RAS International Conference on Humanoid Robots*, 2018-Novem, pp. 587–592. doi: 10.1109/HUMANOIDS.2018.8624973.

[11] Nguyen, N. D. K. *et al.* (2017) ‘Optimal control for stable walking gait of a biped robot’, in *2017 14th International Conference on Ubiquitous Robots and Ambient Intelligence, URAI 2017*, pp. 309–313. doi: 10.1109/URAI.2017.7992738.

[12] Ogata, K. and Brewer, J. W. (1971) *Modern Control Engineering*, *Journal of Dynamic Systems, Measurement, and Control*. doi: 10.1115/1.3426465.

[13] Park, I. W. *et al.* (2007) ‘Mechanical design of the humanoid robot platform, HUBO’, *Advanced Robotics*, 21(11), pp. 1305–1322. doi: 10.1163/156855307781503781.

[14] Pratt, J. *et al.* (2012) ‘Capturability-based analysis and control of legged locomotion, Part 2: Application to M2V2, a lower-body humanoid’, *International Journal of Robotics Research*, 31(10), pp. 1117–1133. doi: 10.1177/0278364912452762.

[15] S., W., J., P. and B., P. (2019) ‘Three-Dimensional Human Gait Pattern: Reference Data for Young, Active Women Walking with Low, Preferred, and High Speeds’, *BioMed Research International*, 2019. Available at:
<http://www.embase.com/search/results?subaction=viewrecord&from=export&id=L625956897%0Ahttp://dx.doi.org/10.1155/2019/9232430>.

[16] Sakagami, Y. *et al.* (2002) ‘The intelligent ASIMO: System overview and integration’, *IEEE International Conference on Intelligent Robots and Systems*, 3, pp. 2478–2483. doi: 10.1109/irids.2002.1041641.

[17] Stephens, B. (2007) ‘Humanoid push recovery’, *Proceedings of the 2007 7th IEEE-RAS International Conference on Humanoid Robots, HUMANOIDS 2007*, pp. 589–595. doi:

10.1109/ICHR.2007.4813931.

[18] Van Tien, A. N. *et al.* (2017) ‘Design of biped walking gait on biped robot’, in *2017 14th International Conference on Ubiquitous Robots and Ambient Intelligence, URAI 2017*, pp. 303–306. doi: 10.1109/URAI.2017.7992736.

[19] Tsagarakis, N. G. *et al.* (2017) ‘WALK-MAN: A High-Performance Humanoid Platform for Realistic Environments’, *Journal of Field Robotics*, 34(7), pp. 1225–1259. doi: 10.1002/rob.21702.

Design and Evaluate the Hardware Framework in Mechanical Ventilator

Anh Son Tran^{1,3}, Ngoc Anh Thu Vuong^{2,3} and Ha Quang Thinh Ngo^{2,3*}

¹ Department of Manufacturing, Faculty of Mechanical Engineering, Ho Chi Minh City University of Technology (HCMUT), 268 Ly Thuong Kiet Street, District 10, HCMC, Vietnam

² Department of Mechatronics, Faculty of Mechanical Engineering, Ho Chi Minh City University of Technology (HCMUT), 268 Ly Thuong Kiet Street, District 10, HCMC, Vietnam

³ Vietnam National University Ho Chi Minh City (VNU-HCM), Linh Trung Ward, Thu Duc District, Ho Chi Minh City, Vietnam

* Corresponding author: nhqthinh@hcmut.edu.vn

Abstract.

In the context of global pandemic, humankind must face high medical risk. To our knowledge, there is currently no efficient way to stop the infectious chain and society suffers the rapidly increasing number of patients. The most important cause of this is the lack of necessary equipments to cure and maintain our living. Once the breath can not be guaranteed, man would fall in the dangerous status. This study aims to design and control a ventilator that is portable, and mass-producible in a short amount of time, which can be of aid to relieve a sudden surge in the demand for ventilators in hospitals, Intensive Care Units (ICU), and the like. They can serve as the temporary alternative solution for mild to moderate patients to alleviate the patient overload, while the more serious patients can be put on heavy-duty, purpose-built mechanical ventilators where the patients may sustain through a long-term sedated state of mandatory invasive breathing. Firstly, the mechanical design is demonstrated and hardware modeling is estimated by mathematical equations. Then, the 3D model is established in virtual environment in order to visualize the whole system. The validation in which the system stability should be respected, consists of various loading cases, different velocities and air flow. The results of this work are to illustrate and verify both in simulations and experiments using the proposed hardware design. From these achievements, it can be seen clearly that our approach to provide the automated breathing machine to sustain the human living is proper, feasible and robust.

Keywords: ventilator, mechanical design, motion control, adaptive control, gripper

1. Introduction

Respiratory failure in extremely widespread disease might be treated with either intubated or non-intubated respiratory support. Non-intubated respiratory support or non-invasive ventilator is favoured since the usage of endotracheal intubation is linked with ventilator-induced lung injury [1]. The non-stop positive air pressure has become the established quality for non-intubated respiratory support, nasal intermittent positive pressure ventilation was gradually common in the several decades ago. Recently, a systematic approach and a more updated meta-analysis of the intermittent positive pressure ventilator was developed, superior to nasal non-stop positive airway pressure in preventing reintubation only in a few day [2]. However, there is no statistical data in using them even though the dangerous risk appears higher and higher.

In the current era, humankind must face to the well-known pandemic COVID-19 [3], which causes a lot of disasters in any country. To survive in this context, patients need the system of non-invasive respiratory support for exchanging the air flow between the human body and the atmosphere. Unfortunately, their lungs are wound, or their health status is too weak to maintain breath by themselves. At this time, mechanical ventilation provides artificial breaths of

inhalation via medical device. The most important problem is that there are not enough artificial ventilation support systems for all of us since the number of patients dramatically increased during such a short time [4]. Even well-equipped hospitals in developed nations still meet the same troubles when the infectious disease spreads in the community. In the poorer countries, the situation in public health is tremendously difficult. Therefore, an attempt to deal with the worldwide challenges of social medicine is to innovate a low-cost, open-source and feasible ventilator [5].

General speaking, there are several types of low-cost ventilators. In [6], researchers studied a microcontroller-driven mechanical ventilator using AmbuBag which is pressed by the arm mechanism. The trajectory of mechanical components is planned by camshaft (CAM) generation. The output results present the time-varying characteristic of tidal volume. With the same method but different mechanism, authors [7] developed a low-cost, open-source ventilator that was initialized by the global shortage of mechanical ventilator for COVID-19 patients. The driving motor, controlled by Raspberry Pi, provides pressure of up to 70 cm H₂O. Additionally, although the design is simple but efficient, the experimental device for ventilation satisfies the desired volume and pressure to clinical requirements [8]. For future steps, developers discuss the reliability of the mechanisms and software, mass production with appropriate standards and regulatory approval or exemption. With portability purpose, investigators in [9] introduce an ease-to-use and mobile version of AmbuBag-based compression machine. This system is manipulated by Arduino and offers various breathing modes with varying tidal volumes. The rate of breathing is from 5 to 40 breaths/minute and the max ratio between inhalation and exhalation is 1:4. The repeatability and precision exceeding personal capabilities of this design are proved in experiments. Although the original design consisting of two paddles is actuated by an electric motor [10], there are still several efforts to represent the pressure-controlled ventilation. It is noted that the usage of electromechanical actuators to press AmbuBag is an excellent solution. Whether the supply of compressed air is available or not, the tidal volume could increase linearly [11].

2. Motivations

Since humankind discovered the Corona disease in 2019, named COVID-19, it has become a world-wide pandemic with considerable growth rate. Many urgent researches have been initiated during a short time in order to save our lives. This infectious disease caused by severe acute respiratory syndrome coronavirus 2 (SARS-CoV-2) [12] normally manifests with few symptoms but lead to a rapidly progressive fatal pneumonia [4]. According to a brief report [3], SARS-CoV-2 virus has resulted in 2.16% mortality from all infected subjects. It is one of the most contagious viruses that human has experienced, expanded across most of People's Republic of China during half a month [13], and later appeared globally within a couple of months [14]. In this context, the ventilation system is usually the principle reason for ill patients to be required in critical care units [15, 16].

In this paper, a study of non-invasive mechanical ventilator has been proposed. Firstly, the block diagram of functional components in overall system is introduced to clarify the role of each part. Secondly, the principle diagram that depicted the hypothetical relations among them is presented to provide an overview of whole ventilator. Then, some calculations are completed to perform the fundamental theory in mechanical design. Later, all elements in the mechanism are built in a model of mechanical ventilator. Besides, Proportional-Integral-Derivative (PID) scheme is employed to ensure the output response reached the desired values. The results of this research are then achieved in order to validate the proposed design. From these outcomes, it is clear that our approach is feasible, effective and capable for the COVID-19 scenario, especially

for its low-cost, open-source and readiness in the poor nations. The rest of this paper is constructed as following. Section 3 demonstrates the inside structure of conceptual scheme and mechanical framework in detail while several achievements in numerical simulation is gained in Section 4. Finally, the conclusions are drawn in Section 5.

3. Proposed Approach

3.1 Theoretical Platform of Mechanical Ventilator

The conceptual design of mechanical ventilator in our research is depicted as Fig. 1. Due to the medical requirements of ventilator notified by World Health Organization [17], this design must satisfy these following constraints:

- Possibility of pressure control ventilation (PCV)
- Peak pressure should be no more than 2 cmH₂O greater than plateau pressure
- PEEP (Positive end-expiratory pressure) must be maintained during expiration
- For the ratio of inspiration phase/expiration phase, the ventilator must provide a ratio in the range of 1:1–1:3
- The ventilator must provide a range of 10–30 breaths per minute

Moreover, in order to be used in Vietnamese hospitals in the context of global pandemic, some technical specifications are integrated into the proposed design:

- **Portability:** the machine design could easily be carried by hands. It might be used in households, healthcare center or hospital. In some emergency cases, the proposed ventilator could be employed in outdoor situations.
- **Simplicity:** the operator does not have to be an expert. A patient or relative could set the working mode and supervise at home.
- **Rapid maintenance and production:** according to the special circumstances of social problems, it lacks the medical force to maintain or repair if the working conditions are not guaranteed. In addition, the manufacturer must produce a lot of machines as soon as possible. The peripheral instruments should be available in the market frequently.

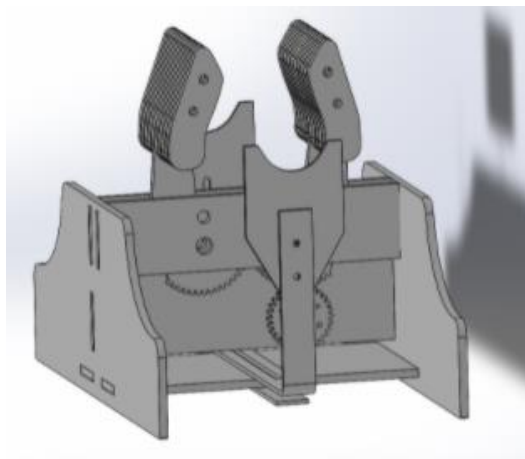


Fig. 1. 3D design of proposed ventilator

3.2 Mathematical Computation of Proposed Model

In Fig. 2, the diagram of the whole machine is sketched out. Nurse or operator chooses the proper values of inputs such as air flow, pressure or tidal volume. Later, the motion controller using microprocessor manipulates the operation of ventilator. Whenever the setting values is stored, these gains are compared with the feedback signals to perform the tracking errors. There are three working modes, child, adult and emergency. Because of the different volumes in lungs and breaths, the mechanical ventilator would decide the suitable working manner for several purposes. The air flow and pressure are installed in advance for both child and adult, while the urgent case depends on the current status of patient. In some cases, depending on the feedback data from patient such as inhalation/exhalation or heart rate, the control signal is varied continuously. From the central processing unit (CPU), the output voltage is sent to mechanical actuator. Based on this command, the driving mechanism provide the sufficient torque to press the AMBU bag. Although it might produce nonlinear characteristic, the high performance of ventilator could be guaranteed. To relay valuable information to the controller, sensors to measure the air flow and pressure are necessary to implement.

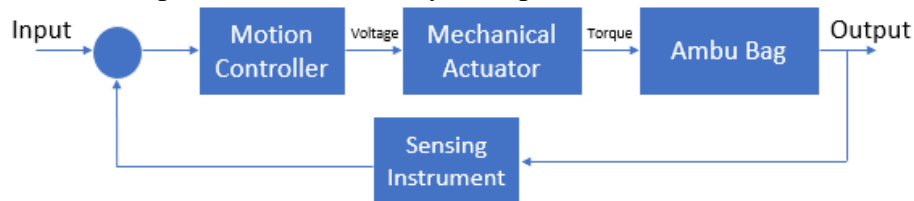


Fig. 2. Block diagram of overall control system

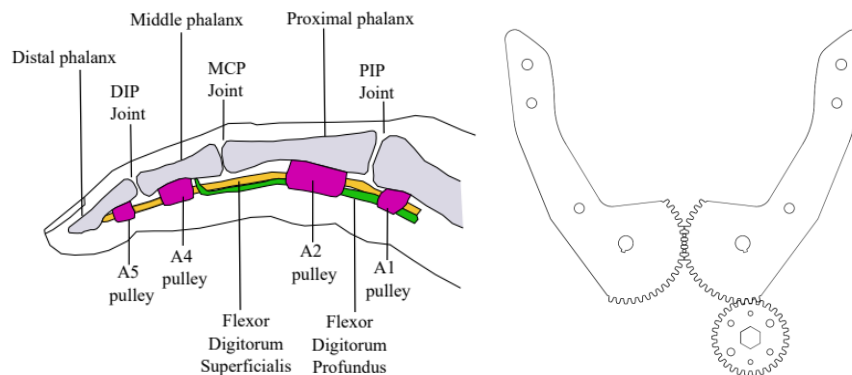


Fig. 3. Demonstration of bio-inspired mechanism for fingers, (a) analysis of structure and (b) mechanical design

To force the AMBU bag, it is essential to mimic the natural gesture of human hand. For the reason that nature is always the best and most efficient design and the hand can conform to the shape of AMBU bag, the interactive torque is evenly distributed so that the contact area and controllability are the greatest. Though the human hand has many joints and Degree-of-Freedom (DOFs), the action of both hand and fingers to press the bag is complicated owing to the multi-DOFs movement with many joints. Inspiring the bio-engineering design, two rigid fingers have curvatures that like the bag, and rotate in tandem around two symmetrical axes so that it ensures the maximum contact area with the least complex and feasible movement. Fig. 3 illustrates the mechanism of two fingers to press the AMBU bag. These two fingers are synchronized by the gear pattern in the bottom with the transmission ratio 1:1 to certify the symmetrical movement.

In addition, one of the fingers is driven by a pinion gear that connected to the geared DC servo motor with the internal ratio of 1:264 and transmission ratio of 1:1.56 to amplify the driving torque.

Separately, the required holding power can be computed from the worst-case values as following

- Maximum pressure at ambu bag: $P_{\text{airway,max}} = 60 \text{ cm H}_2\text{O}$ (pop off relieve valve)
- Maximum respiration rate: $RR_{\text{max}} = 40 \text{ bpm}$
- Minimum inhale/exhale ratio of 1:4: $IE_{\text{ratio,min}} = 4$
- Maximum tidal volume: $V_{\text{max}} = 800 \text{ cm}^3$

It means that in the worst case, our machine needs to squeeze of air at a pressure of 60 cm H₂O, during 0.3 second

$$t_{\text{inhale}}(s) = \frac{60}{RR_{\text{max}}} \times \frac{1}{1 + IE_{\text{ratio,min}}} \quad (5)$$

The volume of air flow needs in the worst-case (peak) scenario is

$$Q_{\text{airflow}} = \frac{V_{\text{max}}}{t_{\text{inhale}}} = 0.0027 \text{ m}^3 / \text{s} \quad (6)$$

In the form of pressurized volume flow, the power output is

$$Power_{\text{airflow}} = P_{\text{airflow,max}} Q_{\text{airflow}} = 16W \quad (7)$$

Reversely, there is amount of power to use for squeezing the AMBU bag lost because of the bag deformation or friction. It is considered that approximately 50% of the force is converted to the pressurized volume flow. Taking this into account, the real power for the gripper is

$$Power_{\text{gripper}} = 2Power_{\text{airflow}} = 32W \quad (8)$$

The actual power from the driving motor must be higher, and this value depends on the mechanical and electrical design. We assume that half of the motor power is lost by mechanical and electrical inefficiencies (gears, thermal dissipation, etc.), then it is computed as

$$Power_{\text{motor}} = 2Power_{\text{gripper}} = 64W \quad (9)$$

To demonstrate our design, the pressing posture of two-finger mechanism is shown in Fig. 4. Three parameters must be measured: finger-bag contact area, finger lever arm length, and sweep angle. In this research, the physical dimensions of these items are,

- Finger-bag max contact area: $A_{\text{bag}} = 90 \text{ mm} \times 115 \text{ mm}$
- Finger lever arm length: $l_{\text{finger}} = 12 \text{ cm}$
- Sweep angle: $\alpha_{\text{sweep}} = 30^\circ$

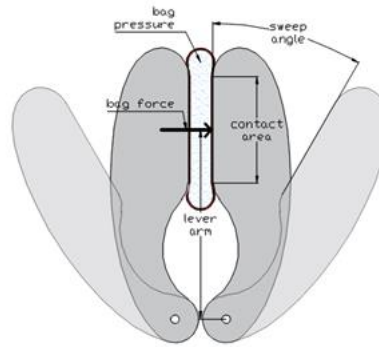


Fig. 4. Graphical illustration of system paramters

Using the same 50% pressure transmission efficiency, the maximum force of the bag on one finger when fully squeezed is

$$F_{finger} = 2A_{bag} P_{airflow,max} = 81.199N \quad (10)$$

The maximum torque on each finger is

$$\tau_{finger} = F_{finger} l_{finger} = 9.74Nm \quad (11)$$

Currently, the required power for two-finger gripper using the sweep angular rate during 0.3 second is

$$P_{finger} = 2 \times \tau_{finger} \omega_{finger} = 34.01W \quad (12)$$

The total power for singler motor when additionally applying the same 50% efficiency of motor and gearbox is

$$P_{motor} = 2 \times P_{gripper} = 68.03W \approx 70W \quad (13)$$

4. Results of Study

To verify the effectiveness of our approach, the proposed model for mechanical ventilator is simulated in this section. As lung compliance fluctuates with pulmonary disease, a ventilator must be able to offer a wide range of pressure in inspiration and sustain high pressure at the end process of exhalation. To adapt with a lung compliance of 60 mL/cm H₂O and an airway resistance of 5 cm H₂O/L, the proposed ventilator could achieve the tidal volume of approximately 500 mL. The results of input flow rate, tracking performance in flow rate and volume for our ventilator are demonstrated in Fig. 6 and Fig. 7 respectively. In general, the average value of flow rate mentioned in [16] is supplied to the lung of patient. In each period, the mechanical ventilator must provide the same flow rate regularly as in Fig. 5. To meet the requirement, the two-finger mechanism warrants frequent operation with sufficient torques. Because of the rapid response, the mechanical actuator completes the journey during a short period. Currently, there is no mechanical structure that satisfy this condition. However, our solution suggests a better solution owing to the flexibility and feasibility of finger-like mechanism.

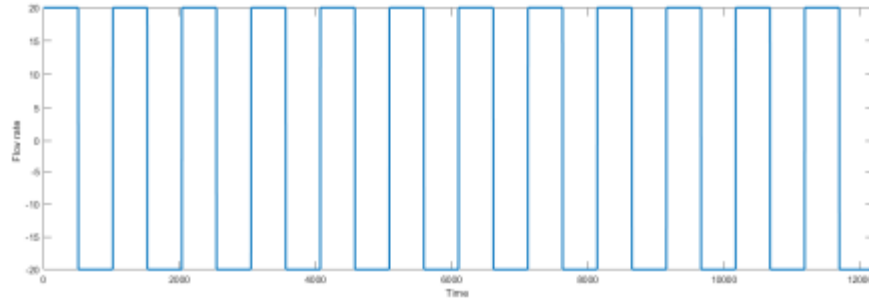


Fig. 5. Simulation result of flow rate to input for respiratory patient

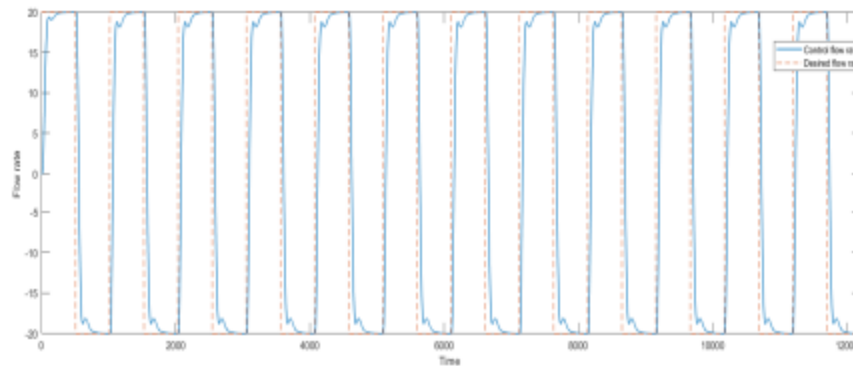


Fig. 6. Simulation result in tracking performance of flow rate for respiratory patient

To visualize the volume control mode response, the tracking performance of proposed controller is verified through the system parameters such volume control and flow rate. Since the nonlinear characteristic of flow rate is difficult to monitor, our research tries to obtain the output results. In Table 1, it can be seen clearly that the response of control flow is critically damped with very fast response time, low RMS (Root-Mean-Square) value of 1.34 and almost zero steady state error, the supplied volume reach around 475ml and identical in all periods. Therefore, the simulation results of flow and volume control are excellent with high tracking performance and high repeatability that would satisfy the requirement for a medical-grade ventilator.

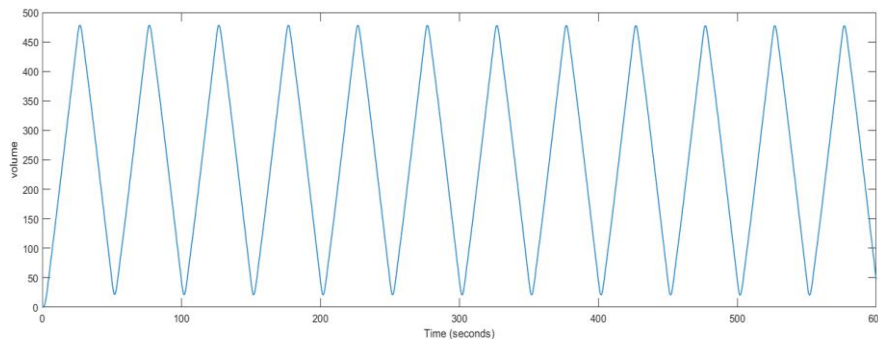


Fig. 7. Simulation result of volume control for respiratory patient

Table 1. List of comparative results for respiratory patient.

Item	Max	Min	Average	RMS (Root-Mean-Square)
Flow rate	3.75	0.85	1.66	1.34
Volume	475	35	220	213.7

5. Conclusions

In this paper, a novel design for mechanical ventilator was presented via systematic analysis and computational theory. The system parameters in detail are identified in order to ensure stable working condition. In the medical field, adaptation and stability as well as the controllability are required, and is one of the most critical issues. The proper framework for mechanical components is suggested so that the desired flow rate in each period could be achieved. From the results of our study, the effectiveness and feasibility of our approach are proved to provide an excellent solution for emergency case.

Acknowledgements

This research is funded by Japan International Cooperation Agency Project for ASEAN University Network / Southeast Asia Engineering Education Development Network (JICA Project for AUN/SEED-Net) in the framework of Special Program For Research Against COVID-19 Japanese Fiscal Year 2020-2021 (SPRAC), with the support of time and facilities from Ho Chi Minh City University of Technology (HCMUT), VNU-HCM.

References

- [1] Pelosi, P., Rocco, P. R. M., & de Abreu, M. G. (2018). Close down the lungs and keep them resting to minimize ventilator-induced lung injury. *Critical Care*, 22(1), 1-8.
- [2] Millar, D., Lemyre, B., Kirpalani, H., Chiu, A., Yoder, B. A., & Roberts, R. S. (2016). A comparison of bilevel and ventilator-delivered non-invasive respiratory support. *Archives of Disease in Childhood-Fetal and Neonatal Edition*, 101(1), 21-25.
- [3] Pfefferbaum, B., & North, C. S. (2020). Mental health and the Covid-19 pandemic. *New England Journal of Medicine*, 383(6), 510-512.
- [4] Watkins, J. (2020). Preventing a covid-19 pandemic.
- [5] Omer, S. B., Malani, P., & Del Rio, C. (2020). The COVID-19 pandemic in the US: a clinical update. *Jama*, 323(18), 1767-1768.
- [6] Islam, M. R., Ahmad, M., Hossain, M. S., Islam, M. M., & Ahmed, S. F. U. (2019, May). Designing an electro-mechanical ventilator based on double cam integration mechanism. In 2019 1st International Conference on Advances in Science, Engineering and Robotics Technology (ICASERT) (pp. 1-6). IEEE.
- [7] Acho, L., Vargas, A. N., & Pujol-Vázquez, G. (2020, September). Low-Cost, Open-Source Mechanical Ventilator with Pulmonary Monitoring for COVID-19 Patients. In *Actuators* (Vol. 9, No. 3, p. 84). Multidisciplinary Digital Publishing Institute.
- [8] Castro-Camus, E., Ornik, J., Mach, C., Hernandez-Cardoso, G., Savalia, B., Taiber, J., ... & Koch, M. (2020). Simple ventilators for emergency use based on Bag-Valve pressing systems: Lessons learned and future steps. *Applied Sciences*, 10(20), 7229.

- [9] Petsiuk, A., Tanikella, N. G., Dertinger, S., Pringle, A., Oberloier, S., & Pearce, J. M. (2020). Partially RepRapable automated open source bag valve mask-based ventilator. *HardwareX*, 8, e00131.
- [10] MIT E-Vent. MIT emergency ventilator project. Available online: <https://e-vent.mit.edu>
- [11] AndalucíaRespira. Available online: <https://www.andaluciarespira.com/en/andalucia-respira-en>.
- [12] Muniyappa, R., & Gubbi, S. (2020). COVID-19 pandemic, coronaviruses, and diabetes mellitus. *American Journal of Physiology-Endocrinology and Metabolism*, 318(5), E736-E741.
- [13] Wang, D., Zhou, M., Nie, X., Qiu, W., Yang, M., Wang, X., ... & Chen, W. (2020). Epidemiological characteristics and transmission model of Corona Virus Disease 2019 in China. *The Journal of infection*, 80(5), e25.
- [14] Lipinski, T., Ahmad, D., Serey, N., & Jouhara, H. (2020). Review of ventilation strategies to reduce the risk of disease transmission in high occupancy buildings. *International Journal of Thermofluids*, 100045.
- [15] Carter, C., Osbourne, M., Agagah, G., Aedy, H., & Notter, J. (2020). COVID-19 disease: Invasive ventilation. *Clinics in Integrated Care*, 100004.
- [16] Zuckerberg, J., Shaik, M., Widmeier, K., Kilbaugh, T., & Nelin, T. D. (2020). A lung for all: Novel mechanical ventilator for emergency and low-resource settings. *Life sciences*, 257, 118113.
- [17] World Health Organization. (2020). Technical specifications for invasive and non-invasive ventilators for COVID-19: Interim guidance, 15 April 2020. World Health Organization. <https://apps.who.int/iris/handle/10665/331792>. Licence: CC BY-NC-SA 3.0 IGO

Towards Motion Capture Using a Swarms of Drones

John Page^{1, *}, Faqihza Mukhlis² and Michael Bain³

^{1,2}School of Mechanical and Manufacturing Engineering, University of New South Wales,
Sydney, Australia

³ School of Computer Science and Engineering, University of New South Wales, Sydney,
Australia

² Engineering Physics Research Group, Institut Teknologi Bandung, Bandung, Indonesia

² Center for Instrumentation Technology and Automation, Institut Teknologi Bandung,
Bandung, Indonesia

*Corresponding author. E-mail: j.page@unsw.edu.au

Abstract

Since it has become practical to create reliable facial recognition algorithms, the technology has found many applications. However, in identifying subjects at a distance and predicting future behaviour, it is quite limited. Motion capture offers some interesting possibilities in this area. It can capture both poise and gait, which can be used as data to identify an individual, assess physical condition, deduce their mood and possibly their intentions. At the moment, Motion Capture is mostly carried out in a studio with controlled lighting and backgrounds and using an actor's interpretation of the required behaviour. The ideal situation would be to capture spontaneous motions in a non-controlled environment. The aim of this paper is to investigate the possibility of UAVs to act as camera platforms and obtain usable data in an uncontrolled environment. There are technical difficulties associated with this. The paper explores the use of technical capabilities developed for the computer game industry, special effects in the film industry, and image manipulation techniques to address these issues. The problems addresses deal with an uncontrolled light environment, capturing a 3D image of the subject clear of background interference, how to mesh the subject's vision, and finally, how to produce a skeleton to map the motion.

Keywords: Motion Capture, Drone Swarms, Poise, Gait

1. Introduction

Since facial recognition software became reliable at identifying people, it has found many applications, from security checks to shopping. This has resulted in a significant debate about the ethical use of such systems (Kostka et al., 2021). Though the artificial intelligence (AI) involved is lauded as mimicking how humans and other sentient entities identify and distinguish a given human, this is only partially true. On the other hand, we can often identify an individual who is known to us long before we can clearly see their face from posture (Ding et al., 2020) and gait (Winiarski et al., 2019). This data is not only distinctive for the individual, but also changes with the individual's desires, emotions and physical state. There is also evidence to suggest such data could help predict future action (Varizi-Pashkam et al., 2015). The problem is that obtaining this data is not simple, which is why we believe there is a role for UAV swarms in this area. Currently, most data is obtained in a highly controlled environment, often using actors whose motions are mapped by targets attached to their bodies. Of course, *acting* angry or fearful is not the same as *being* angry or fearful. Both obtaining the required DATA and processing it into useful information requires the development of new techniques (Rahul, 2018). Fortunately, there

are technical capabilities that can be modified developed for the computer gaming and film industry (Sharma, 2020; Zhang, 2013). It is the aim of this paper to investigate how these techniques might be adapted as a precursor for developing an original UAV system for motion capture.

2. Difficulties Need to be Addressed and Overcome

Before it is possible to determine the motion of a human subject by a drone or flock of drones in an outside environment, a number of requirements need to be addressed. One solution to this problem is to use a simple model. This is done on paper by Xiaowei Zhou, Sikang Liu, Georgios Pavlakos, Vijay Kumar, Kostas Daniilidis and X. Zhou (2018). This is an interesting approach but limiting the detection to a simple skeleton is restrictive.

2.1 The Data Problem

A reasonable video seems to require about 25 frames per second (fps), which quickly generates a large amount of data for a sequence. However, reasonable motion can be achieved with fewer frames and using AI to fill the gaps between the now sparse frames.



Figure 1. A comparison between motion capture; The top image is full frames, the lower reduced frames

In Figure 1, the top image is using all available keyframes. The bottom image has reduced images, about three fps, and the images are taken between the top keyframes and generated by AI interpolation. In these images taken from a video, it is hard to detect a difference, which is also true when the source video is viewed.

2.2 Static

A certain number of conclusions can be drawn from the static information, particularly if there is a wide separation. For example, gender classification can be achieved if the subjects are naked and well away from a defined gender boundary.

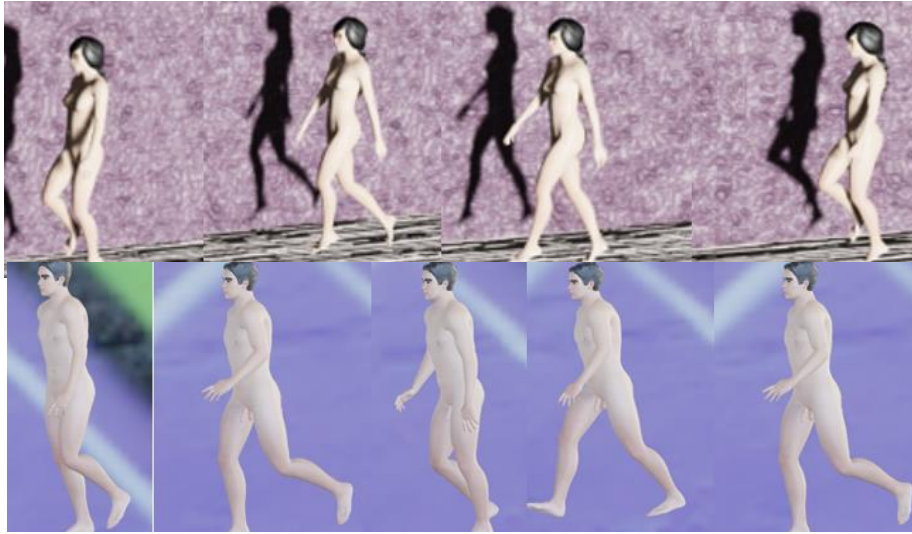


Figure 2. Comparison of a male and female walking caricature

It was found to be quite easy to train an AI system to distinguish between the gender of the two images in Figure 2, given the AI had three-dimensional images to work with (Li et al., 2019). However, it became progressively harder when the subjects were clothed in non-gender specific clothes and less gender stereotypical. Distinguishing the nature of the walk and the motive behind it to draw conclusions was very hard from a static 3D image. A dynamic approach should help as the nature of the motion would appear to become very significant.

2.3 Dynamic



Figure 3. Show a composite image based on the motion capture where the actor is given different instructions

In the composite image in Figure 3, the actress in the motion capture has been given a number of scenarios that resulted in different walking patterns. However, it is very hard from a static image to identify them, despite actors always exaggerating an emotion. Of course, it is easy to tell the one at the end of the line is sad and possibly the one at the front is very energetic, but it is hard to tell from the static image, which is aggressive, while in the dynamic image, it is easy. This is partly because human beings have evolved to adapt their response quickly to human movements, particularly when faced with possible aggression.



Figure 4. Interaction

A lot of information can be obtained when the figures are interacting, even in a static case, see Figure 4. In this example, we can tell that the woman is the dominant individual though we cannot tell their relationship. They could be, among other scenarios, a mother and son, teacher and student or even a storekeeper who has caught a shoplifter. What the static image does not give is a direction the altercation is moving in. Is it settling down or escalating, which might indicate an intervention is required?

2.4 Capturing an image

Capturing a high-definition three-dimensional image can be achieved by either using several cameras simultaneously or moving one camera around a static object. The former is hard to achieve as it requires uniformity of the images collected by different cameras. This can be overcome by post-processing for still images, which is one of the reasons we propose collecting still images and combining them into a video through AI interpolation from limited keyframes. The latter is much harder to achieve if the model is non-static. Once sufficient images are obtained, eight seems to be about a minimum. They are stitched together using features on the images. This means the camera's location is not required. More dramatic features are easier to stitch in practice, which is one reason caricatures in computer-generated movie shots and video games often wear high feature clothing.

2.5 Gathering and Processing the Image

The first stage is to generate a 3D model, which is then meshed. The mesh is used to generate a skeleton or rig.

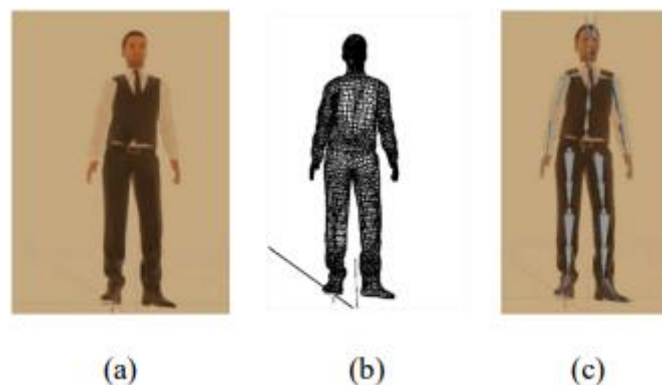


Figure 5. Shows the Three Stages Involved in Animating a Real Character

Figure 5(a) is a three-dimensional image from <https://renderpeople.com/free-3d-people/> (“Free 3D People for Max, Maya, C4D & more,” n.d.). The image is stilted as it was obtained using a single camera moved around the caricature. This involved the subject remaining motionless for a period of time, and the hands are holding supports, now removed, to assist this.

Figure 5(b) shows the same figure meshed. There are a few programs that can be used to do this automatically. The image provided is of a very dense mesh, but in practice, this can be reduced depending on the purpose for which it is generated. When the subject moves, so does the mesh, which could be used to determine or generate the motion but, due to the complexity of the mesh, a rig or skeleton is used.

Figure 5(c) shows the skeleton imposed on the original caricature. This rig was generated from a simple program that requires only ten points to be defined on the subject. An AI-based program then interpolates this, choosing the bones, including finger, and other appendage, bones based on learned relationships. This is quite crude but allows the subject to be manipulated easily. Again, there are several programs to generate the rig demanding different levels of human import.

3. Modifying the Technology for Our Purpose

The technology is designed to capture an individual and place them in a computer-generated scene where they can be manipulated to contribute to a film or video game. What we are attempting to do is to take some keyframes of a human motion and determine the relationship. This is, in a sense, the reverse of using AI to interpolate between keyframes done in video making. We want to establish the rules that drive the motion between keyframes. These should be dependent on a number of factors that it should be possible to determine using classic AI deep learning.

4. Value of Capability

If we can establish the relationship between keyframes or the captured still images in our case, that should provide an insight into what drives the motion. This would be a very useful capability to have. To take a simple example, if a footballer’s motion differed from normal, this could be an indication of a potential injury or a fitness issue. Or in a more complex system like a security checkpoint, if normal behaviour was taken into account using data clustering based on gender, age, ethnicity etc., deviant behaviour could be identified for further investigation as a possible indication of bad intent.

5. Conclusion

This paper is intended only as a first step in investigating whether existing technology could support a UAV based motion capture system. There are two ways drones could be used, either as a swarm taking synchronised pictures of a single drone flying around the subject. The forms would seem to be well supported by current technology later. However, it would create difficulties in stitching the image together. Now we are convinced it is possible to start the next stage of experimental work.

Acknowledgments

The production of this paper depended on the use of several computer programs. They are listed below, and all were cost-free, either as freeware or developments versions.

- **Blender** was the core program used to coordinate the process and generate the output.
- **Casadeur** was used to interpolate between keyframe and to generate a rig (skeleton).
- **MakeHuman** was used to generate human assets.
- **Meshroom** was used to mesh the human figure.

- **Mixamo** was the source of motion capture data.

References

- [1] Ding, W., Hu, B., Liu, H., Wang, X., Huang, X., 2020. Human posture recognition based on multiple features and rule learning. *Int. J. Mach. Learn. Cybern.* 11, 2529–2540. <https://doi.org/10.1007/s13042-020-01138-y>
- [2] Free 3D People for Max, Maya, C4D & more, n.d. Renderpeople. URL <https://renderpeople.com/free-3d-people/> (accessed 6.2.21).
- [3] Kostka, G., Steinacker, L., Meckel, M., 2021. Between security and convenience: Facial recognition technology in the eyes of citizens in China, Germany, the United Kingdom, and the United States. *Public Underst. Sci.* 0963662521100155. <https://doi.org/10.1177/0963662521100155>
- [4] Li, Y., Mahjoubfar, A., Chen, C.L., Niazi, K.R., Pei, L., Jalali, B., 2019. Deep Cytometry: Deep learning with Real-time Inference in Cell Sorting and Flow Cytometry. *Sci. Rep.* 9, 11088. <https://doi.org/10.1038/s41598-019-47193-6>
- [5] Rahul, M., 2018. Review on Motion Capture Technology. *Glob. J. Comput. Sci. Technol., F Graphics & Vision* 18, 23–26.
- [6] Sharma, D., 2020. A Review Paper on Motion Capturing Technology for Gaming. *Int. J. Creat. Res. Thoughts* 8, 5.
- [7] Varizi-Pashkam, M., Sarah, C., Nakayama, K., 2015. Predicting Actions Before They Occur (No. 038), CBMM Memo Series. Center for Brains, Minds and Machines (CBMM).
- [8] Winiarski, S., Pietraszewska, J., Pietraszewski, B., 2019. Three-Dimensional Human Gait Pattern: Reference Data for Young, Active Women Walking with Low, Preferred, and High Speeds. *BioMed Res. Int.* 2019, 1–7. <https://doi.org/10.1155/2019/9232430>
- [9] Zhang, M.Y., 2013. Application of Performance Motion Capture Technology in Film and Television Performance Animation. *Appl. Mech. Mater.* 347–350, 2781–2784. <https://doi.org/10.4028/www.scientific.net/AMM.347-350.2781>
- [10] Zhou, X., Liu, S., Pavlakos, G., Kumar, V., Daniilidis, K., 2018. Human Motion Capture Using a Drone. *ArXiv180406112 Cs*.

Experimental Modelling of Flapping-wing Micro Air Vehicle

Steven Aurecianus¹, Gi Heon Ha², Hoang Vu Phan², Hoon Cheol Park², and Taesam Kang^{1,*}

¹Department of Mechanical and Aerospace Engineering, Konkuk University, Seoul, South Korea, 05029

² Department of Smart Vehicle Engineering, Konkuk University, Seoul, South Korea, 05029

*Corresponding author. E-mail: tskang@konkuk.ac.kr

Abstract

In this study, we constructed dynamic models of a flapping-wing micro air vehicle (FW-MAV), KUBeetle, using grey box and black box approaches in the MATLAB® system identification application. The initial model for grey box approach is based on linearized Newton-Euler equations for near hover flight with rigid body assumption. Furthermore, the filters and servos dynamics are included in the model to accommodate the real system. Proportional-derivative (PD) feedback controller is implemented in the control board to stabilize the KUBeetle during experimental flight. The KUBeetle is an inherently unstable system. Thus, to obtain experimental data, it should first be stabilized with any simple feedback controller. The set of flight data used for system identification are obtained from experimental flights where specific square wave signal is applied to the KUBeetle as reference command. Using the system identification application in MATLAB®, various methods are used to obtain the identified models. Then, these models are evaluated and compared with the flight data using computer simulation. Due to the noise generated by flapping motion and vibration, the fit percentage of the model output and flight data is not too high, especially for angular rate. Generally, the black box model produces higher fit percentage compared to the grey box model. It is because black box model does not need to follow the structure of the derived model and the initial model has some disparities with the real system.

Keywords: System identification, experimental modelling, flapping-wing micro air vehicle, controller design

1. Introduction

Since more than a decade ago, the scope of research on unmanned aerial vehicle (UAV) has been expanding towards more unconventional design, especially flapping-wing micro air vehicle (FW-MAV) [1, 2]. The inspiration in designing the FW-MAVs comes from observing biological system, such as birds and insects. Generally, bird-inspired FW-MAVs flap its wing vertically and have control surface at tail, while insect-inspired FW-MAVs flap its wing horizontally and do not have control surface. Similar to bird flight characteristics, bird-inspired FW-MAVs are not able to stay in one position and have low degree-of-freedoms. In contrary, similar to insect flight characteristics, insect-inspired FW-MAVs are able to remain in one position in the air and perform agile flight maneuvers with high degree of freedoms [3, 4]. Due to these design and flight characteristics, developing insect-inspired FW-MAVs are typically more challenging than developing bird-inspired FW-MAVs. Currently, there are numerous existing insect-inspired FW-MAV designs with various propulsion systems and wing configurations [3]. Some of them have shown successful stable flight, such as Nano Hummingbird [5], Robobee [6], Delfy [7], KUBeetle [8, 9], Robotic Hummingbird [10], Colibri [11], NUS-Robobird [12], and Purdue Hummingbird [13]. In order to stabilize their flight, insect-inspired FW-MAVs generate thrust

and control moment by manipulating their wing kinematics. The flap amplitude, angle of attack, flapping frequency, or stroke-plane angle of the wing can be controlled by actuators, such as motor and servo.

In order to control the FW-MAVs, typically, a control board, which includes microprocessor, sensor, receiver, and antenna, is attached to the robot [3]. The microprocessor as the “brain” of the robot processes the state estimation using the sensor data and run the control algorithm to obtain control output to stabilize the FW-MAV using servo motors. One of the most commonly used sensors is inertial measurement unit (IMU) which can be found in many control boards due to its functionality. In addition, other sensors, such as barometer, laser sensor, and vision sensor, might be included to enhance the performance of the FW-MAV. External devices, such as high-speed camera and motion-capture camera also can be used to replace the onboard sensor [6] or record the attitude of the FW-MAV [7, 8, 14]. The main function of receiver and antenna is to receive reference command from remote control or ground station. The receiver can be replaced with a transceiver which supports two-way communication, so that the flight data or other information can be transmitted to the ground station [15]. Alternatively, the flight data can be recorded into a memory card embedded on the control board [12].

During the development of the FW-MAV, stabilizing the FW-MAV is most important. Many FW-MAVs use proportional-integral-derivative (PID) controller and its variant as their control algorithm due to its feasibility, simplicity, and ease of implementation [8, 10–12]. Even though the FW-MAV can perform stable flight using the simple PID techniques, dynamic model identification is necessary for further analysis and improvement on control algorithm. A lot of efforts have been done for mathematical modelling and system identification to obtain dynamic model of FW-MAV [16–20]. But few of them are used for the controller design and analysis. In [21], the speed of a tailless four-winged FW-MAV is successfully improved based on the analysis of the validated longitudinal mode dynamic model. In another study [15], stable and robust control gains are obtained for an insect-like, tailless FW-MAV using the root locus and H_∞ norm analyses of the dynamic model.

In this study, experimental modelling of FW-MAV is suggested, specifically on pitch motion during free flight. After obtaining the flight data through experimental flight, system identification process is done in MATLAB to obtain gray and black box models. Then, the models are evaluated and compared with the original model. The rest of the paper is arranged as follows: In section 2, the FW-MAV design and dynamic model used in this study are described. In Section 3, the experimental flight setup and results are given. The system identification procedures and results are described and analyzed in Section 4. Finally, conclusion and future research topics are given in Section 5.

2. FW-MAV

2.1 KUBeetle

The flying robot used in this study is an insect-like, tailless FW-MAV called KUBeetle [8, 9], which is shown in Figure 1. The KUBeetle has one pair of wings driven by motor through flapping mechanism to generate thrust. Three servos are used to manipulate the wing kinematics to generate control moment for pitch, roll, and yaw, respectively. The control board is placed between the yaw servo and battery with IMU located perpendicular to the center of gravity. NRF24L01+ transceiver module is connected to the control board for flight data transmission. The data set are transmitted to a monitoring ground system 100 times per second. The total weight of the system is 18.6 g and the center of gravity is located at around 0.75 chord length below the leading edge of the wing.

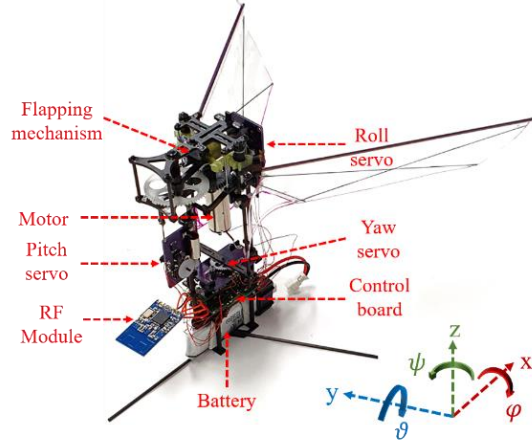


Figure 1. KUBeetle

2.2 Dynamic Model

The dynamic model of the KUBeetle used in this study can be found in [15]. It is derived from the linearized Newton-Euler equation of motion for near hover flight with rigid body assumption [22, 23]. The model is improved further with the addition of filters and servos dynamics. The improved dynamic model is used as the initial model for model refinement in system identification.

3. Experimental Flight

3.1 Experimental Setup

The experimental flight is conducted to obtain the flight data of the KUBeetle for system identification. It is done indoor, in a closed space where there is no wind disturbance. The experimental setup is illustrated in Figure 2. The remote transmitter sends reference commands to the KUBeetle to manipulate the drone. Then, the KUBeetle transmits the flight data, including the state estimation, to the ground station. One of the commands is programmed as trigger signal for the experimental flight, so that the pitch reference command is generated automatically by the control board in the form of square signal. For this experimental flight, the pitch reference command is set as square signal with amplitude $\pm 17^\circ$ and randomized frequency between 0.7 to 5 Hz.

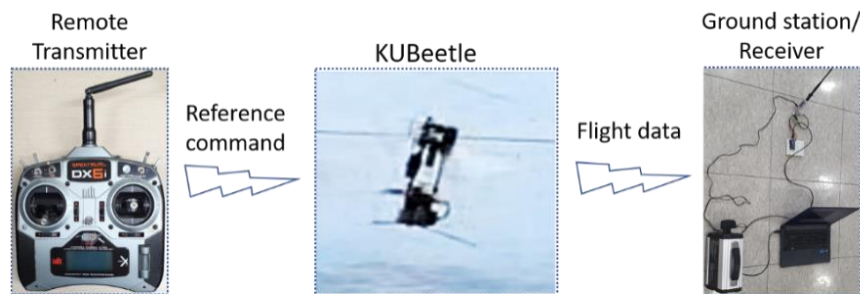


Figure 2. Experimental setup

3.2 Experimental Results

One of the flight data obtained from the experimental flight is shown in Figure 3. It can be observed that the pitch angle follows the pitch reference command sufficiently well with some

delay. The angular rate contains some high frequency noises due to vibration generated by flapping motion.

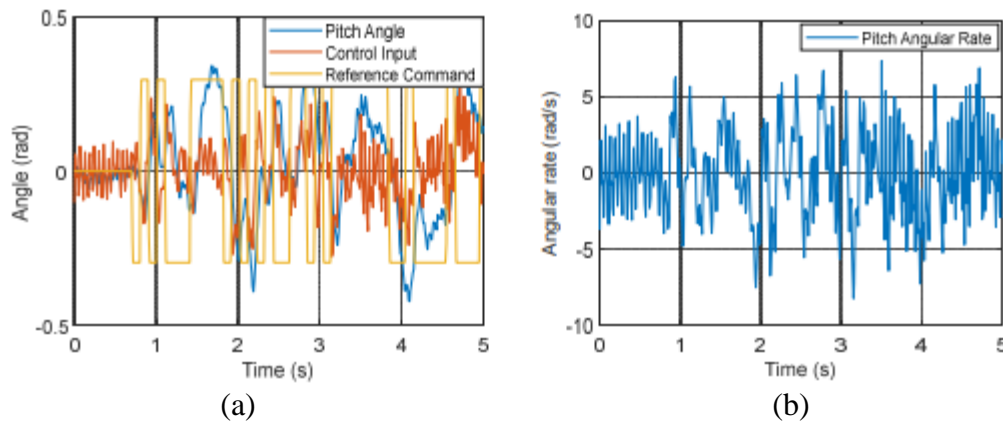


Figure 3. Flight data of pitch: (a) angle and (b) angular rate

4. System Identification

4.1 Black Box Model

The flight data is processed in MATLAB[®] System Identification application using various settings. The control input is set as the model input and the pitch angle and angular rate are set as the model outputs. By using the control input rather than pitch reference command as the model input, an open-loop model is to be obtained. Currently, one of the best and most applicable models is found using Subspace (N4SID) estimation method and Multivariable Output Error State Space (MOESP) weighting scheme. The generated model is a 10th order model with average fit percentage to estimation data of around 33% for angular rate and around 35% for angle. A closed-loop control system is constructed by adding the PD feedback controller to the model for simulation and analysis. The simulation results are shown in Figure 4. The response of the black box model shows a small indication of non-minimum phase characteristic, and the steady state error is relatively lower than the initial model.

4.2 Gray Box Model

The pitch motion is part of longitudinal mode of FW-MAV. Therefore, we use the improved longitudinal mode dynamic model for system identification. PD feedback controller is included as part of the initial model to construct closed-loop model before it is used in the model refinement process. Some parameters on the state space matrices are fixed because the values of these parameters are known, such as parameters of the filters and servo. The coefficients of the filters in the model are equivalent to the coefficients of the digital filters implemented in the control board. In addition, the servo dynamic has been measured and estimated in a previous study [15]. The pitch reference command is set as the model input and the pitch angle and angular rate are set as the model outputs. One of the best and most applicable models is found with average fit percentage to estimation data of around 16.5% for angular rate and around 36% for angle. Considering that only some of the parameters on the initial model are changeable, the relatively low fit percentage indicates that there are some differences between the initial model and the real system. After constructing closed-loop control system with PD feedback controller, the model responses are evaluated. The simulation results are shown in Figure 4. The response of the gray box model becomes more oscillatory and there is not much improvement on steady state error than the initial model.

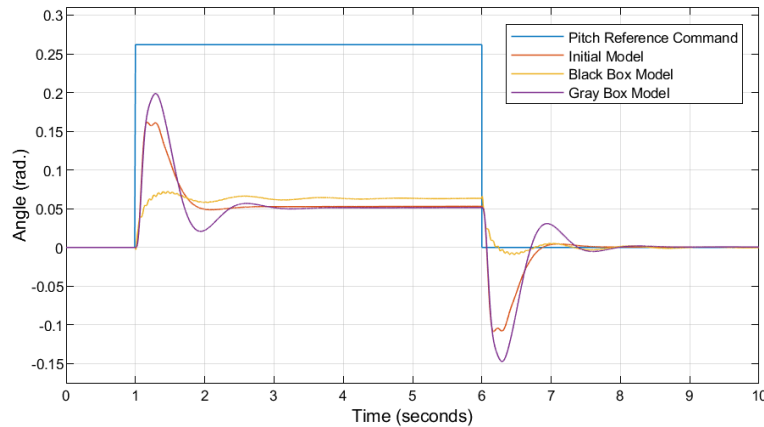


Figure 4. Simulation Results

5. Conclusion

This study shows the process of experimental modelling for pitch motion of FW-MAV. The various methods of system identification produce a varying model with different fit percentage and characteristic. Generally, the generated black box model has higher fit percentage to estimation data than gray box model. It is because some parameters are imposed with restriction so that their values cannot be changed during model refinement. Because the angle data has much less noise than angular rate data, the angle output of the model is usually higher than angular rate output. Further study and analysis are needed to evaluate the generated models.

Acknowledgments

This research is supported by Basic Science Research Program through the National Research Foundation of Korea (NRF) funded by the Ministry of Education (No. 2020R1A6A1A03046811).

References

- [1] Han, J.H., Lee, J.S., Kim, D.K. (2009), “Bio-inspired flapping UAV design: a university perspective”, Health Monitoring of Structural and Biological Systems, Proc. SPIE 7295.
- [2] Tan, X., Zhang, W., Ke, X., Chen, W., Zou, C., Liu, W., Cui, F., Wu, X., and Li, H. (2012), “Development of Flapping-wing micro air vehicle in Asia”, Proceedings of the 10th World Congress on Intelligent Control and Automation, Beijing, pp. 3939-3942.
- [3] Phan, H.V. and Park, H.C. (2019), “Insect-inspired, tailless, hover-capable flapping-wing robots: Recent progress, challenges, and future directions”, Progress in Aerospace Sciences, Vol. 111.
- [4] Sun, M. (2014), “Insect flight dynamics: Stability and control”, Reviews of Modern Physics, Vol. 86, pp. 615-646.
- [5] Keennon, M., Klingebiel, K., Won, H. (2012), “Development of the nano hummingbird: A tailless flapping wing micro air vehicle”, Proceedings of AIAA Aerospace Sciences Meeting including the New Horizons Forum and Aerospace Exposition, AIAA 2012-0588.
- [6] Ma, K.Y., Chirarattananon, P., Fuller, S.B., and Wood, R.J. (2013), “Controlled flight of a biologically inspired, insect-scale robot”, Science, Vol. 340(6132), pp. 603-607.
- [7] Karásek, M., Muijres, F., De Wagter, C., Remes, B. and de Croon, G. (2018), “A tailless aerial robotic flapper reveals that flies use torque coupling in rapid banked turns”, Science, Vol. 361(6407), pp. 1089-1094.

- [8] Phan, H. V., Kang, T., and Park, H. C. (2017), “Design and stable flight of a 21 g insect-like tailless flapping wing micro air vehicle with angular rates feedback control”, *Bioinspiration & Biomimetics*, Vol. 12(3).
- [9] Phan, H.V., Aurecianus, S., Kang, T., Park, H.C. (2019), “KUBeetle-S: An insect-like, tailless, hover-capable robot that can fly with a low-torque control mechanism”, *International Journal of Micro Air Vehicles*.
- [10] Coleman, D., Benedict, M., and Chopra, I. (2015), “*Design, development and flight testing of robotic hummingbird*”, *71st Annual Forum of the American Helicopter Society*.
- [11] Roshanbin, A., Altartouri, H., Karasek, M., and Preumont, A. (2017), “COLIBRI: A hovering flapping twin-wing robot”, *International Journal of Micro Air Vehicles*, Vol. 9(4), pp. 270-282.
- [12] Nguyen, Q. and Chan, W.L. (2018), “*Development and flight performance of a biological-inspired tailless Flapping Wing Micro Air Vehicle with wing stroke plane modulation*”, *Bioinspiration & Biomimetics*, Vol. 14.
- [13] Deng, X., Schenato, L., and Sastry, S.S. (2006), “Flapping flight for biomimetic robotic insects: part II-flight control design”, *IEEE Transactions on Robotics*, Vol. 22(4), pp. 789-803.
- [14] Zhang, J., Tu, Z., Fei, F., and Deng, X. (2017), “Geometric flight control of a hovering robotic hummingbird”, *2017 IEEE International Conference on Robotics and Automation (ICRA)*, Singapore, pp. 5415-5421.
- [15] Aurecianus, S., Phan, H.V., Kang, T., and Park, H.C. (2020), “Longitudinal mode model-based controller design for tailless flapping wing robot with loop shaping compensator”, *Bioinspiration & Biomimetics*, Vol. 15, No. 5.
- [16] Mwongera V. (2015), “A Review of Flapping Wing MAV Modelling”, *International Journal of Aeronautical and Space Sciences*, Vol. 2, p. 17.
- [17] Taha, H., Hajj, M.R., and Nayfeh, A. (2012), “Flight dynamics and control of flapping-wing MAVs: A review”, *Nonlinear Dynamics*, Vol. 70, pp. 907-939.
- [18] Shyy, W., Kang, C. K., Chirarattananon, P., Ravi, S., and Hao, L. (2016), “Aerodynamics, sensing and control of insect-scale flapping-wing flight”, *Proceeding of The Royal Society A*.
- [19] Orłowski, C. T. and Girard, A. R. (2012), “Dynamics, stability, and control analyses of flapping wing micro-air vehicles”, *Progress in Aerospace Sciences*, Vol. 51, pp. 18-30.
- [20] Khan, Q. and Akmeliawati, R. (2021), “Review on System Identification and Mathematical Modeling of Flapping Wing Micro-Aerial Vehicles”, *Appl. Sci.*, Vol. 11(4), p. 1546.
- [21] Kajak, K.M., Karásek, M., Chu, Q.P., and de Croon, G.C.H.E. (2018), “A minimal longitudinal dynamic model of a tailless flapping wing robot for control design”, *Bioinspiration & Biomimetics*, Vol. 14, No. 4.
- [22] Au, L.T.K. and Park, H.C. (2019), “Influence of Center of Gravity Location on Flight Dynamic Stability in a Hovering Tailless FW-MAV: Longitudinal Motion” *Journal of Bionic Engineering*, Vol. 16(1), pp. 130-144.
- [23] Karásek, M., and Preumont, A. (2012), “Simulation of Flight Control of a Hummingbird Like Robot Near Hover,” *Acta Technica CSAV (Ceskoslovensk Akademie Ved)*, Vol. 58(2).

Multi-terrain Hexapod Robot for Search and Rescue Mission

R. Akmeliawati*, D. Harvey, N. Mudisi, S. Lakshmanan, I. Iro and M. Ijala

School of Mechanical Engineering, The University of Adelaide, Adelaide, Australia, SA 5005

*Corresponding author. E-mail: rini.akmeliawati@adelaide.edu.au

Abstract

In this paper, we present our proposed Underground Search & Rescue Robot (USRR), which is capable of detecting and localizing humans underground or in confined spaces. A top-down system engineering approach is utilized in designing and building the robot, and functional analysis is performed in identifying five key functions and corresponding major subsystems of the robot, including the control, power, body frame and locomotion, detection and communication systems. The robot is built based on a synergy of a spider with six, grasshopper-like legs, commonly known as a hexapod. The robot's chassis is designed specifically to increase the functionality of the detection system to facilitate sensors, such as the carbon dioxide sensor, humidity and thermal camera, and other electronic components. The leg module adds stability and aids in mobility while the robot is in motion. Additionally, an interchangeable tip is utilized, allowing the robot to adapt to multiple terrains, such as grass and concrete. The six-legged robot, equipped with obstacle avoidance function, operates on 7.4V LiPO battery, which allows for operations of up to 30 minutes on multi-terrain. The proposed robot offers efficient operation and manufacturing simplicity, manoeuvrability and spacing functionality.

Keywords: Underground rescue robot, Hexapod, Sensor network

1. Introduction

The International Disaster Database (EM-DAT, 2019) reveals that in the last decade, there has been a significant rise in catastrophic events globally, and an even higher increase in fatalities from entrapment of humans as victims are trapped under very heavy and unstable debris. Entrapment under such rubble creates extreme complications causing search and rescue missions, which are particularly dangerous to be performed by humans. Due to the complex and dangerous nature of these rescue missions, they are also time consuming. The current rescue procedures involve a triangulation method where rescue personnel canvas a region believed to be occupied by survivors, digging and calling out for anyone who is able to respond. The rescue teams then commence digging in the direction of the response. However, despite the tremendous efforts, work and time invested into rescue operations, Bartels and van Rooyen (2012) state that the proportion of survivors recovered from collapsed structures is still minimal. Additionally, if survivors are found, it is often hours or even days after rescue efforts had begun.

Reddy *et al.* (2015) explain that due to the unpredictability of the underground environment and extent of accidents from collapses during underground activities, it is extremely difficult for rescue operations to be completed successfully and safely. The most significant factors that affect rescue teams include decreased visibility and the presence of poisonous and explosive gases. Walker (2019) suggests that due to these difficulties, robots for underground missions would be a vital tool for identifying and localizing trapped victims. Reddy *et al.* (2015) emphasize that the first few hours following a disaster are the most crucial and hence, prompt actions are necessary in order to minimize loss of life. As explained in Walker (2019), search and rescue robots are a quick and reliable solution for mapping underground environments and assessing the dangers of the environment. The information acquired from these robots can then

be used to devise an appropriate response, maximizing the number of lives saved. This has motivated the research presented in this paper.

In this paper, we propose an underground search and rescue robot designed to assist human searchers. It is a hexapod robot equipped with thermal camera, humidity and carbon dioxide sensors. This paper is organized as follows. In Section 2, we discuss various types of existing Underground Search and Rescue Robots (USRRs). Section 3 presents our proposed USSR. Its performance is discussed in Section 4. Finally, we conclude this paper in Section 5 by highlighting the merits of the proposed robot.

2. Different Types of Underground Search and Rescue Robots

There are various types of USRRs, such as legged, wheeled and rocker-bogey suspension types. One of the search-and-rescue robots that are currently in use in mining applications is the CSIR-CMERI Subterranean robot (Reddy *et al.*, 2015). This robot has numerous functional requirements, which include search, structural inspection and mapping. It has the ability to manoeuvres over debris and in tight spaces on an interchanging wheel configuration. With sonar technology, the robot is able to avoid obstacles, and is equipped with a camera for the purposes of data collection and mapping the areas of interest (Reddy *et al.*, 2015). As in general subterranean robots need to be capable of operate under a zero-visibility environment, this robot is equipped with an onboard lighting device working in conjunction with an infrared sensor to allow for detection of human body heat and potential fires (Reddy *et al.*, 2015).

Another USRR with water and explosion resistant chassis is reported in (Zhao *et al.*, 2017). The robot is equipped with gas sensors to detect methane, carbon dioxide and oxygen. Infrared sensor and video cameras are used to provide obstacle avoidance function and to obtain real-time footage of the underground condition to the operators. A gyro, an electronic compass with the robot's movement trajectory obtained from its traveling motors is used to solve to localize the robot underground in absence of GPS. A similar concept of USRR, known as the Gemini Scout Search and Rescue Robot, is found in (Quick, 2011). This robot is also equipped with thermal cameras to detect victims, high-resolution cameras for obstacle avoidance, and gas sensors to monitor ambient air quality. It also uses a tethered fiber optic cable for long-range underground communication.

Different from the aforementioned rover type of USRR, multi-jointed snake robot is also used for underground rescue missions. With its multi-joint structure, the robot offers various motion capabilities, including rolling, slithering, and climbing over obstacles (Nichols, 2018). It provides several degrees of freedom that allows it to traverse and manoeuver uneven terrains. The robot is equipped with a camera and a flashlight for obstacle avoidance and victim detection.

3. Proposed Underground Search and Rescue Robot

The proposed USRR is built based on the scenario-based analysis, which was performed for the robot pre-mission, during mission and post mission as shown in Figure 1. This analysis was used to consider in a structured way what the human rescuer needs the robot to do, and output from this analysis helped identify the key functions of the robot and corresponding subsystems, as well as to provide some justification for design targets. The key components identified were the leg modules, chassis, and electronics & control subsystems.

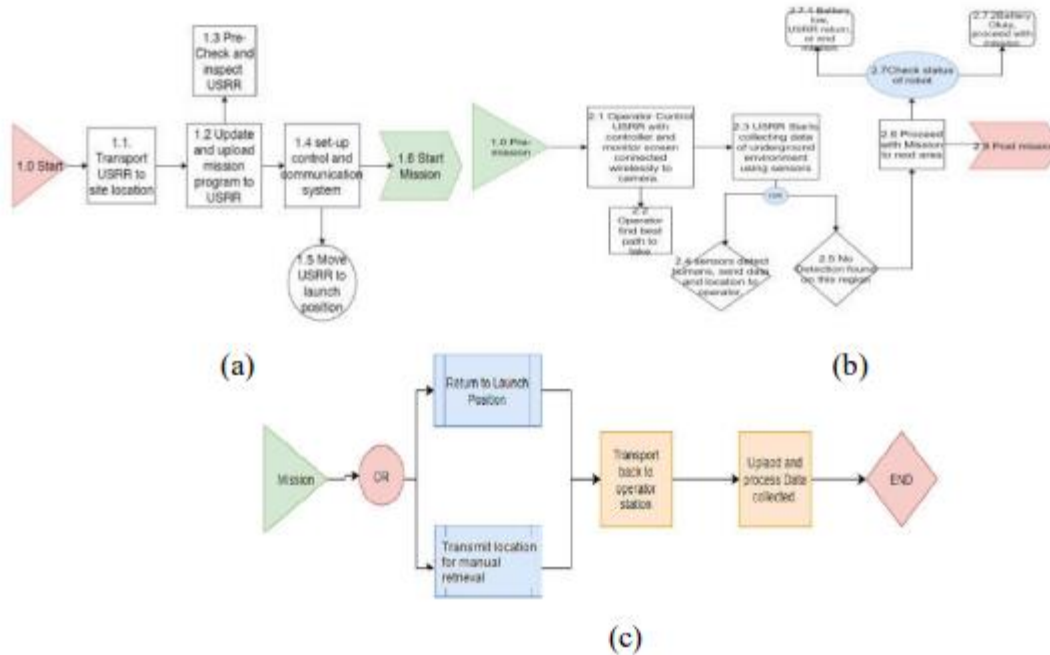


Figure 1. The scenario-based analysis of the proposed USRR for (a) pre-mission, (b) during mission, and (c) post mission

3.1 Leg Module and Gait Motion

The proposed robot is designed to mimic a spider but with six grasshopper-like legs. Each individual leg consists of three segments including the coxa, femur and tibia, as shown in Figure 2. Coxa or base joint provides horizontal motion for the robot to traverse in forwards and backwards directions. The other end of the coxa is connected to the femur, which provides the robot vertical motion at the hip joint. The femur also acts as a connection between the coxa and tibia assisting in rotational motion of the tibia. The tibia is connected to the femur/hip joint forming a revolute pair in the vertical direction, known as the knee joint. This provides three degrees of freedom to one leg and 18 DoF to the overall system. At the end of the tibia, an interchangeable tip is attached, allowing the robot to navigate to various terrains, and providing ease of maneuverability as well as friction to avoid slipping. The robot can adjust its height to prevent the base of the chassis from touching the surface of the terrain and to allow the legs to contract when encountering tight and narrow areas.

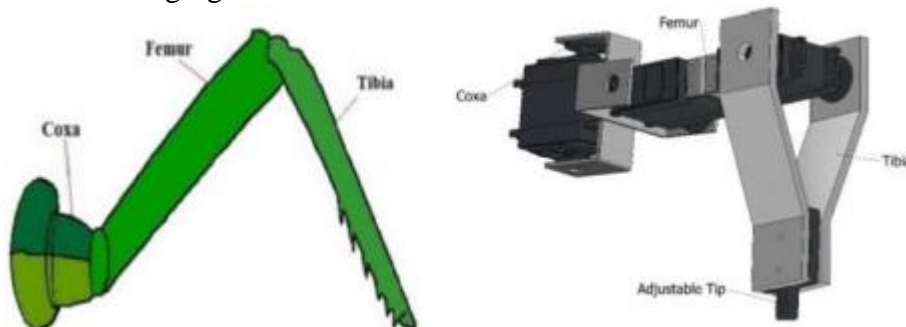


Figure 2. Grasshopper leg structure (Moldovan, 2012) (left) and the proposed Grasshopper-like robot (right)

Three smart servos SCS115 are used in each leg. This type of servo provides a relatively high torque (of 15kg.cm) and position, temperature, speed and voltage feedback. It allows for a rotational motion of 0 - 200°. The servo uses asynchronous serial bus communication, which has the ability to connect up to 253 SCServos to a single serial bus communication network, and they can be controlled either together or independently.

Tripod gait is used to provide stability and optimal speed for the hexapod. Gaits affect the relationship between the motion of the robot and changes in speed and phase. Different gaits result in different speeds and stability characteristics. For instance, the fewer legs on the ground while in stance mode, the faster the robot will be with a reduction in stability and vice versa. The proposed hexapod leg module configuration is shown in Figure 3.

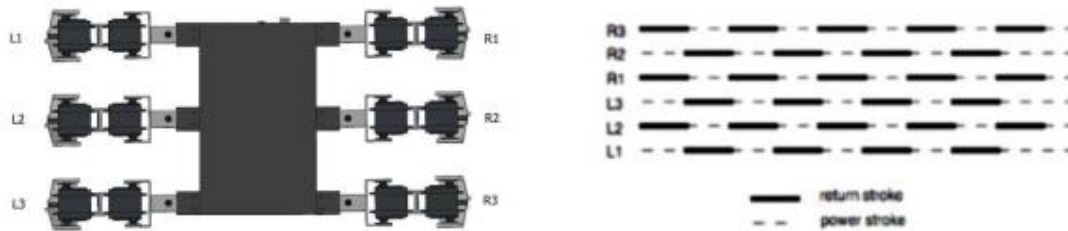


Figure 3. Hexapod leg module configuration and its gait pattern, known as the tripod gait (Wilson, 1966) (right)

Finite element analysis (FEA) was performed to select the materials used for the legs and their structural integrity. The analysis shows that the legs assist each other in carrying a payload when all six legs are on the ground and when only three legs are supporting the payload. The results show that the legs are able to support the robot with the maximum principal stress of less than 0.186 MPa, as shown in Figure 4. Based on the analysis, carbon fiber is selected as the suitable material for the legs as it provides the lowest maximum principal stress and total deformation.

3.2 Chassis

The hexapod required a suitable chassis to house all the necessary components and payloads. This chassis will be the load-bearing platform of the robot, hence directly affecting the robot's stability during operation. The rectangular shape chassis is used to provide sufficient space for all the electronics and power supply module. It is relatively simple to manufacture and stable when the ratio of the femur/tibia link is greater than 0.4 (Saranli *et al.*, 2001). The chassis has protruding parts for attaching three motors on each side. This provides greater degrees of freedom to adjust the angles at which the coxa can be placed to achieve structural stability.

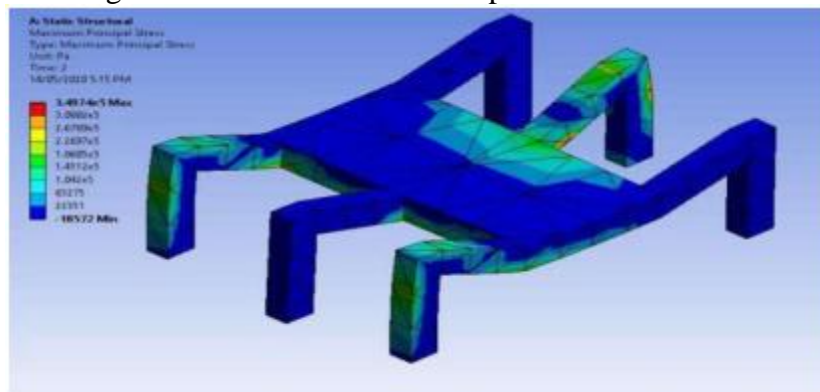


Figure 4. FEA analysis of the hexapod with carbon fiber

3.3 Electronics and Control System

The electronics and control system comprise of microcontrollers, actuators, power system, sensors, bluetooth module and signal conversion board. The block diagram of the control system architecture is shown in Figure 5.

The electronics consists of a 7.4V LiPO connected directly to a signal conversion board also known as the TTlinker board. This signal conversion device can control 18 SCservo motors simultaneously. The Arduino Mega is connected to the TTlinker board via the serial communication port 'Tx' and 'Rx'. HC-10 Bluetooth module is also connected to the Arduino Mega to enable manual control of device using a mobile phone. The Arduino Mega is powered by a 9V External power source. All the detecting sensors are connected to the Arduino Uno. The detection sensors include CO₂, humidity sensor, proximity sensor and a thermal camera.

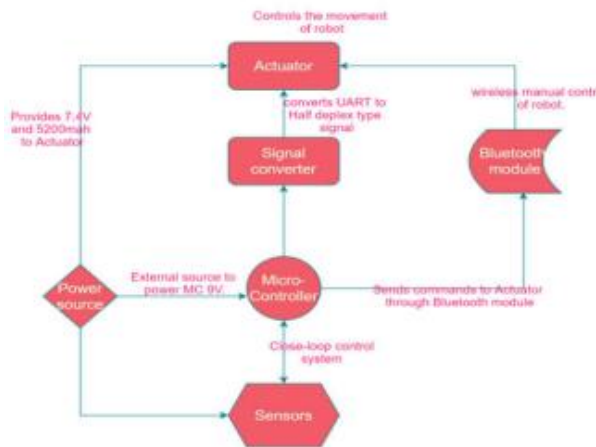


Figure 5. Control Architecture

this information to the Master Arduino Mega. The former is chosen due to its 20 digital I/O pins, of which six can function as Pulse Width Modulation (PWM) and six can be used as analog inputs. It also features a 16 MHz resonator and an ATmega16U2 programmed as a USB-to-serial converter. To use the Arduino Mega to control the SCServo motor motion, a signal conversion device called TTlinker board is used to convert UART signal to HALF Duplex type. This enables the microcontroller to communicate with the SCServos.

3.3.2 Power Source

The main power supply used is a Lithium polymer battery, which provides a maximum voltage of 7.4V with 5200mAh capacity. The maximum continuous operational time of the robot with such power supply is 30 minutes.

3.3.3 Software

Multiple softwares, including Arduino IDE, SCServo Debug and Dable, are implemented to achieve complete control, motion and functionality of electronics platform and mechanical structure of the robot. Dabble is a mobile application interface that connects wirelessly to Arduino mega using HM-10 Bluetooth module. The Dabble application has a gamepad configuration that is reprogrammable using Arduino IDE to control the movement of the robot.

3.3.4 Sensors

Two sensors are installed on the robot, including CO₂ MH-Z16 sensor, which measures the concentration of carbon dioxide with a high sensitivity and resolution, and the D6T-8L-06 thermal sensor, which can detect stationary and moving human presence through non-contact temperature measurement with relatively high accuracy and low noise, humidity sensor, as well as an Arduino smart camera. The thermal camera's detection result is shown in Figure 6.

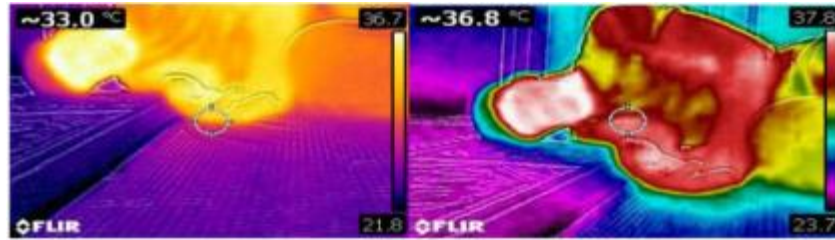


Figure 6. Thermal camera detecting the presence of a man lying on the ground

4. Overall Robot Architecture and Performance

The overall robot architecture is shown in Figure 7.

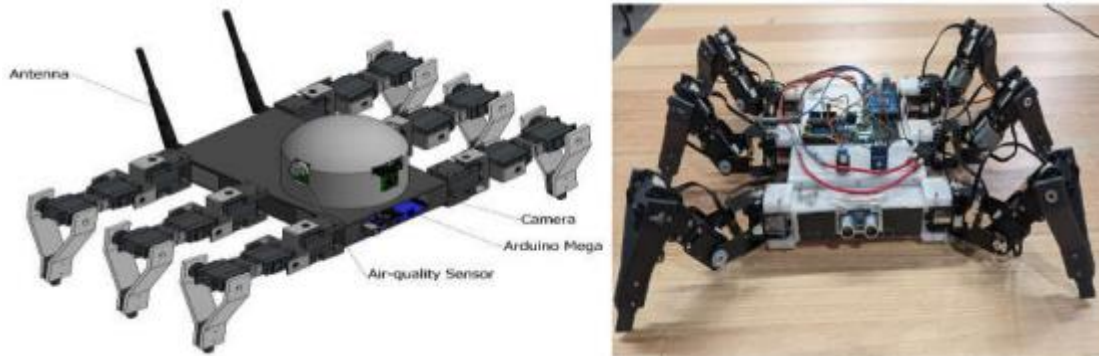


Figure 7. The proposed hexapod USRR

The robot has been tested on various terrains, such as concrete, carpet, glass and tiles as shown in Figure 8. The maximum speed for those terrains (for a continuous 30 minutes operation) are 0.19, 0.37, 0.40, and 0.22 m/s, respectively. Furthermore, the robot can operate with a maximum speed of 0.74 m/s on rough surfaces for approximately 4 minutes.

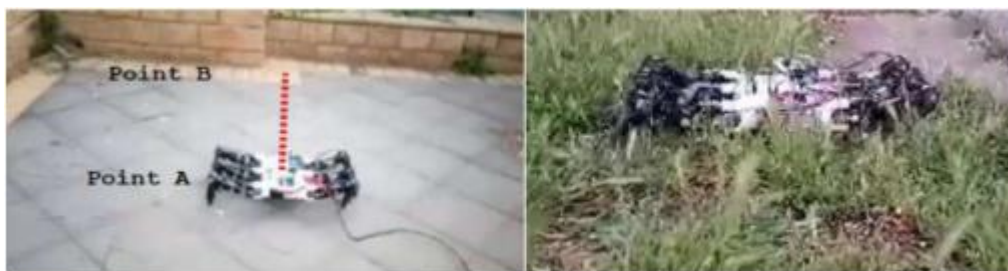


Figure 8. The proposed hexapod on rough surfaces, such as (left) concrete and (right) grass

Red zone area testing is performed to evaluate the performance of the robot. Red zone areas are high priority areas in search and rescue missions where entrapment of people is more probable based on the data collection of the robot. These areas are determined using a fuzzy logic gate control. The floor plan or building map of the rescue area must be present before commencing rescue operations.

The map is split into separate zones in which the USRR will traverse and navigate to detect humans. The zones will then be classified as a red zone should it satisfy any of the following conditions:

- Both the CO₂ sensor and humidity sensor reach a certain threshold of 450ppm or more and 66% or more, respectively.
- An instantaneous rate of change of 100ppm for the CO₂ sensor or 9% change in relative humidity level for the humidity sensor.
- Thermal camera picks up heat signatures of human body parts.

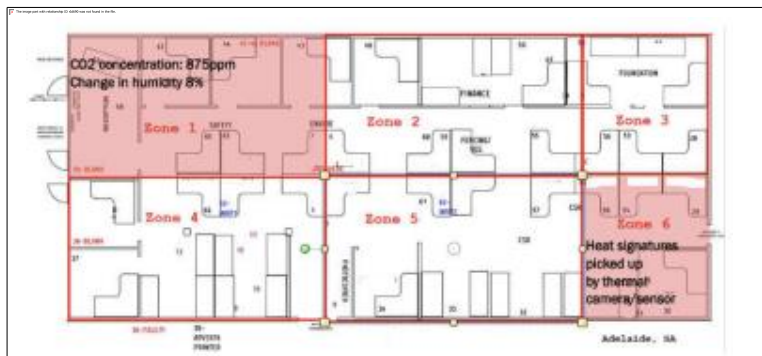


Figure 9. Red zone area testing

wirelessly when the robot is untethered. The buzzer module houses a receiver set to a specific frequency to receive signals. An example of the testing on a site office located in Kilburn, Adelaide is shown in Figure 9 with the implementation of red zone mapping based on data collection from the robot. The robot was able to detect the human presence in Zone 1 and Zone 6 based on the detected CO₂ concentration and heat signature from the thermal camera, respectively.

Multiple tests have been conducted at different ranges from the sensors equipped on the robot for measuring the average concentration of CO₂ in the air, average relative humidity and the temperature output from the thermal camera for different body parts. It is observed that the CO₂ concentration increases to about 450ppm on average and the relative humidity level is close to 66% when detecting a human underground. Additionally, thermal imaging tests suggest that the hand and face are the most sensitive body parts when in the field of view of the camera with an average thermal heat temperature output of 35 degrees Celsius.

5. Conclusion

The hexapod robot for underground search and rescue mission proposed in this paper has been successfully built and demonstrated its efficient operation and manufacturing simplicity, manoeuvrability and spacing functionality. The leg and gait motion, chassis, electronics and control of the USRR have been discussed. We presented a successful integration and implementation of a viable detection system including sensors and camera modules, as well as the CO₂ sensor, humidity sensor, and thermal camera, that enables the robot to detect trapped humans in dark and confined spaces, such as underground.

References

- [1] Bartels, S & van Rooyen, M 2012, "Medical complications associated with earthquakes", *The Lancet*, vol. 379, no. 9817, pp.748-757.

- [2] EM-DAT (2019), CRED / UCLouvain, Brussels, Belgium – www.emdat.be (D. Guha-Sapir) (accessed on 31 May 2020)
- [3] Moldovan, F., Dolga, V., Sticlaru, C. (2012) “A New Type of Walking Robot Based upon Jansen Mechanism”, *Advanced Materials Research*, Vols. 463-464, pp. 997-1001.
- [4] Nichols, G. (2018), “Snakebot Named Ground Rescue Robot of The Year”, ZDNet, available at
- [5] <https://www.zdnet.com/article/snakebot-named-ground-rescue-robot-of-the-year/> (accessed on 31 May 2020).
- [6] Quick, D. (2011), “Gemini-Scout mine rescue robot to lead the way to trapped miners”, available at <https://newatlas.com/gemini-scout-mine-rescue-robot/19543/> (accessed on 31 May 2020).
- [7] Reddy A.H., Kalyan B., Murthy C.S. (2015), “Mine Rescue Robot System—A Review”, *Procedia Earth Planet. Sci.* 11:457–462.
- [8] Saranli, U., Buehler, M., and Koditschek, D. (2001), “RHex: A Simple and Highly Mobile Hexapod Robot”, *The International Journal of Robotics Research*, vol.20, no.7, pp.616-631.
- [9] Walker, J. (2019), “Search and Rescue Robots – Current Applications on Land, Sea, and Air”, available at <https://emerj.com/ai-sector-overviews/search-and-rescue-robots-current-applications/> (accessed on 31 May 2020).
- [10] Wilson, D.M. (1966), “Insect Walking”, *Annual Review of Entomology*, Vol. 11, pp.101-122.
- [11] Zhao, J., Gao, J., Zhao, F., and Liu, Y. (2017), “A Search-and-Rescue Robot System for Remotely Sensing the Underground Coal Mine Environment”, *Sensors* (Basel, Switzerland), 17(10), 2426.

Laser-equipped Drone for Weed Management

R. Akmeliawati*, N. Sergiienko, L. Verbi, L. Hunter, A. Scarfo, C. Alt, B. Pedler
School of Mechanical Engineering, The University of Adelaide, Adelaide, Australia SA 5005

*Corresponding author. E-mail: rini.akmeliawati@adelaide.edu.au

Abstract

Weed control is an expensive process in agriculture due to two main factors, consumables and labour. To obtain a significant saving for the grower, consumables need to be optimised and labour minimised or eliminated. Agriculture in is a significant contributor to Australia's national economy, directly accounting for 2.7% of Gross Domestic Product and 2.5% of employment in 2016-17. In this paper, we demonstrate the potential of an autonomous airborne weed control unit utilising laser technology to control weeds. This work involves design and finite element analysis of the drone and laser-targeting system. A 1 mW laser, mounted on a drone, is powerful enough to be clearly visible from the camera at the desired flight altitude, and has the capability to be remotely triggered by the pilot. The drone is designed to be strong and lightweight as well as to provide sufficient stability and manoeuvrability. Flight tests have been conducted and the overall system can achieve an average of 3 cm accuracy with 3 m flight altitude. The proposed laser airborne weed control utilises a video camera, a LiDAR to measure the altitude of the drone and a micro servo to actuate the laser to target weeds with high accuracy and reliable operation.

Keywords: Weed management, Drone, Laser, Hexacopter

1. Introduction

Agriculture is a large industry in Australia, and as such any reduction in losses will be immensely beneficial to the industry. The use of chemicals in weed management costs the Australian agricultural industry approximately \$1.7 billion a year on average (McLeod, 2018), with 60% of the costs attributed to the growth of wheat and other grains. Additionally, \$2.7 billion is spent on non-chemicals: manual labour, fuel, and maintenance, contributing to a total loss of over \$4 billion a year for weed management.

Uncontrolled noxious weed growth is one of the major detriments in the agricultural industry, causing a reduction in both the yield and quality of crops growing. This is largely due to the competition for nutrients and space between the crops and weed. As a result, action must be taken to carefully control the environment in which the crops are growing. This action is usually performed via manually removing or spraying the weeds when the crops are initially planted, but this results in a large expense of both time and money. The use of manual labour to remove harmful weeds is detrimental in both time and cost effectiveness, leaving a possibility to explore alternate methods.

Throughout the years, the use of herbicides has proven to be an effective method of eliminating weeds in many areas, not just in agriculture, but as is the case with chemicals there is a possibility of adverse effects to non-targeted items. Latha and Gopal (2010) showed after the application of herbicide reduces the population of all bacteria in soil, and only when the concentration of the herbicide was at a concentration of one field rate, was the population able to recover within 30 days. Sanyal and Shrestha (2008) also addressed the issue of herbicide application contributing towards crop diseases and pathogens. Although these interactions can be understood, they have not been completely mapped, and any unknown reactions can prove disastrous towards the crop. As such there is a unique opportunity to develop a non-chemical

method of weed management to reduce the environmental impact directly seen from the use of herbicides.

According to Krishnan (2018), the most widely used weed killer is an herbicide named glyphosate, which interferes with an enzyme that makes amino acids. The crops that have this herbicide sprayed on are often genetically modified such that they are glyphosate resistant, but this is not the case for other plants and organisms in the area. In 2009, the Environmental Protection Agency (EPA, 2020) initiated a review into the hazard that glyphosate could pose to humans, non-target plants and wildlife, as well as a variety of other potential risk factors. This review has continued to the current day with required management measures of the herbicide to keep the risk from exposure to all effected parties low to non-existent. Even with these measures in place, there is still a chance that an unknown reaction could be caused from the application of glyphosate or any of the other herbicides used in the industry. As such there is a unique opportunity to develop a non-chemical method of weed management to reduce the environmental impact directly seen from the use of herbicides.

The method of managing weed growth is generally left to herbicide or mechanical removal. An alternative to chemical or mechanical control is to utilise a laser to shock the foliage and root system of the plant. Mathiassen *et al.* (2006) investigated the effects considering variations in laser power, wavelength, exposure time and spot size for the particular weeds investigated. The findings concluded that for the 5W laser used, control of the specific weeds was possible while only allowing under 1 s of exposure times. However, suggestions were made for further research into different species of plant in addition to power levels and wavelengths of the laser. Research and development continued to achieve optimised performance discussing results from use of a CO₂ (Carbon Dioxide) laser by Marx *et al.* (2012). Using a total period of 108 ms with pulses between 5 and 320 s, a success probability greater than 95% was desired. For monocotyledonous plants, a minimum energy level of 54 J was found to be adequate in early growth. However, high density control scenarios were suggested to be not feasible for laser control in addition to the consideration of legal and size issues with implementing a laser capable of such available energy.

In this paper, we propose a laser airborne weed control (LAWC) which is a remotely operated drone capable of controlling weed growth with an integrated laser-targeting system (LTS). The drone is capable of identifying and targeting weeds to eradicate them from the air with a laser in real-time. This paper is organised as follows. In Section 2, the details of the drone design are presented. Section 3 presents the laser-targeting system. The testing results of the overall system is presented in Section 4. We conclude this paper by highlighting the merit of the created weed management system in Section 5.

2. Drone Design

The proposed LAWC platform is a hexacopter with a mass of 4 kg. It has been selected as the drone for our proposed system as it provides relatively better stability and efficient flight in comparison to other types of rotorcrafts. The system is shown in Figure 1. Airframe subsystems constituting arm assembly and landing gear.

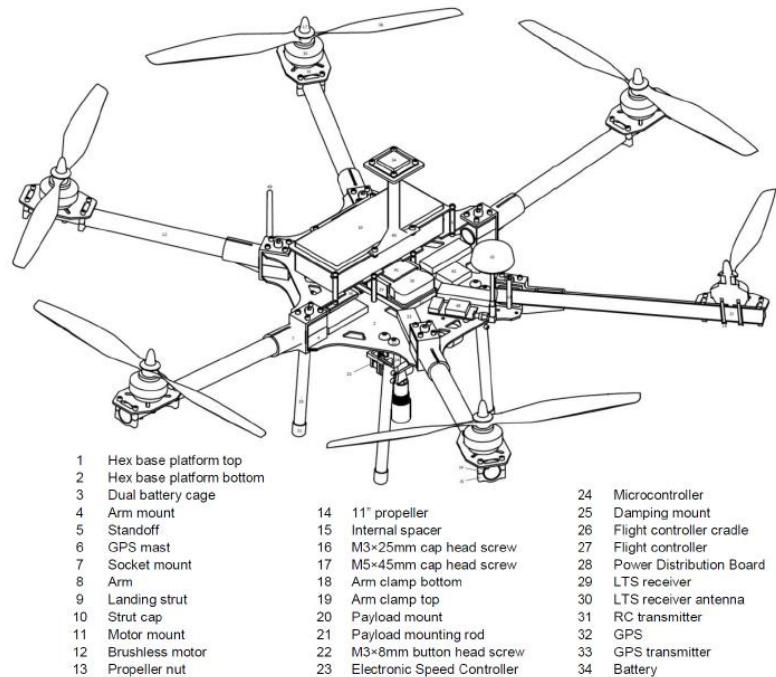


Figure 1. The LAWC

2.1 Airframe Design

The main airframe, which consists of the six arms, is made of pull braided carbon fiber tubes. Other parts such as the arm connectors are made of aluminum alloy and 3D printed PLA. Aluminium parts, mostly mounts and brackets, are manufactured from stock aluminium billet. A symmetric airframe is designed to ensure the centre of gravity coincided with the airframe centroid. In the transverse axis, shown in Figure 2, the centre of gravity is in line with the total airframe centroid. In Figure 2, the centre of gravity is desired to be below the motors. This is necessary to ensure static flight stability necessary for accurate laser targeting. Finite Element Analysis (FEA) has been used to investigate the structural and modal characteristics of the design. Stresses in the arm assemblies for each configuration are verified in static structural FEAs. Each model used unlayered 230 GPa woven carbon fibre.



Figure 2. Centre of gravity of the LAWC, side view

The design consists of 6 arms with the dihedral angle of 5°. Dihedral angle is the angle of elevation of the drone arm and its corresponding motor as shown in Figure 3. The advantages of this design are increased yaw responsiveness and greater stability from disturbances. It also aids in dispersing down-wash spread, which can help protect sensitive payloads such as gimbals from turbulence from the motors. However, this comes at a small loss of vertical thrust of 8.7% due to horizontal thrust component introduced by the angle dihedral. At larger angles, the motor dihedral is also susceptible to greater cross axis error, which occurs when a roll and a yaw response is induced by a disturbance on the drone. Dihedral design is typically used in bigger hexacopters or octocopters due to their larger moment arms and greater resistance to cross axis error.

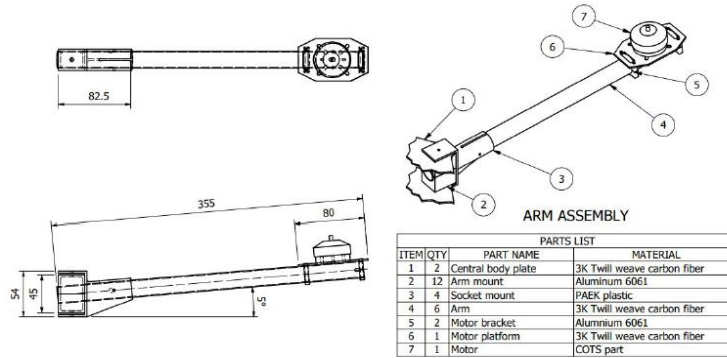


Figure 3. Hexacopter arm with the 5° dihedral angle

During laser-targeting operation, the LAWC will be hovering from an altitude of 2 to 3 m. Consequently, vibrations induced by the motors and propellers will be transmitted through the airframe to the laser-targeting system (LTS). Comparing natural and pre-stressed modal frequencies allows the critical frequencies in the airframe during hover to be determined.

The modal analysis without pre-stress has been conducted (using ANSYS) on the simplified 1/3rd airframe model to determine its natural frequencies. The model consists of two arm assemblies connected by a 120°, or 1/3rd section of the top and bottom hex base frame platforms (refer to Figure 4). This sectioned model is necessary to achieve solution convergence without exceeding node limitations. The 11" nylon propellers are modelled with rotational constraints about the centre of the equivalent motor. A rotational velocity is applied to each propeller in opposite directions at the no-separation connection site. A magnitude of 573 rad/s, or about 5500 rpm, is evaluated using manufacturers' motor thrust tables and system requirements for the thrust-to-weight ratio, assuming an estimated LAWC weight of 4 kg. The natural and pre-stressed modal frequencies in the airframe are simulated for the first 20 vibration modes. The mode is shape for the damped frequency of 101.1 Hz. At the motor operating frequency, 5500 rpm or 91.7 Hz, there is a low risk of resonances amplifying in the airframe. However, the pre-stressed frequency is significantly close to the motor hovering frequency. Consequently, the airframe is predicted to resonate at the 7-th to 8-th mode pre-stressed frequency. The corresponding vibrations are thus mitigated using dampers in the mount of the LTS. Low stiffness rubber vibration isolation mounts are used to dampen these vibrations and prevent oscillations in the laser which would impinge accuracy. These would interface with the bottom of the gimbal and payload mounting platform.

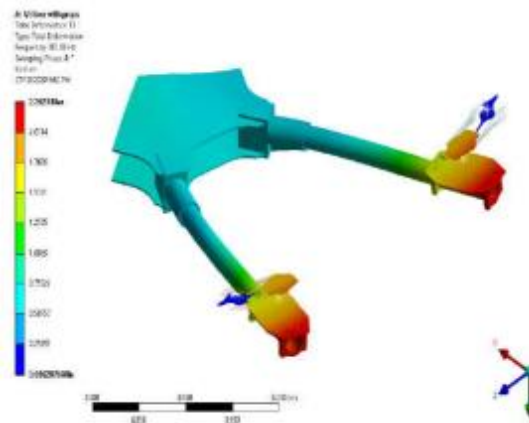


Figure 4. Airframe mode shape at excitation frequency 101 Hz

2.2 Propulsion and Power Systems

The drone is powered by six motors (SunnySky X3508S brushless DC motors) and their corresponding 9 inch-propellers, which provide the total thrust so that the thrust to weight ratio is

2:1 in order to obtain the industry standard optimal total thrust. The drone is powered by one 10,000 mAh 4S LiPo battery to satisfy the maximum electrical supply required for all electrical components is 9841 mAh with a 20% safety factor for 10 minutes flight duration.

2.3 Flight Controller and Telemetry System

A Pixhawk flight controller has been considered due to its full range of customisation and the tuning that it allows. Equipped with accelerometers, a gyroscope, magnetometer and a barometer, the Pixhawk provides most of the sensors required for control of the aircraft; however, an external compass module has been added for improved redundancy. Positioned in the centre of the aircraft, the Pixhawk is accessible by the surrounding ESCs, the payload beneath, and the batteries above. The rotorcraft can operate with only one 10,000 mAh 4S LiPo battery. As the sensors are already integrated in the Pixhawk itself, the use of sensors as an input for the control of the motors is greatly simplified. The controller is also capable of remote communication through the MAVLINK messaging protocol and paired with a ground controller or portable ground control unit (GCU). This allows all the data recorded by the Pixhawk sensors to be transmitted to the pilot and displayed on the GCU. The footage capture by the payload camera is also set up to be received by the pilot on a small, portable screen. The combination allows the pilot to completely understand the movement of the aircraft without having direct visibility of the aircraft.

3. Laser-Targeting System

The laser-targeting system consists of the laser, camera and laser mounting platform. It is designed to satisfy the payload requirements while minimizing total payload weight. The laser is placed at a particular distance from the line of sight of the camera. To simplify the laser actuation, the design will need to minimize the number of degrees of freedom it controls. Aircraft height will determine what corrective laser angle is required from the actuator; thus, a height sensor system is required. Outdoor range sensors are ideal for the target environment as their ideal operating range in broad daylight is within the designed altitude envelope. The systems relationship is detailed in Figure 5, which portrays how the height at which the payload is positioned above the ground surface directly affects the laser angle. Hence, for a varying height, a variable laser angle is required for optimal accuracy.

3.1 Laser

Micro-Laser Module from Digi-Key electronics is used as the laser source since it is extremely compact and has an integrated automatic power control circuit. The relay is utilized to provide a more efficient power shared with the rest of onboard electronics. It is digitally switched by a microcontroller when a logic signal is received from the flight controller auxiliary output. Despite being low power, laser activation still raises safety concerns, and as such a 570 nm laser is desired as it produces a green light which is highly visible. In our case, we utilize a 532 nm laser with the power of less than 1 mW. At this stage, the power level is sufficient to cripple the targeted weeds.

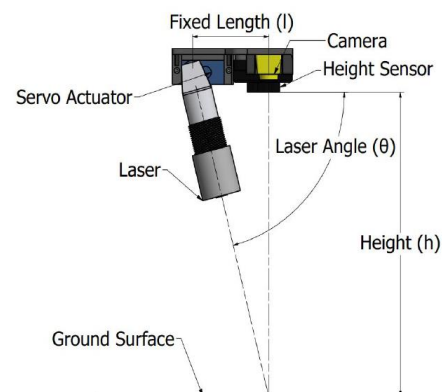


Figure 5. Laser-targeting system

3.2 Camera

Visual telemetry is provided from a First-Person View camera. These are compact, inexpensive and lightweight and are thus utilised in drone applications. To determine the suitability of the camera, the Ground Sampling Distance (GSD) parameter is utilised. The GSD is a measurement of the distance between the centre of adjacent pixels for an image taken directly above a ground surface. The camera specific parameters of the GSD equation (focal length, sensor size and image size) will typically be predetermined for commercially purchased cameras and can only be varied within small ranges. Since different cameras have varying values for these parameters, there may be a level of compromise required to find the optimal design choice. To minimise GSD, a large focal length is required, however this also reduces the field of view. A large field of view expands the coverage area of the camera, minimising the frequency with which the pilot needs to move the aircraft to a new viewing location. In addition to aforementioned factors, the flight height parameter may be dependent on the surrounding environment, or possibly laser requirements, and hence is likely to vary.

3.3 Laser Mounting Platform

The laser mount is designed to control the position of the laser to target the weed. The mount is shown in Figure 6. To control the rotation of the laser a 9G Micro Servo and Arduino are utilized. It is capable of high torque outputs while maintaining high accuracy (0.1°). The laser control system has capability for safety protocols such that the laser may be inoperable if certain conditions are met. The flight controller can output roll and pitch values to the Arduino. and in the case of rotation angles greater than 10° , the laser will turn off such that no bystanders are injured.

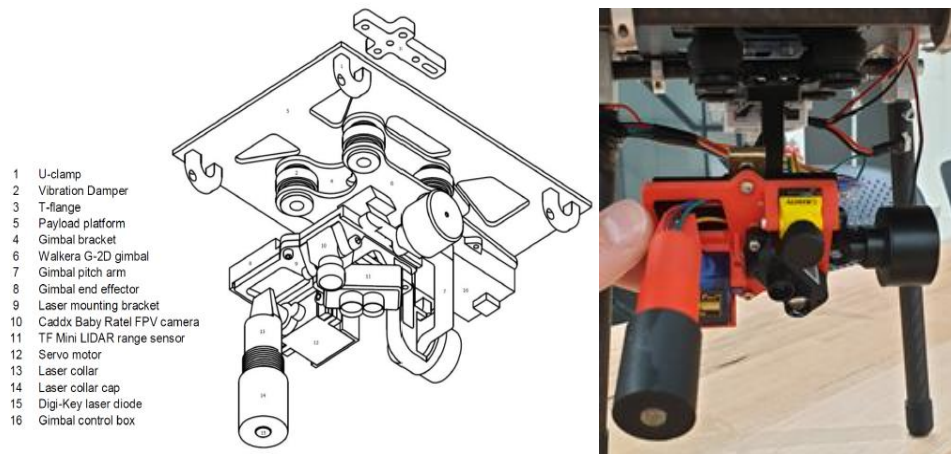


Figure 6. Laser mounting platform

4. Flight Tests and Results

The static testing procedure involves testing the accuracy of the laser targeting system while the LAWC prototype is not in flight. The LAWC prototype with mounted LTS is attached and positioned at varying heights from 2 to 4 m directly above a grid target. Camera telemetry is transmitted to the receiver monitor operated by the pilot. The target centre is re-positioned directly under the centre point of the camera sensor using prompts from the pilot. This process is designed to simulate the pilot positioning the aircraft directly over a weed, using the camera as a visual aid. Once in position, the laser is activated to illuminate a dot on the target. The results are shown in Figure 7.

The dynamic tests have been conducted and the LAWC can achieve a stable flight in excess of 3-min intervals both with and without the LTS. A flight path obtained from the GPS during the dynamic test is shown in Figure 8.

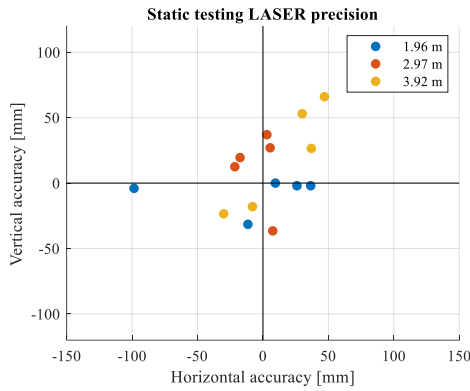


Figure 7. Static test for testing the laser precision

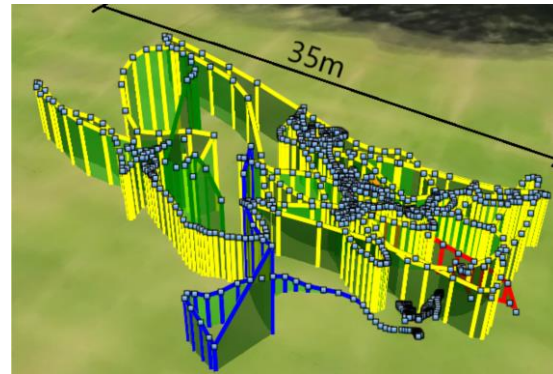


Figure 8. Flight path during dynamic tests

5. Discussion

The scope of work completed in this project was largely focused on producing a working laser targeting system, a supporting airframe and a sufficient propulsion and control system. Integrated avionics and brushless motors with 9" propellers provided a flight time of up to 10 min per battery. The results show a mean spread of 2 to 3 cm of the laser dot. The inaccuracies are largely attributed to gimbal actuations and insufficient fidelity in the LTS servo. In dynamic tests, the LAWC prototype achieves stable flight both with and without the payload.

6. Conclusion

The LAWC proof-of-concept is the first step towards an alternative, environmentally friendly and cost-effective weed management scheme. This project aimed to design, build and test this proof-of-concept to verify the LAWC's capability to simulate the accurate targeting of invasive weed species. The LAWC prototype is split into the LTS, airframe, propulsion, avionics and telemetry subsystems. The LTS, the centre piece of the LAWC, employed gimbal stabilization and autonomous height adjustment abilities. The developed LAWC strives to evolve into a fully autonomous system capable of selectively eliminating weeds over large agricultural fields.

Future work will be dedicated to the automation of both the targeting system and the navigation system. Through computer vision technology, the camera will be able to detect weeds and trigger the laser to fire without assistance from a human pilot.

Acknowledgments

The authors would like to thank the School of Mechanical Engineering and Unmanned Research Aircraft Facility (URAF) of the University of Adelaide, American Institute of Aeronautics and Astronautics (AIAA), and Toptek Composite for the financial and in-kind support as well as expert advice.

References

- [1] EPA (2020), “Glyphosate Environmental Protection Agency,” available at <https://www.epa.gov/ingredients-used-pesticide-products/glyphosate> (accessed 3 October 2020).
- [2] Krishnan, N. (2018), “The environmental impact of the world's most famous weed killer envirobites”, available at <https://envirobites.org/2018/01/19/the-environmental-impact-of-the-worlds-most-famous-weed-killer/> (accessed 3 October 2020).
- [3] Latha, P.C. and Gopal, H. (2010), “Effect of herbicides on soil microorganisms”, *Indian Journal of Weed Science*, 42(3&4), pp.217-222.
- [4] Marx, C., Barcikowski, S., Hustedt, M., Haferkamp, H. and Rath, T. (2012), “Design and application of a weed damage model for laser-based weed control,” *Biosystems engineering*, 113(2), pp.148-157.
- [5] Mathiassen, S.K., Bak, T., Christensen, S. and Kudsk, P. (2006), “The effect of laser treatment as a weed control method”, *Biosystems Engineering*, 95(4), pp.497-505.
- [6] McLeod, R. (2018), “Annual Costs of Weeds in Australia”, eSYS Development Pty Ltd, Centre for Invasive Species Solutions, Canberra, Australia.
- [7] Sanyal, D. and Shrestha, A. (2008), “Direct effect of herbicides on plant pathogens and disease development in various cropping systems”, *Weed Science*, 56(1), pp.155-160.

A Smart Assistant Tool for Ship Machinery Arrangement Using Genetic Algorithm

Trinh Duc Minh¹, Nguyen Duy Anh¹, Tat-Hien Le^{1*}

¹Department of Naval Architecture and Marine Engineering, Ho Chi Minh City University of Technology, Ho Chi Minh City, Vietnam

First author: tdmh.sd20@hcmut.edu.vn; Second author: duyhanhnguyen@hcmut.edu.vn

*Corresponding author. E-mail: hienlt@hcmut.edu.vn

Abstract

The shipbuilding industry is now operating in a competitive market, shipbuilders aim to reduce production time and costs, while making sure the design idea is good enough to avoid serious mistakes. Generally, facility layout problems of the machinery arrangement design are very complex, and needs a lot of man hours. Also, engineers must consider the space allocation of equipment to ensure the pipe route is optimal. In the preliminary design stage, the ship's engine room layout and pipeline routing depend a lot on engineering experiences. This study proposes an optimization algorithm for equipment arrangement in order to meet the design constraints and pipeline route in a ship engine room using the Dijkstra and optimization technique integration. A genetic algorithm was adopted to explore solutions in the search space. The results of layout design optimization will be transferred to the CAD for design team.

Keywords: Layout design optimization, facility layout, machinery arrangement, pipe route

1. Introduction

Due to the direct and tight connection to the efficiency operation and production costs of propulsion system, the arrangement of the machinery parts in a ship's engine room has always been considered a challenging and complex process. Thus, automatic equipment arrangement and pipeline routing in ship engine room has been a topic of interest to many researchers over the last decade [1–7]. In addition to the technical requirements for operation and maintenance, the arrangement of the machinery parts is also analyzed to ensure safety constraints, production costs, as well as routing problems of pipes. This implies that the machinery arrangement is a multi-objective optimization problem with several constraints. In this paper, a new approach is proposed to properly arrange machinery parts and design piping route based on genetic algorithm in order to equip designers with an intelligent tool at the preliminary design stage. Two objective functions related to the optimization of pipe routing and equipment layout area are formulated. In addition, the constraints defined from technical requirements and design criteria are also included in the optimization problem. Nondominated Sorting Genetic Algorithm (NSGA-II) is then employed to solve the multi-objective optimization problem because of its power and reliability [8].

2. Problem Formulation

The tool aims to shorten design time and costs, assists engineers in exploring potential solutions in the preliminary design phase. The equipment and pipes will be arranged automatically and simultaneously with respect to the minimization of following two objective functions:

The first objective function is pipe connection costs, as shown in Eq. (1):

$$f_1 = \sum_{i=1}^N \sum_{j=1}^N RM_{ij} \times L_{ij} \quad (1)$$

where i and j are machines, RM_{ij} is the weight factors, show relationship between i and j that can be scored by experts and designer to show their design recommendation, the RM_{ij} values and their meanings proposed by Lee et al [9] can be used to score the weight factors in this study. L_{ij} is the length of the pipe connecting i and j .

The second objective function is space costs. This objective calculates the ratio between the total area that is not used by the facilities and the total area enveloped by the facility layout. Since the total area of the components is constant, the only way to minimize this function is to place the facilities closer together to reduce the total area of the arrangement, which is given by Eq. (2).

$$f_2 = \frac{A_{unused}}{A_{envelope}} = \frac{A_{envelope} - A_{components}}{A_{envelope}} \quad (2)$$

where $A_{envelope}$ is the minimum space required for the equipment arrangement and $A_{components}$ is the total area of the machines to be arranged in the engine room.

In addition to the minimization of objective functions, the optimization problem must satisfy the following constraints, which will be solved in section 3:

- The guarantee of adequate space for operation, maintenance, repair, walkways, emergency exit. Those constraints could be considered as overlap constraint.
- Piping must be arranged optimally without collisions with minimum lengths and minimum bends while meeting a number of engineering rules.

3. A Smart Assistant Tool

In this section, the implementation of the tool will be briefly described, the model is developed to satisfy some predefined constraints in section 2, objective functions will be minimized using NSGA-II algorithm.

3.1 Propose a new design method

Figure 1 depicts the design process of the proposed method. Thereby, engineers can interact with tools, called human-computer interactions to come up with design concepts. This approach allows vessel data and constraints to be added according to specified requirements and client's preferences [10]. The tool will assist engineers to refer and make effective design plans in a short time. The optimal layout concept is then transferred to Cad drawings.

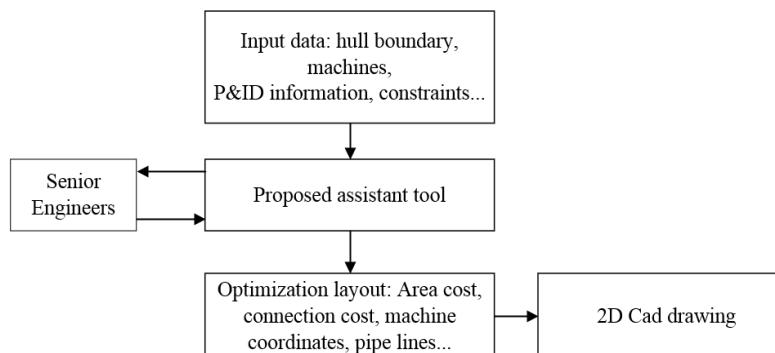


Figure 1. Proposed design method

3.2 Gene representation

Figure 2 shows how to represent machines in this paper. Each machine is represented by a rectangle that surrounds itself, position of the machine is represented by the center of gravity coordinates. Connection gates are represented by inlet and outlet coordinates. The dashed line indicates space required for operation, maintenance and safe distance around the equipment.

Yarpiz proposed a simple method to enforce overlap constraint [11]. Figure 3 shows an example of a solution violating overlap constraint. Potential solutions that violate this constraint will be discarded.

Figure 4 depicts the decoding process of a chromosome to layout, each gene consisting of 3 components X, Y, R, where X, Y are machine central coordinates, and R is direction of rotation. In this case, the chromosome consists of 5 genes representing a layout of 5 machines in engine room. The minimum envelope line describing minimum area required for the machinery arrangement space.

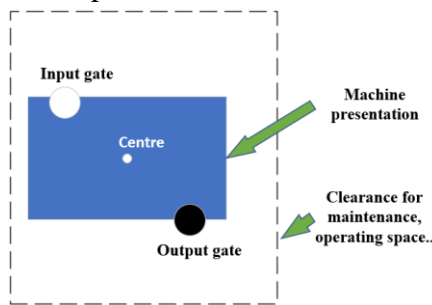


Figure 2. Machine layout representation

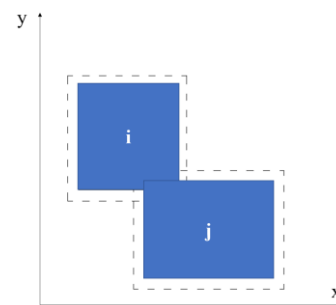


Figure 3. Solution violated overlap constraint

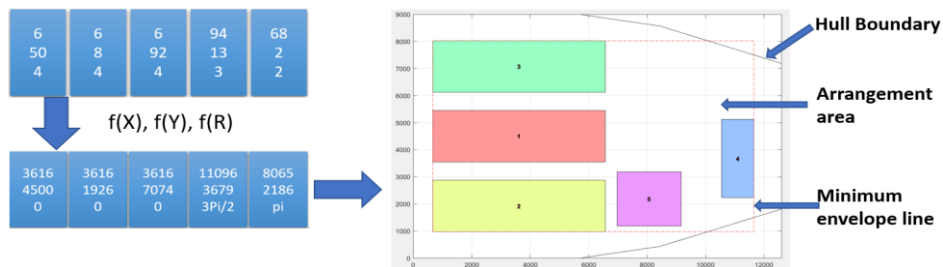


Figure 4. Solution representation

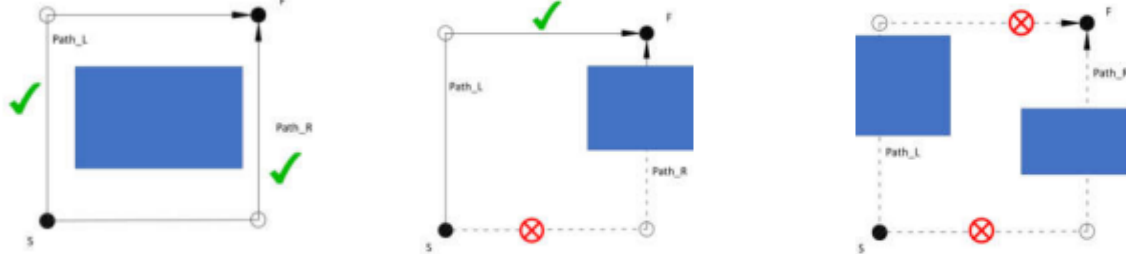
When applying crossover and mutation process, a large number of infeasible solutions are produced, if we only use the penalty function to eliminate those infeasible solutions, we will lose a large number of solutions, which both lowers population diversity and costs time trying to find out potential solutions. Therefore, author proposed a method to improve those infeasible solutions by bringing them from infeasible back to being feasible, then use the penalty function to remove infeasible solutions.

3.3 Pipes and walkways routing

Pipe routing in a large space as a ship engine room with a lot of components (obstacles) is solved using Dijkstra's algorithm in each explored solution to find optimal paths. The Dijkstra's original algorithm finds the shortest path between two given nodes in a created graph considered routing space, as presented in references [12], [13], while NSGA-II algorithm will have to explore many potential solutions in search space. Therefore, we need to have a smart routing strategy that saves computation time, since computation time of Dijkstra's algorithm depends on

the number of vertices. Liu [6] proposed a method, which aim to minimizes the number of vertices, finding optimal paths with minimum lengths and minimum bends in routing space that defined as constraints in section 2. This method is presented as follows:

Figure 5.a shows that both Path_L and Path_R routes satisfy the condition of no collision, so both are candidates for the shortest path from S to F with a least amount of vertices. Similarly, in Figure 5.b only Path_L route satisfies the path from S to F, while Figure 5.c has no feasible path.



(a) Both 2 path routes

(b) Only path_L

(c) No feasible path

Figure 5. Check for routing pipe

Figure 6 depicts the strategy to build routing graph. For each machine, we create 4 corresponding vertices lying on the dashed line with offset distance equal to half the required path width ($Pw/2$). For example, in the left side of Figure 7, we need to route the shortest collision-free pipe path connecting point S to point T. Now Dijkstra's algorithm is adopted to route in the created graph. The result is shown in the right side of Figure 7, the shortest path goes through the predetermined vertices. P1 and P2 are called virtual points, these points are not included in the routing graph to increase calculation speed of Dijkstra's algorithm. For each solution, if any pair of vertices is not connected, it will be considered an infeasible solution and will be discarded.

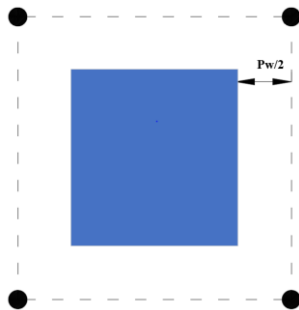


Figure 6. Create vertices for routing graph

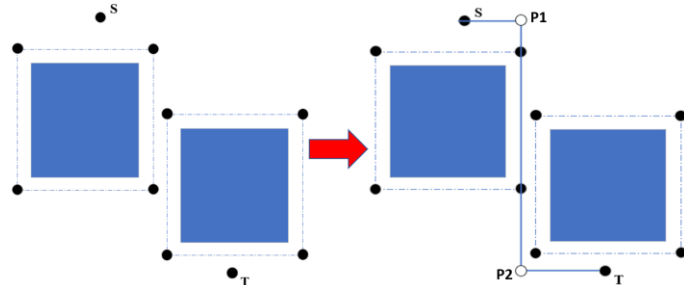


Figure 7. Shortest collision-free pipe path from S to T

3.4 Testing tool

Figure 8 shows a randomly generated solution satisfying the above constraints. In this figure, the blue paths depict the pipes connecting machineries, the pink path depicts pathway in the engine room with predetermined width, assuming the aisle connecting 2 exits is fixed in the engine room. It is clear that this layout concept is a feasible solution. Therefore, in section 4, the tool will be applied for an engineroom design process.

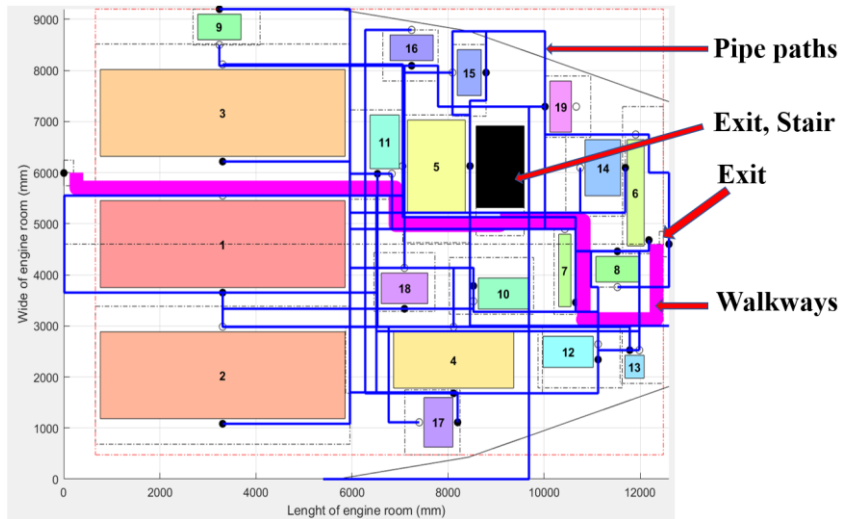


Figure 8. A random solution satisfies predefined constraints

4. Application and results

In this section, the developed tool will be applied for layout design and pipe routing in the engine room of a Platform Supply Vessel (PSV). In this case, only big components are considered, including main engines, auxiliary engines, cooling, fire hydrant, and water treatment equipment. Figure 9 below shows randomly generated solutions that satisfy added constraints. Figure 10 depicts the diversity of the first-generation solutions, with blue dots representing Pareto-optimal solutions that is nondominated by any solution, being chosen as optimal solutions [8]. Figure 11 below also shows the convergence graph of both objective functions over 1500 generations. It can be seen that both objective functions are greatly reduced.

The convergence graph shows that from the 1000th to the 1500th generation, neither objective function can be optimized any further, and it can be concluded that both objective functions converge. Figure 12 shows the Pareto-optimal solutions of the 1500th generation, including 4 candidate solutions, from which engineers can consider choosing a concept that suits their design criteria.

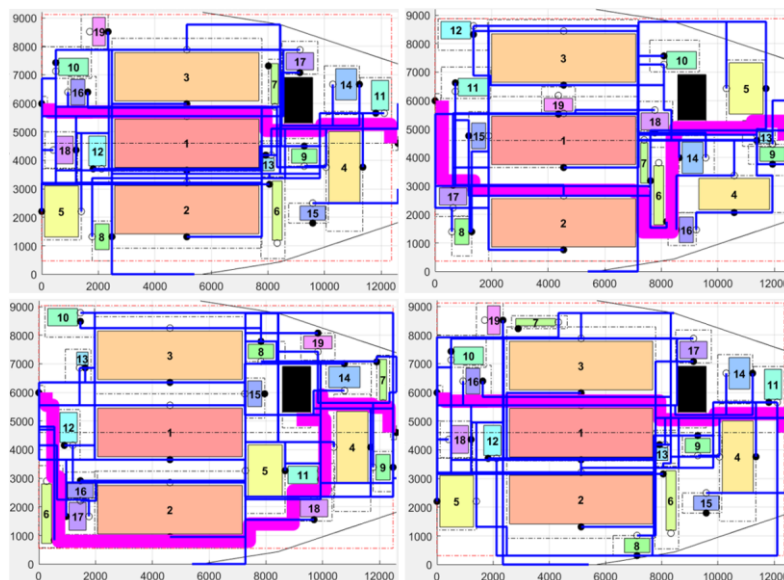


Figure 9. Random solutions

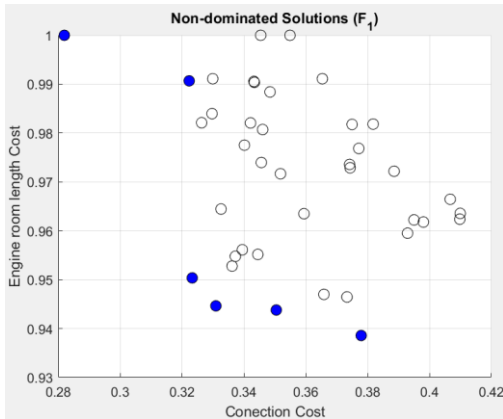


Figure 10. Pareto-optimal solutions of the first generation

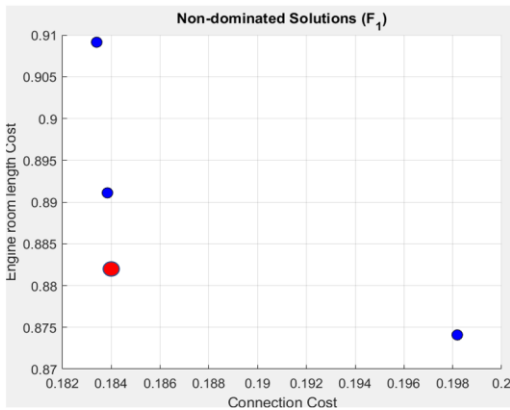


Figure 12. Pareto-optimal solutions of the 1500th generation

For example, the solution represented by red dot in Figure 12 is chosen, and then visual layout of this solution is shown in Figure 13. Finally, this layout concept is automatically converted to Cad drawing format as shown in Figure 14. In this figure, pipes in six different systems are clearly annotated with their respective colors, whereby engineers can more easily distinguish systems and more easily refer to the layout results.

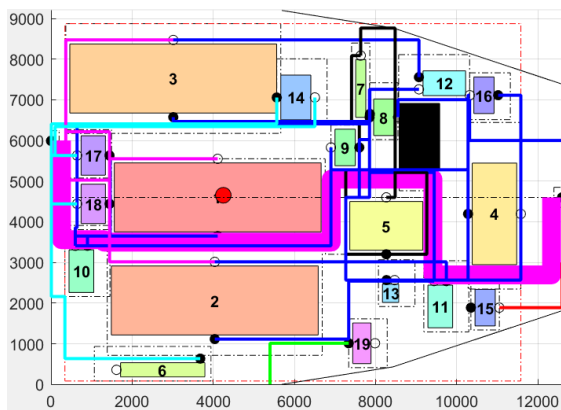


Figure 13. Layout after 1500 generations

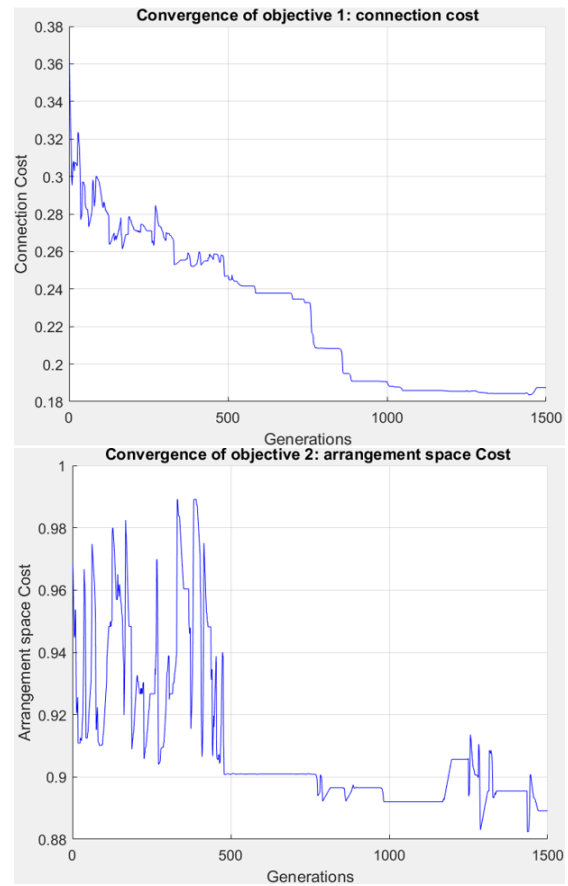


Figure 11. Graph of convergence

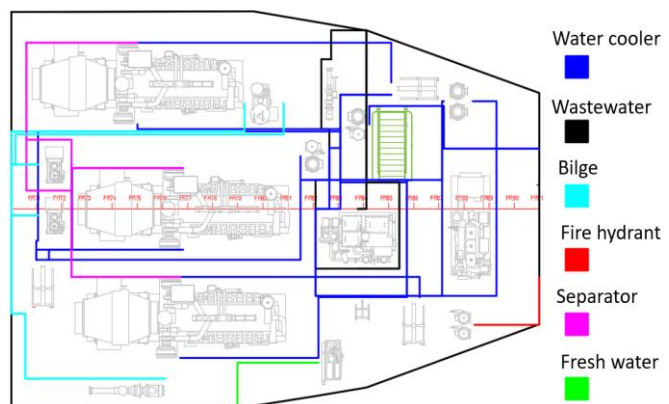


Figure 14. Cad drawing output

5. Conclusions

This paper has developed an assistant tool for ship layout design engineers through the evolutionary optimization process. The potential solutions are explored, guarantee that constraints added by designer are satisfied. Optimal solutions can be converted into engine room layout in Cad drawing. Engineers can reference and modify the design concepts easily. Calculation time has also been optimized through efforts to improve GA's solution searchability and improving routing space by minimizing the number of vertices while ensuring reliability of solutions. As a result, calculation speed significantly increases. The developed tool is shown to be a useful addition to the early concept design of machinery space arrangement.

Acknowledgments

This research is funded by Vietnam National University Ho Chi Minh city (VNU-HCM) under grant number B2021-20-05.

References

- [1] Gunawan, K. Hamada, T. Deguchi, H. Yamamoto, and Y. Morita, "Design optimization of piping arrangements in series ships based on the modularization concept," *Int. J. Technol.*, vol. 9, no. 4, pp. 675–685, 2018, doi: 10.14716/ijtech.v9i4.969.
- [2] S. H. Kim, W. S. Ruy, and B. S. Jang, "The development of a practical pipe auto-routing system in a shipbuilding CAD environment using network optimization," *Int. J. Nav. Archit. Ocean Eng.*, vol. 5, no. 3, pp. 468–477, 2013, doi: 10.3744/JNAOE.2013.5.3.468.
- [3] W. Niu, H. Sui, Y. Niu, K. Cai, and W. Gao, "Ship Pipe Routing Design Using NSGA-II and Coevolutionary Algorithm," *Math. Probl. Eng.*, vol. 2016, 2016, doi: 10.1155/2016/7912863.
- [4] A. Drira, H. Pierreval, and S. Hajri-Gabouj, "Facility layout problems: A survey," *Annu. Rev. Control*, vol. 31, no. 2, pp. 255–267, 2007, doi: 10.1016/j.arcontrol.2007.04.001.
- [5] H. Kimura, "Automatic designing system for piping and instruments arrangement including branches of pipes," *RINA, R. Inst. Nav. Archit. - Int. Conf. Comput. Appl. Shipbuild. 2011, Pap.*, vol. 3, pp. 93–99, 2011.
- [6] Q. Liu, "A rectilinear pipe routing algorithm: Manhattan visibility graph," *Int. J. Comput. Integr. Manuf.*, vol. 29, no. 2, pp. 202–211, 2016, doi: 10.1080/0951192X.2015.1033019.
- [7] R. van der Bles, "A Design Tool for Machinery Space Arrangement," *MSc. Thesis*, 2019.
- [8] K. Deb, A. Pratap, S. Agarwal, and T. Meyarivan, "A fast and elitist multiobjective genetic algorithm: NSGA-II," *IEEE Trans. Evol. Comput.*, vol. 6, no. 2, pp. 182–197, 2002, doi: 10.1109/4235.996017.
- [9] K. Y. Lee, M. Il Roh, and H. S. Jeong, "An improved genetic algorithm for multi-floor facility layout problems having inner structure walls and passages," *Comput. Oper. Res.*, vol. 32, no. 4, pp. 879–899, 2005, doi: 10.1016/j.cor.2003.09.004.
- [10] [10] J. H. Nam and T. H. Le, "Automatic interior space arrangement of mid-sized superyachts using a constraint-based genetic algorithm," *J. Mar. Sci. Technol.*, vol. 17, no. 4, pp. 481–492, 2012, doi: 10.1007/s00773-012-0182-1.
- [11] Yarpiz, "Facility Layout Design and Location Allocation in MATLAB." 2015, [Online]. Available: <https://yarpiz.com/378/ypap109-layout-design>.
- [12] M. A. Javaid, "Understanding Dijkstra Algorithm," *SSRN Electron. J.*, no. November, 2013, doi: 10.2139/ssrn.2340905.
- [13] E. W. Dijkstra, "A Note on Two Problems in Connexion with Graphs," *Numer. Math.*, vol. 271, pp. 269–271, 1959.

LULC Classification with Modified HarDNet-MSEG on Sentinel-2 Satellite Images

Laphonchai Jirachuphun^{1,2}, Pudit Tempattarachoke², Panin Pienroj² and Photchara Ratsamee³
and Nattee Niparnan¹

¹Department of Computer Engineering, Chulalongkorn University, Bangkok, Thailand, 10330

²OZT Robotics Co., Ltd., Bangkok, Thailand, 10500

³Cyber Media Center, Osaka University, Osaka, Japan, 560-0043

{laphonchai, pudit, panin}@oztrobotics.com, photchara@ime.cmc.osaka-u.ac.jp

Abstract

We present techniques and results for land use land cover (LULC) classification on satellite images from Sentinel-2. We modify the input of HarDNet-MSEG to facilitate multiple input channels presented in satellite multi-spectral images. Following a series of experiments, we discover that the combination of only 4 bands of Band 2, Band 3, Band 4 and Band 8 performs best with the consideration of our small dataset. We also modify the model's output so that it suits our usage of semantic segmentation task. Apart from altering the model, we engineer our own loss as a linear combination of Focal Loss and Dice Loss to combat our highly imbalanced dataset. The dataset we used in this study is self-collected from Sentinel-2 official website (<https://www.usgs.gov>) with primary focus on Thailand. We manually label the data as ground truth with the assistance of GIS experts. We use IoU to measure our model's performance and test it against a decision tree model simulating a traditional method and a Feature Pyramidal Network (FPN) model. Our model achieves a mean IoU of 0.841.

Keywords: Land use land cover, LULC classification, Sentinel-2, Satellite images, HarDNet-MSEG

1. Introduction

With increasing satellite usage, there are many applications arising from this technology in different areas, ranging from geology, communication, navigation, the military, to urban planning. Each area has its own use of satellite technology. Navigation, communication and the military use the Global Positioning System (GPS) to calculate the locations of desired points on the Earth, while geology and urban planning use satellite images to understand the physical characteristics of the terrain. There are currently several types of satellites orbiting the Earth, including communications satellites, remote sensing satellites, and navigation satellites. For this work, since we are focusing on land use land cover (LULC) classification from satellite images, we need a remote sensing satellite which measures reflected and emitted radiation from the surface of the Earth. We decide to use free-of-charge satellite imagery sources from Sentinel-2 as our data source.

Sentinel-2 is a sun-synchronous orbit satellite aiming to monitor variability in land surface conditions, which is suitable for our usage. It comprises of two satellites, Sentinel-2A and Sentinel-2B, orbiting on the same orbit path. For Thailand, the revisiting time per satellite is 10 days. With two satellites, we receive multi-spectral images every 5 days. The optical image has 13 channels with one for each spectral band generated from the Multi-Spectral Instrument (MSI) on the satellite. The bands' wavelengths range from the visible range to the shortwave infrared

(SWIR) and their resolution is from 60 to 10 meters. Figure 1 shows the details of the Sentinel-2's bands.

In this paper, we want to classify each pixel in Sentinel-2's images into one of five LULC classes: Bare Soil, Construction, Road, Vegetation, and Water. This task in the machine learning field is called semantic segmentation and most of the work is based on the Convolutional Neural Network (CNN). We decided to modify HarDNet-MSEG [1] for this research. Our ultimate goal is to track long-term changes happening in Thailand, such as detecting flooding, deforestation, or urban expansion. We hope that this work will bring us a step closer to achieving this goal, shown in Figure 2.

Sentinel-2 Bands	Central Wavelength (µm)	Resolution (m)
Band 1 - Coastal aerosol	0.443	60
Band 2 - Blue	0.49	10
Band 3 - Green	0.56	10
Band 4 - Red	0.665	10
Band 5 - Vegetation Red Edge	0.705	20
Band 6 - Vegetation Red Edge	0.74	20
Band 7 - Vegetation Red Edge	0.783	20
Band 8 - NIR	0.842	10
Band 8A - Vegetation Red Edge	0.865	20
Band 9 - Water vapour	0.945	60
Band 10 - SWIR - Cirrus	1.375	60
Band 11 - SWIR	1.61	20
Band 12 - SWIR	2.19	20

Figure 1. Details of Sentinel-2's bands from <https://www.usgs.gov>

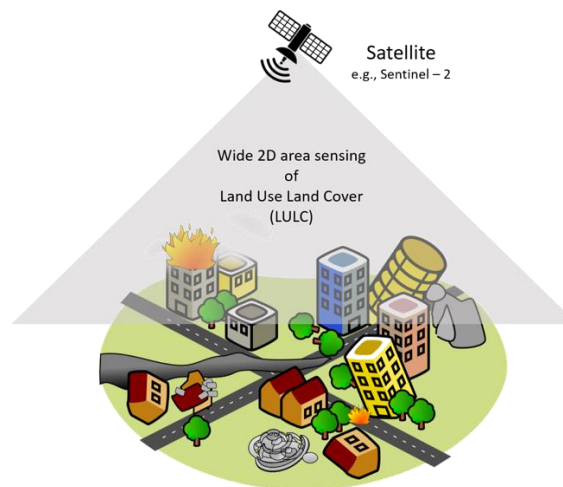


Figure 2. Satellite usage for LULC management

2. Related work

In the past, the LULC problems were solved by traditional methods, including physical property and generalized statistical inferences. Also, deep learning techniques are continually evolving and going beyond the traditional techniques' performance rapidly. In this section, we briefly discuss related work on traditional and deep learning methods for LULC problems. Our discussion, as well as qualitative evaluation in section 4, is mainly focused on deep learning approaches.

2.1 Traditional method

Early attempts to solve LULC tasks were usually derived using prior knowledge of the physical characteristics of the area. Figure 3 illustrates the relation between percent reflectance and the wavelength of common urban materials. By analyzing the wavelength of the reflected light spectrum from each area, we can derive a specific index for each specific material. These specific indexes are then used as main features to classify each pixel into different classes with simple rule-based classification, such as vegetation areas, water, asphalt and others. Well-known indexes derived from these reflectance characteristics which are commonly used to classify land are the Normalized Difference Vegetation Index (NDVI) [2], Normalized Difference Water Index (NDWI) [3] and Normalized-Difference Snow Index (NDSI) [4], etc.

After the rise of machine learning algorithms, the remote sensing research community shifted their main strategies by including more features from different feature engineering techniques [6]. Machine learning techniques unlock the potential to solve LULC problems with higher accuracy, broader classes and more specific types of land. Popular classification algorithms are k-Nearest Neighbour (kNN) [7], Supporting Vector Machine (SVM) [8] and Random Forest (RF) [9].

Thanh Noi, et. al [10] compared different machine learning algorithms to classify multiple classes of Land cover from Sentinel-2 data into 6 different classes; Residential, Impervious surface, Agriculture, Bare Land, Forest and Water. The author concluded that SVM produced the highest accuracy of around 90% precision. Immitzer, *et al.* [11] used NDVI along with other combinations of reflective value of each pixel with RF to classify more specific classes of crop and tree species in Central Europe with an accuracy of around 65-76%.

However, traditional ML techniques present difficulties in feature engineering and feature selection. The current deep learning method helps researchers solve this challenge and gives a breakthrough to the community.

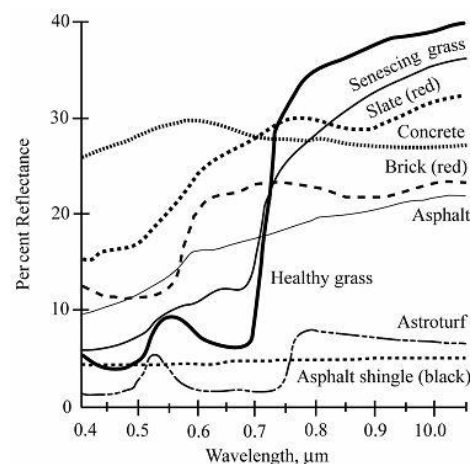


Figure 3. Plot of spectral reflectance for common urban materials relative to wavelength [5]

2.2 Deep learning method

Since the introduction of inception net [12] in 2014, based on a convolution neural network (CNN) architecture, CNN based networks have achieved state-of-the-art results on different computer vision fields. It has been widely used in deep learning tasks. For image segmentation

tasks, one of the fast-growing areas in computer vision, CNN architectures have been ubiquitous, developed as the backbones of the most successful image segmentation models to classify LULC classes.

In recent years, Huang *et al.* proposed a higher accuracy deep learning model for Semantic Segmentation called HarDNet-MSEG [1] that consists of a backbone and a decoder. For the backbone, HarDNet-MSEG implemented Harmonic Densely Connected Network (HarDNet) [13], which reduced most of the layer connections from DenseNet [14] to reduce concatenation cost and balanced the input/output channel ratio by increasing the channel width of a layer according to its connections as the backbone. The decoder part was modified from Cascaded Partial Decoder [15] by adding appropriate convolution and skip connections that are based on Receptive Field Block [16] and Dense Aggregation techniques.

2.3 Positioning of this paper

Although FCNs have achieved huge success in a variety of segmentation problems, including LULC Segmentation [17], the HarDNet-MSEG delivers 0.904 mean Dice and high FPS that is more than the FCN-8 score. Furthermore, it reduces inference time and the amount of training data, which is suitable for our small data set. Hence, we decided to modify HarDNet-MSEG for the LULC classification.

3. Methodology

In this section, we propose a solution for LULC classification on satellite images from the Sentinel-2 satellite. We first analyze different product types of image that Sentinel-2 offers and then discuss our final channel selection for the model considered in our limited dataset. Next, we provide our method of modifying the HarDNet-MSEG's input layer to facilitate the increase in the number of channels for the images. Then, we show how to augment the output layer so that the model will classify each pixel into multiple classes for the LULC task. After that, we discuss how we divide the scene into smaller fixed-sized images for the model and how to merge them back into a complete scene. Then, we examine the loss function we used, and finally, we talk about how we overlaid cloud masks from Sentinel-2 to get our final result. Figure 4 shows the overall picture of our solution.

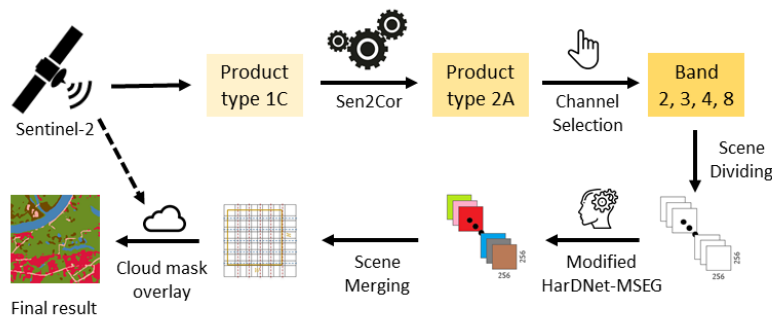


Figure 4. The overall pipeline of our solution

3.1 Product type

Sentinel-2 offers two types of product types: Level-1C and Level-2A. Level-1C image data represents top-of-atmosphere reflectance (TOA), whereas Level-2A data represents bottom-of-atmosphere reflectance (BOA). Figure 5 shows the differences between these two product types. The Level-2A product type is generated from the associated Level-1C product type using the

Sen2Cor processor to eliminate atmospheric factors [18]. We decided to use the Level-2A product type for the model since the quality is far superior, especially in lower-wavelength channels in the images, such as the blue and green channels. However, we find that older images from Sentinel-2 are different and contain some defects because at that time the images were converted using an older version of Sen2Cor. Hence, we settled on using the Level-1C product type and then convert it to Level-2A using the updated Sen2Cor processor.



Figure 5. Level-1C image data (left) and associated Level-2A image data (right) [19]

3.2 Channel selection

Sentinel-2 images contain 13 channels ranging from visible to shortwave infrared, as shown in Figure 1. We analyze a combination of channels for our model and test their performance. First, we removed Band 1, Band 9 and Band 10 from consideration because their primary usage is atmospheric analysis. Next, we removed Band 5, Band 6, Band 7 and Band 8A because their wavelength is close to Band 8 and they are used for classifying different types of vegetation, which is not in the scope of this work. Therefore, we are left with the visible bands (Band 2, Band 3 and Band 4), NIR (Band 8), and SWIR (Band 11 and Band 12). For SWIR, since the resolution is 20 meters compared to the remaining 10 meters, we upscale the images to the same resolution with the nearest neighbor method. We compare different combinations and find that using both visible and NIR gives the best result. We initially assumed that SWIR would be useful when the scenes are covered with Cirrus cloud, which appeared as fogs in RGB images, because their high wavelengths could penetrate the clouds more easily. However, when comparing the results, the performance is relatively the same, which might be possible due to our small dataset and the increase in network size.

3.3 Input modification

Since our input is not the standard 3-channel of RGB images, we modify the encoder part of HardNet-MSEG by adding another layer on top. The added layer is a 1x1 convolutional layer with an input size equal to the number of channels and an output size of 3. We believe this modification performs well because the 1x1 convolutional layer is essentially a linear combination of input channels, which is similar to using multiple indices, such as NDVI or NDWI, in traditional methods. Apart from adding a channel conversion layer, we also decided to connect the layer right after the first HarDBlock with an additional RFB module in the decoder part to preserve finer classification details for the upsampling output. Figure 6 shows these modifications.

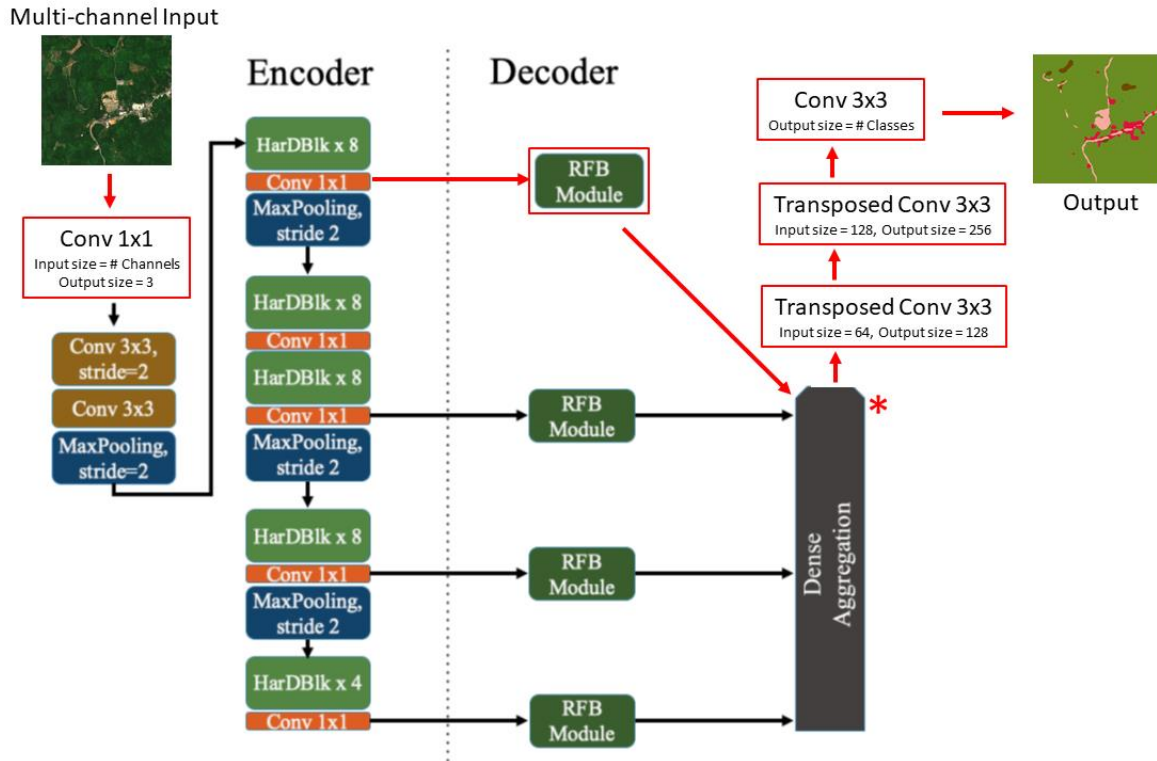


Figure 6. Modified HarDNet-MSEG for LULC task where the red parts show our modifications and the rest are from the original HarDNet-MSEG architecture [1]

3.4 Output modification

In the original HarDNet-MSEG, the author used Bilinear Upsample for the output layer to classify each pixel of the images into either a cancer or not. However, we cannot use the same method for LULC classification, since it requires multiple output classes. First, we replaced a Bilinear Upsample with two transposed convolutional layers and another 3x3 convolutional. We discovered that this change improves performance, particularly at the boundaries of each LULC class. Next, similar to how we modify the input layer, we add a 3x3 convolutional layer with an output size equal to the number of LULC classes at the end of the model. Finally, we use a Softmax activation function to classify each pixel into a LULC class. The modification can be seen in Figure 6.

3.5 Aggregation layer modification

Another part we adjust is in the aggregation layer. As discussed in the previous subsection, we connect the layer right after the first HarDBlock with an additional RFB module and then feed the result to our modified Aggregation block. The changes follow the same technique used in the original Aggregation block. Figure 7 shows this modification. These changes enable us to incorporate finer details of the input images into the model for classification, resulting in improved performance, particularly at the edge.

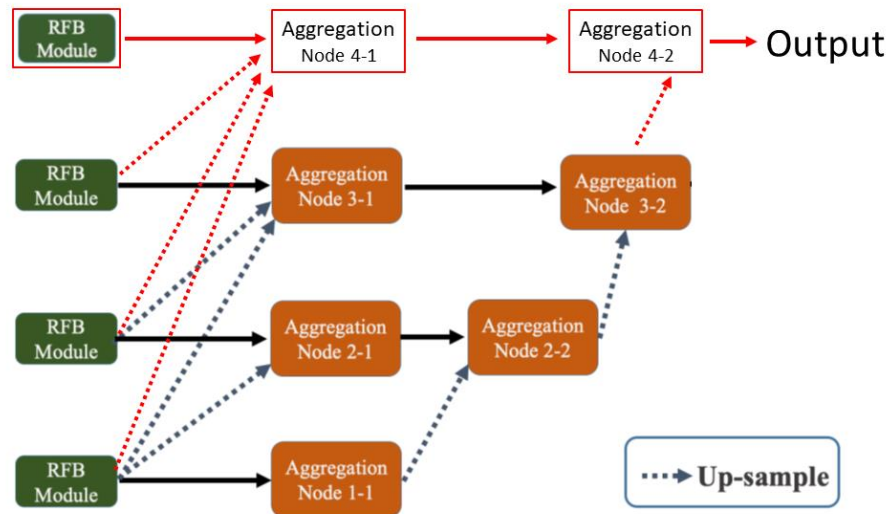
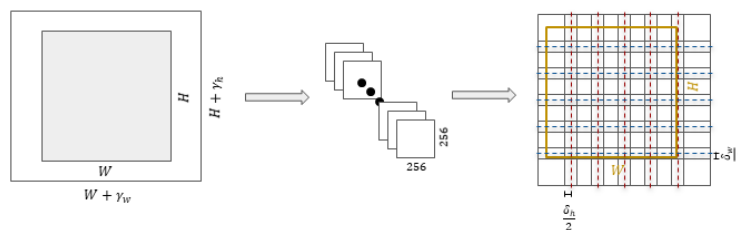


Figure 7. Modified Aggregation block for additional RFB module where the red parts show our modifications and the rest are from the original HarDNet-MSEG architecture [1]

3.6 Scene dividing and merging

Since the model takes only fixed-size images of 256×256 pixels, we need a method to classify images into arbitrary sizes. One common method is to divide the image into multiple smaller patches. However, this method also introduces errors at the boundaries of the patches. Scene dividing and merging shown in Figure 8 is our strategy for merging and smoothing boundary effect that always occurs when model receives non-overlap images. First, we add data ($\gamma_h \times \gamma_w$) from the original image's reflection to edges of each channel $H \times W$, which ensures that of cutting the new image is cut into smaller overlapped patches of 256×256 pixels and the overlapped sizes of δ_w and δ_h for width and height axes, respectively. We assume that the model generates satisfying results from the patch without boundary effect in a non-overlap area and half of the overlapped area closer to the center of the patch. From this assumption, when we merge into the final image, for each pixel, we use the classification of the patch that is closest to that pixel.



**Figure 8. Left side shows original image and the image after adding reflect data
 Middle shows overlapped image patches to be processed with our model
 Right side shows the final image in as a yellow rectangle after the merge where the red and blue dashed lines show the boundary of which patch to use for the classification**

3.7 Loss

In this study, our model is optimized on our own engineered loss function which is a linear combination of a Focal Loss and a Dice Loss.

- 1) Dice Loss: Dice loss measures the Intersection over Union (IoU) between the ground truth and the predicted value. By optimizing this value, we are trying to make sure that the predictions have maximum overlap with the ground truth. The equation for the dice loss is written below:

$$D_{Loss} = 1 - \frac{2 \sum_i^N p_i g_i}{\sum_i^N p_i^2 + \sum_i^N g_i^2} \quad (1)$$

where p_i and g_i represent pairs of corresponding pixel values of prediction and ground truth, respectively. The values of p_i and g_i are either 0 or 1, indicating whether the pixel belongs to the class or not.

- 2) Focal Loss: Focal Loss is designed to address a scenario in which there is an extreme imbalance between classes in the dataset which represents some classes in our dataset. The focal loss is defined as

$$F_{Loss} = -(1 - p_t)^{\gamma} \log(p_t) \quad (2)$$

where p_t is

$$p_t = \begin{cases} p, & \text{when } t \text{ is the current class} \\ 1-p, & \text{otherwise} \end{cases} \quad (3)$$

where p is the model's estimated probability for each class.

By optimizing the focal loss, our model can overcome the class imbalance problem in the dataset.

We combined both losses with a linear combination in order to maximize the prediction precision of Dice Loss while preserving the ability to combat the class imbalance from Focal Loss. The final loss equation is written as:

$$Loss = \alpha F_{Loss} + \beta D_{Loss} \quad (4)$$

where α and β are real numbers that we need to tune and F_{Loss} and D_{Loss} are Focal loss and Dice loss predicted from our model relative to the ground truth. We choose $\alpha = 1$ and $\beta = 1$ which yields the best prediction outcome. Finally, we assign different weights for each LULC class to combat the unbalanced in our dataset even more, especially in a Road class which will be discuss later in section 4.

3.8 Cloud mask overlay

Even though our model also predicts Cloud class, we only use visible and NIR bands, in which we leave out the SWIR bands that are useful for cloud detection. Nevertheless, Sentinel-2 provides a cloud mask for Dense cloud. This cloud mask depicts all pixels that have characteristics of Dense cloud, which is calculated from Band 2, SWIR, and Band 10. Therefore, we use the cloud mask from Sentinel-2 and overlay it on top of our classification result to get our final result.

4. Experiment and Results

For this section, we discuss the LULC classes we selected, the dataset we used and the result of our experiment.

4.1 LULC Classes

The purpose of this work is to create a system that can monitor the macro-to-micro changes in the land in Thailand. The core of this system is a LULC classification algorithm developed in this study. Our ultimate goal is to develop a hierarchical classification that can detect changes on a macro scale using Sentinel-2, then use different data sources on a micro scale. We want to be able to track urban expansion, deforestation as well as disasters for emergency response, such as flooding. This hierarchical classification will be discussed more in section 5. Considering our usage and image resolution, we decided to use a total of five LULC classes of Construction, Road, Bare soil, Water and Vegetation with an addition Cloud class for detecting macro changes. The description and percentages of each class are shown in Table I.

Table 1. Details and descriptions of LULC classes

Class name	Description/Example	Percentage
Construction	Building, House, Factory	9.31%
Road	Road, Tollway, Runway	4.73%
Bare soil	Soil, Sand, Beach	16.23 %
Water	River, Lake, Ocean, Pond	14.25 %
Vegetation	Forest, Farm, Lawn, Tree	52.21 %
Cloud	Dense cloud	3.27 %

4.2 Dataset

For data preparation, we manually select satellite images from different times and different areas in Thailand and nearby regions taken by Sentinel-2. The reason we only select data from this region is because we want to create a LULC classification model specifically for Thailand with our interested LULC classes. Furthermore, we believe that this dataset will help the model yield a better result than training from a more generalized dataset. The characteristics of land surfaces usually differ greatly from one geographic location to another. One obvious example is that Thailand has no snow.

After we select the images, all channels from the images are cropped into square patches of 256x256 pixels in order to optimize HardNet-MSEG's performance. The data was then manually labeled into six classes per pixel with the guidance of GIS experts. We label the images with PixelAnnotation tools [20] based on their RGB appearances compared with high-resolution images from Google Map, along with other false color composition images in the QGIS software [21].

In this study, we used a total of 193 images for training data and 54 images for testing data. Apart from our limited dataset, one of the challenges is the severity of imbalanced classes. We alleviate this problem by manually adding areas with a high concentration of the lacking classes, such as Road, and removing images with abundant classes, such as Vegetation. Table I summarizes the final composition of our dataset.

4.3 Result

We show results from our experiment in this section. Firstly, we calculated a confusion matrix of our model on the test dataset where the columns are predicted classes and the rows are actual classes, as shown in Table II. The confusion matrix is normalized by row.

Table 2. Confusion matrix of our model on the test dataset where the columns are predicted classes and the rows are actual classes

	Construction	Road	Bare soil	Water	Vegetation	Cloud
Construction	0.908	0.013	0.019	0.023	0.036	0.001
Road	0.012	0.911	0.033	0.018	0.026	0.001
Bare soil	0.014	0.017	0.848	0.053	0.067	0.001
Water	0.011	0.007	0.065	0.881	0.035	0.001
Vegetation	0.007	0.010	0.023	0.011	0.945	0.004
Cloud	0.001	0.002	0.005	0.003	0.018	0.971

Secondly, we tested our model on a totally unseen dataset. The result can be seen in Figure 9. The first three scenes are areas in Thailand. In the first one, we evaluated how well our model performed against a scene with moderate cloud coverage. We tested the second one with a scene containing salt fields, beaches and ocean. The third scene is obscured by Cirrus cloud which appears as fogs. The fourth one is an airport under ongoing construction in Koh Kong, Cambodia. The last one is a 256x256 image patch.

Thirdly, we quantitatively compared our model with a decision tree model and a FPN [22]. We use the decision tree model because it is similar to the traditional method for LULC classification. For FPN, it is an advanced deep learning method, which is a fairer comparison. All the models are trained on the same training set and tested on the same test set. We calculate IoU and mean IoU in Table III. Although our model performs slightly worse in the Bare soil and Water classes, the overall performance is better especially in the Construction and Road classes.

Table 3. Performance comparison on different models with IoU metric

Model	Construction	Road	Bare soil	Water	Vegetation	Cloud	Mean
Decision Tree	0.363	0.178	0.587	0.908	0.849	0.692	0.596
FPN	0.605	0.471	0.844	0.962	0.897	0.781	0.760
Our solution	0.865	0.757	0.782	0.825	0.917	0.904	0.841

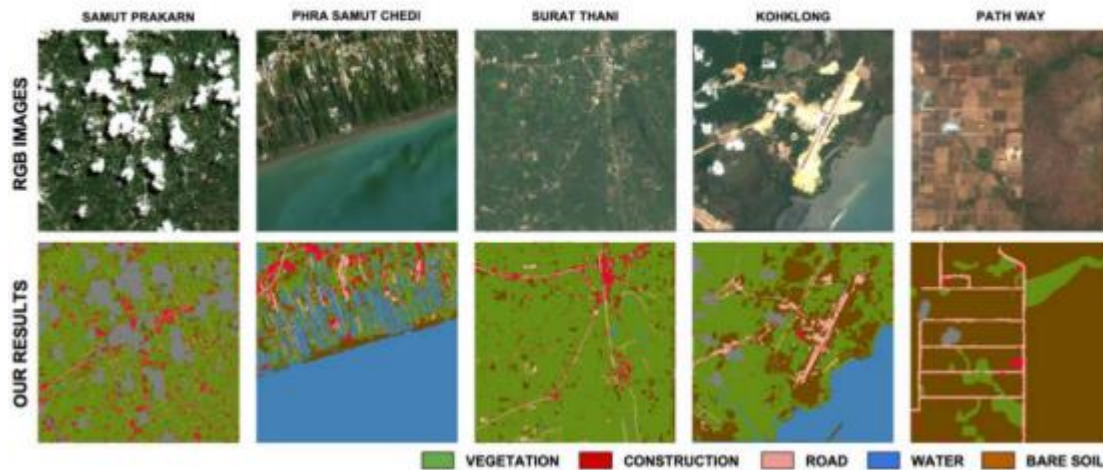


Figure 9. RGB images and our predicted segmentation results from the modified HardNet-MSEG on unseen examples

5. Conclusion

In this paper, we provide a method for LULC classification on Sentinel-2 imagery. We decided to use product type 1C and convert it to 2A using the Sen2Cor protocol. Only visible and NIR bands are used as input to our model. We modified the model from HardNet-MSEG to increase its performance and allow the model to perform semantic segmentation tasks.

As has been briefly discussed in the previous section, our final goal of this work is to create a system that can monitor changes happening on the land in Thailand from a macro scale to a micro scale. First, the system will observe large scale changes with satellite images, which can be a fusion of multiple satellite data sources. Then, when we detect the changes, we can use images from airplanes or pico-satellites to understand them in more detail. Finally, if the need arises, we can deploy drones to obtain close-up images. Undeniably, the LULC classes will become more and more specific and defined in a hierarchical manner. Despite the fact that majority of the system is still in the works, this research is a critical component of the system.

References

- [1] C.-H. Huang, H.-Y. Wu, and Y.-L. Lin, “Hardnet-mseg: A simple encoder-decoder polyp segmentation neural network that achieves over 0.9 mean dice and 86 fps,” arXiv preprint arXiv:2101.07172, 2021.
- [2] D. W. Deering, “Rangeland reflectance characteristics measured by aircraft and spacecraft sensors,” Ph.D. dissertation, Texas A M University, 1978.
- [3] B. cai Gao, “NdwI—a normalized difference water index for remote sensing of vegetation liquid water from space,” *Remote Sensing of Environment*, vol. 58, no. 3, pp. 257–266, 1996. [Online]. Available: <https://www.sciencedirect.com/science/article/pii/S0034425796000673>
- [4] D. K. Hall and G. A. Riggs, “Normalized-difference snow index (ndsi),” 2010.
- [5] S. E. through Earth Observation(SEOS). Science education through earth observation(seos). [Online]. Available: <https://seos-project.eu/>
- [6] D. Phiri, M. Simwanda, S. Salekin, V. R. Nyirenda, Y. Murayama, and M. Ranagalage, “Sentinel-2 data for land cover/use mapping: A review,” *Remote Sensing*, vol. 12, no. 14, 2020. [Online]. Available: <https://www.mdpi.com/2072-4292/12/14/2291>
- [7] G. Guo, H. Wang, D. Bell, and Y. Bi, “Knn model-based approach in classification,” 08 2004.
- [8] T. Evgeniou and M. Pontil, “Support vector machines: Theory and applications,” vol. 2049, 01 2001, pp. 249–257.
- [9] T. K. Ho, “Random decision forests,” in *3rd International Conference on Document Analysis and Recognition*, Montreal, QC, 14–16 August 1995. pp. 278–282. IEEE, 1995.
- [10] P. Thanh Noi and M. Kappas, “Comparison of random forest, k-nearest neighbor, and support vector machine classifiers for land cover classification using sentinel-2 imagery,” *Sensors*, vol. 18, no. 1, 2018. [Online]. Available: <https://www.mdpi.com/1424-8220/18/1/18>
- [11] M. Immitzer, F. Vuolo, and C. Atzberger, “First experience with sentinel-2 data for crop and tree species classifications in central europe,” *Remote Sensing*, vol. 8, no. 3, 2016. [Online]. Available: <https://www.mdpi.com/2072-4292/8/3/166>

- [12] C. Szegedy, W. Liu, Y. Jia, P. Sermanet, S. Reed, D. Anguelov, D. Erhan, V. Vanhoucke, and A. Rabinovich, “Going deeper with convolutions,” in *Computer Vision and Pattern Recognition (CVPR)*, 2015. [Online]. Available: <http://arxiv.org/abs/1409.4842>
- [13] P. Chao, C.-Y. Kao, Y.-S. Ruan, C.-H. Huang, and Y.-L. Lin, “Hardnet: A low memory traffic network,” in *Proceedings of the IEEE/CVF International Conference on Computer Vision*, 2019, pp. 3552–3561.
- [14] G. Huang, Z. Liu, L. Van Der Maaten, and K. Q. Weinberger, “Densely connected convolutional networks,” in *Proceedings of the IEEE conference on computer vision and pattern recognition*, 2017, pp. 4700–4708.
- [15] Z. Wu, L. Su, and Q. Huang, “Cascaded partial decoder for fast and accurate salient object detection,” in *Proceedings of the IEEE/CVF Conference on Computer Vision and Pattern Recognition*, 2019, pp. 3907–3916.
- [16] S. Liu, D. Huang *et al.*, “Receptive field block net for accurate and fast object detection,” in *Proceedings of the European Conference on Computer Vision (ECCV)*, 2018, pp. 385–400.
- [17] A. B. S. Nayem, A. Sarker, O. Paul, A. Ali, M. Amin, A. Rahman *et al.*, “Lulc segmentation of rgb satellite image using fcn-8,” *arXiv preprint arXiv:2008.10736*, 2020.
- [18] M. Main-Knorn, B. Pflug, J. Louis, V. Debaecker, U. Muller-Wilm, “ and F. Gascon, “Sen2cor for sentinel-2,” *10* 2017, p. 3.
- [19] T. E. S. Agency(ESA). Level-2a. [Online]. Available: <https://sentinels.copernicus.eu/web/sentinel/user-guides/sentinel2-msi/product-types/level-2a>
- [20] A. Breheret, “Pixel Annotation Tool,” <https://github.com/abreheret/PixelAnnotationTool>, 2017.
- [21] QGIS Development Team, QGIS Geographic Information System, QGIS Association, 2021. [Online]. Available: <https://www.qgis.org>
- [22] T.-Y. Lin, P. Dollar, R. Girshick, K. He, B. Hariharan, and S. Belongie, “Feature pyramid networks for object detection,” 2017.

A Comparison of Kalman Filters for Unmanned Aerial Vehicles Attitude Estimation Using Real Flight Test Data

Dung Van Vu*, Thanh Truong Nguyen, Dong Thanh Nguyen, and Thap Khac Nguyen
Flight Instrument Center, Viettel High Technology Industries Corporation, Hanoi, Vietnam,
11209

*Corresponding author. E-mail: dungvv23@viettel.com.vn

Abstract

This paper studies Unmanned Aerial Vehicles (UAV) attitude estimation based on an Attitude Heading Reference System (AHRS). A novel approach of unscented Kalman filter (UKF) is implemented with low-cost sensor systems for real fixed-wing UAV in GPS-denied environment. We introduce a nonlinear filter for the airspeed data instead of the ground speed obtained from GPS for calculating the Euler angles. These angles are used for the correction instead of the accelerometer and the magnetometer data directly. Compared with the standard UKF, the proposed filter reduces the number of so-called sigma points, which leads to the lower computational cost. In the flight test, we use a high-accuracy system to generate the reference attitude, which is only used for comparing estimated attitude angles from Kalman filters. An algorithm is presented to eliminate the misalignment of this high-accuracy sensor system and the UAV's autopilot one. Real flight test results are provided to validate the effectiveness of the proposed UKF against the extended Kalman filter (EKF) based on accuracy estimation and against the standard UKF based on the computational cost.

Keywords: UAV, AHRS, Attitude estimation, Kalman filter, Quaternion

1. Introduction

Recently, unmanned aerial vehicles (UAV) have attracted much research attention from the control system society because of attractive applications in both military and civilian fields such as aerial surveying, monitoring, pipeline inspection, and satellites. Micro-Electro-Mechanical-Systems (MEMS) development has provided a solution to the UAV attitude estimation problem, which requires a lightweight, low-cost, and low-energy sensor system [1]. A well-known attitude estimator, namely an Attitude and Heading Reference System (AHRS), fuses data from MEMS sensors, including three-axis gyroscopes, three-axis accelerometers, and three-axis magnetometers to give information about the UAV's orientation [2-3]. Safe and reliable flights require enough accurate UAV's angles; however, data from sensors are often noisy due to their nature. Therefore, the minimization of the noise effects based on the filters plays an essential role in the UAV angle estimation problem. Surveys [4-5] presented many attitude filtering techniques; however, most advanced filters are difficult to implement in real-time embedded processors due to computational complexity. An extended Kalman filter that provides the sub-optimal solution based on the linearization of the UAV kinematic equation has been used widely because of low computation cost [6-7]. However, linearization can lead to the divergence of estimation if the sampling time is not short enough. To deal with this difficulty, an unscented Kalman filter was introduced [8-10], which estimates the mean and the covariance matrix based on the selected appropriate points, namely sigma points, instead of linearization. The performance of the UKF has been proven in a wide range of both state estimation and parameter estimation. The more accuracy of UKF compared with EKF can also be found in simulations [8-9]. Authors in [11] also compared UKF and EKF to estimate quaternion motion of the human

head or hand orientation tracking. The UKF for spacecraft attitude estimation can be founded in [12]. However, to our best knowledge, few papers have compared EKF and UKF algorithms based on real flight sensor data and implementing the UKF in the real embedded flight processors. Reference [13] introduces the UKF for a fixed-wing UAV and compares the UKF and EKF. Nevertheless, this comparison was performed based on Matlab simulations and the configuration sensor data, not flight data. The experimental results did not compare UKF with EKF and prove the UKF's performance because the noisy reference angles were obtained from GPS and a vision system instead of a high-accuracy sensor. Real-time processors require computationally efficient algorithms; thus, reference [8] studied the computational cost. Authors in [8] stated that for state estimation, the UKF and EKF have equal complexity $\mathcal{O}(d^3)$, where d is the size of the covariance matrix; thus, reducing d plays a key role in decreasing the computational cost, making the UKF easy to implement in real autopilot systems.

In this paper, the attitude estimation of a UAV is studied. Off-the-shelf and low-cost sensors, which are implemented in the UAV, consist of a three-axis gyroscope, a three-axis accelerometer, a three-axis magnetometer, and a pitot tube. The raw sensor data are filtered with proposed algorithms to yield a measured UAV attitude combined with the predicted attitude from an integration quaternion-based kinematic equation. The novel UKF approach is introduced with reducing the number of sigma points to obtain the lower computation, which makes this filter able to be implemented in real UAVs with a low-cost microprocessor. The real-time flight results are used to compare three algorithms, including the standard EKF, the standard UKF, and the proposed UKF.

The remainder of this paper is organized as follows. Section II contains background on the attitude estimation problem and Section III presents the proposed UKF. The flight test results are provided in Section IV, and Section V concludes this papers.

2. Preliminaries

2.1 Kinematic equations

Consider two orthogonal right-handed coordinate frames, including the inertial frame and the body frames, which are oriented in its north, east, and down axes. The rotation of the body frame with respect to the inertial frame can be parameterized by the Euler angles, as known as roll ϕ , pitch θ , and yaw ψ . However, this representation can lead to the so-called gimbal lock phenomenon; therefore, quaternions, which yield non-singularity and the linear kinematic equations, have been widely used for attitude parameterization in modern-day applications. The normalized quaternion $q = [q_0, q_1, q_2, q_3]^T$ is obtained from the attitude $\eta = [\phi, \theta, \psi]^T$ as $q_0 = c_{\phi'} c_{\theta'} c_{\psi'}$, $q_1 = s_{\phi'} c_{\theta'} c_{\psi'}$, $q_2 = c_{\phi'} s_{\theta'} c_{\psi'}$, $q_3 = c_{\phi'} c_{\theta'} s_{\psi'}$, where $\phi' = 0.5\phi$, $\theta' = 0.5\theta$, $\psi' = 0.5\psi$, c_x and s_x represent $\cos(*)$ and $\sin(*)$. We also can compute the Euler angles as

$$\phi = \text{atan2}\left(2(q_2 q_3 + q_0 q_1), 1 - 2(q_1^2 + q_2^2)\right), \theta = -\text{asin}\left(2(q_1 q_3 - q_0 q_2)\right), \psi = \text{atan2}\left(2(q_1 q_2 + q_0 q_3), 1 - 2(q_2^2 + q_3^2)\right).$$

Now, with the angular velocity $\omega = [\omega_x, \omega_y, \omega_z]^T$ expressed in the body frame, where the roll rate, the pitch rate, and the yaw rate are denoted by ω_x , ω_y , and ω_z respectively, the kinematic equation of UAV attitude can be written based on quaternions, expressed as $\dot{q} = \frac{1}{2} \underbrace{\begin{bmatrix} 0 & -\omega \\ \omega & [-\omega \times] \end{bmatrix}}_{A(\omega)} q$.

This quaternion-based kinematic equation, which is used widely for UAV attitude estimation,

can determine the UAV attitude by measuring the angular velocity and integration. However, the measured angular velocity usually has noise and bias; thus, the attitude obtained using only the kinematic equation's integration tends to drift over time and be noisy. Thus, it is vital to fuse other sensors to obtain a more accurate estimation.

2.2 Sensor models

The three-axis gyroscope whose output is modeled as $\tilde{\omega} = \omega + \beta + v_{\omega}$, where $\tilde{\omega}$ and ω denote the measured and real angular velocity, β denotes the bias term, and v_{ω} represents the Gaussian white noise. The bias term β can be assumed to be slowly varying during the flight; thus, it can be modeled simply as $\dot{\beta} = -\tau\beta + v_{\beta}$, where v_{β} is the Gaussian white noise and τ is a small positive constant.

As stated above, using only the gyroscope with integration leads to inaccurate attitude estimation; thus, a three-axis accelerometer, a three-axis magnetometer, and a pitot tube are usually combined with the gyroscope to give a good estimation of attitude. The accelerometer measures the specific acceleration in the body frame, $\tilde{f} = a^b - g^b + v_f$, where \tilde{f} is the accelerometer output, a^b and g^b represent the acceleration vector (including the linear acceleration and the Coriolis acceleration) of the UAV with respect to the inertial frame and the gravitational acceleration, expressed in the body frame, and v_f is the process noise, which mostly depends on the perturbation of motors. Using filtered measurements obtained from the accelerometer and estimating the gravitational acceleration g^b expressed in the body frame yields roll and pitch angles, which will be called measured roll and pitch angles. That is, the following equation is used to compute $\hat{\phi}$ and $\hat{\theta}$ after obtaining \hat{g}^b as $\hat{g}^b = \text{DCM}(\hat{\phi}, \hat{\theta}, \hat{\psi})[0, 0, g_e]^T = g_e [-s_{\hat{\theta}}, s_{\hat{\theta}}c_{\hat{\phi}}, c_{\hat{\phi}}c_{\hat{\theta}}]^T$, where g_e is the Earth gravitational acceleration constant.

A three-axis magnetometer is used to obtain the measured yaw after computing measured roll and pitch angles. The magnetometer measurement model is $\tilde{m} = m_b^b + m_e^b + v_m$, where \tilde{m} denotes the magnetometer output, m_b^b and m_e^b denote the magnetic field vectors generated by the UAV and the Earth expressed in the body frame, and v_m represents the measurement noises. It is assumed that $\|m_b^b\| \ll \|m_e^b\|$, that is, $m_b^b \approx 0$. Magnetometer noise is generated by hard iron and soft iron noises, which can be eliminated by the calibration process. The filtered output \hat{m} of the calibrated magnetometer, which has axes align with the gyroscope axes, can be used to compute the measured yaw as $\hat{m} = \text{DCM}(\hat{\phi}, \hat{\theta}, \hat{\psi})[m_e, 0, 0]^T$, where m_e denotes the magnitude of Earth magnetic field.

Therefore, the measured attitude angles can be obtained from filtering the output of the accelerometer and magnetometer. These measured Euler angles are fused with the UAV attitude given by integrating the quaternion-based kinematic equation. Hence, it is important to compute \hat{g}^b and \hat{m} simply and enough accurately. To this end, other sensors are added to get a more accurate estimation, such as the Global Positioning System (GPS) and a pitot tube. GPS is an all-weather, worldwide, and reasonable cost system; however, it is low-rate updated and noisy, especially, can be jamming or cannot work in some special environments. A pitot tube is also a low-cost sensor and gives an airspeed estimation of UAV, which can be fused with the

accelerometer to obtain the more accurate value of \hat{g}^b . In this paper, a nonlinear airspeed filter measured from the pitot tube is proposed to increase airspeed estimation accuracy.

3. Filtering algorithm

In this paper, we design the UKF shown in Table 1 for the state $x = \text{vec}(q, b) \in \mathcal{R}^7$, thus the dynamic matrix F in step 1 is computed as $F(\omega, q) = I_7 + \begin{bmatrix} A(\omega) & B(q) \\ O_{3 \times 4} & -\tau I_3 \end{bmatrix} \Delta t$ and $B(q) = \frac{-1}{2} \begin{bmatrix} -\vec{q}^T \\ q_0 I_3 + [\vec{q} \times] \end{bmatrix}$. In step 2, the predicted matrix is updated to a new value P^* if and only if $P_q^* = P^*(1:4, 1:4)$ is positive-definite; thus, the lower-triangle matrix S computed by the efficient Cholesky algorithm is always well-defined. Selecting appropriate vectors called sigma points in designing the UKF yields more accurate nonlinear estimation than EKF [8-10]. In step 3, we compute 9 sigma points, where $[S]_j$ denotes the j -th column of the matrix S and

$$\begin{cases} \alpha = 10^{-4}, \beta = 2, \lambda = 7(\alpha^2 - 1), \gamma = \alpha\sqrt{7}, \gamma_i = \gamma, \varepsilon_i = i \forall i = 1:4; \gamma_i = -\gamma, \varepsilon_i = i - 4 \forall i = 5:8; \gamma_9 = 0 \\ \mu_i = \xi_i = 0.5(7 + \lambda)^{-1} \forall i = 1:8; \mu_9 = (3 + \lambda)(7 + \lambda)^{-1}; \xi_9 = \mu_9 + 1 + \beta - \alpha^2 \end{cases}$$

Compared with the standard UKF in [13], the proposed UKF is computationally efficient because it reduces the number of sigma points (from 15 to 9) and the dimension of squared-root matrix (from 7 to 4), which is based on the fact that the attitude does not depend on the bias term.

The noise of the accelerometer usually comes from the perturbation of motors, so the Chebyshev filter should be used to filter raw data of specific acceleration, that is $\hat{f} = \text{Chebyshev}(\tilde{f})$. Determining the cut frequency by other tests leads to a 2-order Chebyshev filter design, which is easy for implementation.

In [13], the gravitational acceleration was estimated by GPS, which is low-updated, and easy jamming or spoofing. In this paper, the UAV velocity is approximated by airspeed, which is measured by a pitot tube and filtered by the following nonlinear filter $\dot{\hat{v}}_a = f_{\text{pitot}}(\tilde{v}_a - \hat{v}_a) \text{sat}(\rho_1 + \rho_2^2(\tilde{v}_a - \hat{v}_a)^2)$, where \hat{v}_a and \tilde{v}_a denote the filtered airspeed and raw airspeed, f_{pitot} is the sampling frequency of the pitot tube, $\text{sat}(\cdot)$ denote the saturation function, and $\rho_1 < 1$ and ρ_2 are two designed positive parameters. Note that the smaller ρ_1 leads to the greater smoothing of filtered airspeed, and parameter ρ_2 can be considered a threshold of noise. These parameters are determined offline by changing them to obtain the best filtered airspeed from raw airspeed data. Note that this filter can be considered a low-pass filter with the adjustable gain $\text{sat}(\cdot)$ that increases if the error between raw data and filtered data increases leads to the faster convergence while remaining smooth. Based on filtered airspeed, the term \hat{g}^b can be computed as $\hat{g}^b = -\hat{f} + [\hat{v}_a, \hat{v}_a \tilde{\omega}_z, -\hat{v}_a \tilde{\omega}_y]^T$. This approximation is based on the UAV's velocity mostly from the component in the x -body axis. Now, measured attitude is computed in step 6 based on filtered sensor data as $\hat{\eta} = [\hat{\phi}, \hat{\theta}, \hat{\psi}]^T$, $\hat{\phi} = \text{atan2}(\hat{g}_2^b, \hat{g}_3^b)$, $\hat{\theta} = \text{atan2}\left(-\hat{g}_1^b, \sqrt{(\hat{g}_2^b)^2 + (\hat{g}_3^b)^2}\right)$,

$\hat{\psi} = \text{atan2}(s_{\phi}\hat{m}_3 - c_{\phi}\hat{m}_2, c_{\phi}\hat{m}_1 + s_{\phi}(s_{\phi}\hat{m}_2 + c_{\phi}\hat{m}_3))$. In this paper, we use the Euler angles as measured vector while in the other papers, it can be the accelerometer output, magnetometer output, and/or the entries of DCM matrix. The UKF algorithm is repeated until the UAV stops.

Table 1. Proposed Unscented Kalman filter

1	Compute dynamic matrix $F = F(\tilde{\omega} - b^+, q^+)$. Predict $x^- = Fx^+$ and normalize q^- .
2	Predict $P^* = FP^+F + Q$. If $P_q^* > 0$ then $P^- = P^*$, $S = \sqrt{P_q^*}$ end , where $P_q^* = P^*(1:4, 1:4)$.
3	Sigma points $\sigma_i = q^- + \gamma_i [S]_{e_i}$ and $\eta_i = \text{EulerOfQuat}(\sigma_i)$ where $i=1:9$.
4	$\bar{\eta} = \sum_{i=1}^9 \mu_i \eta_i$, $P_{q\eta} = \sum_{i=1}^8 \xi_i (\sigma_i - q^-)(\eta_i - \bar{\eta})^T$, $P_{\eta\eta} = R + \sum_{i=1}^9 \xi_i (\eta_i - \bar{\eta})(\eta_i - \bar{\eta})^T$.
5	Compute the Kalman matrix $K = \begin{bmatrix} P_{q\eta} P_{\eta\eta}^{-1} \\ O_{3 \times 3} \end{bmatrix}$. Correct the matrix $P^+ = P^- - \begin{bmatrix} P_{q\eta} \\ O_{3 \times 3} \end{bmatrix} K^T$.
6	If Receive data from sensors then $\hat{g}^b, \hat{m}, \hat{v}_a = \text{Filter}(\tilde{f}, \tilde{m}, \tilde{v}_a)$ and $\hat{\eta} = \text{EulerOfIMU}(\hat{g}^b, \hat{m})$.
7	Correct $x^+ = x^- + K(\hat{\eta} - \bar{\eta})$ and normalize q^+ end .

4. Flight test results

4.1 Flight test set up

The proposed algorithm is implemented in an actual fixed-wing UAV with a real flight test to verify the theoretical analysis. Sensors MEMS IMU Module ADIS16467-2 and Digital Magnetometer HMR2300 are used for UAV attitude estimation. It is vital to obtain the real attitude to validate the algorithms; thus, the high-accuracy sensor Ixblue Phins Surface PH2647 is attached to the UAV cabin. Data from this sensor Ixblue are used only for comparing UKF and EKF algorithms and not for UAV attitude estimation. The gyroscope of ADIS16467-2 has the configuration: in run-bias stability of $2.5^\circ/\text{hr}$, angular random walk of $0.15^\circ/\sqrt{\text{hr}}$, output noise of $[0.05, 0.08, 0.08]^\circ/\text{sec}$, and rate noise density of $[0.002, 0.003, 0.003]^\circ/\sqrt{\text{Hz}}$. The accelerometer of ADIS16467-2 has in run-bias stability of $13\mu\text{g}$, velocity random walk of $0.037 \text{ m/sec}/\sqrt{\text{hr}}$, output noise of 2.3mg , noise density of $100\mu\text{g}/\sqrt{\text{Hz}}$. The digital magnetometer has the accuracy of $\pm 1\text{Gauss} 0.5\% \text{FS}$, the offset error is approximated at $0.10\% \text{FS}$, the output rate selectable between 10 and 154 samples/sec. Lastly, Ixblue Phins Surface has the heading with GPS/USBL/LBL which is 0.01° secant latitude, and the roll and pitch dynamic accuracy (no aiding) is 0.01° . Our autopilot works with the frequency 100Hz. All configuration data of sensors are based on its datasheets.

After the flight test, UKF and EKF algorithms are performed in the Matlab software with real flight data from UAV sensors. Estimated Euler angles are compared with the UAV attitude from the high accuracy Ixblue sensor, which is considered the real UAV attitude. Our autopilot system and Ixblue Phins Surface are independent of each other; Ixblue data are reference UAV Euler angles used to test the UKF and EKF algorithm's efficiency only. The misalignment between our AP and the Ixblue is removed by letting the UAV not move during T (s) and then use the following algorithm in Matlab after the flight test.

4.2 Alignment algorithm

To alignment two frames of Ixblue and our AP, first we calculate the attitude when the UAV is not moving as $\eta_{Ix}^o = \frac{1}{T} \int_0^T \eta_{Ix}(t) dt$ and $\eta_{AP}^o = \frac{1}{T} \int_0^T \eta_{AP}(t) dt$. With an arbitrary vector ζ , from two equations $\zeta_{Ix} = \text{DCM}(\eta_{Ix})\zeta_i$ and $\zeta_{AP} = \text{DCM}(\eta_{AP})\zeta_i$ where ζ_{Ix}, ζ_{AP} , and ζ_i is the coordinate of ζ in Ixblue-, AP-, and inertial- frames, we have $\zeta_{Ix} = \Pi \zeta_{AP}$, where $\Pi = \text{DCM}(\eta_{Ix}^o) \text{DCM}^T(\eta_{AP}^o)$ is a constant DCM between AP and Ixblue. Now, the estimated attitude of Ixblue-frame are computed based on Euler angles obtained from AP according to $\zeta_{Ix} = \underbrace{\Pi \times \text{DCM}(\eta_{AP})}_{\Sigma} \zeta_i$ as

$$\phi = \text{atan2}(\Sigma_{23}, \Sigma_{33}), \theta = -\text{asin}(\Sigma_{13}), \psi = \text{atan2}(\Sigma_{12}, \Sigma_{11}).$$

These attitudes obtained from two algorithms, including conventional EKF (in blue) and the proposed UKF (in red), and the sensor Ixblue Phins Surface (in black) are compared and shown in Fig. 1. Figure 2 depicts the estimated attitude deviations between two Kalman filters and Ixblue.

Compared with the EKF, the UKF generates a closer roll angle to the Ixblue sensor. Between 400s and 500s, the EKF fails to estimate the roll angle and makes it drift. In contrast, the UKF remains the performance and keeps tracking the roll angle of Ixblue continuously. The difference between the UKF and EKF algorithms is clarified when comparing the pitch angle. All the time, the EKF cannot track the pitch angle of Ixblue like the UKF. From 400s to 700s, we try to increase the UAV's velocity to test the algorithm's performance at a high-level velocity and slow down at the end; and figures show that the EKF is affected by the UAV's variation. In this flight test, the UKF shows the best performance at the pitch angle comparison; and the error between the UKF and the Ixblue can be overlooked. For yaw angle comparison, as shown in the figures, the UKF is still better than the EKF. Figure 3 indicates that the proposed UKF's computational cost is less about 2 times than the standard UKF's one in [13] while the estimation errors are the same, which makes the proposed UKF is easy to implemented in low-cost sensor systems than the conventional UKF.

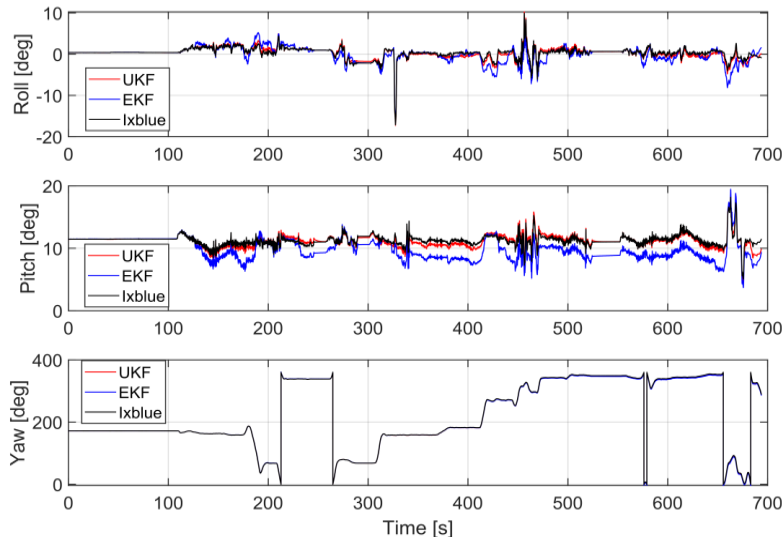


Figure 1. Euler angles vs. time. Red: UKF, blue: EKF, black: Ixblue

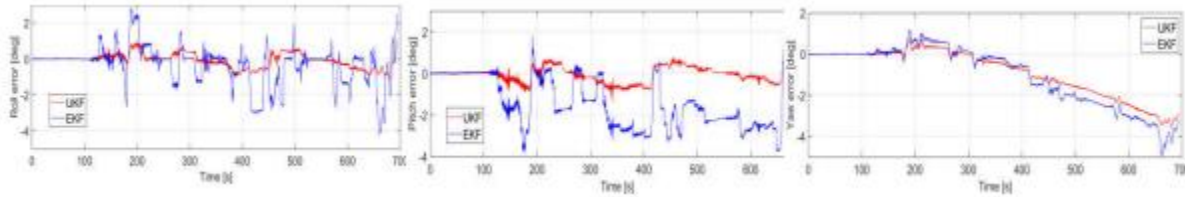


Figure 2. Errors of attitude. Red: UKF, blue: EKF. Left to right: roll, pitch, and yaw

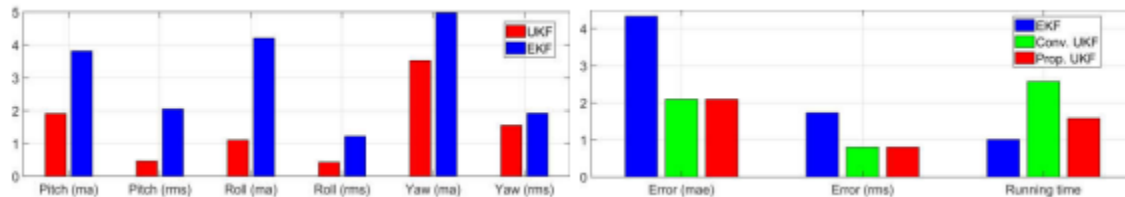


Figure 3. Compare Kalman filters. MA and RMS: maximum absolute and root mean squared (in degree). Running times: 1 unit=40s. Blue: EKF, Red: Proposed UKF, Green: Conventional UKF [13]

5. Conclusion

This paper proposes a novel approach of unscented Kalman filter that fuses the measured data from filtering the raw sensor data and integrating the quaternion-based kinematic equation to estimate the UAV attitude in GPS-denied environment. This algorithm has a more accurate estimation than the EKF and has low computational cost than conventional UKF; thus, it can be implemented in real UAVs with a low-cost microprocessor. The real flight test shows the better performance of the proposed UKF compared with the EKF and the standard UKF, which supports the theoretical analysis.

References

- [1] Z. Wachter, “A cost effective motion platform for performance testing of mems-based attitude and heading reference systems,” *Journal of Intelligent & Robotic Systems*, vol. 70, no. 1, pp. 411–419, 2013.
- [2] W. Geiger, J. Bartholomeyczik, U. Breng, W. Gutmann, M. Hafen, E. Handrich, M. Huber, A. Jackle, U. Kempfer, H. Kopmann *et al.*, “Mems imu for ahrs applications,” in *Proceedings of IEEE/ION PLANS 2008*, 2008, pp. 225–231.
- [3] M. Cordero, F. Alarcon, A. Jimenez, A. Viguria, and A. Ollero, “Survey on attitude and heading reference systems for remotely piloted aircraft systems,” in *2014 International Conference on Unmanned Aircraft Systems (ICUAS)*. IEEE, 2014, pp. 876–884.
- [4] J. L. Crassidis, F. L. Markley, and Y. Cheng, “Survey of nonlinear attitude estimation methods,” *Journal of guidance, control, and dynamics*, vol. 30, no. 1, pp. 12–28, 2007.
- [5] E. J. Lefferts, F. L. Markley, and M. D. Shuster, “Kalman filtering for spacecraft attitude estimation,” *Journal of Guidance, Control, and Dynamics*, vol. 5, no. 5, pp. 417–429, 1982.
- [6] G. Mao, S. Drake, and B. D. Anderson, “Design of an extended kalman filter for uav localization,” in *2007 Information, Decision and Control*. IEEE, 2007, pp. 224–229.
- [7] A. G. Kallapur and S. G. Anavatti, “Uav linear and nonlinear estimation using extended kalman filter,” in *2006 International Conference on Computational Intelligence for Modelling*

Control and Automation and International Conference on Intelligent Agents Web Technologies and International Commerce (CIMCA '06). IEEE, 2006, pp. 250–250.

[8] R. Van Der Merwe and E. A. Wan, “The square-root unscented kalman filter for state and parameter-estimation,” in *2001 IEEE international conference on acoustics, speech, and signal processing. Proceedings (Cat. No. 01CH37221)*, vol. 6. IEEE, 2001, pp. 3461–3464.

[9] E. A. Wan and R. Van Der Merwe, “The unscented kalman filter for nonlinear estimation,” in *Proceedings of the IEEE 2000 Adaptive Systems for Signal Processing, Communications, and Control Symposium (Cat. No. 00EX373)*. Ieee, 2000, pp. 153–158.

[10] S. J. Julier and J. K. Uhlmann, “New extension of the kalman filter to nonlinear systems,” in *Signal processing, sensor fusion, and target recognition VI*, vol. 3068. International Society for Optics and Photonics, 1997, pp. 182–193.

[11] J. J. LaViola, “A comparison of unscented and extended kalman filtering for estimating quaternion motion,” in *Proceedings of the 2003 American Control Conference, 2003.*, vol. 3. IEEE, 2003, pp. 2435–2440.

[12] J. L. Crassidis and F. L. Markley, “Unscented filtering for spacecraft attitude estimation,” *Journal of guidance, control, and dynamics*, vol. 26, no. 4, pp. 536–542, 2003.

[13] H. G. De Marina, F. J. Pereda, J. M. Giron-Sierra, and F. Espinosa, “Uav attitude estimation using unscented kalman filter and triad,” *IEEE Transactions on Industrial Electronics*, vol. 59, no. 11, pp. 4465–4474, 2011.

Long Range Delivery Experiment using a VTOL Type UAV -A Case Study of the Medical Supply Delivery Between Remote Islands-

Kazuo Watanabe^{1*}, Masafumi Miwa², and Shinya Takatsuka³

1 Technology Integration Office, WorldLick & Company Co., Ltd., 98-2, Iwagakakiuchi,
Kamigamo, Kyoto, Japan, 603-8053.

2 Graduate School of Technology, Industrial and Social Sciences, Tokushima University, 2-1
Minamijosanjima, Tokushima, Japan, 707-8501.

3 Digital Design Lab, ANA HOLDINGS INC, Shiodome City Center, 1-5-2 Higashi-
Shimbashi, Minatoku, Tokyo, Japan, 105-7140.

*Corresponding author. E-mail: k.watanabe@skylinkjapan.com

Abstract

In Japan, which consists of more than 6,800 islands, marine transportation is essential for supporting people's lives in the marine area. However, the number of ferries connecting remote islands is limited, and the travel time takes longer, so the rapid supply of daily necessities and medicines is an issue. To develop supplemental transportation way, 32 km round trip BVLOS (Beyond Visual Line of Sight) goods transportation experiment between remote islands using a Wingcopter, a VTOL aircraft, was conducted in Goto Island Nagasaki, Japan. The autopilot UAV that took off from the main island was equipped with an LTE communication system to enable real-time monitoring of telemetry information and FPV images. After landing at the destination, a nurse at the clinic retrieved the medicines and then flew the return trip without changing the battery. The medical supply transport experiment was carried out in March 2021, making two round trips for 72 km. During the flight, no communication failure or aircraft trouble occurred. The flight speed was 80-120 km, and the flight time was about 35 minutes, not including the waiting time on the island where it arrived. After the 32 km round trip flight, the remaining battery power was more than 30%, confirming that the aircraft can sufficiently withstand long-distance transportation.

Keywords: VTOL, BVLOS, Transport, Island, Medical supply

1. Introduction

In Japan, the so-called Level 4 BVLOS (Beyond Visual Line of Sight) will be implemented in 2022, which is the automatic navigation over urban areas by Unmanned Aerial Vehicles (UAVs, drones) without visual inspection (JAXA, 2017). Level 4 BVLOS is expected to be used to transport goods and will require a variety of technological innovations and functional integration to safely deliver heavy objects from several kilometers to several tens of kilometers away. Ahead of the Level 4 operation, experiments and market development are actively underway to develop automatic and non-visual navigation in uninhabited areas (Level 3 operation), which is one step ahead of the Level 4 operation, with particular focus on the transportation of goods between mountainous regions and remote islands.

There are more than 6,800 islands in Japan, and marine transportation is an important infrastructure that supports the lives of the residents. However, the number of ferry services is limited, and travel is time-consuming. Therefore, drones have been attracting attention as an efficient method of transporting medical supplies and daily goods. However, the aircraft that have been used in existing experiments are mainly multi-rotor type aircraft, and their flight range

is limited to a few kilometers due to their characteristics of high battery consumption. Therefore, the transportation distance is limited for inter-island transportation.

The Wingcopter is a vertical takeoff and landing (VTOL) aircraft that combines the characteristics of both multi-rotor and fixed-wing aircraft. It can fly long distances with low battery consumption and rotary-wing aircraft, carrying a large payload, and does not require a wide takeoff and landing area. In this paper, we report on the improvement of the system based on the past trials (Watanabe and Miwa, 2020) and the experiment of transporting pharmaceuticals using LTE communication.

The goals of the experiment using the LTE communication system and VTOL aircraft are: i) to transmit telemetry information and FPV images to the ground in real-time without interruption, ii) to allow the Wingcopter to fly safely over the target range, and iii) to transport supplies without changing batteries on the outward and return trips.

2. Outline of the Experiment

2.1 Organizations

This experiment was conducted by the six organizations listed in Table I. ANA Holdings Inc. was in charge of overall coordination, flight application to the Civil Aviation Bureau, drone operation management, and operation of the pharmaceutical delivery management system. Takeda Pharmaceutical Co., Ltd. was responsible for the management of pharmaceutical wholesalers and development of the pharmaceutical delivery scenario. Nagasaki University coordinated with medical personnel engaged in online medical treatment and medication guidance, and drug transportation. NTT DOCOMO, Inc., as a mobile service provider, provided an LTE communication network and assisted in the formulation of the flight plan considering the radio wave conditions. WorldLink & Company, Co., Ltd. provided the aircraft and technical support for the operation (ANA, 2021). Tokushima University developed the communication systems.

Table I. List of the organization and their roles

Organization Name	Role
ANA Holdings Inc.	Overall coordination, flight application submission, drone operation management and operation of the pharmaceutical delivery management system.
Takeda Pharmaceutical Co., Ltd.	Management of pharmaceutical wholesalers and development of the pharmaceutical delivery scenario.
Nagasaki University	Coordination with medical personnel engaged in online medical treatment and medication guidance, and drug transportation.
NTT DOCOMO, Inc.	Providing an LTE communication network and assisted in the formulation of the flight plan considering the radio wave conditions.
WorldLink & Company, Co., Ltd.	Providing the aircraft and technical support for the operation.
Tokushima University	Development of the communication systems.

2.2 Flightpath and Operations

In this experiment, the aircraft flew from the takeoff point at 32°41'38 "N, 128°51'24 "E in Fukuejima, Goto City, Nagasaki Prefecture, to Hisaka Island, located 16 km away at 32°47'58 "N, 128°52'23 "E. The aircraft was loaded with medical supplies at the takeoff point. After retrieving the supplies at Hisaka Island, the aircraft returned to the takeoff point without changing the battery. Therefore, the total distance flown at one time was about 32 km. This drone transportation is the longest distance record in Japan.

Figure 1 shows the flight path. Takeoff was from the breakwater at Fukue Port, and after vertical takeoff, the drone shifted to horizontal flight at an altitude of 150 m above the ground with a maximum speed of 120 km/h. The drone landed on Hisaka Island. As it approached the landing site at Hisaka Island, it gradually descended the altitude, and the plane shifted from horizontal flight mode to copter mode before landing. Pilots capable of manual control were stationed at the takeoff and landing points in case of emergencies, but all takeoffs and landings can be performed automatically under normal circumstances.

The experiment was carried out on March 25, 2021, with two round-trip flights. The schedule and route on the day of the flight were notified in advance to the ferry operator, local fishing cooperative, etc., and on the website to inform all related parties.



Figure 1. Location of the Goto island and flight path for the experiment
(*Blue dotted line shows the ferry route)

3. Aircraft and Operation Systems

3.1 Aircraft

Wingcopter Heavy Lift 178, a VTOL aircraft manufactured by Wingcopter GmbH., was used for the experiment. The aircraft flies as a four-rotor multi-copter in the copter mode by the thrust generated by these rotors, as shown in Fig. 2. After taking off vertically, the four rotors are tilted, and the aircraft flies as a twin-engine aircraft using the thrust of only the front two rotors and the lift of the main wings. The rear two rotors, which are stationary, are folded to reduce drag during horizontal flight. There is a removable cargo box underneath the fuselage, in which the cargo is stowed. The maximum takeoff weight is 16kg, of which the aircraft weight is 7.5kg, accounting for about half the total weight. From the remaining takeoff weight of 8.5kg, the weights of the battery (6-cell 16,000 mAh), cargo case, FPV camera, and communication system are as shown

in Table II. Since three batteries were used in this experiment, the weight of the loadable capacity was 0.7kg.



Figure 2. Wingcopter HL178 in copter mode with removable cargo box

Table II. Weight of the aircraft and payload

Items	Weight (kg)
Body	7.5
Buttery@3units	5.4
Cargo Box	1.4
Communication system	0.7
Buttery for Communication system	0.3
Remaining loadable capacity	0.7
Total	16

3.2 Communication System Configuration

The system configuration for this experiment is shown in Figure 3. BVLOS needs to maintain constant communication with the aircraft so that the status of the aircraft can be monitored at all times. In order to meet this requirement, we redesigned the control, communication, and power systems to be redundant. In addition, a video communication device was installed to enable operation from an FPV angle.

Two types of radio-controlled transmitters and receivers can be selected using a selector circuit for the control system (MM Switch). This system enables independent manual operation at the start and endpoints. In addition, a Raspberry Pi-based device was placed between the LTE terminal and the flight controller (FC) to enable command transmission by the Ground Control Station (GCS) using the MavLink protocol through a modem or LTE line. For the GCS, we used the freeware QGround Control, which enables us to monitor the aircraft from two locations at the takeoff and landing points simultaneously using LTE lines. For communication redundancy, we installed a 2.4GHz communication device, P2400 (Microhard), for receiving telemetry information and MavLink communication, and a 5.7GHz receiver, HN10TR (BODUK), for receiving FPV images of the aircraft. These two kinds of signals can achieve by installing one each at the takeoff and landing sites.

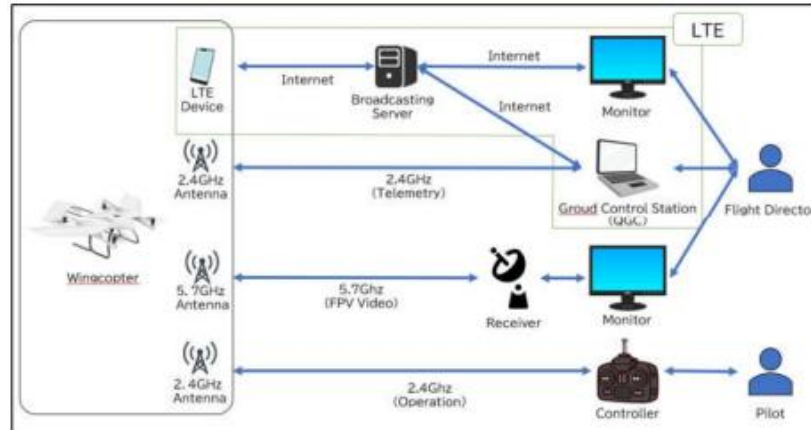


Figure 3. Communication system configuration

The flight logs are stored in the FC and can be retrieved by connecting to a PC running the QGC via USB. In this experiment, we developed a system to display various telemetry information of the Wingcopter and estimate the wind direction and speed during the flight. After the end of the flight, we collected and analyzed the flight logs with the cooperation of AirData (AirData, 2021), a cloud-based flight log management service.

3.3 The Intervention of the Pilot During Flight

In this experiment, the aircraft is navigated automatically in both copter mode for takeoff and landing and plane mode for horizontal flight. However, suppose there is a large error between the coordinates of the landing site and the GPS information provided by the aircraft. In that case, the radio controller transmitter can switch to manual control.

A two-person team carried out the work at the takeoff and landing points of the flight: a pilot who carries the radio-controlled transmitter and controls the aircraft. A flight director checks the telemetry information displayed on the QGC on a PC monitor and sends MavLink commands as necessary. The operator holds the radio-controlled transmitter at all times to avoid obstacles within the radio-controlled transmitter's range. Besides, it can send RTL (Return to Land) commands to abort the mission and return to the home position via MavLink when the radio-controlled transmitter enters the LTE-only communication state. In this way, the operator can always intervene.

4. Results

4.1 First Flight

The first round trip flight was conducted in the morning. The weather was cloudy, the temperature on the ground was 17.5 degrees Celsius, and the wind speed on the ground was 5m/s. The wind direction was north. The maximum flight speed and flight time for the outward trip were 118km/h and 16 minutes, and for the return trip, 115km/h and 11 minutes, respectively. Differences in flight speed between outward and return flights were due to the aircraft being pushed by the wind from the north.

The telemetry information from the 2.4GHz band was interrupted at about 5km from the takeoff point. Still, the LTE communication was stable for telemetry information and images and could be monitored until the landing.

As for the battery, Figure 4 shows that there was a sudden drop in voltage and capacity immediately after takeoff and just before landing. This indicates that a large load is placed on the battery during takeoff and landing in copter mode, which is a characteristic power consumption

trend of VTOL aircraft. During level flight, recovery and a gently decreasing trend of the remaining battery power were observed, with a remaining power level of about 50% during outward landing and about 30% during the return flight. There was no collapse of the loaded cargo, and the flight was very stable.

4.2 Second Flight

During the second round trip flight in the afternoon, the weather was clear, and the temperature on the ground was 18.2 degrees Celsius. The wind speed on the ground was 5.8 m/s northward on the outward trip and 6.1m/s northeastward on the return trip. The maximum flight speed and duration for the outward flight were 127km/h and 14 minutes, respectively, and 111km/h and 11 minutes for the return flight. The maximum speed of the outbound flight exceeded that of the return flight despite the headwind being unknown.

As in the first round trip flight, the telemetry information using the 2.4GHz band was interrupted at about 5km from the takeoff point, but the LTE communication was stable for both telemetry information and images and could monitor during flight.

As for the battery, Figure 5 shows the same trend as the first round trip. A sharp drop in voltage and capacity occurred immediately after takeoff and just before landing. The remaining power level at the landing on the outbound flight was 50% and about 30% on the return flight. There was no collapse of the loaded cargo, and the flight was very stable.

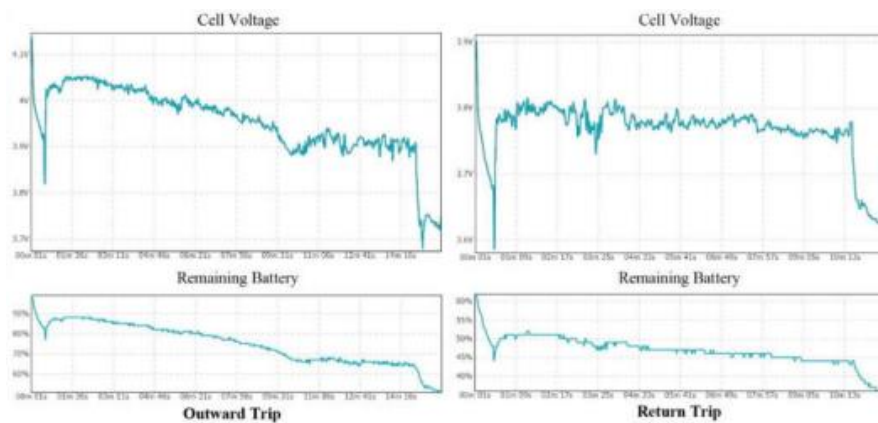


Figure 4. Outbound battery consumption during first round trip

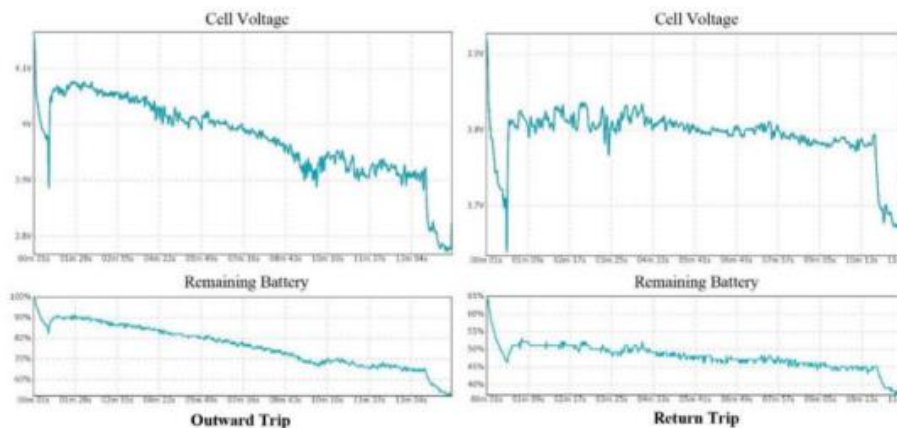


Figure 5. Outbound battery consumption during second round trip

5. Conclusion

In this study, as a demonstration of long-distance transportation, a 32-km transportation experiment was conducted on a remote island using a Wingcopter, a VTOL aircraft, and an LTE communication system. The objectives of this experiment were: i) to transmit telemetry information and FPV images to the ground in real-time without interruption, ii) to allow Wingcopter to fly safely over the target range, and iii) to transport goods without changing batteries on the outward and return trips. For i), we could monitor telemetry information and FPV images in real-time by redundant communication using 2.4 GHz, 5.7 GHz, and LTE bands. For ii), the flight was very stable without collapsing the cargo. As for iii), we were able to return the aircraft with 30% remaining power without changing the battery for a route of 16km one way and 32km round trip. This means that we were able to demonstrate that long-distance transportation is possible without having to assign an engineer to operate the aircraft at the receiving end.

From the results, we can conclude that this experiment was generally successful.

Acknowledgements

We would like to thank Goto city officers, medical staff, and Hisaka island residents for the warm support. This work was conducted under the project entitled “Project to Promote the Introduction of Advanced Technologies to Simultaneously Realize Social Innovation and Decarbonization of Logistics” funded by Organization for the Promotion of Low Emission Vehicle.

References

- [1] AirData (2021), <https://app.airdata.com/main?flight=last>
- [2] ANA Holdings Inc. (2021), “Medical supply delivery using fixed-wing vertical takeoff and landing (VTOL) drones.”, Press release, available at: <https://www.anahd.co.jp/group/pr/202103/20210310.html> (accessed 30 May 2021).
- [3] Japan Aerospace Exploration Agency (JAXA) (2017), “R&D Program of Small UAS Traffic Management in Japan”, ICAO Asia Pacific UAS Task Force 1st meeting, Bangkok, Thailand, pp.2-4, available at: <https://www.icao.int/APAC/Meetings/2017%20APUASTF1/SP03.pdf> (accessed 30 May 2021).
- [4] Watanabe, K. and Miwa, M. (2020): “Long-distance BVLOS transportation experiment with VTOL Wingcopter”, SICE Symposium on System Integration Division, 2A1-07.

Using Telematics to Improve EMTs' Response Times After Traffic Accidents Saving up to 2000 Lives per Year

Mark Haley^{1*}

¹Analytical Software Inc. President, 8505 Broad Meadow Lane, McKinney, Texas 75071 USA,
Previously Professor, China University

*Corresponding author. E-mail: Haley@Provenrobotics.com

Abstract

There were 36,096 traffic deaths in 2019 in the U.S., however telematics and data from onboard vehicle sensors could expedite the response times of first responders after traffic accidents thereby saving lives. 10% of fatal U.S. crashes were reported in over ten minutes. This paper identifies how to automatically report more vehicle accidents within seconds. In 2021, the European Union was far ahead of the U.S. in the ability to automatically report vehicle accidents since after April 2018 all European Car Makers have been required to include eCall, an automated emergency call technology. When a crash occurs, eCall sends the location and also indicates if the airbags were deployed. It's crucial that Emergency Medical Technicians (EMTs) deliver accident victims to advanced medical care at hospitals within the Golden Hour, the crucial hour after an accident when doctors have the best chance to save lives. The method of treating trauma is called the "Advanced Trauma Life Support (ATLS)". In the U.S., only 10% of drivers permitted sharing telematics vehicle data, however with bigger automobile insurance discounts, better technology, laws mandating onboard vehicle technology to automatically report accidents and protection on privacy, more U.S. drivers could be enticed to share this data. This would expedite response times and improve the chances for survival of hundreds of US vehicle accident victims each year. If a system such as eCall was fully implemented in the U.S, it could save over 1,300 lives per year and up to 2,000 lives total in the U.S. and the EU.

Keywords: optimization, eCall, EMTs, first responders, privacy

1. Introduction

After vehicle accidents, it is crucial that the victims receive advanced medical care at hospitals within the Golden Hour after the crash to ensure that the victim will have the best chance of survival. Per the American College of Surgeons, "The concept of the "Golden Hour" emphasizes the urgency necessary for successful treatment of injured patients and is not intended to represent a fixed time period of 60 minutes. Rather, it is the window of opportunity during which doctors can have a positive impact on the morbidity and mortality associated with injury". [1] The method of treating trauma is called the "Advanced Trauma Life Support (ATLS)", and was developed in 1976 based on those seriously injured. "Studies have shown that approximately 50% of fatalities occur within minutes, 30% within a couple of hours, and 20% during the following days and weeks". [2][3] Also, studies have show that the fatality rate is twice as high in rural areas versus cities where the accidents are reported more quickly.[4][5] This paper shows that the response time to meet that Golden Hour is much more difficult in U.S. versus urban areas like Europe where there are more medical facilities near most accidents. Advanced telematics are the ideal U.S. option to expedite response time for medical care. eCall could save 700 lives per year in EU & 1,300 lives per year in the US.

YouTube Video - eCall 911 - <https://youtu.be/ZWiFprFIIsE>

2. Purpose - EU's eCall versus U.S. Telematics to Improve America's Vehicle Safety

Telematics is the combination of telecommunications, onboard vehicle or other sensors or even phones which can help expedite safety. On a more limited basis, it has been used in the U.S. by insurance companies to monitor drivers to encourage them to improve their driving skills by avoiding excessive speeds or braking, thereby reducing their insurance premiums. On the other hand, the European Union's eCall is used to report an accident, with GPS location and whether the airbag was deployed. Europe is far ahead of the US in implementing real-time responses to accidents, and this paper shows how the U.S. can significantly improve its systems and thereby save lives. This paper also provides an option which goes far beyond eCall with a broader solution which can save even more lives.

While eCall is crucial for Europe, this paper shows the EU's analysis used to justify eCall overstated by over 3 times the projected lives saved. The EU's analysis failed to address the crucial issue of the impact on rural versus urban areas. The EU justified the eCall based on projected saved lives in Scandinavian countries which are much less congested than Europe. Europe has 262.2 people per square mile (Table 2), which is over 7 times more congested than Norway, which only has 35.6 people per square mile. On the other hand, this paper correctly bases the savings in U.S. lives on the population density of the U.S. versus Europe where the U.S. is roughly 1/3 as congested as Europe. Also, the case for eCall is weaker in densely populated countries like Japan, Korea, China etc.

Therefore, while the EU originally suggested eCall would save 2,500 lives per year, as shown in Tables 1 and 2, the actual projected number of saved lives per year may be only 730 lives, which is less than 1/3 of the original projection. While this is extraordinary, projected forecasts on such a crucial issue need to be more precise, such as the methodology used in the paper. In less congested areas, the distance to hospitals is further and the time for emergency calls made by other people who witnessed the accident is much longer. For example, in remote areas of the U.S. such as Alaska, Nevada, Idaho, Wyoming, Utah and Montana, etc., it can be hours or even days before another vehicle might drive by in a remote area. The person in the accident could be unconscious or without a phone and might not be able to call for help. And in many remote areas of the U.S., there is no cell phone service.

As an example, one of the most remote areas in the lower 48 is the Frank Church-River of No Return Wilderness, which covers 2.37 million acres, the largest US wilderness in the lower 48 states. It has limited if any cell phone coverage, including the nearby roads. For example, Dixie Idaho (population 2019, 3237) near this area had limited cell coverage (2019).

Also, in Big Bend National Park, the drive from the Castolon Visitor Center to the Mariscal Mine, a drive of 35 miles which takes roughly 2 hours and 30 minutes to cover has sporadic cell coverage. Large areas in Alaska have almost no coverage. This paper shows that the U.S. which is almost 1/3 as congested as Europe (Table 2) could save over 1,300 lives per year.

$$TRT = \text{Time 911 call} + \text{Time at accident} + \text{Time to Hospital} \quad (1)$$

Here, the Total Response Time (TRT) equals: (1) the time before the 911 call is made, which without eCall is much longer in rural areas than urban areas since more people are likely to report an accident in congested areas when the victim might be unconscious; (2) the time at the accident where the victim must be extricated from vehicle while providing emergency triage. This would be similar whether in urban or rural areas; and (3) the time to travel to the hospital which depends on the distance to the hospital and whether the victim is airlifted to hospital. In remote areas, this would obviously be longer. eCall or other telematic systems reduce the time before the emergency call is made, and this time is most significant in rural areas such as much

of the U.S. and Norway (Table 2). The TRT time should be less than the Golden Hour needed to ensure the optimal medical care.

2.1 Vehicle Deaths in the U.S. versus the EU

In 2019, there were roughly 280 million vehicles in both the U.S. and the EU, however the U.S. had more than double the number of deaths per million people, 110 versus 50.9 for the EU (Table 1 [6],[7],[8]). However, the average U.S. driver covers almost double the miles of driver in the EU (13,476 U.S. versus 7,440 EU). The net result is that the deaths per million population adjusted for the miles driven is similar, 92.2 deaths in the EU versus 110.0 deaths in the U.S.

Table 1 - Vehicle Related Deaths in the U.S. and the EU

	<u>European Union (EU)*</u>	<u>United States (US)*</u>
Population (Millions)	447.7	328.2
Vehicle Fatalities (2019)	22.800	36.096
Deaths per Million Pop.	50.9	110.0
Number of Vehicles (Mil.)	280	284
Number of Miles Driven**	7.440	13.476
Deaths adjusted by Miles Driven	92.2	110.0

* The population, fatalities, death per million, is 2019 and the EU excludes Britain from EU Commission and US Federal Highway Adm. **Miles driven is DOT March 2018

3. Design/Methodology/Approach - EU's eCall versus U.S.'s Limited Telematics

EU's eCall focuses on expediting EMT's response times after vehicle accidents while the U.S. telematics options are more focused on improving driver safety before crashes and collecting data on their driving habits.

3.1 EU's eCall

eCall was developed by the European Union to improve driver safety. In 2018, it mandated that all new vehicles must include a telematic device which automatically reports vehicle accidents by calling Europe's emergency number, 112. This number is the equivalent of the U.S.'s 911. Then, emergency personnel are sent to the accident site to bring the victims to the hospital. EU's rationale for this requirement was clear: "While new automotive technologies have resulted in a sharp drop in the number of fatalities – which have fallen by 57.5% since 2001, the numbers are still high. By speeding up emergency response times by 40% in urban areas and 50% in the countryside, it is estimated that eCall could help prevent 2,500 road deaths and save EUR 26 billion every year." [9][10] However, more recent, detailed cost benefit analysis indicated only a 3.2% reduction in fatalities or roughly 730 lives saved once eCall is fully implemented [2][3]. The number of lives saved is higher in rural areas since the response time is much longer and the chances that someone reports the accident is much lower in remote areas (or late at night in urban areas). The hardware cost for eCall is as little as 30 Euros (1.22 Euros/dollar * 30 = \$36.6).

3.2 Potential Number of Lives Saved by Implementing a System like EU's eCall in the U.S.

As noted previously, the EU could save about 730 lives per year related to vehicle accidents once eCall is fully implemented [2] [3]. Norway, a rural country and a focal point of one of these studies had a projected 4% improvement in lives saved of lives, while the UK, a congested county with about 712 people per square mile, had a savings of 2%.

The number of projected saved lives in the U.S. assuming a linear relationship between density and lives saved could be 1,336* per year once a system similar to eCall is fully

implemented in the U.S. This is based on the 3.7% saving in lives (3.7% * 36,096). This is a higher % savings versus the EU since the U.S. is much less congested than the EU. In 2019, there were 92.9 people per square miles in the U.S. versus 262.2 in the EU. Alaska only had 1.1 people per square mile. While the arguments were strong for EU’s eCall, the mandate for implementing a U.S. type cCall system is even more compelling since the U.S. would save a projected 600 more lives per year than the EU.

Table 2 - Projected Lives Saved/yr. vs. Population Density once eCall is Fully Implemented

	<u>Area</u> <u>Square Miles</u>	<u>Population</u> <u>(Millions)</u>	<u>People/</u> <u>Sq Mile</u>	<u>Density</u> <u>vs. Norway</u>	<u>% Lives</u> <u>Saved</u>
European Union (EU)	1,707,642	447.7	262.2	7.36	3.2%
United States (US)	3,531,905	328.2	92.9	2.61	3.7%
Norway	148,729	5.3	35.6	1.00	4.0%
Britain	93,628	66.7	712.4	19.99	2.0%
Alaska	663,300	0.7	1.1	0.03	

* % Lives saved calculated based on linear relation vs. Norway and Britain

3.3 Worldwide Impact

Up to 2,000 or more lives per year could be saved by using an eCall system in the U.S. and the EU. Table 3 shows that in 6 key countries, the total lives saved could be over 4,700 lives per year. Even though China is over 4 times as crowded in people per square mile compared to the U.S., China’s large population results in even more potential lives saved than the U.S.

Table 3 - Potential Worldwide Lives Saved/yr. if an eCall type system is Implemented

	<u>Population</u> <u>(Millions)</u>	<u>Land Area</u> <u>Sq miles</u>	<u>Traffic</u> <u>Fatalities</u>	<u>People/</u> <u>Sq. Mile</u>	<u>Deaths/</u> <u>10,000</u>	<u>Lives</u> <u>Saved/Yr.</u>
China	1,398	3,600,950	63,194	388	4.5	1,808
US	328	3,531,905	36,096	93	11.0	1,345
EU	447	1,707,642	22,800	262	5.1	736
India	1,366	1,147,960	151,113	1,190	11.1	732
Vietnam	96	119,720	7,600	802	7.9	124
Japan	126	140,752	3,920	895	3.1	53
					Total	<u>4,798</u>

Population and Fatalities are 2019 except China (2018)

3.4 Difficulty in Calculating Lives Saved Using EU’s eCall due to COVID-19 impact on Driving

Unfortunately, due to COVID-19, it will be difficult to accurately calculate the impact of eCall on saved lives since the number of miles driven in both the U.S. and the EU significantly declined in 2020 (over 10 percent) and their driving patterns changed dramatically. And less miles driven results in fewer deaths. Moreover, people tended to drive more for local shopping and not to their jobs. While the highways were less crowded, it appeared that there was more speeding, resulting in more high-speed accidents. Once the miles driven in both the EU and the U.S. return to pre-COVID-19 levels, a more accurate analysis of a fully implemented eCall or other technologies could be more accurately calculated.

3.5 How eCall and Other Real-time Telematics Solutions Work

Figure 1 shows how a general telematic solution such as the EU’s eCall works.

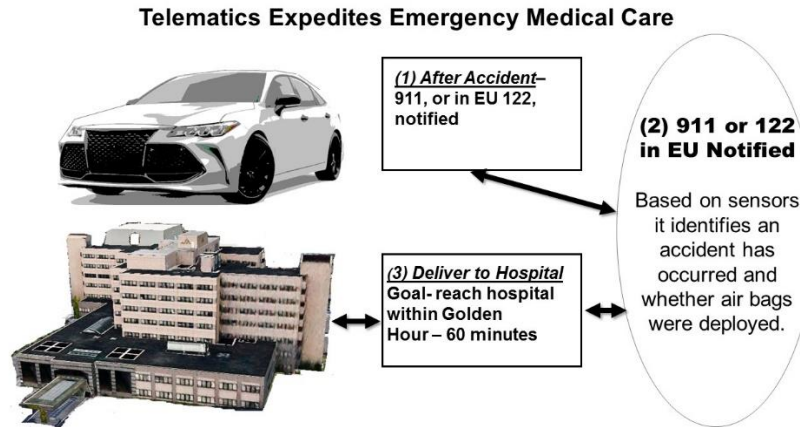


Figure 1 - How Telematics, such as eCall, Notify EMTs after Accidents

After an accident is detected by sensors and/or a device in the vehicle, including even cell phones, an emergency message is automatically sent to 911, or for the EU 112. In the case of GM's OnStar™, it notifies a call center, which then notifies 911.

3.6 U.S. Telematics - GM's OnStar™

GM's OnStar™ is a subsidiary of GM. It was a pioneer in the telematics safety systems when it was formed in 1996. It provides a number of services, the primary one, is emergency calling and automatic crash response plus roadside assistance during breakdowns. GM charges for basic service was \$29.99 per month in May 2021. [11] While OnStar™ originally included Europe and South America, those 2 areas were discontinued on Dec. 31st, 2020. Also, their Hands-free phone option will discontinue in 2022 due to the widespread use of cell phones. After 2022, GM's service will focus on accident and roadside services. Nevertheless, GM's OnStar™ is a bright spot in emergency service versus other U.S. general telematics services.

3.7 Other U.S. Telematics - Mainly oriented towards Improving Driver Safety/Reducing Insurance Premiums

In general, most U.S. telematics services offered in 2021 are oriented towards: (1) helping drivers improve their driving skills by not speeding or rapidly braking and (2) helping the insurance industry collect data so they can identify the drivers who deserve the lowest insurance premiums. The major flaw of the system is that it's not focused on expediting EMTs quickly responding to accidents.

Almost all major U.S. automobile insurance companies offer insurance discounts if their customers use telematics devices in their cars. These firms and their service names include Allstate Drivewise, Farmers Signal, Liberty Mutual RightTrack, Nationwide Insurance SmartRide, Progressive Insurance Snapshot, Travelers Insurance IntelliDrive, State Farm Drive Safe & Save and USAA [12]. They offer discounts in exchange for letting them track their customers' driving habits and suggesting driving improvements.

Over time, any discounts may be reduced if a driver exhibits risky driving habits such as speeding. The telematics tracks the driver's speed, acceleration, and if they're using their phone, etc. Some of these systems use the driver's phone to track them while others such as Nationwide SmartRide are devices connected to the car's onboard diagnostics (OBD) system. Good drivers can have lower insurance premiums. And insurance companies have access to a massive amount of driving data for their customers. Unfortunately, unlike GM's OnStar™ or EU's eCall, many of these systems don't provide automatic notification of accidents. In short, they are excellent sources of information for insurance companies, but they do not focus on expediting EMTs during a crash.

3.8 U.S. Telematics - Consumers are worried about Privacy

Nationwide Insurance Company’s survey on Dec. 9, 2020 revealed that customers would consider “a telematics device to capture their driving behavior if it provided a discount, yet only 10% of consumers report actually using one... 62% of consumers have privacy concerns about the information telematics is capturing. However, the survey also showed that this barrier may be easy to overcome and lead to a conversation about telematics discounts as 65% of respondents say they would allow a telematics device to capture their driving behaviors if it provided them a discount.” [13]

This survey underscores the problems of telematics in the U.S., it is primarily being used to collect massive amounts of data on driver safety, which is crucial to the insurance industry to identify good drivers and adjust insurance premiums. However, it fails to focus on the issue of expediting EMT’s response time to accidents, which could save thousands of lives.

3.9 Amount of Data available onboard Vehicles versus Key Data for Telematics

The amount of data onboard the latest automobiles is massive, especially for autonomous cars which have a large number of sensors including cameras, radar and LiDAR. They track driving information 360 degrees around the self-driving vehicle, including up to 250 meters ahead. This could be terabytes of data per hour. For comparison, a 90-minute Hollywood movie is over 200 GB of data. This vehicle data is used to precisely steer the car, making multiple driving decisions every millisecond. The distances for the sensors in this chart are based on a Tesla 2021 sales brochure.

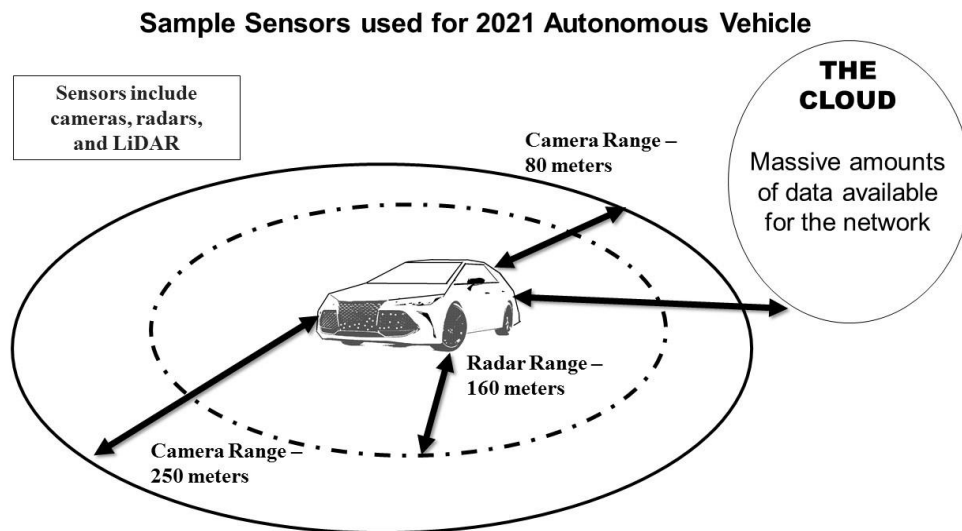


Figure 2. The Massive Amounts of Data from onboard Autonomous Vehicles

Only a small percent of this data is shared over the network. For example, EU’s eCall system emergency message is only 128 characters long, including the GPS location and whether the airbags have been deployed. This makes the system very flexible since the bandwidth can be limited and the accident information can still be quickly routed to the EMTs.

4. Findings - The U.S. Telematics Vehicle Safety System is Inferior to the EU’s eCall

This paper is a crucial call to action for the U.S. government to mandate a similar system to EU’s eCall on all new cars sold in the U.S. This could save over 1,300 U.S. lives per year at a cost as low as \$37 per vehicle. While most current U.S. telematics systems provide key information for the insurance industry, they are not focus on expediting EMTs response for

accidents which is crucial in the Golden Hour after an accident. Low-cost technology is available now if the U.S. government sets standards quickly to match the EU's eCall system.

5. Originality - This paper outlines the 1st step in improving U.S./EU Vehicle Safety

eCall or GM's OnStar™ are the crucial first steps in improving EMTs response time after vehicle accidents. This paper was written after Mark Haley filed a patent on a more extensive system of safety which goes beyond eCall to provide a more robust response to emergencies. This patent will be published in a few months after this paper, and it provides more details about a system that goes beyond eCall and should be adopted in both the EU and the U.S. in order to potentially save even more lives by expediting EMT's response time after vehicle accidents.

References

[1] American College of Surgeons (2008). *Atls, Advanced Trauma Life Support Program for Doctors*. Amer College of Surgeons. ISBN 978-1880696316.

[2] European Commission. Commission staff working paper: Impact assessment accompanying the document "commission recommendation on support for an EU-wide eCall service in electronic communication networks for the transmission of in-vehicle emergency calls based on 112 (eCall)". 2011. ref SEC (2011)1019 final.

[3] "Europe (EU28) vs. Norway - Assessment of Socio-economic Impact of In-vehicle Emergency Call (eCall)", Ann-Helen Brembo, June 2016, NTNU, Norwegian University of Science and Technology, Department of Telematics, Master of Science in Communication Technology, p. 37.

[4] Mell, H., Mumma, S., Hiestand, B., Carr, B., Holland, T., Stopyra, J. (2017, July 19). Emergency medical response times in rural, suburban and urban areas [Editorial]. *JAMA Surgery* DOI: 10.1001/jamasurg. 2017. 2230

[5]. Gonzalez RP, Cummings GR, Phelan HA, Mulekar MS, Rodning CB. "Does increased emergency medical services prehospital time affect patient mortality in rural motor vehicle crashes? a statewide analysis. *Am J Surg*. 2009;197(1):30-34. Abstract

[6] Federal Highway Administration. 2020. Highway statistics, 2019. Washington, DC: US Department of Transportation

[7] US DOT Miles Driven, March 29, 2018 <https://www.fhwa.dot.gov/ohim/onh00/bar8.htm>

[8] EU miles driven- 12,000 km <https://www.odyssee-mure.eu/publications/efficiency-by-sector/transport/distance-travelled-by-car.html#:~:text=Large%20discrepancy%20of%20the%20average,the%20EU%20as%20a%20whole.>

[9] EUSPA, "eCall: 2 Years of Saving Lives", March 31, 2020 <https://www.euspa.europa.eu/newsroom/news/ecall-2-years-saving-lives>

[10] Henriksson, E. M., Oström, M. Eriksson, A. (2001) Preventability of vehicle-related fatalities. *Accident Analysis and Prevention*, 467-475

[11] 5/18,2021, GM's call center indicated that the charge for the basic service was \$29.99 per month.

[12] Jason Metz, "How Usage-Based Insurance Works", *Forbes*, May 11, 2021 <https://www.forbes.com/advisor/car-insurance/usage-based-insurance/>

[13] Nationwide Survey, Dec. 9, 2020 <https://news.nationwide.com/120920-survey-consumers-are-more-ready-to-use-telematics-than-in-years-past/>

Demonstration of a Visible Light Communication System Using LED and Low-cost Low-quality Camera

Nguyen Hoang Nam^{1,2*}

¹Institute of Control Engineering and Automation, Hanoi University of Science and Technology, Hanoi, Vietnam

²School of Electrical Engineering, Hanoi University of Science and Technology, Hanoi, Vietnam

*Corresponding author: nam.nguyenhoang@hust.edu.vn

Abstract

The content of this article presents the theory of communication technology by visible light (LED) combined with Camera by C-OOK (Camera On-Off Keying) method. In addition, the design and testing of a communication system using LED and Camera helps us evaluate results for research in some specific applications such as navigation, traffic problems, advertising, and medical.

Keywords: Visible Light Communication, Camera On - Off Keying, LED, IEEE 802.15.7m

1. Introduction

Nowadays, the demand for wireless communication is increasing day by day. It is gradually replacing wired communication with its many advantages such as: easy to install and popular data transmission without dependence on wires. Wireless technology based on radio frequency (RF) is slowly running out of resources and tightly regulated. In addition, to improve the data rate, a higher frequency is required. However, higher frequencies are associated with dangers to human health. Therefore, visible light communication is being developed and has great potential for the future.

2. Overview

2.1 Introduction to the light transmission system

Studies on using visible light to transmit data are also becoming more popular with feasible new technologies including Communication with Visible Light (VLC), Optical Wireless Communication (OWC)/Optical Camera Communication (OCC), each of which can replace RF communication. The advancements of VLC or OWC/OCC compared to RF communication according to [1] and [2] can be summarized as follows:

- Light waves do not negatively affect human health if supported by dimming and non-blending methods.
- Depending on the results of research with many different people, it proves that optical modulation frequencies up to 200Hz can be considered without affecting the human eye.
- The bandwidth of the visible light is 1000 times greater than the RF bandwidth.
- Visible light waves are more cost effective. In addition, visible lighting is available in street and vehicle lighting infrastructures, helping to reduce the costs of implementing VLC and OWC/OCC systems compared to deploying RF systems.

Therefore, many companies are investing most of their budgets in research into this new technology. Optical Camera Communication (OCC) refers to the wireless communication between optical sources (LED) and the camera. The camera is used to receive data from the LED. This technology can be implemented in all cameras as well as in smartphones as it is

capable of processing images. LED lights are created to replace filament lights, neon lights or seven-segment screens in small and medium lighting systems, because of its efficient energy usage, high illumination capacity and durability. Besides, LEDs have a small response time to voltage changes, so it is possible to use high frequency continuous on and off LED bulbs to encode a piece of information in a certain rule.

A microcontroller is used to encode and control high-frequency LED bulbs. This frequency should be high enough that the human eye cannot perceive the switching “on” and “off” of the LED, not to affect the lighting ability. Therefore, the LED will be used as the encoded signal generator. In addition, at the receiver, a camera is used to record the on-off status of the LED and decode it for data information.

Because of the popularity of both LED bulbs and cameras, light communication systems have the potential to develop in the future and can be applied in many different fields such as receiving signals from signs, outdoor billboards, indoor LED lighting, communication between vehicles, etc...

2.2 Some optical camera communication standards

A light communication system consists of one or more high-frequency LED lights that are continuously turned on and off to carry encrypted information, and a camera used to capture the information emitted by the LED. Depending on the LED control and information encoding method, there are different communication standards such as S2-PSK and C-OOK [3], moreover, there are some other communication methods.

The S2-PSK method uses 2 LEDs to encode the signal, of which 1 LED carries a reference signal that functions like the clock for the system. The other light will encrypt the data. This method is applicable for low-speed cameras, around 30fps. However, the disadvantage of this method is that the transmission speed is not high, it cannot transmit a lot of data, but can provides a quite long transmission distance.

There is also another method, C-OOK, which uses only a single LED that is turned on and off at high speed to carry information. Because the camera's scanning speed is limited, when scanning from above, there will be a difference in light intensity, thereby creating bright and dark fringes. By encoding and decoding these patterns, we transmit and receive the information. There are also several other communication methods, in this article mainly presents C-OOK encryption method.

3. Effects of camera parameters in OCC

The choice of a camera receiver affects the selection of the signal formats transmitted by the LEDs. Notably, Some camera type limit OCC performance. Therefore, developers should understand and consider these factors carefully in specific applications. These four main camera parameters: shutter speed, frame rate, scroll speed and focal length, which are discusses in four sections as follows.

3.1 Camera shutter speed

Today digital cameras can be divided into two categories: those that use mechanical shutter and those that use electronic shutter. The shutter is a very important parameter because it determines the exposure time and entails a variety of visual effects. For cameras that use a mechanical shutter, inside the lens, there is a shield black screen in front of the sensor, it is usually in a flat form called the shutter. The mechanical shutter consists of two shutters: the front shutter and the rear shutter. In today's digital cameras, these two shutters are arranged vertically (top - bottom). With film cameras, these two shutters are usually arranged horizontally, and the camera is arranged vertically. In the normal state, the sensor is always covered in front. When

shooting (exposure) starts, the front shutter pulls down so that the sensor starts exposure, then the rear shutter pulls down to cover the sensor to end the exposure. The length of time that the shutter stays open is known as the shutter speed or exposure time because it is also the length of time that the sensors are exposed to light. When the shutter is open, all pixels in the image are captured at the same time.

Shutter speed is measured in seconds or fractions of a second like 1, 1/60s, 1/125s, 1/250s ... The longer the exposure time, the more the light will enter the sensor, it makes the photo brighter. However, it will cause motion blur. For a light communication system, to be able to capture the status of the blinking LED bulb, the shutter speed needs to be adjusted to a low level for eliminating noise caused by outside light.

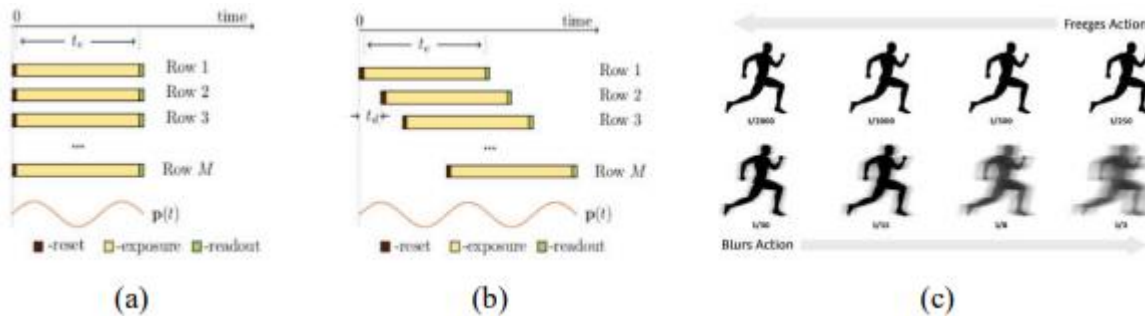


Figure 1. Camera working mode of (a) global shutter; (b) rolling shutter and (c) effect of shutter speed on movement

Today, digital cameras are equipped with two main image sensor technologies [4]: Charge Coupled Device (CCD) and Complementary Metal-Oxide Semiconductor (CMOS). A digital camera captures an image by converting light from an object into an electronic signal in a CCD or CMOS image sensor. Consequently, the amount of light intensity falling on the image affects the amount of the signal generated by these image sensors. That means a digital camera also requires some of the same mechanism to operate the shutter as a mechanical film camera. Currently, the two main shutter mechanisms of action are adopted in digital cameras, and both are supported by the CCD/CMOS image sensor. Hence, digital cameras can be classified by shutter operations as rolling shutter and global shutter mechanisms.

A global shutter captures the entire frame at a time. Thus, all pixels in an image are read out at the same time. In contrast, a rolling shutter camera scans rows of pixels. The pixel rows are read at once, this creates a delay in the final frame known as the rolling effect. The rolling effect can occur when the rolling shutter camera captures moving subjects.

Exposure time is the amount of time the camera shutter opens when the camera is shooting. Based on the exposure time, the camera's shutter speed can be calculated. The exposure time significantly affects the signal to noise ratio (SNR or E_b / N_0). The higher the SNR achieved, the longer the exposure time is configured. However, when the exposure time is long enough, the total light noise can decrease the communication bandwidth.

3.2 Camera frame rate

The camera's frame rate (fps) is the number of frames that a camera recorded in 1 second. Faster frame rates result in faster, smoother images while slower frame rates result in slower, wobbly images. Today, the common frame rates on camera are 30fps, 60 fps, 120 fps and 960 fps [5]. Frame rates between 25-30 fps are commonly used as standard rates, images are smooth and do not cause eye strain. Besides, the frame rate of the camera depends partly on the storage and image processing speed of the microcontroller in the camera, the frame rate is sometimes

fluctuated and unstable. Therefore, receiving information and decoding at different transmission rates is a great difficulty. The camera frame rate plays an important role in OCC because it affects the communication data rate in OCC [6]. Basically, the OCC data rate can be calculated based on the camera's frame rate as follows.

$$R_{bps} = R_{fps} \times N_{bpf} \quad (1)$$

where R_{bps} is the OCC bit rate (bits per second - bps), R_{fps} is the camera's frame rate, and N_{bpf} is the number of bits per frame.

Variable framerate is one of the current camera problems. Many cameras were not working at a fixed frame rate, and frame rate changes are unpredictable. Therefore, sampling and decoding transmitted data with random sampling time is a major challenge in OCC. Actual camera frame rate can be estimated by measuring the time interval between two images taken in succession.

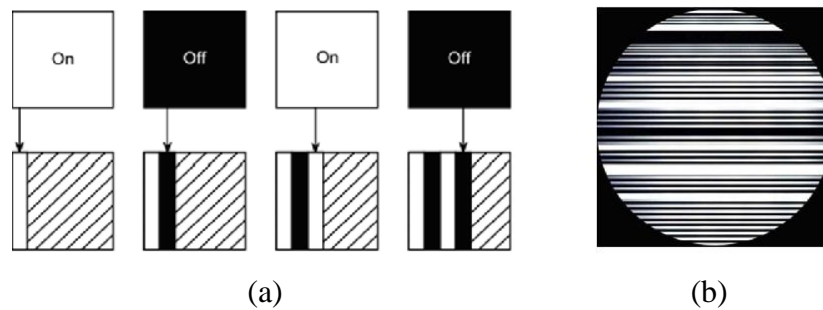


Figure 2. OOK for (a) On/Off status and (b) result with rolling shutter camera

3.3 The camera shutter's rolling speed

Today's digital cameras are often equipped with a rolling shutter, also known as an electronic shutter. This electronic shutter uses CMOS sensors [7] in place of the mechanical shutter. This sensor works by the principle of converting images to electronic signals. The CMOS sensor integrates a logic circuit to process the signal right at the light receiving points and the image is captured in photoside rows. Therefore, cameras using CMOS electronic shutter are often not able to take all the pixels at once, but by gradually scanning the pixels horizontally or vertically. In light communication systems, these cameras can produce alternating color lines when recording an LED is being switched on and off continuously at high frequency in Figure 2.

In OCC, different light clock speeds of the Tx light signal can cause different widths of the stripes in the photograph. The width of the stripe also depends on the camera image sensor resolution. The width of the stripes (measured in pixels) can be calculated using the following equation:

$$N_{pixel/bit} = \frac{F_s}{2 \times f_{Tx}} \quad (2)$$

where $N_{pixel/bit}$ is the number of pixels per stripe, F_s is the camera's rolling rate, f_{Tx} is the Tx optical pulse rate.

3.4 Focal Length

Focal length is the distance from the image sensor and the optical center of the lens when the lens focuses at infinity. The focal length affects the size of the image taken directly. It also affects the Field-of-view of the camera. The longer the focal length, the greater the magnification ability.

The relationship between the focal length and shooting distance is shown in the following equation:

$$\frac{d[m]}{H_{LED}[m]} = \frac{f[mm]}{h_{LED}[mm]} \quad (3)$$

where f is the focal length, d is the shooting distance, H_{LED} is the actual LED size, and h_{LED} is the LED size in the captured image.

From the equation, we can estimate the maximum communication distance in OCC if we know the LED light size and camera focal length. Theoretically, according to Nyquist's sampling theorem, OCC can function when the LED size in the captured image is only 2 pixels. In this case, the maximum contact distance is estimated using the equation:

$$d = \frac{f \times H_{LED}}{2 \times N \times h_{ISmax}} \quad (4)$$

H_{LED} is the actual LED size (in m). N is the number of pixels of an image, h_{IS} is the image sensor size (in mm). Practically, it is necessary to consider the strength of the Tx light sources. If the light intensity of the Tx signal is too low, the camera may not detect the light source pixels among the background noise pixels [8,9].

4. Design and testing communication system using led and camera

4.1 Hardware in the test

Arduino Uno is an opensource 8-bit microcontroller circuit board based on Microchip ATmega328 microcontroller developed by Arduino. The circuit board is transmitted device equipped with 10mm diameter white LED that has 3.2V operation voltage and 20° view angle. The camera has low-cost low-quality specifications: 1.3Mpixel resolution, 30fps frame rate and 30600Hz rolling rate.

4.2 Measure the rolling speed of the camera

Due to the action of the rolling shutter mechanism, a rolling effect can occur when moving subjects are captured. In previous part, the shutter camera captures an image not by capturing the entire scene at once, but by scanning the scene horizontally or vertically. In OCC, a rolling shutter camera can produce different stripes in an image when shooting frequency conversion LEDs. From (2), it is known that:

$$F_s = 2 \times N_{pixel/bit} \times f_{Tx} \quad (5)$$

where $N_{pixel/bit}$ is the number of pixels per stripe, F_s is the camera's rolling rate, f_{Tx} is the Tx optical pulse rate.

The Rx uses a shutter camera, so it knows the rolling speed to accurately sample from the Tx signal. However, the camera's rolling speed has not been offered in any commercial products. Therefore, a measurement test should be performed to determine the rolling speed. The Tx transmitter will transmit an optical pulse with a known frequency, the Rx receiver is responsible for calculating the number of pixels per bit (number of pixels per stripe). At the transmitter, we use Arduino UNO R3 to generate PWM pulses with bit sequence 0101010101... with a frequency of 200Hz using interrupt of Timer/Counter1. Figure 4.a shows the results of the LED when it is emitted at 200Hz. To calculate the number of pixels per stripe (pixels per bit) we must count the number of stripes obtained per pixel length on the image, then calculating the number of pixels per stripe based on the formula below:

$$N_{pixel/bit} = \frac{\text{sampling-pixel-length}}{\text{Number-of-stripes-sampled}} \quad (6)$$

Number-of-stripes-sampled is the number of stripes, sampling-pixel-length is sampling pixel length. Figure 4.a shows sampling-pixel-length = 285 - 55 = 230 (pixels), Number-of-stripes-sampled = 3. Applying (6), F equals 30668Hz and $N_{\text{pixel/bit}}$ is 76.67 pixel/bit.

From the above experiment with testing and sampling results many times with different frequencies, it shows that the camera rolling speed is being measured at about 30600Hz. Knowing the camera rolling rate is very important in sampling and decoding information in optical camera communication.

4.3 Design communication system using LED and Camera

Figure 3.a shows the Rx design scheme. Initially, the Running Length Limit (RLL) data is Manchester encoded, Manchester encoded to maintain DC balance at Tx light intensity, providing error detection ability and clock recovery ability for Tx signal.

In this experiment, the input bit sequence 00 is encoded Manchester, the result is 0101 and add the SF packet detection bits 011100 (According to Manchester encoding), finally obtained the bit string 0111000101. This bit string is generated by PWM pulses that push out the LED with a customizable frequency using a Timer/Counter1 Interrupt (in this experiment the pulse frequency is 2200Hz).



Figure 3. Diagram of Tx pulse modulation (left) and Rx decoding (right)

The diagram in Figure 3.b shows the Rx decoding procedure. The decoding process begins with preprocessing and down-sampling to provide the input 1D image. The down-sampled 1D image is then discarded. Removing a trend from the data can help the Rx decoder focus on fluctuations in the trend data. The input 1D data is then ready for SF detection. It decodes the data to obtain packed data, then Manchester decodes it to obtain the bit string you want to send. The entire process is programmed in the LabVIEW language.

4.4 Results obtained

Tx transmitter with an optical frequency of 2200Hz sends out DS 0111000101 (10 bits) bit sequence. Due to the capabilities of the camera as well as the size of the LEDs, to obtain a minimum of one DS package, the distance should not be too far. Three tests will correspond to three different distances between receiver and transmitter.

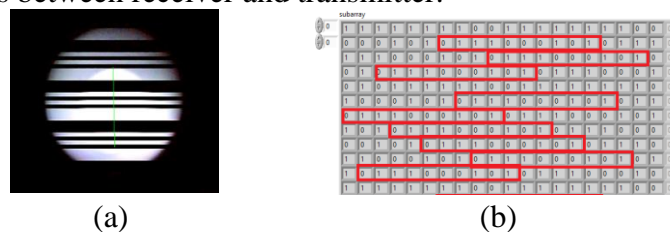


Figure 4. LED on-off at distance of 10cm (a) and resulting bit value array obtained per frame captured (b) from a camera with a Tx light frequency of 200Hz

Sampling following the green line in Figure 4.a, it will give us the number of stripes or the corresponding number of bits depending on the length of the line. In this experiment, a test with different line lengths is carried out, resulting in a 2D array of the resulting bits. The number of elements in the array corresponds to the number of bits captured per frame. Figure 4.b shows the results of the array obtained when performing the experiment at a distance of 10 centimeters and taking 20 bits per frame. The number of elements per column corresponds to the number of sampled frames. In these experiments, 30 frames (30 lines of result arrays) were sampled, equivalent to the recording time in approximately 1s of the camera). Each frame can receive a bit sequence at Tx or not. The next work is to sample 30 frames and compute the bitrate acquisition rate at the Tx end of the frames (dominant frame rate). Then, we examine this rate according to the number of bits per frame. This is important to survey and evaluate the optimal line length to get the maximum rate of Tx first bit sequence. This helps to collect data at the most effective rate. The rate of frames that receive the Tx bit sequence (dominant frame rate) will be examined and plotted according to the number of bits taken per frame. The specific experiment is calculating the rate of frames obtained Tx bit sequence corresponding to taking the number of bits in each different frame (calculate the times with the number of bits per frame 12, 14, 16, 18, 20, 22, 24, 26, 28, 30 respectively - the number of bits must be greater than 10 bits at the beginning of the Tx). Figure 5 shows the array of values of the resulting bit sequence, corresponding to each row, it is a frame captured by the camera. At the transmitter, data is transmitted with the 10-bit sequence (0111000101), so if 20 bits are taken per frame, a high ratio Tx transmitter DS packet is obtained.

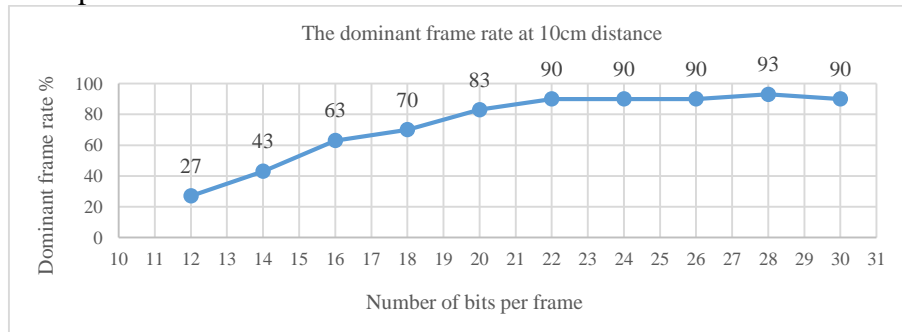


Figure 5. The dominant frame rate at 10cm distance

Development direction of the topic

Although communication by light is not a new topic, there are not many studies in Vietnam, but light communication methods have a great potential to apply and develop in the future in the fields of transport, medical, positioning, combined with available technologies such as IoT in developing 5G technology. In addition, the lighting and advertising use mainly LED bulbs, which can be modulated to become signal transmitters, which is a huge advantage in terms of infrastructure for development and application. One of the uses of visible light communication technology that the team is working on is positioning in buildings where GPS cannot interfere. Specifically, buildings will be installed LED lighting systems which carries location information and blinking at frequencies above 200Hz that are not affect the human health. The smartphone front camera of the user points to the position of the LED, with installed software and will decode the exact location in the building. In addition, the research team is also developing smart hospital applications with this LED-based localization system. All up-to-date medical record information of a patient will be displayed on the doctor's smartphone. This helps to make medical examination and treatment more effective in the future.

References

- [1] P. H. P. *et al.*, "Visible Light Communication, Networking, and Sensing: A Survey, Potential and Challenges", *IEEE Communication Surveys & Tutorials*, chap 17. s.l.:s.n., pp. 2047-2077, September 2015.
- [2] Duc, T. M., "*Novel Hybrid Temporal-Spatial Phase Shift On-Off Keying for Optical Camera Communications*", s.l.: s.n., 2018.
- [3] Duy Thong Nguyen, 2018. *Opticalpress*, available at:
<https://opticalpress.com/2018/09/05/c-ook-customizing-ook-for-optical-camera-communication-2/>.
- [4] IEEE-SA, "IEEE 802.15.7-2018-IEEE Standard for Local and metropolitan area networks--Part 15.7: Short-Range Optical Wireless Communications", s.l.: s.n., 2018.
- [5] H. Nguyen, *et al.*, "The Impact of Camera Parameters on Optical Camera Communication", *International Conference on Artificial Intelligence in Information and Communication (ICAIIIC)*, February 2019.
- [6] L. U. Khan, "Visible light communication: Applications, architecture, standardization and research challenges", *Digital Communications and Networks*. s.l.:s.n., pp. 77-78, May 2017.
- [7] Axis Communication, "CCD and CMOS sensor technology", Technical white paper, 2010, available at: https://www.axis.com/files/whitepaper/wp_ccd_cmos_40722_en_1010_lo.pdf
- [8] Trang Nguyen *et al.*, "2D-OFDM for Optical Camera Communication: Principle and Implementation", *IEEE Access*. s.l.:s.n., pp. 29405-29424, February 2019.
- [9] Trang Nguyen, *et al.*, "Design and Implementation of a Novel Compatible Encoding Scheme in the Time Domain for Image Sensor Communication", *Sensors*, Vol 16, 2016.

Low-cost 2D LIDAR System on Autonomous Robot for 3D Scanning and Modeling Unknown Areas

Hoang-Nam NGUYEN^{1*}

¹Hanoi University of Science and Technology, Hanoi, Vietnam

*E-mail: nam.nguyenhoang@hust.edu.vn

Abstract

Robots and automatic machines appear popularly in every aspect of industry, as well as daily life and are become more and more intelligent than. Step by step, robots can take human places in doing dangerous job in hazardous environment, or works which needed high level of accuracy. One of the research team's works is building a low-cost autonomous LIDAR robot who can 3D scan and model/map the environment from a low-cost 2D LIDAR and aiming to rebuild the LIDAR manufacturer's PC-based application because of the huge amount of raw data transmits to PC. With powerful computation resources like edge computing nowadays, an autonomous robot can use some complexity algorithms to recalculate and rebuild the digital mapping without PC. So, the autonomous robot can run through, survey, and monitoring caves, shafts, forests, ancient buildings, or remnants of natural disaster. And with digital maps in hand, more useful indoor applications for smart buildings can be created.

Keywords: Autonomous Robot, Environment Modeling, Digital Mapping, LIDAR, Unknown Areas

1. Introduction

Autonomous robot is one type of automation robot that can move and do some specific tasks automatically. They are now used popularly in large factories to reduce human effort. They are also used as our eyes in unknown or dangerous places, with many advance components equipped to give them the ability to operate stably and highly accurate in hazardous environment. Autonomous robot can run on rubber wheels or crawler. In this research, a basic autonomous robot that can detect and avoid obstacles was built, and with the 2D LIDAR technology attached. LIDAR sends laser pulses that are reflected by the obstacles with its distance. The distance is calculated by Time of Flight (TOF) measurement. For indoor navigation, LIDAR is fused with inertial sensor for localization. But 3D LIDAR system that can capture accurate 3D point clouds is very expensive, such as like Velodyne LIDAR system in Google's Waymo autonomous car which costs more than \$50,000. To reduce the price, some cameras are used along with LIDAR for mapping [1-4]. Some differently 3D sensing technologies are available, each with their own advantages and disadvantages. These differ in the type of rotating mechanism lasers system or the solid state LIDARS. The solid state LIDARS is now popular due to their size and architecture on a single silicon chip. But the cost remains high.

The research team aims to build a low-cost autonomous LIDAR robot who can 3D scan and model/map the environment from a low-cost 2D LIDAR. And the second work is rebuilding the LIDAR manufacturer's PC-based application to embedded with edge computing resources on autonomous robot. The data acquired by LIDAR sensors is huge and can be calculated only on edge computing platforms. In [5], another research team tried to generate 3D map at known locations and secondly by using one 2D LIDAR for mapping and localization. This approach is time consuming and can only be used for low-speed platforms. In addition, due to the movement of the robot there is vibration causing errors in positioning and localizing [6 - 7]. For precise

control, it is needed to have the accuracy of the motors [8], different step sizes of servo motor was analyzed to 3D mapping with number of scanning points and scanning time required. A discussion will be planned for this. With the second aiming, an algorithm of rebuilt the 3D cloud points is tried in an application based on Windows Forms of Microsoft Visual Studio to modeling 3D data that was received from low-cost 2D LIDAR.

The paper is structured as follows: Section 2 describes the proposed autonomous robot with 8-bit microcontroller ATmega2560 and autonomous algorithm for the robot; computer application is rebuilt and presented in Section 3. Section 4 shows experimental results, the calibration and some discussion. Section 5 concludes the paper.

2. Autonomous Robot

2.1 Main components

An autonomous robot is programmed with a microcontroller ATmega2560 and an H bridge L298 circuit to allow DC motors to run forwards or backwards [8]. In the body, an accelerometer is used to measure the acceleration combined with a gyroscope to help determine orientation [9 - 10]. The InvenSense MPU-6050 sensor contains a MEMS accelerometer and a MEMS gyro in a single chip. It is very accurate, as it contains 16 bits analog to digital conversion hardware for each channel. This sensor uses the I2C communication with the microcontroller [11]. In addition, two HC-SRF04 ultrasonic sensors are added [12] to detect obstacles in front of the robot. The autonomous algorithm used here is wall-following algorithm. If there is an obstacle, the autonomous robot can rotate 45 degrees to the left. The important component is LIDAR Lite v3 sensor provided by Garmin which measures distance with 905nm-wavelength laser [13]. The data of LIDAR sensor is transfer through ESP8266 Wi-Fi module to the PC. After having initially chosen power supply source IC for this autonomous robot, Table 1 shows the calculated power consumption to ensure of all components being used in Table 1.

Table 1. Total component consumption of the autonomous robot

No	Component	Quantity	U,V	ΣI_{\max} , mA	ΣP_{\max} , mW
1	ATmega2560	1	5	14	70
2	ESP8266	1	3.3	215	710
3	MPU6050	1	3	0.5	1.5
4	L298D	1	5	24	120
5	HC-SR04	2	5	60	300
6	DC engine	4	7.4	1000	7400
7	LIDAR Lite v3	1	5	120	600
8	Servo	2	4.8	500	2400
9	DRV8825	1	5	30	150
10	Stepper motor	1	6	1000	6000
Total				2964.5	17751.5

The power supply for the robot is three Ultra-Fire batteries with the voltage of 3.7V and have a capacity of 4800mAh for each cell, so the total energy is as in Equation (1), so we can calculate the robot can work continuously in three hours:

$$A = 3 * U * (I * t) = 3 * 3.7 * 4800 = 53280(mWh) \quad (1)$$

2.2 Localizing and route mapping

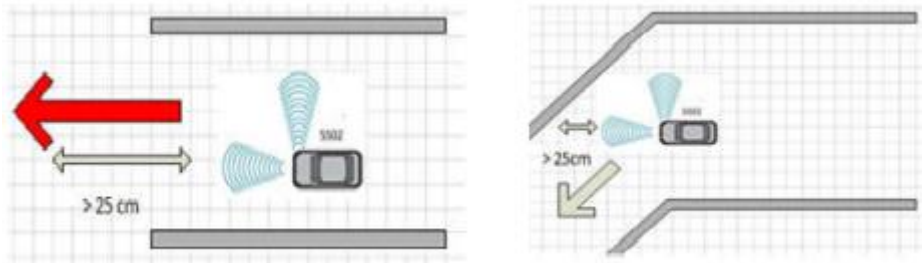
The requirement for auto-moving task is making the robot run automatically in 15 seconds, then it stops for the LIDAR sensor scan the environment and process those data, send it to PC through Wi-Fi. After the sending process is completed, it completes one cycle of the working process, and the total process is repeated until the whole area being scanned completely.

The main cases when running in unknown areas of the autonomous robot are showed in Figure 1:

- **Case 1:** When the autonomous robot maintains constant distance from the right wall, and there is no obstacles in a radius of 25cm in front, a robot will decide to move straight ahead.
- **Case 2:** When the autonomous robot rotates its couple of sonar sensors 45 degrees to the left, and the right sensor detect obstacle below a radius of 25cm in the right, the robot decided to move left by 45 degrees.
- **Case 3:** Like case 2, but a robot detect obstacle from the front sensor below a radius of 25cm, the robot decided to move right by 45 degrees.
- **Case 4:** When the robot is beside the left wall, it will not detect that wall to follow due to not having sensor on the left side, so it will try to rotate to the right 45 degrees each time to find a wall to follow. To avoid rotating endlessly, we have set a variable which determined the maximum times a robot can rotate to find a right wall. After exceeding this value, the robot will move straight ahead till it meet the next obstacle, and we move to case 5.
- **Case 5:** When the robot moving straight ahead and facing the in front obstacle below the radius of 25cm from the robot, it will decide to move left 90 degrees and continuously follow that obstacle as a new right wall.
- **Case 6:** When the robot moving straight ahead and realizes it has just lost its right wall to follow, it will try to rotate to the right 45 degrees each time to find a wall to follow. To avoid rotating endlessly, we have set a variable which determined the maximum times a robot can rotate to find a right wall. After exceeding this value, the robot will move straight ahead till it meet the next obstacle, and we move to case 5.

The MPU6050 calculates yaw angle, which mean the rotate angle around z-axis, to determine the direction of the robot on the ground. Combined with distance data from LIDAR it can be localized the robot comparative with the area. Before calculating yaw angle, DMP determined Quartenion that is defined like a complex with 3 virtual elements:

$$q = w + x*i + y*j + z*k = w + v \quad (2)$$



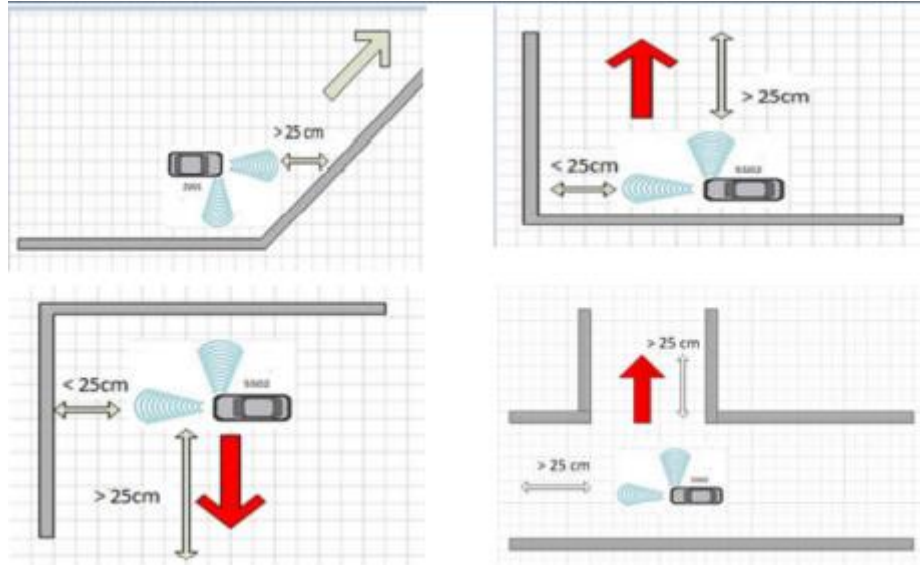


Figure 1. Main cases in unknown areas of the autonomous robot

Apply to our spatial rotation, suppose we have a vector of rotation axis \vec{u} (\vec{u} must be a vector unit, which mean $u_x^2 + u_y^2 + u_z^2 = 1$) and rotation angle θ (be plus when its direction follow right-hand rule), we will have a rotation quartenion like this:

$$q = \cos \frac{1}{2} \theta + u * \sin \frac{1}{2} \theta = \cos \frac{1}{2} \theta + (u_x * i + u_y * j + u_z * k) * \sin \frac{1}{2} \theta \quad (3)$$

The values of Quartenion: w, x, y, z are saved sequentially in each couple of 8-bit packet-buffer registers (contains values measured by a sensor). MPU6050 default amplitude of gyro value is $\pm 2g$ (correspond with the sensitivity of 16,384 LSB/g), so then the yaw can be calculated from Quartenion by this formula:

$$Yaw = \arctan\left(\frac{2 * q[x] * q[y] - 2 * q[w] * q[z]}{2 * q[w] * q[w] + 2 * q[x] * q[x] - 1}\right) \quad (4)$$

After having calculated yaw angle of MPU6050 throughout the robot's running process, based on its yaw changing level, we can find out if it has changed direction or not.

2.3 3D coordinate scanning

After having determined the robot's position, based on distance data from LIDAR, we can calculate the coordinates of each point of the surrounding area that be scanned by LIDAR. About the moving part of LIDAR, a stepper motor is used to provide 360 degrees scanning horizontally, and to create lifting angle for 3D scanning, the sensor is attached to a servo. The lifting angle we created here is from -20 to 20 degrees, equivalent to angle of servo from 140 to 180 degrees (160 degrees is parallel with ground surface, this value depends on each specific project), and the stepper we used is 200 steps one (meaning it completes one round by moving 200 steps), so 1 step is equivalent to 1.8 degrees.

For each point, the LIDAR scans from the surrounding area, includes a package of numeric data enough to define that point: position of stepper compares with the starting position facing ahead to the direction of a robot; lifting angle; distance from sensor to that point and of course, yaw angle defines which direction the robot is moving is also important. Data received from LIDAR will be passed to ATmega2560 through I2C protocol, and then from ATmega2560 to

ESP8266 through UART protocol. After the transmitting process is complete, the register will be clear for the next data to come up. The ESP8266 module will be used as an Access Point with the default IP address and port number is 8000. The PC will be connected to the Wi-Fi created by ESP8266 and will be provided a client IP. Transmitting-receiving process continuously.

3. Computer Application

A PC program is written in C#. The Windows application has two main features:

- **2D-scan:** LIDAR is set on 2D scanning mode to hold in a plain parallel with the ground and scans 360° around it. In this mode, data is collected continuously in just 1 section of examined area. Data about coordinates scanned will be saved in text file.
- **3D-scan:** In this mode, a servo with attached sensor will be activated and provide lifting angle from -20° to 20°, providing the autonomous robot more detail information about the 3D model of the area. Data about coordinates scanned will be saved in text file.

3.1 2D-scan

A message will be sent under the form of one string from PC to ESP8266 through Wi-Fi connection to activate the 2D-scan process. The robot will be controlled, the stepper with a LIDAR sensor attached above it to move each step and scan in one section parallel with ground until getting enough distance data from 200 steps. Then the data will be transmitted to ESP8266 through UART and to PC through Wi-Fi connection.

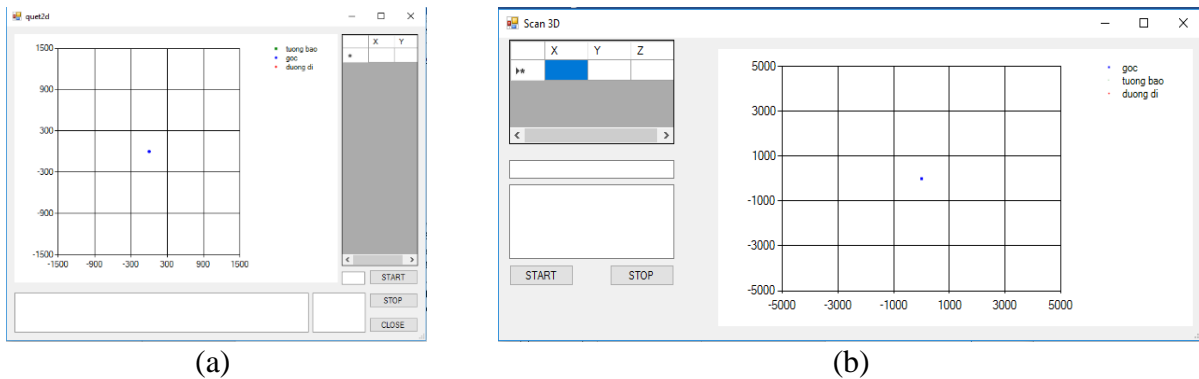


Figure 2. PC interface of the (a) 2D-scan process and (b) 3D-scan process

Data is sent to the computer as a string. The string will carry information of 10 datasets including distance and angle. Particularly for the first series, in addition to angle and distance data, there is further data on the direction of motion of the vehicle and the coordinates of the vehicle, which are marked before and after by a default character for the process of interpretation. Once enough data has been received (400 datasets), the software will calculate the coordinates of the points corresponding to each dataset of angle and distance according to the formula:

$$\begin{aligned} x &= pos_1 - dis * \cos \alpha \\ x &= pos_2 - dis * \sin \alpha \end{aligned} \quad (5)$$

where (pos_1, pos_2) is the coordinates of the robot; α is a rotation angle of the stepper motor; dis is the distance corresponding to the obstacle (mm).

After being received successfully, the data will be saved in text file for further work.

3.2 3D-scan

Like 2D-scan operating method, but different in that to have the 3D coordinate of environment, a servo is used to provide lifting angle to LIDAR system. It provides a solution of scanning not only horizontally like in the 2D mode, but also vertically to offer the 3D-view of an examined area [14].

In this mode, the data sent to the computer will also have the angle of the servo. The coordinates of the vehicle compared to the 2D sweep will be added the altitude. Considering the robot is on a flat surface, the height of the robot is unchanged, and the coordinate value of the robot on the z axis is 0. Considering the coordinates of the robot are (x_0, y_0, z_0) with $z_0 = 0$, we can calculate the coordinates [15] of points in the surrounding area that are scanned according to the formula:

$$\begin{aligned} x &= x + dis * \cos \alpha \\ y &= x + dis * \sin \alpha \\ z &= dis * \sin \theta \end{aligned} \quad (6)$$

where (x, y, z) are the coordinates of the scanned point; α is a rotation angle of the stepper motor; θ is the lifting angle created by a servo; d is a distance corresponding to the point (mm).

After receiving and processing data successfully, the dataset will be saved in text file for further work.

4. Measurement and Calibration

The LIDAR Lite v3 was connected to 8-bit microcontroller ATmega2560 and the embedded program was run with Arduino Library for the LIDAR Lite v3 provided by Garmin. After the experiments, the sensor can only provide truthful and stable results at the minimum distance of about 0.3m. It is necessary to compare the constant bias with real distances (about 0.2m).

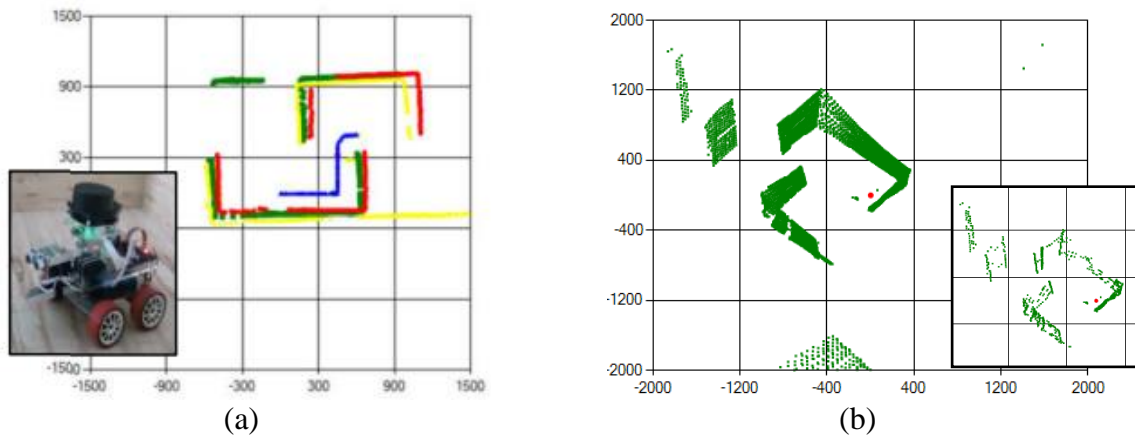


Figure 3. The 2D tracking path (a) and the 3D-scan process result (b)

Figure 3a shows that the red line is the model surrounding space. The blue line is the actual tracking path of the robot. The green dots-line are model surrounding positions from the surveyed data of LIDAR sensor on the robot when it moves on the model map. The obtained results have errors. The cause of these errors here is the slippage of the robot wheel when turning. More survey is needed to consider the error of the MPU6050 and LIDAR sensor. For these problem, two corresponding solutions are arranged in order of priority. Correction the zero-point of sensor's measurement by adding supplemental value to the register of sensor, in this

LIDAR Lite v3 sensor is the register at address of 0x13 for zeroing work. By doing this, the constant bias in distance measurements can be erased. After making several distance measurements from LIDAR Lite v3 sensor, one ruler is needed to compare with the real distances, one convert table was constructed from error measurement to standard one. Using some suitable and effective interpolating methods, approximation will be calibrated for the measurements of sensor that below 1m.

5. Conclusion

The research team has built a motion assist system in combination with low-cost 2D sensor to make scanning 3D environment easier and more convenient. This system was tested in practice model and results are relatively accurate. During testing, the robot sends data to the computer every 200ms through Wi-Fi. This selected period is to avoid the data loss compared to the period of 150ms as shown in Figure 3b. Another test and advanced version are developed: one successful print 3D parts of the mechanical system, a combination between the LIDAR parts and sensors into a complete sensor. The next version will be improved product form, stability of the system.

References

- [1] De Silva V et al., “Robust fusion of LiDAR and wide-angle camera data for autonomous mobile robots”, Vol 18, 2018
- [2] Endres F et al., “3-D Mapping with an RGB-D camera”, IEEE Trans. Robot. 30, 2014, p. 177–87
- [3] Kitayama D et al., “3D map construction based on structure from motion using stereo vision”, 4th Int. Conf. Informatics, Electron. Vision, ICIEV 2015, p. 1–5
- [4] Balasubramanian K et al., “Object recognition and obstacle avoidance robot”, Chinese Control Decis. Conf., CCDC 2009, 3002–3008
- [5] Kang X et al., “3D reconstruction assessment framework based on affordable 2D lidar”, IEEE/ASME Int. Conf. Adv. Intell. Mechatronics, AIM 2018–July, p. 292–299
- [6] Bosse M et al., “Zebedee: Design of a spring-mounted 3-D range sensor with application to mobile mapping”, IEEE Trans. Robot. Vol. 28, 2012, p. 1104–1123
- [7] Ocando M.G. and Certad N., “Autonomous 3D mapping of an environment, while simultaneously making 2D SLAM, using a single 2D LIDAR and ROS”, 2017, p. 2–7
- [8] Al Williams (2002), “*Microcontroller projects using the Basic Stamp*”, 2nd Ed.
- [9] LiveScience, “*Accelerometer vs. Gyroscope: What's the Difference?*” <https://www.livescience.com/40103-accelerometer-vs-gyroscope.html> (Accessed 10 April 2021)
- [10] SparkFun Electronics, “*How a Gyro Works*” <https://learn.sparkfun.com/tutorials/gyroscope/how-a-gyro-works> (Accessed 10 April 2021)
- [11] Arduino Playground, “*MPU-6050 Accelerometer + Gyro*” <https://playground.arduino.cc/Main/MPU-6050> (Accessed 10 April 2021)
- [12] Carnegie Mellon, Robotics Academy, “*What is an Ultrasonic Sensor*” http://education.rec.ri.cmu.edu/content/electronics/boe/ultrasonic_sensor/1.html

(Accessed 10 April 2021)

[13] Garmin, “*Lidar Lite v3 Operation Manual and Technical Specifications*”

[14] G. Scott Owen (1998) *3D Rotation*

www.siggraph.org/education/materials/HyperGraph/modeling/mod_tran/3drota.html

(Accessed 10 April 2021)

[15] Dan Sunday, “*Polyline Decimation (any Dim)*” <http://geomalgorithms.com> (Accessed 10 April 2021)

A Novel Approach in Simulation of Flow over Sphere From Low to High Reynolds Numbers

Anh Huy Huynh^{1,2}, Buu Hung Tran^{1,2}, Thi Hong Hieu Le^{1,2*}, Ngoc Hien Nguyen³ and Quang Le Dang^{1,2}

¹*Department of Aerospace Engineering, Faculty of Transportation Engineering, Ho Chi Minh City University of Technology (HCMUT), 268 Ly Thuong Kiet Street, District 10, Ho Chi Minh City, Vietnam*

²*Vietnam National University Ho Chi Minh City, Linh Trung Ward, Thu Duc District, Ho Chi Minh City, Vietnam.*

³*RMIT University, Australia*

*Corresponding author. E-mail: honghieu.le@hcmut.edu.vn

Abstract

In this article, a Python-based tool for OpenFOAM 6 is developed to perform simulations of flow over a stationary sphere from low to high Re in an effortless and time-saving manner. The three stages of a conventional CFD including meshing, simulation and data analysis, and input variables (Reynolds numbers, geometries, etc.,) are parameterized in a single algorithm and executed automatically. The simulated results from Re = 1000 to Re = 1.5x10⁶ are obtained. The flow characteristics (such as drag coefficients, drag crisis phenomena) are validated with experiments to verify different flow regimes. The results showed that the proposed approach has a good agreement with experiments in comparison with other numerical simulations, especially in the drag induced regime. Thereby, the proposed techniques can be applied to data for the simulation of arbitrary obstacles.

Keywords: Drag crisis phenomena, laminar turbulent transition, CFD, convergence criteria, mesh quality, OpenFOAM, SIMPLE, RANS, turbulent models

Nomenclature

AR	=	aspect ratio
CFD	=	Computational Fluid Dynamics
OpenFOAM	=	Open source Field Operation And Manipulation
SALOME	=	external meshing generation
SIMPLE	=	semi- Implicit Method for Pressure Linked Equations
checkMesh	=	mesh checking utility of OpenFOAM
Re	=	Reynolds number
I	=	the turbulence intensity of the fluid
C_D	=	drag coefficient
ν	=	fluid kinematic viscosity
ω	=	turbulent kinetic energy diffusion rate
μ	=	dynamic viscosity of the fluid
ρ	=	Air density
c, D	=	sphere's diameter

1. Introduction

Flow over a sphere is a topic that has been studied extensively by theory, experiment and CFD. In the CFD approach, one can only manually set up and run a simulation of a single case at a time. If a person wants to investigate another case, he/she needs to change various settings. The chances of getting errors during these changes are high due to many unseen reasons (i.e human error). Thus, there arises the need for automatic simulation for tasks that require repeated steps.

In this study, a Python library is developed to automatically access and modify the file settings of OpenFoam directory from geometry definition, meshing, boundary definition, solver setting, stimulation running and post processing. This way, the input and output data can be controlled and collected, but more convenient and less time consuming.

In this work, over twenty cases covering the wide range of flow over a sphere from $Re = 3.4 \times 10^5$ to $Re = 1.5 \times 10^6$ are simulated using this program. The results showed that the proposed approach has a good agreement with experiment in comparison with other numerical simulations, especially in the drag induced regime. The Python library is promising as a good tool to study the flow over arbitrary geometries. The rest of this paper is organized as follows. In Section 2, a brief overview of drag crisis phenomena and experiment on flow past a sphere are described. In Section 3, the research method is presented with computational domain, mesh setting, turbulent models, y^+ , etc. Automatic simulation analysis results are mentioned in Section 4. Some concluding remarks are provided in Section 5.

2. Literature Review

2.1 Drag crisis phenomenon

Drag crisis is a phenomenon in which drag coefficient drops off suddenly as Reynolds number increases. This phenomenon was first published by Gustave Eiffel in 1912. Eiffel made this discovery in his experiment study about flow over a sphere with a smooth surface. He found a drop in the drag force as the flow speed increased above a critical Reynolds number of 200,000 and continued to drop until about $Re = 300,000$ [1].

Due to increasing Reynolds number, the boundary layer transits from laminar flow to turbulent flow and the flow separates farther downstream. At this time, the majorly of drag is the pressure drag. As a result, the boundary layer separation point appears at the back of the body. The posterior track becomes thinner and narrower, resulting in the decrease in the slope of the pressure drag.

2.2 Experiments on the flow past sphere

The comprehensive coherent presentation has been made on the transitional process of flow past an isolated stationary smooth sphere from laminar flow to highly turbulent regimes. According to the available findings from published literature, a regime map has been presented to categorize the flow into eight different regimes [2]. A summary of the five typical ranges is outlined below:

- 1) Regime IV-separating vortex tubes regime ($800 < Re < 3000$): The velocity gradients in the shear layer cause pulsation behaviour leading to the formation of vortex tubes.

- 2) Regime V – The Subcritical regime ($3000 < Re < 3.4 \times 10^5$): The drag coefficient in this regime becomes almost independent of the Reynolds number.
- 3) Regime VI – The Critical Regime ($3.4 \times 10^5 < Re < 4.4 \times 10^5$): A rapid drop in the drag coefficient is observed in this regime, which persists from $Re = 3.4 \times 10^5$ to $Re = 4.4 \times 10^5$, with the lowest value of $C_D \approx 0.1$, being reached at around $Re = 3.7 \times 10^5$.
- 4) Regime VII – The supercritical regime ($4.4 \times 10^5 < Re < 1.5 \times 10^6$): A gradual increase in drag coefficient is observed with an increase in Re in this region.
- 5) Regime VIII – The transcritical regime ($Re > 1.5 \times 10^5$): Increase in drag coefficient which happens due to the upstream shift of the separation point transitioning the boundary layer from laminar to turbulent.

3. Research Methodology

3.1 Computational model

In this study, a spherical model with a diameter of 0.1 m and a turbulence intensity of 0.6% is used for automatic numerical simulation. Firstly, the geometry of the spherical model is implemented by SALOME software. The computational domain has a rectangular shape and dimensions of $20c$, $14c$, $11c$ on the Ox , Oy and Oz axes respectively whereas c is sphere's chord. The boundary faces for the computational model are set up as shown in Fig. 1. The sphere is located symmetrically about the x -axis in the middle of the domain. The distance from the centroid of sphere to the Inlet, Symmetry, both right and left Walls planes are respectively $7c$, $5.5c$, $7c$.

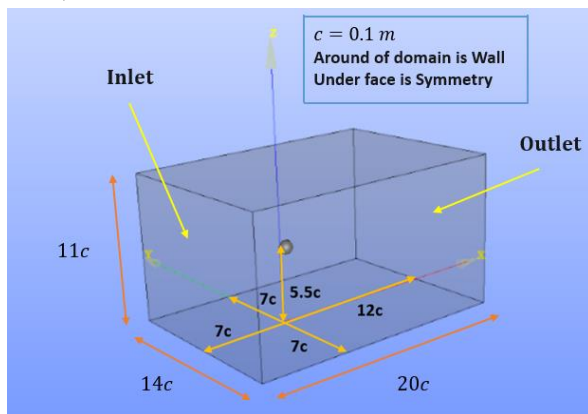


Figure 1. Conditions and dimensions of domain

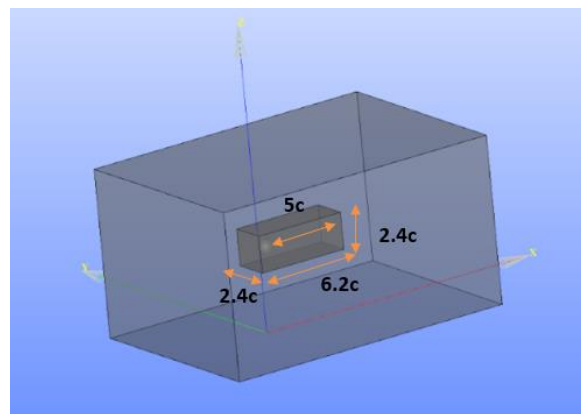


Figure 2. Sub-mesh domain size

In the next step, SALOME software is applied to create the background structured mesh with 401,576 uniform hexahedron cells. The mesh quality is almost perfect, shown by the cell aspect ratio of 1 and near zero skewness and non-orthogonality values. In the process of refining the mesh, in order for the problem to have the accurate result quickly and with less resource consumption, a rectangular sub-mesh domain is created with the dimensions of $6.2c \times 2.4c \times 2.4c$ (Fig. 2). The dimensions of the auxiliary mesh box domain must be carefully chosen so that the physical behaviour of the wake downstream can be kept track of. Two structural meshes for the

entire computational model are built for grid convergence study. Table 1 shows the basic parameters regarding the two meshes.

Table I. The parameters of two meshes

	Refinement level in subdomain	Refinement level on the sphere	nSurfaceLayers	Expansion ratio	Total cells
Mesh 1	2	6	11	1.4	2,658,866
Mesh 2	3	6	17	1.3	4,716,571

3.2 Algorithm of the automatic operation of wide range Reynolds numbers

This study aims at building an algorithm to run automatically numerical simulation for the fluid flows passing the sphere from the laminar to fully turbulent regime in Reynolds range $1000 \leq Re \leq 1.5 \times 10^6$. According to literature, the flow behavior around the sphere is affected by the Reynolds number. The choice of turbulent models and the non-dimensional y^+ values are well considered with respect to Reynolds numbers. Mesh is therefore created differently at each Reynolds number. The proposed algorithm is utilized to tune the appropriate mesh qualities in order to execute multi Reynolds cases. Moreover, the routine can also show mesh quality evaluation standards. The specific meshing parameters and meshing results will be presented in section 4.

Table II. Selection of turbulent models and y^+ value at different Reynolds regimes

Regime	Reynolds number	Turbulent models	y^+
<i>Sub-critical regime I</i>	$1000 \leq Re \leq 10000$	$k - \omega SST$	1
<i>Sub-critical regime II</i>	$10^4 \leq Re \leq 2 \times 10^5$	$k - \omega SST$	5
<i>Critical regime</i>	$2 \times 10^5 \leq Re \leq 6 \times 10^5$	<i>TransitionSST</i>	15
	$6 \times 10^5 \leq Re \leq 8 \times 10^5$		20
<i>Supercritical</i>	10^6	$k - \varepsilon$	25
	1.5×10^6		30

The process of mesh generation includes the change of the mesh parameters in the snappyHexMesh dictionary and the performance of OpenFOAM interactions on the terminal. The mesh parameters that need to be changed are box level, expansion ratio, number of surface layers and the first layer thickness. The box level, expansion ratio and number of surface layers change according to the type of mesh, while the first layer thickness is calculated based on the Reynolds number.

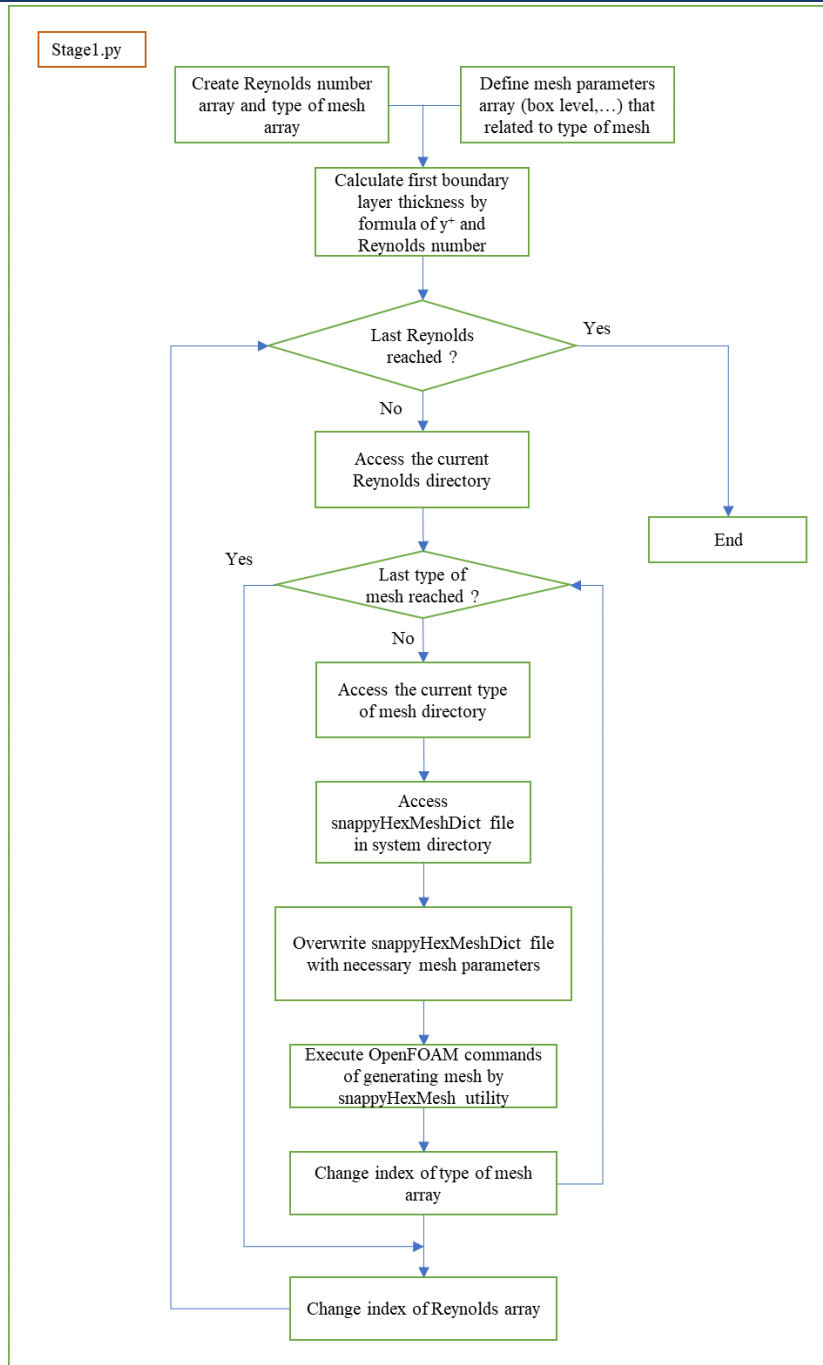


Figure 3. Detail block diagram of automatic mesh generation algorithm

4. Results

4.1 Mesh quality evaluation

The result graphs are obtained after running the mesh quality evaluation algorithm. According to this result, all sets of meshes satisfy the grid evaluation criteria. Sensitive criteria (AR, skewness, etc.) are at a low level, thus they can be used to perform numerical simulation problems automatically. It is noticeable that the average duration for building a mesh structure at a given Reynolds number varies from 200 seconds to 300 seconds.

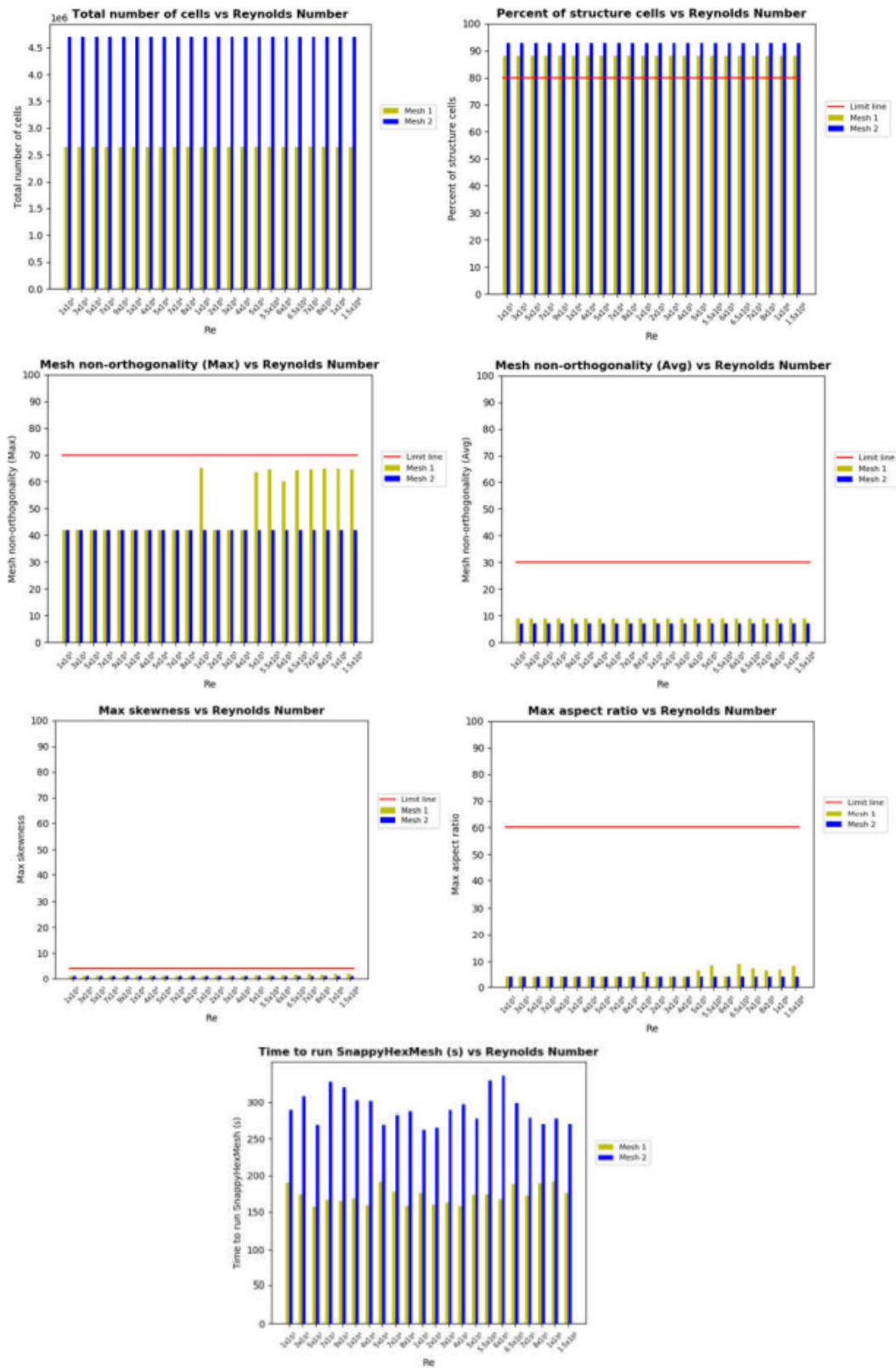


Figure 4. Mesh quality evaluation graph

4.2 Residuals

Figure 5 shows a typical residual chart of one simulation at Reynolds number $Re = 3 \times 10^5$. As Reynolds increases, the flow changes from laminar to turbulent, the convergence graph becomes more fluctuating and unstable, but acceptable residuals of flow quantities are still achieved approximately after 5000 iterations.

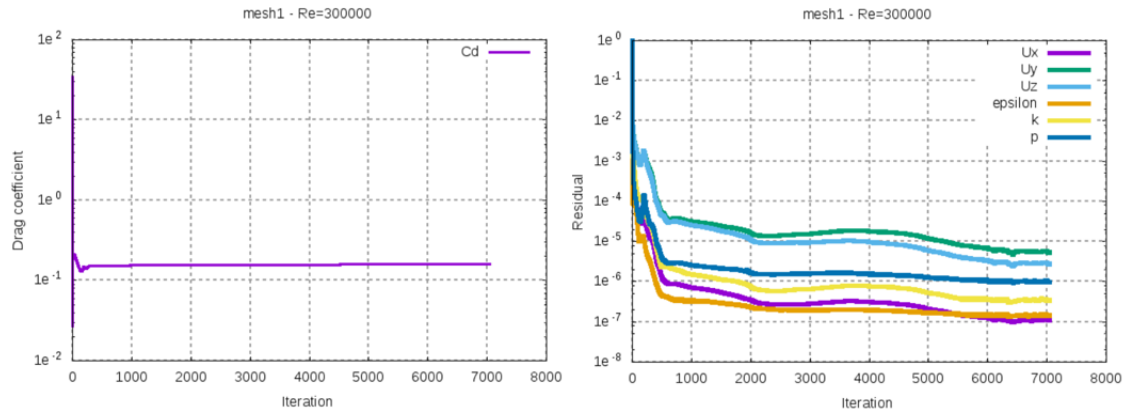


Figure 5. The residual convergence charts $Re = 3 \times 10^5$

4.3 Drag coefficient

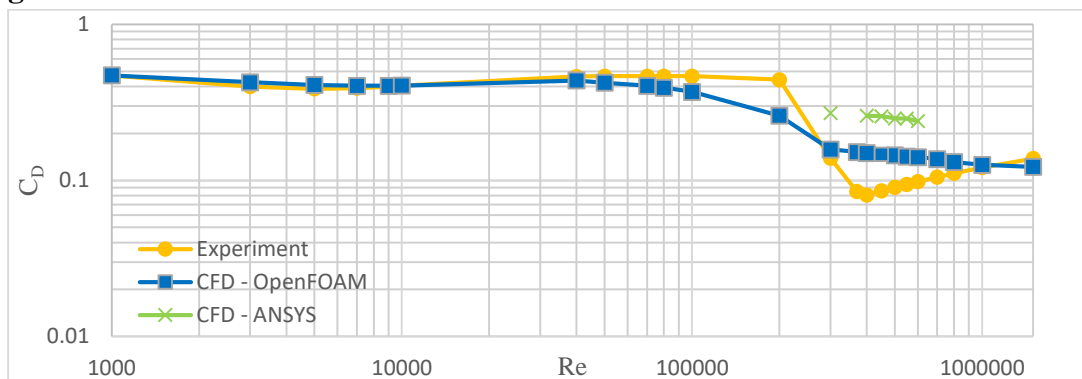


Figure 6. Drag coefficients on the stationary sphere versus Reynold numbers

After calculating the automatically numerical simulation by Python, the drag coefficients according to Reynolds are obtained. Grid independence check is verified for the two structured meshes as mentioned in Table 1. These results agree with those conducted by experiment in Ref. [4] and by ANSYS-Fluent's simulation in Ref. [5]. In the subcritical regime ($1000 \leq Re < 10^5$) the drag coefficient calculated from OpenFOAM is almost close to the experimental results. In the critical regime $2 \times 10^5 \leq Re < 6 \times 10^5$, the area where the drag crisis phenomenon occurs, there is a significant difference between the OpenFOAM results and the experimental results [4]. In general, in this area, the drag coefficient has decreased but has not dropped to the slope of the experimental curve. The transition from laminar to turbulent region is a very sensitive area, the numerical simulation results are easy to deviate from the experiment. This study proposed a more appropriate turbulence model than $k-\omega$ SST that can accurately simulate flow in this area. In the supercritical regime ($6 \times 10^5 \leq Re < 1.5 \times 10^6$), there is quite a difference between the two results. In OpenFOAM simulation, this region tends to decrease further as Reynolds increases.

Besides, about experimental results, after the drag crisis occurs, the drag coefficient starts to increase slowly again.

4.4 Flow field

The results of the velocity, direction flow of velocity vectors, pressure, turbulent kinetic energy field for each Reynolds region are output according to the automatic display algorithm. Since we have divided Reynolds corresponding to the fluid behavior over the sphere, we only give illustrative results at some of the Reynolds in that region. At low Reynolds, in the subcritical regime, the velocity field at the upper and lower of the sphere are almost symmetric. As the Reynolds increases in the critical and supercritical regime, the flow becomes more chaotic and the velocity field is no longer symmetrical and turbulent.

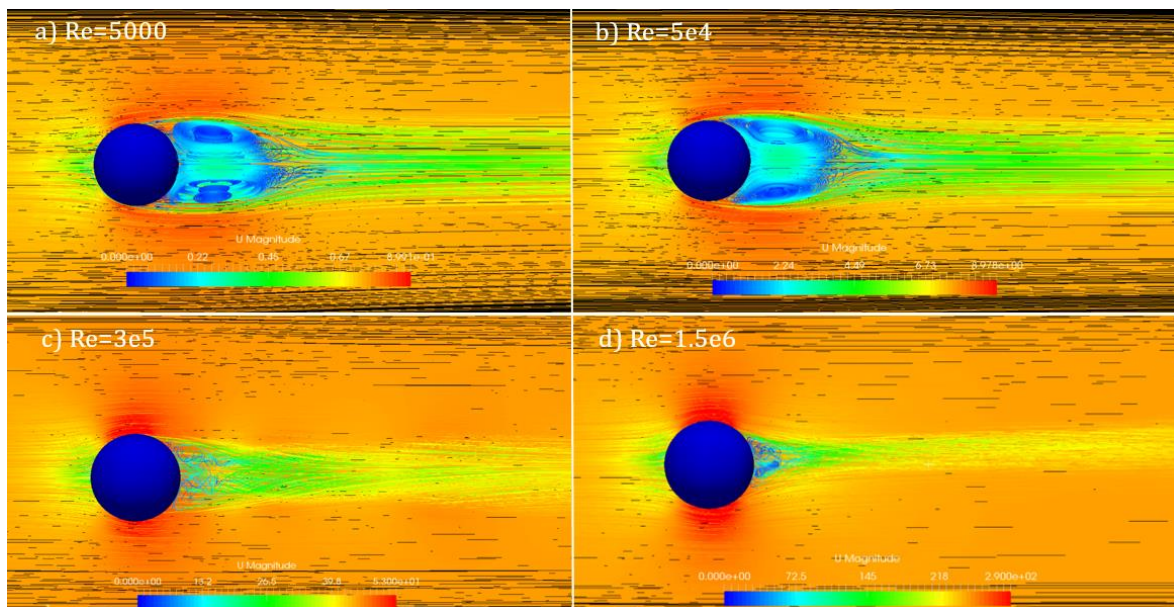


Figure 7. Velocity and streamlines at various Reynold regimes

5. Conclusion

In this paper, a single algorithm to control the automatic simulation of the OpenFOAM program is developed and provides reasonable results for the case study of the flow over a stationary sphere in a wide range of Reynolds numbers. The program will be utilized to study more complicated geometries in the future. However, when changing to other objects, it should be noted that the mesh parameters must be analyzed and calibrated again to ensure that all meshes are created well and satisfy the mesh evaluation criteria.

Acknowledgments

This research is funded by Vietnam National University Ho Chi Minh City (VNU-HCM) under grant number C2020-20-14. We acknowledge the support of time and facilities from the Hyper Computing Lab, Ho Chi Minh City University of Technology (HCMUT) and VNU-HCM for this study.

References

- [1] P.Dong, 2018, ‘An experiment study about drag crisis phenomenon on teardrop model’, MA thesis, National Cheng Kung University, Tainan, Taiwan.
- [2] Shashank S. Tiwari, Eshita Pal , Shivkumar Bale , Nitin Minocha , Ashwin W. Patwardhan,, Krishnaswamy Nandakumar, Jyeshtharaj B. Joshi, 2020, ‘Flow past a single stationary sphere, 2. Regime mapping and effect of external disturbances’, Powder Technology, Vol. 365, no. 0032-5910, pp. 215-243
- [3] H.K.Versteeg and W.Malalasekera, T 2007, ‘An introduction to Computational Fluid Dynamics’, Pearson Education.
- [4] Ing. Jan Dumek, 2018, ‘*Aerodynamic Parameters for Description of Flight of Rotating Volleyball*’, MA thesis CTU in Prague, faculty of mechanical engineering, Mechanical Engineering.
- [5] C.H.Yen, 2017, ‘Numerical study of flow past a solid sphere at high Reynolds number’, IOP Conference Series: Materials Science and Engineering, Vol. 243, no. 012042
- [6] The OpenFOAM Foundation Ltd, ‘OpenFOAM USER GUIDE,’ viewed July 4 2018, <<https://openfoam.org/resources/>>
- [7] J. John D. Anderson, 2011, ‘*Fundamentals of Aerodynamics*’, McGrall-Hill.

Path Planning Technology of Unmanned Vehicle Based on Improved Deep Reinforcement Learning

Luhe Wang¹, Jinwen Hu¹, Zhao Xu^{2*}, Lei Lu¹

1. School of Automation, Northwestern Polytechnical University, Xi'an 710129, China
E-mail: luhe_wang@foxmail.com, hujinwen@nwpu.edu.cn, nodainoben@mail.nwpu.edu.cn

2. School of Electronics and Information, Northwestern Polytechnical University, Xi'an 710129, China
E-mail: zhaoxu@nwpu.edu.cn

Abstract

As the basic problem of unmanned vehicle navigation control, path planning has been widely studied. Reinforcement learning (RL) has been found an effective way of path optimization for the highly nonlinear and unmodeled dynamics. However, the RL based methods suffer from the "dimension disaster" under the high-dimension state spaces. In this paper, the path planning of an unmanned vehicle with collision avoidance is considered, and an improved Deep Q-Network (DQN) algorithm is proposed to reduce the computation load in the high-dimension state space. First, the states, actions and rewards are determined based on the task requirement, and a smoothing function is defined as an additional penalty term to modify the basic reward function. Then, the two-dimension grid of the state space is mapped to a gray image, which is applied as the input of a neural network, i.e., the Q-Network. Finally, simulation results show that the modified DQN algorithm is more stable, and the fluctuation frequency is significantly reduced.

Key Words: Reinforcement learning, path planning, DQN

1. Introduction

All aspects of our life enjoy the convenience brought by artificial intelligence, especially the intelligent robot^[1]. To meet national strategy and market driven demand, the research of robot is more and more in-depth in the academic circles, in which robot navigation and path planning is an important problem in the field of robot research.

The original intention of path planning is to make the robot get the best navigation, reduce the redundant path in the process of autonomous motion, and help improve work efficiency of the producer in the process of production and processing. The existing path planning algorithms can be divided into classical and intelligent algorithms. The classical algorithms can be divided into heuristic search algorithm, potential field algorithm and sampling based algorithm, and are mainly used to solve the problem of optimal path calculation when the environment is completely known and basically fixed, mobile agents located accurately and meeting the relevant trajectory. However, the amount of calculation is huge, and the limitation is high. For example, A* algorithm^[2] often can not give feasible solutions in solving high-dimensional problems, the artificial field potential method^[3] finds it difficult to design in gravity and repulsion, and its application space is very limited. The probability graph method^[4] and the fast exploration random tree method^[5] are very dependent on the distribution of sampling points, which is not easy to grasp. After decades of development, traditional algorithms have been mature and made systematic.

In recent years, the related improvement methods based on traditional algorithms have been combined the idea of artificial intelligence^[6-7]. The early intelligent algorithm is represented by genetic algorithm^[8] and neural network^[9]. The emerging path planning algorithm is based on reinforcement learning method^[10]. Although the intelligent algorithm based on reinforcement learning is not necessarily optimal each time, the judgment speed is very fast, and through a certain period of learning, its overall efficiency is much higher than the traditional algorithm. Reference [11] studies the efficiency of different reinforcement learning algorithms for agent obstacle avoidance, but the simulation experiment is a 6x6 grid map, there is no experimental study on larger grid environment, and the obstacles are sparse, which has little practical significance. The research in [12] shows that it is completely feasible to use DQN to realize the navigation of mobile robot without creating a map, and path planning is preliminarily realized using DQN in raster map, and better result never obtained before is obtained. However, in [12], the convergence of DQN algorithm is weak, and the convergence of the algorithm is not improved. Although [13] studies the path planning problem of three-dimensional space unmanned vehicle based on DQN, the algorithm framework is similar to that of two-dimensional obstacle avoidance environment. It is the improvement and application of DQN algorithm in specific scenes, and the convergence speed is higher than that of DQN algorithm, but it does not explain the accuracy of the algorithm. In [14], the DNN network is used to build a deep reinforcement learning framework to study the obstacle avoidance path planning of unmanned vehicles. By repeating its algorithm, this paper finds that although the DQN method based on DNN can get the optimal path, the success rate is very low, and the algorithm framework is not worth promoting. In addition, more and more scholars have used deep reinforcement learning algorithm to solve problems in various industries, and they are relatively mature in path optimization^[15-16].

To sum up, the existing research on the application of reinforcement learning technology to solve path planning problems focus on whether the algorithm converges, and does not discuss whether the convergence result of each operation of the algorithm is optimal or the accuracy of the convergence result. Using DQN algorithm to solve the obstacle avoidance path planning of unmanned vehicle in discrete space, this paper further discusses the success rate and application effect of DQN algorithm in path planning. Firstly, four motion directions are set based on the research scene, and the grid coordinates are used to record the current position of the unmanned vehicle. Secondly, based on the basic principle of reinforcement learning and the characteristics of the environment, a smoothing function is defined as an additional penalty term to modify the basic reward value. Thirdly, two-dimensional grid image with the current position information of the unmanned vehicle is mapped to the gray image as the input of the neural network, and the Q-Network is trained to form the value network based on the memory bank and the target network design algorithm process. Finally, the simulation experiment is carried out, the results show that the improved DQN algorithm based on the characteristics of the scene is more stable, and the fluctuation frequency is significantly reduced.

The arrangement of this paper is as follows: Section 2 describes the relevant elements of unmanned vehicle path planning. Section 3 briefly introduces the basic principle of reinforcement learning and the framework of path planning based on the DQN algorithm, which is followed by the modified algorithm. Simulations are carried out in Section 4 and the results show the effectiveness of the modified algorithm. Section 5 concludes the paper.

2. Description of Route Planning Elements

2.1 Problem Description

Figure 1 is a $m \times n$ grid map (m and n are arbitrary integers). Each grid in the map represents a location state. The agent is represented by a red box, the target point is represented by a yellow circle, and the remaining black and white boxes represent obstacles and barrier free areas respectively. Different map environments can be formed by changing the distribution of black obstacles. In this paper, the agent is explored to complete the collision free optimal path planning from any starting point to the end point through interactive learning with the environment when the environment state is unknown.

2.2 State Information and Action Space

The simulation experiment is written in Python language, and the visual interface is built by using Python toolkit Tkinter. As shown in Figure 1, each grid can be uniquely represented by the coordinates of the upper left and lower right vertices, so the current state information of the agent can be marked $S = [x_1, y_1, x_2, y_2]$, where x_1 and y_1 represents the abscissa and ordinate of the upper left corner of the grid and the abscissa and ordinate of the lower right corner of the grid. The first grid in the upper left corner of the map is marked as $[0,0,1,1]$, and the lower right corner is $[m-1, n-1, m, n]$.

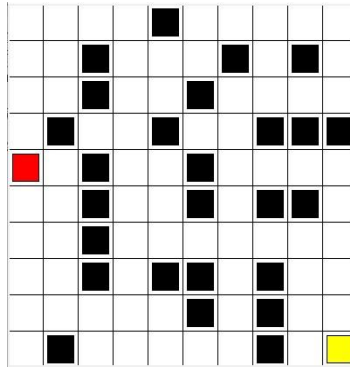


Fig 1. Scene design of unmanned vehicle path planning

Because the experimental environment of this paper is a two-dimensional discrete grid space, the grid occupied by the red box is the real-time position of the agent in the environment. In the simulation environment, it is stipulated that the agent can only move up, down, left and right in four directions, and the agent can only move one grid every time it performs an action. Therefore, the action space is represented by the following set

$$A = \{ "up", "down", "left", "right" \}.$$

3. Unmanned Vehicle Path Planning Based on Q-Network Reinforcement Learning

Reinforcement learning is a way for an agent to optimize its behavior in an unknown environment. The purpose of learning is to seek the strategy $\pi(s)$ to maximize the cumulative reward, that is, to seek the optimal strategy $\pi^*(s)$.

$$q_*(s, a) = R_s^a + \gamma \sum_{s' \in S} P_{ss'}^a \max_{a'} q_*(s', a') \quad (1)$$

$$\pi^*(a|s) = \arg \max_a q_*(s, a) \quad (2)$$

(1) is to solve the value function of the optimal action, R_s^a is the reward feedback under the state S , γ is the discount factor, $P_{ss'}^a$ is state transition probability, $q_*(s', a')$ represents the value of the optimal action under the next state, and $\pi^*(a|s)$ of (2) is the optimal strategy.

This experiment explores the path planning of unmanned vehicle in unknown environment, so it is model-free learning, and it does not need to know the transition probability P_{ss}^a . In order to simplify the calculation and improve the efficiency, the following expression is usually used to replace the update process of the above value function.

$$Q(s, a) = Q(s, a) + \alpha(R + \gamma Q(s', a') - Q(s, a)) \quad (3)$$

$$\pi^*(a | s) = a^* = \arg \max_{a \in A} Q(s, a) \quad (4)$$

The optimal strategy is $\pi^*(a|s)$ and the action value function $Q(s, a)$ represents the value of the selected action a in state s . The difference between $Q(s, a)$ and the value function in (1) and (2) is that $Q(s, a)$ is not strictly derived from the Bellman equation, but obtained by simplifying the Behrman equation by artificially specifying a more reasonable learning rate α and discount factor γ .

3.1 Reinforcement Learning Framework

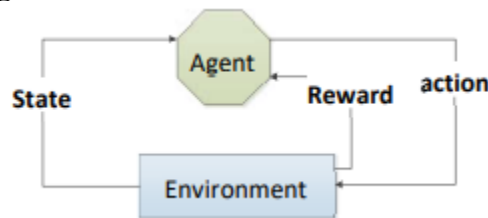


Fig 2. Reinforcement learning framework

The reinforcement learning framework of unmanned vehicle path planning is established, which mainly composed of environment and agent. In this paper, the unmanned vehicle is studied as an agent. The state of the environment is the current position $S = [x_1, y_1, x_2, y_2]$ of the agent. The agent decides an action according to the current state for the next moment. After the action is executed, the environment will change, and a reinforcement signal will be generated to feed back to the agent. So far, the agent interacts with the environment to complete a cycle. As shown in the Figure 1, the model is represented as the interaction process between agent and environment.

3.2 DQN Model

In the early research, some scholars used Q-learning in reinforcement learning to complete obstacle avoidance in static unknown environment^[17] and path navigation in three-dimensional environment^[18]. Then in 2010, Jaradat et al. first used Q-Learning for path navigation in dynamic unknown environment^[19]. With the deepening of research, scholars found that the size of the state space of ordinary Q-learning algorithm will become extremely large when facing large and complex environments, then face the disaster of dimensionality. In 2013, Google Deep-Mind team first combined convolutional neural network with Q-learning and proposed the concept of DQN. Then Deep-Mind and other teams and research institutions successively optimized and improved the DQN algorithm^[20], and reinforcement learning algorithm officially emerged. In this paper, convolution neural network is used to approximate $Q(s, a)$ to solve the problem of "dimension disaster".

3.2.1 Structure Design of Q-Network

Q-Network consists of input layer, convolution layer, all connected layer and output layer, as shown in the Figure 4. Convolution neural network needs to take the picture as the input state information, in order to reduce the amount of convolution calculation, we map the input image

into a numerical matrix as the input of neural network. The barrier free area is represented by 0, and the barrier grille is represented by 1. In addition, the grid represented by its current coordinate is represented by a value of 2 to distinguish feasible paths and obstacles. As shown in Figure 3, the RGB 3D image is transformed into a $m \times n \times 1$ grayscale by matrix mapping, which greatly improves the computational efficiency of the convolutional network. The convolution layer uses a three-layer convolution network to extract the features of the input information. After the feature extraction of the image, the output information $Q(s,a)$ is obtained by connecting the flatten layer and the all connected layer.

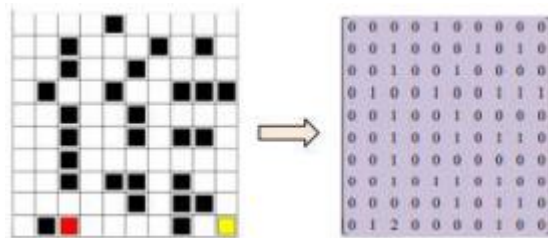


Fig 3. RGB image mapping

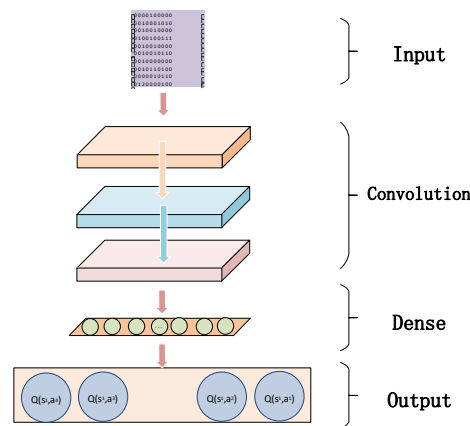


Fig 4. Neural network structure

Adjusting the weight of the neural network can change the size of the output value function Q in each action direction. The purpose of training the neural network is to find a group of appropriate weights, so that the agent can start from the starting point and act according to the maximum Q value of the neural network output under the weight in each state, so as to make the planned path optimal. Compared with Q -learning, the neural network in DQN algorithm is equivalent to Q table.

3.2.2 Action Strategy

Strategy is an action basis, and the next action mode of the agent will be adjusted according to the strategy. In this paper, agents learn by trial and error in the process of path planning, then use the learned knowledge to select the optimal action. Therefore, agents should fully explore the environment to accumulate experience in the early stage of training and use value function to select actions in the late stage of training. In this paper, we use the ϵ - greedy strategy that ϵ changes with the number of training.

$$\pi(a | s) = \begin{cases} \arg \max_{a \in A} Q(s, a) & \text{if } num > \varepsilon \\ \text{random action} & \text{if } num < \varepsilon \end{cases} \quad (5)$$

num is a system generated random decimal between 0 and 1. At the beginning of iteration, when the value of ε is large, the system randomly selects the action with the probability of ε , and uses the value function to select the action with the largest corresponding state action value with the probability of $1 - \varepsilon$. With the increase of the number of iterations, ε decreases gradually. When the number of iterations reaches a certain number, the agent completely relies on the value function and no longer explores the environment.

The reward function plays a guiding role in training. According to the characteristics of reinforcement learning, agents will get different cumulative rewards when they take different paths to the destination, and the cumulative reward of the optimal path should be the largest, so the basic reward function is designed as follows

$$R = \begin{cases} 1 & \text{reach the target point} \\ -1 & \text{encounter obstacles} \\ -0.1 & \text{others} \end{cases} \quad (6)$$

If Q-learning algorithm is directly combined with neural network, there will be two problems: ① As a kind of supervised learning, deep learning needs a large number of labeled samples. Reinforcement learning is that agents search for data samples by themselves, which is small in number and sparse in size with delay. ② Deep learning requires that each data sample is independently distributed, but the data samples obtained by reinforcement learning are not independent. In order to solve the defects of this reinforcement learning algorithm, two improvement directly use (6) as the basis of iterative updating of reinforcement learning value function, although the optimal planning path can be obtained, the success rate is less than 50%. The specific experimental results are shown in the experimental analysis in Section 4. In this paper, according to the characteristics of the experimental scene, the smooth function is added to greatly increase the success rate of the experiment.

Directly using (6) as the basis of iterative updating of reinforcement learning value function, although the optimal planning path can be obtained, the success rate is less than 50%, the specific experimental results are shown in the experimental analysis in Section 4. In this paper, according to the characteristics of the experimental scene, the smooth function is added to greatly increase the success rate of the experiment.

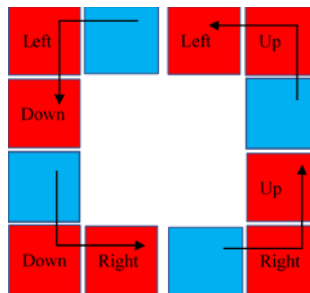


Fig 5. Four cases of car turning

The obstacles built in this experiment are not evenly distributed, and the optimal path is between the dense obstacles. If the car wants to find the optimal path in the training process, it is bound to hit the wall many times. Therefore, the car tends to take the route that is not easy to hit

the wall, which leads to the unsatisfactory training effect of using R as the reward function directly. It is found that whether the experimental result is the optimal solution largely depends on the action direction of the first step of the car, and the optimal path is the smoothest path, and the turning times of other paths to the destination are greater than the optimal solution. Therefore, the smooth function is defined to limit the turning times of the car, and the penalty value of the turning nodes of the clearance joint is different to help the car find the optimal path. Define penalty function as:

$$P_u = \begin{cases} 0 & \text{Turn} \\ -0.5 & \text{No Turn} \end{cases} \quad (7)$$

In this paper, the direction of two consecutive movements is used as the basis to judge whether the car is turning. Figure 5 shows four situations in which the car turns. The blue square represents the relative position of the agent in the first place, and the two red squares crossed by the black arrow represent the action direction of the agent in the next two steps.

3.2.4 Memory Bank and Target Network

Schemes are proposed: Experience Playback and Fixed Q-Target.

Experience Playback: Firstly, a memory bank is established to store the data (s, a, r, s') generated by the agent when exploring the environment. When the neural network is trained with the data, the agent can randomly extract some data from the memory bank for repeated learning. The method of random extraction is to destroy the close relationship between the data and make its update more efficient.

Fixed Q-Target: In this method, the neural network used in DQN is cloned once. The cloned network has the same architecture as the original network, but the parameters are different; we call it the target neural network. The parameters of the original network are updated with the training process. The parameters of the target neural network are copied from the original network with a certain number of training rounds. By setting the target neural network separately and freezing its parameters temporarily, the correlation of data is reduced, and the stability of neural network is guaranteed.

During the training process, DQN is updated by continuously adjusting the network parameters through the gradient descent method. The error function equation used is as follows:

$$Loss = (r + \gamma \max Q(s', a', \theta'_i) - Q(s, a, \theta_i))^2 \quad (8)$$

where $\max Q(s', a', \theta'_i)$ is the output of the target network, $Q(s, a, \theta_i)$ is the output of the estimated value network, and θ_i and θ'_i are the parameters of the estimated network and the target network respectively. The process of updating is to select a batch of sample data from the memory, in which each sample is expressed as (s, a, r, s') , calculate the action value function of state s by using the estimation neural network $Q(s, a)$, calculate the action value function of state s' by using the target neural network $Q(s', a')$, and then update the parameter θ of the prediction network using the gradient descent method according to the error function $\theta \theta \alpha \gamma_{t+1} = +_t$ In (9), $r + \gamma \max Q(s', a', \theta')$ $\theta_{t+1} = \theta_i + \alpha [r + \gamma \max Q(s', a', \theta') - Q(s, a, \theta)] \nabla Q(s, a, \theta)$ (9) is the target action value function and θ' is the parameter of the target network. When the above process has been executed for a certain number of times, the parameters θ of the prediction network are copied to the target network, that is, the parameters of the target network are updated.

3.3 Algorithm Flow Design

Define the action memory set M , which contains $action_1$ and $action_2$ variables, and store the two consecutive action directions of the car in the process of moving. The initial position of the agent is $(0,0)$, and action a_1 is selected and executed according to the ε -greedy strategy make agent transfer to the next state s' and get reward r_1 . Turn action a_1 to $action_1$. Save (s, a_1, r_1, s') to the memory. In state s' , the agent selects and executes action a_2 according to the ε -greedy strategy and transfer to state s'' to get reward r_2 . Turn action a_2 assignment to $action_2$. Judge $action_1$ and $action_2$ to see whether it will make the car turn, assign a value to Pu , and save $(s', a_2, r_2 + Pu, s'')$ to the memory, repeat the above operation for many times to accumulate a large number of sample data. When the system meets the indicators set by the program, samples will be randomly selected from the memory to train the neural network, input s to the estimated value network to get $Q_{estimate}$, input s' to the target value network to get Q_{target} , get the error function according to (8), and update the estimated value network parameters using (9) of gradient descent method. After a certain number of times or rounds of training, the parameters of the estimated value network are assigned to the target value network. The neural network is continuously optimized through many rounds of training, so it is necessary to slowly increase ε in the later stage, so that the agent can choose the optimal action $a = \arg \max Q(s, a_i)$ according to the value function with greater probability. In order to speed up the experimental convergence as much as possible and reduce the training plot, only a negative reward is given when it collides with the obstacle, and the agent is not reset to the initial position. In the process of updating $action_1$ and $action_2$, $action_2$ always stores the current action direction, and $action_1$ stores the action direction of the last car.

4. Simulation Analysis

Take the simulation environment of 10×10 as an example. First, we do 30 experiments on the DQN algorithm before the improvement, as shown in Figure 7, The abscissa represents the number of experiments, and the ordinate represents the results of each experiment. It can be seen that the experimental results are not stable and fluctuate continuously in a small range, which indicates that in the process of many experiments, it is difficult to guarantee the optimal planning results based on DQN algorithm, and most of them are suboptimal solutions with little difference from the optimal results.

The experimental results based on the improved DQN algorithm are shown in Figure 8. We can see that after the improvement, there are more optimal results in the path planning of the agent. Compared with the experimental results before the improvement, Figure 8 shows that the improved DQN algorithm is more stable, the fluctuation frequency decreases significantly, and the success rate of the algorithm increases from 30% to 73.3%, which shows that it is effective to directly limit the number of car turns.

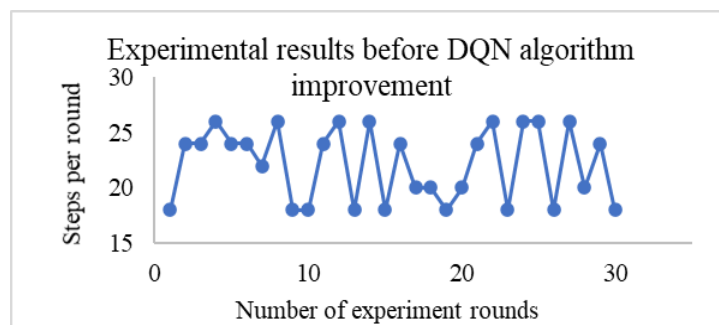


Fig 7. Experimental results before DQN algorithm improvement

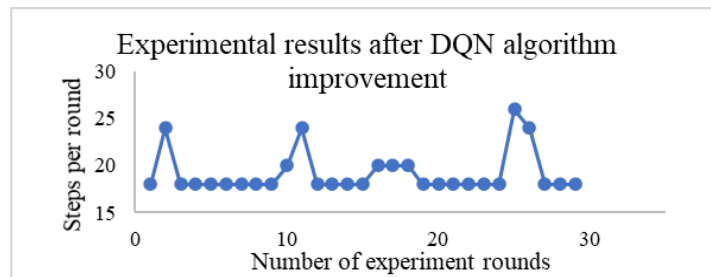


Fig 8. Experimental results after DQN algorithm improvement

Through the above improvement measures, it can be seen that the path planning based on DQN algorithm is difficult to have absolutely accurate planning effect like the traditional algorithm. The reward function designed at the beginning of this paper does not consider the cost penalty of each step, and only gives -1 and 1 reward values, which is a sparse reward measure, so in most cases, the reward value returned by an agent in a state is zero. When the above reward function is changed to (6), the result will reach a better convergence state. In order to make the results more stable, this paper adds some restrictions, so that the accuracy of DRL results can be improved from 30% to 73%. To achieve 100%, we need more accurate restrictions for deep reinforcement learning.

Through the recurrence and improvement of DQN algorithm, we can see that deep reinforcement learning is more likely to have good performance when it meets the following conditions: ① Data acquisition is very easy and easy to express. ② The reward function is easy to define. ③ The guidance signal refers to the feedback signal given by the environment to guide the agent to approach the optimal solution in the learning process. If the guidance signal is sparse or there are many punishment signals, the agent may not be guided for a long time, and eventually lead to stagnation in a certain state, or form a dead cycle in several positions, so it is the most important. Every change of state gives the agent a certain guidance feedback, and timely feedback helps the agent converge to the optimal solution quickly.

5. Conclusion

Based on reinforcement learning theory, an obstacle avoidance path planning model of unmanned vehicle is established. In order to solve the problems of sparse reward distribution in grid environment and the algorithm is not suitable to converge to the optimal result, a smoothing function is constructed to modify the reward function according to the characteristics of obstacle space. In order to solve the problem of convolution neural network with large amount of calculation and tedious feature extraction, a gray image is constructed instead of RGB three-dimensional color image to participate in the training of neural network. The simulation results show that the training method can effectively improve the accuracy of obstacle avoidance path planning, the intelligent obstacle avoidance algorithm of unmanned vehicle based on deep reinforcement learning has high accuracy under the premise of ensuring the speed, and the application effect is good.

Due to the shorter development time of deep reinforcement learning, and the application time in control field is shorter, so there are still many aspects which need to be improved. Such as in simulation experiments, based on deep reinforcement learning, although the simulation results are good, it is not really applied to practice, and its real performance needs to be further proved.

References

- [1] Xuedong Jing, Ya-nan Chen, Yuquan Xue. Study on Path Planning for Family Service Robot Based on Improved Genetic Algorithm. *Chinese Intelligent Systems Conference*. 2019:621-631.
- [2] Hart P E, Nilsson N J, Raphael B. A formal basis for the heuristic determination of minimum costpaths. *IEEE Transactions on Systems Science and Cybernetics*, 1968, 4(2): 100-107.
- [3] Khatib O. Real-time obstacle avoidance for manipulators and mobile robots. *The International Journal of Robotics Research*, 1986, 5(1): 90-98.
- [4] Kavraki L E, Svestka P, Latombe J C, et al. Probabilistic roadmaps for path planning in high-dimensional configuration spaces. *IEEE Transactions on Robotics and Automation*, 1996, 12(4): 566-580.
- [5] Lavalle S M . Rapidly-exploring random trees : A new tool for path planning. *Computer ence Dept*. Oct, 1998, 98.
- [6] Xiu Yue, Chaofeng Zhang, Wei Zhang, et al. UAV Path Planning Based on A* Algorithm and Improved Simulated Annealing Algorithm. *Control Engineering (in Chinese)*, 2020,27(8):1365-1371.
- [7] Koenig S, Likhachev M. Fast replanning for navigation in unknown terrain. *IEEE Transactions on Robotics*, 2005, 21(3): 354-363.
- [8] Chunmiao Wang, Y. C. Soh, Han Wang, et al. A hierarchical genetic algorithm for path planning in a static environment with obstacles. *Canadian Conference on Electrical and Computer Engineering, and Congres Canadien en Genie Electrique et Informatique (CCECE2002CCGEI)*, vol.3.2002:1652-1657.
- [9] Y. Chen and W. Chiu, Optimal robot path planning system by using a neural network-based approach, *2015 International Automatic Control Conference (CACS)*, Yilan, Taiwan, 2015:85-90.
- [10] Sutton, R. & Barto, A. Reinforcement Learning: An Introduction (MIT Press, 1998).
- [11] Sijia Liu, Xiangrong Tong. Urban transportation path planning based on reinforcement learning. *Journal of Computer Applications (in Chinese)*, 2021, 41(1) : 185 – 190.
- [12] Panov A I, Yakovlev K S, Suvorov R. Grid path planning with deep reinforcement learning: Preliminary results. *Procedia Computer Science* , 2018,123:347-353.
- [13] Shuo Feng, Hong Shu, Buqing Xie. 3D Environment Path Planning Based on Improved Deep Reinforcement Learning .*Computer Applications and Software (in Chinese)*, 2021, 38(1): 250-255.
- [14] Zhirong Liu, Shuhai Jiang, Wenwen Yuan, Chenhui Shi, Robot Path Planning Based on Deep Q-Learning, *Measurement and Control Technology (in Chinese)*, 2019, 38(7):24-28.
- [15] Yao Dong, Yingying Ge, Hongyong Guo, et al. Path Planning for Mobile Robot Based on Deep Reinforcement Learning. *Computer Engineering and Applications (in Chinese)*, 2019 , 55(13):15-19,157.
- [16] Xingxing Liang, He Feng, yang Ma, et al. Deep Multi-Agent Reinforcement Learning: A Survey . *ACTA AUTOMATICA SINICA (in Chinese)*,2020, 46(12): 2537–2557
- [17] William D. Smart, Leslie Pack Kaelbling. Effective reinforcement learning for mobile robots.2002 *IEEE International Conference on Robotics and Automation (ICRA 2002)*, vol.4.2002:3404-3410.

[18] Beom H R, Cho H S. A sensor-based navigation for a mobile robot using fuzzy logic and reinforcement learning. *IEEE Transactions on Systems, Man and Cybernetics*, 1995, 25(3):464-477.

[19] Jaradat M A K, Al-Rousan M, Qadan L. Reinforcement based mobile robot navigation in dynamic environment. *Robotics & Computer Integrated Manufacturing*, 2011, 27(1): 135-149.

[20] Mnih V, Kavukcuoglu K, Silver D, et al. Human-level control through deep reinforcement learning. *Nature*, 2015, 518(7540):529.

Obstacle Avoidance System on an Omni X Drone Based on Neural Network, Computer Vision and Mavlink Protocol

Tran Quang Khoi^{1,*}, Ngo Khanh Hieu^{2,*}, Le Dinh Anh Huy² and Truong Lu Tien²

¹Real-time Robotics Viet Nam Company Limited, 40/10 Khong Tu Street, Hiep Phu Ward,
District 9, Thu Duc City

²VNU-HCM Key Laboratory for Internal Combustion Engine

*Corresponding author. E-mail: khoi.tran@rtrobotics.com, ngokhanhhieu@hcmut.edu.vn

Abstract

The paper presents preliminary research results after implementing an obstacle avoidance program based on a cheap camera input video and a neural network to process the frames and command the drone to stop. The program includes 2 modules implemented on a Jetson Nano single board computer and can achieve real time performance at 40 FPS. The neural network is developed in Python using the Pytorch framework and based on the DroNet model. The control module is developed in Python and communicates with the drone via Mavlink protocol. The network succeeds in detecting obstacles at accuracy up to 80% even in low light conditions. The system reaction delay reaches 300ms and can stop the vehicle moving at speed 0.65m/s effectively. The results in this paper demonstrate the potential of this approach for further development of an omni obstacle avoidance system using only cameras in the future. Based on real-world results, the authors showed that a good outcome is achievable with only cheap devices and can be implemented easily on agriculture drones which are familiar nowadays on Vietnamese rice fields. Besides, the paper also proposes several solutions to increase the neural network's accuracy and most importantly the real-time performance on multi stream input which is essential for an omni obstacle avoidance system with multiple cameras onboard the drone.

Keywords: Autonomous navigation, Pi camera, DroNet, Pytoch, Mavlink, Ardupilot, Obstacle Avoidance

Nomenclature

FPS=Frame Per Second

1. Introduction

Today, more sophisticated drones are playing an important role in real-life applications. Complex flight missions that require coordinated work between control systems, navigation, and awareness of real-world situations sometimes take place out of the blue.

Studies in 2012[1] show that the use of mapping techniques in obstacle avoidance requires reconstructing those obstacles in 3D space. Approaches such as [1] use GPS to calculate the state, the camera to determine where the area is, and the lidar to find an obstacle in the line of sight. In addition, the authors [2] also used optic flow to evaluate the directional feedback when encountering obstacles and stereo vision to identify obstacles. Grzonka et al. [3] use the SLAM algorithm on a quadcopter capable of determining the current position of the aircraft and reconstructing the map with the least error.

In 2013, the authors in [4] used the Dagger algorithm to train a drone on how to act when encountering obstacles, similar to a human pilot. According to the algorithm presented, the ability to learn is based on the responses to recorded situations. In the article [5], the author trains a Deep Learning Network model with the main function of recognizing trails along cliffs. Using

RGB color images from a camera onboard the drone, the system can recognize real-life situations.

The DroNet network [6] was built as an inevitable result of the development of UAV techniques for detecting the path as well as identifying the collision situation. The network is trained on images obtained from outdoor data collection and can avoid the need of basic tasks such as “Localization, Mapping, and Planning” that the mapping method requires.

For methods to identify obstacles by creating a map of the surrounding environment, typically the SLAM algorithm, it is necessary to reconstruct the 3D model of the environment from which to determine the coordinates and the path. The problem is that the system needs to perform a huge amount of computation and decide only after having full data on the 3D map around the aircraft.

For the method using the deep learning reinforcement network, after training the computer with a sufficiently large amount of data, the computer's artificial neural network is able to receive predictions of the steering angle and the situation of a collision without mapping the surrounding environment.

The use of neural networks is also highly feasible because embedded computers are getting more and more powerful and are equipped with GPUs and TPUs to process artificial neural networks at high speed, so that the processor can handle situations without transmitting data to the ground station, which will increase the system's real-time responsiveness. In addition, the system does not need to be equipped with additional peripheral sensors such as radar, lidar, etc., thereby reducing the cost of the obstacle avoidance system.

In this study, the authors succeeded in implementing an artificial neural network built on the DroNet network architecture [6] using the Pytorch platform. This neural network is called P-DroNet and operates on a Jetson Nano embedded computer which communicates and controls the drone via Mavlink protocol and can achieve real-time performance up to 70 FPS.

2. Implementation

Converting DroNet from Keras framework to Pytorch brings many computational advantages on GPU in speeding up computation. Pytorch is supported by NVIDIA directly on Jetson Nano's Jetpack software suite. Therefore, by successfully converting DroNet to Pytorch, Jetson Nano is expected to be able to process this neural network faster than the one on Keras.

DroNet network architecture is shown in Figure 1. The authors have kept this architecture and simply converted to Pytorch framework to operate on Jetson Nano.

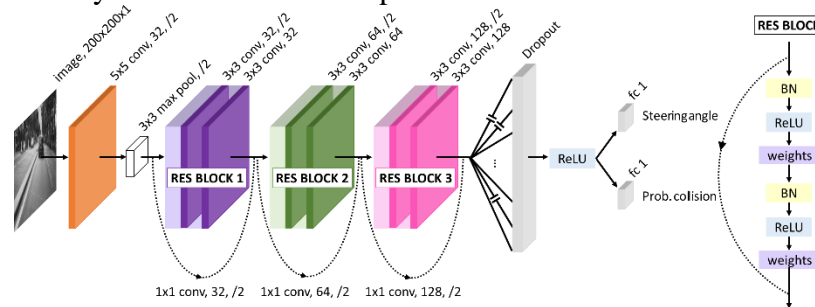


Figure 1: DroNet CNN architecture [6]

The DroNet network structure is converted to the Pytorch framework thanks to the nn.Module modules [7], Dataset and Data Loader as shown in Figure 2. These modules divide data into training, testing, and validation sets.

The method of training and evaluating the network is quite different from the Keras framework that the University of Zurich has applied before. The authors use model.train() to set

the training state for the model. In each loop, the data is forwarded through the model to return the corresponding output, calculate the loss value and optimize to the smallest possible value.

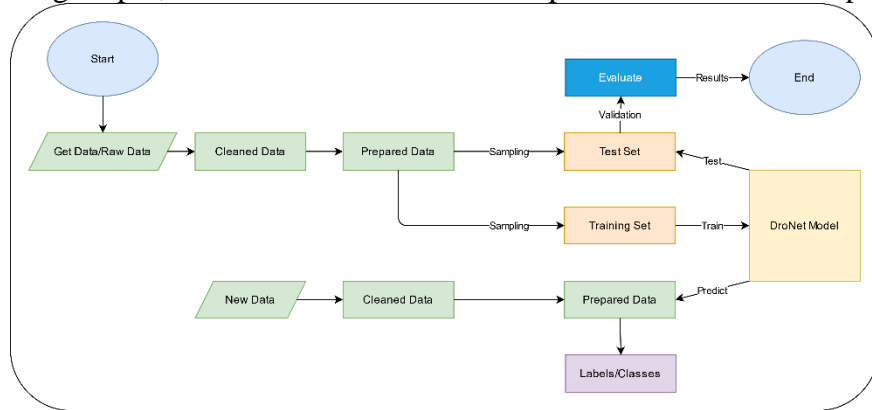


Figure 2: Retrain DroNet

In addition, the fine-tuning of the DroNet network is also applied to achieve higher accuracy (Avg. accuracy) by adjusting the learning rate to minimize the global loss.

2.1 P-DroNet on Pytoch and Jetson Nano

The DroNet network based on the PyTorch framework achieves a processing speed of > 40 FPS at the resolution of 320x240 pixels when combined with the control algorithm on Jetbot. The desired speed when deploying to the drone is 70 FPS at resolution of 256x144 pixels as shown in Figure 3 below. It can also be seen that when reducing the resolution of input frames, the collision prediction ability of P-DroNet changes from 0.92(true) to 0.34 (false).

Currently, the experiments presented in the next section are conducted based on 320x240 pixel input with the network performance about 40 FPS.

The P-DroNet is trained to raise the “stop” signal at a distance of 40cm. In reality, this distance may vary depending on the controlled system itself (quadcopter or jetbot) and the light conditions. The authors carried on experiments in section 3 to verify this distance in real situations.

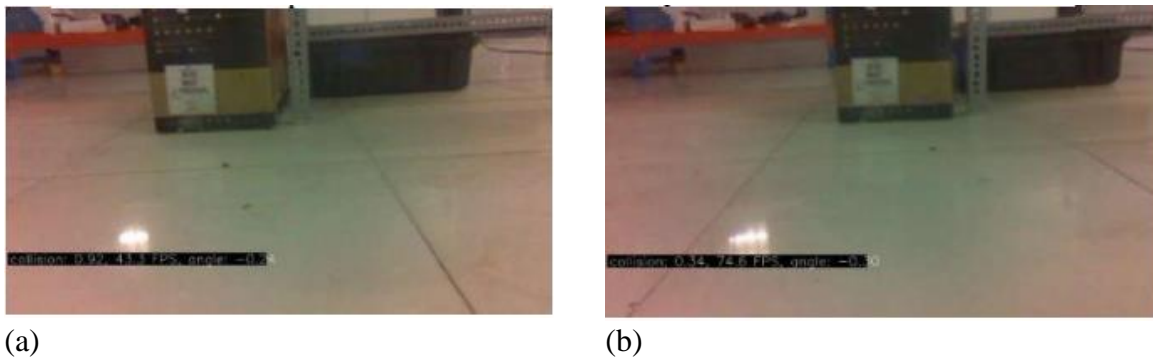


**Figure 3: (a) Inference DroNet on Jetson Nano 320x240 pixels at 43 fps;
(b) Inference DroNet on Jetson Nano 256x144 pixels at 74 fps**

2.2 Ardupilot and mavlink control

Most small drones are equipped with Ardupilot or PX4 flight control software on a flight control unit such as the Pixhawk Cube in Figure 4. The Jetson Nano acts as a companion computer and can send/receive commands.media via the highly structured and extensible MAVLink[8] packets, allowing the user to fully control the vehicle.



Figure 4: Pixhawk Orange Cube Flight Controller

2.3 Jetbot

Jetbot is deployed on land before implementing P-DroNet on aerial drones. In Figure 6, the Jetbot is an OmniX ground vehicle using Mecanum wheels. These Mecanums allow Jetbot to move in omni directions on the ground similar to a drone in the air. Jetbot is equipped with a Jetson Nano computer that both recognizes a collision situation based on input from the Pi V2 IMX219 camera with a 160-degree FOV and sends a control signal to (Cube) to stop the device in the event of a collision.

Before the emergency stop signal is sent, the Jetbot is controlled by the RC signal from the operator via the Radiomaster TX16S controller. Control channels are set by default.



Figure 5: Radio control Radiomaster TX16S



Figure 6: Jetbot implemented with P-DroNet onboard Jetson Nano

2.4 P-DroNet and Mavlink control program structure

The diagram below shows the control program structure that the authors put on Jetbot to deploy obstacle detection and emergency stop system using camera, P-DroNet and MAVLink packet system.

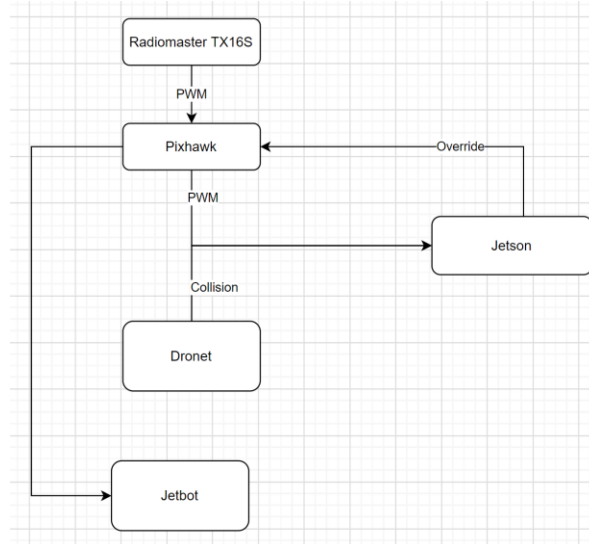


Figure 7 : Main program flowchart

3. Real world performance

The experiments are carried on below to estimate the accurate and responsiveness of the obstacle avoidance system in a variety of situations, including complex ambient light changes or when obstacle suddenly appears.

Besides, the authors also measure the real-time performance of the obstacle avoidance system to evaluate the feasibility of the approach.

3.1 DroNet and P-DroNet comparison

To compare the performance of DroNet in Pytorch, DroNet and P-DroNet are retrained with more datasets in Viet Nam. Training and evaluation of P-DroNet are done with the combination of Udacity dataset and dataset at RTR company. Both networks are capable of identifying collision situations in an environment in VietNam after retraining. The P-DroNet occurs overfitting so the early stopping method is applied as shown in Figure 8.

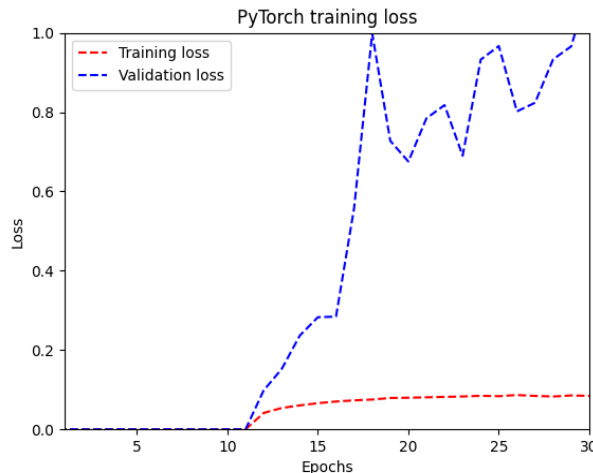


Figure 8: The loss function of P-DroNet

The comparison results are presented in Table 1. Accuracy results are based on Avg.accuracy and F-1 score. Avg.accuracy indicates how accurately a collision is detected. At 80.8%, this is a good result. The F-1 score calculates accuracy only in the group that has a collision. The higher the F-1 score, the less imbalanced the network is.

Table 1: Training result of DroNet and P-DroNet on both datasets

Model	Avg. accuracy	F-1 score	Processing time [fps]
DroNet	95.4 %	0.901	20
P-DroNet	80.8 %	0.882	30

It can be seen that the network structure after converting to the Pytorch platform has significantly lower accuracy results, but has superior processing speed, suitable for applications that need fast response time.

3.2 Simple situations

The simple situations are placed into two main contexts. In the first scenario, which can be seen in Table 2, the Jetbot moves to the subjects; the remaining context in Table 3 is the subject approaching Jetbot (which is standstill).

In those scenarios, objects are placed at a distance of 200 cm from the Jetbot. In the first scenario, the Jetbot is expected to stop when it encounters an obstacle within the designed recognition range. The collision distance is recorded when the Jetbot recognizes the collision. In all scenarios, the Jetbot stopped without collision. Objects are wall, person, big box, small box, black object.

Scenario 1: The Jetbot approach the obstacle:

Table 2: The Jetbot approach the obstacle in simple scenario

Obstacle	Distance [cm]	
	Normal condition	light Low light condition
Wall	115	180
Person	85	67
Packages	50	50
Box	63	73
Black object	83	74

Scenario 2: The object approaches the Jetbot:

Table 3: The Jetbot standstill in simple scenario

Obstacle	Distance [cm]	
	Normal light condition	Low light condition
Wall	-	-
Person	82	49
Packages	83	64
Box	43	50
Black object	52	60

In the above situations, the P-DroNet performs well in most of the situations within the range at a distance of 40 cm to 180 cm in both normal and low-light conditions.

The experimental image of P-dronet detecting a person in the obstacle situation where the Jetbot moves to the objects is compared with the Dronet on the Drone in Figure 9.



Figure 9: (a) Avoiding a person in Dronet; (b) Avoiding a person in P-Dronet

3.3 Sudden situations

Jetbot faces some unexpected situations where pedestrians move ahead; cut the Jetbot moving trajectory or suddenly stop in front of Jetbot.

The unexpected collision situation is reconstructed to evaluate the obstacle detection distance between the Dronet and P-Dronet networks in Figure 10 below. The person moves forward and suddenly hinders Jetbot's movement, thereby the collision distance is estimated since Jetbot encounters an obstacle and stops completely. The distance is considered suitable for Dronet in the case of normal light with a speed of 0.4 m/s.

In Figure 11a, the unexpected happens when a pedestrian from a distance approaches a moving Jetbot. Jetbot suddenly stops when it detects that someone appears in the field of view when the collision value increases gradually. And the Jetbot continues to move when there is no obstacle visible to the camera or the collision value decreases.

In Figure 11b, the pedestrian starts to move from behind, then passes in front of the Jetbot and then suddenly stops. Once an impending collision situation is detected, the collision value continuously increases as the distance between the person and the Jetbot is shortened. In both of the above tests, Jetbot recognized a collision situation well at a distance of less than 40 - 50 cm.

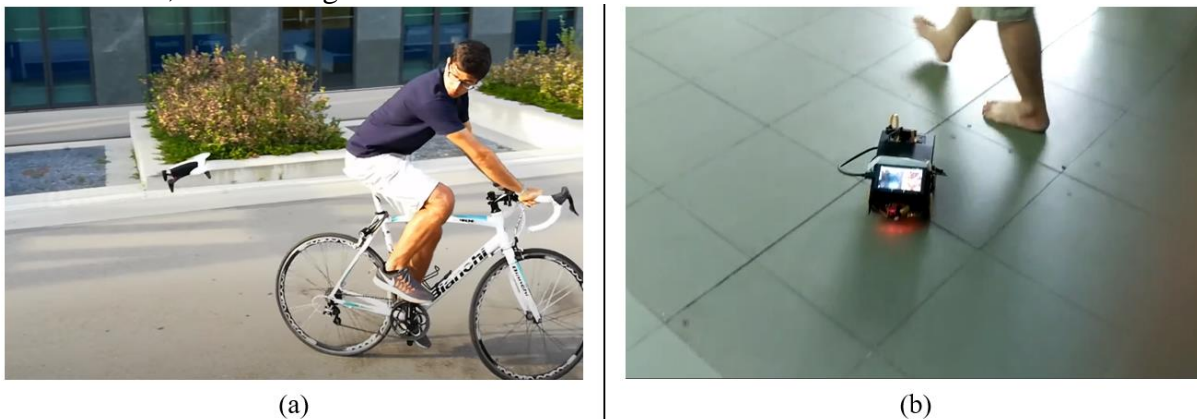
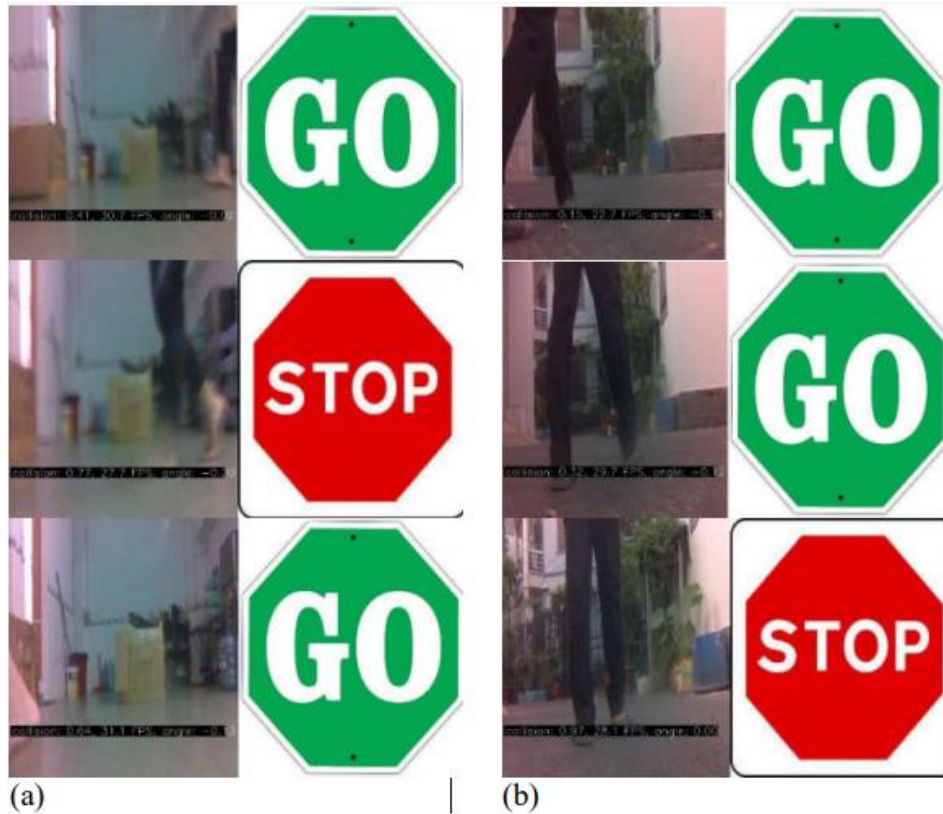


Figure 10: (a) People cross over the Drone in Dronet; (b) People cross over the Jetbot in P-Dronet



**Figure 11: (a) Person suddenly appeared in front of Jetbot;
 (b) People are moving and suddenly stop in front of Jetbot.**

3.4 Complex light environments

In the complex lighting environment, P-DroNet shows many limitations. In environments with a lot of reflection, P-DroNet is confused when it encounters high reflection subjects. The results are similar to when a backlit situation happens.

Environments with complex lighting conditions cause P-DroNet to fail under certain circumstances. This has been foreseen as an inherent weakness of camera solutions.

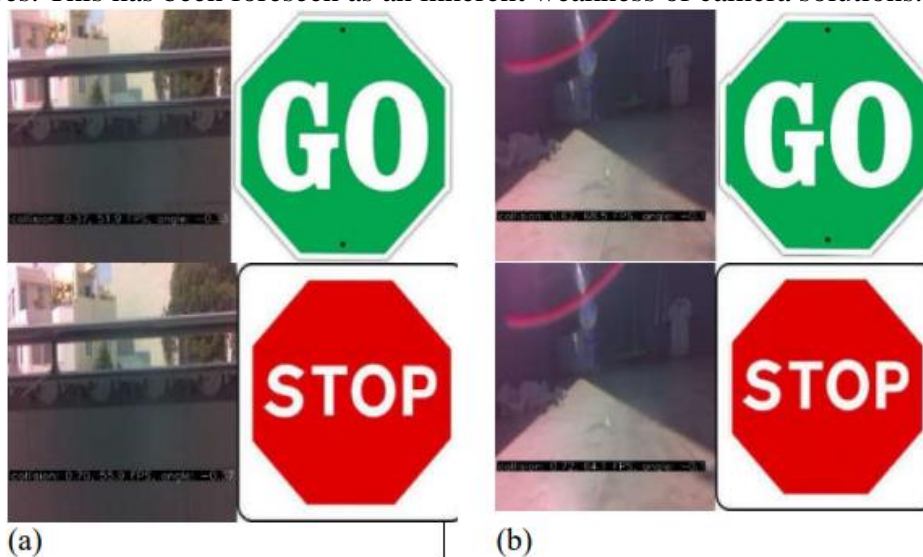


**Figure 12: (a) In case of complicated lighting environment;
 (b) In case of a backlit environment**

3.5 Real-time performance

P-DroNet's real-time performance can reach 30 FPS at 320x240 Pixels and up to 70 FPS at 256x144 pixels. This is good enough to put into applications that need fast response times. However, at 70 FPS, the network needs to be improved in accuracy.

In addition, the overall processing speed of the system including P-DroNet and the control system via MAVLink is also affected by the speed of MAVLink packets. In this study, the authors set the signal rate to send and receive at 20ms (equivalent to 50 FPS) to meet the processing capacity of P-DroNet at ~40 FPS.

When operating, the entire program consumes about 20-30% of the Jetson Nano's CPU usage. Therefore, it can be seen that the P-DroNet network structure is relatively lightweight and can still be improved on this embedded computing platform.

4. Conclusion

In this paper, we have achieved some positive results in the approach using camera and neural network to build an obstacle avoidance system for UAV which control the Jetbot via the Mavlink protocol.

The P-DroNet network built on the Pytorch platform showed good performance and accuracy referenced to the original DroNet network [1]. From this result, it is possible to combine this network with other applications on Jetson Nano or Jetson NX single board computers without any conflict.

Although the P-DroNet artificial neural network is capable of operating at high speeds, up to 70 FPS on a Jetson Nano, that is still not enough for some real-life situations. Experiments show that the system's effectiveness is still quite limited in situations where people or obstacles appear suddenly. These situations may require frame rates of up to 100 FPS or more to respond effectively.

The study also shows that the method of using artificial neural networks operating on embedded computers onboard drones has great potential in developing an efficient and economical obstacle avoidance system capable of 360 observations around the aircraft. Such systems can be implemented into low-cost drones used in agriculture to ensure safety without increasing product costs too much.

5. Future work

In this research, the obstacle avoidance system was only implemented on Jetbot, which is an omni rover instead of a quadcopter. Subsequently, some further development for this application can be (1) Implement the obstacle avoidance system to quadcopter and examine its capability in real life; (2) Enhance the real-time performance of the program by optimizing the use of Jetson Nano's GPU, thereby increasing the system reaction when obstacles are detected; (3) Build a synchronous camera system to examine the aircraft's surroundings, which will serve as the foundation for developing a 360-degree obstacle avoidance system using only cameras. That should be a game changer in the field of autonomous vehicles, delivery drones, agricultural drones. (4) Combine the P-Dronet network with some other neural networks, which allows the system to detect and classify obstacles based on existing data. As a result, there will be more complicated actions the drone can do when obstacles appear on its way.

Acknowledgments

This study was carried out within the cooperation between Real-time Robotics Vietnam and VNU-HCM Key Laboratory for Internal Combustion Engine.

References

- [1] S. Scherer, J. Rehder, S. Achar, H. Cover, A. Chambers, S. Nuske, and S. Singh (2012), “River mapping from a flying robot: state estimation, river detection, and obstacle mapping” *Autonomous Robots*, vol. 33, no. 1-2, pp. 189–214.
- [2] Hrabar, S., & Gaurav, S. (2009). “Vision-based navigation through urban canyons”. *Journal of Field Robotics*, 26(5), pp. 431–452.
- [3] Grzonka, S., Grisetti, G., & Burgard, W. (2009). “Towards a navigation system for autonomous indoor flying”. In *IEEE international conference on robotics and automation, ICRA '09*, New York: IEEE Press, pp. 2878–2883.
- [4] S. Ross, N. Melik-Barkhudarov, K. S. Shankar, A. Wendel, D. Dey, J. A. Bagnell, and M. Hebert (2013), “Learning monocular reactive UAV control in cluttered natural environments,” in *IEEE Int. Conf. Robot. Autom. (ICRA)*, pp. 1765–1772.
- [5] A. Giusti, J. Guzzi, D. C. Cirean, F. L. He, J. P. Rodriguez, F. Fontana, M. Faessler, C. Forster, J. Schmidhuber, G. D. Caro, D. Scaramuzza, and L. M. Gambardella (2016), “A machine learning approach to visual perception of forest trails for mobile robots,” *IEEE Robotics and Automation Letters*.
- [6] Antonio Loquercio, Ana I. Maqueda, Carlos R. del-Blanco, and Davide Scaramuzza (2018), “DroNet: Learning to Fly by Driving”, *IEEE ROBOTICS AND AUTOMATION LETTERS*.
- [7] PyTorch 1.9.0 Documentation, available at: <https://pytorch.org/docs/stable/nn.html>
- [8] MAVLink Developer Guide, available at: <https://mavlink.io/en/>

Implementing Lean and Sweep Method for Optimization of Gas Turbine Blade by Computational Fluid Dynamics

Zung Pham Ngoc¹, Anh Nguyen Tuan¹, Vu Hoang Nhu¹ and Nhu Van Nguyen^{1,*}

¹Jet Engine Center, Viettel Aerospace Institute, Thach That, Hanoi, Viet Nam, 100000.

*Corresponding author. E-mail: vannn3@viettel.com.vn

Abstract

This paper presents the optimization of rotor axial turbine blade of a gas turbine engine using sweep and lean blade method. With the help of computational fluid dynamics (CFD) solver, fluid flows over these modified geometries generated from the original sample were analyzed. The effect of the lean and sweep of the rotor blade in one gas turbine stage on its performance have been investigated. Due to the spatial structure of the flow, there are secondary flows, which are an additional source of loss of kinetic energy, and an additional source of losses. Losses associated with the flow of gas in the nozzles and channels of the working blades, as well as losses of kinetic energy associated with the output speed of the gas are called “flow losses” and considered by the district efficiency, reduce the heat transfer converted into mechanical work. The most important task in the operation of a gas turbine is to achieve higher efficiency and reduce losses. Using lean and sweep blade helps to reduce flow losses. Using optimal variant with lean rotor blade, it is observed that the stage efficiency increases by 1.12% for operating design, while the power increases by 0.59 MW.

Keywords: Gas turbine, lean and sweep blade, optimization, stacking line, CFD

Nomenclature

φ =lean angle

γ =sweep angle

P_0 =total pressure

T_0 =total temperature

η_{ad} =turbine adiabatic efficiency

N = turbine power

M =torque per blade

ζ =total loss

\bar{l} =relative blade height

1. Introduction

Investigations on gas turbine engine components are carried out to develop the new products. The need for high efficiency turbo machines has led to a high demand for high efficiency compressor and turbine blades. Small improvements in performance may result in remarkable saving in operating costs. With the ever-increasing requirements for high aerodynamic performance blades, aerodynamic optimization is of great importance for industrial and aerospace applications. Gas turbine performance can be improved by reducing secondary flow losses at end-walls and blade tip or by optimizing the 3D blade shape geometry [1].

The most important goal in the operation of turbine engine is to achieve higher performance. For this purpose, the blades should be designed and shaped so that they cause minimum flow losses, and the boundary conditions are controlled. The second and most difficult challenge in minimizing flow losses is to minimize the losses near the hub, which are caused by the secondary flow losses. Currently, in the three-dimensional engineering design of blades, blade sweep and lean (dihedral) blades are used for the control of secondary flows in order to reduce the corner stall and prevent low-momentum fluids from returning to the row of blades. With the rapid progress in computational power, the optimization of turbine components based on 3D flow analyses and evolutionary global algorithms has been growing considerably in recent years [2-4].

The designing method of axial flow turbine based on the three-dimensional flow analysis has been developed remarkably in recent years with the rapid enhancement of computational power. Accurate flow prediction inside a turbine rotor using CFD is difficult due to its extremely complex features: three-dimensional, unsteady and vortical nature of flow in the blade passage. However, CFD has obvious advantages compared to traditional experimental analysis. CFD helps us analyze the effects of individual feature more easily compared to the experimental method.

Recently, the use of sweep, lean, stacking line in rotational direction in axial flow turbine blade has become a matter of interest in the design of turbomachinery blades. These blade shape parameters, which form a three-dimensional stacking line, are generally introduced to reduce shock losses, corner separation in the blade hub, and tip clearance losses in turbine blade [5]. The effect of blade sweep and lean on fan performance is explained in this paper. The important point regarding the shockwaves is that the shockwave must impact the casing wall vertically. Thus, the effects of shock sweep near the casing wall and hub are inevitably lost. As the hub's boundary layer influences the flow behavior at the root of blade, the effect of blade tip clearance on performance is also severe.

2. Geometry of Turbine Stage

The object of this paper is gas turbine rotor blade of a turbojet with a rotating speed of 24000 rpm at the maximum thrust of 400 kgf. Fig. 1 represents the meridional view and blade to blade section of the turbine stage.

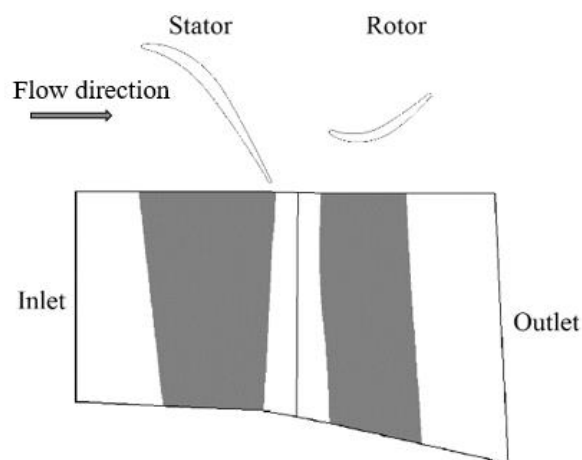


Figure 1. Meridional and mean section blade to blade view

The geometrical specifications of the considered stage have been summarized in Table 1.

Table I. Geometrical parameters of first stage

Parameter (at mean section)	Unit	Stator	Rotor
Mean diameter	mm	130.69	129.66
Blade height	mm	44.9	45
Chord	mm	40.5	22.5
Number of blades	-	32	53
Inlet metal angle, degree	degree	15	66
Outlet metal angle, degree	degree	77	70

3. Methodology and numerical analysis

The overall procedures of optimization by lean/sweep blade are shown in Fig. 3. First, variables for optimization are selected, then experiments points are determined with design of experiments method to minimize the number of calculations. In the next step, the original shape is modified for each experimental point. Then, each experimental point is obtained by CFD simulation and results analysis to find optimal point.

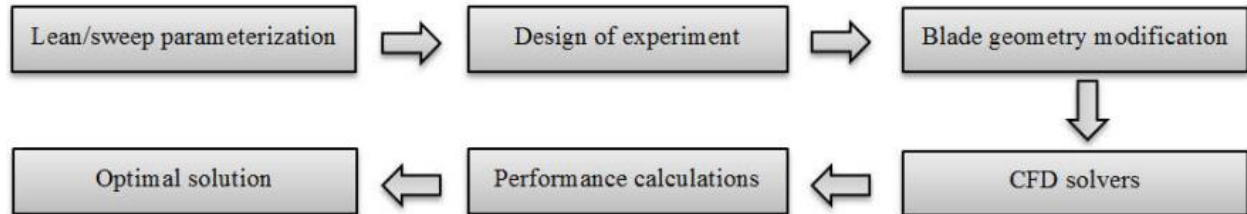


Figure 2. Optimization progress

3.1 Construction method of lean and sweep

Lean or sweep is formed by giving the axis of the blade shape in second-order curve, which is given by the lean (sweep) angle φ (γ) and the relative length (Δl) of the curved blade section at hub and tip.

$$\bar{\Delta l} = \frac{\Delta l}{H} \cdot 100\% \quad (1)$$

It should be mentioned that, in consideration of the changes of relevant constraints, the changes of blade lean (sweep) forward or backward and the degree of lean towards or contrary to the turbine direction of rotation (axial direction), the shapes of the modified geometries have been so designed as to prevent the impact with adjacent blades.

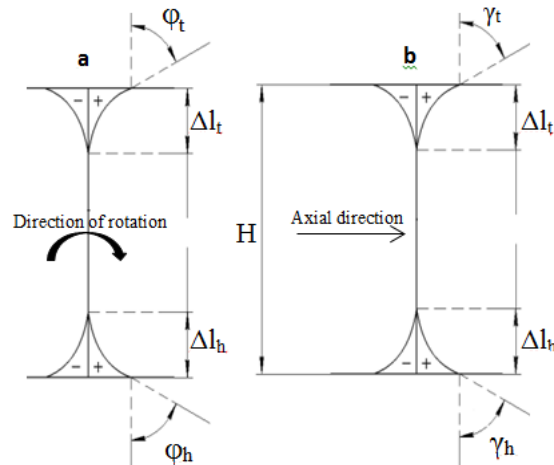


Figure 3. Lean (a) and sweep (b) schema for turbine blade

Modifying the geometry of rotor blades is generally accomplished by making changes to the profile of blade sections or changing the stacking line of blade sections. In the present paper, the stacking line was modified by changing the arrangement of blade section, without changing their profiles, and then the desired geometry was produced. The lean and sweep schema for turbine blade with convention of positive and negative directions for angle is shown in the Fig. 3.

The original shape was imported then modified in software program AxStream. The AxStream is software platform for multidisciplinary design, analysis and optimization provides an integrated and streamlined approach to turbomachinery design programming using diagrams. AxStream allows the change of stacking line along the axial or direction of rotation to create lean and sweep blade.

3.2 Simulation method

Simulation method of flow processes in turbomachines was implemented in the commercial package Ansys. After creating the considered 3D lean and sweep geometries, the geometries were imported to module Ansys TurboGrid to generate the computational grid.

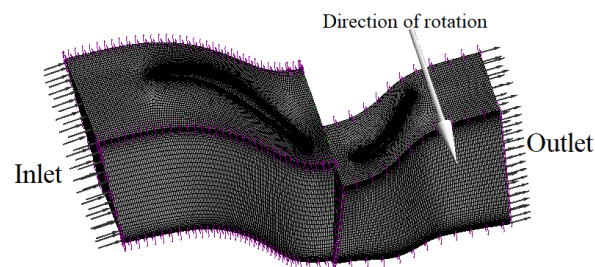


Figure 4. Structured mesh of turbine stage

In order to increase quality of simulation, the mesh structure around the blade became very fine using the adjustments of the y^+ method, whose value was considered as below 5 with SST k-w turbulence model. SST k-w is turbulence model, which is improved from standard k-w model, and is a highly accurate and reliable method for various types of flow. In total, a mesh density of more than 5 million elements was established for the whole stage geometry. Fig. 4 presents the structured mesh of turbine stage, which was created with module Ansys TurboGrid.

The Ansys CFX module was used to numerically solve the turbine flow problem. The boundary conditions apply to the average section of the stator inlet and rotor outlet, which is presented in Table 2.

Table II. Boundary conditions

Parameters	Unit	Value
Total pressure at stator inlet	kPa	420
Total temperature at stator inlet	K	1100
Speed of rotation, rpm	RPM	24000
Static pressure at rotor outlet, kPa	kPa	190

The turbine stage is solved in steady-state analysis type. For the steady stage RANS solution, interface type is chosen as mixing plane to approach ensuring the more realistic (in terms of steady averaging) flow behavior. Also, a physical time step of 10⁻⁴ and residual convergence value of 10⁻⁶ were used as well.

In this study, adiabatic efficiency η_{ad} is selected as an objective function for the shape optimization of the blade, and is defined as follows:

$$\eta_{ad} = \frac{(P_{0exit} / P_{0inlet})^{(\gamma-1)/\gamma} - 1}{T_{0exit} / T_{0inlet} - 1} \quad (2)$$

where P_0 and T_0 are the total pressure and total temperature, respectively.

In addition, turbine power is also a parameter of interest and is calculated according to the formula:

$$N = M \cdot \frac{\pi \cdot n}{30} \quad (3)$$

where N is the power (W); M is the torque ($N.m$) that can be calculated from the simulation result; n is the speed of rotation (rpm).

4. Discussion and analysis

The dependences of power, efficiency on the values of lean (sweep) are also considered. According to the simulation results, for negative Δl at the tip, the blade pressure side tends to lean towards the positive axial direction, which causes the gap at blade tip to increase and causes the air pressure zone to be unevenly divided, leading to increased thickening of boundary layer, which create more energy losses. In this paper, the optimal variants were found with $\Delta l_t = 25\%$, $\Delta l_h = 0\%$; $\phi_t = 30^\circ$, $\phi_t = 0^\circ$ (variant a); $\Delta l_t = 20\%$, $\Delta l_h = 0\%$; $\phi_t = -15^\circ$, $\phi_t = 0^\circ$ (variant c).

In all variants with sweep of the rotor blade in the tip region, the gap between the shroud and blade increases and the pressure field is redistributed, which leads to a decrease in the thickness of the boundary layer in front of the rotor blade (the flow is more strongly pressed against the bypass) and, accordingly, decrease kinetic energy losses. Fig. 5 describes a few typical cases of losses increases at the tip and the root sections. The total losses in the step for all the investigated

structures increase by 0.06-0.16 %, which leads to decrease stage efficiency. Distribution of losses along the blade height was shown in Fig. 5.

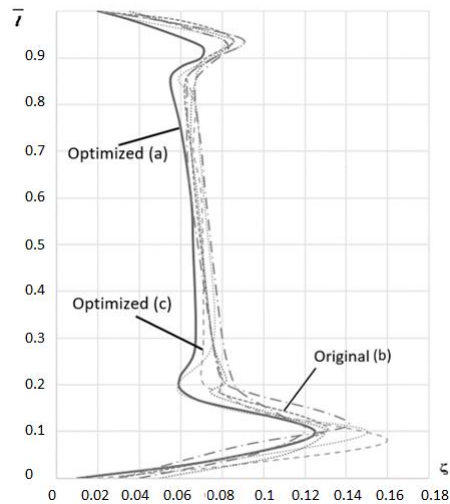


Figure 5. Distribution of losses along the blade height

Considering the overall flow effects, the 3D analysis was performed at 95% blade section; due to the stage being an acoustic pass stage at lower blade sections, the shock pattern is not observed completely, and this is due to the low value of Mach number in these regions. Fig.6 shows the change of relative Mach number at 95% span.

The relative Mach number represents the relative velocity of the current and has a big influence on performance. It can be seen that in the original case, there is an uneven distribution of Mach number; there are regions with the much larger Mach number and this causes shock waves, leading to current turbulence, causing a lot of energy losses, reducing turbine efficiency. However, observing the two optimal cases, it can be seen the Mach coefficients are distributed more evenly on blade to blade section and meridional section. At the same time, the point of sudden large Mach coefficient will no longer reduce the turbulence area, shock waves and the impact on the blade pressure side and suction side, which contributes to reducing energy losses caused by shock waves.

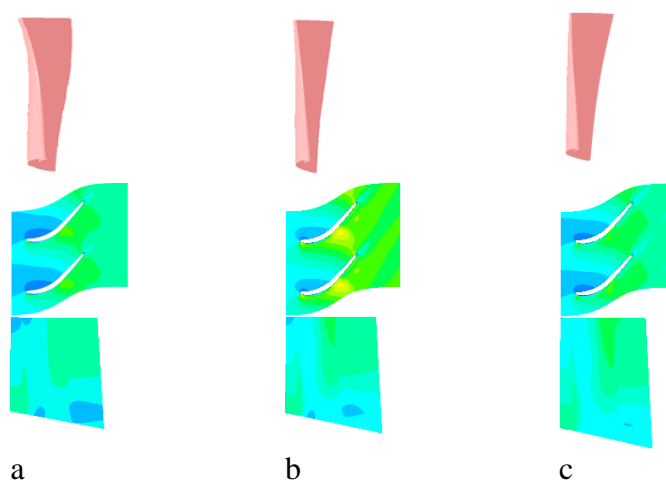


Figure 6. Mach number contours of the 95% blade section

Similar to the Mach number distribution, the pressure field is also more evenly distributed in the two optimal cases. Large areas of pressure present at the tip blade are removed and lead to

reduce blade stress. The flow pressure at the blade outlet is reduced but not much, so it is not clearly shown in the Fig.7, but the reduced pressure also lead to increase the expansion ratio, the energy of the flow is converted to more mechanical energy to increase turbine power.

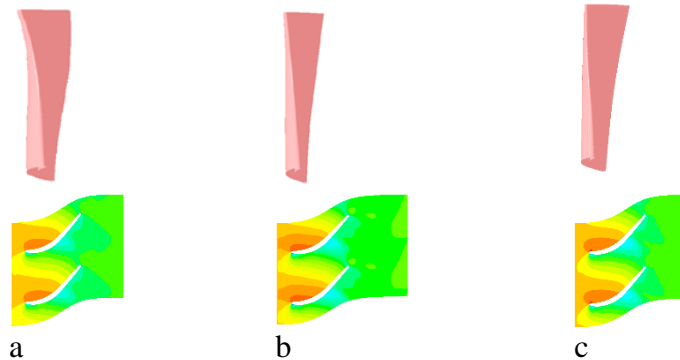


Figure 7. Static pressure contours of the 95% blade section

As mentioned above, at the root of blade, the formation of additional pressure gradients in the radial direction, which contribute to pressing the flow to the hub. The use of lean/sweep blade led to the appearance of a transverse-radial pressure gradient along the height of the blade at the points of curvature of the blade along height. The vortex under the action of the transverse-radial pressure gradient on the blade is displaced towards the flow core, which leads to decrease flow at the root and tip, where there are more vortices.

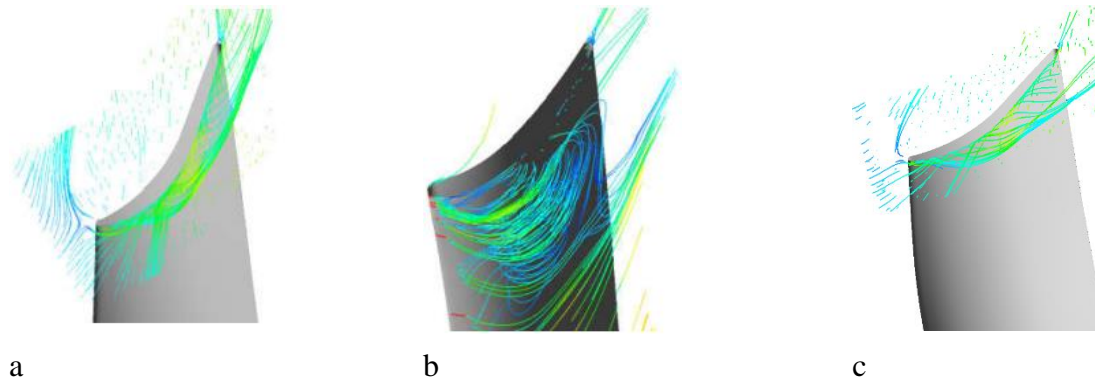


Figure 8. Tip vortex at blade gap

As seen from Fig. 8, for the largest Δl and ϕ_h value, shock wave (vortex) are formed near the hub at the exit of rotor. We use optimal lean angle lead to reduce vortex near the hub and tip. In operation mode with very high rotation speed and high pressure and temperature conditions, the flow is always unstable and air bubbles, spiral air vortex appear cause pressure difference. The optimization in this paper helps to reduce air vortex, which appears during the turbine operation. Fig. 8 shows the reduction of vortex at the tip of blade. This helps to stabilize the outlet flow angle, decrease energy losses caused by the deflection angle of the outlet velocity vector.

When optimal variant (a) with lean blade is used, it is observed that the stage efficiency increases by 1.12% for operating design, while the power increases by 0.59 MW and efficiency increases by 0.79%, power increases by 0.33 MW with variant (c). Some important charts describing turbine characteristics are shown from Fig. 9 to Fig. 12.

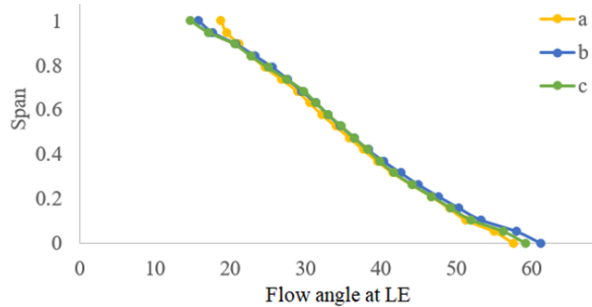


Figure 10. Flow angle at leading edge

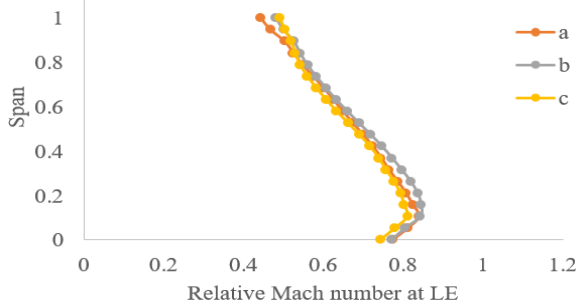


Figure 12. Relative Mach number at leading edge

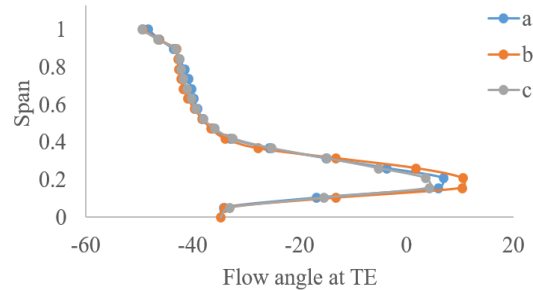


Figure 11. Flow angle at trailing edge

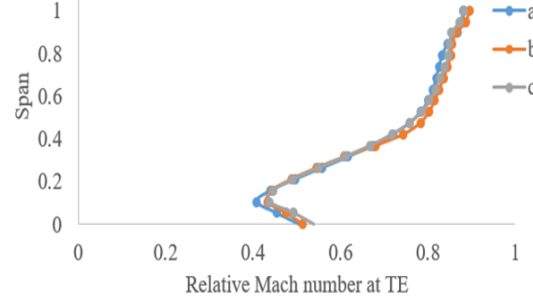


Figure 13. Relative Mach number at trailing edge

5. Conclusions

Using verified numerical simulation models and the genetic algorithm, the effects of lean and sweep blade on the turbine performance are studied. The present optimization method led to decrease blade losses at hub and tip, reduce vortex at the boundary, which decrease turbine performance. It successfully improves 0.59 MW power and 1.12 % in the turbine stage total-to-total efficiency in its design and off-design speeds, respectively. Lean and sweep method with suitable angle and relative length help to reduce air vortex and energy losses by secondary flow, friction caused by flow with high velocity, pressure and temperature. The results of this paper provide a basis for research, evaluation and manufacturing of turbine blades with curved profiles for the manufacture of jet engines.

Acknowledgment

The authors are grateful for the academic support and the continued assistance in this work from the members of Jet Engine Center of Viettel Aerospace Institute.

References

- [1] Abolhassan Asgarshamsi, Ali Hajilouy-Benisi and Ahmad Assempour (2014), “Multi-Point Optimization of Lean and Sweep Angles for Stator and Rotor Blades of an Axial Turbine”, Proceedings of ASME Turbo Expo 2014: Turbine Technical Conference and Exposition GT2014 June 16 – 20, 2014, Düsseldorf, Germany
- [2] Arabnia, M. and Ghaly, W. (2010), “On the use of Blades Stagger and Stacking in Turbine Stage Optimization”, Proceeding of ASME Turbo Expo, GT2010-23399, Glasgow, UK.
- [3] Arabnia, M., Sivashanmugam, V.K. and Ghaly, W. (2011), “Optimization of an Axial Turbine Rotor for High Aerodynamic Inlet Blockage”, Proceeding of ASME Turbo Expo, GT2011-46757, Vancouver, British Columbia, Canada.
- [4] Sivashanmugam, V.K., Arabnia, M. and Ghaly, W. (2010), “Aero Structural Optimization of an Axial Turbine Stage in Three Dimensional Flow”, Proceeding of ASME Turbo Expo, GT2010-23406, Glasgow, UK.

Combustion Analysis for Small Gas Turbine Engine Using Computational Fluid Dynamics (CFD)

Quoc-Huy Nghiem^{*}, Cong-Anh Pham, Quang-Hai Nguyen and Nhu-Van Nguyen

Jet Engine Center, Viettel Aerospace Institute, Viettel Group

^{*}Corresponding author. E-mail: huynq80@viettel.com.vn

Abstract

This work introduces a numerical method for modeling and simulating the combustion of a small gas turbine engine, which might be beneficial in the early stages of combustor design and development when the design engineer has a large number of models and ideas to consider, and it is impractical to do experiments at this stage. This method employs the RANS method with the k-epsilon turbulence model and the standard wall function for the entire flow field, while the non-premix model was used to simulate the chemical reaction. The injection of fuel is also modeled using the Rosin-Rammler distribution and the Secondary Breakup model. This concept is commonly used in the design of jet engine. The outcomes are compared to the design parameter range, which is chosen by the designer. These values are selected from a great number of other studies that have been confirmed, validated, and widely accepted. The distribution of temperature is displayed to estimate the length of the flame and to show the critical area where the temperature reaches the maximum value. Following the CFD calculation procedure, the designer can build some engine prototypes to conduct tests to check if the design meets design criteria. The results of experiments can be used to validate the CFD results, making the CFD method more accurate and feasible.

Keywords: CFD, Combustor, Non-premixed, TAB

Nomenclature

PF=Pattern Factor, *dimensionless*

PLC=Pressure loss coefficient, *dimensionless*

PT-in=Total pressure at inlet, [*K*]

PT-out=Total pressure at outlet, [*K*]

TT-in=Total temperature at inlet, [*atm*]

TT-out=Total temperature at outlet, [*atm*]

1. Introduction

The performance of a combustion chamber or combustor is calculated in the design phases of a jet engine using ideal thermodynamic cycles. Some of the most important parameters like efficiency, lost pressure, and output temperature are computed using constant parameters such as inlet temperature, mass flow, and total pressure [1]. The engineer chooses the value of these parameters based on certain features of the combustor they are interested in.

This method can provide a decent estimate of overall performance, but cannot fully describe the flow's characteristics inside the combustor. The velocity, pressure, and temperature distribution throughout the combustor cannot be predicted. The effects of airflow in primary, secondary, and dilution zones are also unpredictable. As a result, the combustor wall may be inefficiently cooled and get damaged. The temperature at the outlet is another critical parameter

that can have a direct impact on the performance and durability of the combustor wall and turbine downstream [2]. In practice, the temperature changes from the combustor's inner to outer case, but in principle, it is assumed to be constant. Therefore, the engineer who designs the combustor must pay great attention to the distribution of aerodynamic characteristics within the combustor. The experiments can be carried out, but it is more difficult and require a lot of time to do so in the initial design phases because the engineer needs to change the parameters or combustor geometry frequently to archive the best performance.

This problem can be handled by modeling and simulating the combustion using the CFD approach. CFD is a strong and dependable tool for simulating combustion. Some of the top simulation software, such as ANSYS, has been developed as a reliable, rapid, and low-cost process for modeling and calculating combustor performance [3]. This strategy can accelerate the entire design process, save a significant amount of time, and assist the engineer in archiving the optimal combustor model.

The content below presents a numerical method, using ANSYS Fluent Software R19.2 to predict the aerodynamics phenominal inside a combustor. This combustor is part of an engine prototype research project that was created from the ground up.

2. Geometry and modeling of combustors

The combustor is built to use in a small jet engine. Figure 1 shows the 3D CAD image of the conventional annulus combustor. The length of this model is 536 mm. The annular inlet diameters are 260 and 300 mm. The minimum and maximum diameters of the internal domain are 72 and 350 mm. The outlet is slightly larger than the inlet, with diameters of 105 and 150 mm.

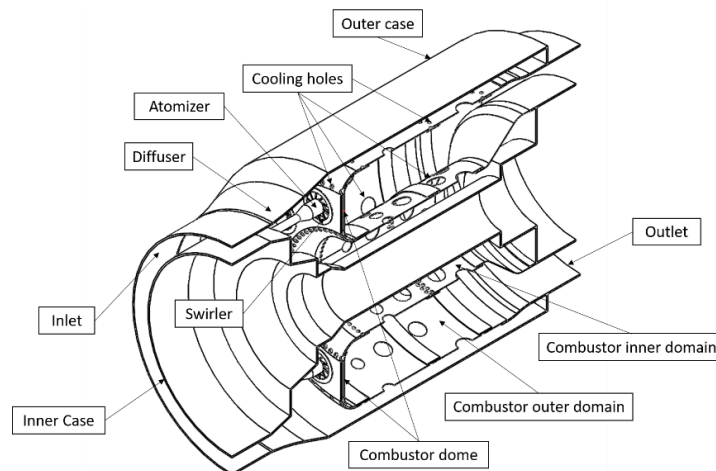


Figure 1: 3D CAD model of designed combustor

The entering air flow is assumed to be compressed and preheated. The velocity is decelerated after passing through the diffuser and is then separated into two primary streams. The first stream enters the combustor dome before being twisted by ten swirlers. As mentioned in document [4], this stream should contain 12% of the total mass flow rate of the air inlet and serves as the combustion's oxidizer. The second stream enters the inner and outer annulus domains and is utilized to cool the combustor.

The fuel is jet-a1, which is commonly used on airplanes and consists primarily of kerosene. It is injected into the combustor domain by ten evenly arranged atomizers. The injections are

represented mathematically by the Rosin-Rammler distribution. The TAB is chosen as the secondary break-up model [5]. The injection settings are selected from the atomizer parameters supplied by the manufacturer [6]. The mean diameter and spread parameter are the two most important values. The mean diameter chosen for the injection of the current under-research engine is the Sauter diameter [7], which is equal to 65 μm and the spread factor is 3.2. The injection origin is $(x; y; z) = (0; 0.1120; 0)$.

To reduce the amount of time calculated, the combustor domain is separated into ten domains, each with its own atomizer and swirler. The periodic boundary condition is used as the interface surface of two continuous domains. Figure 2 depicts the fluid domains that are utilized for simulation along with the main zones, and Figure 3 shows the mesh of the combustor model. The simulation employed the hybrid poly-Hexa core meshing method to achieve a high-quality mesh while maintaining the number of elements around 11 million, which is adequate to obtain dependent and acceptable results and to perform well with the current computer configuration. According to an earlier research, the mixing zone in which the fuel is injected and combustion occurs should have the element size of smaller than 1 mm [8].

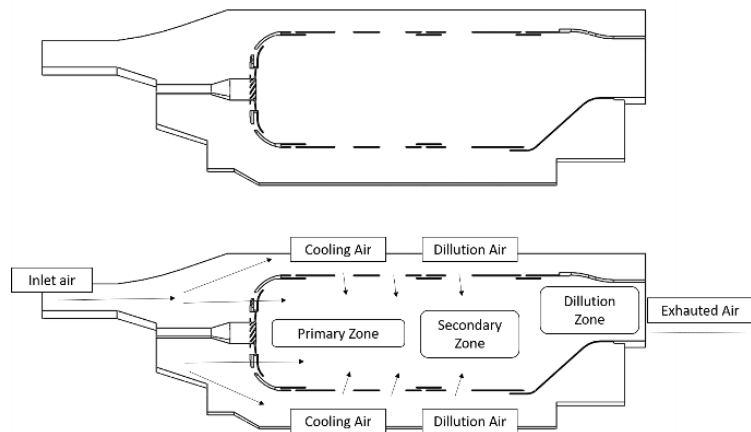


Figure 2: Fluid domain and main zones of combustor

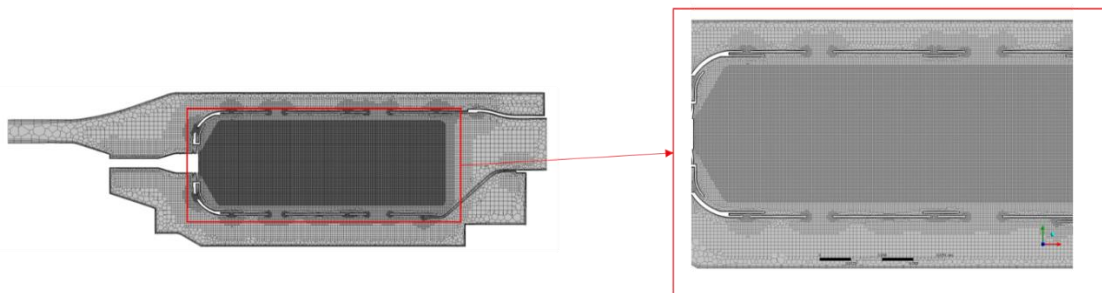


Figure 3: Mesh of the combustor model. The mixing zone domain is meshed with cell element size equal to 0.5mm

The combustion is performed at atmospheric pressure, with an operational pressure of 4.2 atm. The turbulence model k-epsilon, standard wall function is employed for modeling the airflow. This model offers fast and robust performance. The wall treatment of the k-epsilon model is less strict than in the SST model. The non-premixed combustion model with 20 species is used for chemical reactions and is supplied as a PDF table. The Thermo-chemistry and its relationship with turbulence are provided in this PDF table.

For the boundary condition, the mass flow rate of the air inlet is 8.6kg/s or 0.86 kg/s for each periodic domain. The air temperature is 470K, and the total pressure is 4.7 atm. These conditions are derived from the compressor performance of the engine. The study is only concerned with the aerodynamic phenomenon of the combustor, hence heat transfer is ignored. Therefore, the wall boundary condition is adiabatic and no-slip.

The final results show the pressure, velocity, and temperature distributions inside the combustor. Surface integral is used to determine other essential characteristics, such as total pressure loss, average temperature at exit, and mass flow rate through the cooling hole to evaluate the combustor performance. These results are compared to design criteria to verify that the model is as close to the design intention as possible.

3. Design criteria

The following provides the values of the expected design parameters and performance of the combustor mentioned above, which are selected from other previous researches. [2] [4] [9] [10]

- The air average-temperature at the exit is 1150K, which is sufficient for the turbine material.
- Mass flow rate entering the combustor's dome contains 12-20% of the total mass flow rate. The rest enters the annulus domain.
- Mass flow rate distribution of primary zone is 30-40% of the total, for secondary is 20-30%, and for dilution is 40-65%.
- The flame must not reach the turbine outlet.
- The temperature profile at the outlet is as uniform as possible.
- Total pressure loss is less than 7%.
- The Pattern Factor (PF) of the total temperature at the outlet is less than 0.25.

4. Results and discussion

The table below displays the estimated mass flow rate distribution inside the combustor as well as the CFD results:

Table 1: CFD mass flow rate distribution results

Zone	Hole name	Percentage of total mass flow rate (%)	Total (%)
Primary	Swirler	12	39.5
	Cool dome	8	
	Cool Primary	15.5	
	Cool 1	4	
Secondary	Cool Secondary	15.5	22.5
	Cool 2	7	
Dilution	Cool 3	7	38
	DL 3	31	

These CFD results are very close to the design criteria in terms of mass flow distribution for the combustor's zone. The surface integral calculation is used to derive the average temperature at the outlet. This resulted in a value of 1148 K, which is close to the predicted design value. Figures 4 describes the temperature distribution at a cross-section, middle plane, and wall of the combustor. It shows that the flame does not expand out of the combustor, which is very beneficial in design to avoid turbine damage and increase the engine lifetime. It is shown that the cooling air is ineffective, as there are some areas of the wall where the temperature reaches its maximum value. It can lead to damage of the combustor wall or reduce service time. The temperature profile shown in Figure 5 can be used to indicate the temperature distribution at the outlet. A dimensionless measure called Pattern Factor can be used to determine whether the temperature profile is acceptable or not. It is calculated by the following equation [4]:

$$PF = \frac{T_{t-max} - T_{t-out}}{T_{t-out} - T_{t-in}} \quad (1)$$

While $T_{t-max} = 1236K$ is the maximum total temperature in the profile, $T_{t-out} = 1148K$ is the average total temperature at the outlet and $T_{t-in} = 470K$ is the total temperature at the inlet [2].

Hence:

$$PF = \frac{1236 - 1148}{1148 - 470} = 0.125.$$

The pressure drop coefficient along the combustor is calculated by the equation:

$$PLC = 1 - \frac{P_{t-out}}{P_{t-in}} \quad (2)$$

While $P_{t-out} = 4.7 atm$ is a boundary condition, and $P_{t-in} = 4.4 atm$ is calculated by surface integral. Hence:

$$PL = 1 - \frac{4.4}{4.7} = 0.0638 = 6.38\%.$$

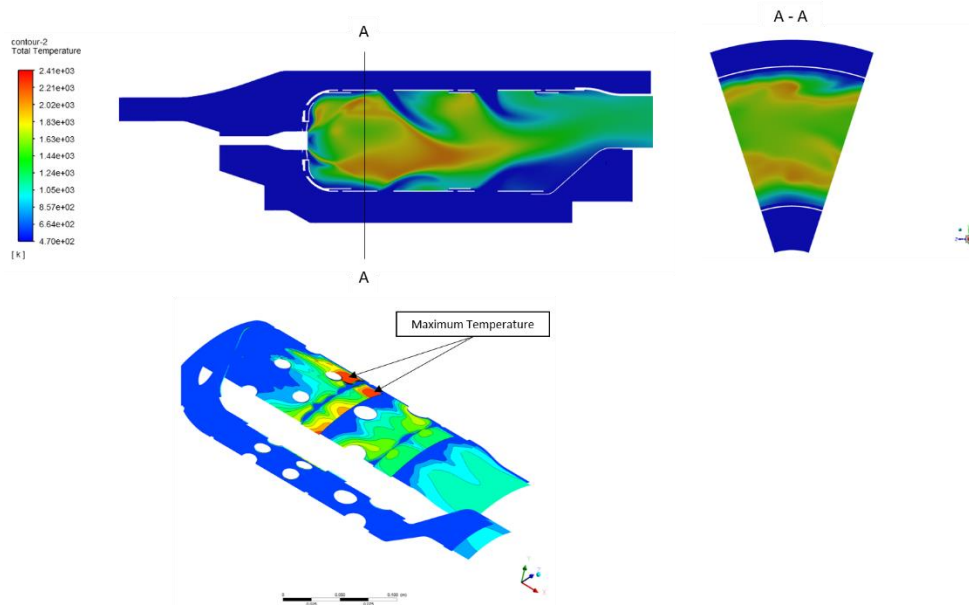


Figure 4: Total temperature distribution at middle plane and cross section plane (0.02 m from injection origin and parallel with inlet)

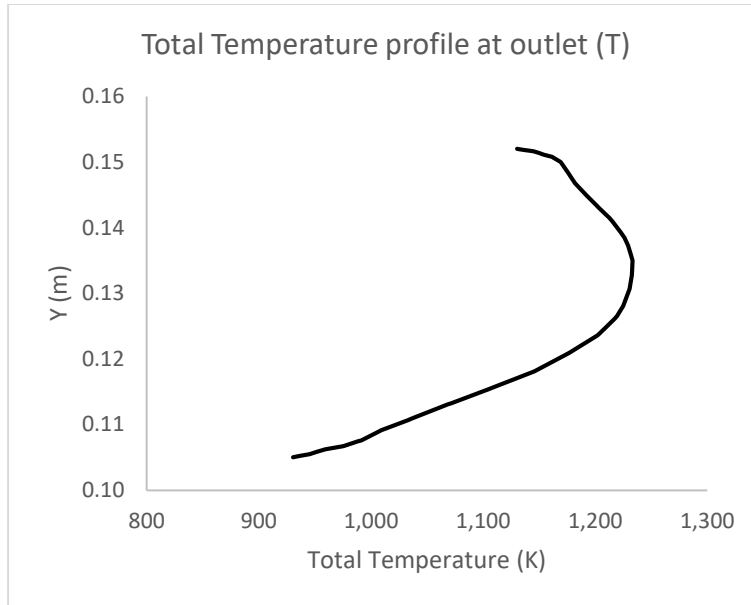


Figure 5: Total temperature profile at outlet

Figure 6 shows the injection diameter. It can be seen that all the fuel particles are evaporated and burnout, which means that there is no remaining fuel after combustion.

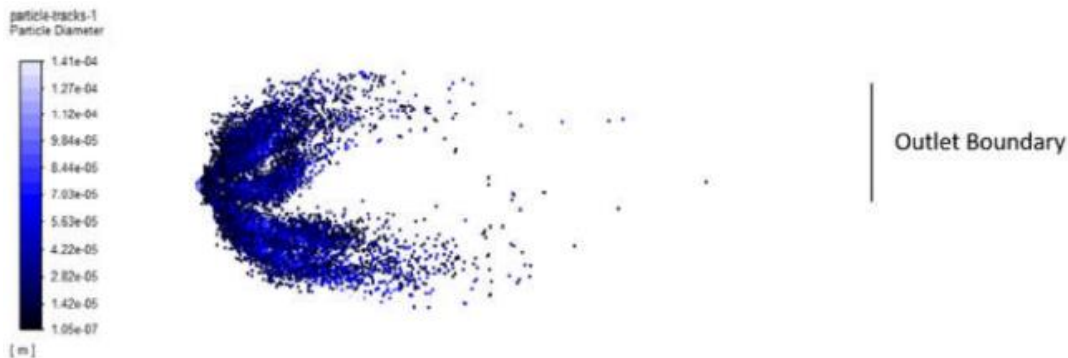


Figure 6: Injection diameter

5. Conclusion

The research findings show that the numerical method produced acceptable values that were quite close to the design criteria. The temperature is adequate for the turbine, and the profile is even. It has the potential to alleviate thermal stress within the turbine structure. The flow's aerodynamic features are useful to the combustor's performance. However, the total temperature at the combustor wall reaches the maximum value in some areas, which can affect the durability and longevity of the combustor.

In conclusion, the CFD approach offers a quick and strong solution for studying the characteristics of the combustor. This method can be applied to other combustor configurations to determine which model has the best performance or meets the engineer's requirements. Following that, engineers can create a prototype model to test the performance of the combustor to guarantee that the design is flawless.

References

- [1] J. D. Mattingly, "Aircraft Gas Turbine Engine," in *Elements of Propulsion: Gas Turbines and Rockets*, AIAA, 2006, pp. 233-259.
- [2] D. R. B. Arthur H. Lefebvre, *Basic Considerations*, CRC Press, 2010, pp. 1-34.
- [3] ANSYS, "Gas Turbine Simulation," ANSYS, [Online]. Available: <https://www.ansys.com/applications/gas-turbines>. [Accessed June 2021].
- [4] A. S. C. Priyant Mark, "Design and analysis of annular combustion chamber of a low bypass turbofan engine in a jet trainer aircraft," *Propulsion and Power Research*, no. 5(2), pp. 97-107, 2016.
- [5] P. J. Łukasz Jan Kapusta, "JET AND DROPLET BREAKUP MODELLING APPROACHES," *Journal of KONES Powertrain and Transport*, vol. 2, no. 3, 2015.
- [6] L. H. IKEUCHI & Co., *Catalog on Hydraulic Spray Nozzles*, H. IKEUCHI & Co., LTD.
- [7] V. G. M. Arthur H. Lefebvre, *Atomization and Sprays*, CRC Press, 2017.
- [8] A. L. A. A.-T. Daniel Lörstad, "Investigation of siemens sgt-800 industrial gas turbine combustor using different combustion and turbulence models," *Turbomachinery Technical Conference and Exposition*, 2016.
- [9] Y. P. L. J. H. L. a. Y. W. Y. P. Zhang, "Design and Numerical Simulation of a Micro-Gas Turbine," *Journal of Applied Fluid Mechanics*, vol. 12, no. 5, pp. 1707-1718, 2019.
- [10] R. E. P. S. Talita Mitsue Onose Araujo Cunha, "Dimensioning of a combustion chamber for microturbine based on automotive turbocharger," *17th Brazilian Congress of Thermal Sciences and Engineering*, 2018.

The Comparison Results of Numerical Simulation with Experimental Data for Axial Turbine of Small Turbojet Engine

Hung Vu Xuan*, Anh Pham Tuan, Lanh Chu Duy, Nhu Van Nguyen

Jet Engine Center, Viettel Aerospace Institute, Thach That, Hanoi, Viet Nam, 100000

* *Corresponding author* E-mail: Hungvx3@viettel.com.vn

Abstract

Small turbojet engines are widely implemented in high-speed Unmanned Air Vehicles (UAVs) and high-speed target drones. In order to set up an accurate numerical model of the engine that includes realistic representations of the turbomachinery (i.e. experimentally validated performance maps) and estimates of pressure losses in ducting, CFD validation are required. This work presents the single stage axial flow turbine CFD validation at operating points using two different solvers k- ϵ and SST turbulence model for mass flow rate, total pressure, and temperature distribution compared to the experiment data. This study analyzed the stage performance of an axial turbine using a computational tool for simulating the steady state three-dimensional viscous flow. A computational fluid dynamics software was used to solve the RANS equations with the k- ϵ and SST turbulence model. Validations about the numerical scheme and the test of turbine performance at various operating speeds are conducted. The results show that verified CFD solvers are capable in predicting the turbine performance. This work provides the reliable axial turbine performance analysis methodology with the verified CFD solvers for the future turbine design.

Keywords: Computational fluid dynamics (CFD), Turbine Experiment Data, Turbine Design, Small Gasturbine

Nomenclature

Mfr	=	Gas mass flow rate through turbine
CFD	=	Computational fluid dynamics (CFD)
Cp	=	Specific heat capacity
$Pt5$	=	Total pressure at turbine outlet
$k-\epsilon, SST$	=	Turbulence model
$Tt5$	=	Total temperature at turbine outlet

1. Introduction

Gas turbine engine study has always been of undeniable significance and interest among industry and academy, ever since the birth of its concept. It is widely used to power aircraft, ships, trains, generators, etc., because of its advantages such as high power-to-weight ratio, comparatively small sizes, availability for various fuels, and such other advantages. Several types of gas turbines have been developed and realized in practice in order to fulfill different application requirements. Advantages and disadvantages exist simultaneously for every engine; thus, a compromised selection should be reached. The cutaway view of the AMT Olympus engine is shown in Fig. 1 for demonstration, consisting of three main components: compressor, combustor and turbine.

In this study, the performance of an axial turbine in a gas turbine engine is investigated. The turbine is an essential part in the engine operation cycle because it provides power for driving the compressor. Preliminary study of axial turbine has been conducted by other researchers. Johan George Theron Basson [1] conducted design and numerical study on axial turbine applied for small turbojet engine, providing the foundation for following up investigations on this axial turbine design. Zafer Leylek [2] utilized a time-accurate computational approach to investigate into performance modeling small gasturbine components. Schluter and Wu [3] developed an integrated RANS-LES computation method to simultaneously predict the performance of several components in gas turbine engine. Silva, D.T. and Tomita, J.T. [7] discuss the influence of two different turbulence models in fully turbulent flow $k-\epsilon$. The results are discussed for each turbulence model based on the solution from CFD tool analyzing the distribution of fluid properties along the turbine blade span. The main results showed that the Spalart-Allmaras model shows better results than the $k-\epsilon$ model for high pressure ratios. At high pressure ratios, boundary layer separation can occur on the turbine blade suction side. The $k-\epsilon$ turbulence model, which uses wall functions, cannot obtain, in some cases, accurate results under these conditions and engineering problems. With the Spalart-Allmaras turbulence model the equation is integrated until the wall, respecting the values of y^+ following the model recommendations. An detailed discussion and comparison between the results of a high pressure turbine flow field using different turbulence models, including a seven equations model and the well known two-equation SST turbulence model, was described in the work developed by Tomita, J. T., Silva, L. M. and Silva, D. T. [8]. In this work, the models were compared for different mesh types as structured and unstructured and its application for different turbulence equations within an axial turbine: the one equation turbulence model of Spalart-Allmaras and the two equations turbulence model. Their approach proved its accuracy and efficiency with simple test cases and was a good demonstration of numerical prediction. Based on previous study, computational approach on AMT Olympus turbine is utilized, to further verify the reliability of CFD method for turbo machinery study. The comparison of numerical results and available experimental data is conducted for validation, and flow field analysis is also considered to better understand the performance of axial flow turbine.

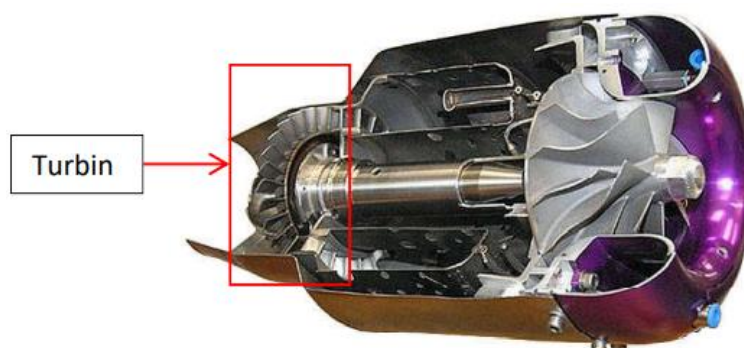


Figure 1. Cross section view of engine AMT Olympus HP [4]

2. Validate Numerical simulation of axial flow turbine

2.1 Blade Geometry

The AMT Olympus HP axial turbine is chosen as the testing model, as it is a well documented experiment [3]. The turbine cross section view is shown in Fig. 2. In total, 29 rotor blades and 22 stator blades compose the full circular of the compressors. In this study, due to concerns about computational time and resources, only one blade passage from the stage is

meshed and used for subsequent computational approach, to represent the full circular during this numerical study. Thus, rotor fluid passage and stator fluid passage are used with periodic boundary condition applied in azimuthal direction.

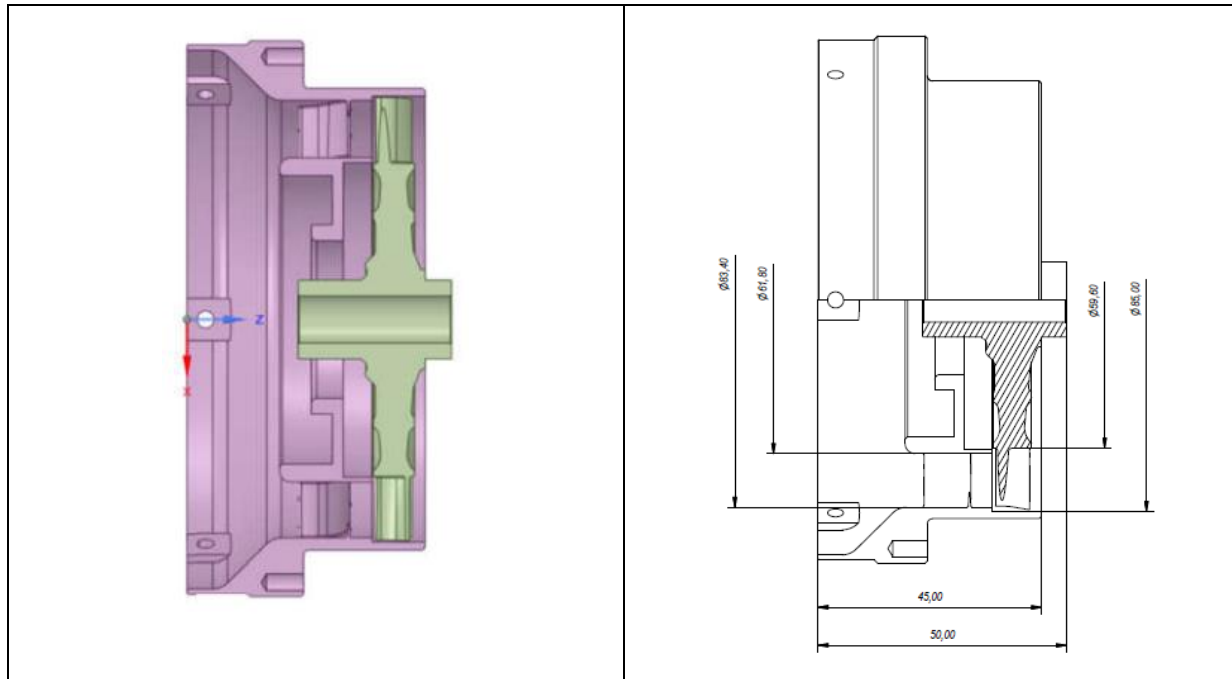


Figure 2. Geometry of turbine

2.2 Mesh generation

A structured mesh is generated for the computational domain using the packet TURBOGRID of software ANSYS 19.0 R2. The tip clearance gap 0.25 mm in this study. The grid is formed separately for the rotor and stator fluid domain. Mesh refinements are conducted near blade leading and trailing edge regions. Near wall treatment is also employed and a y^+ value is adapted to 1 for SST turbulence model, and from 30 to 300 for k - ϵ turbulence model. Our domain length, grid independence independent study suggests that 7 mm length of inlet and outlet domain, 524.000 mesh cells for k - ϵ turbulence model, and 1.890 million mesh cells are sufficient in producing sufficiently accurate results.

2.3 Boundary Condition

The design operation parameters and the available experimental data of AMT Olympus HP turbine are referred for the specification of boundary conditions in the simulations. Total pressure ratio, total temperature for inlet boundary and static pressure out outlet boundary conditions are applied. The initial gauge pressure values are defined for inlet & outlet boundaries, based on experimental data. Periodic boundary conditions are implemented to both rotor & stator domain in the azimuthal direction and it represents the full circular by allowing fluid variables across the boundary continuously. All wall boundaries are defined as adiabatic, with no heat flux through wall allowed in this study. The operating speed is set as 80%, 90%, 100% of design speed respectively for the rotor domain, while the stator domain remains stationary. This is for the purpose of understanding turbine performance characteristics at both high and relatively low operation speed. The mixing Plane method is chosen to address the rotor-stator interaction, where flow data is circumferentially averaged. The k - ϵ and SST turbulence

model is selected from our validation study and engineering experience. Boundary conditions are applied for numerical simulation of axial turbine in this case following Table 1.

Table I. Boundary conditions for numerical simulation

Parameter	Unit	80% speed	90% speed	100% speed
Total pressure at turbine inlet	Bar	2.338	2.838	3.585
Total temperature at turbine inlet	K	849	955	1171
Static pressure at turbine outlet	Bar	1.095	1.136	1.23
Turbulent intensity	%	5	5	5
Fluid: Air ideal gas with Cp	J kg ⁻¹ K ⁻¹	1158.3	1158.3	1158.3

2.4 Numerical flow chart

A steady state density-based algorithm is used, which solves the continuity equation and momentum, energy, species transport as a coupled set of equations using an ideal gas. An implicit formulation is used for numerical solutions and 1st order upwind scheme is utilized to discretize both flow and turbulent viscosity. A low under relaxation factor value and small courant number are applied at the start of simulation to aid convergence. Each computation takes approximately 4 hours to reach the final convergence on 25 processors.

2.5 Turbulence Model Comparison

To close the Reynolds-Averaged Navier-Stokes (RANS) equation, turbulence models have been created to provide additional modelling of the nonlinear Reynolds stress. In this section, the comparison of two most commonly employed turbulence models, K-epsilon (k- ϵ) and SST (SST) models, are conducted. These models provide approaches to compute the turbulence viscosity with relatively low cost. Different turbulence models possess their own superiority in dealing with different problems, and that's why this validation study is conducted, to determine the most suitable turbulence model in handling our problems.

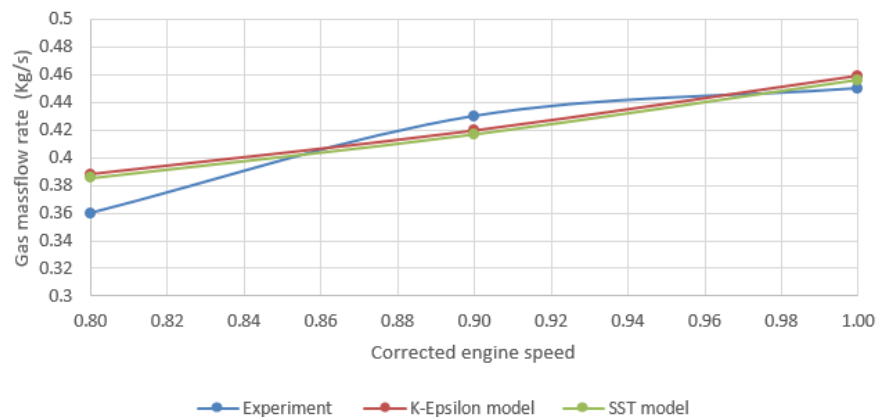


Figure 3. The dependence of gas mass flow rate on corrected engine speed

The comparison of numerical results and experimental data about gas mass flow rate through turbine at 80%, 90%, 100% design speed is firstly presented. Generally, numerical results are close to experimental data and the largest deviation is observed at around 0.0255kg/s Mfr, where numerical result is 7% difference from experimental data. Fig.3 show that Pt5 slightly increases with the increase of engine speed. Numerical results generally predict a smaller Pt5 than that of experimental data, and a comparison of Pt5 also at 90% engine speed shows 5.6% underestimation of experimental data. The comparison of numerical results and experimental data at 80%, 90%, 100% design speed are presented. Fig. 4 shows that when turbine is operating at 100% design speed, numerical results for Pt5 from both turbulence model testing are very close to experimental results.

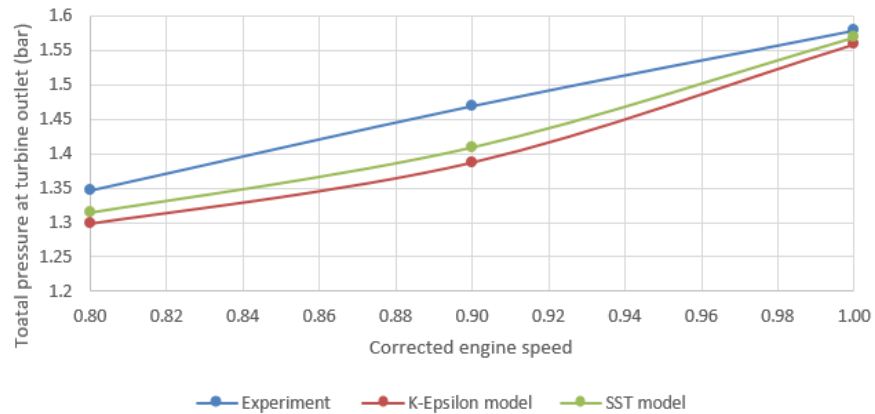


Figure 4. The dependence of total pressure at turbine outlet on corrected engine speed

The numerical results from K-epsilon (k- ϵ) and SST (SST) models underestimate the experimental data by 3.6% and 2.3% at experimental data Pt5 at 80% design speed. Fig. 5 shows the numerical prediction of Tt5 changes with the increase of engine speed. The K-epsilon (k- ϵ) and SST (SST) turbulence model generally follow the trend of Tt5 change from experiment, showing a general increase of Tt5 until the engine speed achieve 100%. SST turbulence model generates better capture and gives closer prediction in Pt5 and Tt5 values and an acceptable distribution changes with various engine speed. At 100% designed engine speed, the K-epsilon (k- ϵ) model underestimates experiment by 1.2% for Pt5 and 0.35% for Tt5, while the SST model underestimates the experiment by 0.6% for Pt5 and 0.08% for Tt5. In general, SST model gives better results in predicting turbine performance at high operation speed.

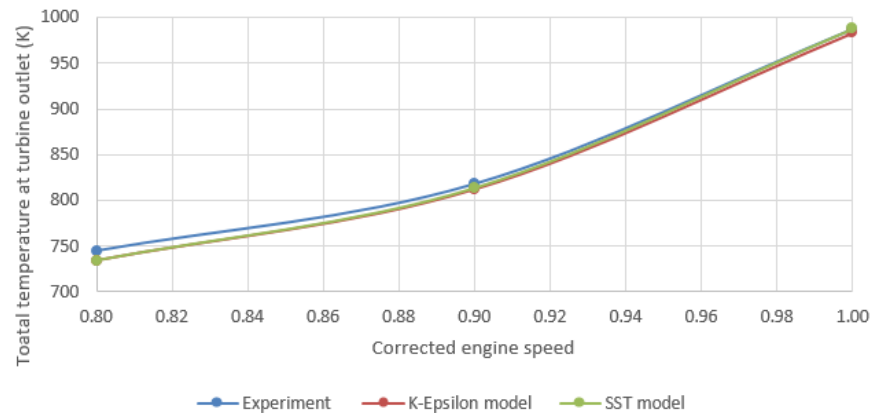


Figure 5. The dependence of total temperature at turbine outlet on corrected engine speed

Based on our numerical study in this section, SST turbulence model more accurately predicts turbine performance at both high and low operation speed conditions.

3. Conclusion

This CFD solvers evaluation and analysis are presented and shown for the axial turbine analysis with the experiment data comparison. This numerical study demonstrates that the proposed CFD method is capable in predicting axial turbine performance reliably. Parameters indicating the turbine performance as gas mass flow rate, total pressure and temperature at turbine outlet are also discussed from the thermodynamic point of view and the high deviation between CFD results and experiment data are identified. The SST turbulence model is suitable for numerical simulation to predict performance of axial turbine. This work strengthens the understanding of axial turbine operation and provides valid results for further computational study about single-stage, or even multi-stage axial turbine.

Acknowledgment

The authors are grateful for the academic support and the continued assistance in this work from the members of Jet Engine Center of Viettel Aerospace Institute.

References

- [1] Johan George Theron Basson, “Design methodology of an axial flow turbine for a micro jet engine”. Master Thesis, Stellenbosh University, 2014.
- [2] Zafer Leylek, Wesley S. Anderson, Glen Rowlinson and Nigel Smith, “An investigation into performance modeling of a small gas turbine engine”, in Proceedings of *ASME Turbo Expo 2013: Turbine Technical Conference and Exposition GT2013 June 3-7, 2013*, San Antonio, Texas, USA.
- [3] Schluter, J.U., et al., “A framework for coupling reynolds-averaged with large-eddy simulations for gas turbine applications”. *Journal of Fluids Engineering*, 2005. 127: p. 806-815.
- [4] <https://ecommerce.aviationeu.supplies/en/81-gas-turbines-and-jet-aircraft-engines->
- [5] Aungier, R. H., 2006. “Turbine aerodynamics”. 1st ed. New York: ASME press.
- [6] A. Horoufi and M. Boroomand, “Design and Construction of Microjet Engine at Amirkabir University of Technology,” in *45th AIAA/ASME/SAE/ASEE Joint Propulsion Conference, 2009*.
- [7] Silva, D.T.; Tomita, J.T., 2011, “ Axial Turbomachinery Flow Simulations with Different Turbulence Models”. ITA. São José dos Campos, SP, Brazil.
- [8] Tomita, J.T.; Silva, L.M.; Silva, D.T., 2011, “Comparison Between Unstructured and Structured Meshes With Different Turbulence Models for a High Pressure Turbine Application”. Proceedings of *ASME Turbo Expo 2012, GT2012-6990*, June 11-15, 2012, Copenhagen, Denmark.

The Control Methodology for Jet Engine of Unknown Characteristics

Huy Hoang Nguyen^{1*}, Van Son Bui², Thanh Nam Trinh³, Nhu Van Nguyen⁴ and Quang Hai Nguyen⁵

¹*Jet Engine Center, Viettel Aerospace Institute, Thach That, Hanoi, Viet Nam, 100000.*

**Corresponding author. E-mail: hoangnh261@viettel.com.vn*

Abstract

This paper provides a method to build a control algorithm for a jet engine of unknown characteristics. Experiments were conducted on different types of jet engines and simulations were performed using Matlab software. Jet engine control models have been developed for different operating speed ranges. On that basis, the control coefficients corresponding to each model were selected. Safe operating limits of the engine have been added to create a complete control algorithm. The control algorithms work stably with two different types of engines, showing the applicability of the method to many different jet engines. The method can be considered as a basis for application to other types of gas turbine engines such as turbofan or turboprop, turboshaft.

Keywords: algorithm, experiment, model, coefficient

Nomenclature

rpm = round per minute

PID = Proportional–Integral–Derivative controller

EGT = Exhaust gas temperature

ECU = Engine Control Unit

1. Introduction

Gas turbine engine control methodology is an important technology in the engine research and development process. Most studies in this field focus on building control algorithms from thermodynamic models of engines. A jet engine designer who has a nonlinear thermodynamic model can easily come up with the right control algorithm for his engine [1]. This is the traditional and natural way to design engine control algorithm. However, without the thermodynamic nonlinear model, this approach is not feasible. The purpose of this article is to provide a method of building a stable and reliable control algorithm for a jet engine with unknown characteristics. The approach of this paper is from an experimental perspective. Firstly, the article presents how to build a hardware and software platform. Then, the experimental method of identifying the engine's response model is described. Section 4 explains how to build control algorithm structure and select coefficients using Matlab Simulink software. Finally, the control algorithm's quality is evaluated by the Nyquist stability criterion and by the actual test in Section 5.

The study was carried out on two different turbojet engines, AMT Nike and AMT Olympus. Their thrusts are up to 75kgf at 65000rpm and 25kgf at 108500rpm, respectively, according to the manufacturer's information. These are all single-shaft turbojet engines with centrifugal compressors. Main engine components are the inlet, compressor, combustion chamber, turbine and exhaust. A turbojet engine is a gas turbine engine that works by compressing air with an inlet and a compressor (axial, centrifugal, or both), mixing fuel with the compressed air, burning the mixture in the combustor, and then passing the hot, high pressure air through a turbine and a

nozzle. Thrust is generated by the high velocity air passing through the nozzle. Turbine is driven by power from the hot, high pressure air. Turbine rotor and compressor rotor are connected through a shaft, so the driving turbine rotates the compressor.

2. Build open-loop control platform

The engine control system comprises an engine control unit (ECU), a rotational speed sensor, an EGT sensor, an ignitor fuel solenoid valve, a main fuel solenoid valve, a fuel pump, an electric starter motor and an ignition device. These components are connected to each other as shown in the Fig.1

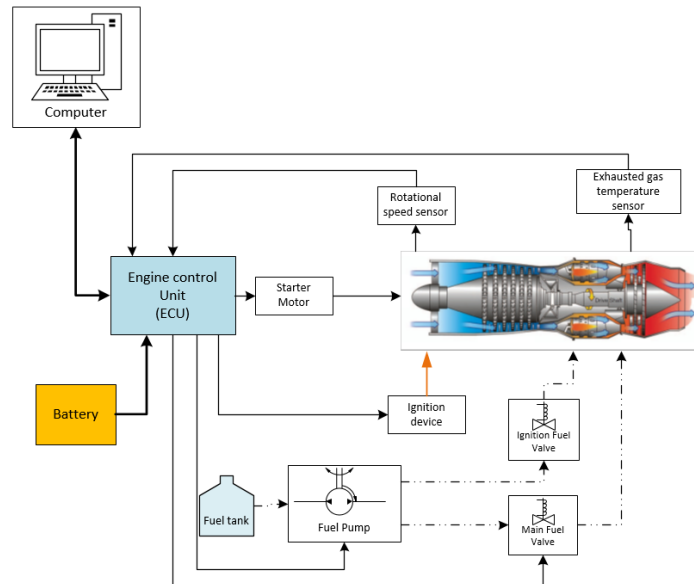


Figure 1. Diagram of turbojet engine control system

The engine control unit has been designed and fabricated by authors. The central microcontroller embedded in the circuit is STM32F4. The ECU is responsible for communicating with the computer, reading the sensors, and controlling the actuators to control the engine. The interface software is designed to include the functions of displaying the state of rotational speed, EGT, giving commands to control each actuator, controlling the engine by manual mode and automatic mode.

The first step in control methodology is the starting method. The process of starting the engine is the process by which the engine changes from the static state to the Idle state (self-sustaining without the assistance from starter motor). This method was found by an experimental approach. It consists of an open-loop control sequence of actuators. Firstly, the igniter is activated, then the starter motor and fuel pump, ignition solenoid valve operate. The engine rotation speed increases gradually, and when the engine is close to idle state, the main fuel solenoid valve works, then the starter motor, ignition device and ignition solenoid valve are stopped working. When the engine reaches Idle state, we can control the engine to change speed manually by changing the fuel flow into the combustion chamber. The open-loop control method for turbojet engines is the basis for the development of the closed-loop control method.

3. Engine model identification

The PID control algorithm is selected for closed-loop control of jet engines. However, because jet engines have a nonlinear response model, using the same set of control coefficients

for the entire operating range according to the engine's rotational speed will not result in good control quality. Therefore, the control coefficients that change according to the operating state of the motor will provide better control quality. To find these sets of control coefficients, we need to build the response models corresponding to them. The engine's operating ranges from Idle to full speed is divided into smaller ranges. Corresponding to each range, a linear response model of the engine will be built by identification method from experimental data [4]. Experiments for the purpose of model identification comprise of following stages: starting, open loop controlling the engine to the range that needs to identify the model, and controlling fuel pump according to a pre-programmed pulse. This particular pulse is designed to make the engine showing its response characteristics [2]. Experimental data is sampled every 0.06s and stored in the computer to serve the analysis and build the control model. Fig.2 shows data from one experiment.

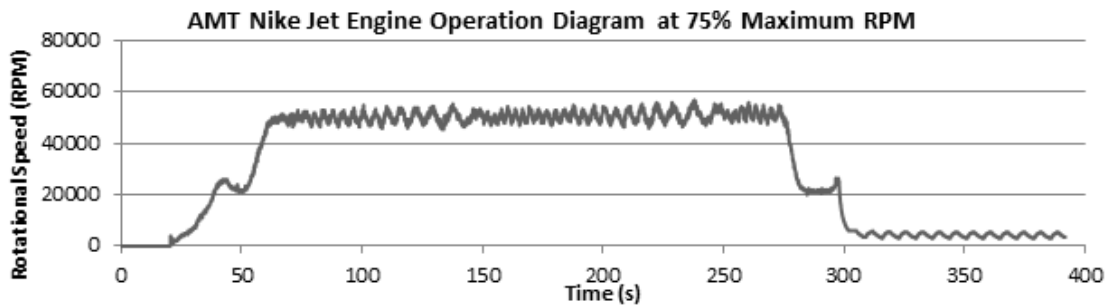


Figure 2. AMT Nike jet engine experimental data at the range 70-80% maximum RPM

Input data (fuel pump controlling pulse) and output data (rotational speed) of model identification experiments are synchronized in time. Noisy data is removed [3]. Then, a linear transfer function model representing the relationship between output and input data for each engine operating range is built using System Identification tool in Matlab. Transfer function model structure with 1 zero point and 2 poles is chosen to represent the engine model because they have minimum degree and an allowable dynamic evolution [1]. Details of the transfer functions of AMT Nike engine their reliability are listed in the table below

Table 1. AMT Nike engine's transfer function models

Operational Range	Engine's transfer function model	Matching Reliability
From Idle to 60% maximum RPM	$\frac{1896s + 4.411e05}{s^2 + 241.3s + 409.1}$	62.02%
From 60% to 70% maximum RPM	$\frac{2278s + 91.55}{s^2 + 1.963s + 0.08126}$	67.75%
From 70% to 80% maximum RPM	$\frac{3437s + 61.45}{s^2 + 2.029s + 0.04979}$	61.59%

4. Design a closed-loop control algorithm

Diagram of PID closed loop control algorithm is set on Matlab Simulink tool for each model, in which setpoint is the desired rotational speed value, input is the instantaneous rotational speed value and output is the result of the controller to control to the fuel pump. Because differential

term in PID controller is sensitive to sensor signal noise, this term is removed and the controller becomes PI [5].

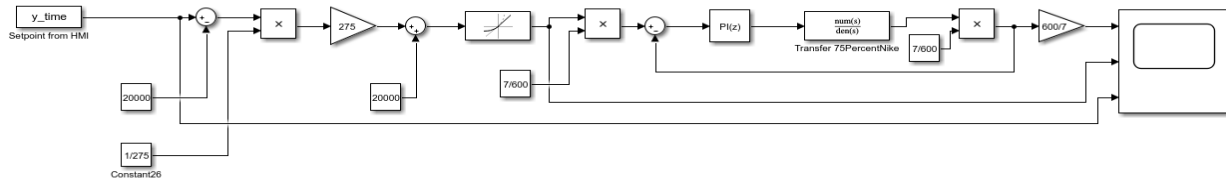


Figure 3. Diagram of closed loop control algorithm for AMT Nike engine

The control coefficients are selected using the PID Tuner tool. Choice of response time of 4s for Olympus engine and 7.45s for Nike engine and high robustness results in low overshoot, convergent control. The PID Tuner tool's interface is shown in Fig.4.

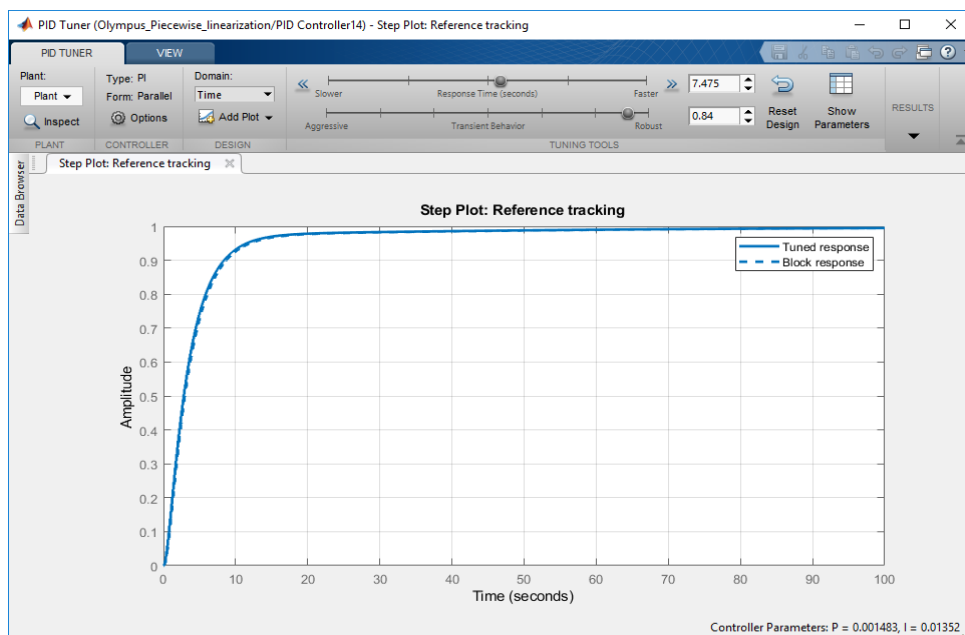


Figure 4. PID Tuner tool's interface

In order for the engine control system to operate safely and stably, operation limiters need to be added to prevent engines from surging. Since the thermodynamic characteristics of the engine are unknown, in this study, only limits on maximum engine rotational speed and acceleration were established. To limit the rotational speed, the maximum value of the fuel pump control pulse is defined. To limit the engine's acceleration, a limit of variation for the PI controller setpoint over a delta t time is given. According to experiments with the Nike engine, a maximum setpoint variation of 4300rpm per second is suitable; for Olympus, this value is 8000 rpm per second.

5. Evaluate control system's quality

The Nyquist stability criterion is used to evaluate the quality of the closed-loop control algorithm. Open-loop transfer functions of closed-loop control systems are calculated, and their Nyquist plots are used to evaluate control systems's quality. Open-loop transfer functions of the closed-loop control systems are listed in the table below:

Table 2. Open-loop transfer functions of the closed-loop control systems

Operational range	Engine's transfer function model	Open-loop transfer functions of the closed-loop control systems	Poles
From Idle to 60% maximum RPM	$\frac{1896s + 4.411e05}{s^2 + 241.3s + 409.1}$	$\frac{22s^2 + 5275s + 10347}{s^3 + 241.3s^2 + 409.1s}$	$s_1 = 0$ $s_2 = -239.5925$ $s_3 = -1.7075$
From 60% to 70% maximum RPM	$\frac{2278s + 91.55}{s^2 + 1.963s + 0.0812}$	$\frac{23.1648s^2 + 49.4617s + 1.9}{s^3 + 1.963s^2 + 0.08126s}$	$s_1 = 0$ $s_2 = -1.9207$ $s_3 = -0.0423$
From 70% to 80% maximum RPM	$\frac{3437s + 61.45}{s^2 + 2.029s + 0.0497}$	$\frac{2.2176s^2 + 44.3924s + 0.79}{s^3 + 2.029s^2 + 0.04979s}$	$s_1 = 0$ $s_2 = -2.0042$ $s_3 = -0.0248$

The Nyquist plots of engine control systems are shown as follow:

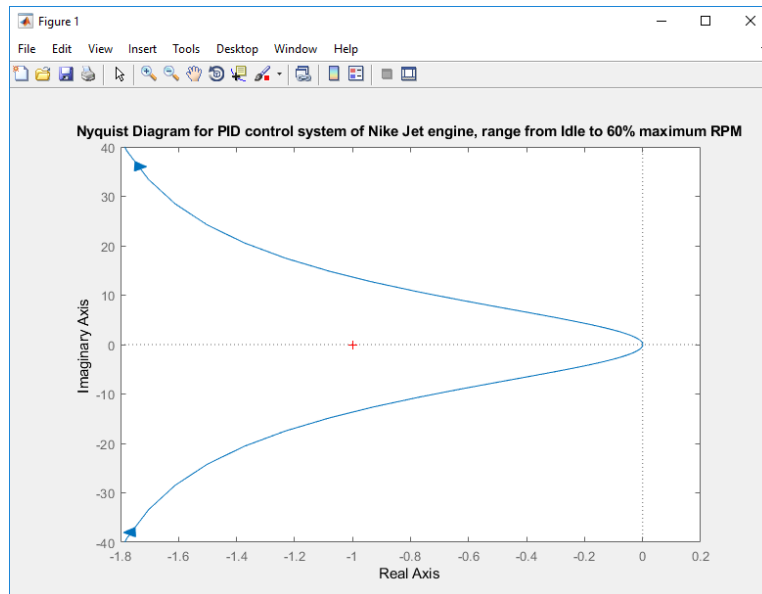


Figure 5. Nyquist plot for PID control system of Nike Jet engine, from Idle to 60% maximum RPM

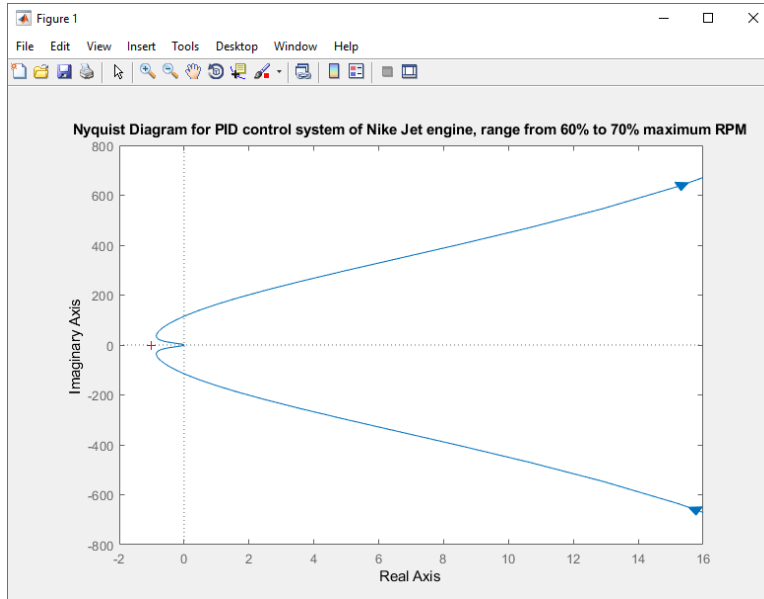


Figure 6. Nyquist plot for PID control system of Nike Jet engine, from 60% to 70% maximum RPM

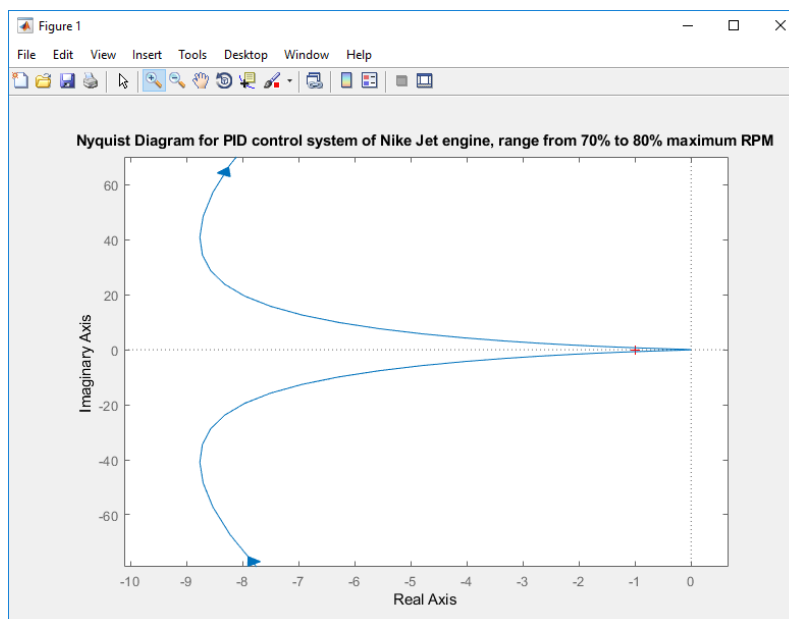


Figure 7. Nyquist plot for PID control system of Nike Jet engine, from 70% to 80% maximum RPM

The Nyquist plots of the open-system transfer functions do not cover the point -1 in the increasing direction of s (arrow direction). Besides, apart from pole 0, all poles of open systems lie to the left of the imaginary axis, so according to the left-hand rule of the Nyquist stability criterion, closed-loop systems are stable.

The complete control algorithm is programmed into embedded code for the STM32F4 microcontroller. The control coefficients are embedded in a 2-column matrix K_p , K_i with rows corresponding to the motor rotation speed ranges. When programming embedded algorithms, care should be taken so that during the transition between operating ranges, the output signal pulse is always continuous and not jerky. Finally, a test to confirm the operation of the control

algorithm is performed. Fig.8 and Fig.9 show the test results that confirm the operation of the control algorithm with AMT Nike and AMT Olympus engine, respectively. In the figures, THR is rotational speed setpoint that ECU receives from interface software and RPM is the engine's rotational speed in real time.

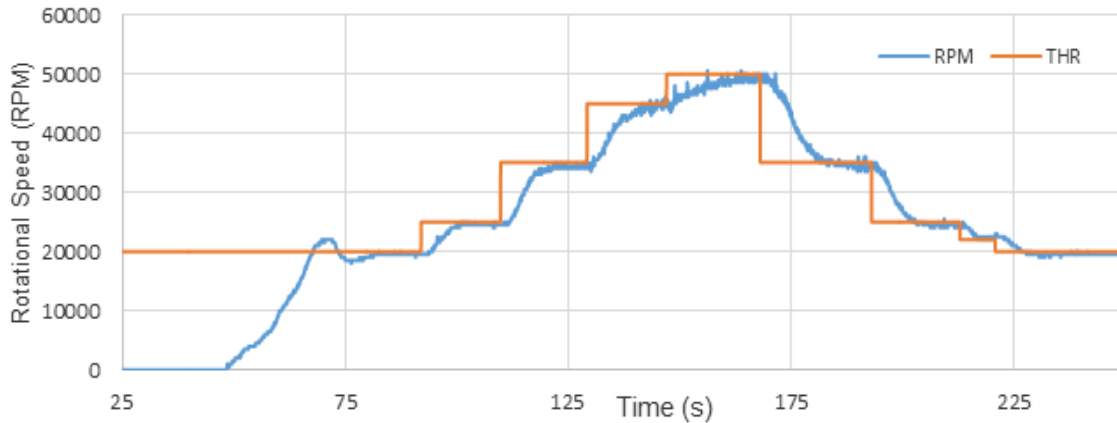


Figure 8. Test results of AMT Nike engine closed-loop control algorithm

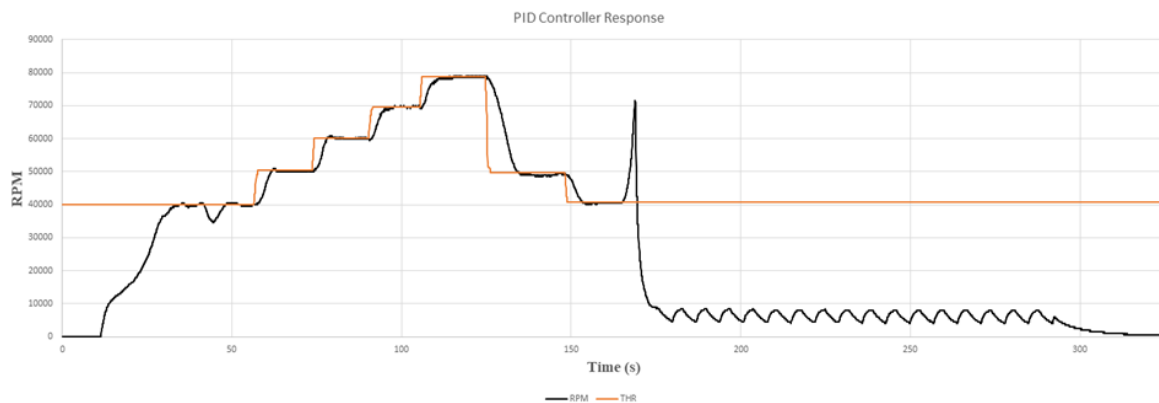


Figure 9. Test results of AMT Olympus engine closed-loop control algorithm

6. Conclusions

The quality of the closed-loop control algorithm has been confirmed. The control result is convergence, the rotational speed is not excessive, the response time is about 7.5s, which coincides with the simulation of coefficients selection by PID Tuner tool. The closed-loop control algorithm has proven to be stable and reliable in practice. This method can be extended to apply to other types of gas turbine engines such as turbofan, turboprop, turboshaft. The results of this paper provide a basis for research, evaluation and manufacturing of Engine control unit with closed-loop control algorithm for jet engines.

Acknowledgments

The authors are grateful for the academic support and the continued assistance in this work from the members of Jet Engine Center of Viettel Aerospace Institute.

References

Gennady G.Kulikov, Haydn A. Thompson (Eds.), "Dynamic Modelling of Gas Turbines, Identification, Simulation, Condition Monitoring and Optimal Control", Springer-Verlag, London 2004.

Evans C., “Identification of linear and nonlinear systems using multisine signals, with a gas turbine application”, Ph.D. dissertation, University of Glamorgan, School of Electronics, UK, 1998.

Schoukens J, Pintelon R, Vandersteen G, Guillaume P, “Frequency-domain system identification using nonparametric noise models estimated from a small number of data sets”, *Proceeding of Automatica*, 1997:33:1073-1086

Ahmed M. shehata, Mohamed K. khalil, Mahmoud M. Ashry, “Controller Design for Micro Turbojet Engine”, *Proceeding of 2020 12th International Conference on Electrical Engineering (ICEENG)*, Cairo, Egypt, 2020

M. M. Ashry, Z. Z. Kamalova, and T. V. Breikin, “Tuning of digital PID controller parameters using local optimal control”, *Proceeding of 16th Mediterranean Conference on Control and Automation Congress Centre*, Ajaccio, France Jun 2008

Reverse Engineering and Aerodynamic Analysis of a High-speed UAV Inverted V-tail Using XFRL5

Do Hoang Huy^{1,*}, Ngo Khanh Hieu^{1,2}

¹ *Aerospace Engineering Department, Ho Chi Minh City University of Technology, VNU-HCM*

² *VNU-HCM Key Laboratory for Internal Combustion Engine*

**Corresponding author. E-mail: huy.do99@hcmut.edu.vn*

Abstract

This paper proposes an effective way of reverse analysis of the high-speed fixed-wing unmanned aerial vehicle (UAV) as a part of preliminary design stage. The methodology in this paper is developed to analyze the aerodynamic characteristics and the aerodynamic coefficients including lift, drag, and pitching moment variations versus the angle of attack of the High-speed UAV using XFRL5 software. XFRL5 software is also used for analyzing the stability and control of the aircraft. After receiving the 3D model from our partner, the airfoil was interpolated to find its geometry. After that, with the help of XFRL5, the airfoil characteristics were found. Then, High-speed UAV 3D model was created in XFRL5 for analyzing its aerodynamic characteristics. The analyzed results were compared with aircraft specifications. The results showed the feasibility to apply XFRL5 software to obtain configuration of UAVs operating at low Reynolds Numbers. In the future, without changing the design, the aerodynamics performance of the High-speed UAV will be modified to become more suitable for the Low-speed UAV using XFRL5.

Keywords: XFRL5, Preliminary design, UAV inverted V-Tail configuration

1. Introduction

XFRL5 is an analysis tool for airfoils, wings, and planes operating at low Reynolds Numbers. XFRL5 software is an effective tool for analyzing design. XFRL5 has been applied for analyzing aerodynamic characteristics in many studies. For instance, Sudhakar et al. (2011) [1] obtain the aerodynamic characteristics of a modified airfoil geometry using the reverse design method of XFRL5. The airfoil aerodynamic performance was compared with the original airfoil to provide better longitudinal stability for a MAV configuration based on the analysis results from XFRL5. Aerodynamic performance of VTOL (vertical take-off and landing) blended wing body aircraft was analyzed with VLM (vortex-lattice method), NLL (Non-linear numeric lifting line), and CFD (computational fluid dynamics) methods by Vuruşkan et al. (2014) [2]. XFRL5 software was used to analyze the used airfoil characteristics. The results of VLM and CFD methods were more compatible with experimental data existing in literature more than NLL method.

This study is the first stage of a project which is a part of the collaboration between VNUHCM Key – Lab for Internal Combustion Engine and Real-Time Robotics Vietnam Ltd. (RTRs) to modify a high-speed UAV inverted V-tail (HSUAV) to a low-speed UAV inverted V-tail (LSUAV) includes design, manufacture prototype and flight testing the UAV.

As reverse engineering is the cheapest and fastest method, it will be used to recreate the model. HSUAV has a non-traditional design with a unique fuselage shape, inverse V-tail, and elliptical wing. Therefore, traditional analysis is going to take a long time and probably not fidelity. For that reason, XFRL5, the medium-fidelity software, is used to reverse-engineering the configuration design of a UAV.

In this study, XFLR5 is used to analyze existing airfoil aerodynamic characteristics of high-speed UAV inverter V-tail (see Fig. 1) with the aim of modifying this HSUAV configuration design into an LSUAV configuration design for wild area aerial protective inspector in Vietnam. First, the airfoil of the HSUAV was interpolated from a 3D model sent from RTRs. Then, airfoil aerodynamic coefficients are analyzed with the help of XFLR5. After that, aerodynamic characteristics are analyzed using XFLR5 software. The analysis results of the reverse design airplane would be compared with the original one to show the feasibility of the reverse analysis method for UAV models.

Once the methodology proves its reliability, it can be used in reverse engineering to modify or enhance aircraft performance. This method introduces one of the least expensive and most efficient ways to reverse engineering an existing aircraft design. The exploration of the aircraft design leads to recreation and innovation for more advanced design.

2. Aerodynamic characteristics

2.1 Aerodynamic characteristics of the main wing airfoil

One of our research presented in [3] verify that the use of a multifidelity analysis tool like XFRL5 could help to evaluate the aerodynamic characteristics of the airfoil.

The main wing airfoil of the HSUAV is interpolated from 3D model sent from RTRs (see Fig. 2).



Figure 1. A design of HSUAV for wild area aerial protective inspector



Figure 2. Main wing airfoil of HSUAV interpolated from 3D model

Geometrical features of the airfoil:

- Maximum camber thickness: 11.7 %
- Maximum camber thickness position: 38 %
- Camber: 3.6 %
- Camber: 27 %

Figure 3 below shows the simulation results of main wing airfoil aerodynamic characteristics at Reynold Number at the velocity of 35 m/s. Reynold number at this position:

$$Re = (35 \times 0.113 / 2.75 \times 10^{-5}) = 1.4 \times 10^5$$

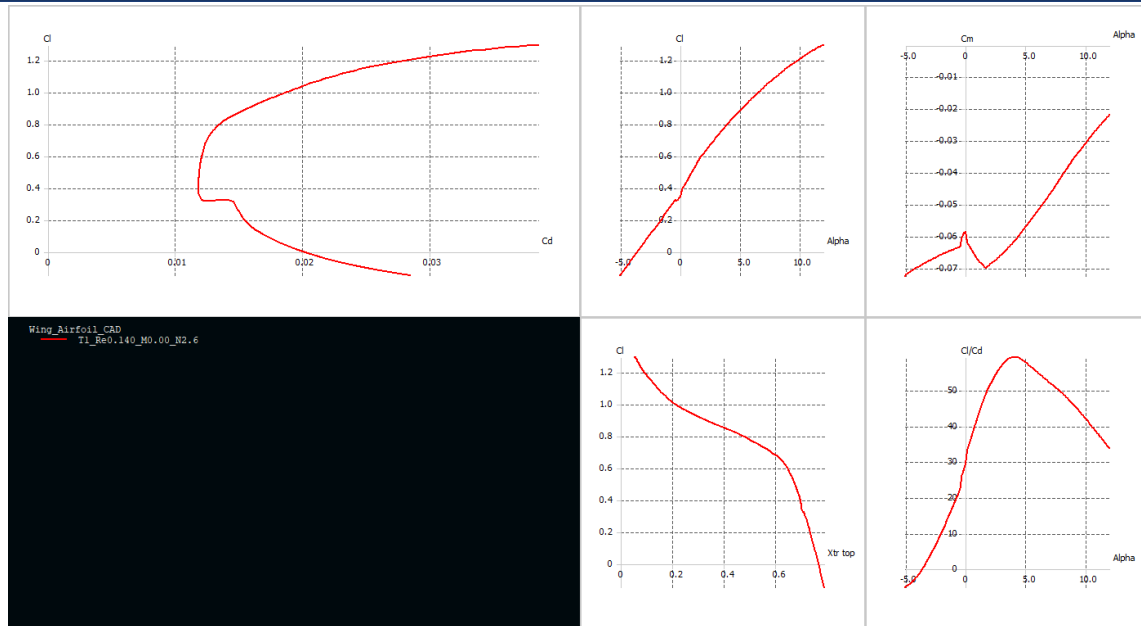


Figure 3. The aerodynamic characteristics of the main wing

Some of characteristic of the airfoil at Reynold number 1.4×10^5 :

- $C_l = 0.094 \times \alpha + 0.3685$ with (α : degree)
- $C_{l_\alpha} = 0.094 (1/\text{deg}) = 5.3858 (1/\text{rad})$
- $\alpha_{0L} = -3.92$ (degree)
- C_l / C_d reach a peak at approximately 59 with angle of attack: 4 degree
- $C_{m,c/4}$ at angle of attack of 1°, 2°, 3°, 4°, are -0.0668; -0.0687; -0.0655; -0.0617 respectively
- $C_{l,\max} = 1.35$ at $\alpha_{\text{stall}} \approx 15$ degree

2.2 Aerodynamic characteristic of the “High-Speed UAV inverted V-tail”

XFLR5 is a software that could implement for analyzing the aerodynamic study as well as the stability and control analysis in aircraft design studies [4]. HSUAV 3D geometry was provided by RTRs in STP form (see Fig. 4). The HSUAV configuration design is the following:

- Maximum take-off weight: 9 kg
- Wingspan: 1.919 m
- Wing area: 0.217 m^2
- Aspect ratio: 17
- Mean camber line: 0.113 m
- Swept back angle of the main wing: 1 degree
- Dihedral angle of the main wing: 0 degree
- The area of horizontal tail: 0.0362 m^2
- Dihedral angle of the tail: -30.5 degree

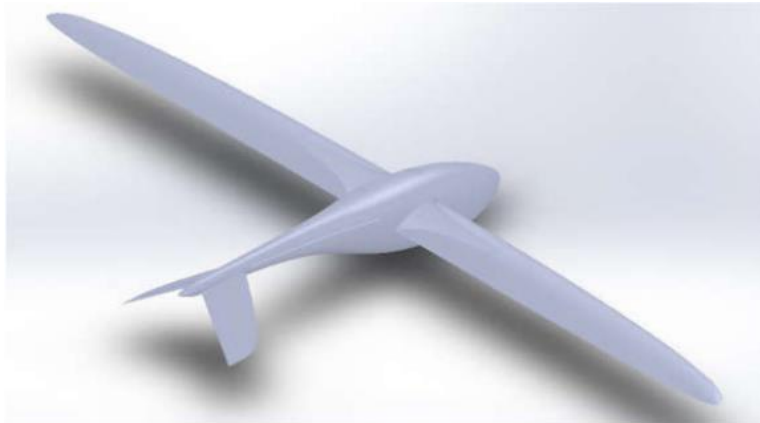


Figure 4. 3D model of the existing HSUAV configuration

From HSUAV 3D model and specifications, 3D model implemented in XFLR5 consists of wings, fuselage and inverted V-tail:

- Assume that the main wing has a weight of 2 kg and its center of gravity based on 3D geometry in XFLR5
- Assume that fuselage has a weight of 2 kg and its center of gravity based on 3D geometry in XFLR5
- Mass of the tail is known with the assumption that density of it is the same as the main wing (the same material).
- Battery and payload weight is assumed to be 4.8 kg (ensure that the take-off weight is 9 kg)
- Angle of incident of the wing is 2 degree
- Angle of incident of the tail is -2 degree
- The coordinate is set so that the origin of coordinate at leading edge (LE) of the airfoil is at the main wing chord root.

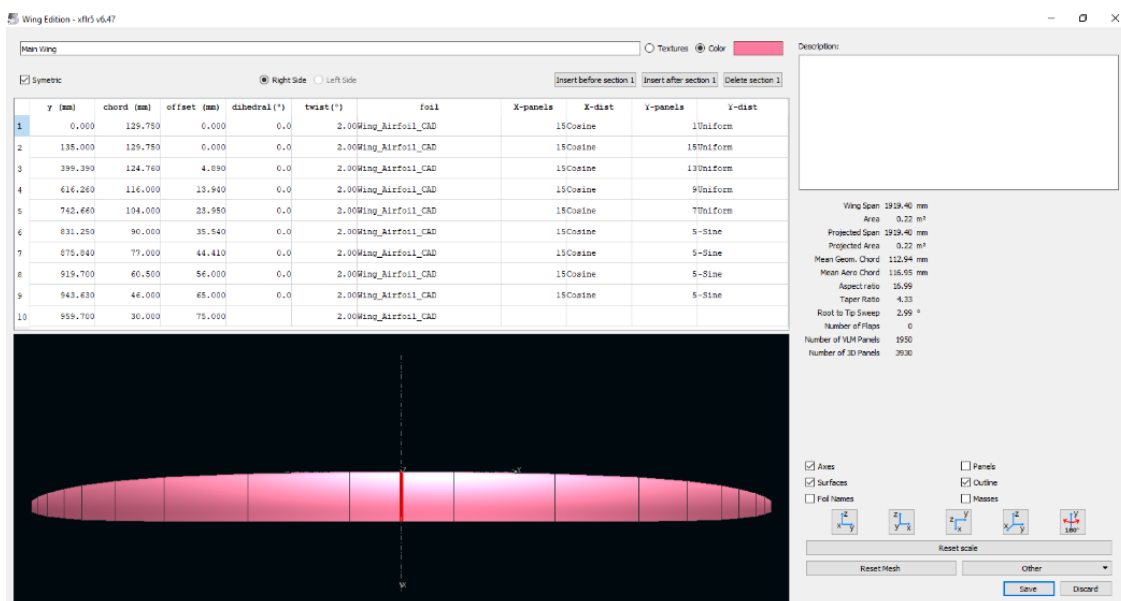


Figure 5. Geometry of the main wing in XFLR5

Figure 5 shows the the main wing geometry set up in XFLR5 with 1 section at root and 9 more from root to tip.

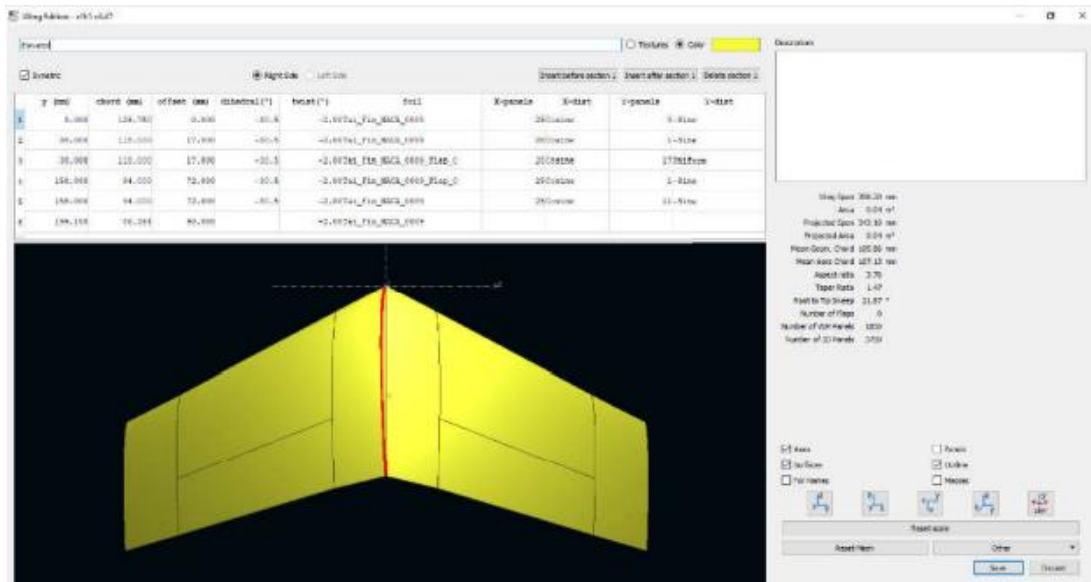


Figure 6. Tail set up in XFLR5

Figure 6 shows set up 3D geometry for the tail of HSUAV with 4 sections on each side. Figure 7 shows set up 3D geometry for the fuselage of HSUAV with 13 sections interpolated from 3D model.

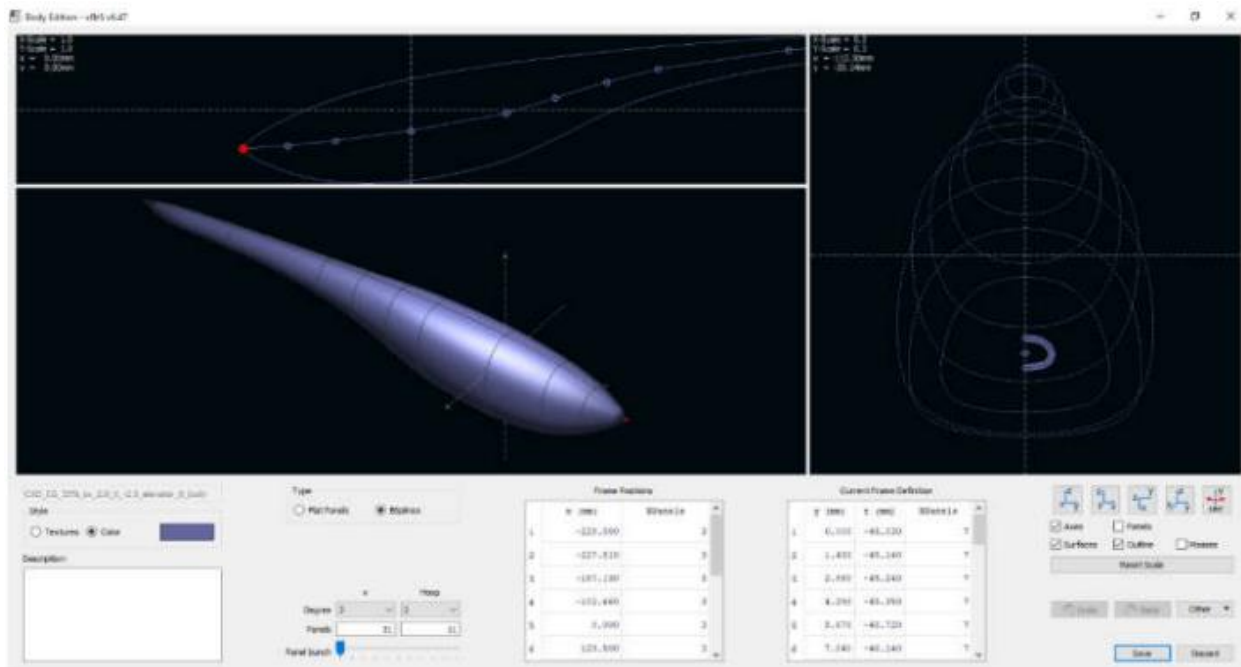


Figure 7. Fuselage set up in XFLR5

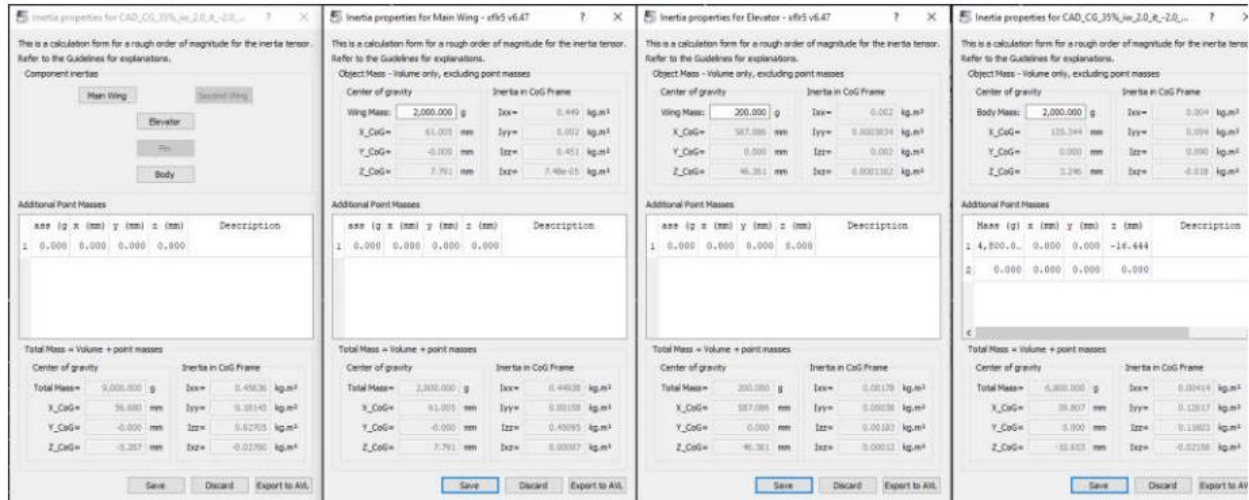


Figure 8. Mass distribution of HSUAV in XFLR5

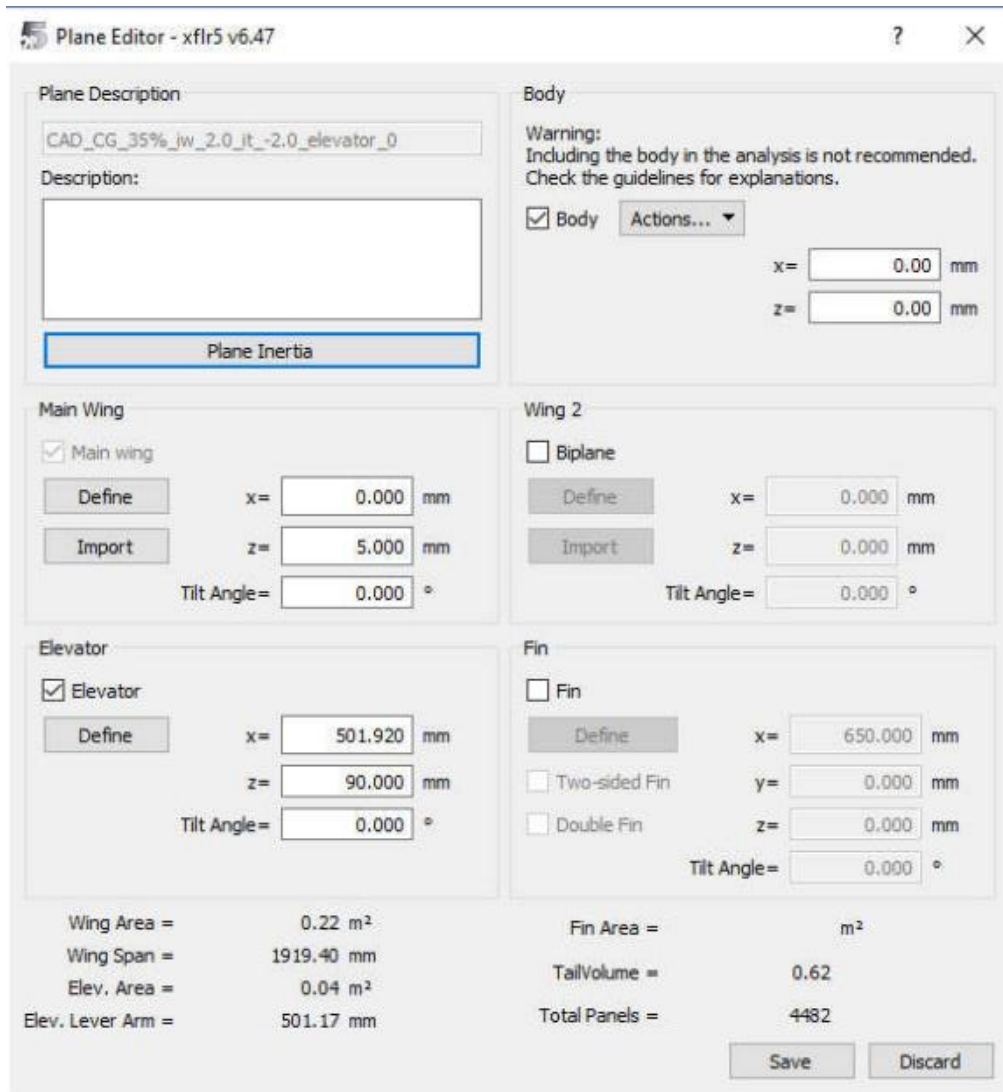


Figure 9. Plane editor in XFLR5



Figure 12. The pitching moment characteristic according to the angle set by the elevator at the center of gravity

The HSUAV model pitching moment curve at the center of gravity 36.5% of the mean camber shows a stable longitudinal static response. An important static stability characteristic must be met during the preliminary design analysis of the UAV. However, to be able to fly at a lift coefficient (C_{L_cruise}) of 0.6, it is necessary to set the trim angle of the height rudder (Up - negative elevator deflection) with an angle of -6.7 degrees. Figure 12 shows that the pitching moment characteristic of the HSUAV model at 36.5% center of gravity position of the average wing at the trim angle of the Elevator is -6 degrees:

$$C_{M_elevator_up_6} = -0.2418 \times C_L + 0.1357$$

$$\rightarrow C_{L_trim} = 0.5612 \text{ (level flight lift coefficient where pitching moment is zero)}$$

$$\rightarrow \alpha_{trim} = 2.6^\circ$$

$$\rightarrow V_{cruise} = \sqrt{(2 \times 9 \times 9.806) / (1.12 \times 0.217 \times 0.5612)} = 36 \text{ (m/s)}$$

The cruising speed of the HSUAV model at the trim angle of the Elevator is -6 degrees at the center of gravity 36.5% of the mean camber compared to the 35 m/s setting speed for the C_{L_cruise} of 0.6 indicating consistency of the analytical results (see Fig. 14). Figure 13 shows the distribution of pitching moment coefficients along the wingspan of the main and horizontal wings of the “High Speed UAV” model at an incident angle of 2.6 degrees.

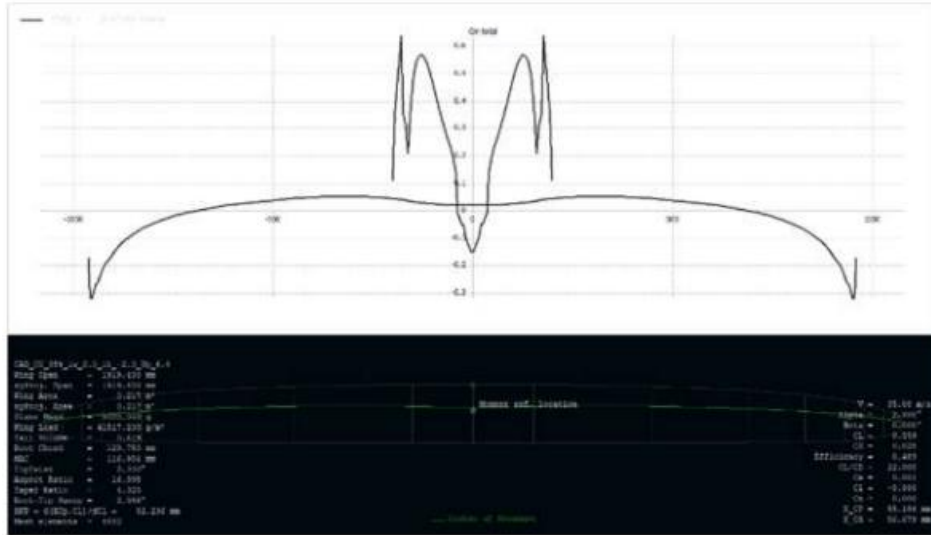


Figure 13. Distribution of pitching moment on the main wing and on horizontal tail with the trim angle of -6 degree

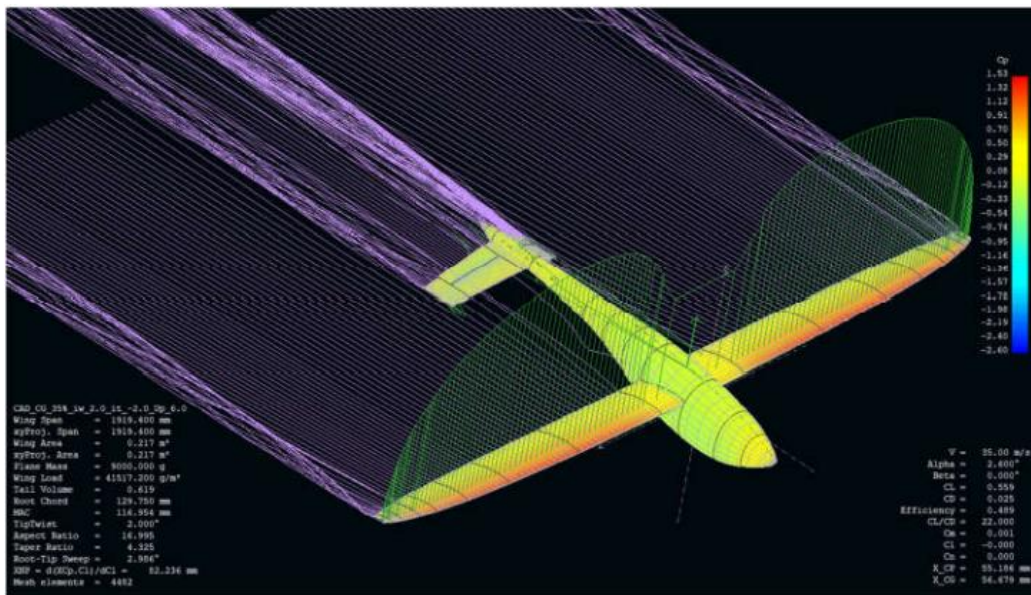


Figure 14. Streamlines and lift distribution at CG and elevator trims at -6 degree (Isometric view)

The HSUAV drag coefficient is 0.02 (lift-to-drag ratio is 22). Therefore, the HSUAV required thrust and required power could be calculated to fly at the velocity of 36 m/s and take-off weight of 9kg:

$$T_{req} = 0.5 \times 1.12 \times 36^2 \times 0.217 \times 0.025 = 3.94 \text{ N}$$

$$P_{req} = 3.94 \times 36 / 0.489 = 290 \text{ W}$$

With four propellers, each propeller will produce at least 1N when the aircraft flies at 36 m/s. Some of the propeller models that can be used for the above “High Speed UAV” model from the UIUI Propeller Database [6] are: APC Thin Electric; Master Airscrew GF has a pinwheel diameter of 11 inches, pinwheel pitch from 8 inches to 10 inches.

3. Conclusion

The HSUAV has the following design configuration features based on reverse survey from its 3D geometry:

- The design center of gravity is in the region from 36.5% to 38% of mean camber of the main wing.
- The main wing and the tail angle of incident is 2° and - 2° respectively.
- Trim angle of the elevator when the model flies at the design speed is -5° to -6°.
- Pitching moment vs lift coefficient characteristic of: $C_{M_elevator_up_6} = -0.2418 \times C_L + 0.1357$
- Characteristic of total lift coefficient: $C_L = 0.0902 \times \alpha + 0.3242$
- Total drag coefficient at design speed: $C_D = 0.025$
- Neutral point is 58.5% of mean camber.
- Propulsion system can use 4 propellers with the specifications: \emptyset 11 inches, pitch 8 inches: 10 inches

The analytical results were then compared with the HSUAV specifications. The analytical lift and drag coefficients are close to those of the HSUAV. The HSUAV stability-analyzed outcomes show that the plane will fly stably. Therefore, the results show great success.

The HSUAV aerodynamic characteristics reverse-calculation results presented in the above sections show the feasibility to apply XFRL5 software for the unmanned aircraft reverse design at a low Reynolds number.

With its proven reliability, we can now confidently use this method for reverse engineering UAV designs.

4. Future work

In this research, aerodynamic performances of reversal designed HSUAV were analyzed with the help of XFRL5. In the next stage, aerodynamic performance will be enhanced for the LSUAV as a part of our contact. After that, a prototype will be manufactured. Low-speed UAV will be made mainly of balsa wood. Then it will take to the skies for the first test flight.

Acknowledgments

This study was carried out within the cooperation between Real-time Robotics Vietnam and VNU-HCM Key Laboratory for Internal Combustion Engine.

References

- [1] S. M. S. R. G. M. K. T. A. Sudhakar, "Experimental Studies on SM4308 Airfoil at Low Reynolds Numbers.," 2011.
- [2] A. Ö. U. Y. M. İ. G. Vuruşkan, "Dikey İniş Kalkış Yapabilen Bir İnsansız Hava Aracının (Turaç*) Aerodinamik Analizi," V. ULUSAL HAVACILIK VE UZAY KONFERANSI. Kayseri: Erciyes University., 2014.
- [3] Ngo Khanh Hieu, Huynh Thien Loc, "Airfoil Selection for Fixed Wing of Small Unmanned Aerial Vehicles," Lecture notes in Electrical Engineering 371, Springer, 2015.
- [4] P. Q. V. D. A. B. Ngo Khanh Hieu, "Design of a Small UAV Combined Between Flying-Wing and," International Journal of Transportation Engineering and Technology, vol. 2, no.

- 5-1, Special Issue: Experiments Researches in Aeronautical Engineering, pp. 1-6, 2016.
- [5] G. Vietnamese Research Cooperation on Wind Power Initiative, "DeVie Wind Turbine project, German," 4/2017 – 11/2018.
- [6] P. Tsilingiris, "Thermophysical and transport properties of humid air at temperature range between 0 and 100°C," *Energy Conversion and Management*, vol. 49, pp. 1098-1110, 2008.
- [7] <http://www.xflr5.tech/xflr5.htm>.
- [8] XFRL5 – Analysis of foils and wings operating at low Reynolds numbers, Guidelines for QFLR5 v0.03, October 2009.
- [9] U. P. Database, <https://m-selig.ae.illinois.edu/props/volume-1/propDB-volume-1.html>.
- [10] A. p. database, <https://www.apcprop.com/technical-information/performance-data/>.

Numerical Study of the Laminar Separation Bubble during Drag Crisis over the Teardrop Model

Thi Hong Hieu Le^{1,2*}, Dinh-An Nguyen^{1,2} and Ngoc Hien Nguyen³

¹*Department of Aerospace Engineering, Faculty of Transportation Engineering, Ho Chi Minh City University of Technology (HCMUT), 268 Ly Thuong Kiet Street, District 10, Ho Chi Minh City, Vietnam*

²*Vietnam National University Ho Chi Minh City, Linh Trung Ward, Thu Duc District, Ho Chi Minh City, Vietnam.*

³*RMIT University, Australia*

*Corresponding author. E-mail: honghieu.le@hcmut.edu.vn

Abstract

This paper presents the numerical approach to study the mechanism and properties of the laminar separation bubble, which occurs on a symmetrical model during drag crisis. The model implemented in this paper has a teardrop shape, generated by 2 different-diameter circles for head and tail, and symmetrical NACA airfoil for the body part. The critical Reynolds regime is numerically defined from 2.5×10^4 to 5.5×10^4 , compared to the experimental result from 4.3×10^4 to 6.3×10^4 . In this regime, drag crisis occurs and the model suffers from a sudden drop from ~ 0.41 to ~ 0.09 in drag coefficient with a slight increase in Reynolds. The computation also successfully captures the image of the structure of flow in laminar separation bubble region; therefore, the physical data of each particle is analyzed. This paper applies Semi-Implicit Method for Pressure-Linked Equation (SIMPLE) algorithm to solve the incompressible Navier-Stokes equations in both scalar and vector variables, with the accuracy of Second Order Upwind scheme. A combination of Reynolds averaged Navier-Stokes (RANS) with $k-\omega$ SST turbulence model is employed in OpenFOAM platform based on its good behavior in adverse pressure gradient and separation flow. Flow turbulence intensity effect on drag crisis phenomenon is computed and discussed comprehensively.

Keywords: Drag crisis phenomenon, laminar separation bubble (LSB), CFD, RANS, turbulence model $k-\omega$ SST

Nomenclature

c =chord of the teardrop model

C_p =pressure coefficient

C_D =drag force coefficient

1. Introduction

Drag crisis is described as an object experiences a sudden drop in drag coefficient in a particular Reynolds number regime. Experiments on this phenomenon on circular cylinder and sphere have been investigated. Teardrop geometry is regularly used to make the bicycle frame and considered for frame revolution, which can reduce up to 95% of drag in a specific range of speed. There were many experiments and numerical studies of this phenomenon on other objects such as sphere and cylinder. Therefore, a numerical simulation for teardrop model is presented to validate the results that were done by experiments in P. Dong *et al.* research [1]. The main

features of this paper are to make a comparison of drag coefficient line between numerical simulation and experimental results during drag crisis, to visualize the footprint of phenomenon and structure of streamline, and to observe the effects of turbulence intensity of flow on the phenomenon.

The numerical simulation focuses on solving incompressible Navier-Stokes equation in both scalar and vector variables using the Second-order upwind scheme and the Semi- Implicit Method for Pressure Linked Equations (SIMPLE) algorithm. Computations are conducted only two-dimensionally (2D) to capture the structure of flow and streamlines in the present work. Steady solver “*simpleFoam*” in OpenFOAM platform using the RANS simulation and $k-\omega$ SST turbulence model as its sub-dictionary is run to regard the footprint of bubble formation.

2. Literature review

Concepts of boundary layer and critical Reynolds regime are presented fundamentally. Boundary layer is the thin viscous region adjacent to the body, very thin compared to the extent of the rest of the flow, but this layer causes various effects and aerodynamic phenomena [2]. Drag crisis mainly occurs due to the boundary separation, in the free shear layers of this region. In terms of the second concept, drag crisis only occurs in a defined Reynolds regime of each specific airfoil shape.

2.1 Phenomenon mechanism

The drag crisis phenomenon is basically caused by the laminar-turbulent transition. The transition consists of the following processes, explained by J. T. Kegelmann and T. J. Mueller [3]: firstly, laminar and stable flow forms unstable 2D Tollmien-Schlichting waves; then, they develop to 3D waves and eddies, then vortex breakdown occurs and fluctuates fully, and finally some turbulent spots are forms, the flow becomes totally turbulent. The boundary layer transition processes are theoretically classified into 3 scenarios: *Natural transition*, *Bypass transition* described as the flow may skip the early stages of natural instability and move directly to vortex breakdown stage or turbulent spots formation, and *Separated-flow transition* in which “bubble shape” recirculation flow region called laminar separation bubble (LSB) is created.

2.2 Construction of laminar separation bubble (LSB)

Laminar separation bubble (LSB) sketched in Figure 1 is formed when the flow of boundary layer faced an adverse pressure gradient, which has great enough magnitude to separate the flow from wall. At S (Separation point), the flow is divided into two regions [4]. The first one is between mean dividing streamline ST'R and the wall; this region has re-circulatory streamlines, known as bubble. The second one is between ST'R and border of boundary layer S''T''R'', consists of free shear layers, which are unstable and undergo a transition from laminar to turbulence stage at T (Turbulence point). In this region, the separated shear layer curves back to the airfoil surface to form a shallow region of recirculation flow. Moreover, there is a near-vacuum region, known as “*dead air*” region, locates under the detached shear layer behind the separation point S, thereafter is a recirculation zone extends to R (Reattachment point) [5]. With the presence of bubbles on the surface, the pressure distribution coefficient remains nearly constant between points S and T, which means the pressure gradient of the boundary layer streamline equals zero from the separation to transition points. Then, it suffers a sudden drop from transition to reattachment points, which means there is a great pressure gradient of flow in this region.

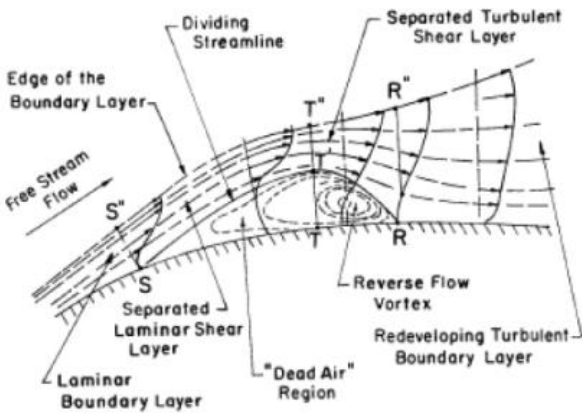


Figure 1. Section view of LSB [6]

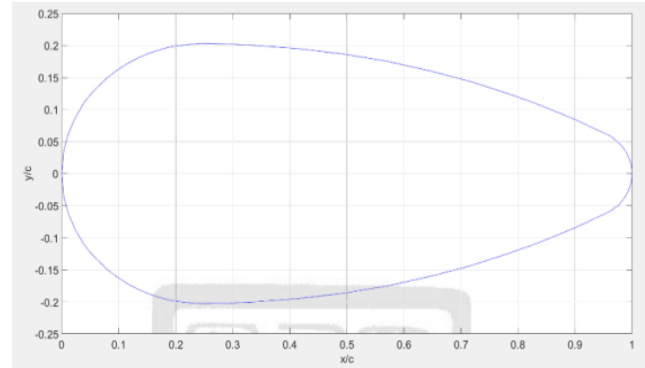


Figure 2. Teardrop model: symmetric shape, chord 0.1m, relative maximum thickness 40% at the quarter chord

3. Implementation of model in Openfoam

3.1 Problem identification

Teardrop airfoil is generated as a combination of symmetrical NACA airfoil for the body part, and circular cylinder for head and back parts, with its characteristics mentioned in the Figure 2. Computational domain with boundary condition is illustrated in Figure 1, Figure 3, and Figure 4. Numerical simulations are carried out for various Reynolds number in the range 10^4 to 10^6 . Inlet velocity U_{Re} is calculated based on the Reynolds formula, which is the ratio of inertial forces to viscous forces within a fluid

$$Re = \frac{\rho U_{Re} c}{\mu}$$

where $\rho = 1.204 \text{ kg} / \text{m}^3$ is fluid density; $\mu = 1.8 \times 10^{-5} \text{ kg} / \text{ms}$ is fluid dynamic viscosity; $c = 0.1 \text{ m}$ is chord of airfoil.

3.2 Computational region and grid

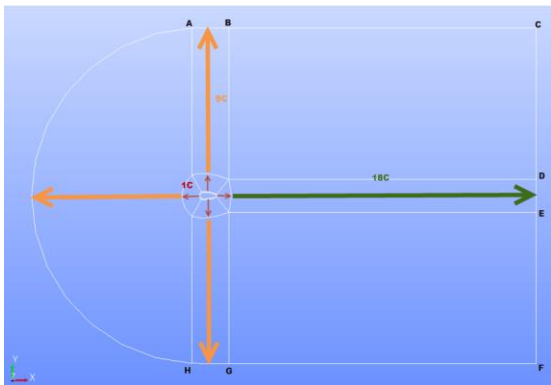


Figure 3. U-grid domain with sub-region added

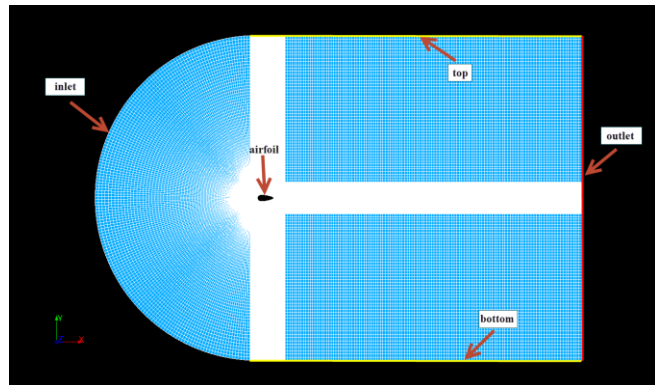


Figure 4. Boundary patches defined in polyMesh

This paper uses three main meshes to compare with experimental result in [1]. Table I gives miscellaneous important data of each mesh. Mesh *M1* is the name of mesh type without boundary layer region. Mesh *M2_fine* is the name of mesh type with the added boundary layer

region, and has the same number of cells grid with mesh M1. Mesh $M2_coarse$ has the same structure with mesh $M2_fine$ but with a lower number of cells. The purpose of making $M2_coarse$ is to compare with $M2_fine$ to evaluate the result and decide the most effective and efficient mesh based on different criteria.

Table I- Details of the finite element meshes used

	$M1$	$M2_fine$	$M2_coarse$
Nodes	742,210	742,210	297,020
Elements	370,150	370,150	147,800
Faces	745,035	745,820	299,320
Boundary layers (added)	0	100 layers	50 layers
Expansion ratio		1.15	1.15
First grid layer thickness	$570\mu m$	$47.5\mu m$	$95.2\mu m$
Maximum $y+$	4.562	1.009	1.952
Average $y+$	1.664	0.29	0.566

3.3 Turbulence models applied $k-\omega$ SST

The most advanced feature of this turbulence is it shows great sensitivity to the free stream value of ω whereas it behaves much better near the wall. Moreover, there are positive responses for its good behavior in adverse pressure gradients and separation flow, which is vital for visualizing the structure of flow in LSB region.

4. Numerical result verification

This part continues to study the physical properties of LSB and drag crisis phenomenon influenced by various factors. The results are compared with the experimental data given.

4.1 Drag coefficients comparison in different instances

This section gives a comparison of drag coefficient distribution using different types of grid to find the optimal solution. Additionally, the effect of turbulence intensity on drag crisis phenomena is discussed comprehensively to understand how this factor impacts the transition term of boundary layer and free shear layer.

4.1.1 Relationship between drag crisis and Reynolds regime.

The experiment taken by P. Dong [1] is designed to avoid 3D effects by extending the wingspan to approximate the wind tunnel diameter. Therefore, all the data collected is considered 2D data. The chart below provides drag coefficients comparison between his experimental result and numerical simulation results.

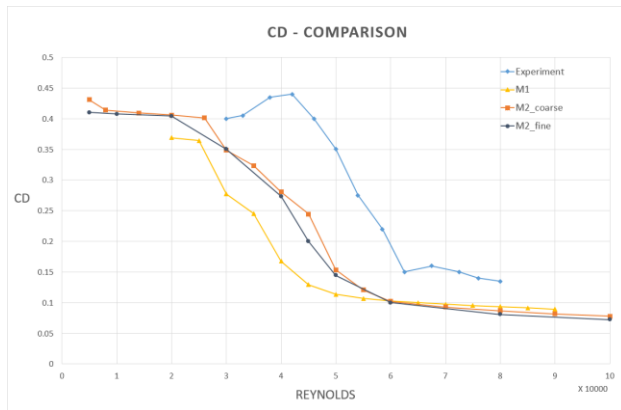


Figure 5. Comparison of drag coefficient among three meshes and experiment result

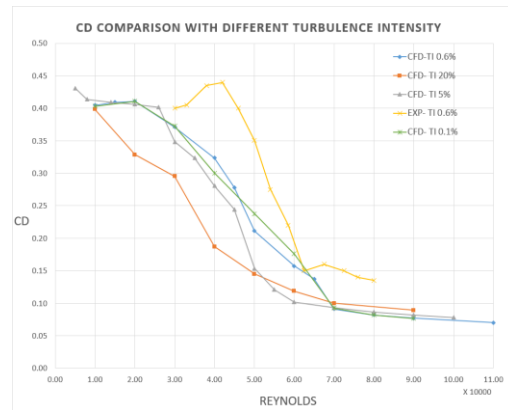


Figure 6. Distribution of drag coefficient with different turbulence intensity and comparison with experiment result

Compared to the measurements from the experiment, all three grid results predict the drag-crisis at a slight lower Reynolds number. There are several hypotheses to explain this difference. Compared to the measurements from the experiment, all three grid results predict the drag-crisis at a slight lower Reynolds number. There are several hypotheses to explain this difference. First, in a numerical research to investigate the drag crisis occur on a circular cylinder, G. Chopra assumed that the chosen computation model is the reason for this drag curve shift. In his research, the drag curve provided by LES with the Smagorinsky model is in the closest agreement with experimental data [7]. The actual critical Reynolds regime shifts to the regime located behind, at lower Re. Second, P. Dong's experiment [1] is well organized to set as a 2D experiment. However, it is still not a fully 2D experiment and thus, there are still any oscillation factors can affect the result. Third, the result is grid quality dependent. This is also hypothesized in S. Mittal *et al.* paper [8]. They make five different grids with different refinement levels and domain sizes. Due to the available computational resources, mesh refinement is the priority method to improve the result.

4.4.2 Effect of turbulence intensity on drag crisis.

Researches have proved that turbulence intensity can prevent the flow to form LSB because higher turbulent fluid has much energy. Hence, the flow can pass the adverse pressure gradient region and no separation occurs. The diagram in Figure 6 shows the comparison of drag coefficient curves with different turbulence intensity, from $I = 0.1\%$ to $I = 20\%$. The drag curve shifts to the left of the diagram, which means the drag crisis phenomenon occurs at lower Reynolds regime, when the flow increases turbulence intensity property.

Additionally, this tendency was investigated in K. Son *et al.* research about the effect of free-stream turbulence on the flow over a sphere in its critical Reynolds regime. They confirmed that the drag decrease with increasing turbulence intensity because free-stream turbulence promotes transition to turbulence both in the boundary layer and free shear layer [9].

This adjustment is explained by the ideas of laminar flow energy. At lower Reynolds number, the laminar flow energy is small. But the turbulence intensity of flow at far field provides energy to keep the flow attach on the surface until it reaches the separation point. Hence, when the Reynolds number in this regime increases, reattachment happens. Therefore, the shift of C_D curve to the left as increasing turbulence intensity is reasonable.

4.5 Structure of flow and particles inside LSB visualization and discussion

In this section, the structure of flow, streamline and spectrum of variables calculated by $k-\omega$ SST turbulence model will be analyzed at the Reynolds number 3×10^4 representing the flow with laminar separation bubble formation (LSB) in critical regime number as in Figure 7. The flow is transient, unsymmetrical distribution and has different images in different time directories. The spectrum of all variables will be visualized by preset rainbow and changed to log scale mode when is necessary to investigate small gradient regions. The LSB is only found in simulation with turbulence intensity equal to 0.6% and smaller, with $I = 5\%$ and above, Paraview is unable to be visualized. The data used in this section is collected from the cases that apply turbulence intensity $I = 0.6\%$, equals to the intensity value utilized in P. Dong experimental research [1]. The streamlines of flow structure are also analyzed to comprehensively understand the flow structure inside LSB.

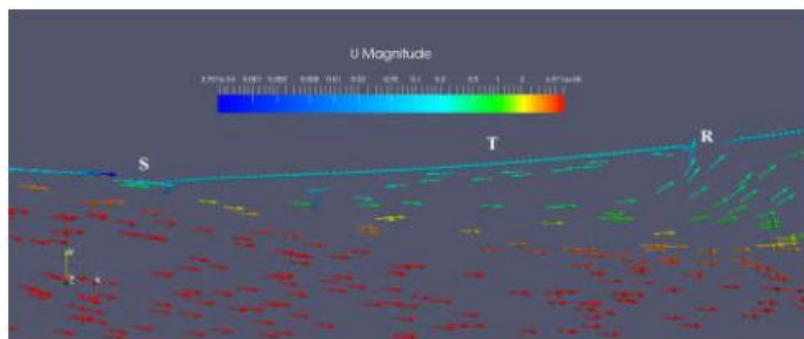


Figure 7. Streamline of short bubble at $Re= 3 \times 10^4$ with glyph mode being applied

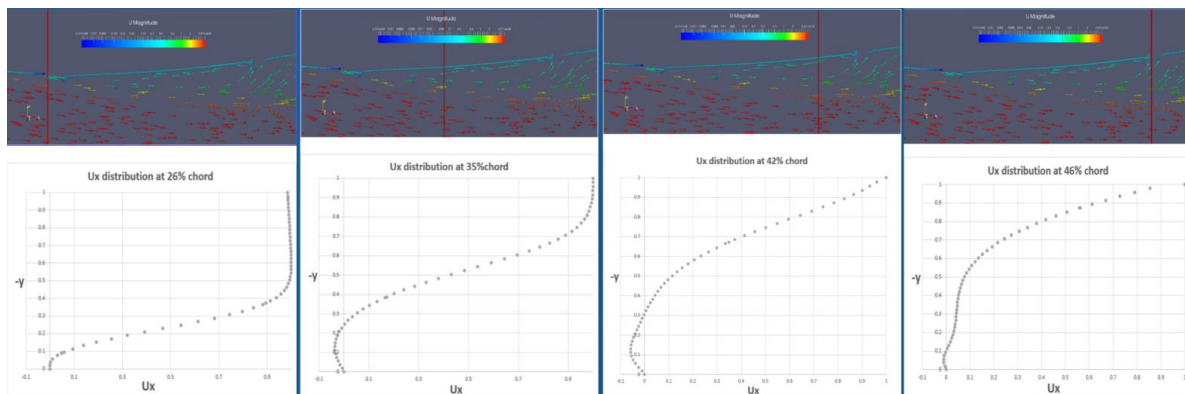


Figure 8. Pressure distribution on upper and lower surface at $Re= 3 \times 10^4$

As we can see, the streamline in the lower region in the Figure 7 is similar to the streamline of the bubble described in [10]. *Glyph* mode is applied to observe the fluid flow direction. The separation, turbulence and reattachment points are marked by S, T and R letters. To conclude that this region is LSB, the fluid particle velocity at the above 3 points is investigated. Using four planes perpendicular to the surface, the data of each particle are collected to make these diagrams below. Both y and U_x have been transferred to dimensionless factors; y is divided by the boundary region thickness and U_x is done by the free-stream velocity.

In Figure 8, the 26% chord location stands for the S separation point when 35% and 42% chord locations stand for T turbulence transformation region and 46% chord location is R reattachment point. The velocity distribution trend matches with the theoretical distribution diagram which has been presented in Figure 1.

The pressure coefficients C_p in Figure 9 between the two bars belongs to the region from 26% to 46% chord, the distribution is very similar to the theoretical one as sketched in Figure , C_p remains approximately constant between separation point S and transition point T, then suffers a sudden drop from point T to reattachment point R. Figure 10 illustrating the pressure field confirms the dissymmetric characteristics of the flow field by the presence of the separation bubble on the lower surface of the teardrop model.

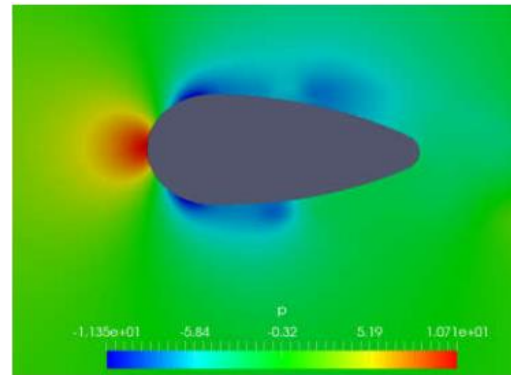
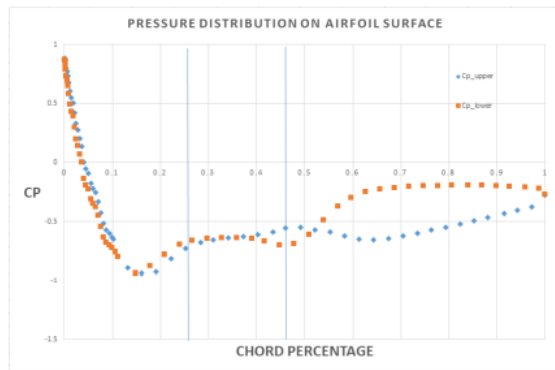


Figure 9. Pressure distribution on upper and lower surface at $Re= 3 \times 10^4$

Figure 10. Pressure field at $Re= 3 \times 10^4$

5. Conclusion

In conclusion, the steady solver *simpleFoam* using the combination of RANS simulation and $k-\omega$ SST turbulence model can successfully simulate the flow over teardrop model during drag crisis phenomenon. The critical Reynolds regime for a teardrop shape model within the drag crisis is defined from 2.5×10^4 to 5.5×10^4 using mesh M2 coarse. This range is different from the experimental measurement given in P. Dong thesis [1], which was reported in the Reynolds number range 4.3×10^4 to 6.3×10^4 . The reasons are hypothesized as the grid is quality dependence, the correction of RANS simulation and chosen turbulence model or the experiment is not completely two-dimensional. However, the numerical result is capable of predicting the drag crisis phenomenon tendency and utilizing to visualize the structure of flow, especially the particles inside LSB. Moreover, free-stream turbulence plays an important role in the formation of the laminaer separation bubble (LSB). Drag crisis phenomenon occurs at lower Reynolds regime when the flow increases turbulence intensity property. This inverse ratio exists because the free-stream turbulence promotes transition to turbulence both in the boundary layer and free shear layer.

Acknowledgments

This research is funded by Vietnam National University HoChiMinh City (VNU-HCM) under grant number C2020-20-14. The authors acknowledge the support of time and facilities from the Hyper Computing Lab and the Ho Chi Minh City University of Technology (HCMUT).

References

- [1] P. Dong, J. J. Miao and Z. Alaeddine, "An experiment study about drag crisis phenomenon on teardrop model," The 3rd SAWAE 2018 Workshop, Taiwan, 2018.

- [2] J. John D. Anderson, "Fundamentals of Aerodynamics," 5th ed., vol. 4, New York, McGraw - Hill, 2011, pp. 965-1046.
- [3] F. White, *Viscous Fluid Flow*, 3rd ed., McGraw- Hill, 2005.
- [4] M. M. O'Meara and T. J. Mueller, "Laminar Separation Bubble Characteristics on an Airfoil at Low Reynolds Numbers," *AIAA Journal*, vol. 25, no. 8, pp. 1033-1041, 1987.
- [5] N. D. Sandham, "Transitional separation bubbles and unsteady aspects of aerofoil stall," *The Aeronautical Journal*, vol. 112, no. 1133, 2008.
- [6] L. Amy, S. Jonathan and W. Redha, "PIV and Volumetric 3D Measurements of Separated Turbulent Boundary Layers on a NACA4412 Hydrofoil," in *50th AIAA Aerospace Sciences Meeting including the New Horizons Forum and Aerospace Exposition*, 2012.
- [7] G. Chopra and S. Mittal, "Numerical simulations of flow past a circular cylinder," in *Fifteenth Asian Congress of Fluid Mechanics*, 2017.
- [8] S. P. Singh and S. Mittal, "Flow past a cylinder: shear layer instability and drag crisis," *International Journal for Numerical methods in Fluids*, vol. 47, pp. 75-98, 2005.
- [9] K. Son, J. Choi, W. P. Jeon and H. Choi, "Effect of free-stream turbulence on the flow over a sphere," *Physics of Fluids*, vol. 22, 2010.
- [10] G. Chopra and S. Mittal, "The intermittent nature of the laminar separation bubble on a cylinder in uniform flow," *Computers and Fluids*, 2016.

SPONSORS

